fracture mechanics

Proceedings of the Twelfth National Symposium on Fracture Mechanics

ASTM STP 700

AMERICAN SOCIETY FOR TESTING AND MATERIALS

FRACTURE MECHANICS

Proceedings of the
Twelfth National Symposium
on Fracture Mechanics

A symposium sponsored by
ASTM Committee E-24 on
Fracture Testing of Metals
AMERICAN SOCIETY FOR
TESTING AND MATERIALS
Washington University
St. Louis, Mo., 21-23 May 1979

ASTM SPECIAL TECHNICAL PUBLICATION 700
P. C. Paris
Washington University
symposium chairman

04-700000-30

AMERICAN SOCIETY FOR TESTING AND MATERIALS
1916 Race Street, Philadelphia, Pa. 19103

Library of Congress Catalog Card Number: 79-55188

NOTE

The Society is not responsible, as a body,
for the statements and opinions
advanced in this publication.

Printed in Baltimore, Md.
July 1980

Foreword

This publication, *Fracture Mechanics,* contains papers presented at the Twelfth National Symposium on Fracture Mechanics which was held 21-23 May 1979 at Washington University, St. Louis, Missouri. The American Society for Testing and Materials' Committee E-24 on Fracture Testing of Metals sponsored the symposium. P. C. Paris, Washington University, presided as symposium chairman.

Related ASTM Publications

Part-Through Crack Fatigue Life Predictions, STP 687 (1979), $26.65, 04-687000-30

Fracture Mechanics Applied to Brittle Materials, STP 678 (1979), $25.00, 04-678000-30

Fracture Mechanics, STP 677 (1979), $60.00, 04-677000-30

Elastic-Plastic Fracture, STP 668 (1979), $58.75, 04-668000-30

Fractography in Failure Analysis, STP 645 (1978), $36.50, 04-645000-30

Flaw Growth and Fracture, STP 631 (1977), $49.75, 04-631000-30

A Note of Appreciation to Reviewers

This publication is made possible by the authors and, also, the unheralded efforts of the reviewers. This body of technical experts whose dedication, sacrifice of time and effort, and collective wisdom in reviewing the papers must be acknowledged. The quality level of ASTM publications is a direct function of their respected opinions. On behalf of ASTM we acknowledge with appreciation their contribution.

ASTM Committee on Publications

Editorial Staff

Contents

Introduction

This volume represents the Proceedings of the Thirteenth National Symposium on Fracture Mechanics, a very special symposium in a number of ways.

First, it was held at Washington University on 21-23 May 1979, under the Technical Chairmanship of Professor Paul C. Paris. Dr. Paris, along with Professor G. R. Irwin, was one of the founders of the National Symposium on Fracture Mechanics when it was initiated in 1965 at Lehigh University. Further, when ASTM Committee E-24 took over the sponsorship of the symposium in 1969, Dr. Paris became Chairman of E-24's Symposium Committee and remained an important element in the planning of many of the symposia up to and including 1979. The Thirteenth Symposium was a significant technical success, attested to by the breadth of national and international authors and subject matter which follow. We are indebted to Paul Paris for this fine meeting in the excellent facilities of Washington University.

Second, the Thirteenth Symposium was a notable one for the acknowledgment given to an E-24 contributor whose untimely death shocks the fracture industry. Special recognition was made to the valuable association of Dr. Kenneth Lynn of the Atomic Energy Commission with the fracture testing, materials evaluation, and energy industries. The occasion was marked by a presentation to Dr. Lynn's widow, and by the opening of the Kenneth Lynn Laboratory at Washington University.

Finally, the meeting was notable for its international impact, as papers were included from experts from Great Britain, Hungary, Japan, France, and West Germany. These, together with contributions from an impressive list of U.S. experts, assure the lasting value of this volume.

On behalf of the membership of ASTM Committee E-24 on Fracture Testing, the ASTM Symposium Committee chaired by Dr. Jerry Swedlow, and the fracture community in total, I want to express my appreciation to Dr. Paris for his role as Technical Chairman of the meeting. In addition, I would like to recognize the efforts of Tina Paris, Louise Cummings, Mario Gomez, and the ASTM Staff, notably Joseph J. Palmer, for their parts in other arrangements for the meeting.

J. G. Kaufman

Chairman, Committee E-24.

Jaap Schijve[1]

Prediction Methods for Fatigue Crack Growth in Aircraft Material

REFERENCE: Schijve, Jaap, **"Prediction Methods for Fatigue Crack Growth in Aircraft Material,"** *Fracture Mechanics: Twelfth Conference, ASTM STP 700,* American Society for Testing and Materials, 1980, pp. 3-34.

ABSTRACT: In the first part of the paper a survey is given of relevant knowledge on fatigue crack growth and qualitative and quantitative understanding of predictions. Aspects of cycle-by-cycle predictions and characteristic K prediction methods are discussed. In the second part recent work on prediction problems is reported. This includes (*a*) crack growth under flight-simulation loading with crack closure measurements, (*b*) predictions for flight-simulation loading based on a constant crack opening stress level, and (*c*) crack growth under pure random loading with different S_{rms}-values, two irregularities and two crest factors.

The random load tests were also carried out to explore the usefulness of K_{rms}. The paper is concluded with some indications for future research and a number of conclusions.

KEY WORDS: crack propagation, fatigue (materials), predictions, flight-simulation loading, random loading, crack closure, fractures (materials)

Nomenclature

a	(Semi) crack length
Δa	Increment of a in one cycle
C	Geometry factor, or crest factor
da/dn	Crack growth rate
K	Stress intensity factor
k	Irregularity factor
P	Load
R	$S_{\min}/S_{\max}$
S_{mf}	Mean stress in flight
S_{op}	Crack opening stress

[1]Professor, Production and Materials Group, Department of Aerospace Engineering, Delft University of Technology, Kluyverweg 1, Delft, The Netherlands.

t Thickness
W Specimen width
γ S_m/S_{rms}

Fatigue cracks in aircraft structures and materials are still an urgent problem for reasons of both safety and economy. Unfortunately, prediction of crack growth is a complicated problem because many aspects are involved. One significant feature is the complex nature of load-time histories occurring in service. Progress of improving prediction techniques is made slowly. However, modern experimental techniques and computer facilities suggest that further improvements are possible. In the first part of this paper a survey is given of the present state of knowledge on fatigue crack growth including qualitative and quantitative understanding of predictions. Reference is made in this part to developments in experimental techniques and indications obtained from fatigue of aircraft structures.

The second part is dealing with some recent work on prediction fatigue crack growth in aluminum alloys, carried out in the Department of Aerospace Engineering, Delft University of Technology, Delft, The Netherlands. This includes: (*a*) crack growth under flight-simulation loading with crack closure measurements, (*b*) crack growth predictions for flight-simulation loading based on a constant crack opening stress level, and (*c*) crack growth under random loading to explore the usefulness of K_{rms} and to observe effects of irregularity and crest factor.

The paper concludes with a brief discussion on the relevance of research programs for solving the problem of crack growth prediction techniques and a summary of some conclusions.

Aspects of the Problem of Fatigue Crack Growth

Any newcomer in the field of fatigue must be overwhelmed by the vast amount of literature. J. Y. Mann compiled about 6000 references over the period 1951 to 1960 [*1*][2], and probably more appeared in years afterwards. The subject index of Mann's book illustrates the abundant variety of aspects associated with fatigue problems.

Numerous papers on theoretical or experimental studies refer to practical problems, but usually this is done in a superficial and indirect way. The impression emerges (right or wrong) that fatigue and fracture mechanics have become disciplines in themselves with a practical significance, which should be self-evident. It is a relevant question then to see which problems we try to solve and which problems we should try to solve. This point will be elaborated in this paper to some extent with respect to fatigue crack growth.

[2]The italic numbers in brackets refer to the list of references appended to this paper.

For this purpose some aspects of the state of knowledge have to be recapitulated. The areas that will be discussed herein are as follows:

1. Laboratory observations on fatigue crack growth.
2. Theoretical prediction methods.
3. Developments in experimental procedures.
4. Service experience.
5. Practical relevance of research programs.

The first four items are discussed hereafter, while the last one is briefly touched upon in the discussion at the end of this paper.

Laboratory Observations on Fatigue Crack Growth

It is convenient to divide fatigue life into two periods: (1) crack initiation period, and (2) crack growth period. The life is completed by final failure in the last cycle. Microscopical studies have shown that crack initiation occurs early in the fatigue life if not immediately. However, microcrack growth usually is a slow process for a long time and this may be considered as part of the initiation period. The crack growth period then starts when a macrocrack is present. Although it is difficult to define the transition from the initiation period to the crack growth period, some comments may clarify the idea. In the first period microcrack growth is still a local process with hardly any effect on macroscopic stress and strain distributions. However, in the second period, fatigue is no longer a localized surface phenomenon, and stress and strain distributions are significantly affected by the crack. Bulk properties of the material become important. One significant conclusion is: predictions of crack initiation life on one hand and predictions of crack growth on the other hand require different prediction techniques. For predictions on the initiation period K_t-factors and a Neuber-type analysis can be relevant. However, for crack growth predictions other means should be adopted.

A number of relevant aspects of macrocrack growth include the following: early initiation, striations, Δa during load increase only, stress ratio (R) effects, load sequence effects (interaction effects), crack closure, and environmental effects.

Striations are a well-known feature by now, frequently used to indicate the nature of service fatigue failures. Striation patterns have shown that some crack front advancement (Δa) occurs in every load cycle. This has prompted prediction techniques to calculate Δa for each cycle (see later). Originally it was proposed by Paris et al [2] that the crack rate was a function of the range of the stress intensity factor (ΔK), which was approximated by a simple power relation

$$\Delta a = \frac{da}{dn} = C\,\Delta K^m \tag{1}$$

It was observed later that the effect of the stress ratio $R = S_{min}/S_{max}$ could not be ignored. The so-called Forman equation is a well-known relation including this effect

$$\frac{da}{dn} = \frac{C\Delta K^m}{(1 - R)K_c - \Delta K} \tag{2}$$

More empirical relations can be found in the literature, but a derivation on physical arguments appears to be very problematic.

Some decades ago it was observed that peak loads produced large delays of crack growth. An illustration from Ref *3* is given in Fig. 1. Such delays have led to the definition of so-called interaction effects. It implies that Δa in a load cycle will depend on what occurred in the preceding cycles. Similarly, a load cycle will affect Δa in subsequent cycles. Actually interaction effects have to be expected, because Δa will depend on such factors as crack tip blunting, shear lip developments, crack closure, cyclic strain hardening and residual stresses around the crack tip, all factors produced by the preceding load history [*4*]. Apparently the phenomenon can be rather complex.

Sequence effects are the result of interactions. In Fig. 1 the same peak load cycle is applied in two different sequences (Case A: positive → negative, Case B: negative → positive), and the growth delays are highly different. It may be argued that the example in Fig. 1 is not a good one, because the maximum load range A_1A_2 (downwards) occurs in Case A but not in Case B. Similarly, B_1B_2 (upwards) occurs in Case B but not in Case A. This distinction should be made because it is expected that crack extension (Δa) will occur during increasing load only. This was recently confirmed by work of Bowles [*5*], who

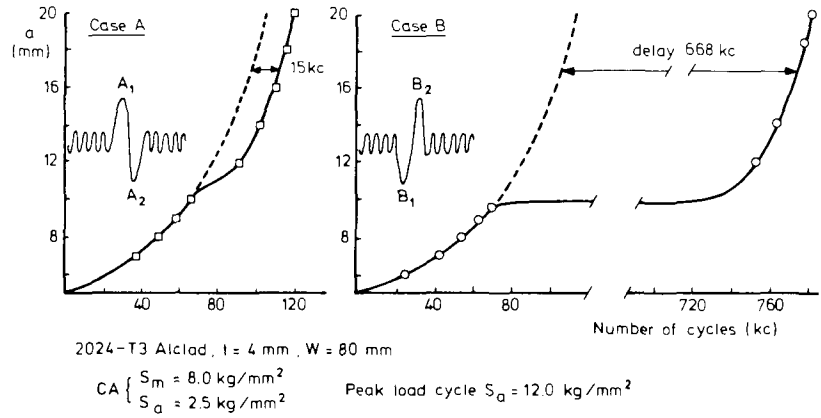

FIG. 1—*Different delays depending on sequence in peak load cycle* [3] (*Note: 2024-T3 Alclad,* t = *4 mm,* W = *80 mm; CA* S_m = *78.5 N/mm²,* S_a = *25.4 N/mm²; Peak load cycle* S_a = *118 N/mm²*).

developed a new technique for fatigue crack tip observations. The distinction should also be expected from considerations on reversed plasticity and crack closure (see in later section).

Crack closure has now become a well-known phenomenon, but it remains a remarkable fact that it was overlooked for so many years until Elber in 1968 discovered this phenomenon [*6*]. Until that time crack growth delays were explained by residual compressive stresses in the crack tip area ahead of the crack. Fatigue crack growth should be considered as the result of cyclic slip at the crack tip, and the conversion of this microplasticity into crack extension [*7*], which can be activated by the environment [*8*]. It should not be expected that residual stress will affect slip, but it may well promote the conversion of slip into crack extension. It is important to realize that this requires the crack tip to be open. A stress singularity at the crack tip is present only if crack closure has been removed. It is difficult then to see how residual stresses ahead of the tip could be important. The more essential part of the question is whether the crack is open or not, and this depends on the plastic deformations left in the wake of the crack.

Finally reference should be made to environmental effects on fatigue crack growth. Obviously the effect will depend on the material-environment combination. Our knowledge of crack growth under corrosive conditions is increasing, but the subject is too extensive to be summarized here. One observation should be mentioned. For crack growth in aluminum alloys the aggressive component of normal air is water vapor. Small amounts are sufficient to produce a saturated damaging effect under load frequencies occurring in practice. From this argument and from the observation that crack extension occurs under increasing load only, it was deduced that an accelerated test to simulate service loading can be allowed [*9*]. This was confirmed by flight-simulation tests at 10, 1, and 0.1 Hz, which gave the same crack growth rates. Such a "time compression" is probably not allowed for mild steel in salt water environments.

Theoretical Prediction Techniques

The major aspects to be recognized here are as follows:

1. Type of loading—constant-amplitude (CA) loading and variable-amplitude (VA) loading.
2. Geometry of crack front—straight crack front (plane problem) and curved crack front (three-dimensional problem).
3. Type of prediction method—cycle-by-cycle method and characteristic K method.

The most simple problem is the prediction of a simple through crack in a structure of sheet material under CA loading. For the material concerned,

crack growth data should be available as graphs or analytical relations, representing

$$\frac{da}{dn} = f(\Delta K, R) \tag{3}$$

Many data have been published, but it is also easy to determine the relationship in a fairly small number of tests on simple specimens. Secondly, K-values for the case of application are required. Sometimes K-values can be directly obtained from handbooks [*10–12*]. In other cases calculations have to be made, either by clever superpositions of known solutions, or by finite element methods. Several successful applications have been reported in the literature.

A relatively simple three-dimensional problem is a semi-elliptical surface crack in the center of a plate specimen. The value of K varies along the crack front. Reasonably accurate K-values seem to be available for semi-elliptical cracks [*13*]. Unfortunately, if the crack grows according to Eq 3, the shape will not remain semi-elliptical. As a result, the problem of a semi-elliptical crack, which is so easily specified, requires already a fairly elaborate amount of calculations to predict how the curved crack front will move onwards.

VA loading offers significant prediction problems in view of the interaction effects defined before. Several methods have been proposed (reviewed in Ref *4*) and two main lines will be recapitulated here.

Cycle-By-Cycle Calculations—These calculations start from simple crack length additions

$$a = a_o + \Sigma \Delta a_i \tag{4}$$

where a_o is the initial crack length and Δa_i is the crack length increment in cycle (i), and these increments have to be predicted. The Willenborg model [*14*] and the Wheeler model [*15*] are accounting for interaction effects by

$$\Delta a_i = \beta_i \left(\frac{da}{dn}\right)_{CA} \tag{5}$$

with

$$\left(\frac{da}{dn}\right)_{CA} = f(\Delta K_i, R_i) \tag{6}$$

similar to Eq 3, while β_i accounts for the interactions. In both methods β_i is assumed to depend on plastic zone sizes associated with load cycle (i) and the preceding cycles. Simple assumptions are made for this purpose. As a result crack growth delays after a peak load are obtained, but negative interactions

(crack growth accelerations) can not be predicted, although they do occur [3].

From a physical point of view, crack closure appears to offer better arguments for interaction effects [16]. Then Eqs 5 and 6 have to be replaced by

$$\Delta a_i = \left(\frac{da}{dn}\right)_{CA} = f(\Delta K_{\text{eff},i}) \tag{7}$$

which is the relationship between crack rate and ΔK_{eff} as proposed by Elber [6]. The problem still remains to calculate the crack-opening stress level (S_{op}) in cycle (i) from which $\Delta K_{\text{eff},i}$ has to be deduced

$$\Delta K_{\text{eff}} = C \cdot (S_{\max} - S_{\text{op}}) \cdot \sqrt{\pi a} = C \Delta S_{\text{eff}} \sqrt{\pi a} \tag{8}$$

Different delays in Fig. 1 for Case A and Case B can be understood if crack closure is considered. In Case B the load range $B_1 B_2$ will cause a large plastic zone. If the crack tip is penetrating into this zone, it will meet with a high crack opening stress level and significant growth retardation will occur. In Case A an equally large plastic zone will occur at peak load A_1 and the crack tip will be plastically opened. The load range $A_1 A_2$ will then cause a considerable reversion of plasticity ahead of the crack tip. As a result lower crack opening stress levels will follow later on and the delay is much smaller. Both analytical studies on cyclic plasticity at the crack tip [17–19] and some experimental evidence [20,21] confirm the argumentation. Some work is now going on to introduce crack closure into cycle-by-cycle calculations for complex load time histories [21–23]. It is easily understood that elasto-plastic calculations for each load cycle is a rather elaborate procedure. It then seems reasonable to look also for acceptable simplifications.

Elber [24] measured S_{op} during random load tests with a short return period, and he found it to be approximately constant during a test. He then defined effective stress ranges of the random loading by

$$\Delta S_{\text{eff}} = S_{\max} - S_{\text{op}} \text{ if } S_{\min} < S_{\text{op}} \tag{9}$$

and

$$\Delta S_{\text{eff}} = S_{\max} - S_{\min} \text{ if } S_{\min} > S_{\text{op}} \tag{9a}$$

It means that those parts of stress ranges which are above S_{op} are supposed to be effective. Subsequent derivations of equations in Ref 24 are not rather explicit, but it is equivalent to substituting ΔS_{eff} according to Eqs 9 and 9*a* into Eq 8 and ΔK_{eff}-values thus obtained into Eq 7. No further interactions are supposed to occur. In a later section of this paper, the idea will be carried on somewhat further in view of application to flight-simulation test results. It

should be pointed out here that an approximately constant S_{op} can be applicable only if the VA-loading may be considered to be stationary as discussed in Ref *25* (fourth lecture). It implies that load sequence properties should be constant, while crack growth on a macro-scale should not show apparent discontinuities (that is, delays observable from the crack growth curve).

Characteristic K Methods—These methods were adopted in the literature for random loading and flight-simulation loading. It requires that the VA-loading is stationary and fully characterized by a single stress level, S_{char}. A characteristic K-value is easily defined

$$K_{char} = CS_{char}\sqrt{\pi a} \tag{10}$$

The crack rate should then be a function of K_{char} only. Paris [*26*] adopted this idea for random loading, for which Eq 10 becomes

$$K_{rms} = CS_{rms}\sqrt{\pi a} \tag{11}$$

Crack growth results can then be represented by

$$\frac{da}{dn} = f(K_{rms}) \tag{12}$$

and this has found some confirmation in the literature [*27-29*]. It should be clear that Eq 12 represents empirical results, which can be used for prediction purposes if the same type of random loading applies, including the same S_{rms}/S_m ratio. Writing Eq 12 in a more general form

$$\frac{da}{dn} = f(K_{char}) \tag{13}$$

an inherent advantage and disadvantage of the characteristic K method will be recognized as follows:

1. Any change of a nominal or local stress level in a structure does usually not affect the character of the VA-loading in service. Effects of such changes on crack growth rates can thus be derived from an empirical relation like Eq 13 obtained from simple laboratory specimens.

2. The disadvantage is that the empirical relation in Eq 13 has to be established for each relevant VA-loading and unfortunately many types of VA-loadings occur in various structures. For instance, random loadings are not of the same type if the spectral density functions are different, or if the crest factor or the S_{rms}/S_m ratio are different (discussed further in section on crack growth under random loading).

The applicability of Eq 13 to flight-simulation loading was checked fairly

extensively at the National Aerospace Laboratory in Amsterdam. The mean stress in flight, S_{mf} was adopted as the characteristic stress level to define K_{mf} analogous to Eq 11. It was hoped to find a unique correlation between da/dn (growth rate per flight) and K_{mf}, but the first results were not very positive [*30*]. It was argued that similar crack rates to be obtained require similar K-values, and in addition similar dK/da-values to account for the preceding history. Usually the requirements of both similar K and similar dK/da are incompatible. Later on more data of flight simulation tests were compiled by Wanhill [*31*]. He concluded that K_{mf} could be used for crack growth prediction as a first approximation, provided the flight-simulation loading is stationary. He emphasized that K_{mf} cannot account for load spectrum variations, such as different truncation levels, different numbers of low-amplitude cycles, etc.

Experimental Developments

Some developments have had a most significant impact on fatigue research programs. The combination of closed-loop fatigue machines with computer controlled programs should be especially mentioned here. A closed-loop electrohydraulic loading system can apply any load time history that can be generated as an electrical command signal. Computer controlled signal generation has led to most versatile possibilities for programming of load-time histories. It includes aspects as load sequences, wave shapes, and frequency. Moreover, any random sequence of loads can exactly be reproduced in subsequent tests. Flight-simulation tests and random load tests can now be adopted for a variety of testing purposes. It has already initiated a standardizing of two different types of flight-simulation loading (TWIST [*32*] and FALSTAFF [*33*]) and probably more will follow. It is also easily understood that the characteristic K-method requires basic material test data under relevant loading histories. Without computer controlled fatigue machines this would be practically impossible.

Another development to be mentioned here is the automatic measurement of crack length by the electrical potential drop method. Each type of specimen has to be calibrated for this purpose. Computer control is possible again. It is now possible to obtain crack growth data for any type of load sequence by employing routine procedures.

Service Experience

One might hope that service experience on fatigue problems is well documented in the literature, but this is only partly true. Table 1 helps clarify the situation. Most information in the literature is on the origin of cracks. If cracks are found in service it is a highly practical question to know whether it

TABLE 1—*Crack growth in real structures.*

Origin of Cracks	Source of Information
Incidental cases (corrosion pits, damage, etc.)	aircraft in service
Systematic occurrence (bolt and rivet holes, fillet, etc.)	full-scale test component tests

is an isolated case or a symptomatic one. Solutions to cure the problem will depend on the answer to this question. Remedial actions are taken as soon as a crack is noted because it should not be there. As a result crack growth data from service experience are highly exceptional, and moreover the load history will not be accurately known. The best data are coming from full-scale tests and component testing, usually carried out to prove the fail-safety of a new structure. Such data are scattered through the literature and usually the description is not sufficiently complete to be used by other investigators for checking prediction methods. Moreover, real structures do not have the geometrical simplicity of laboratory specimens. Nevertheless, a coordinated program to compile available data of crack growth in structures, with relevant information on the structure and its fatigue loading, would be most instructive to set the scene of the prediction problem.

Results of Some Recent Crack Growth Studies

Crack Growth Under Flight-Simulation Loading

Tests were carried out on sheet specimens (thickness = 2 mm, width = 100 mm) of 2024-T3 Alclad and 7075-T6 Clad material. A standardized flight-simulation loading (TWIST [*32*]) was used. Different truncation levels were adopted and the well-known effect of faster crack growth for lower truncation levels was found (Fig. 2). During these tests numerous crack closure measurements were made with a crack opening displacement (COD) meter. It was hoped that the tests would indicate higher crack closure levels if the truncation level was higher. This would offer an explanation for the truncation effect and perhaps a basis for improved prediction techniques based on crack closure. Unfortunately, the crack closure measurements showed a rather chaotic picture which did not allow a simple evaluation [*34*]. However, two lessons could be learned from the results:

1. The most severe flights with the highest maximum loads significantly changed the crack closure level.
2. The COD meter was located in the center of the specimen during all measurements, since locating the meter near the crack tip for all measurements is very elaborate. Unfortunately, a determination of S_{op} becomes less accurate.

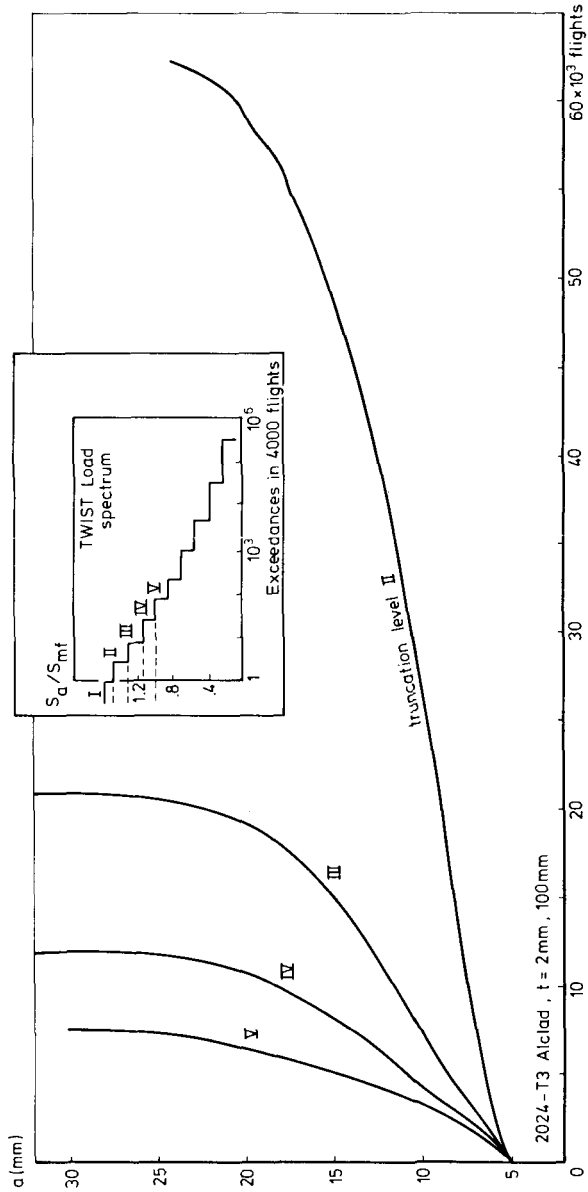

FIG. 2—*Effect of truncation level on crack growth curves.*

Examples of crack closure measurements are shown in Fig. 3. During a severe flight (No. 2936), a significantly enlarged plastic zone is formed ($r_p \sim [K_{max}/S_{0.2}]^2/\pi = 1.45$ mm), and plastic crack tip blunting will occur. As a result S_{op} is relatively low immediately after this flight (A_1 in Fig. 3), and the nonlinear behavior below A_1 shows that the crack is not fully closed under the compressive load applied. After the severe flight, the crack tip has to grow into the newly formed plastic zone, and this implies that S_{op} now is very high (see Point C_2 after flight No. 3180). The crack has grown then from 12.1 to 12.5 mm ($\Delta a = 0.4$ mm). The *P*-COD record contains two linear parts (A_2B_2 and C_2D_2) from which the first one (A_2B_2) is parallel to A_1B_1. Equal compliances indicate equal crack lengths, which means that the crack was open until $a = 12.1$ mm during the load increase A_2B_2. However, the very last part of the crack (from $a = 12.1$ mm to $a = 12.5$ mm) was still closed during A_2B_2, while it was opened during the load increase B_2C_2. During further crack growth S_{op} is decreasing (Points $C_3 \rightarrow C_4 \rightarrow C_5 \rightarrow C_6$), but then another severe flight occurs (No. 3841). The same process is repeated and after flight No. 4105 even three linear parts can be observed: (1) A_7B_7 parallel to A_1B_1 corresponding to $a = 12.1$ mm, (2) C_7D_7 parallel to C_6D_6 corresponding to $a = 17.5$ mm, and (3) E_7F_7 corresponding to $a = 20.1$ mm. The successive openings are schematically shown in Fig. 4.

In Fig. 3, A_2B_2 and C_2D_2 correspond to $a = 12.1$ mm and $a = 12.5$ mm respectively; that is, the slope difference is no more than 3 percent. Although this can be observed, it will be clear that the transition points B_2 and C_2 cannot be accurately indicated. In spite of this, it is evident that the line $C_6C_5C_4C_3C_2$ (and also the line E_8E_7) are going upwards. It means that S_{op} during the first part of crack growth after a severe flight will be extremely high. This was confirmed in more accurate measurements during CA tests after a peak load [*4*]. In later flights in Fig. 3, S_{op} comes down, but it is possible that the linear parts C_3D_3, C_4D_4, and C_5D_5 (corresponding to apparently open cracks) consist of two linear parts with almost equal slope as a result of somewhat less severe flights in between. It should be realized that the very end of a crack (tenths of millimeters and even smaller) can be closed, while this cannot be observed empirically. At the same time one must face the problem that the physical meaning of

$$\Delta K_{eff} = K_{max} - K_{op} \tag{14}$$

as it was originally suggested by Elber [*6*] might break down if a very minute part of the crack tip is closed only.

The *P*-COD records with more than one linear part are obtained as a result of local contacts behind the crack tip (Fig. 4). This phenomenon was observed before [*20*], and apparently it also follows from analytical studies [*17,19*]. It may be expected that it can be included in a cycle-by-cycle calculation in the future. At the same time it has to be recognized that the above

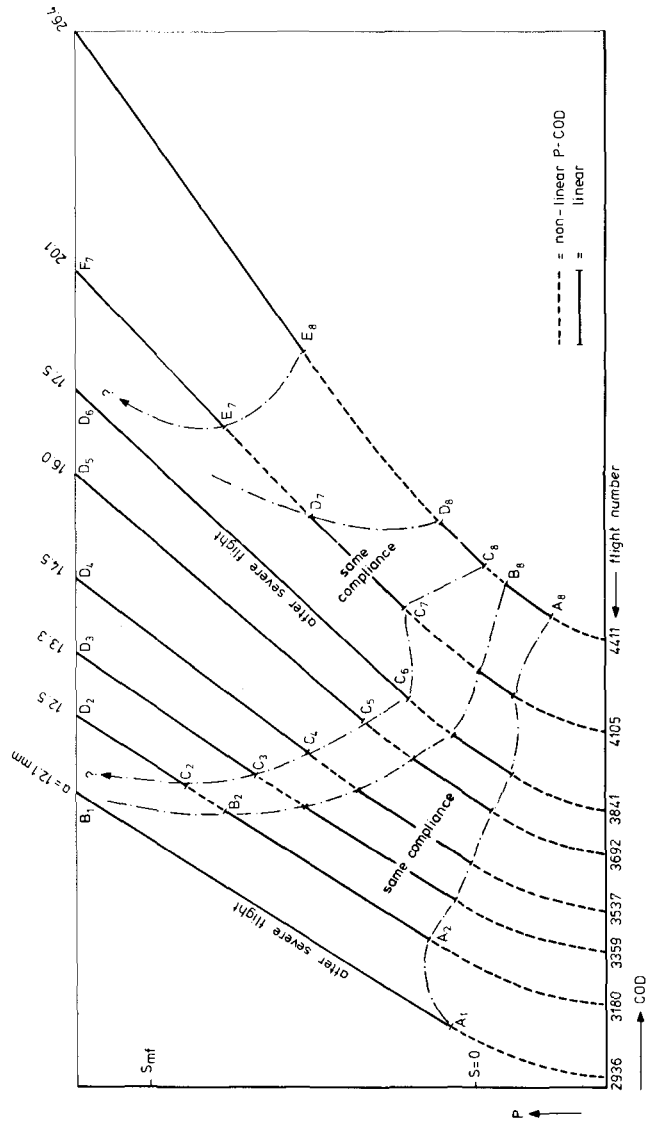

FIG. 3—*Crack closure measurements during a flight-simulation test on a 7075-T6 sheet specimen.*

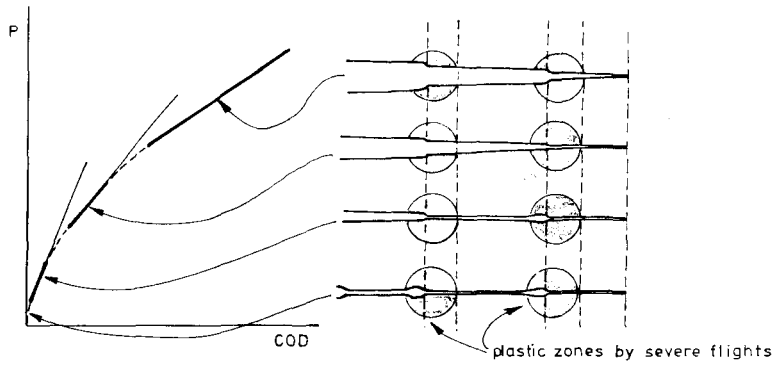

FIG. 4—*Schematic picture of crack opening in different stages during a flight simulation test.*

evidence of flight-simulation tests indicates that crack closure will be then rather complex.

Secondly, a formal application of ΔK_{eff} may not be fully justified any longer from a physical point of view. There is a limit to the level of sophistication that is still feasible. Under such conditions simplified approaches, giving sufficient credit to physical observations, should be explored. The introduction of an average crack closure level for a stationary VA loading should be considered as such an approach.

Crack Growth Predictions for Flight-Simulation Tests

In a previous investigation [*35*], crack growth was studied under flight-simulation loading with the following main variables: (*a*) different truncation levels, (*b*) omission of low-amplitude cycles, and (*c*) omission of ground-to-air cycles. Some other aspects studied were omission of taxiing loads in the ground-to-air cycle (GTAC), application of gust cycles in a programmed low-high-low sequence instead of a random sequence, and application of all gust cycles in reversed order. Especially the first three issues, implying fairly drastic load spectrum variations, seem to be critical for proving the validity of a prediction model. This is one reason to adopt the result of Ref *35* for a first exploration. The second reason is that CA test results were also obtained for the materials testsed in Ref *35*.

The model to be discussed here starts from Elber's observation, which was an approximately constant crack opening stress level during pure-random-load tests [*24*]. Three basic assumptions for the model are:

1. During a stationary VA loading, the crack opening stress level (S_{op}) may be regarded to be constant.
2. The value of the constant S_{op} under stationary VA-loading is a function

of the maximum stress $(S_{max})_{VA}$ and the minimum stress $(S_{min})_{VA}$ occurring in the VA loading. Moreover, this function is the same one applicable to CA loading.

3. Stress ranges are effective as far as they are above S_{op} (Fig. 5).

The third assumption was adopted by Elber [*16*], see Eqs 9 and 9*a* but instead of the second one he used S_{op}-values measured in the random load tests for which predictions were made. However, it is thought that the second assumption on S_{op} involves some obvious elements. The maximum load in a stationary VA test will determine the maximum plastic zone. This zone should have a large effect on the plastic deformation left in the wake of the crack, which causes crack closure. Some substantiation comes from simple measurements (light reflection) on plastic deformation around cracks grown under flight-simulation loading (Ref *25*, second lecture). For a flight-simulation test it implies that S_{op} will depend on the truncation level of the load spectrum. It should also be expected that the minimum stress level will be significant in view of reversed plasticity, occurring in the crack tip plastic zone. Confirmation is offered by analytical work [*17–19*]. Consequently, the stress ratio for stationary VA loading defined as

$$R_{VA} = \frac{(S_{min})_{VA}}{(S_{max})_{VA}} \tag{15}$$

should be a significant parameter to estimate $(S_{op})_{VA}$, which has been as-

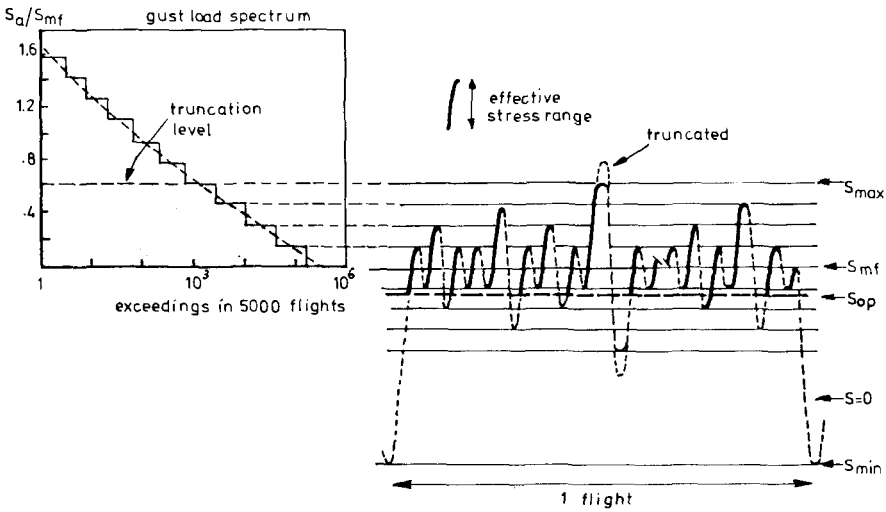

FIG. 5—*Example of flight profile (low truncation level) with* S_{op} *level and effective stress ranges.*

sumed to be constant. The validity of the model has been checked as yet for 2024-T3 sheet material only. For this material Elber found [*16*]

$$\frac{\Delta K_{\text{eff}}}{\Delta K} = \frac{S_{\max} - S_{\text{op}}}{S_{\max} - S_{\min}} = 0.5 + 0.4R \tag{16}$$

which can be also written as

$$S_{\text{op}} = S_{\max}(0.5 + 0.1R + 0.4R^2) \tag{17}$$

The applicability of this equation on our own CA data was checked first. These data include S_a-values corresponding to R-values 0.73, 0.52, 0.23, 0.03 and -0.11. An R effect was clearly observed, but plotting da/dn as a function of ΔK_{eff}, brought all data points on a single curve with a very narrow scatter band [*36*]. This curve has been used for the predictions on the flight simulation tests.

According to assumption (2), Eq 17 now implies

$$(S_{\text{op}})_{\text{VA}} = (S_{\max})_{\text{VA}}\,[0.5 + 0.1(R)_{\text{VA}} + 0.4(R)_{\text{VA}}{}^2] \tag{18}$$

where $(R)_{\text{VA}}$ follows from Eq 15. It is noteworthy that the applicability of Eq 18 can be checked for Elber's own random load test results, because he reports $(S_{\max})_{\text{VA}}$ and $(S_{\min})_{\text{VA}}$. For six different random load histories in Ref *24*, the results are shown next. Although there are differences, the comparison is promising.

$(S_{\text{op}})_{\text{VA}}$ in MPa	Measured	104	53	87	102	56	89
	Eq 18	102.8	51.4	86.6	102.8	51.4	86.6
Difference, (%)		−1.2	−3.0	−0.5	0.8	−8.2	−2.7

Predictions on crack growth rates for the flight-simulation tests in Ref *35* will now be made. Previously, the VA loading was required to be stationary in order to justify a constant S_{op}. Another advantage of the stationarity should be exploited. The crack extension in cycle (i) according to the crack closure concept adopted will be equal to

$$\left(\frac{da}{dn}\right)_i = f(\Delta S_{\text{eff},i}) \tag{19}$$

If there are n_i stress ranges $\Delta S_{\text{eff},i}$ in a certain period, the average crack growth rate in that period follows from

$$\left(\frac{da}{dn}\right)_{VA} = \frac{\Sigma n_i \left(\frac{da}{dn}\right)_i}{\Sigma n_i} \tag{20}$$

In this equation $(da/dn)_{VA}$ and $(da/dn)_i$ should apply to the same a-value and da/dn data have to be derived from CA tests plotted as a function of ΔK_{eff}.

Predictions of da/dn for the test series with various types of flight-simulation loading can now be made. Steps to be followed are:

1. For each test series calculate S_{op} from S_{max} and S_{min} (Eqs 15 and 18).
2. For each possible effective stress range (Fig. 5), determine how many times (n_i) it will occur.
3. For each effective stress range, determine the related crack rate from the CA data in the form $da/dn = f(\Delta K_{eff})$.
4. Combine information from Steps 2 and 3 by substitution in Eq 20 to give $(da/dn)_{VA}$.

The last Steps 3 and 4 have to be repeated for a sufficient number of a-values to see how the predicted crack rate depends on crack length. It still should be pointed out that Step 2 can be done in two different ways. One way is a simple counting analysis with S_{op} as a kind of lower boundary condition. Another method followed here is to calculate the statistical expectation from the statistical data on flight types and gust cycles [*37*].

Although this work is still being continued, illustrative results can be presented. Predicted crack growth rates are presented in Figs. 6 through 8 together with test results. Predicted crack growth lives are obtained by integrating the inverse of the growth rate over a crack growth interval from $a =$ 14 mm to $a = 50$ mm. Results are compared with test data in Figs. 9*a–d*. In these figures predictions based on noninteraction (ignoring crack closure) are shown also.

Effect of Truncation—Figure 6 shows that there is moderate agreement between predicted and actual crack rates. Figure 9*a* confirms the trend of increasing crack growth life for higher truncation levels. Apparently, the trend is also indicated by the S_{op} model. If crack closure is ignored (noninteraction), the latter figure shows that there is no predicted effect of the truncation level at all. This is not surprising because the rarely occurring high loads hardly contribute to a noninteractive damage summation.

Omission of Low-Amplitude Cycles—Omitting low-amplitude cycles of the flight-simulation tests implied a lower number of cycles per flight. An extreme case was also investigated (that is, to have only one positive gust per flight, that means the largest one occurring in each flight). Omitting cycles gave lower crack rates as should be expected, and this empirical trend is also

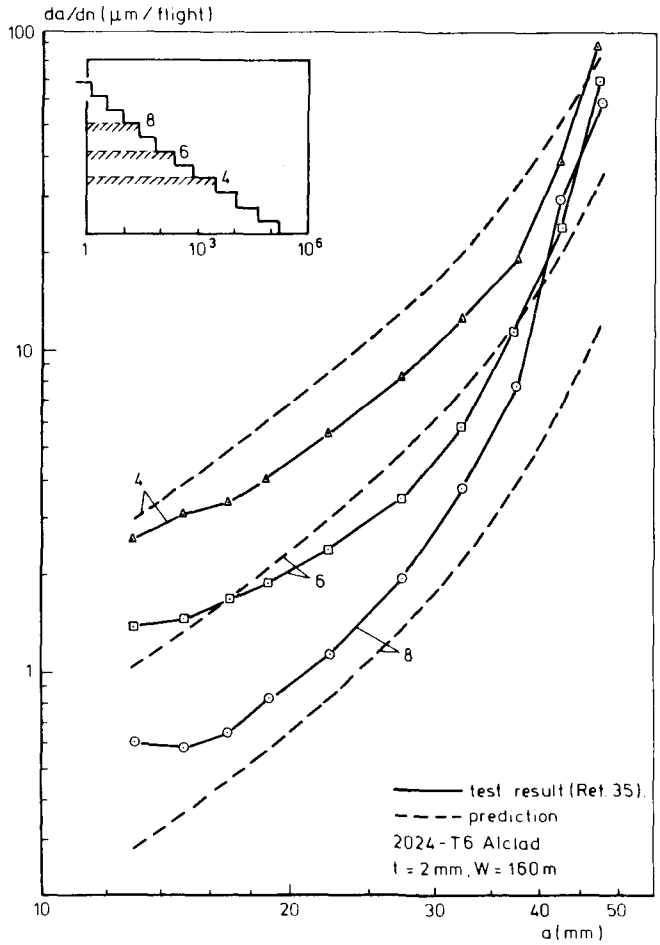

FIG. 6—*Effect of truncation level on crack growth rate in flight-simulation test.*

predicted (Figs. 7 and 9*b* and *c*). It should be noted that a 1:1 relation between predicted life and test life, a result sometimes observed in Fig. 9, does not imply that the crack growth rate is also accurately predicted (Fig. 6 through 8). For a reliable prediction method it should be required that the growth rate is predicted reasonably well. A good prediction of crack growth life is then obtained automatically.

Omitting Ground-to-Air Cycles (GTAC)—The results in Figs. 8 and 9*d* are somewhat disappointing. The tests indicate a significant growth rate reduction if the GTAC are omitted. The prediction gives a small reduction only. The latter results are obtained because omitting the GTAC changes $(S_{min})_{VA}$ from -3.4 to $+0.4$ kg/mm^2, and R_{VA} from -0.250 to $+0.029$;

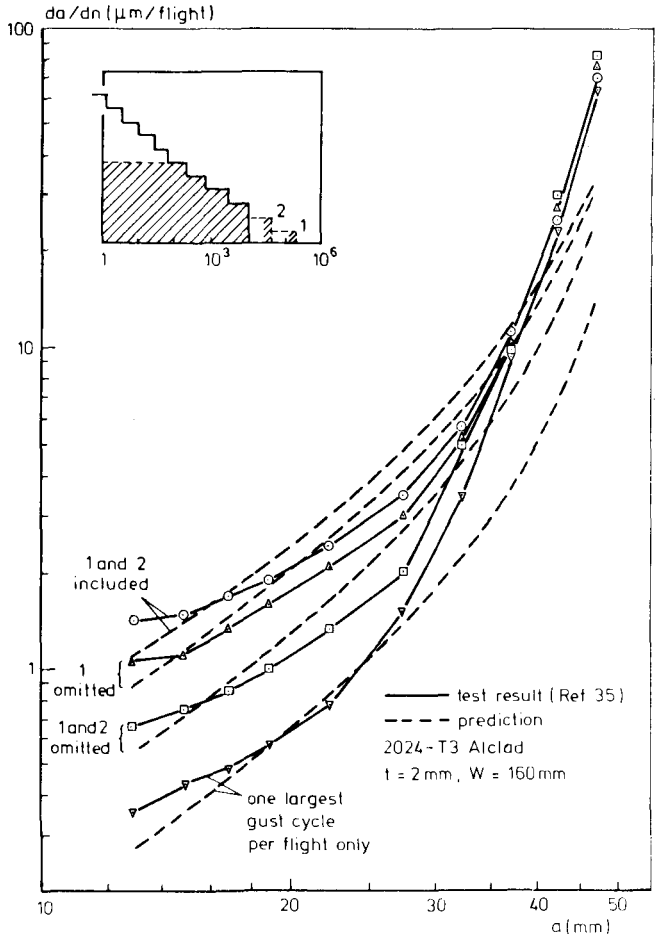

FIG. 7—*Effect of omitting low-level amplitude cycles on crack growth in flight-simulation tests.*

whereas, S_{op} changes from 6.80 to 6.845 kg/mm^2 only. The small change of S_{op} explains the predicted results obtained. At this point it should be asked, how a fairly drastic change of S_{min} can give such a small change of S_{op}. To answer this question, Elber's results leading to Eq 18 have been replotted in Elber's manner (Fig. 10*a*), and in another way preferred by the author (Fig. 10*b*). Clearly enough Elber's results do not extend any further down as $R = -0.1$, and an applicability below this value was never claimed. Figure 10*b* shows that Elber's function for S_{op} goes through a minimum at $R = -0.125$, and it would be rather strange if such a minimum would exist. Elasto-plastic analysis of Newman [*17*] indicated the trend of the dotted line in Fig. 10*b*, which appears to be more plausible. A similar trend was also predicted by

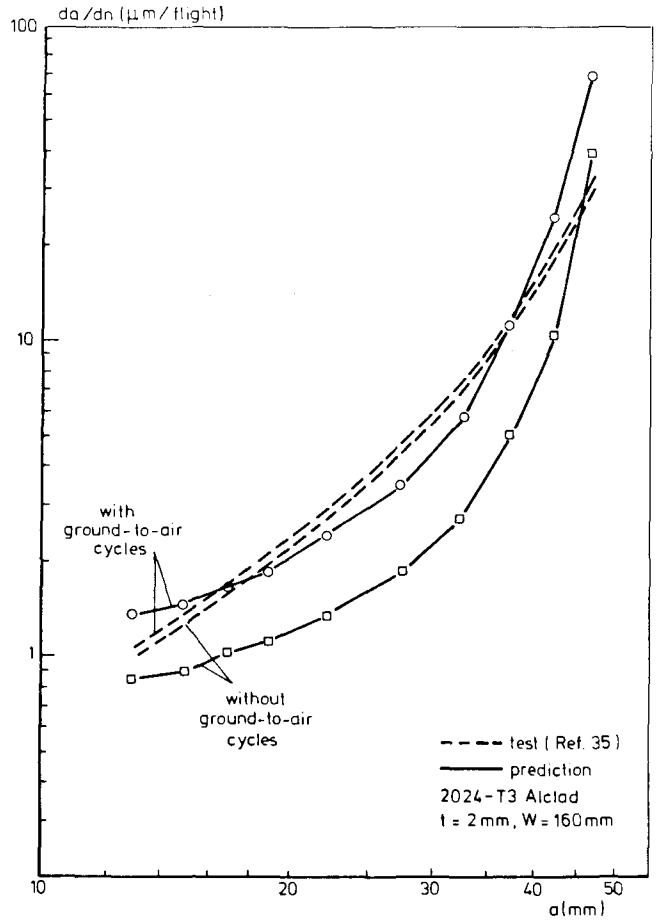

FIG. 8—*Effect of omitting ground-to-air cycles on crack growth in flight-simulation tests.*

Führing [*19*]. As a matter of fact, other lines can be drawn through Elber's data points giving credit to the expected trend following from analytical work. From such a line a larger shift of S_{op} after removing the GTAC would have followed, and a more significant effect would have been predicted as indicated by the test results.

It is thought that a systematic picture is emerging from the above results. A model with a constant crack opening stress level, depending on maximum and minimum stress in a stationary VA loading, is capable of predicting the trends of significant load spectrum variations. The quantitative accuracy is still insufficient, but this may well be a consequence of insufficient knowledge about crack opening stress levels.

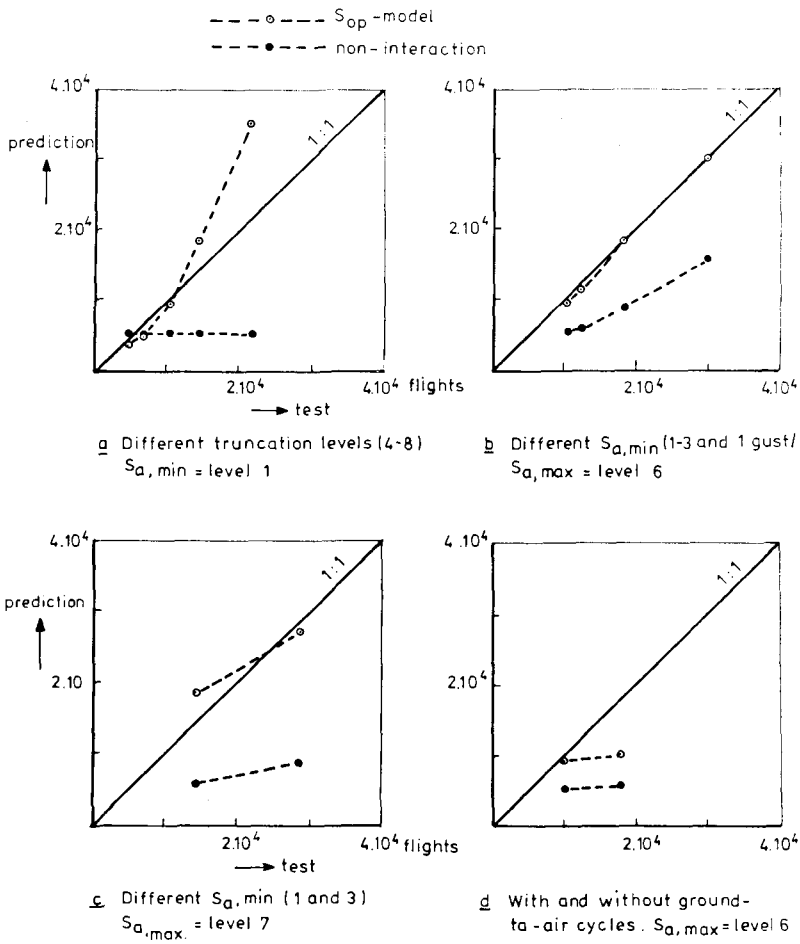

FIG. 9—*Crack propagation lives* (a = *14 mm to* a = *50 mm*), *comparison between prediction and test results of flight-simulation tests.*

Elber's formula, Eq 16, assumes S_{op} to be independent of crack length and K_{max}. However, both analytical studies [*17,19,38*] and experimental work [*20,39*] have shown that some effects do exist. In Fig. 10*b* Newman's curve applies to $S_{max}/S_{0.2} = 0.4$, but he found different results for other $S_{max}/S_{0.2}$ ratios.

The literature cited indicates lower S_{op}/S_{max} for high K_{max}-values. It is noteworthy then, that experimental curves in Fig. 6 through 8 merge together for large a-values corresponding to high K-values.

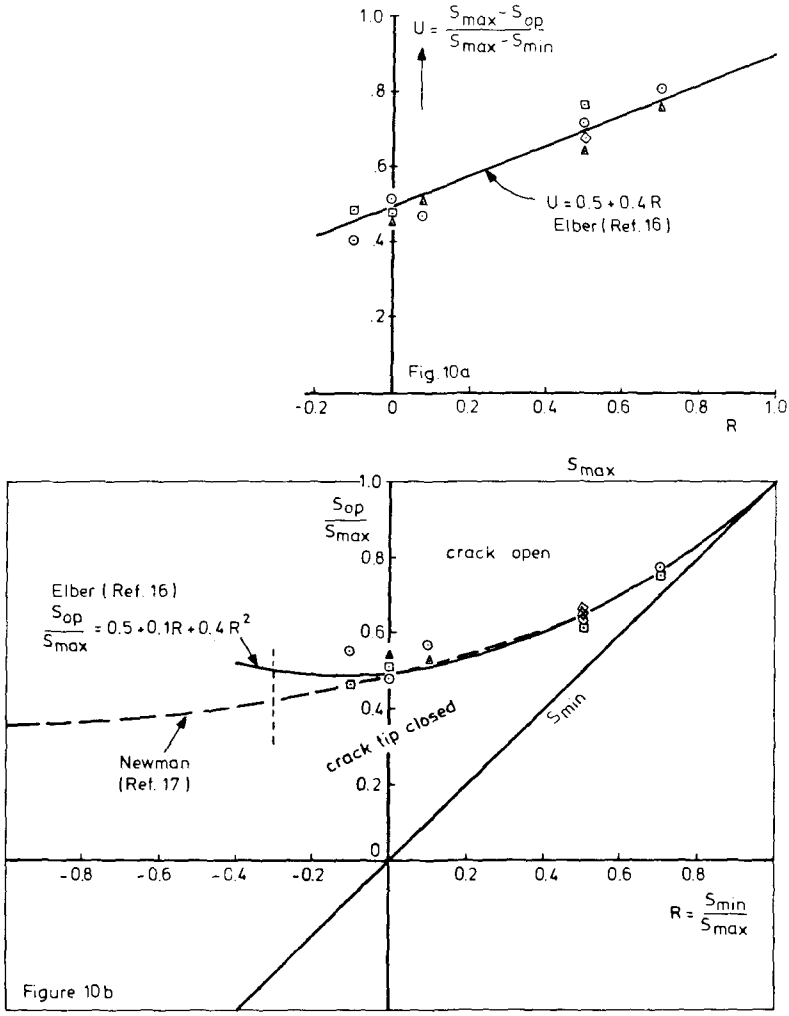

FIG. 10—*Crack-opening stress as a function of* R. *Experimental results of Elber.*

Crack Growth under Random Loading

An investigation on the applicability of K_{rms} for correlating crack growth under random loading was started some time ago and is still being continued. Variables of the first test series [*40*] were: S_{rms}, irregularity factor k, and truncation of high amplitudes (crest factor C). Tests were carried out on 2024-T3 Alclad sheet specimens (thickness = 2 mm, width = 100 mm) with a central crack. The random load was applied by computer control of a closed loop fatigue machine. For this purpose, a load signal generating pro-

cedure, developed in Germany, was adopted [*41*]. It starts from a two-dimensional density function proposed by Kowalewski, which can be written as

$$h(M, A)\, dM\, dA = \frac{1}{I^2\sqrt{2\pi(1-I^2)}} \cdot \exp\left[\frac{-(M/\sigma)^2}{2(1-I^2)}\right] \cdot \frac{A}{\sigma} \exp\left[\frac{-(A/\sigma)^2}{2I^2}\right] d\left(\frac{M}{\sigma}\right) d\left(\frac{A}{\sigma}\right) \tag{21}$$

The range between two successive peak values (a maximum p and a minimum q or the reverse) is equal to $2A$ with a mean value M. The irregularity factor $k(= 1/I)$ is defined as the ratio of the number of peak values and the number of mean crossings, and σ is the standard deviation of the random signal. Defining S_{rms} as the root-mean-square of $(S - S_m)$ implies that $S_{rms} = \sigma$. Both σ and k can be derived from the power spectral density function, $\Phi(\omega)$, assuming the random signal is Gaussian.

Equation (21) is used to fill a matrix with numbers corresponding to the frequency of occurrences of ranges between 32 p-levels (maxima) and q-levels (minima). The computer makes a random walk through the matrix, which produces a random signal satisfying Eq 21. Two specimens are shown in Fig. 11 for a narrow band random signal and a broader band signal.

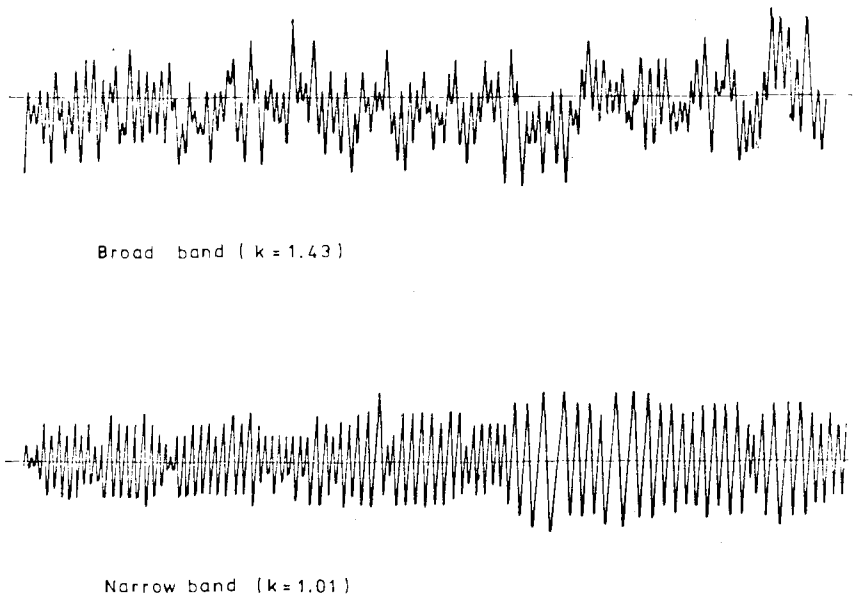

FIG. 11—*Samples of load histories in random load test.*

In the tests the ratio $\gamma = S_m/S_{rms}$ was kept constant ($\gamma = 3.28$), which should be required for the applicability of K_{rms} ($= CS_{rms}\sqrt{\pi a}$). The return period of the random signal was chosen to correspond to 10^6 positive zero crossings (actually mean crossings). As a result the crest factor C, defined by

$$C = \frac{S_{\max} - S_m}{S_{rms}} \tag{22}$$

becomes $C = 5.25$. Crack growth tests were carried out at five different S_m-values. Averages of two tests are presented in Figs. 12 and 13 for broad- and narrow-band loading, respectively. It was hoped that both figures would confirm the applicability of

$$\frac{da}{dn} = f(K_{rms}) \tag{23}$$

However, a small but systematic effect of S_m is observed. Higher S_m-values give slightly higher crack rates. Consequently, an average curve in Figs. 12 and 13 representing Eq 23 can be applicable only in an approximate way.

On the average crack rates in Fig. 13 for narrow band random loading are about 1.5 times faster than for broadband random loading in Fig. 12. In both figures the cycle definition for *da/dn* is one minimum plus one maximum. However, if the definition of one cycle is based on two mean crossings the factor 1.5 reduces to $(1.01/1.43) \times 1.5 = 1.06$, and the difference between crack rates should be considered as negligible. A similar trend was found in Ref *28*.

A somewhat more significant effect is observed if the random signal is artificially truncated until $S_{\max}/S_{\text{rms}} = 3.31$ (Figs. 14 and 15). In practice, mechanical systems with their own characteritic response will usually damp high amplitude excitations. Since such a truncation was known to have a significantly harmful effect on crack growth under flight-simulation loading, it appeared desirable to see whether this also applied to pure random loading. The results in Fig. 14 again indicate some effect of S_m, while Fig. 15 illustrates the effect of truncation. A fairly drastic truncation increased the crack rate 1.3 to 2 times. This is a fairly modest effect as compared to the effect observed in flight-simulation tests.

Discussion

In the first part of this paper, physical aspects of fatigue crack growth relevant to prediction methods were surveyed. This was followed by a discussion on two different prediction methods: (1) cycle-by-cycle calculations and (2) characteristic K methods. The significance of crack closure for explaining interaction effects was emphasized. In the second part, aspects of both

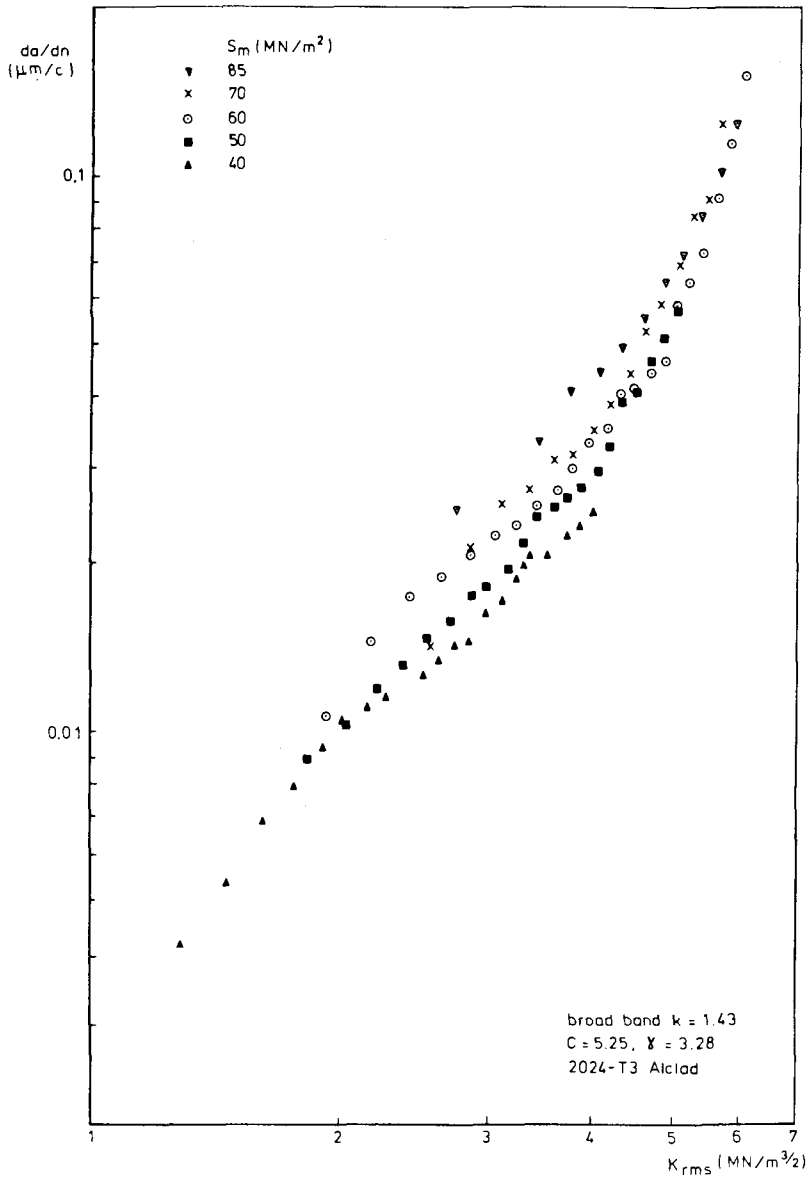

FIG. 12—*Crack growth rates for broadband random loading.*

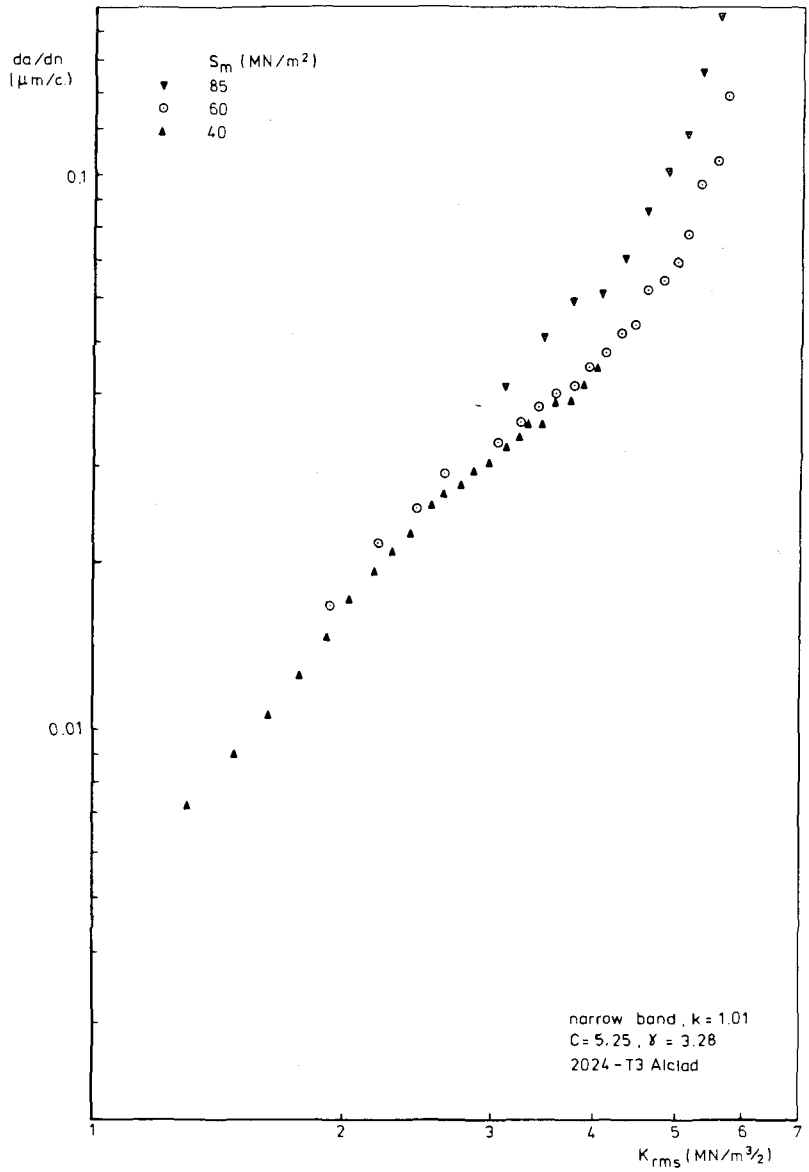

FIG. 13—*Crack growth rates for narrow band random loading.*

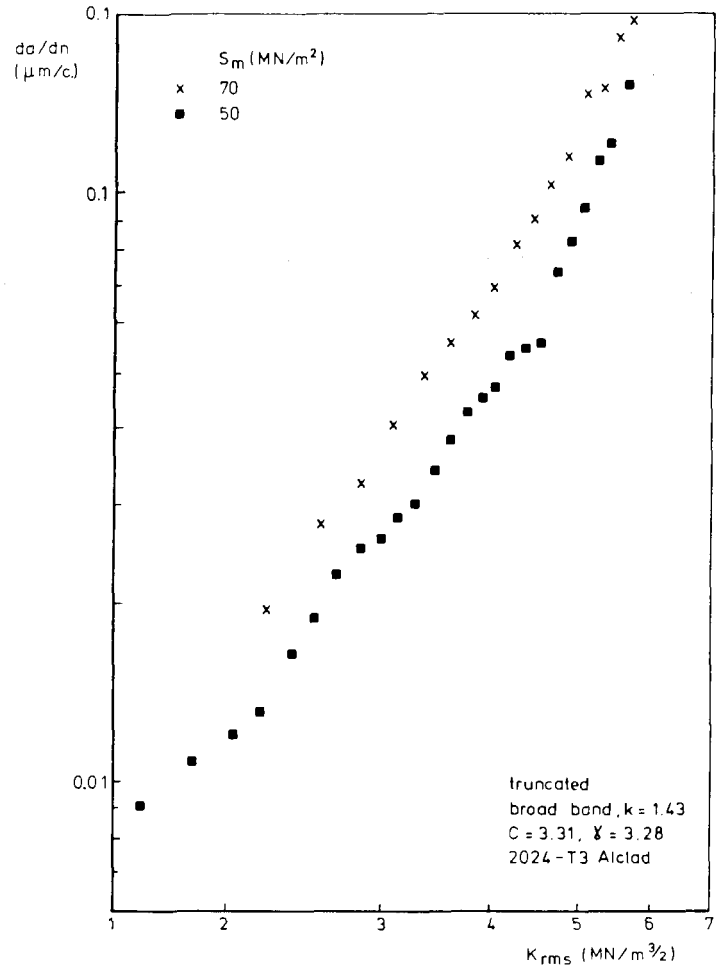

FIG. 14—*Crack growth rates for truncated broadband random loading.*

methods were studied as part of recent test series. It is obvious that a cycle-by-cycle calculation is more universal than the characteristic K-method. The problem is that a cycle-by-cycle prediction method to be accepted should include the possible occurrence of both positive and negative interactions. So far the introduction of crack closure seems to be the only available way to satisfy this requirement. However, a cycle-by-cycle calculation then becomes fairly elaborate. A sufficient simplification to avoid this was to adopt a constant crack-opening stress level, which was considered to be justified for a stationary VA loading. Results thus obtained indicate that such a calculation model might open a useful perspective. However, it was also clear that the

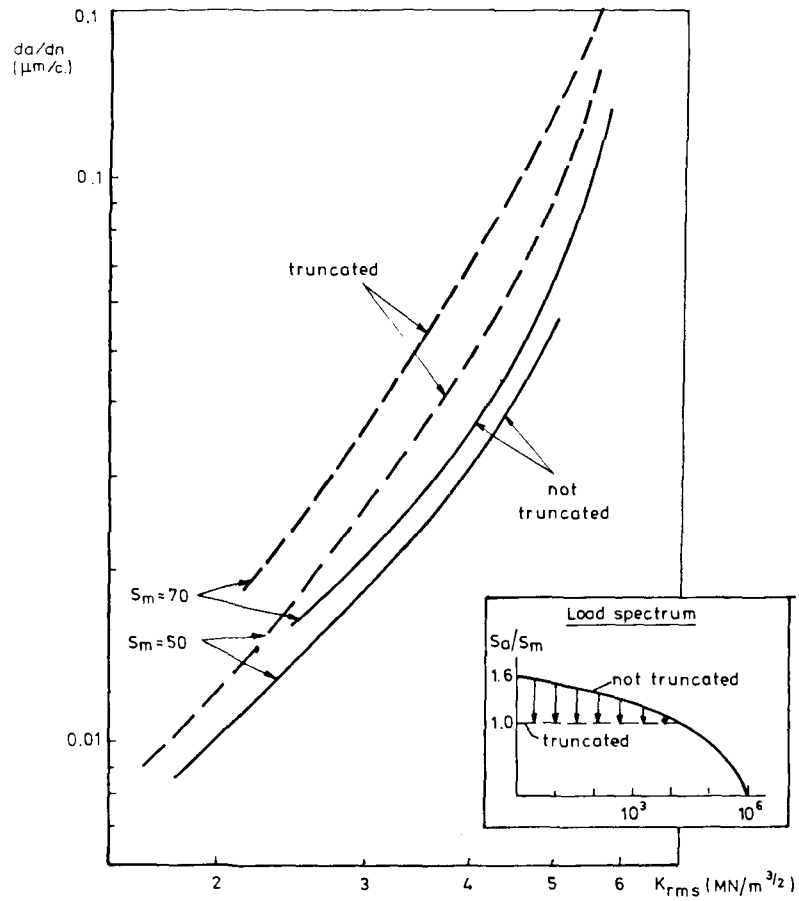

FIG. 15—*Effect of truncation on crack growth under random loading (curves derived from Figs. 12 through 14).*

quantitative knowledge of crack opening stress levels is still insufficient. It is stimulating to see that this can be improved by elasto-plastic analysis, but measurements seem to be desirable as well.

An important practical point is that the major part of present research is restricted to through cracks in sheet materials. It was pointed out that cracks with curved crack fronts offer additional problems, while brief reference was made to limited information of fatigue crack growth in service. Anyhow, many cracks in service are known to have curved crack fronts. It is sufficient to refer to semi- or quarter-elliptical cracks at bolt holes in joints. In view of the practical relevance of such cracks it is definitely desirable to compile more data on crack growth of various types of cracks.

To summarize some indications of previous parts of the paper, the following points may be observed:

1. Until now much research was carried out on the effects of peak loads in CA tests or other very simple loading programs. Beyond any doubt this has been very useful to recognize and understand interaction effects. A second benefit of this type of test is that it stimulated analytical studies employing elasto-plastic mechanics, which proved to give most useful indications. We thus have learned to appreciate available tools for developing prediction techniques.

2. At the same time there is a risk to overlook the question of which problem one wants to solve. That problem is to predict crack growth of cracks with curved crack fronts as well, in components with more complex geometries than a sheet specimen, under highly variable fatigue loads. Since information of crack growth under such conditions will not come from service experience, it has to be generated in the laboratory.

Some recommendations appear to be a logical outcome now:

1. Crack growth data should be produced under well specified conditions concerning the following aspects:

(*a*) Materials and specimen geometry should be representative for details of aircraft structures, which are supposed to have a critical nature.

(*b*) Fatigue loads to be applied should cover a variety of load-time histories which are relevant for aircraft utilization.

2. For the evaluation of prediction techniques to be applied on the above test results, sufficient basic information must also be made available with respect to:

(*c*) Basic crack growth data for the material concerned,

(*d*) Crack closure behavior of the material, and

(*e*) Relevant K-values.

It will be understood that a plea is made here for approaching the problem from the practical side. If we would stidk to a step-by-step evolution from simple cases to more complex problems, there is a certain risk of never reaching a practical solution.

Concluslons

1. Pertinent physical information on the process of fatigue crack growth is now available. It provides guidelines to account for load cycle interactions in the prediction of fatigue crack growth under VA loading. Crack closure is an important observation in this respect.

2. A cycle-by-cycle prediction method is more universal than a method based on characteristic K-values. However, the former one is more elaborate, while satisfactory methods are not really established as yet.

3. Crack closure measurements were made during flight-simulation tests on two aluminum alloy sheet materials. The results illustrate that crack closure can be a fairly complex phenomenon during service simulation loading. The effect of severe flights on the crack opening stress level (S_{op}) was clearly noted.

4. For the prediction of crack growth under stationary VA loading it was proposed that: (*a*) S_{op} may be considered to be constant, (*b*) the level of S_{op} depends on the maximum and the minimum stress occurring in the VA loading, and (*c*) this dependence is the same one applicable to CA loading. This method was applied to flight-simulation test results with essentially different load spectra and the results appear to be promising. However, more quantitative information on S_{op} levels is desirable.

5. Crack growth tests under pure random loading (with $S_m/S_{rms} = 3.28$) were carried out on 2024-T3 Alclad specimens. Five different S_m-values and two irregularity factors were used. As a rough approximation the growth rate for different S_m-values is a function of K_{rms} only. However, a small but systematic effect of S_m was recognized. The growth rate (millimetres per mean crossing) was practically similar for narrow band ($k = 1.01$) and broadband ($k = 1.43$) random loading. If the maximum stress amplitudes of the random loading were truncated a significant increase of the growth rate was observed.

6. It appears that crack growth data for more practically relevent cracks are highly desirable. Guidelines for research on this topic have been outlined briefly.

References

[*1*] Mann, J. Y., *Bibliography on the Fatigue of Materials, Components and Structures*, Vol. 2, 1951-1960, Pergamon Press, London, 1978.

[*2*] Paris, P. C., Gomez, M. P., and Anderson, W. E. "A Rational Analytic Theory of Fatigue," *The Trend in Engineering*, Vol. 13, 1961, pp. 9-14.

[*3*] Schijve, J., *Engineering Fracture Mechanics*, Vol. 6, 1974, pp. 245-252.

[*4*] Schijve, J. in *Fatigue Crack Growth Under Spectrum Load, ASTM STP 595*, American Society for Testing and Materials, 1976, pp. 3-23.

[*5*] Bowles, C. Q., "The Role of Environment, Frequency and Wave Shape during Fatigue Crack Growth in Aluminum Alloys," Ph.D. thesis, Delft University of Technology, Delft, The Netherlands, Aug. 1978 (also Department of Aerospace Engineering, Report LR-270, 1978).

[*6*] Elber, W., "Fatigue Crack Propagation," Ph.D. thesis, University of New South Wales, Australia, 1968 (see also *Engineering Fracture Mechanics*, Vol. 2, 1970, pp. 37-45).

[*7*] Schijve, J. in *Fatigue Crack Propagation, ASTM STP 415*, American Society for Testing and Materials, 1967, pp. 415-457.

[*8*] Vogelesang, L. B., "Some Factors Influencing the Transition from Tensile Mode to Shear Mode Under Cyclic Loading," Department of Aerospace Engineering, University of Delft, Delft, The Netherlands, Report LR-222, 1976.

[*9*] Schijve, J., "Fundamental and Practical Aspects of Crack Growth under Corrosion Fatigue Conditions," *Proceedings*, Institution Mechanical Engineers, Vol. 191, 1979, pp. 107-114.

[*10*] Tada, H., Paris, P., and Irwin, G., "The Stress Analysis of Cracks Handbook," Del Research Corp., Hellertown, Pa., 1973.

[11] Sih, G. C., "Handbook of Stress Intensity Factors for Researchers and Engineers," Lehigh University, Bethlehem, Pa., 1973.
[12] Rooke, D. P. and Cartwright, D. J., "Compendium of Stress Intensity Factors," Her Majesty's Stationery Office, London, 1976.
[13] Newman, J. C., Jr., "A Review and Assessment of the Stress-Intensity Factors for Surface Cracks," NASA TM 78805, National Aeronautics and Space Administration, Washington, D.C., Nov. 1978.
[14] Willenborg, J. D., Engle, R. M., and Wood, H. A., "A Crack Growth Retardation Model Using an Effective Stress Concept," AFFDL-TM-FBR-71-1, Air Force Flight Dynamic Laboratory, Dayton, Ohio, 1971.
[15] Wheeler, O. E., *Journal of Basic Engineering, Transactions* of the American Society of Mechanical Engineers, 1972, pp. 181-186.
[16] Elber, W. in *Damage Tolerance in Aircraft Structures, ASTM STP 486*, American Society for Testing and Materials, 1971, pp. 230-242.
[17] Newman, J. C., Jr., in *Cyclic Stress-Strain and Plastic Deformation Aspects of Fatigue Crack Growth, ASTM STP 637*, American Society for Testing and Materials, 1977, pp. 56-80.
[18] Ogura, K. and Ohji, K., *Engineering Fracture Mechanics*, Vol. 9, 1977, pp. 471-480.
[19] Führing, H., "Elastic-Plastic Crack Closure Analysis of Dugdale Crack Plates Based on Fracture Mechanics," (in German), Report of Institut für Statik und Stahlbau, Technische Hochschule, Darmstadt, Heft 30, 1977.
[20] Paris, P. C. and Hermann, L., Lecture presented at the International Union on Theoretical and Applied Mechanics colloquium, 30 Aug.-4 Sept., Delft, The Netherlands, 1976.
[21] Bell, P. D. and Wolfman, A. in *Fatigue Crack Growth Under Spectrum Loads, ASTM STP 595*, American Society for Testing and Materials, 1976, pp. 157-171.
[22] Eidinoff, H. L. and Bell, P. D., "Application of the Crack Closure Concept to Aircraft Fatigue Crack Propagation Analysis," *Proceedings* of the International Committee in Aeronautical Fatigue Symposium, Darmstadt 1977, paper 5.3
[23] Dill, H. D. and Saff, C. R. in *Fatigue Crack Growth Under Spectrum Loads, ASTM STP 595*, American Society for Testing and Materials, 1976, pp. 306-319.
[24] Elber, W. in *Fatigue Crack Growth Under Spectrum Loads, ASTM STP 595*, American Society for Testing and Materials, 1976, pp. 236-247.
[25] Schijve, J., *Engineering Fracture Mechanics*, (four lectures on fatigue), Vol. 11, 1979, pp. 167-221.
[26] Paris, P. C., "The Growth of Fatigue Cracks Due to Variations in Load," Ph.D. thesis, Lehigh University, Bethlehem, Pa., 1962.
[27] Paris, P. C., *The Fracture Mechanics Approach to Fatigue, Fatigue an Interdisciplinary Approach*, Syracuse University Press, Syracuse, N.Y., 1964, pp. 107-132.
[28] Smith, S. H., *Fatigue Crack Growth Under Axial Narrow and Broad Band Random Loading, Acoustical Fatigue in Aerospace Structures*, Syracuse University Press, Syracuse, N.Y., 1965, pp. 331-360.
[29] Swanson, S. R., Cicci, F., and Hoppe, W., in *Fatigue Crack Propagation, ASTM STP 415*, American Society for Testing and Materials, 1967, pp. 312-362.
[30] Schijve, J., Jacobs, F. A., and Tromp, P. J., "Fatigue Crack Growth in Aluminum Alloy Sheet Material under Flight-Simulation Loading, Effects of Design Stress Level and Loading Frequency," NLR TR 72018, Amsterdam, The Netherlands, 1972.
[31] Wanhill, R. J. H., "Engineering Application of Fracture Mechanics to Flight Simulation Fatigue Crack Propagation," International Conference in Fracture Mechanics in Engineering Application, Bangalore, March 1979 (also NLR MP 78015).
[32] de Jonge, J. B., Schütz, D., Lowak, H., and Schijve, J., "A Standardized Load Sequence for Flight Simulation Tests on Transport Aircraft Wing Structures," LBF Report FB-106, NLR TR 73029, March 1973.
[33] Anonymous, "Description of a Fighter Aircraft Loading Standard for Fatigue Evaluation: FALSTAFF," Combined report of the NLR, LBF, IABG and F+W, March 1976.
[34] Provó Kluyt, J. C., "Significance of Crack Closure for Crack Growth in 7075-T6 and 2024-T3 Al Alloys under Flight Simulation Loading with Different Truncation Levels," (in Dutch), Ph.D. thesis, Department of Aerospace Engineering, Delft University of Technology, Delft, The Netherlands, April 1978.

[35] Schijve, J., Jacobs, F. A., and Tromp, P. J., Crack Propagation in Aluminium Alloy Sheet Materials under Flight Simulation Loading," NLF TR 68117, Amsterdam, 1968.

[36] Schijve, Jaap, "The Stress Ratio Effect on Fatigue Crack Growth in 2024-T3 Alclad and the Relation to Crack Closure," Memorandum M-336, Department of Aerospace Engineering, Delft, The Netherlands, Aug. 1979.

[37] Schijve, J., "Statistical Transformations of Load Histories Applied in Flight-Simulation Tests," Department of Aerospace Engineering, Delft University of Technology, Delft, The Netherlands, Memorandum M-303, 1978.

[38] Führing, H. and Seeger, T., *Engineering Fracture Mechanics*, Vol. 11, 1979, pp. 99-122.

[39] Katcher, M. and Kaplan, M. in *Fracture Toughness and Slow-Stable Cracking, ASTM STP 559*, American Society for Testing and Materials, 1974, pp. 264-282.

[40] ten Have, A. A., "K_{rms}-correlation in Digitally Generated Random-Load Fatigue Tests on 2024-T3 Al Sheet Material, Ph.D. thesis, Department of Aerospace Engineering, Delft University of Technology, Delft, The Netherlands, Oct. 1978.

[41] Fischer, R., Hück, M., Köbler, H. G., and Schütz, W., "Criteria for the Evaluation of Fatigue Strength of Materials and Components at Present and in the Future," (in German), Industrie Anlagen-Betriebsgesellshaft Report 14224601, 1975 and Laboratorium Für Betriebsfestigkeit, Report 2909, 1975.

R. M. Pelloux,[1] *M. Faral,*[1] *and W. M. McGee*[2]

Fractographic Measurements of Crack-Tip Closure

REFERENCE: Pelloux, R. M., Faral, M., and McGee, W. M., **"Fractographic Measurements of Crack-Tip Closure,"** *Fracture Mechanics: Twelfth Conference, ASTM STP 700,* American Society for Testing and Materials, 1980, pp. 35-48.

ABSTRACT: Relative changes in striation spacing resulting from a sudden change of the load range were used to measure crack-tip closure under plane-strain conditions. The tests were performed in a 2124-T351 aluminum alloy. The difference between the opening and closure rates of the crack tip was quantitatively measured by comparing striation spacings for two different programmed load blocks. It is concluded that crack-tip closure occurs principally in the plane-stress region of the crack front. In the center of the specimen, under plane strain, the average value of K_{op}/K_{max} is less than 0.20 for ΔK varying from 10 to 35 MPa$\sqrt{m}$.

KEY WORDS: crack tip closure, crack tip opening, fatigue crack growth, programmed loads, electron fractography, aluminum alloy fractures (materials), crack propagations

Since the crack-tip closure concept was introduced by Elber [*1*],[3] a large number of theoretical and experimental investigations of this phenomenon have been carried out. A thorough review [*2*] of the experimental results published so far show large discrepancies in closure measurements. These discrepancies are due to differences in techniques; that is, they are all macroscopic techniques. These techniques include surface displacement gages, photography, laser interferometry, electrical potential, ultrasonics, photoelasticity, and bulk interferometry.

By contrast with this extensive work, the authors decided to use a microscopic technique to measure K_{op}. This technique makes use of electron-fractography and of programmed load testing to correlate a change in striation spacing with a sudden change of the stress intensity factor range.

[1]Professor of metallurgy and research assistant, respectively, Department of Materials Science and Engineering, Massachusetts Institute of Technology, Cambridge, Mass. 02139.

[2]Research engineer, Engineering Structures and Materials Laboratory, Lockheed-Georgia Co., Marietta, Ga. 30063.

[3]The italic numbers in brackets refer to the list of references appended to this paper.

The preliminary results of this fractographic approach were reported in a previous paper [3]. Since then a quantitative analysis of the results was performed by comparing the crack tip opening and closure displacements as a function of the applied stress. This paper reports on the quantitative analysis of the crack closure measurements obtained by the fractographic technique.

Materials and Test Procedures

All the fatigue tests were performed on compact tension specimens (width (W) = 63.5 mm, thickness (B) = 12.7 mm) in the long transverse orientation. The alloy 2124-T351 was received from Alcoa as fully heat-treated plates, 12.7 mm thick. Alloy 2124-T351 was selected because it is relatively free of large inclusions and it shows well-defined fatigue striations. Chemical composition and mechanical properties of the alloy are given in Table 1.

The tests were run at 10 Hz with $R = 0.05$. K_{max} varied with crack length from 11 to 38 MPa$\sqrt{m}$ from the beginning to the end of each test. The load block diagrams referred to as R and T, respectively, in Figs. 1 and 2 were inserted when the crack lengths reached values corresponding to K_{max} levels of 11, 13.8, 16.5, 22, and 33 MPa$\sqrt{m}$. The load blocks were run at 0.25 Hz, and the load output was recorded on a chart recorder. All the tests were performed on a servohydraulic machine interfaced with a digital computer. Crack length was monitored with a ×30 traveling microscope by reading a reference grid engraved on one side of each specimen. Crack length measurements were accurate to ±0.025 mm. All the tests were designed so that the crack front would advance beyond the boundaries of the plane-stress plastic zone size created by the overloads D and H of the block diagrams R or T before the next block program was applied.

Electronfractography was performed by scanning microscopy of the fracture surfaces and by transmission electron microscopy of two stage plastic-carbon replicas. The shadowing direction was opposite to the crack growth direction. All the fractographic results for the closure measurements were

TABLE 1—*Alloy 2124-T351.*

Chemical Composition					
Al	Cu	Mg	Mn	Fe	Si
balance	3.84	1.33	0.46	0.09	0.05

Long Transverse Tensile Properties		
Yield Stress	Tensile Strength	Elongation, %
296 MN m^{-2}	451 MN m^{-2}	25

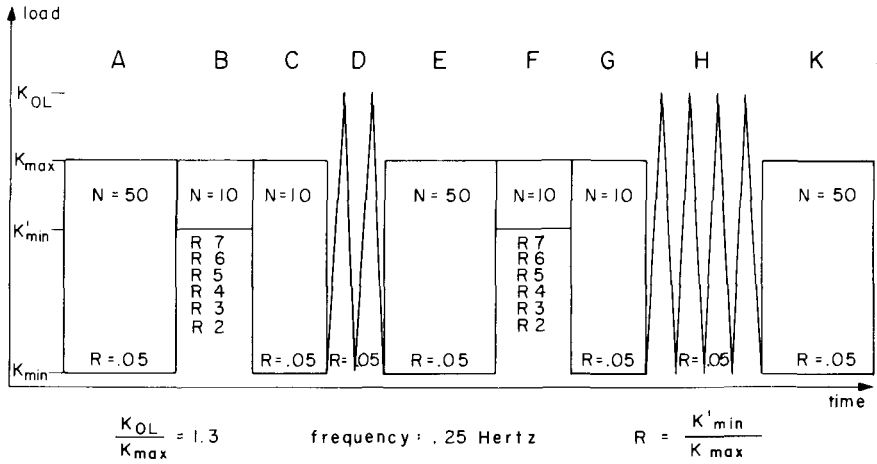

TYPE R BLOCK DIAGRAM

FIG. 1—*Description of the* R *load program.*

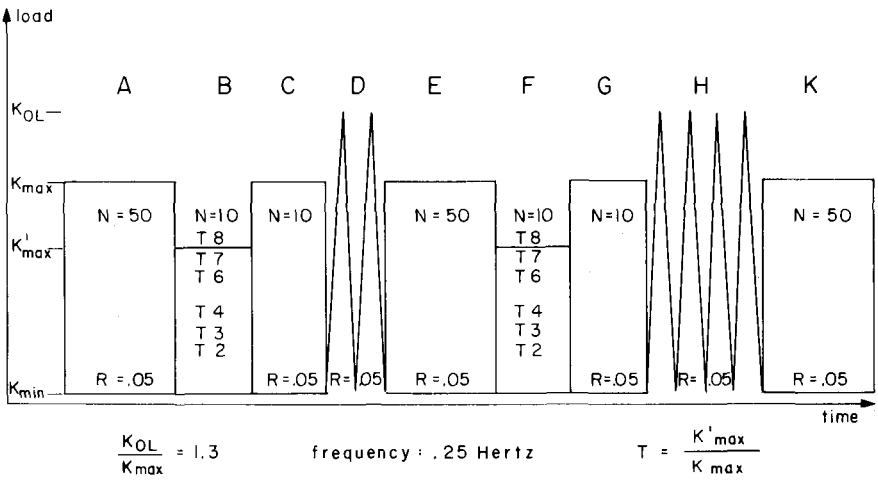

TYPE T BLOCK DIAGRAM

FIG. 2—*Description of the* T *load program.*

taken from the plane strain region of each specimen typically along a 5-mm length of the crack front at the midsection of the specimen.

Principle of the Fractographic Technique

The general principle of the fractographic technique is based on the one to one correlation between crack tip opening displacement and crack advance per cycle, *da/dn*. This correlation has been demonstrated previously [*4*] for aluminum alloys in the range of stress intensity factors studied here; that is, from 10 to 40 MPa$\sqrt{\text{m}}$. The principle of the method is shown in Fig. 3 with two load blocks, *A* and *B*. In Fig. 3, if $K_{min}\,A > K_{op}$, the striations of the *A* cycles will be smaller than the baseline striations. On the other hand, if K_{min} $B < K_{op}$ there will be no difference between the base line striations and the *B* cycles striations.

Calculations of the crack tip opening displacements (CTODs) for different load ranges are included in Fig. 2 in order to show the difference between the cyclic CTOD associated with reversed plastic flow and the monotonic CTOD resulting from a load excursion (cycle 456), which extends the plastic zone beyond the steady-state cyclic plastic zone. On the basis of the CTOD calculations, there will be a difference between the striation spacings of load cycle 456 and cycle 78. These CTOD calculations can be done either with the assumption that $K_{op} = 0$, or that K_{op} has a finite positive value.

One may assume in a first approximation that *da/dn* per cycle is proportional to the CTOD effective with CTOD_{eff} being defined as follows

$$\text{CTOD}_{eff} = A\left(\frac{\Delta K_{eff}}{2YE}\right)^2$$

where

Y = flow stress,
E = elastic modulus, and
A = constant.

With

$$\Delta K_{eff} = \frac{K_{max} - K_{op}}{K_{max} - K_{min}} \cdot \Delta K_{appl}$$

$$\Delta K_{eff} = U \cdot K_{appl} \qquad \text{if } K_{op} > K_{min}$$

$$\Delta K_{eff} = \Delta K_{appl} \qquad \text{if } K_{op} < K_{min}$$

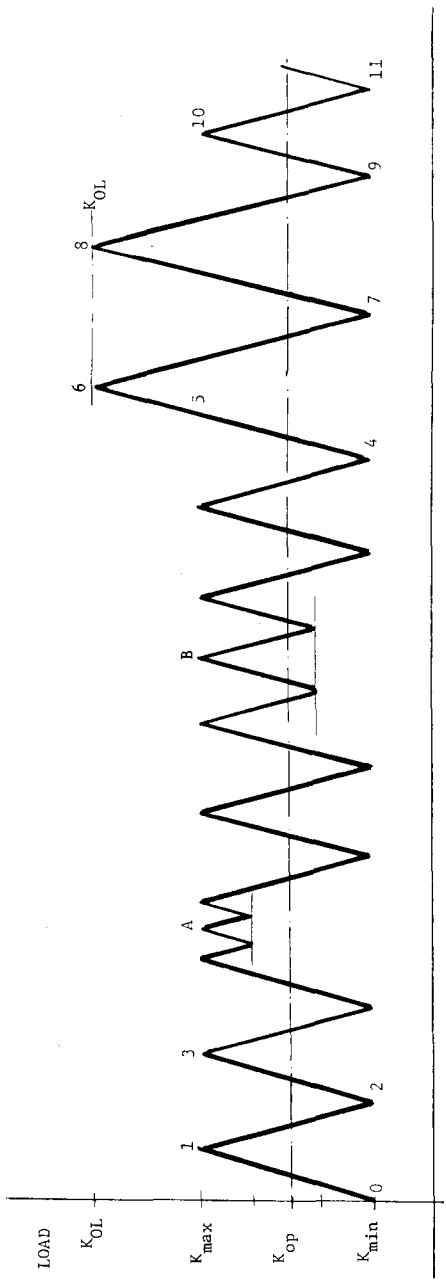

FIG. 3—*Sketch of a sequence of programmed loads showing the principle of the fractographic technique. The* A *block will show striations smaller than base line striations 01 or 23. The* B *block will show striations identical to the base line striations 01 or 23. The authors deduce, therefore, that* $K_{min\ B} < K_{op} < K'_{min\ A}$.

Test Programs

The methodology described in Fig. 3 was used with the fractographic data obtained from the block diagrams R and T shown in Figs. 1 and 2. The programmed load blocks shown in Figs. 1 and 2 were designed as follows:

1. Block *A* (50 cycles) is the continuation of the steady-state crack growth condition at 0.25 Hz instead of 10 Hz.
2. Block *B* (10 cycles) is used to obtain a measurement of K_{op} by (*a*) varying ΔK_B and keeping K_{max} constant in the type *R* tests; (*b*) varying ΔK_B and keeping K_{min} constant in the type *T* tests.
3. Block *C* (10 cycles) is designed to show that the base line crack growth rate and the closure effect are not affected by block *B*. Block *C* also serves to separate *B* from the load marker *D*.
4. Block *D* (2 cycles) is a crack front marker which is used to locate *B* and also to introduce a crack retardation effect and a change of K_{op}.
5. Block *E* (50 cycles) allows a steady crack growth rate to develop after the overloads. *E* will also provide a measure of the retardation effect due to block *D*.
6. Block *F* (10 cycles) is identical to block *B* and by comparing (da/dn_E) to (da/dn_F), one can calculate K_{op} following the *D* overloads.
7. Block *G* (10 cycles) is identical to block C.
8. Block *H* is a four loads crack front marker (different from *D*).
9. Block *K* is a return to the baseline load range before the frequency was returned to 10 Hz.

Type R *Tests Shown in Fig. 1—*

$$R = \frac{K'_{min}}{K_{max}} \text{ for block } B$$

The notation of *R*5, *R*6 refers to $R = 0.5$, $R = 0.6$. If $(\Delta K)_B$ is such that $K'_{min\,B} < K_{op}$ there will be no fractographic difference in da/dn spacing between *A* and *B* and *C*. If $(\Delta K)_B$ is such that $K'_{min\,B} > K_{op}$, one can determine K_{op} from a single test.

$$\frac{(\text{CTOD})_A}{(\text{CTOD})_B} = \frac{(da/dn)_A}{(da/dn)_B} = X = \frac{(\Delta K_{eff\,A})^2}{(\Delta K_B)^2} = \frac{(K_{max} - K_{op})^2}{(K_{max} - K'_{min})^2}$$

that is

$$\frac{K_{op}}{K_{max}} = 1 - \sqrt{X}\,(1 - R)$$

X is obtained from the fractographic measurements of da/dn averages for blocks A and B.

Type T *Tests Shown in Fig. 2—*

$$T = \frac{K'_{\max} \text{ for block } B}{K_{\max} \text{ for block } A}$$

The notation T_4, T_5 means $T = 0.4$, $T = 0.5$.

A CTOD analysis gives the following relations between CTOD ratios and da/dn ratios

$$\frac{(\text{CTOD})_A}{(\text{CTOD})_B} = \frac{(da/dn)_A}{(da/dn)_B} = X = \frac{(\Delta K_{\text{eff}A})^2}{(\Delta K_{\text{eff}B})^2} = \frac{(K_{\max} - K_{\text{op}})^2}{(K'_{\max} - K_{\text{op}})^2}$$

that is

$$\frac{K_{\text{op}}}{K_{\max}} = \frac{1 - T\sqrt{X}}{1 - \sqrt{X}}$$

Again X will be obtained from the ratio of fractographic measurements.

The dependence of the calculated CTOD upon ΔK or $K_{\max}$ is given graphically in Fig. 4, which presents three nondimensional sketches of CTOD (da/dn per cycle) versus K. Figure 4*a* shows that for a given value of K, the value of CTOD during closure of the crack tip is greater than during its opening. This observation is directly derived from the "reversed plasticity" behavior of the plastic zone at the tip of a fatigue crack [5]. Also, if one assumes a constant loading rate, the crack tip opens up at a faster rate at the end of the cycle than at the beginning. The reverse is true during

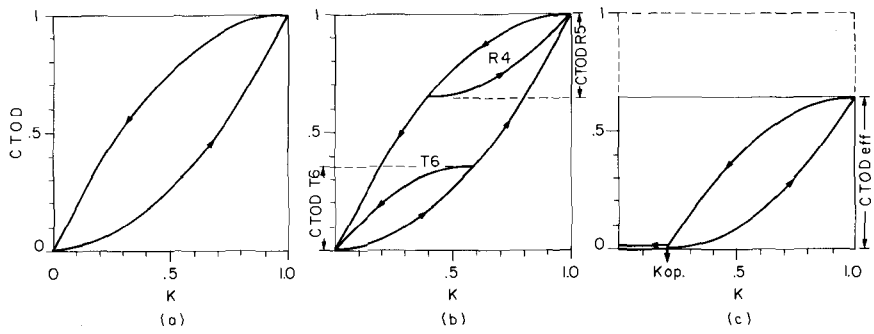

FIG. 4—*Sketches of the CTOD versus* K *relationships*; (a) *CTOD versus* K *during opening and closure*, (b) *CTOD versus* K *for* R5 *and* T6, *and* (c) *CTOD versus* K *with closure at* K_{op}.

unloading. Figure 4*b* gives an illustration of the CTOD sequence for a *B* cycle for *R*4 and *T*6 for the case where $K_{op} = 0$. Finally, in Fig. 4*c* one sees that a finite value of K_{op} results in a CTOD effective which is much lower than the expected CTOD.

So far it was assumed that $K_{op} = K_{closure}$ as shown in Fig. 4*c*. Neumann [*6*] has shown by a finite element analysis that K_{op} could be different from K closure with K_{op} being a strong function of R, the loading ratio. If one assumes with Neumann, that $K_{op} \neq K_{closure}$, then we can see that the *B* blocks of the *R* programs will measure a $K_{closure}$, while the *B* blocks of the *T* program will measure a K_{op}. For this work with a steady-state $K_{min}/K_{max} = 0.05$, the authors have assumed $K_{op} = K_{closure}$ in order to facilitate the interpretation of the fractographic results.

Crack retardation following the *D* loads is measured directly by comparing $(da/dn)_E$ to $(da/dn)_C$. This retardation effect is the result of an increase in K_{op} following the two overload cycles of *D*. K_{op} following *D* could also be determined by comparing $(da/dn)_E$ to $(da/dn)_F$.

Test Results

A log-log plot of da/dn versus ΔK for steady crack growth rate ($R = 0.05$) is best represented by the following equation

$$\frac{dl}{dn_{\text{in.}}} = 8 \times 10^{-8} \Delta K^3 \, (\Delta K \text{ in ksi}\sqrt{\text{in.}})$$

in the range 5×10^{-6} in. $< dl/dn < 5 \times 10^{-4}$ in. Extensive measurements of striation spacings show an excellent agreement between microscopic and macroscopic crack growth rates in the range of growth rates mentioned above.

Some typical fractographs of the *R* programs are given in Figs. 5–8. Figure 5 which is a scanning electron microscope (SEM) fractograph of *R*2 shows clearly the positions of the crack front for overloads *D* and *H*. The 30 percent overloads result in a well-defined crack-tip stretching associated with the large fatigue striations. Each side of the matching faces of the fracture surfaces shows the same stretched ridges. For $\Delta K < 16.5$ MPa$\sqrt{\text{m}}$, the fatigue striations were not clearly resolved with the SEM and the transmission electron microscope (TEM) replica technique was used extensively. Figures 6 and 7 show low- and high-magnification fractographs for *R*5 at 16.5 MPa$\sqrt{\text{m}}$. All the striation measurements were taken on 8 by 10 in. enlargements of the micrographs in order to obtain maximum accuracy. Note that since the method uses ratios of mean striation spacings, there was no need for tilt corrections. A typical *R*2 program is shown in Fig. 8. The difference in striation spacing between *B* and *A* and *C* blocks is very small, indicating that K_{min} of *B* block is slightly above K_{op}; that is, K_{op} is of the order of $0.2\,K_{max}$.

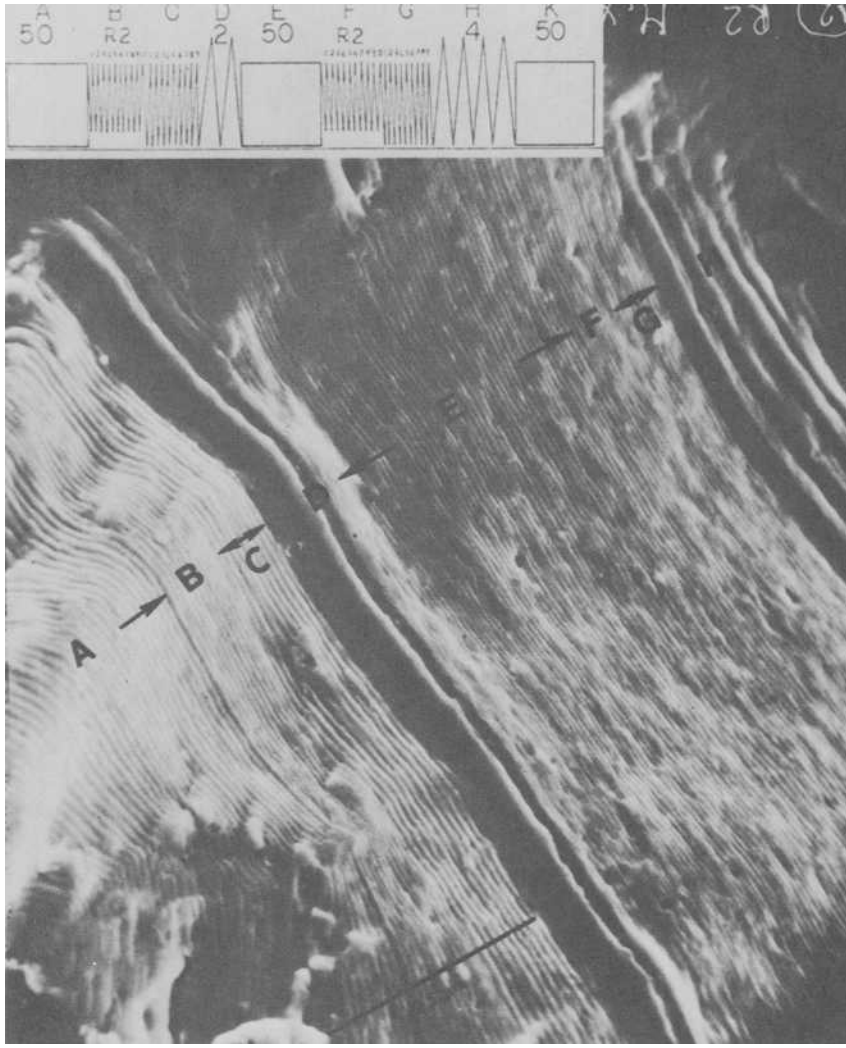

FIG. 5—*An SEM fractograph of* R5 *showing overload blocks* D *and* H.

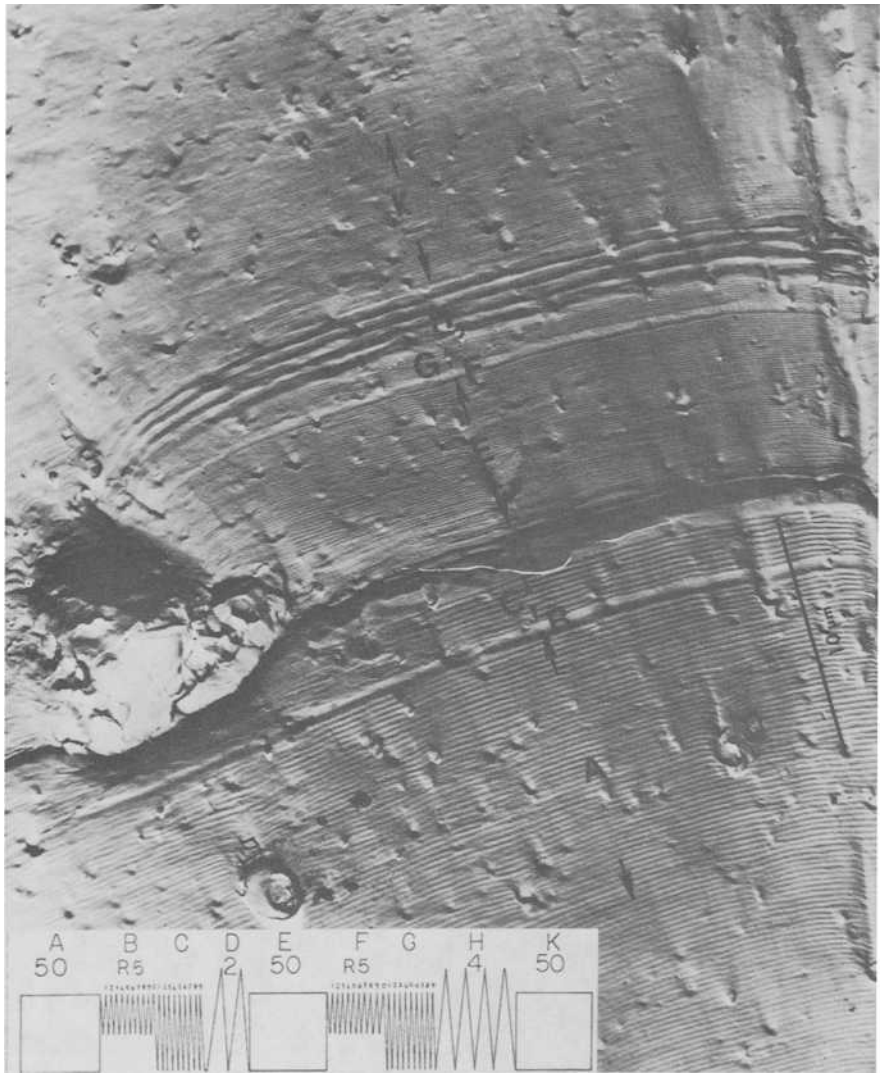

FIG. 6—*A typical* ABCDEFGHK *sequence for* R5 (*TEM replica*—K_{max} = *11 MPa*$\sqrt{m}$).

clearly an increase in K_{op}/K_{max} to a value of 0.3 at the surface and 0.2 in the center of the crack front.

The *T* tests, which measure a K_{op} instead of $K_{closure}$, seem to indicate a high value of K_{op}. For instance, 20 cycles of *B* block with a *T*3 program do not show any striations. It seems that the problem of measuring a K_{op} with the *T* program is related to the number of cycles of the *B* block and the microscopic resolution of the *B* fatigue striations. The tests performed so far

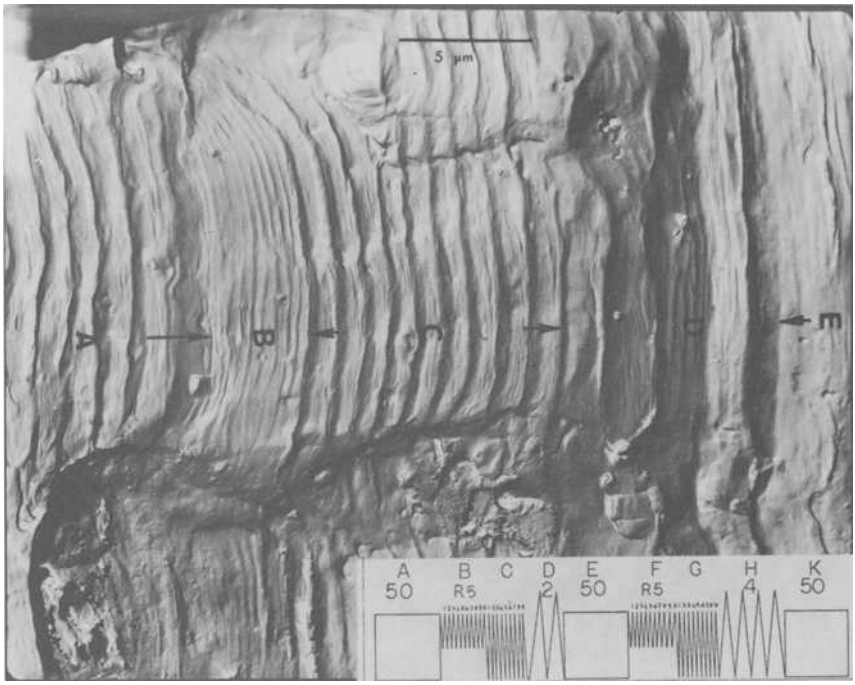

FIG. 7—*A sequence* ABCD *for* R5 (*TEM replica*—$K_{max} = 15.7\ MPa\sqrt{m}$).

had too few cycles in the *B* block of the *T* program. A residual stress effect could also account for the high K_{op} measurements obtained with the *T* programs.

Discussion

The following observations have been made:

The fractographic technique is good enough to show that closure in the plane-strain region of the specimen is very small. Closure in the plane-stress part of the crack front can be detected by the inflection point on the *R*-curves (Fig. 9). We found $K_{closure}/K_{max} < 0.2$ during steady-state crack growth and $K_{closure}/K_{max} \simeq 0.3$ following a 30 percent overload.

The programmed loads fractography technique used to study crack closure is very powerful although it is limited to crack growth rates greater than 5×10^{-6} in. The best application of the technique is its use to verify finite element models of crack growth under programmed loads.

The test results confirm McEvily's model [*7*] that closure is a localized phenomenon associated with stretched ligaments near the surface of the

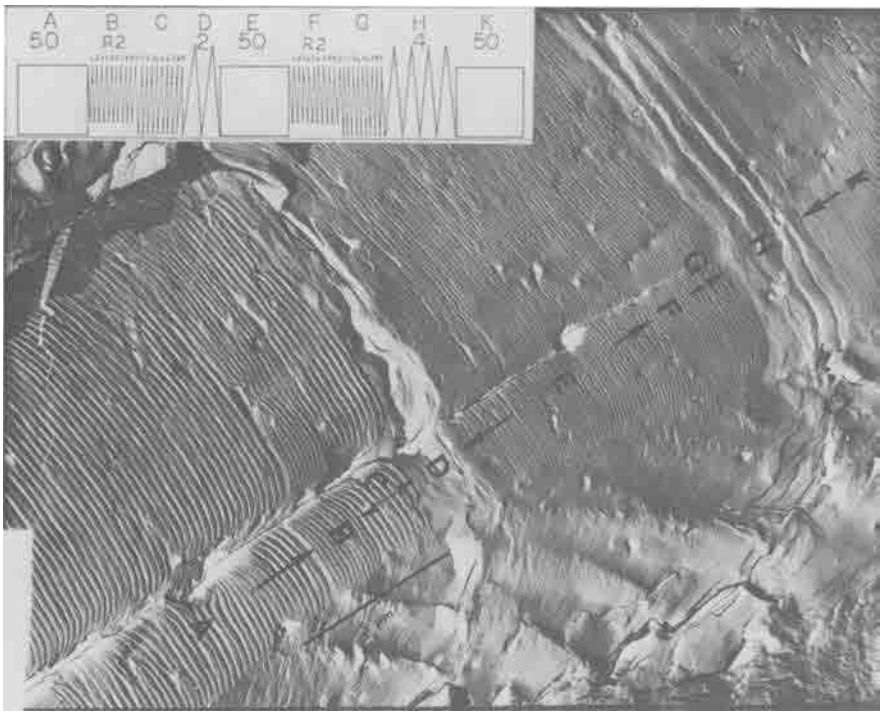

FIG. 8—*A typical sequence* ABCDEFGHK *for* R2 (*TEM replica*—K_{max} = *11 MPa*$\sqrt{m}$).

specimen in the pseudo-plane stress region. Figure 10 is a sketch showing the closure sites as a function of σ/σ_{max}.

The marked difference between the cyclic and monotonic calculations of CTOD is observed with the two cycles of the *D* overloads. The first *D* striation is much larger than the second *D* striation. Microscopic crack retardation measurements following the *D* and *H* overloads have been performed. The results will be reported in a second paper.

Conclusions

1. Fractographic measurements of crack closure show that crack closure is very small in the plane-strain region of a crack tip.

2. Values of $K_{op}/K_{max} < 0.20$ were measured for 2124-T351 aluminum alloy in the range of ΔK-values of 10 MPa$\sqrt{m} < \Delta K < 35$ MPa$\sqrt{m}$.

3. An increase in K_{op} from 0.2 to 0.3 was observed following two cycles of overload of 30 percent above K_{max}.

4. In spite of its limitations the fractographic technique is very useful to investigate the crack tip behavior in the plane strain part of the specimen.

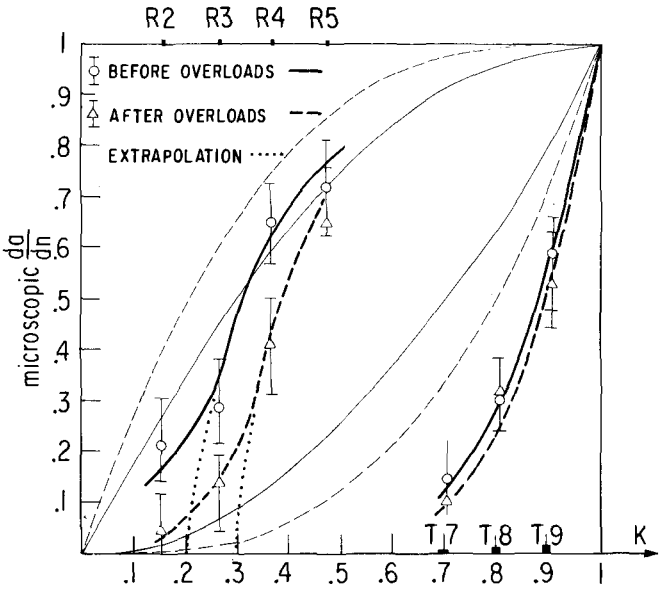

FIG. 9—*Summary of the crack growth rate data for the* R *and* T *programs. The data is reported as* $da/dn_A/da/dn_B$ *for* R *and* T *programs before the overloads* D *and as* $da/dn_F/da/dn_E$ *after the overloads* D.

Acknowledgments

The authors would like to acknowledge the National Science Foundation for their financial support of this research work through the Massachusetts Institute of Technology's Research Center for Materials Science and Engineering. M. Faral was supported by a grant of the French Ministry of Foreign Affairs for the scholastic year 1976 through 1977.

References

[1] Elber, W. in *Damage Tolerance in Aircraft Structures, ASTM STP 486*, American Society for Testing and Materials, 1971, pp. 230-242.

[2] Faral, M., "A Fractographic Study of Crack Closure," M.S. thesis, Massachusetts Institute of Technology, Cambridge, Mass.

[3] Pelloux, R. M., Faral, M., and McGee, W. M., *Fatigue of Engineering Materials and Structures*, Vol. 1, 1979, pp. 21-35.

[4] McMillan, J. C. and Pelloux, R. M. in *Fatigue Crack Propagation, ASTM STP 415*, American Society for Testing and Materials, 1967, pp. 505-532.

[5] Rice, J. R. in *Fatigue Crack Propagation Fatigue, ASTM STP 415*, American Society for Testing and Materials, 1966, p. 247.

[6] Newman, J. C., Jr., in *Mechanics of Crack Growth, ASTM STP 590*, American Society for Testing and Materials, 1976, pp. 281-301.

[7] McEvily, A. J., "Current Aspects of Fatigue," presented at the Fatigue 1977 Conference, University of Cambridge, England, 28-30 March 1977.

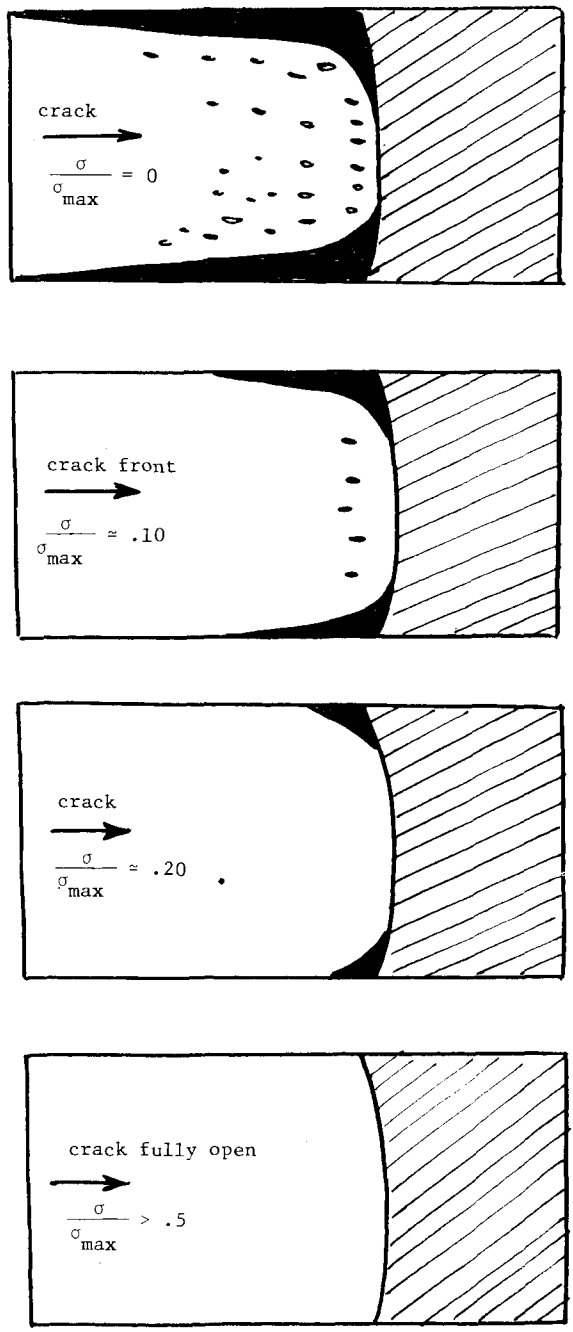

FIG. 10—*Sketch showing the closure contact areas as a function of the ratio* σ/σ_{max} *during opening of the crack.*

R. W. Hertzberg,[1] *M. D. Skibo,*[2] *and J. A. Manson*[1]

Fatigue Crack Propagation in Nylon 66 Blends

REFERENCE: Hertzberg, R. W., Skibo, M. D., and Manson, J. A., **"Fatigue Crack Propagation in Nylon 66 Blends,"** *Fracture Mechanics: Twelfth Conference, ASTM STP 700,* American Society for Testing and Materials, 1980, pp. 49-64.

ABSTRACT: Fatigue crack propagation (FCP) rates were measured in nylon 66, an impact-modified nylon 66, and in blends of the two resins as a function of the stress intensity factor range ΔK and cyclic frequency. Significant reductions in FCP rates were observed with increasing additions of the impact-modified polymer to pure nylon 66, though the relative ranking of the various blends was found to depend on the magnitude of ΔK and test frequency. These differences were related to specimen heating associated with certain blend compositions and high ΔK levels. Crack tip temperatures increased with increasing ΔK level and were as high as 125°C (257°F) in the impact-modified nylon 66 that had been moisture equilibrated at room temperature. Other tests revealed that this material represents the first polymeric solid to exhibit higher fatigue crack growth rates with increasing cyclic frequency.

KEY WORDS: fatigue (materials), crack propagation, fracture mechanics, engineering plastics, hysteretic heating, frequency, impact modification, nylon 66 blends, plasticity corrections, modulus normalization, fractures (materials)

The current demand for light-weight structural materials has directed the attention of component designers to the increasing use of engineering plastics. Though a number of these materials may possess satisfactory tensile strength and modulus, their selection for certain applications has been restricted by their low toughness. Considerable success in overcoming this property deficiency has been achieved through the addition of a rubbery second phase to such amorphous and mesomorphic polymers as polystyrene (PS) and poly(vinyl chloride) (PVC). These materials have been shown to possess superior toughness, resulting from enhanced localized shear banding and crazing [*1,2*].[3] A parallel improvement in fatigue resistance has also

[1] New Jersey Zinc professor and professor of chemistry, respectively, Materials Research Center, Lehigh University, Bethlehem, Pa. 18015.

[2] Formerly, research associate, Materials Research Center, Lehigh University, Bethlehem, Pa. 18015; presently, Sandia Laboratory, Livermore, Calif. 94550.

[3] The italic numbers in brackets refer to the list of references appended to this paper.

been noted [*3–7*]. For example, fatigue crack growth rates in neat PVC have been reduced by as much as two orders of magnitude with the addition of 6 to 14 percent of a methacrylate-butadiene-styrene copolymer (MBS).

Since crystalline polymers as a class are generally stronger and tougher than most amorphous polymer counterparts, including rubber-modified blends, there has been less incentive for the development of an impact-toughened crystalline polymer. Recently, however, an impact-toughened semi-crystalline nylon 66 was introduced by the DuPont Chemical Company with the designation of Zytel ST801. This blend possesses Izod toughness values more than an order of magnitude greater than those exhibited by unmodified nylon 66 in both the wet and dry as-molded conditions [*8*]. In addition, ST801 exhibits pronounced surface lubricity. This latter property is especially desirable in applications involving the need for a minimization of friction such as in mechanical slides and gear drives not requiring oil.

As a result of its superior strength, toughness, and lubricity, this material already is finding application in components subjected to repeated loadings. For this reason, a thorough understanding of the fatigue response of this material is needed. This paper is concerned with an evaluation of the fatigue crack propagation (FCP) behavior of ST801 as well as intermediate blends of ST801 and pure nylon 66. In addition, attention is given to the effect of cyclic frequency on both FCP rates and cyclic lifetimes.

Cyclic frequency was chosen as a major test variable in this investigation based on numerous and conflicting reports of its influence on cyclic life [*9–20*]. On one hand, standard reversed bending experiments conducted with various polymeric solids at 30 Hz, according to ASTM Test for Flexural Fatigue of Plastics by Constant-Amplitude-of-Force (D 671-71), have shown that failures in unnotched specimens can take place by either mechanical or thermal processes. Regarding the latter, cyclic induced hysteretic heating is known to cause specimen softening and eventual melting. Since the rate of hysteretic heating is related directly to the test frequency, an increase in test frequency has been often associated with attenuated fatigue life [*9,10,21*]. By sharp contrast, an entirely different frequency dependence has been observed in fatigue crack propagation experiments involving precracked test specimens. For some polymers, FCP rates decreased with increasing cyclic frequency while in other polymers, FCP rates remained unchanged with different test frequencies [*2,13–20*]. Numerous studies have shown that the beneficial influence associated with fatigue testing at higher cyclic frequencies in some polymers was attributed to a resonant condition between machine test frequency and the jump frequency of segmental motions associated with the β-damping peak [*13–16*]. It has been argued that this damping condition, when localized at the crack tip, leads to crack-tip blunting and associated reduction in FCP rates. Pertinent to this paper, this rationalization of material behavior has been supported

by FCP experiments conducted on rubber modified poly(phenylene oxide) and acrylonitrile-butadiene-styrene. Since no damping information is available regarding Zytel ST801 or blends containing Zytel ST801 and nylon 66, it is not clear what type of frequency sensitivity might be found in these materials. Furthermore, the frequency sensitivity of FCP rates might be expected to depend on the blend ratio with the latter affecting overall damping response.

Experimental Procedures

Most of the materials used in this investigation were received in the form of dry, as-molded plaques (76 by 128 by 7.5 mm) of pure nylon 66 (Zytel 101), Zytel ST801, and blends containing 25, 50, and 75 percent Zytel ST801. These plaques were stored in a dessicator to preclude moisture pickup. In addition, certain tests (description follows) were performed on Zytel ST801, which was moisture equilibrated in laboratory air.

Compact tension fatigue specimens were machined to a width of 61 mm and a height-to-width ratio of 0.6. Initial notches were introduced both parallel and perpendicular to the injection molding direction. After machining, all specimens were stored again in a dessicator except those specimens that had already absorbed moisture.

All fatigue testing was performed on an 8.8-KN MTS machine. To minimize total test time, specimen precracking to initiate a sharp crack from the machined notch was usually carried out at 50 to 100 Hz. In the high concentration ST801 blends, however, this usually resulted in excessive crack tip heating. To eliminate the possibility that this heating might affect subsequent FCP measurements, all specimens were allowed to cool for at least 1 h before actual data collection commenced. Crack propagation data were obtained at test frequencies of 1 to 100 Hz. For the more compliant ST801-nylon 66 blends, the test machine was incapable of supplying sufficient displacement to generate 100 Hz at the desired load. Consequently, these materials were tested at a maximum frequency of 30 to 50 Hz. A traveling microscope was used to make crack length measurements over typical increments of 0.15 to 0.30 mm. The test machine was stopped briefly (usually for a period less than 15 s) for such readings. Crack growth rates were related to the crack tip stress intensity factor range ΔK where $\Delta K = Y\Delta\sigma\sqrt{a}$, and $Y = 29.6 - 185.5\ (a/w) + 655.7\ (a/w)^2 - 1017\ (a/w)^3 + 638.9\ (a/w)^4$. The load ratio R (that is, K_{min}/K_{max}) was held constant at 0.1.

A thermocouple was placed within a test plaque of moisture equilibrated ST801 to permit measurement of the crack tip temperature. A 1.6-mm hole was drilled from the top of the specimen to the plane of the machined notch and about 15 mm from the notch tip. The hole was filled from the

bottom with an epoxy resin using a hypodermic syringe. Before the epoxy resin had cured, the thermocouple was inserted with the junction being located along the anticipated crack plane.

Results and Discussion

Comparative Fatigue Behavior

A series of fatigue tests was conducted to determine the FCP response of dry, as-molded blends of Zytel 101 containing 0, 25, 50, 75, and 100 percent ST801 both parallel and perpendicular to the injection molding direction. Single experiments were conducted on these five materials in each orientation. In addition, some additional data were obtained from other specimens tested at two different test frequencies. No significant variation in FCP rates (less than 20 to 30 percent) as a function of specimen orientation was noted in any of these materials when tested at 10 Hz (Fig. 1). In view of this apparent isotropic response, these data were taken to represent essentially duplicate tests of all five material blends.

Certain trends in fatigue crack propagation behavior are to be noted. The pure nylon 66 polymer (Zytel 101) exhibited a log-log linear relationship between the FCP rate da/dN and the stress intensity factor ΔK. For the ST801-101 blends, a definite break in the curve is noted, corresponding to a change in the dependence of da/dN on ΔK. (Even pure Zytel 801 shows a modest change in slope above $\Delta K \approx 3$ MPa$\sqrt{\text{m}}$.) From Fig. 2 it is seen that the point of inflection, corresponding to the $da/dN - \Delta K$ slope change, decreased to lower ΔK levels with increasing amounts of Zytel 801. All slopes were lower at lower ΔK levels, hereafter referred to as Region I; the slopes were higher at the higher ΔK levels (that is, Region II). It is clearly evident that pure nylon 66 exhibited the highest crack growth rates and hence the poorest fatigue resistance of all the blends. A significant reduction in FCP rates was observed with increasing addition of ST801 to pure nylon 66, though the relative ranking of the various blends was found to depend on the stress intensity factor range ΔK.

The enhancement of fatigue resistance in the rubber-modified crystalline blends is, therefore, similar to that observed in the rubber-modified amorphous plastics as discussed earlier [*5-7*]. At this point it is not clear what micromechanisms are responsible for the attenuated crack growth rates in the ST801 blends. For example, it is possible that the superior fatigue properties of the ST801 blends may have been derived as a direct result of the presence of the toughening second phase or as a result of the very fine nylon 66 spherulite size (less than 1-μm diameter) associated with the ST801 polymer.

During the course of these fatigue experiments, it was observed that the crack-tip region became hot to the touch, particularly at high ΔK levels.

Since the pure ST801 material experienced the greatest amount of heating, an attempt was made to quantify the temperature rise at the crack tip in this polymer. The plaque used in this experiment was moisture-equilibrated at 50 percent relative humidity. The variation in thermocouple temperature readings as a function of the distance between the thermocouple and the advancing crack front is shown in Fig. 3. It is seen that significant specimen heating occurred when the crack tip was as much as 14 mm from the thermocouple location with the temperature rising to 125°C (257°F) when the crack tip reached the location of the embedded temperature probe. (At this point, the stress intensity factor was 3.2 MPa$\sqrt{\text{m}}$.) Research in progress has shown that the specimen crack-tip temperature elevation depends strongly on both moisture content of the nylon 66 and on the amount of ST801 in the blend. For example, dry nylon 66 experienced no crack tip heating, whereas a specimen equilibrated with moisture at 50 percent relative humidity revealed a 15°C (59°F) crack-tip temperature elevation [*22*]. Likewise, the extent of crack-tip heating in dry specimens decreased with decreasing ST801 content from a maximum of 55°C (131°F) in pure ST801 to 5°C (41°F) in the 25 percent ST801 material [*23*]. Though the 125°C (257°F) crack-tip temperature in the moisture equilibrated ST801 specimen probably represents a "worst case" situation, it is clear that all of the dry specimens containing ST801 had experienced varying amounts of hysteretic heating. As a result, the yield strengths and elastic modulii of these specimens would be expected to decrease and adversely affect fatigue resistance.

Other experimental findings provide additional confirmation for the deleterious influence of gross specimen heating on fatigue crack propagation behavior in some of these nylon blends. Transient decreases in FCP rates were noted following any lengthy interruption in specimen cycling. A corresponding increase in specimen stiffness was found with each such rest period. Both observations are consistent with the fact that the specimen should become cooler with prolonged interruption in load cycling. It was also found that FCP rates at 10 Hz in ST801 were higher immediately after having been precracked at 50 Hz as compared with precracking at 10 Hz or after allowing for a suitable rest period following precracking at the higher frequency.

The relative ranking of these nylon blends in terms of their fatigue resistance can now be reexamined in light of the preliminary specimen temperature measurements and other considerations. An attempt has been made to account for the shift in slope of the $da/dN - \Delta K$ plots in terms of a plastic zone correction. In this manner, an effective crack length and associated effective ΔK-value (ΔK_{eff}) can be defined and compared against the effective crack growth rate (also taking into account the change in effective crack length). Since the crack-tip temperature is presumed to increase continuously with increasing ΔK level, the proper choice of the

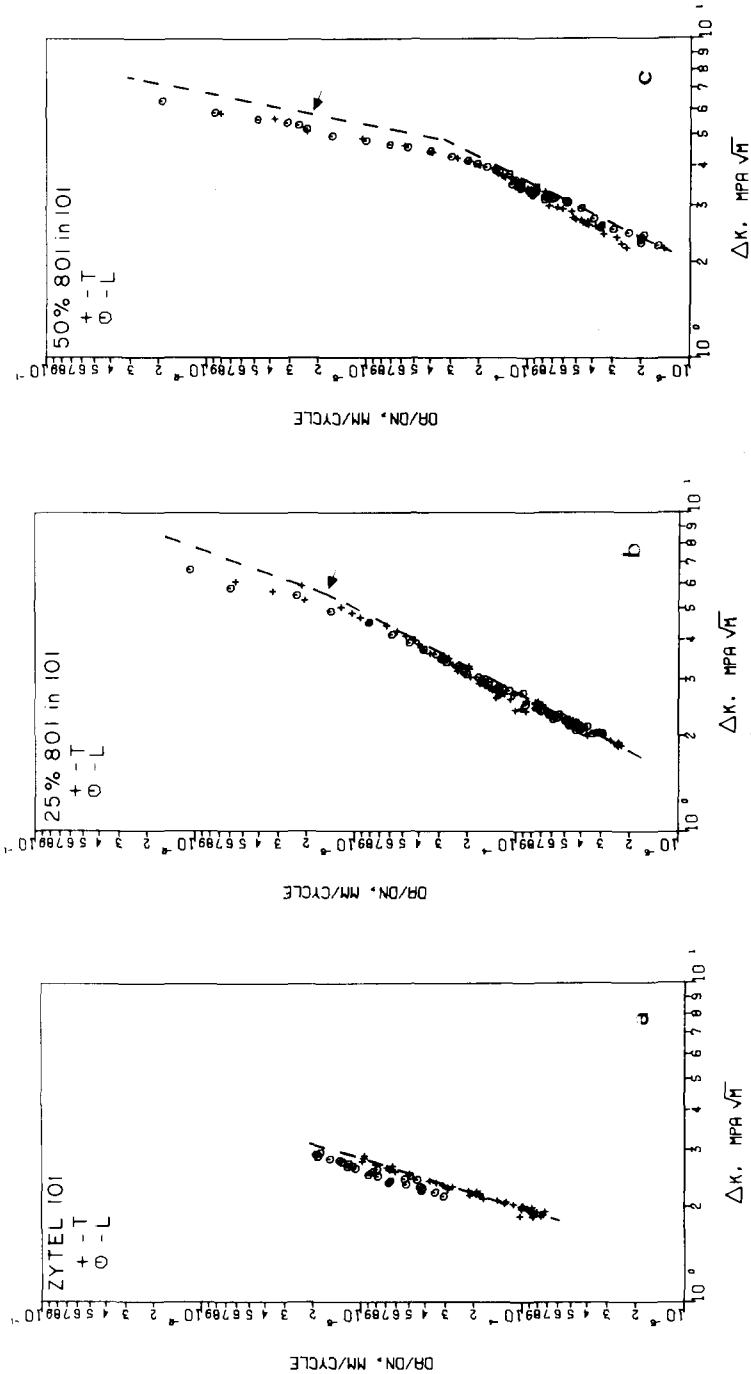
ZYTEL 101
+ - T
⊖ - L
a
50% 80I in 101
+ - T
⊖ - L
c
25% 80I in 101
+ - T
⊖ - L
b
ΔK, MPA √M
DA/DN, MM/CYCLE

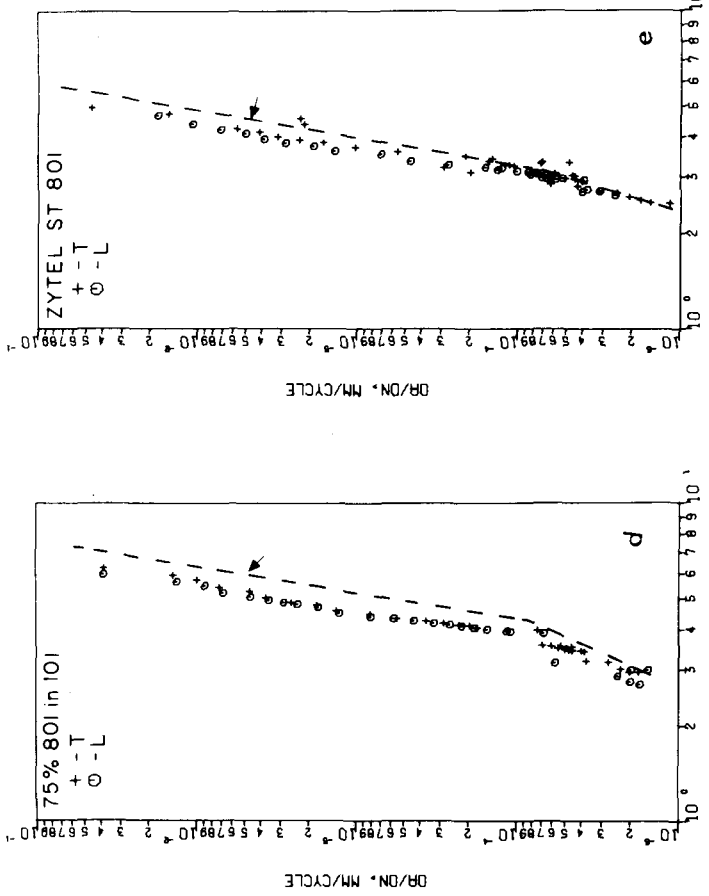

FIG. 1—Fatigue crack propagation in dry nylon 66 blends at 10 Hz—(a) pure nylon 66 (Zytel 101); (b) 25 percent Zytel 801 in 101; (c) 50 percent Zytel 801 in 101; (d) 75 percent Zytel 801 in 101; and (e) pure Zytel 801. Dashed lines represent data corrected for the crack tip plastic zone.

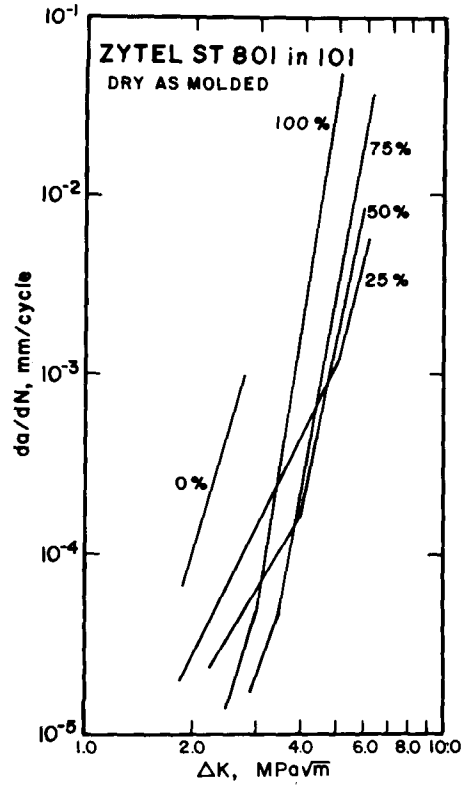

FIG. 2—*Fatigue crack propagation behavior in Zytel 801/101 blends tested at 10 Hz—uncorrected for crack-tip plasticity.*

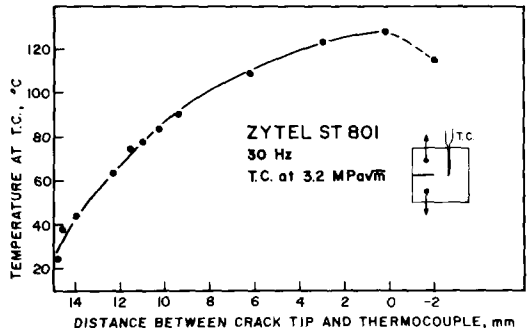

FIG. 3—*Thermocouple temperature as a function of its distance from the crack tip. Specimen moisture equilibrated to 50 percent relative humidity.*

yield strength value for use in the plastic zone size computation is unclear. As a first approximation, room temperature yield strength values for each blend were used for the data corresponding to Region I (from 78 MPa for nylon 66 to 56 MPa for ST801). The yield strengths used to correct the Region II data were based on values corresponding to crack tip temperature measurements from current though incomplete studies (78 MPa for nylon 66 to 42 MPa for ST801). The plastic zone correction was assumed to reflect half of the Dugdale plastic strip dimension (that is, $\pi/16\, K_{max}{}^2/\sigma_{ys}{}^2$). Plastic zone size-corrected data are shown in Fig. 1 as dashed lines. The arrow indicators shown in the ST801 data correspond to a plasticity correction of 15 percent to the applied ΔK-value. Any larger correction at still higher ΔK levels was truncated at a maximum ratio $\Delta K_{eff}/\Delta K_{app} = 1.15$. When these data are compared directly (Fig. 4), it is seen that though the FCP data from the ST801-rich blends are shifted the most, the ranking of the various materials is relatively unchanged.

It is informative also to normalize the FCP data relative to specimen stiffness since crack growth rates are known to increase with decreasing

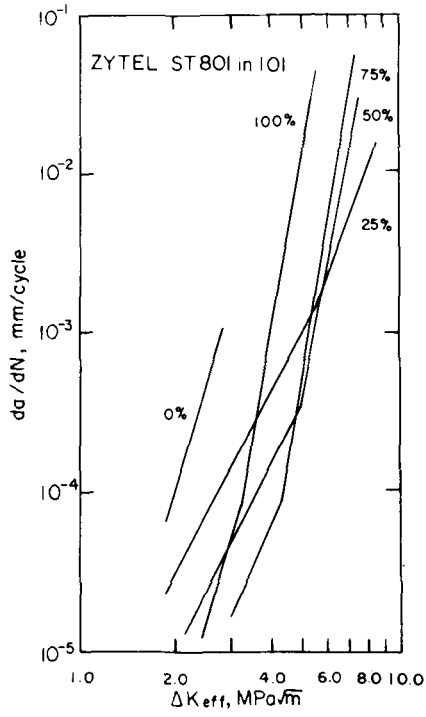

FIG. 4—*Fatigue crack propagation behavior in Zytel 801/101 blends tested at 10 Hz—corrected for plasticity.*

elastic modulus [*3*]. To this end, the crack growth rate curve for each material was normalized by the dynamic modulus for that particular blend. The use of the dynamic modulus rather than the tensile or flexural modulus for the data normalization is based on previous results that showed the elastic modulus of several polymers during fatigue cycling of compact tension specimens to be in agreement with values reported from dynamic mechanical measurements [*24*]. Using a modulus ratio between nylon 66 and pure ST801 of 2.4, based on preliminary measurements by Webler [*25*], the moduli of all blends were assumed to decrease linearly from a value of 4.2 GPa for dry nylon 66 [*24*] to 1.75 GPa for dry ST801. When the $da/dN - \Delta K_{eff}$ results shown in Fig. 4 are normalized by these respective moduli values, it is seen that the ST801 blend is now the most fatigue resistant material examined in this investigation (Fig. 5). Since no data are available to determine the extent of specimen heating during the FCP tests, it was not possible to modify the normalization procedure, using elevated temperature modulus values. From the foregoing computations, we conclude that the relatively poor FCP response of the ST801-rich blends

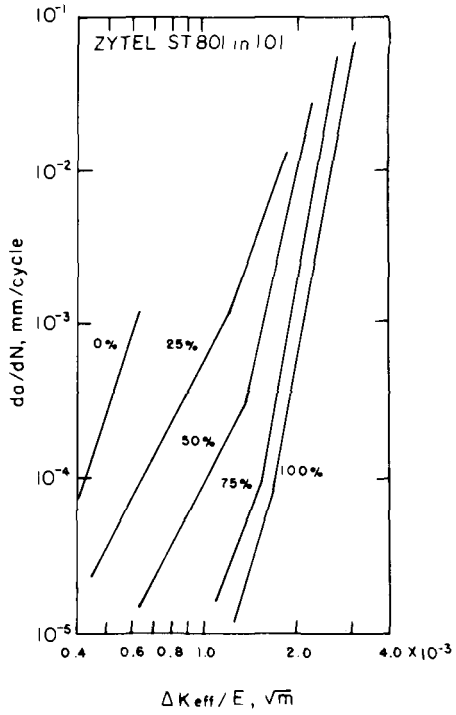

FIG. 5—*Fatigue crack propagation behavior in dry Zytel 801/101 blends. Data corrected for crack-tip plasticity and normalized with respect to elastic modulus.*

in Region II was due to lower yield strengths, which in turn gave rise to larger plastic zones than in the lean ST801 blends and lower elastic modulii, the latter resulting in larger cyclic strains per unit stress intensity level. This situation was aggravated by hysteretic heating-induced further reductions in these two properties.

Since the extent of specimen heating will depend upon such geometrical factors as specimen thickness, specimen planar dimensions and associated stress intensity factor calibration, and net section stress, the relative fatigue performance of the ST801 blends will depend on specimen geometry. For example, some crack-tip heating was generated in a compact tension (CT) specimen whereas a single edge notched (SEN) specimen experienced considerably greater heating across the entire unbroken ligament when tested at a comparable ΔK level. Since the Y-calibration factor for the CT specimen is roughly five times greater than that for the SEN specimen, the gross stress in the SEN specimen would have to be five times greater than a CT specimen of the same crack length. This much higher gross stress in the SEN specimen is believed to be responsible for the observed difference in the extent of specimen heating. As such, one must proceed cautiously when attempting to apply, in a design situation FCP data from the ST801 material if component heating occurs.

Frequency Effects on FCP Response

The pronounced degree of specimen heating measured in ST801 blends at high ΔK levels provides the first opportunity to determine whether FCP rates in a polymeric solid might increase with increasing frequency. As noted earlier, fatigue crack growth rates in all other engineering plastics have either remained unchanged or decreased with increasing test frequency. Any differences between the FCP-frequency sensitivity of the ST801 blends and these other materials may well lie in the much greater degree of damping that takes place within the 801/101 blend crack tip damage zone. In some of these materials, the increase in temperature that takes place in this zone is apparently more intense so as to cause general softening of the specimen. To verify this point, a series of additional fatigue tests were conducted to determine the FCP-frequency sensitivity of nylon blends containing 0, 25, 50, 75, and 100 percent ST801. These experiments were conducted over a frequency range from 1 to 100 Hz with the maximum permissible frequency being dependent on the specific blend and the limitations of the test machine. For example, tests of pure ST801 were conducted at frequencies only as high as 30 Hz since the large compliance of this material did not permit the required test loads to be applied with any greater machine cyclic frequency. The fatigue results for this material are shown in Fig. 6a. Clearly, FCP rates at a given ΔK level are seen to increase with increasing cyclic frequency. ST801, therefore, represents the first polymeric

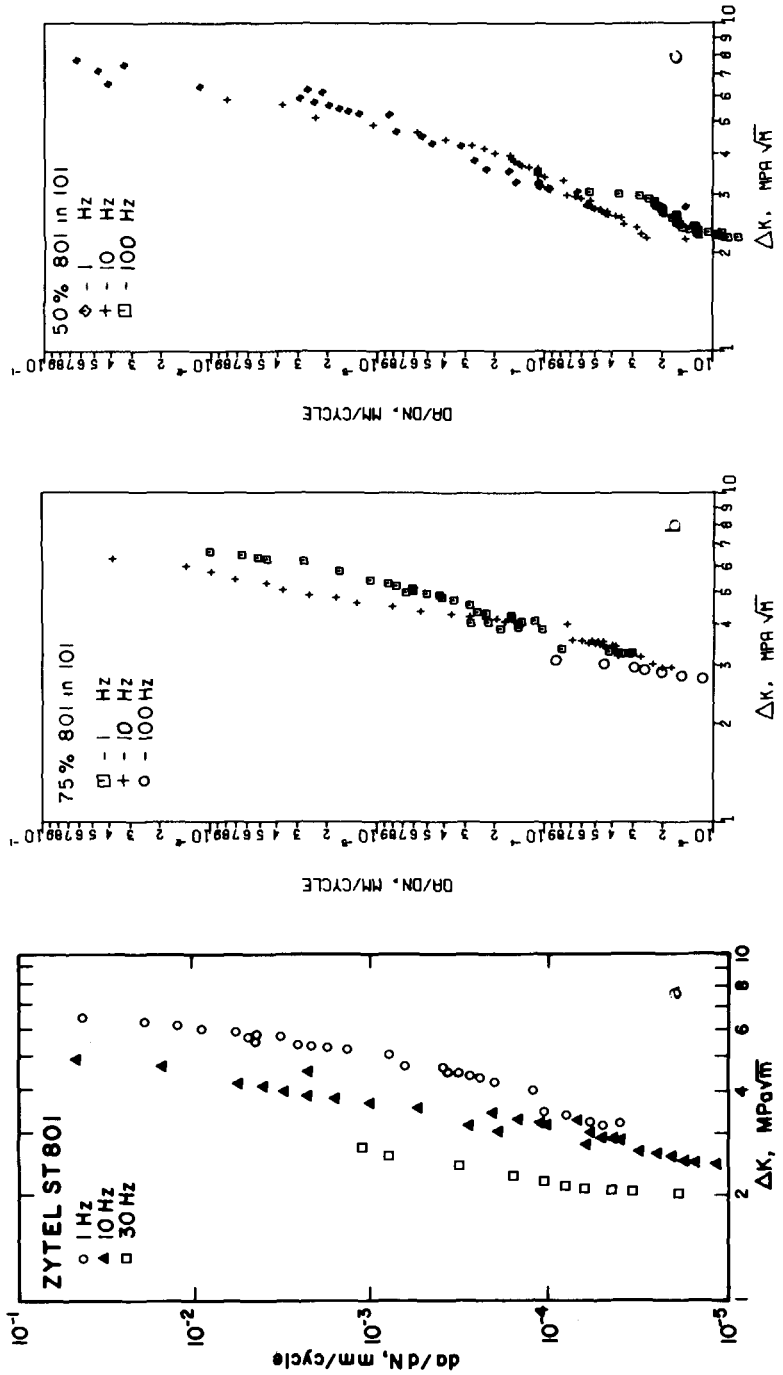
ZYTEL ST 801
1 Hz
10 Hz
30 Hz
da/dN, mm/cycle
ΔK, MPa√m
a
75% 801 in 101
1 Hz
10 Hz
100 Hz
DA/DN, MM/CYCLE
ΔK, MPA √M
b
50% 801 in 101
1 Hz
10 Hz
100 Hz
DA/DN, MM/CYCLE
ΔK, MPA √M
c

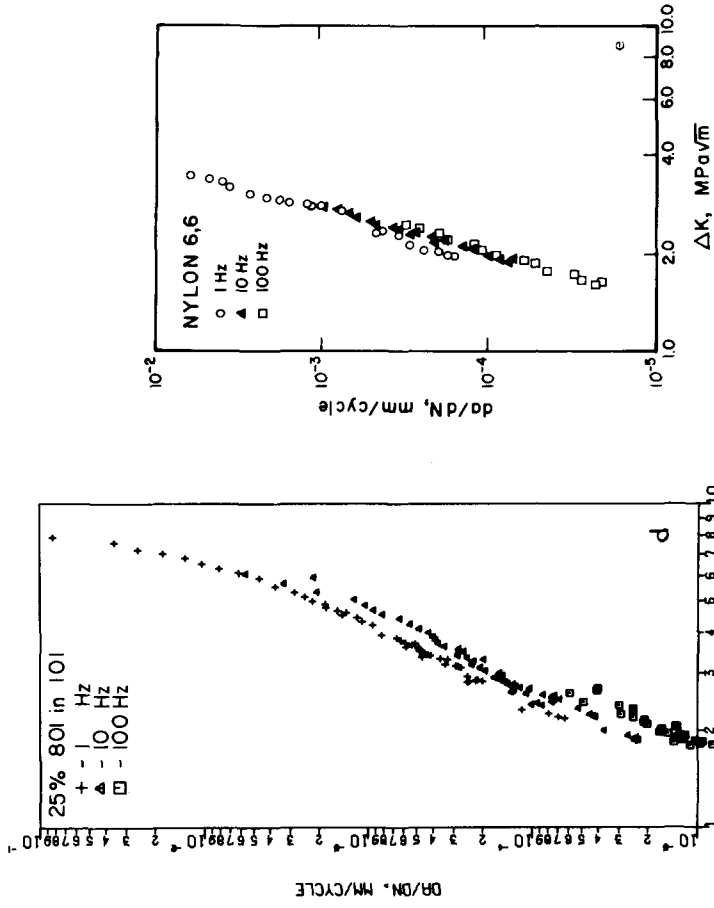

FIG. 6—*Effect of cyclic frequency on fatigue crack propagation response in Zytel 801/101 blends. All specimens tested in the dry as-molded condition except Zytel ST801 1-Hz data, which correspond to moisture equilibration at 50 percent relative humidity.*

solid reported to exhibit higher fatigue crack growth rates with increasing cyclic frequency. As stated above, this behavior is believed to be caused by large-scale crack tip damping that results in appreciable specimen heating. The smaller degree of frequency sensitivity noted at low ΔK levels in this material is attributed to an associated smaller plastic zone size that decreases the amount of hysteretic energy available for specimen heating.

With a 75:25 blend of ST801 and nylon 66, higher crack growth rates again were observed with increasing test frequency, though to a much smaller degree as found with pure ST801 (Fig. 6*b*). This is believed to be related to a lesser amount of damping in this polymer blend. The 50:50 ST801-nylon 66 blend revealed no clearly defined frequency sensitivity, reflecting a balance between the deleterious effect of hysteretic heating induced specimen softening and a beneficial effect of localized crack tip blunting, which acts to decrease the effective ΔK level at the crack tip (Fig. 6*c*). The results shown in Fig. 6*d* suggest that the limited amount of ST801 in the 25:75 ST801-nylon 66 blend serves mainly to blunt the crack and contributes little to overall specimen heating. Consequently, FCP rates are seen to decrease slightly with increasing test frequency, thereby showing this material to behave like a number of other engineering plastics [*3,13-20*]. Lastly, FCP rates in the pure nylon 66 showed no frequency sensitivity in the range from 1 to 100 Hz (Fig. 6*e*) [*13,24*]. As discussed earlier, this insensitivity of FCP rates to cyclic frequency in pure nylon 66 may be attributed to the absence of a resonant condition between machine test frequency and the jump frequency of segmental motions associated with the β-damping peak [*13-16*].

When the results shown in Fig. 2 and 4 are reexamined, it is desirable to separate specimen hysteretic heating effects from fundamental differences in fatigue response among the various nylon blends examined in this investigation. This may be done by making FCP data comparisons at a lower test frequency—say 1 Hz. Such a comparison is made in Fig. 7*a*, where reduced FCP rates are shown to correspond to increasing ST801 content. Note that the greatest influence of ST801 additions on fatigue resistance occurs at lower concentrations and becomes minimal at concentrations greater than 75 percent. This behavior closely parallels results reported previously for the PVC-MBS rubber-modified system [*7*].

As a final note, plastic zone corrections and modulus normalization of these 1-Hz FCP data clearly reveal that ST801 exhibits the greatest fatigue resistance (Fig. 7*b*). The fact that the ST801 fatigue resistance ranks highest when evaluated at 1 Hz as opposed to 10 Hz is attributed to specimen heating and associated loss of stiffness at the higher test frequency.

Conclusions

The fatigue resistance of Zytel ST801 (an impact-toughened nylon 66), nylon 66, and 25, 50, and 75 percent blends of these two compositional

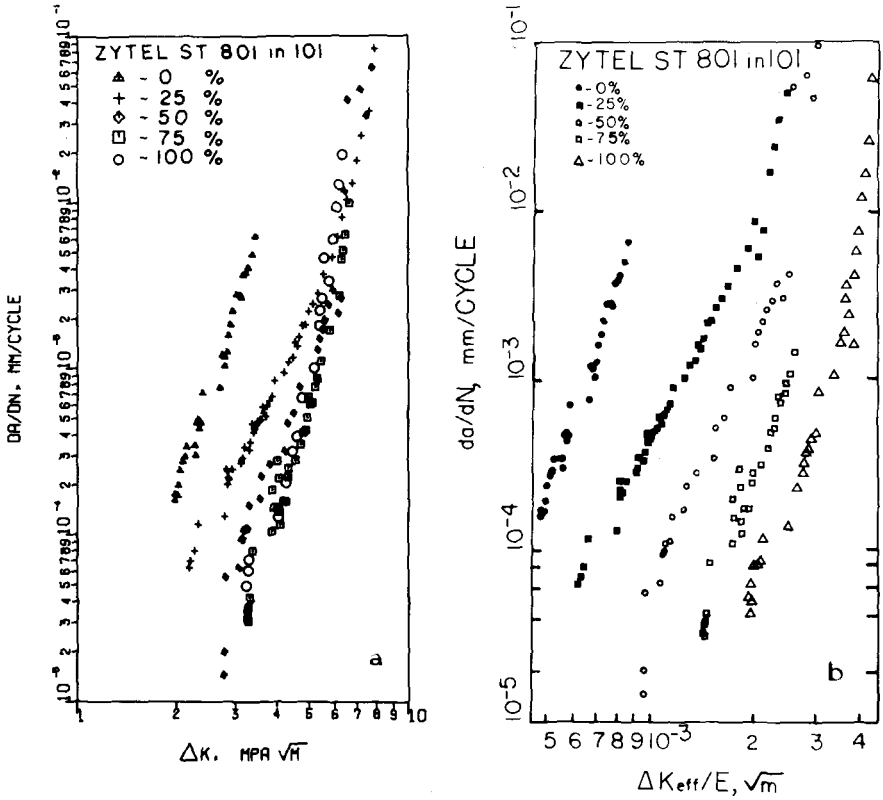

FIG. 7—*Fatigue crack propagation behavior in Zytel 801/101 blends tested at 1 Hz*—(a) *uncorrected data, and* (b) *data corrected for crack tip plasticity and normalized with respect to elastic modulus.*

extremes has been examined with a significant reduction in FCP rates being observed with increasing addition of ST801 to pure nylon 66. The relative ranking of the various blends was found to depend, however, on the stress intensity factor range, ΔK, and test frequency. A considerable degree of hysteretic heating has been noted in blends containing large amounts of ST801 with crack tip temperatures in moisture equilibrated ST801 recorded to be as high as 125°C (257°F). Experiments have shown that FCP rates in ST801 nylon 66 blends either increase, decrease, or remain unchanged as cyclic frequency is increased. By itself, ST801 represents the first polymeric solid reported to exhibit higher fatigue crack growth rates with increasing cyclic frequency. It is proposed that these FCP variations reflect the balance between gross hysteretic heating (which lowers the elastic modulus overall) and crack-tip blunting (due to highly localized heating).

Acknowledgments

This work was supported by funds from the E. I. du Pont deNemours & Co.; The Office of Naval Research; and the Materials Research Center, Lehigh University. The cooperation of E. Flexman, Jr. (du Pont) was especially appreciated along with the experimental assistance of P. E. Bretz, M. T. Hahn, and S. M. Webler.

References

[1] Buchnall, C. B., *Toughened Plastics,* Applied Science Publishers, Ltd., London, 1977.
[2] Manson, J. A. and Sperling, L., *Polymer Blends and Composites,* Plenum Press, New York, 1976.
[3] Manson, J. A. and Hertzberg, R. W., *Critical Review of Macromolecular Science,* Vol. 1, 1973, p. 433.
[4] Manson, J. A. and Hertzberg, R. W., *Journal of Polymer Science and Polymer Physics Education,* Vol. 11, 1973, p. 2483.
[5] Skibo, M. D., Janiszewski, J., Kim, S. L., Hertzberg, R. W., and Manson, J. A., *Society of Plastic Engineers Technical Papers,* Vol. 24, 1978, p. 304.
[6] Skibo, M. D., Janiszewski, J., Hertzberg, R. W., and Manson, J. A., *Proceedings,* International Conference on Toughening of Plastics and Rubber Institute, July 1978, England, p. 25.1.
[7] Skibo, M. D., Manson, J. A., Webler, S. M., Hertzberg, R. W., and Collins, E. A., *ACS Symposium Series,* Vol. 95, American Chemical Society, Washington, D.C., 1979, p. 311.
[8] Flexman, E. A., *Proceedings,* International Conference on Toughening of Plastics, July 1978, England, p. 14.1.
[9] Riddell, M. N., Koo, G. P., and O'Toole, J. L., *Polymer Engineering Science,* Vol. 6, 1966, p. 363.
[10] Koo, G. P., Riddell, M. N., and O'Toole, J. L., *Polymer Engineering Science,* Vol. 7, 1967, p. 182.
[11] Crawford, R. J. and Benham, P. P., *Journal of Material Science,* Vol. 9, 1974, p. 18.
[12] Crawford, R. J. and Benham, P. P., *Journal of Mechanical Engineering Science,* Vol. 16, No. 3, 1974, 1978.
[13] Hertzberg, R. W., Manson, J. A., and Skibo, M. D., *Polymer Engineering Science,* Vol. 15, No. 4, 1975, p. 252.
[14] Manson, J. A., Hertzberg, R. W., Kim, S. L., and Skibo, M. D., *Polymer,* Vol. 16, 1976, p. 479.
[15] Skibo, M. D., Hertzberg, R. W., and Manson, J. A., *Proceedings,* 4th International Conference on Fracture, June 1977, University of Waterloo Press, Waterloo, Canada, p. 1127.
[16] Hertzberg, R. W., Manson, J. A., and Skibo, M. D., *Polymer,* Vol. 19, 1978, p. 359.
[17] Waters, N. E., *Journal of Material Science,* Vol. 1, 1966, p. 354.
[18] Mukherjee, B. and Burns, D. J., *Polymer Engineering Science,* Vol. 11, 1971, p. 433.
[19] Hertzberg, R. W. and Manson, J. A., *Journal of Material Science,* Vol. 8, 1973, p. 1554.
[20] Arad, S., Radon, J. C., Culver, L. E., *Journal of Mechanical Engineering Science,* Vol. 13, 1971, p. 75.
[21] Ferry, J. D., *Viscoelastic Properties of Polymers,* Wiley, New York, 1961.
[22] Bretz, P. E., unpublished research.
[23] Hahn, M. T., unpublished research.
[24] Hertzberg, R. W., Skibo, M. D., Manson, J. A., and Donald, J. K., *Journal of Material Science,* Vol. 14, 1979, p. 1754.
[25] Webler, S., unpublished research.

B. N. Leis[1] *and Akram Zahoor*[1]

Cyclic Inelastic Deformation Aspects of Fatigue-Crack-Growth Analysis

REFERENCE: Leis, B. N. and Zahoor, Akram, **"Cyclic Inelastic Deformation Aspects of Fatigue-Crack-Growth Analysis,"** *Fracture Mechanics: Twelfth Conference, ASTM STP 700,* American Society for Testing and Materials, 1980, pp. 65-96.

ABSTRACT: The objective of this paper is to examine the general utility of a *J*-based analysis of cyclic plasticity aspects in fatigue-crack growth. Preliminary analysis of data which indicates *J* may be appropriate is reviewed, and it is shown that these data represent a unique test case where cyclic plasticity aspects may be inconsequential. Details of the *J*-integral are elaborated in the sense of possible limitations to the usefulness of the deformation theory in applications to cyclic plasticity. The phenomenology of fatigue crack growth under variable amplitude loading is reviewed, and residual deformations and stresses at the crack tip and in the wake of the crack are identified as essential features of the history dependent flow process associated with crack growth. Each of these aspects is elaborated and discussed with regard to the use of a single characterizing parameter; first for stationary, then for growing cracks. It is observed and concluded that *J* controlled near field (J_{NF}) must be used on a cycle-by-cycle basis if a *J* based analysis is to potentially account for cyclic plasticity. A number of crucial analytical and experimental tests of the ability of *J* (J_{NF}) to adequately characterize these effects are enumerated. It is also concluded that the use of a single parameter *J* based analysis for fatigue-crack-growth assessment in structures subjected to variable amplitude loading may be tenuous.

KEY WORDS: J-integral, cyclic plasticity, *J* near field, fatigue crack growth, deformation theory, fractures (materials), crack propagation

The last twenty years have been witness to a renaissance in the design-analysis philosophies and technologies related to the structural fatigue damage process. Toward the end of the 1950s, Paris et al [*1,2*][2] made use of the formalization of Irwin [*3,4*] that characterized the linear elastic near crack-tip stress field to describe the fatigue crack growth rate in tension panels. Somewhat later, in the early 1960s, Smith [*5*] introduced the concept

[1]Principal and research scientist, respectively, Battelle Columbus Laboratories, Columbus, Ohio 43201.

[2]The italic numbers in brackets refer to the list of references appended to this paper.

that fatigue life was controlled by local stresses and strains and pointed out the importance of notch root residual stresses. Some years later, these thoughts were echoed by Grover [*6*] and thereafter by Crews and Hardrath [*7*] in 1966 and by Topper et al [*8*] in 1968, the latter suggesting the local stress-strain approach in the context of Neubers' [*9*] rule. In 1968, Rice [*10*] (and others, for example, see Ref *11*), introduced the concept of a path independent (J) integral that was advanced as being useful to describe the nonlinear near crack-tip field. Also in 1968, Neuber [*12*] demonstrated that the near field surrounding a crack-like defect obeyed the same form of relationship derived for notches. Finally, in that same year, Hutchinson [*13*], and Rice and Rosengren [*14*], developed descriptions of the plastic stress-strain fields for power-law hardening materials in the context of tension loaded center cracked (Mode I) panels.

The first noted analytical developments were derived and presented in the restricted and rigorous framework associated with continuum mechanics analyses. These developments have nevertheless been adapted to the solution of a broad range of practical problems. Paris et al [*1,2*], Schijve et al [*15*], and Topper et al [*8*] etc., postulated two basic technologies in the context of these developments. These authors utilized parametric forms extracted from the rigorous mechanics in conjunction with the assumption that such parameters establish similitude between the damage rate process in a structure and that operative in a reference data base [*16*]. One of these technologies [*8*] sought to assess the damage rate in terms of crack nucleation using small diameter smooth specimens. The second [*1,2,15*] sought the prediction of crack growth using data developed from sharply flawed geometries. Both technologies therefore, facilitated the use of simply developed test data to assess the damage rate in a structure.

The just noted nucleation and growth technologies have evolved along divergent paths until recently. The nucleation technology utilized a nonlinear, history dependent approach to assess damage at notch roots and other fatigue critical locations. A nonlinear approach was adopted largely as a consequence of test data for notched coupons that showed nominal stress based (linear elastic) analysis failed to account for local residual stresses developed during a preload cycle in otherwise constant amplitude cycling (for example, see Ref *16*). On the other hand, carried by early successful correlation of constant amplitude data and the simplicity of linear elastic mechanics as compared to nonlinear solutions, the crack growth technology focused on linear elastic characterization of the driving force for crack growth, elastic stress intensity factor, K. More recently, because of inherent limitations in linear elastic fracture mechanics (LEFM) analysis in situations where either the near crack-tip plasticity is not so confined or the flow process and the displacement field in the wake of the crack exhibit a history dependence due to variable amplitude cycling, there has been a tendency towards inelastic measures such as the J-integral for fatigue crack growth analysis.

The purpose of this paper is to assess the utility of single parameter fields such as J-integral to characterize the inelastic flow process during fatigue crack growth. In so doing, the tie between the idealized rigorous mechanics of this flow process and the practicalities of the history dependent crack growth process is examined. Consider this tie in the context of Fig. 1 which schematically depicts the role of logic and models in the evolution of engineering analysis. Note that the deductive logic, rigorous mathematics, and rational mechanics of the applied mechanics discipline are transformed into useful and practical physical models for engineering analysis through inductive logic and sometimes arbitrary postulates. Often this inductive logic and the arbitrary postulates begin as rational speculation initiated and substantiated by experiments and observation. With a view to Fig. 1, this paper discusses the assumptions inherent in nonlinear mechanics analysis in the context of the phenomenology of damage and, through inductive logic and postulates, examines the applicability of the analysis in terms of appropriate experimental results. Because many of the issues considered relate to the history dependence of the plastic flow process, analogies will be drawn with the corresponding problems in the now well developed nonlinear nucleation analyses [*17-19*].

Specifically, the paper concentrates on a J-integral analysis of fatigue crack growth, since related preliminary data correlation is encouraging [*20*]. First, the fundamental postulate that some measure of J relates one to one with an increment of crack advance is examined in terms of current observations. Of particular concern here is the assumption of similitude in the damage rate processes made when the rate process in some laboratory test is used to assess the damage rate in a structure or other specimen geometry. Next, the phenomenology of fatigue crack nucleation and growth is examined to show that both can be considered to be a consequence of reversed plasticity. Because both share a common mechanism, observations related to the history dependence of the flow process in nucleation analysis can be used later to help resolve corresponding problems in propagation analyses.

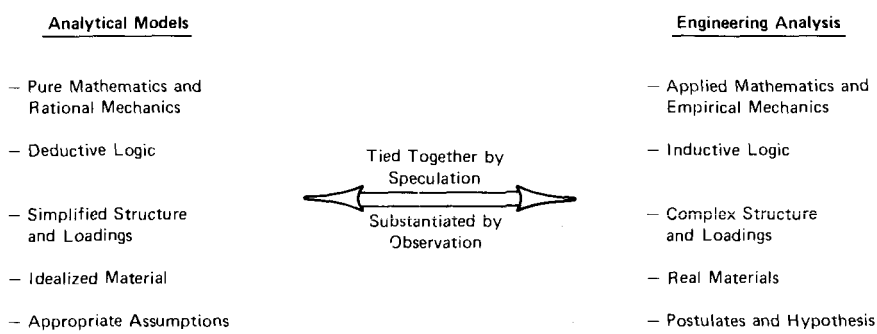

FIG. 1—*Role of logic and mechanics in developing engineering analysis.*

Thereafter, inelastic fields in cracked domains are discussed in terms of the J-integral and the related assumptions of the deformation theory are elaborated; both stationary and growing cracks being considered. Then the cyclic inelastic flow process in singly and multiple connected domains is elaborated, and an approach, which facilitates the use of the deformation theory to model this process, is advanced, discussed, and demonstrated as being useful in the context of stationary cracks. A rational definition for the range of J; ΔJ, follows directly from these considerations. Problems associated with the growing cracks are then examined. Finally, critical analytical and experimental tests of the general utility of J to deal with fatigue crack growth analysis which follow from this consideration of both stationary and growing cracks are elaborated.

J Based Correlation of Fatigue Crack Growth Rate Data

Over the last decade, several authors have addressed fatigue crack growth analysis under, or near, limit load-displacement cycling. Early efforts [*21*] centered around the inelastic stress-strain intensity concept introduced by Neuber in 1968 [*12*] and by others [*13,22*]. More recently, interest has focused on the use of a J based analysis [*20,23,24*]. The form of these descriptions of the near crack-tip field can be shown to be comparable. Not surprisingly then, data correlation on either basis yields comparable results. As shown in Fig. 2, reproduced from Ref *20*, the degree of consolidation achieved using such inelastic parameters is remarkable at least for crack growth in laboratory samples under a cyclic history with a monotonically increasing peak cyclic value of J.

Several open questions remain regarding the consolidation shown in Fig. 2. To what extent is this correlation a consequence of the character of history imposed? That is, can any general conclusions be drawn in view of this correlation of data developed for a cyclic history with a monotonically increasing peak value of J? Also, how can one apply the results of this correlation to the analysis of crack growth in structural geometrics subjected to other constant or variable amplitude histories? That is, what requirements must be imposed to establish similitude between the damage rate process in this test data and that in other components subjected to other loadings?

There are two central issues examined by such questions. First, under what circumstances can a deformation theory crack tip characterizing parameter like J be used in cyclic loadings? Second, given a correlation such as in Fig. 2, which suggests a one to one correspondence between some measure of J and fatigue crack growth rate, what requirements must be imposed to ensure similitude between the damage processes being compared? If such are necessary, will these requirements be so restrictive that data, such as in the figure, will have no general utility? Both central issues will be examined in this paper.

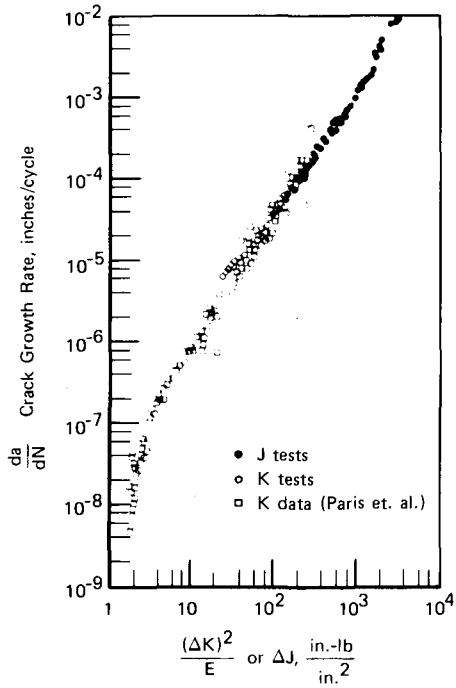

FIG. 2—*Correlation of fatigue crack growth data in terms of* J *and* K [20].

Before passing to further consideration of these questions, some comment on the approximate and preliminary nature of the data analysis of Fig. 2 appears appropriate. First, a deep-crack compliance based approach was used to estimate the maximum value of J associated with crack opening, J_{max}. This formula was applied in situations where the remaining ligament supports other than bending stresses. Thus, there may be some question as to the interpretation and accuracy of J. Second, this formulation was applied, for a portion of the data correlated, in situations where the apparent value of J_{Ic} for the material was significantly exceeded so that their stationary crack value of J_{max} neglects the decrease in J_{max} due to stable tearing at the crack tip. Indeed, it is quite remarkable that this tearing, coupled with fatigue crack advance (two crack advance mechanisms), are correlated by the value of J_{max}.

Such problems aside (as Paris has noted "Mother Nature is not too harsh after all" [*25*]), the definition of ΔJ of Dowling and Begley [*20*] does consolidate these data. With regard to Fig. 3, also reproduced from Ref *20*, note from Part (*a*) of the figure that the ratio of the minimum to maximum loads changes from cycle to cycle (that is, R changes in a LEFM-ΔK context). But more importantly, Part (*b*) shows that the value of J_{max} (or ΔJ) increases on

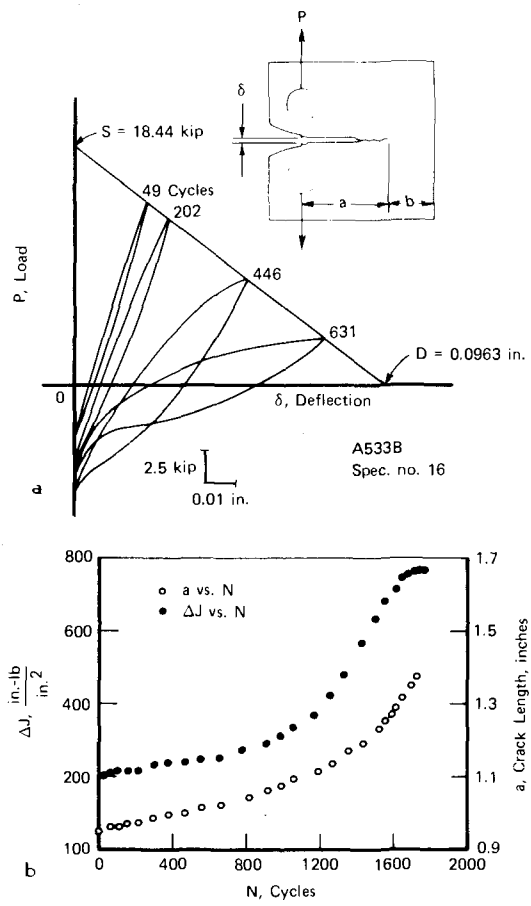

FIG. 3—*Aspects of a* J *based analysis for fatigue crack growth* [20]—(a) *load versus deflection hysteresis loops during deflection control to a sloping line; and* (b) *variation with cycles of crack length and* J.

each cycle. The question might be asked of this and other such data consolidations [*23,24*]—does J (ΔJ) work because its value is monotonically increasing as in its successful applications to elastic plastic crack initiation in fracture toughness testing? (That is, does ΔJ work because prior cyclic near tip history is wiped out on each new cycle?) If so, these data represent a unique test history that may be of limited direct significance either in attempts to develop fatigue crack growth rate data in the region of general yielding, or in demonstrating the utility of J in fatigue crack growth analysis. That it is essential to account for such history effects may be inferred by analogy to their significance in nonlinear nucleation analysis [*19,26*]. But before this analogy is ascribed significance, it must be shown that fatigue crack nucleation and growth share a common mechanism, as discussed next.

Phenomenology of Fatigue Crack Nucleation and Growth

The fatigue damage process can be considered as the coupled action of cyclic inelastic strain and tensile stress. It is considered to occur in the uniform section of a low cycle fatigue (LCF) test specimen or at a crack tip. That is, an element of material suffering fatigue damage does not know if it is in a smooth LCF specimen, at a notch root, or at a crack tip. (However, it does suffer different damage rates that pertain to the geometry and its location within it.) Several authors have presented microstructural evidence which support this posture. Laird [*27*] has indicated that the mechanical response of the LCF specimen is a macroscopic measure of the reversed plasticity damage process leading to nucleation. Thus, variables such as stress and strain which depict mechanical response may serve as measures of the reversed slip damage process during nucleation. Comparable to nucleation, Neumann [*28*], Broek [*29*], and others indicate the growth of nucleated cracks is a geometric consequence of slip. As such, during crack growth, measures of the propensity to slip (near crack tip stress and strain) or the extent of slip (changes in crack tip geometry or position) may serve as near crack tip measures of the crack growth process [*30*].

In view of the foregoing, the key point is that nucleation and growth share a common mechanism so that understanding gained in modeling nucleation can be brought to bear, by analogy, to models of growth. Given that nucleation and growth share a common mechanism, it follows that the need to define nucleation and growth regimes is artificial in a micromechanics sense. It has, however, been convenient to introduce such a division because the total damage process spans a scale from angstroms to meters—ten (or more) orders of magnitude. Indeed, the above noted two basic technologies evolved largely for this reason. (That is to say, the macromechanics which deal with macrogrowth in the context of a homogeneous isotropic media cannot be expected to deal with the failure process that leads to slip band decohesion and nucleation. Similarly, the macromechanics that deal with nucleation cannot be expected to deal with failure at the atomic scale.)

The two just noted basic technologies, therefore, find their application to artificial phases of the total damage process by virtue of the data base used to calibrate them. One, the LCF geometry, emphasizes nucleation and the associated damage process. The other, the fatigue crack growth (FCG) geometry emphasizes the macrogrowth damage process. Neither explicitly models the damage process that occurs, rather they utilize parametric forms that reflect this process and must therefore be calibrated using test data.[3] Both basic technologies assume that if the damage processes are similar in different components, the damage rate in one can be assessed using data

[3]It is significant to note that many authors have postulated apparently successful models of constant amplitude fatigue crack growth based on LCF concepts [*31*]. Others have successfully formulated models of LCF behavior based on FCG analysis [*24*]. Such formulations often compare closely; what differs are the empirical constants and their values.

developed from the other. As noted earlier, some circumstances under which this similitude between damage processes is difficult to achieve due to inelastic (history dependent) action will be elaborated in terms of the J based near-tip stress-strain measures of the propensity to slip discussed in the next section.

Stress-Strain Fields in Cracked Domains

Several reviews exist that document the nature of the inelastic stress-strain field in a cracked domain. Early reviews [*32,33*] have concentrated on antiplane problems. Subsequent reviews [*34*] have addressed inplane problems in power-hardening materials in the context of the deformation theory of plasticity. Because in the present, the authors consider fatigue crack growth where crack extension increments are small in a given cycle, the near-tip field is examined in the sense of small strains and rotations. This is not to say that such a field exists at a propagating crack tip. Rather it is done in the spirit that such a field may, through parametric representation, characterize the driving force for crack growth. In this respect, it is presumed that inadequacies in this representation are geometry independent and occur to the same extent from crack tip to crack tip in a given material. As noted earlier, if such is the case, the increment in crack advance is uniquely characterized by the parameter and is simply determined by calibration tests. For the linear elastic case, K [*3*] is such a parameter.

Near Crack-Tip Field and the J-Integral

For present purposes, suffice it to state that near tip stress and strain fields[4] can be characterized [*13,14*] with reference to Fig. 4 by

$$\sigma_{ij} = \sigma_o \left(\frac{J}{\mathrm{r}\,\sigma_o\epsilon_o}\right)^{\mathrm{n}/(\mathrm{n}+1)} f_{ij}(\theta,n)$$

$$e_{ij} = \epsilon_o \left(\frac{J}{\mathrm{r}\,\sigma_o\epsilon_o}\right)^{1/(\mathrm{n}+1)} g_{ij}(\theta,n) \qquad (1)$$

The nomenclature is defined in Fig. 4 except for $g_{ij}(\theta,n)$ and $\mathrm{f}_{ij}(\theta,n)$, which are universal functions of θ that depend only on n, and for J, which denotes the J-integral [*10*] which is a measure of the dominant singularity at the crack tip. McClintock [*35*] suggested the form of Eq 1 with regard to the work of Refs *10* and *13*.

[4]The term near field is taken herein to mean the dominantly proportional field characterized by J.

The integral J is defined with a view to Fig. 5 as

$$J = \oint_\Gamma \left(W dx_2 - n_j \sigma_{ij} \frac{\partial u_i}{\partial x_j} \, ds \right) \tag{2}$$

for two dimensional problems. In the equation, $n_j\sigma_{ij}$ is the traction vector defined by the outward normal n_j to the contour Γ, ds is an increment of distance along the contour, u_i is the displacement vector, and W is given by

$$W = W(\epsilon_{ij}) = \int_o^{\epsilon_{ij}} \sigma_{pq} \, d\epsilon_{pq} \tag{3}$$

Again in the context of the deformation theory, J can be defined with reference to Fig. 6 as [*10,34*]

$$\mathrm{J} = - \frac{\partial (U/B)}{\partial a} = - \int \frac{\partial P}{\partial a} \cdot d\delta_p = \int \frac{\partial \delta_p}{\partial a} \cdot dP \tag{4}$$

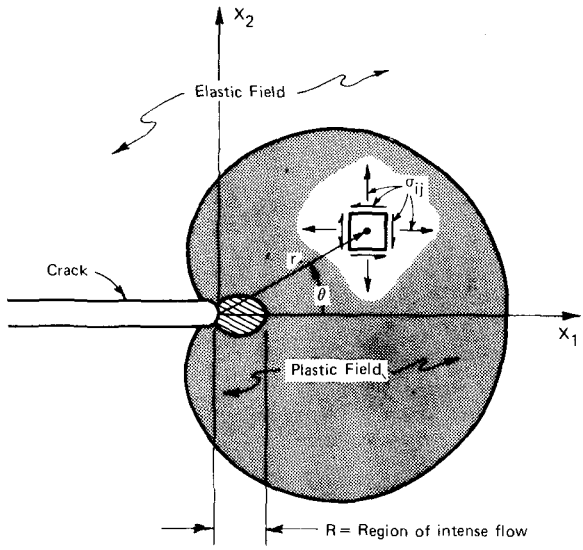

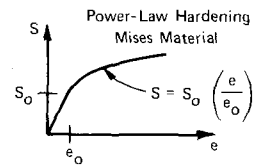

FIG. 4—*Elastic plastic field in relation to* J.

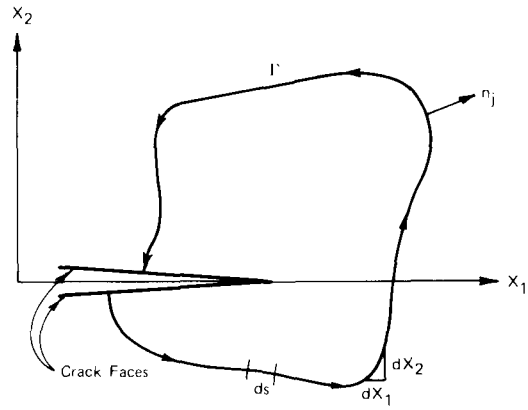

FIG. 5—*Notation related to* J.

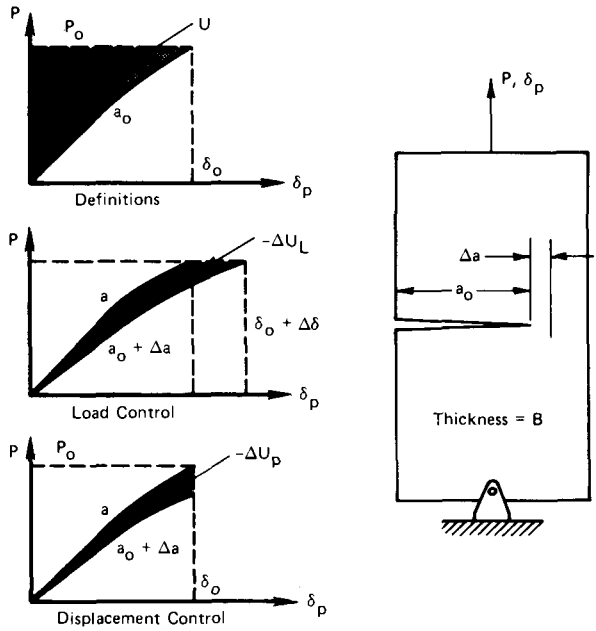

FIG. 6—*Potential energy interpretation of* J.

In this equation U/B is the potential energy normalized per unit thickness. Under limit load conditions, $\partial P/\partial a$ is constant, so that

$$J = -\frac{\partial P}{\partial a}\delta_p \tag{5}$$

for displacement control. In cracked domains characterized by a single length dimension involving the crack size, Rice et al [*36*] have shown that J in Eq 4 can be evaluated in terms of a pseudo-potential energy defined as the work producing displacement of the load due only to the presence of the crack. Thus, with a view to Fig. 7

$$J = \frac{2}{Bb} \times \text{area} \tag{6}$$

Restrictions to Ensure the Validity of J

J is defined in the context of the deformation theory and as such is subject to certain restrictions. Most notably, $W(\epsilon_{ij})$ is a path independent function so that in a plasticity sense, the loading must be monotonic and

$$\epsilon_{ij}{}^{p} = \lambda S_{ij} \tag{7}$$

where $\epsilon_{ij}{}^{p}$ is the plastic part of the total strain tensor, $\epsilon_{ij}{}^{t}$, ($\epsilon_{ij}{}^{t} = \epsilon_{ij}{}^{e} + \epsilon_{ij}{}^{p}$, $\epsilon_{ij}{}^{e}$ = elastic part), S_{ij} is the deviatoric stress tensor, and λ is a scalar proportionality factor. Also J is defined in terms of small strains and rotations, so that the region of intense plastification at the crack tip is not inherent in J. If the single parameter J is to characterize the fracture process, the near field must be dominant, that is, the flow process must be J controlled [*37*]. Related to this is the issue of path independence. McMeeking's [*38*] conclusion is that J is effectively path independent within the region where small strain theory is applicable. But, as noted by Rice [*39*], situations where prior

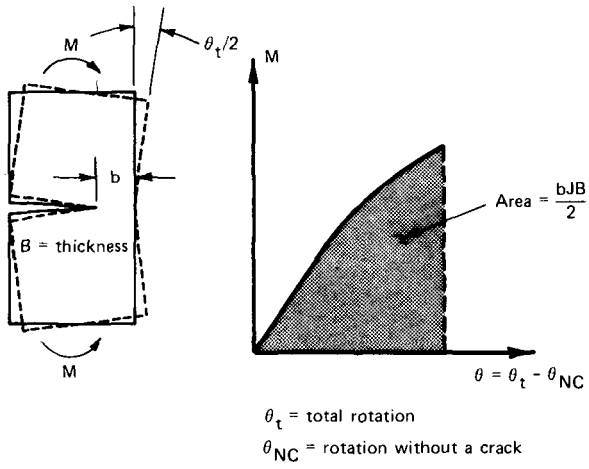

FIG. 7—*Evaluation of* J *for a deeply cracked beam.*

cycling (as in fatigue) introduces residual stresses could lead to path dependence at distances that are large compared to the crack tip opening displacement (CTOD).

There are also limitations to the utility of a parameter defined for stationary cracks subjected to monotonic loadings when extended to applications where the crack advances and the loading is cyclic, as in the fatigue crack growth process examined here. One must first define a range of J, ΔJ, that is consistent with both LEFM and the cyclic control condition. Given such a definition, one must also establish the increment of crack growth over which the driving force for growth is characterized by J for the crack's initial position. These issues are elaborated on, in turn, by analogy to crack advance under monotonically increasing load in the following.

Clearly, the applicability of the J-integral rests on how well the assumptions of the deformation theory of plasticity are justified for the problem under consideration, which as noted above requires proportional stressing throughout the body. Under monotonically increasing load or load-point displacement, crack growth invariably involves unloading at the trailing portion of the advancing crack tip and some nonproportional loading. (Cyclic loading gives rise to cyclic plasticity and its residual effect on the crack tip which in turn creates a more complex stress-strain field and nonproportional loading.) Unfortunately, it is rather difficult to quantify these effects in terms of crack tip characterizing parameters like J at this time. Fortunately, however, the strict requirements of the deformation theory, can be somewhat relaxed in some circumstances [*40*].

The satisfaction of Drucker's [*41*] basic requirements (inequalities) for a strain hardening material may be assumed as the basis for justification for such relaxation. For example, a consequence of Drucker's inequality on positive work requirements for a yield surface which is not smooth (no unique normal) is that the strain rate, $d\epsilon_{ij}^{p}$, must merely point towards the convex region bounded by the cone of normals to the yield surface [*40*]. Deformation theory may still be used for further successive plastic deformation as long as the strain vector, $d\epsilon_{ij}^{p}$, points toward the convex region and is bounded by normals to the yield surface at the point. It is in this spirit, that even though departure from proportional strains may occur, the J-integral may be used as the crack-tip characterizing parameter given that other restrictions, such as those just set forth, are imposed.

Restrictions, postulated in the context of crack growth under monotonically increasing load or load-point displacement, regarding the existence of predominantly proportional strain [*37*] may be interpreted for fatigue crack growth if the effects of cyclic plasticity, crack growth, etc., can be viewed as resulting in a region of nonproportional strains. If after N number of cycles of fatigue loading, the region of proportional strains dominate, that is to say if predominantly proportional strains still exist, then J will still control the damage process occurring at the crack tip. By analogy to Ref *37*, the

dominance of proportional strains requires that (*a*) the crack growth, *da*, should be small compared to the characteristic length of the region controlled by the singular crack tip field, Eq 1, and (*b*) the parameter

$$\omega = \frac{dJ}{da} \cdot \frac{b}{J} \gg 1 \tag{8}$$

where

dJ = the increment of J in N number of cycles,
J = the maximum value of J in N cycles,
da = the crack growth in N cycles, and
b = the remaining ligament.

The lowest value of ω which ensures the dominance of proportional field is not known yet. But, ω-values as low as ten have been found to work well for stable crack growth under monotonically increasing load or load point-displacements. For fatigue crack growth, the lower limit on ω has to be found experimentally.

Consider now the operational definition of the range of J, ΔJ, for fatigue loading. For a given material and type of constraint ahead of the crack tip, J can be expressed as a function of applied load and crack length (Eq 4). Under monotonically increasing P or δ, there exists a unique value of J. However, if the same equation is applied for a loading-unloading cycle in a spectrum, the value of J will not be unique because it will depend on the past history of cyclic plastification. In order to account for the hysteresis effects which will vary from one situation to another (for example, a laboratory specimen to a real structure) it then becomes necessary to define J on cycle by cycle basis, which in turn means that the stress-strain field left over from the previous cycle should be incorporated in the next cycle. Moreover, during crack growth, the contribution to J due to the increment in da should be included. In fatigue crack growth, the contribution of this term is small in a cycle, but may become significant over an accumulated number of cycles. Finally, the problem of bifurcation in the force displacement path due to crack closure must be also addressed.

Each of the just noted restrictions on the validity of the deformation theory, the cyclic uniqueness of J, and the issues related to J based similitude in the damage rate process, are dealt with after the next section.

Having defined the formalism to characterize the near tip field in terms of Fig. 1, the applied mechanics description of the idealized problem, the physical reality that must be characterized in an engineering analysis of the problem will be presented in the following section. Thereafter, these two will be tied together through inductive logic and postulates substantiated by observation and then problems in evolving the rigorous mechanics to deal

with plasticity aspects of fatigue crack growth will be identified and discussed.

Cyclic Plasticity in Cracked Domains

Phenomenology

If attention is limited to a conservative (linear) system, Eq 1 indicates the $1/r$ singularity in the product of stress and strain, for the nonlinear case appears as the usual $1/\sqrt{r}$ in either stress or strain found for LEFM. As a consequence of the linear elastic response, it follows from Eq 1 that

$$J = \frac{\alpha K^2}{E} = G \tag{9}$$

where

α = 1 for plane stress and $1 - \nu^2$ for plane strain, and
G = the Griffith energy.

Equation 9 is considered valid into the region of confined flow since such a restriction is imposed on K. Clearly, however, the equation only has meaning in a practical sense so long as K establishes similitude between cracked bodies. Similitude in the sense of LEFM leads naturally to a restriction on the ratio of plastic zone size to crack size and other relevant dimensions of the cracked body. Likewise it requires that the fields through and into which the crack grows are comparable. As such, load histories that lead to different elastic-plastic distributions of stress and strain preclude the use of the single parameter K to define these distributions. Thus, while the far field stresses and crack geometries may be identical (identical K), K provides a unique characterization of stress-strain fields only if the loading histories are also identical; it is likewise for a far field assessment of the near field through the presumed path independence of the J-integral. Such a point may seem trivial in the context of fracture criteria, and indeed it is since the loadings increase monotonically. It also may seem trivial for cyclic (fatigue) loadings if the cyclic histories do not create residual fields that differ.[5]

To be ascribed any general utility in fatigue crack growth data correlation or in analysis of crack in structural configurations, a J based analysis must be capable of accounting for history dependence. Thus, the problem arises:

[5]It might be noted in this regard that the correlation of the fatigue data by Dowling [*20*] was found for cyclically increasing ΔJ histories, some values of which were well above J_{Ic} for the material examined. It should be emphasized that previous successes with fatigue crack growth data correlation for near limit load cycling using an inelastic stress intensity [*21*] have been achieved only in the context of a constant amplitude history.

given one can suitably define a range in J for fatigue tests, how does one account for differences in the history in the structure as compared to that in the reference data base developed in the laboratory sample.[6] Differences in the history between the laboratory idealization of constant amplitude cycling and service loadings are apparent as retardation, crack closure, etc., in LEFM analysis. These effects are a manifestation of current plastic action on the near tip stress-strain field and of current and prior plastic flow on the force displacement field both ahead and in the wake of the crack. A variety of phenomenological observations clearly indicate the significant impact of these plasticity related consequences on the growth rate [*42*]. Likewise, the material ahead of the crack plastic zone undergoes cyclic damage that may change the microstructure as compared to constant amplitude. Similitude in this complex scenario may be difficult to approximate if not impossible to achieve. The extent to which it is achieved may not be important for histories that erase the effects of prior plastic action. But for histories that involve a range of applied stresses or blocks of small and large stresses, the growth rate at lower levels will be sensitive to microstructural preconditioning [*43*].

Consider this phenomenology in the context of similitude between damage processes; one is a reference state and the other occurs in some other test specimen or in a structural component. For a reference state such as that represented by the data in Fig. 2, some numerical value of J relates to a history independent flow process in a cracked domain which, except in its latter stages at large crack sizes, reflects limited closure of the crack faces. Furthermore, the range of J presented on the abscissa has been defined in a fashion that attempts to circumvent closure problems, consistent with the requirement that the work producing displacement be due only to the presence of an open crack. For this range of J to relate uniquely to crack growth, it is necessary that J be computed in accordance with a definition that is valid for the problem at hand, the computed value of J uniquely reflects the near field, and the material at the tips of two fields with equal J possess a statistically equivalent resistance to crack growth.

The present paper addresses only the validity and uniqueness of J, leaving the third aspect of microstructural preconditioning for subsequent examination. These two will be examined in remaining segments of this section. Cyclic plasticity in gradient fields will be examined in terms of recent experimental and analytical studies [*19,26,44*]. The analogy between these studies and the response of cracked domains will be developed for stationary cracks in terms of both force-displacement and stress-strain fields.

Cyclic Plastic Flow in Gradient Fields

The just noted factors occur at crack tips and are a consequence of the gradient due to the crack. If the crack is far removed from other stress raisers that

[6]Dowling expressly avoided such effects ([*20*], p. 95).

may elevate K (or J) as compared to a cracked panel, then the gradient is due solely to the crack. To the extent that crack advance is small in fatigue loadings as compared to elastic plastic fracture, some insight as to the plasticity at a crack tip can be gained from a consideration of that at a notch root. For such purposes the crack is presumed stationary.[7] Of course, because the flow at the crack tip is more confined, near tip constraint is not reflected to the same extent. The flow processes at cracks and notches may, however, be analogous. This section will examine this analogy in the context of models of the gradient fields developed in nonlinear analyses for crack nucleation, for example, Ref *19*.

Notch Analogy to a Stationary Crack

Linear elastic approaches to assess crack advance (LEFM ΔK; Refs *1,2,15,16*) and crack nucleation (LEFM $\Delta K/\sqrt{\rho}$; Ref *45*) equate the damage rate to a parameter that is linear in far field stress. Thus, the damage rate is postulated as being directly proportional to the far field stress. Nonlinear analysis for crack nucleation, however, estimates the damage rate in terms of the far field stress transformed into critical location measures of damage, then damage is assessed. Thus, in contrast to linear approaches that involve a single step to assess damage, nonlinear nucleation analysis involves two steps. It will now be demonstrated that the first of these nonlinear transformations, illustrated in Fig. 8, must be applied on a reversal-by-reversal basis if the merits of nonlinear analyses are to be exploited. By analogy, it will be postulated that J must likewise be applied reversal by reversal if the utility of this nonlinear parameter is to be exploited fully in fatigue crack growth analysis.

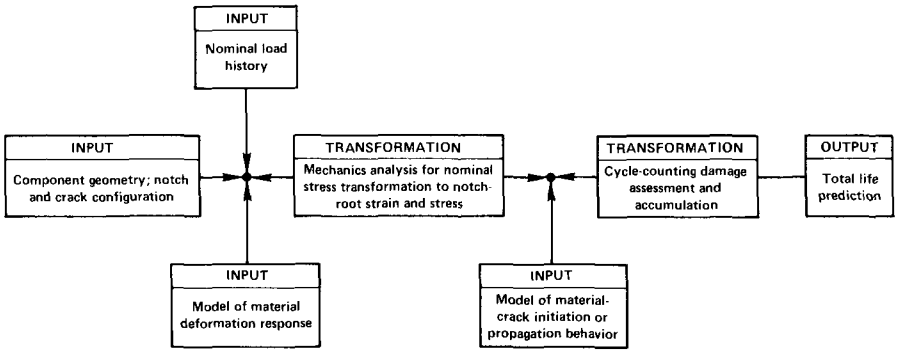

FIG. 8—*Essential features in the direct fatigue-analysis procedure.*

[7]The assumption of a stationary crack may not be physically realistic. If on one reversal the crack grows out of the J-controlled regime or extensive unloading occurs, the utility of J as a characterizing parameter is questionable. For other situations, the assumption of the stationary crack does not impact on the analogy drawn.

The analogy is developed first in terms of the deformation response of an element of material loaded uniaxially and subjected to a variable amplitude strain sequence, as shown in Fig. 9*a*. With reference to the figure, note that such hysteresis typically exhibits the many transient responses characteristic of metals subjected to cyclic load identified in Part *b* of the figure. Constant amplitude transients, cyclic hardening-softening and cyclic relaxation (the counterpart of cyclic creep in load control), have been identified and modeled since the 1950s and 1960s, respectively. Memory, the term applied to the material's repository for prior inelastic strain sequences, is illustrated in Part *c* of this figure. The notion of memory has been identified in rheological studies since the 1950s. The response shown in Part *a* can be simulated in a very simple way if the memory is accounted for. Such uniaxial models can be extended to multiaxial behavior through the introduction of equivalence criteria, but again memory must be accounted for in these models.

Models to simulate responses such as that of Fig. 9*a* have been postulated in the context of the deformation theory [*9,26,44*] and, as evident in Fig. 10*a*, are quite accurate. The essence of these models is that a unique relationship between stresses, σ_{ij}, and strains, ϵ_{ij}, exists in six dimensional stress and strain spaces for either ranges or amplitudes, provided that hysteresis segments defined by these relationships are established from reversal end point to reversal end point and memory is accounted for in the models. On a given reversal, the loading is monotonically increasing in view of the sign convention of Fig. 10*b*. Such a path is characterized by a form that embodies Eq 7, which may be stated as

$$\sigma = \mathbf{f}(\epsilon) \tag{10}$$

On a given reversal, such a path could be also expressed in terms of potential functions

$$\epsilon = \frac{\partial \phi(\sigma)}{\partial \sigma}, \qquad \sigma = \frac{\partial \psi(\epsilon)}{\partial \epsilon} \tag{11a}$$

$$\phi(\sigma) = \int_O^\sigma \epsilon d\sigma \quad \text{and} \quad \psi(\epsilon) = \int_O^\epsilon \sigma d\epsilon \tag{11b}$$

Equations 11*a* and *b* are strictly valid for conservative systems in the same sense that J has been derived. (See Eqs 2, 3, and 7.) The essential point is that equations of this form have been successfully applied in engineering models of cyclic stress-strain response. This success follows, however, only when the equations are applied cycle by cycle and memory is accounted for in the models.

To draw an analogy between the above cycle-by-cycle application of the

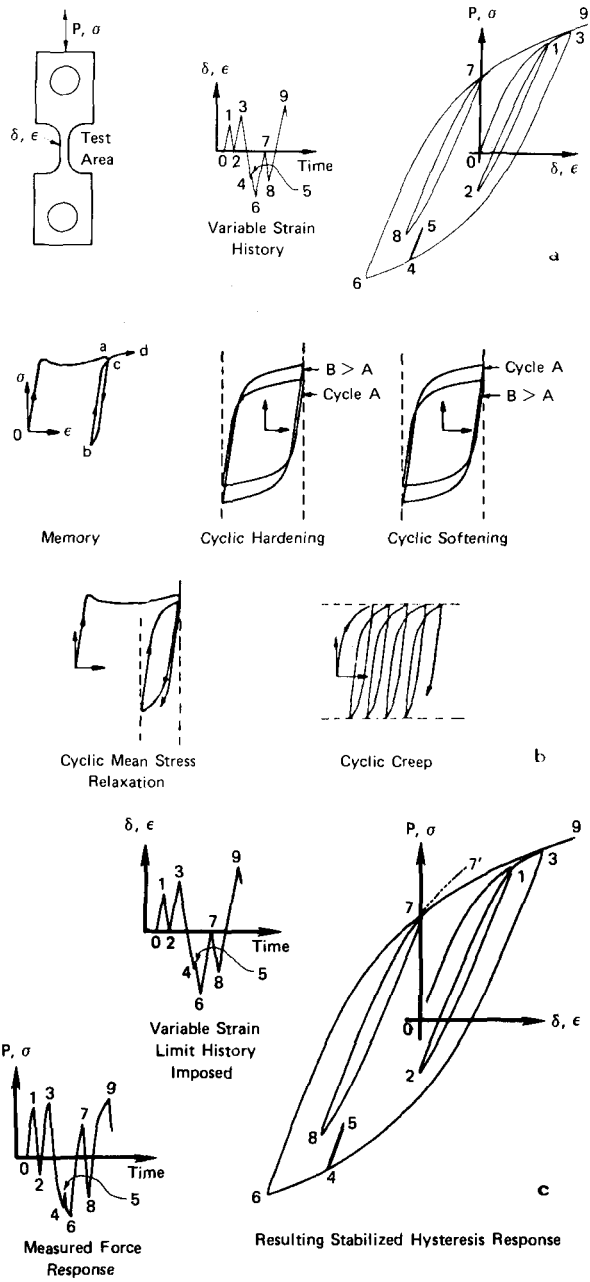

FIG. 9—*Essential features of the cyclic plastic flow process*—(a) *hysteresis in the cyclic plastic flow process for a uniaxial sample;* (b) *cyclic inelastic material deformation behavior; and* (c) *illustration of memory of prior plastic deformation.*

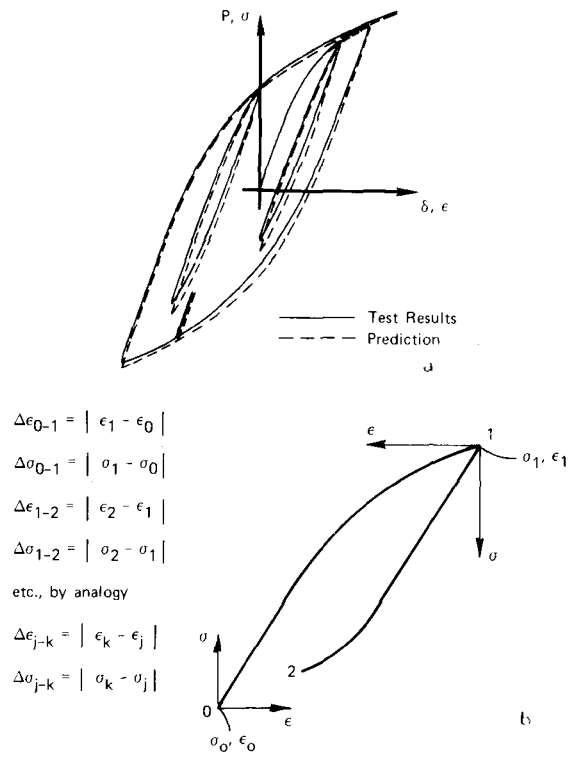

FIG. 10—*Modeling of cyclic plastic flow process*—(a) *prediction superposed on test results for a beam in pure bending* (*after Ref* 19); *and* (b) *sign convention for loop segments.*

deformation theory and application of J requires the existence of similar functions at the scale of the cracked domain (compare Eq 3). Therefore, consider next the force-displacement response of a doubly connected domain, a circularly notched plate, results for which are shown in Fig. 11*a*. Note from this figure that the force-displacement response exhibits the same character as that developed in stress-strain space for a similar forcing function (compare Figs. 9*a* and 10*a*). That is to say, the character of the response in stress-strain space is conserved in this particular transition from material element to structure.[8]

In view of the foregoing, for the class of structures and loadings represented in Fig. 11*a*, the force-displacement response apparently can be stated as potential functions analogous to Eqs 11*a* and *b* as long as the segments defined by these relationships are assembled in accordance with the structures memory of prior inelastic flow. Thus, by analogy to Eqs 11*a* and *b*,

[8]This has been demonstrated for a variety of model structures [*19*].

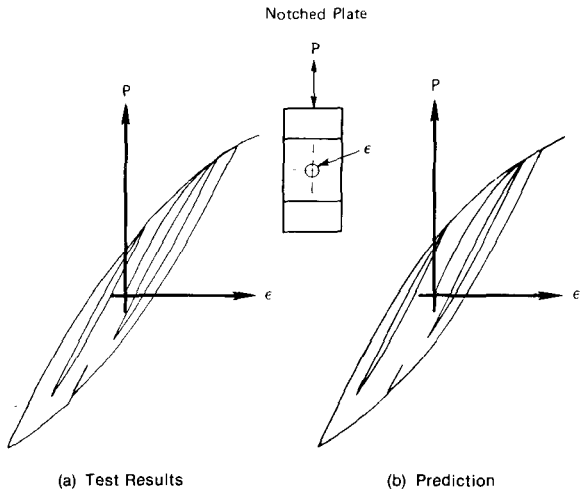

FIG. 11—*Comparison of the predicted and measured far field force-local strain response for a notched plate subjected to variable amplitude loading (after Ref* 19).

segments of the force-displacement response shown in Fig. 11*a* can be expressed in the general form

$$\underline{P} = \underline{F(\Delta)} \tag{12}$$

With regard to Fig. 11*b*, note that when hysteresis segments are defined by Eq 12 and coupled together in accordance with the materials (structures) memory for prior inelastic flow, the response in Part (*a*) of the figure can be accurately simulated. The key point here is that potential functions such as Eqs 3 and 10 through 12 can be utilized in engineering models of the force displacement response of a doubly connected domain. Care must, however, be taken to apply this deformation theory on a reversal-by-reversal basis consistent with the concept of memory; otherwise, deformation theory will, in general, lead to significantly erroneous predictions. It follows then by analogy that J must be likewise applied on a reversal-by-reversal basis if this deformation theory is to prove useful in fatigue crack growth analysis.

Note that the force displacement response just discussed involves a far field (nominal) force and the displacements integrated over a short gage length for an element of material at the notch root. The question arises—does the response in all elements follow such a function and is this response unique? Recent work [*19,46*] suggests that, if the strains and rotations are small, bifurcation and global instability are precluded, the external loading is proportional, and the material is cyclically stable, all material elements are pro-

portionally stressed and deform in-phase with the loading.[9] In such cases, the force displacement relationships expressed as potential functions are postulated as being unique. Of course, numerically different functions exist for different material elements. With regard to cracked domains and J, such functions are postulated as being unique for a stationary crack outside the zone of intense plastic flow. Such functions are dependent strongly on the crack size in the same way that they depend on the notch configuration. For propagating cracks, such functions are postulated as being unique so long as unloading occuring during extension is not significant. This, of course, limits the extension on a given reversal.

Consider in view of the foregoing, the evaluation of J based on its pseudo-potential energy interpretation. As given earlier in Eq 4, J can be interpreted as the potential energy difference between two identically loaded specimens of unit thickness having neighboring crack sizes [*10*]: $J = -\partial U/\partial a$. With respect to Fig. 6, the $P - \delta$ relationships involved are unique in the context of the preceding discussion. (Since such an approach to evaluate J is valid regardless of the extent of the elastic-plastic field or the size of the crack, care must be taken to use the work associated with the crack, (that is, $\delta_{\text{crack}} = \delta_{\text{total}} - \delta_{\text{no crack}}$.) Consequently, unique values of Jda or J for the case of certain deep crack configurations are found as a function of load and crack length from compliance techniques [*36,47,48*]. Now, in the case of fatigue cycling, the range J would sensibly be equal to

$$\Delta J = |J_1 - J_0| \tag{13}$$

along a given segment, where J_0 and J_1 are the values of J at the end points of the $P - \delta$ segment as illustrated in Fig. 12. As indicated in the figure, the near field value of ΔJ is equal to $J_{\max}$ over a given cycle.

Whereas Eq 12 defines hysteresis paths that are geometrically similar for both ascending and descending paths, such paths are not always obtained in the force-displacement response of cracked domains. Indeed as evident in Fig. 3*a*, bifurcation in these paths does occur due to crack closure and concomitant load transfer across these faces during both loading and unloading. As noted earlier, such bifurcation invalidates the use of deformation theory for models of notch response such as that in Fig. 11.

Clearly closure and the associated bifurcation indicate J is not globally path independent. But the utility of J in such cases is not contingent on global path independence. It does, however, require that J be, to an engineering approximation path, independent in a portion of the cracked

[9]In multiaxial states, such relationships exist only in the sense of postulated equivalence quantities. Principal strains and stresses computed from equivalent strains do not necessarily satisfy equilibrium or compatibility.

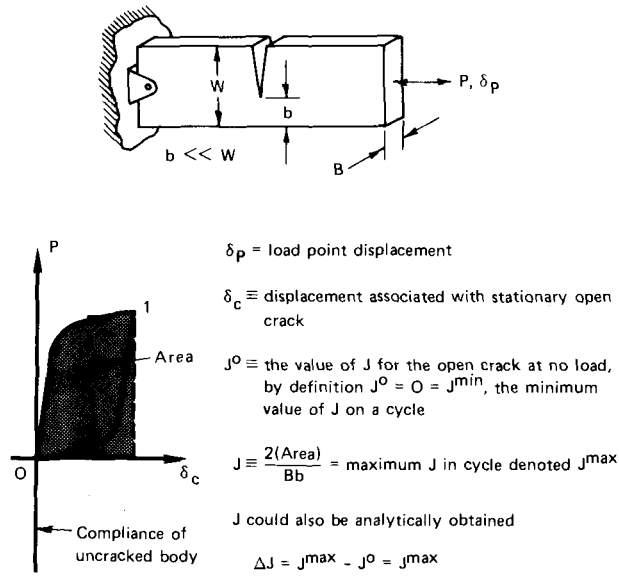

FIG. 12—*Definition of* ΔJ *for an example case of a deeply cracked beam.*

body that contains the crack tip and plastic zone. Expedient use of J in fatigue crack growth analysis would require that the near field response be a unique function of the far field load-displacement response provided load transfer across crack faces is accommodated. Figure 13 schematically characterizes the concept of near field J, J_{NF}, representative of the dominantly proportional field in contrast to the more usual far field value. Of course, the range of J_{NF} must correspond to that value defined for the reference damage data (compare Fig. 2) if the damage processes are to be compared. Given J_{NF} is so evaluated, it is reasonable to postulate the existence of closed force displacement loops with geometrically similar ascending and descending branches (as in Fig. 9). As such, the response may be characterized by the form of Eq 12. Dowling and Begley [*20*] and Mowbray [*23*] have in their operational definition of ΔJ based on crack related work producing displacement, partially accounted for these possible differences between J and J_{NF}.

The just noted use of J_{NF} parallels the essence of the first step in the nonlinear nucleation analysis shown earlier in Fig. 8. With regard to nonlinear nucleation analysis, this first step is essential in situations where far field measures of the damage process (for example, K_t) fail to portray the notch root damage rate because of history dependent plastic action. In such cases, local residual fields not only relate nonlinearly to, but also may have a sense opposite to, the applied far field loading. For such cases, the local con-

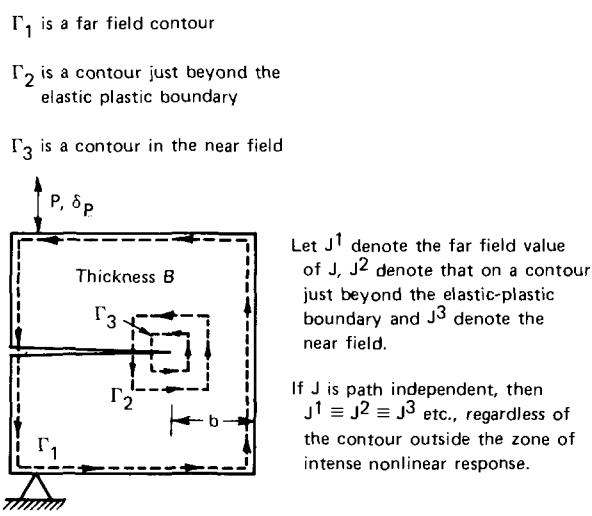

FIG. 13—*Concept of near field* J *in applications to variable amplitude cyclic histories.*

trol condition is provided from [*49*] either accurate finite element analyses (FEM), approximate notch analysis (for example, Neubers' rule) or the strain equivalence principle. As evident in Ref *18*, this refinement yields accurate estimates of the local damage rates.

Unfortunately, computation of J on a contour near the crack tip does not follow from simple rules as those used for notches (for example, Neubers' rule). Thus, in a practical sense difficulties remain in both computing and implementing J_{NF}. Moreover, it is not clear as to the existence of a J controlled near field, J_{NF}, and the demarcation between J_{FF} and J_{NF}.

Thus far, the uniqueness of J and ΔJ have been postulated by analogy to other applications of the deformation theory to cyclic loading problems. It has been noted that, for the uniqueness of J to be retained in such problems, the J-integral approach must be applied on a load reversal by load reversal basis. In the sense that laboratory testing leads to often symmetric closed loops in force-displacement space, the reversal-by-reversal application of J through ΔJ for purposes of fatigue analysis requires closed loops be identified in a variable amplitude J sequence such as would be found in some structural application. By way of analogy, consider the response shown in Fig. 9*a*. Rainflow cycle counting, introduced in Japan in 1968 by Endo [*50*] and popularized on this continent by Dowling since 1973 [*51*], is used to identify closed loops for purposes of damage assessment in crack nucleation analysis. It is known for comparable crack nucleation problems that both the range of the damage parameter and its mean value influence the damage rate. This is also true for confined plasticity in fatigue crack growth using

LEFM [*42*]. It is likely then that parameters that couple the range of J and its mean value (compare Fig. 12) such as that form postulated by Walker [*52*] for LEFM analysis may be appropriate.[10] Such problems are, however, beyond the scope of the present paper.

Stress-Strain Response in the Near Crack-Tip Field, Stationary Cracks

Consider now the stress-strain response in the near crack-tip field for a stationary crack. The near crack-tip field exists as a compatible displacement field confined by some elastic field in all but limit load cycling cases. Depending on the relative size of the plastic zone embedded in the elastic field, the plastic zone will be constrained by the elastic field in a manner which depends on the load sequence and magnitude. This constraint leads to essentially fully reversed stressing in material elements in the intensely deformed region. However, moving away from this zone to the elastic-plastic boundary, material elements will sustain a residual stress that may remain active or cyclically relax. A region of complex response such as this exists at notch roots [*49*], yet the force displacement response in such regions is still apparently unique as is evident in Fig. 11, and so can be characterized in Eq 12.

The residual stress field near the notch is only apparent when the strain field in this zone is mapped into stresses (see footnote 9). As such the question must be raised—are far field force-displacement estimates of J sensitive to this local residual field, which can act locally to either close or open the crack and alter growth rates in order of magnitude.[11] Again, however, it must be emphasized under these conditions that the near field characterized by a far field value of J can only be valid if there is path independence throughout the body. Consequently, the value of J_{NF} must be evaluated on a contour that reflects the near field stress-strain state, that is, in the J dominated zone. By analogy to the notch and in light of Refs *19,26,44,46*, it is probable that all material elements within deform in phase in the near field. If such is the case, the deformation theory is valid and J_{NF} is unique for purposes of engineering analysis.

In view of the foregoing, a far field value of ΔJ by itself cannot be expected to correlate damage rates at crack tips if the residual fields differ. Of course if the difference is only minor, ΔJ will appear adequate. Also, if the subsequent J history at the crack tip wipes out the difference between residual fields, ΔJ will correlate damage rate data. One such case is a stable increasing ΔJ history in fatigue testing, as for example Ref *20*.

The question to be asked is—if far field compliance measures of J are in-

[10] It might be noted that the Walker parameter has the same general form as other parameters that have been useful in nonlinear nucleation analysis (for example [*53,54*]).

[11] Consider here results for a single tension overload in an otherwise constant amplitude history [*55*]. For such problems, closure in the wake of the crack is minimal. There is, however, a compression field at the crack tip for the tension overload case that may act to retard growth.

adequate, can the global path dependence of Eq 2 be utilized to measure the extent of the residual field by its analytical evaluation along a contour in the J dominated process zone? Unfortunately, reversed plasticity solutions for J on various contours in the plastic zone are lacking, even for simple coupon geometries. A related question also arises—given the near tip residual field can be represented in terms of the local path independence of J_{NF}, how does one apply J_{NF} concepts to structures with complex redistribution through plastic action? Also, how does one deal with structural applications where the far field loading is out of phase so that not even global force-displacement relationships for the structure are unique? Unfortunately, this last problem is beyond the scope of the present knowledge so that attention is hereafter limited to uniaxially loaded coupon specimens.

The above issues cast considerable doubt on the general utility of J based analysis for fatigue crack growth. Little can be rigorously said presently about these uncertainties. However, one can identify several crucial tests that can be formulated to quickly ascertain the potential utility of J. These are collectively examined after the consideration of advancing cracks in the next section.

Force-Displacement Fields in Cracked Media-Stable Propagating Cracks

Aside from problems in the definition of J and ΔJ and the limitation in crack advance per cycle detailed earlier, propagating cracks pose one further significant problem. Under the action of variable amplitude loading, prior tension (or compression) overloads generate nonplanar crack faces as illustrated in Fig. 14. Upon release of the external load, contact between adjacent asperities results, and load transfer occurs across them. To the extent that several such asperities may exist due to a range of overloads, the near crack tip field again can be no longer prescribed by a far field (global) evaluation of J (or ΔJ). However, as for the stationary crack given that the compatible displacement field in the remaining ligament can be approximated from the far field force displacement response, the associated boundary conditions could be imposed so as to compute J_{NF} on a scale refined to reflect the near crack tip response. This concept has been shown in Fig. 13. Note that tension overloads reduce the load for crack closure through contact of asperities, whereas compression overloads would increase the load. Of course, overloads of mixed sign would result in an effect related to the dominant plastic field and the magnitude of the subsequent load cycles. Such shrinking of the contour used to compute J could lead to an effective J concept that parallels that for the LEFM K [*42*].

In contrast to the prior introduction of J_{NF} for stationary cracks, the influence of history dependent flow in the wake of the crack on J_{NF} changes as the crack grows. Eventually, the near field may grow out of the region influenced by residual deformations. Alternately, some subsequent overload

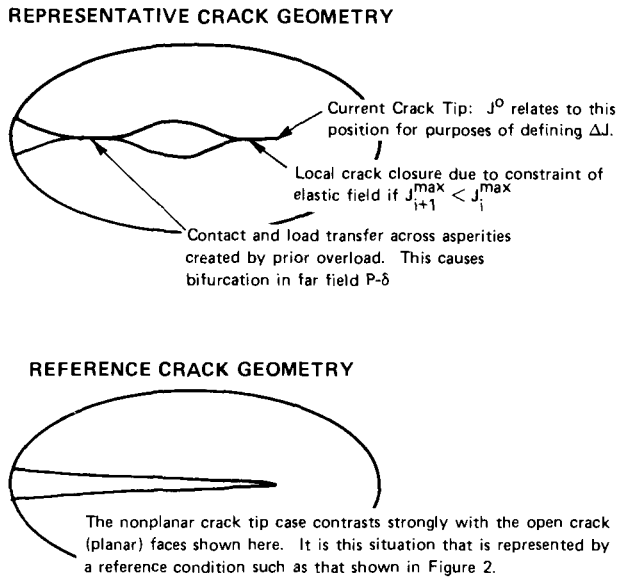

FIG. 14—*Nonplanar crack faces due to history dependent residual deformations.*

may wipe out the influence of prior residual deformations. Thus, the logistics of computing and implementing a concept like J_{NF} are much more involved than for a stationary crack. And, as with stationary cracks, there is uncertainty as to both the validity of deformation theory and the existence and uniqueness of J_{NF}.

Unless a concept such as J_{NF} is valid, it is unlikely that a single parameter measure of the near field will provide general utility in fatigue crack growth analysis. The next section, therefore, outlines several crucial tests that serve to assess the existence and uniqueness of J_{NF}. In view of the above, residual stresses at stationary crack tips, bifurcation and near tip closure, material transient response in the plastic zone, and residual deformations in the wake of the crack must be examined by such crucial tests.

Commentary on Crucial Tests of *J*-Based Fatigue Crack Propagation Analysis

Clearly, if J or J_{NF} concepts are to be useful in fatigue analysis for other than data correlation of unique (trivial) test cases, the just elaborated difficulties must be resolved. A number of crucial tests can be identified, some analytical, others experimental. The analytical tests are essential to evaluate the value of J_{NF} under various conditions of closure and material transient

response.[12] Results of appropriate parametric analysis will facilitate direct determination of the validity of deformation theory and the existence, uniqueness, and utility of the J_{NF} concept. Certain experiments provide indirect assessment of these same issues without recourse to the idealizations and assumptions in analysis.

From an analytical point of view, it is essential to show that a unique value of J_{NF} exists as a function of crack length for a given far field value, J_{FF}. This requires J_{NF} to be virtually path independent at least within the plastic zone but away from the intensely nonlinear region. For simplicity and convenience in analysis, J_{NF} should be path independent over some portion of the body that encloses the plastic zone. To facilitate analysis, the value of J_{FF} should likewise be reasonably path independent over a substantial segment of the body and be related to J_{NF} as a function of crack length and far field load.

If such studies fail to indicate the existence and uniqueness of a concept such as J_{NF}, J based analysis can be of little practical utility in general applications to fatigue crack growth studies. However, if the existence and uniqueness of J_{NF} is indicated, parametric analysis can be gainfully employed to assess the sensitivity of the (presumed unique) value of J_{NF} to a range of overload levels first for stationary, then for growing cracks. In the first instance, the relationship obtained would serve to make the first transformation indicated in Fig. 8. Guidance as to the sensitivity of J_{NF} to load transfer across crack faces as a consequence of prior overloads would allow as a function of crack position from the parametric study of overloads as a function of crack position. While such parametric results would be strictly valid for a given boundary value problem, much of the response simulated in the analysis is a local effect. As such, any relationships between J_{NF} and J_{FF} so developed might scale approximately to other geometries on the basis of J_{FF} as a function of crack size.

Parametric analysis also can be used to assess the sensitivity of J_{NF} to different degrees of transient material response in the plastic zone. For certain classes of materials, such studies will indicate the error in estimating J_{NF} assuming stable material response. If J_{NF} is shown to be only mildly dependent on this transient response, one of the major concerns for the utility of J becomes practically inconsequential.

From an experimental point of view, one very simple test condition could indirectly explore many of the same aspects. As an example, a compact tension specimen instrument with near tip clip gages, as well as the usual load point clip gage, might be subjected to the incremental step-tests shown in Fig. 15. Such tests would indicate if the near tip displacement response is a unique nonlinear function of far field load. Appropriately instrumented

[12] As Rice [*39*] indicates, results of such analysis may not lend themselves to conclusive interpretation.

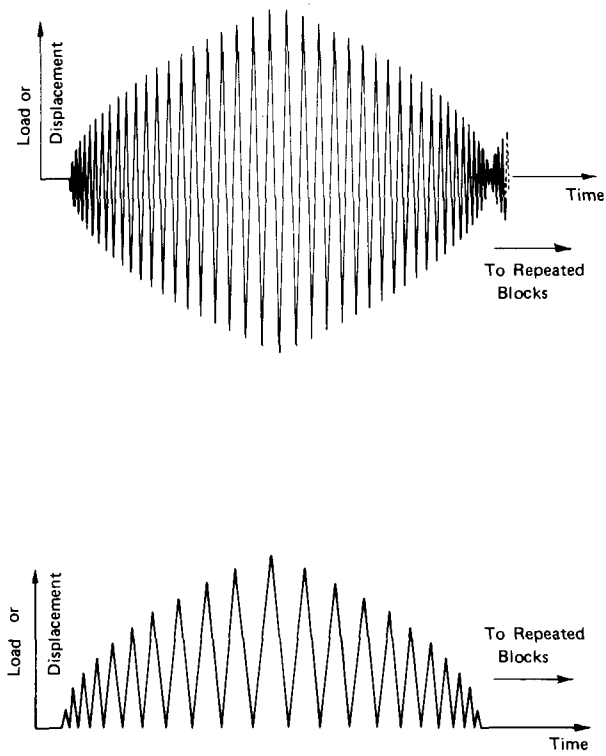

FIG. 15—*Incremental step histories*—(a) *symmetric incremental step test, and* (b) *asymmetric incremental step test.*

specimens would indicate the extent of the near field region related to J_{NF} in terms of elements of material observed to deform somewhat out of phase with the far field because of closure effects. For such a study, care must be taken to guard against crack advance so that a tough steel may be the best test material.

The type of load history shown in Fig. 15 also provides for the study of history effects on the far field value of J. For stationary cracks, these effects are due to transient response (compare Fig. 9*b*) in the plastic zone (as is evident at notch roots [*55*] at loads well below limit load). They cause the force-displacement response to change throughout the body, as is evident in Fig. 16 in terms of the notch root and far field stress-strain response of a notched coupon subjected to several blocks of the history in Fig. 15*a*. Likewise, this load history could be used to study the effects of prior overloads on J_{NF} and the attendant crack growth by including a block of cycles for each peak shown in Fig. 15.

By imposing blocks of this history shown in Fig. 15, the near and far field displacement response can be compared as a function of far field load. If for

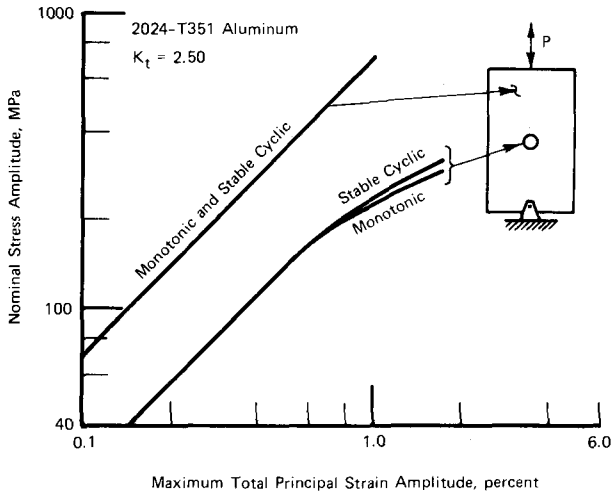

FIG. 16—*Transient response in the near and far fields of a notched plate—FEM results* [53].

such a history these responses are comparable, it is likely for that material that J_{NF} and J_{FF} relate one to one. Thus, J_{FF} may be adequate for crack growth analysis under reasonably general load histories. Also by imposing such a history, the far field value of J could be determined as a function of crack position. If this definition of J_{FF} does not differ significantly as compared to results for static loading, the value of J_{FF} can be considered for practical purposes history insensitive. Furthermore, if crack growth for such a history is found to be essentially history insensitive, the value of J_{FF} probably could be used for general purpose crack growth analysis for that material.

Unfortunately, based on results for notched plates [*19*], it is unlikely that these trends will develop, except for the very soft steels and near limit load cycling. In all other situations, the results of the previously noted analysis will be necessary if J based concepts are to find general utility in fatigue crack growth analysis.

Summary and Conclusion

The problems in the analysis of fatigue crack growth using a single parameter characterization of the crack tip field have been enumerated. Included in this discussion were local residual stress and displacement fields associated with overloads in variable amplitude service loads, transient material response, and similitude between J fields as required in comparing some reference data base with the damage process in a structure for purposes of crack growth analyses. These problems have been discussed in terms of the requirements for the validity of the deformation theory. It has been em-

phasized that these problems exist because of differences between various damage states being compared in terms of J for purposes of fatigue crack growth analysis. Because these differences result in a path dependence of J_{FF} as compared to J_{NF}, the concept of a near field value of J was introduced. Discussion focused then on the existence and uniqueness of J_{NF} and on relationships between J_{NF} and J_{FF}. In that J_{NF} must exist and be unique and simple relationships must exist between J_{FF} and J_{NF} if J based concepts are to be useful in fatigue crack growth analysis, several crucial tests of the potential utility of J in such analysis were outlined. Throughout, the discussion was augmented and interpreted in terms of experience and test results for nonlinear analysis to assess structural fatigue crack nucleation.

Based on the results and discussion of this paper, the following can be concluded:

1. Preliminary indications of the utility of J based fatigue crack propagation analysis represent unique experimental conditions where cyclic plastic aspects have not been explicitly explored. Such data consolidation is a necessary but not sufficient condition to demonstrate the utility of J based concepts in applications to fatigue crack growth analysis in structural components subjected to generalized loadings.

2. History dependent residual stresses, residual deformations, and transient material response may confound the general utility of a deformation theory. To circumvent these difficulties requires the cycle-by-cycle evaluation of J at a scale that reflects nonlinear action related to those history dependent phenomena. The value of J so defined was termed J controlled near field, J_{NF}.

3. Crucial tests of the utility of a J based analysis of fatigue crack propagation can be elaborated in terms of J_{NF}.

4. For general structures subjected to variable amplitude loading, fatigue crack growth analyses based on J concepts may be tenuous.

References

[1] Paris, P. C., Gomez, M. P., and Anderson, W. E., *The Trend in Engineering,* Vol. 13, 1961, pp. 9-14.

[2] Paris, P. C., "The Growth of Fatigue Cracks Due to Variations in Load," Ph.D. thesis, Lehigh University, Bethlehem, Pa., 1962.

[3] Irwin, G. R., *Transactions* of the American Society of Mechanical Engineers, ASME, *Journal of Applied Mechanics,* 1957.

[4] Irwin, G. R. in *Fracture I, Handbook der Physik VI,* Flugge, Ed., Springer, Berlin, 1958.

[5] Smith, C. R. in *Fatigue Testing of Aircraft Structures, ASTM STP 338,* American Society for Testing and Materials, 1962, pp. 241-250.

[6] Grover, H. J., "Fatigue of Aircraft Structures," NAVAIR, 1966.

[7] Crews, J. H., Jr., Hardrath, H. F., *Experimental Mechanics,* Vol. 6, No. 6, June 1966, pp. 313-320.

[8] Topper, T. H., Wetzel, R. M., and Morrow, JoDean, *Journal of Materials,* Vol. 4, No. I, March 1969, pp. 200-209; see also NADC-ST-6818, Naval Air Development Center, Sept. 1968.

[9] Neuber, H., *Journal of Applied Mechanics,* Vol. 28, No. 4, Dec. 1961, pp. 544-560.
[10] Rice, J. R., *Journal of Applied Mechanics,* 1968, pp. 379-386; see also Brown University Report E39, May 1967.
[11] Eshelby, J. D. in *Solid State Physics,* Vol. 3, Academic Press, 1956.
[12] Neuber, H., *Journal of the Mechanics and Physics of Solids,* Aug. 1968, pp. 289-294.
[13] Hutchinson, J. W., *Journal of the Mechanics and Physics of Solids,* Vol. 16, 1968, pp. 337-347.
[14] Rice, J. R., and Rosengren, G. F., *Journal of the Mechanics and Physics of Solids,* Vol. 16, 1968, pp. 1-12.
[15] Schijve, J., Broek, D., and deRijk, P., "The Effect of the Frequency of an Alternating Load on the Crack Rate in a Light Alloy Sheet," NLR Report M 2092, National Aerospace Institute, 1961.
[16] Schijve, J., "The Accumulation of Fatigue Damage in Aircraft Materials and Structures," AGARD-AG-157, Advisor Group on Aeronautical Research and Development, 1972.
[17] Leis, B. N., *Journal of Testing and Evaluation,* Vol. 5, No. 4, July 1977, pp. 309-319.
[18] Leis, B. N., "An Approach for Fatigue Crack Initiation Life Prediction with Applications to Complex Components," in *Fatigue Life of Structures Under Operational Loads, Proceedings* of the Ninth International Committee on Aeronautical Fatigue Meeting, ICAF Document 960, Laboratorium fur Betriebsfestigeit, May 1977, pp. 3.4/1-47.
[19] Williams, D. P., Lind, N. C., Conle, F. A., Topper, T. H., and Leis, B. N. in *Mechanics in Engineering,* University of Waterloo Press, Waterloo Ont., Canada, 1977, pp. 291-311.
[20] Dowling, N. E. and Begley, J. A. in *Mechanics of Crack Growth, ASTM STP 590,* American Society for Testing and Materials, 1976, pp. 82-103.
[21] Gowda, C. V. B., Leis, B. N., and Topper, T. H. in *Proceedings,* International Conference on Mechanical Behavior of Materials, Kyoto, Japan, Vol. II, 1972, pp. 187-198.
[22] Hilton, P. D. and Hutchinson, J. W., *Engineering Fracture Mechanics,* Vol. 3, 1971, pp. 435-451.
[23] Mowbray, D. G. in *Cracks and Fracture, ASTM STP 601,* American Society for Testing and Materials, 1976, pp. 33-46.
[24] Kaisand, L. R. and Mowbray, D. G., "Relationships Between Low Cycle Fatigue and Fatigue Crack Growth Rate Properties," unpublished manuscript, Materials and Process Laboratory, General Electric Co., 1978.
[25] Paris, P. C. in *Flaw Growth and Fracture, ASTM STP 631,* American Society for Testing and Materials, 1977, pp. 3-27.
[26] Conle, F. A., "A Computer Simulation Assisted Statistical Approach to the Problem of Random Fatigue," M.A.Sc. thesis, University of Waterloo, Waterloo, Ont., Canada, March 1974.
[27] Laird, C., oral discussion of several papers at the Symposium on Fatigue Mechanisms, Kansas City, 1978, based on recent work to be published.
[28] Neumann, P., "The Geometry of Slip Processes at a Propagating Fatigue Crack," *Acta Metallurgica,* Vol. 22, 1974, p. 1167.
[29] Broek, D., *Metallurgical Reviews,* Vol. 19, 1974, pp. 135-182.
[30] Broek, D. and Leis, B. N., "Fatigue Crack Initiation and Growth Analysis for Structures," SAE Paper No. 790511, Society of Automotive Engineers, 1979.
[31] Tompkins, B., *Philosophical Mag.,* Vol. 18, 1968, p. 1041.
[32] McClintock, F. A. and Irwin, G. R. in *Fracture Toughness and its Applications, ASTM STP 381,* American Society for Testing and Materials, 1965, pp. 84-113.
[33] Rice, J. R. in *Fatigue Crack Propagation, ASTM STP 415,* American Society for Testing and Materials, 1967, pp. 247-311.
[34] Rice, J. R. in *Fracture, Vol. II,* H. Leibowitz, Ed., Academic Press, New York, 1968, pp. 191-311.
[35] McClintock, F. A. in *Fracture, Vol. III,* H. Leibowitz, Ed., Academic Press, New York, 1971, pp. 47-225.
[36] Rice, J. R., Paris, P. C., and Merkle, J. in *Progress in Flaw Growth and Fracture Toughness Testing, ASTM STP 536,* American Society for Testing and Materials, 1973, pp. 231-245.
[37] Hutchinson, J. W. and Paris, P. C. in *Elastic Plastic Fracture, ASTM STP 668,* American Society for Testing and Materials, 1979, pp. 37-64.

[38] McMeeking, R. M. in *Flaw Growth and Fracture, ASTM STP 631,* American Society for Testing and Materials, 1977.
[39] Rice, J. R. in *Numerical Methods in Fracture Mechanics,* Jan. 1978, pp. 434-449.
[40] Budiansky, B., *Journal of Applied Mechanics,* Vol. 26, 1959, pp. 259-264.
[41] Drucker, D. in *Calculus of Variations and its Application,* L. M. Graves, Ed., McGraw Hill, New York, 1958, pp. 7-22.
[42] Broek, D., *Engineering Fracture Mechanics,* Nordhoff, The Netherlands, 1974.
[43] Ritchie, R. O., *Journal of Engineering Materials and Technology,* Vol. 99, No. 3, 1977, pp. 195-204.
[44] Leis, B. N., "Fatigue Analysis to Assess Crack Initiation Life for Notched Coupons and Complex Components," Ph.D. thesis, University of Waterloo, Waterloo, Ont., Canada, Sept. 1976.
[45] Barson, J. M. and McNicol, R. C. in *Fracture Toughness and Slow-Stable Cracking, ASTM STP 559,* American Society for Testing and Materials, 1974, pp. 183-204.
[46] Lind, N. C. and Mroz, Z. in *Proceedings,* IABSE Symposium of Resistance and Ultimate Deformability of Structures Acted on by Well-Defined Repeated Loads, Lisboa, 1973, pp. 9-14.
[47] Begley, J. A. and Landes, J. D. in *Fracture Toughness, ASTM STP 514,* American Society for Testing and Materials, 1972, pp. 1-20.
[48] Bucci, R. J., Paris, P. C., Landes, J. D., and Rice, J. R. in *Fracture Mechanics, ASTM STP 514,* American Society for Testing and Materials, 1972, pp. 40-69.
[49] Leis, B. N. and Sampath, S. G., "Development of an Improved Method of Consolidating Fatigue Life Data," NASA CR 145312, National Aeronautics and Space Administration, Washington, D.C., Aug. 1977.
[50] Matsuishi, M. and Endo, T., "Fatigue of Metals Subjected to Varying Stress," Paper presented to Japan Society of Mechanical Engineers, Fukouka, Japan, March 1968; see also Endo, T., Mitsunaga, K., Takahashi, K., Kobayashi, K., and Matsuishi, M., "Damage Evaluation of Metals for Random or Varying Load," paper presented at 1974 Symposium on Mechanical Behavior of Materials, Kyoto, Japan, Aug. 1974.
[51] Dowling, N. E., *Journal of Testing and Evaluation,* Vol. 1, No. 4, July 1973, pp. 271-287.
[52] Walker, K. in *Effects of Environment and Complex Load History on Fatigue Life, ASTM STP 462,* American Society for Testing and Materials, 1970, pp. 1-14.
[53] Smith, K. N., Watson, P., and Topper, T. H., *Journal of Materials,* Vol. 5, No. 4, Dec. 1970, pp. 767-778.
[54] Leis, B. N., *Journal of Pressure Vessel Technology, Transactions,* American Society of Mechanical Engineers, Vol. 99, No. 4, Nov. 1977, pp. 524-533.
[55] Schijve, J. and Broek, D., "Crack-Propagation Tests Based on a Gust Spectrum with Variable Amplitude Loading," *Aircraft Engineering,* Vol. 34, 1962, pp. 314-316.
[56] Leis, B. N., Gowda, C. V. B., and Topper, T. H. in *Cyclic Stress Strain Behavior-Analysis, Experimentation and Failure Prediction, ASTM STP 519,* American Society for Testing and Materials, 1973, pp. 133-150.

W. G. Clark, Jr.[1]

Effect of Prestressing on Stress-Corrosion Crack Initiation in High-Strength Type 4340 Steel

REFERENCE: Clark, W. G., Jr., **"Effect of Prestressing on Stress-Corrosion Crack Initiation in High-Strength Type 4340 Steel,"** *Fracture Mechanics: Twelfth Conference, ASTM STP 700,* American Society for Testing and Materials, 1980, pp. 97-111.

ABSTRACT: A preliminary investigation was conducted to evaluate the influence of both tension and compression prestressing (in air) on the subsequent stress-corrosion crack initiation behavior of two high-strength AISI type 4340 steels, 1240-MPa (180-ksi) and 1480-MPa (215-ksi) yield strength. Crack initiation testing was conducted with edge-notched, round tensile specimens subjected to a hydrogen sulfide (H_2S) gas environment. Test results are expressed in terms of the critical combination of maximum elastically calculated notch stress and square root of the notch radius required to induce stress-corrosion cracking. Results show that prestressing can have a significant effect on subsequent stress-corrosion behavior. In general, tension prestressing increased the resistance to stress-corrosion crack initiation and compressive prestressing decreased the resistance. The susceptibility to stress-corrosion crack initiation was increased by as much as a factor of 4 to 1 as the result of compressive prestressing.

KEY WORDS: initiation, stresses, corrosion, fractures (materials), notch, steels, crack propagation, corrosion

Recently, experimental data have been developed which demonstrate that a modified fracture mechanics approach may provide a widely applicable quantitative method for the characterization of environment induced (stress-corrosion) crack initiation behavior at blunt notches in high-strength steels.[2] The essence of the proposed technique is to establish the critical combination of maximum elastic notch stress, σ_{max}, and notch root radius, r, required to yield stress-corrosion crack initiation and subsequently, to relate these parameters to the applied maximum stress and notch radius

[1] Manager, Fracture Mechanics, Structural Behavior of Materials Department, Westinghouse Research and Development Center, Pittsburgh, Pa. 15235.

[2] Clark, W. G., Jr., in *Flaw Growth and Fracture, ASTM STP 631,* American Society for Testing and Materials, 1977.

associated with a component of given material exposed to a particular environment. The fracture mechanics relationship between effective stress intensity, K_I and notch radius is used to compute σ_{max} as follows[3]

$$K_I = \lim_{r \to 0} \frac{(\pi)^{1/2}}{2} (r)^{1/2} \sigma_{max} \tag{1}$$

$$\sigma_{max} = \frac{2K_I}{(\pi r)^{1/2}} \tag{2}$$

This approach to the determination of σ_{max} yields results similar to the more conventional stress concentration techniques but in many cases, determining σ_{max} from K_I is more easily accomplished. In an actual application, the value of K_I is determined by assuming that the notch is a crack with a depth equivalent to the notch depth. K_I is determined from the appropriate stress intensity expression for the geometry and loading configuration involved and σ_{max} is determined from Eq 2. The values of σ_{max} and r associated with the component involved are then compared with the critical combination of σ_{max} and r required to induce stress-corrosion cracking. The critical values of σ_{max} and r, typically expressed as σ_{max}* versus $\sqrt{r}$, must be determined experimentally for the specific material and environment involved. Such data developed for two high-strength AISI type 4340 steels using several test specimens and notch sizes are shown in Fig. 1. Note the geometry independent nature of the relationship between σ_{max}* and $\sqrt{r}$ and the onset of stress-corrosion cracking. This characteristic provides the basic advantage of the σ_{max}* approach to stress-

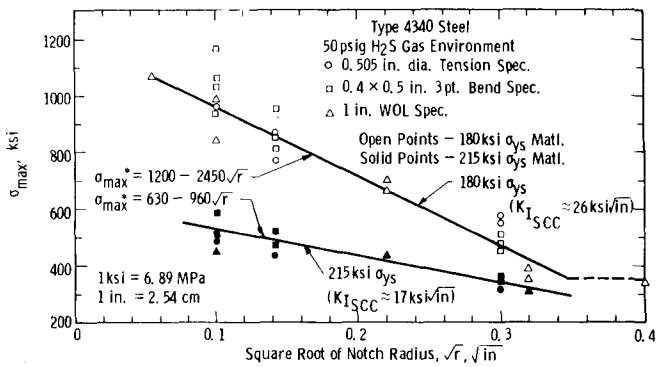

FIG. 1—*Maximum failure stress versus* $\sqrt{r}$ *(1 ksi = 6.89 MPa).*

[3]Clark, W. G., Jr. in *Cracks and Fracture, ASTM STP 601,* American Society for Testing and Materials, 1976.

corrosion crack initiation. Specifically, simple laboratory test specimens can be used to predict the stress conditions required to induce stress-corrosion cracking which in turn, can be related to the stress conditions associated with actual components. Consequently, the σ_{max}* concept offers significant potential as a valuable tool for material selection and hardware design.

The σ_{max}* concept described above and in footnote 2 is a relatively new development, and substantial additional testing and analyses are required to adequately verify the usefulness of this concept as a valuable design parameter. Such effort involving very long-time crack initiation testing, various environments, different notch geometries and lower-strength materials is currently underway and will be reported upon completion. Note also that the σ_{max}* concept addresses the stress or strain (σ_{max}* versus $\sqrt{r}$ can be related to localized strain, see footnote 2) conditions required to develop stress-corrosion cracking at a notch and not the time involved for the crack to develop. The characterization of incubation time in terms of σ_{max}* and $\sqrt{r}$ is also currently under investigation.

Despite the limited amount of data available and the large amount of verification testing yet required, the σ_{max}* versus $\sqrt{r}$ concept appears to offer a unique quantitative approach to the characterization of stress-corrosion crack initiation behavior which in turn, can provide a valuable tool for the evaluation and further understanding of the mechanisms of stress-corrosion cracking. One area of particular concern involves the influence of prestressing on the subsequent development of stress-corrosion cracking at blunt notches.

This paper describes the results of a preliminary evaluation of the effect of both tension and compression prestressing (in air) on the stress-corrosion crack initiation performance of two high-strength AISI type 4340 steels exposed to a hydrogen sulfide gas (H_2S) environment. The results are expressed in terms of the maximum elastically calculated notch stress associated with prestressing and the subsequent σ_{max}* parameter required to develop a stress-corrosion crack. Crack initiation results developed with and without prestressing are compared.

Material and Specimen Preparation

The material involved in this investigation consisted of quenched and tempered AISI type 4340 steel heat treated to 1241-MPa (180-ksi) and 1482-MPa (215-ksi) yield strength levels. The 1241-MPa (180-ksi) yield strength material was obtained as 7.62-cm (3-in.) thick forged plate, and the 1482-MPa (215-ksi) yield strength material was obtained as 14.05-cm (7.5-in.) diameter forged bar stock. The nominal chemical composition, heat treatment, and room temperature tensile properties of the forgings are summarized in Table 1. The room temperature fracture toughness deter-

TABLE 1—*Chemical composition, heat treatment and room temperature tensile properties of materials investigated.*

Material	Chemical Composition, weight %								
	C	Mn	Si	P	S	Ni	Cr	Mo	V
1241 MPa (180 ksi) yield	0.36	0.63	0.25	0.010	0.010	2.54	0.86	0.39	0.093
1482 MPa (215 ksi) yield	0.41	0.81	0.27	0.006	0.009	1.88	0.91	0.37	...

	Heat Treatment
1241 MPa (180 ksi) yield	Austenitized 4 h at 849°C (1560°F), water quenched; double tempered 4 h at 582°C (1080°F) and furnace cooled.
1482 MPa (215 ksi) yield	Austenitized 2 h at 816°C (1500°F), oil quenched; tempered 10 h at 316°C (600°F) and air cooled.

	Tensile Properties at 23.9°C (75°F)			
	Tensile Strength MPa (ksi)	Yield Strength (0.2 % offset) MPa (ksi)	Elongation in 50 mm (2 in.), %	Reduction in Area, %
1241 MPa (180 ksi) yield	1338 (194)	1234 (179)	14	46
1482 MPa (215 psi) yield	1724 (250)	1482 (215)	10	38

mined in accordance with ASTM Test for Plane-Stain Fracture Toughness of Metallic Materials (E 399-74 is 165 MPa$\sqrt{m}$ (150 ksi$\sqrt{in.}$) and 82.4 MPa$\sqrt{m}$ (75 ksi$\sqrt{in.}$) for the 1241-MPa (180-ksi) and 1482-MPa (215-ksi) yield strength material, respectively. The K_{Iscc}[4] for these materials in a 345 kPag (50 psig) H_2S gas environment measured as the result of both long-time constant displacement and rising load tests is 28.6 ± 5.5 MPa$\sqrt{m}$ (26 ± 5 ksi$\sqrt{in.}$) for the 1241-MPa (180-ksi) yield material and 18.7 ± 3.3 MPa$\sqrt{m}$ (17 ± 3 ksi$\sqrt{in.}$) for the 1482-MPa (215-ksi) yield material [*2*].

Figure 2 shows the 1.28 cm (0.505-in.) diameter edge-notch, round tensile specimens used for all crack initiation testing conducted in this investigation. The notch details and corresponding stress concentration factors, K_t, are also included in Fig. 2. Note that the notch depth is the same for each of the three notch radii, 0.48 cm (0.188 in.). In all cases the test specimens were taken from the "as received" material, such that the plane of the notch was parallel to the long-transverse direction of the plate (radial plane of the bar) and perpendicular to the major axis of the original forging.

[4] K_{Iscc} equals the value of the plane-strain stress intensity factor below which an existing crack will not grow due to stress corrosion.

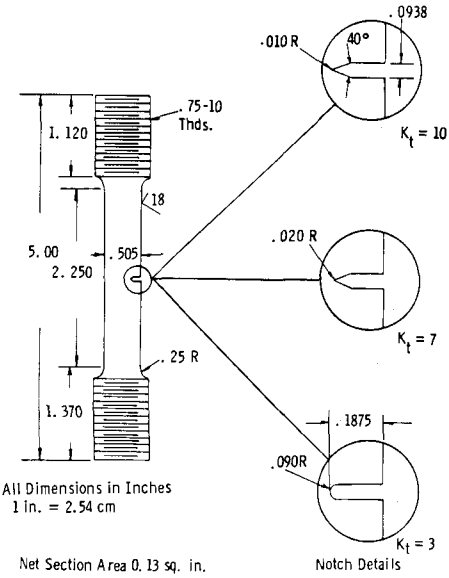

FIG. 2—*Notched tensile bar used for crack initiation studies (1 in. = 2.54 cm).*

Experimental Procedure

All of the stress-corrosion crack initiation testing involved in this investigation was conducted at room temperature 26.7°C (80°F) in a 345-kPa gage (50-psi-gage) H_2S gas[5] environment in accordance with the rising-load, accelerated stress-corrosion test procedure described by Clark and Landes.[6] Specifically, the notched specimens were subjected to slow-rate tensile loading (500 lb, 2.22 MN/min) in the H_2S gas and the load corresponding to the onset of stress-corrosion cracking determined. Because of the extremely rapid rate of crack growth associated with stress-corrosion cracking in the material-environment system involved here (high-strength 4340 steel exposed to H_2S gas), the load corresponding to the initiation of a crack is essentially identical to the load required to cause failure of the specimen. Thus, in this investigation, specimen failure and crack initiation are synonymous.

Figure 3 presents a schematic illustration of the environmental chamber used to conduct the hydrogen sulfide crack initiation tests.

Prior to crack initiation testing, as defined above, several specimens of each of the three notch radii involved were subjected to either compressive or tensile loading in a laboratory air environment. In each case, the maxi-

[5] Volume percent, 99.6, (liquid phase) H_2S, typically 31-ppm water.

[6] Clark, W. G., Jr., and Landes, J. D., *Stress Corrosion—New Approaches, ASTM STP 610,* 1976.

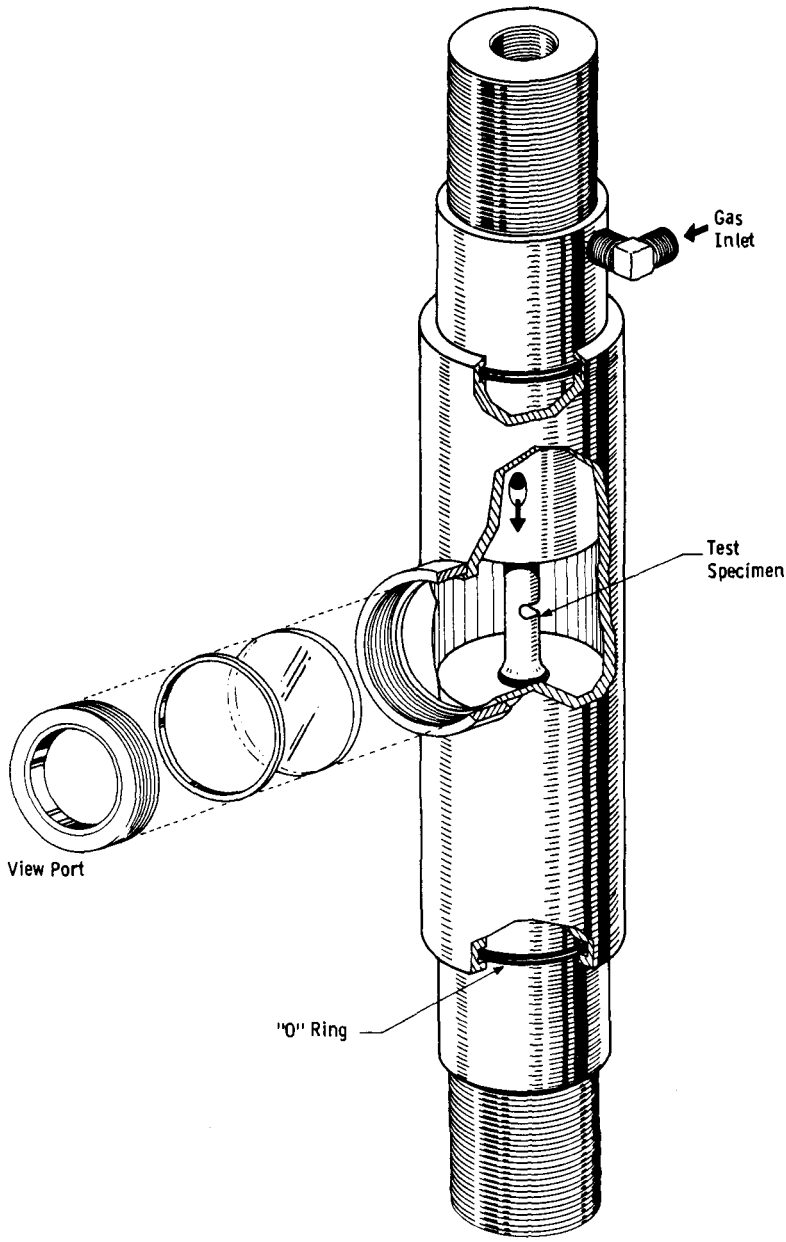

FIG. 3—*Environment chamber used for crack initiation testing (tensile specimens).*

mum air environment preload was maintained for 15 min and the notch surface examined (under load) carefully with a X30 binocular microscope to identify any evidence of cracking developed as the result of prestressing. None of the tests reported here revealed any evidence of cracking due to the prestress loading.

In addition to the prestress testing, a series of notched specimens (not prestressed) were also tested in tension to failure in laboratory air. These results were used to establish guidelines for the prestressing operation. Prestressing was limited to stress levels less than 80 percent of the air environment fracture stress.

Experimental Results

Tables 2 and 3 present the results of all blunt notch testing for the 1241 MPa (180 ksi) and 1482-MPa (215-ksi) yield strength steels, respectively. The prestressing and failure (initiation in the case of the H_2S tests) conditions are noted. The results are expressed in terms of the applied load, P; the net section stress, σ_{net} ($P \div$ net section area); the maximum elastically calculated notch-stress, σ_{max}, and the nominal stress intensity factor, K_I. K_I is computed from the cracked body stress intensity expression for the edge-notch specimen involved (see footnote 2). For the test specimen and notch depth used here, $K_I = 7\ P$. σ_{max} is computed from Eq 2 when $K_I = 7\ P$ ($\sigma_{max} = 7.9\ P/\sqrt{r}$). The results of the air-environment tension tests to failure are also noted in Tables 2 and 3.

Figures 4 and 5 present the results of prestressing in air (expressed in terms of the net section stress) on the subsequent σ_{net} value required to produce specimen failure (crack initiation) in H_2S gas. This method of presenting the data was chosen only to provide a convenient graphical display of the raw test result, and it must be recognized that such a plot is not geometry independent. However, these data do illustrate the potential significant effect of prestressing on subsequent stress-corrosion crack initiation behavior. Note from Fig. 4 that tension prestressing appears to have a small beneficial effect on the resistance to stress-corrosion crack initiation in the 1241-MPa (180-ksi) yield strength steel. In addition, compressive prestresses on the order of -902 MPa (-130 ksi) appear to have little if any effect on crack initiation behavior. However, compressive stresses beyond -902 MPa (-130 ksi) have a very significant effect on initiation behavior. Specifically, for all notch sizes, compressive stresses on the order of -1110 MPa (-160 ksi) reduce the net section stress for crack initiation by nearly 50 percent compared to nonprestressed specimens.

Figure 5 shows that the effect of prestressing in air has an even more dramatic effect on subsequent stress-corrosion crack initiation in the 1482-MPa (215-ksi) yield strength material. Note that for each notch geometry evaluated, there appears to be a consistent effect of prestress

TABLE 2—*Summary of blunt notch test results for 1241-MPa (180-ksi) yield strength type 4340 steel.*[a]

	Prestress Conditions (air)						Failure Conditions (H_2S gas, 50 psig)							
	Load, P		σ_{net}		σ_{max}		Load, P		σ_{net}		σ_{max}		K_I	
Notch Radius	MN	(kip)	MPa	(ksi)	MPa	(ksi)	MN	(kip)	MPa	(ksi)	MPa	(ksi)	MPa$\sqrt{m}$	(ksi$\sqrt{in.}$)
0.025 cm (0.01 in.)	89	(20)	1061	(154)	10 890	(1580)	68	(15.2)	806	(117)	8268	(1200)	117	(106)
		0		0		0	69	(15.5)	819	(119)	8433	(1224)	119	(108)
		0		0		0	53	(11.9)	634	(92)	6477	(940)	91	(83)
		0		0		0	54	(12.2)	648	(94)	6641	(964)	94	(85)
	76	(−17)	902	(−131)	9253	(−1343)	67	(15.0)	792	(115)	8165	(1185)	116	(105)
	89	(−20)	1061	(−154)	10 886	(−1580)	30	(6.8)	358	(52)	3700	(537)	53	(48)
0.05 cm (0.02 in.)	89	(20)	1061	(154)	7117	(1120)	76	(17.0)	903	(131)	6559	(952)	131	(119)
		0		0		0	60	(13.5)	716	(104)	5209	(756)	105	(95)
		0		0		0	69	(15.5)	820	(119)	5980	(868)	120	(109)
	76	(−17)	902	(−131)	6559	(−952)	76	(17.0)	903	(131)	6559	(952)	131	(119)
	76	(−17)	902	(−131)	6559	(−952)	85	(19.0)	1006	(146)	7330	(1064)	146	(133)
	93	(−21)	1116	(−162)	8102	(−1176)	38	(8.5)	448	(65)	3280	(476)	66	(60)
0.228 cm (0.09 in.)	107	(24)	1275	(185)	4299	(624)	101	(22.7)	1205	(175)	4065	(590)	173	(157)
		0		0		0	95	(21.3)	1130	(164)	3817	(554)	162	(147)
		0		0		0	98	(22.0)	1164	(169)	3941	(572)	167	(152)
	76	(−17)	902	(−131)	3045	(−442)	98	(22.0)	1164	(169)	3941	(572)	167	(152)
	107	(−24)	1275	(−185)	4299	(−624)	69	(15.5)	820	(119)	2777	(403)	118	(107)
							Air Test Results (No Prestress)							
0.025 cm (0.01 in.)							100	(22.6)	1199	(174)	12 298	(1785)	174	(158)
0.05 cm (0.02 in.)							104	(23.4)	1240	(180)	9025	(1310)	179	(163)
0.228 cm (0.09 in.)							116	(26.0)	1378	(200)	4658	(676)	198	(180)

[a]Edge notched round tension specimens 1.28 cm (0.505 in.) in diameter, 0.48 cm (0.188 in.) notch depth.

TABLE 3—*Summary of blunt notch test results for 1482-MPa (215-ksi) yield strength type 4340 steel.*[a]

	Prestress Conditions, air						Failure Conditions (H_2S gas, 50 psig)							
	Load, P		σ_{net}		σ_{max}		Load, P		σ_{net}		σ_{max}		K_I	
Notch Radius	MN	(kip)	MPa	(ksi)	MPa	(ksi)	MN	(kip)	MPa	(ksi)	MPa	(ksi)	MPa$\sqrt{m}$	(ksi$\sqrt{in.}$)
0.025 cm (0.01 in.)	80	(18)	950	(138)	9797	(1422)	45	(10.0)	530	(77)	5443	(790)	77	(70)
	62	(14)	744	(108)	7620	(1106)	40	(9.0)	475	(69)	4899	(711)	69	(63)
		0		0		0	28	(6.2)	330	(48)	3376	(490)	48	(44)
	62	(−14)	744	(−108)	7620	(−1106)	8	(1.8)	90	(13)	950	(138)	13	(12)
0.05 cm (0.02 in.)	102	(23)	1219	(177)	8874	(1288)	51	(11.5)	592	(86)	4437	(644)	89	(81)
	76	(17)	902	(131)	6559	(952)	62	(14.0)	744	(108)	5401	(784)	108	(98)
		0		0		0	36	(8.0)	427	(62)	3087	(448)	62	(56)
	76	(−17)	902	(−131)	6559	(−952)	26	(5.8)	310	(45)	2239	(325)	45	(41)
0.228 cm (0.09 in.)	129	(29)	1536	(223)	5195	(754)	83	(18.7)	992	(144)	3348	(486)	142	(129)
	107	(24)	1275	(185)	4299	(624)	93	(21)	1116	(162)	3762	(546)	160	(145)
		0		0		0	58	(13)	689	(100)	2329	(338)	99	(90)
	76	(−17)	902	(−131)	3045	(−442)	31	(7)	372	(54)	1254	(182)	53	(48)
							Air Test Results (No Prestress)							
0.025 cm (0.01 in.)							91	(20.5)	1088	(158)	11 155	(1619)	151	(143)
							98	(22.0)	1164	(169)	11 974	(1738)	169	(154)
0.50 cm (0.02 in.)							116	(26.0)	1378	(200)	10 031	(1456)	200	(182)
							126	(28.3)	1502	(218)	10 920	(1585)	218	(198)
0.228 cm (0.09 in.)							145	(32.5)	1722	(250)	5 822	(845)	247	(225)

[a] Edge notched round tension specimens 1.28 cm (0.505 in.) in diameter, 0.48 cm (0.188 in.) notch depth.

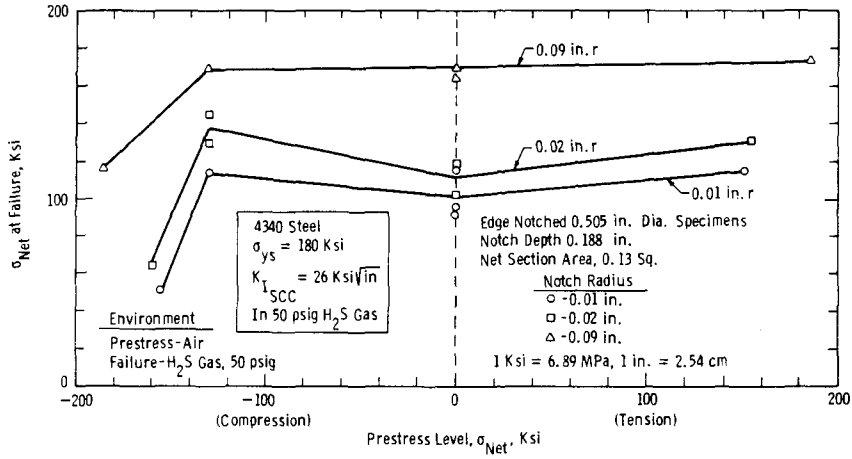

FIG. 4—*Effect of prestressing on net section failure stress in H_2S gas (1 ksi = 6.89 MPa, 1 in. = 2.54 cm).*

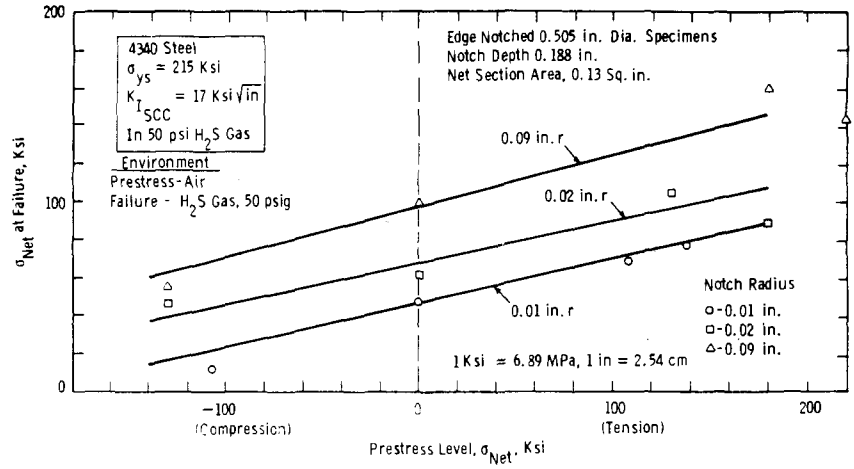

FIG. 5—*Effect of prestressing on net section failure stress in H_2S gas (1 ksi = 6.89 MPa, 1 in. = 2.54 cm).*

level on subsequent crack initiation behavior. Specifically, these limited data imply that a direct relationship exists between the magnitude of the prestress level and the net section stress required to induce cracking. Figure 5 shows that the critical net section stress level required for crack initiation can vary by a factor of as much as 4 to 1 with prestress levels between 1241 MPa (+180 ksi) and −902 MPa (−130 ksi). Note that for each notch radius, tension prestressing increased the σ_{net}-value required for

cracking and compressive prestressing decreased the critical value of σ_{net}. Clearly, prestressing in air prior to exposure to an aggressive environment can have a very significant effect on blunt-notch stress-corrosion crack initiation. In particular, the potential detrimental effect of compressive prestressing must be addressed in actual design considerations. The importance of this behavior is further illustrated by the fact that in the case of the 1482-MPa (215-ksi) yield strength material containing a 0.025-cm (0.01-in.) radius notch and subjected to compressive prestressing at −744 MPa (−108 ksi); failure subsequently occurred in H_2S gas at a σ_{net} level lower than that required to cause failure with an equivalent existing precrack (90 MPa, 13 ksi versus 173 MPa, 25 ksi).

Although the potential significance of the effect of prestressing on subsequent stress-corrosion crack initiation performance is clearly apparent from the consideration of data expressed in terms of net section stress (Figs. 4 and 5), such results are not applicable to other configurations. In order to develop data which can be related to other loading situations and thus, provide useful design information, it is necessary to consider the σ_{max}* concept discussed previously. The results of all blunt notch testing expressed in terms of the elastically calculated maximum notch stress and corresponding $\sqrt{r}$ are presented in Figs. 6 and 7 for the 1241-MPa (180-ksi) and 1482-MPa (215-ksi) yield strength materials, respectively. In these figures, the solid curve represents σ_{max}*, the critical combination of σ_{max} and $\sqrt{r}$ associated with the onset of stress corrosion cracking in H_2S gas (from Fig. 1, no prestressing). The starred points present the results of the air environment fracture tests. The open points show the specific prestress σ_{max} level (in air), and the corresponding solid points (connected by the dashed lines) show the σ_{max} level associated with the subsequent onset of stress-corrosion cracking in H_2S gas. Figures 6 and 7 also show the pattern of prestressing used in this investigation. Specifically, the fracture strength (expressed as σ_{max}) for each notched bar was determined in air, and these values were established as the limits for prestressing. Subsequently, the test specimens were subjected to both tension and compression prestressing at σ_{max} levels on the order of 80 percent of the σ_{max} associated with failure in air. It was expected that prestressing at stress levels near the fracture strength of the materials would reveal the largest potential effect of prestressing on crack initiation performance.

Figures 6 and 7 show that for both steels and all notch radii, tension prestressing results in an elevation of the σ_{max} level required to yield stress-corrosion crack initiation. Again, as in the consideration of the σ_{net} data (Figs. 4 and 5), somewhat more resistance to cracking is developed by tension prestressing in the higher-strength steel than in the lower-strength material. The significance of compressive prestressing on the susceptibility to stress-corrosion crack initiation is also apparent in both Figs. 6 and 7. Examination of the data shown in Fig. 6 for the lower strength steel

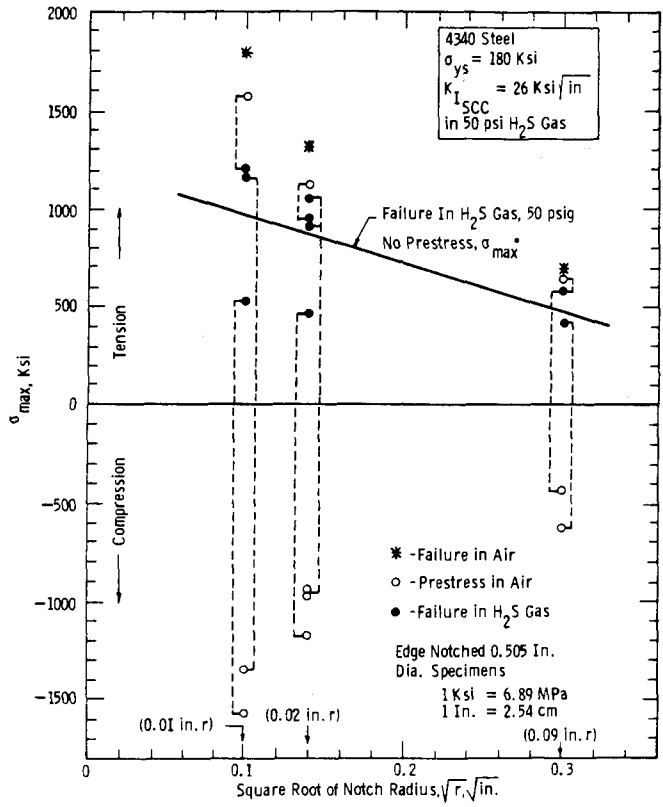

FIG. 6—*Effect of prestressing on* σ_{max} *at failure (1 ksi = 6.89 MPa, 1 in. = 2. 54 cm).*

indicates relatively little effect of prestressing on the 0.228-cm (0.09-in.) radius notch test results. However, the overall magnitude of the prestressing level is also significantly lower than that encountered in the other test specimens. For the smaller notch radii tests, the effect of compressive prestressing can be very significant, reducing the σ_{max} value for crack initiation by 50 percent. However, as shown in Fig. 6, the potential detrimental effect of compressive prestressing appears to be strongly dependent on the specific compressive prestress level. Note that only a small difference in compressive prestress level accounts for the large decrease in crack initiation resistance. Such behavior implies that some kind of threshold level may exist above which compressive prestressing has little effect on subsequent crack initiation behavior. Sufficient test data were not available to examine this phenomenon in the higher strength material (Fig. 7). As was the case for tension prestressing, compressive prestressing appears to have a more significant effect on the higher-strength steel than on the lower strength-material.

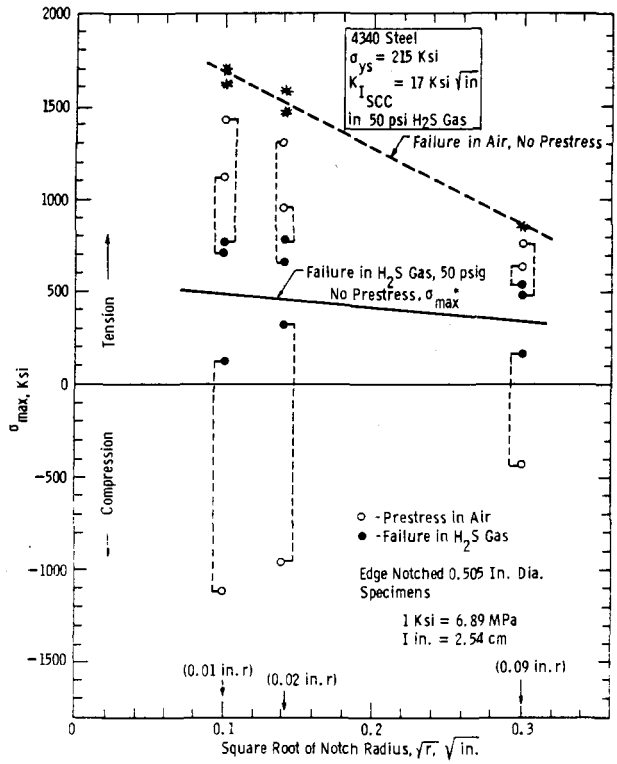

FIG. 7—*Effect of prestressing on* σ_{max} *at failure (1 ksi = 6.89 MPa, 1 in. = 2.54 cm).*

Discussion

The results of this investigation, although preliminary in nature, clearly demonstrate the potential significance of prestressing in air on the subsequent stress-corrosion crack initiation performance at blunt notches in high-strength steels. The fact that virtually all engineering structures are likely to be subjected to overloads or prestressing as the result of proof-testing, fabrication, and shipping and handling prior to exposure to service makes the consideration of prestressing effects an important practical concern. The data presented here show that prestressing can either increase or decrease susceptibility to stress-corrosion crack initiation, and the expected behavior can be characterized in terms of the elastically calculated maximum notch stress. Compressive prestressing tends to increase the susceptibility to cracking, and tension prestressing reduces the susceptibility. Obviously, this behavior is related to the magnitude of residual stresses associated with the specific prestressing conditions. Compressive prestressing results in residual tension stresses which ultimately combine

with the subsequent applied tensile stress to produce cracking at lower applied stresses than those required for cracking without prestressing. The opposite conditions prevail for tensile prestressing resulting in an apparent increased resistance to cracking. Whether residual stresses alone account for the behavior observed in this investigation cannot be determined from the data currently available. Prestressed air tests must be conducted and the results compared with equivalent environmental tests to develop a quantitative measure of the specific role of residual stresses in stress-corrosion crack initiation.

The tests conducted in this investigation with edge-notched tensile specimens are limited to the evaluation of net section prestress levels on the order of the yield strength of the material (limit load conditions for a tensile test). However, often in real applications it is possible to develop significantly higher stress levels that could have even more effect on subsequent stress-corrosion behavior. Consequently, the results of this study cannot be considered to reflect the maximum potential effect of prestressing on crack initiation performance.

The variation in the effect of prestressing on stress-corrosion crack initiation behavior encountered between the two steels investigated here implies that it is rational to expect significant differences in behavior between more dissimilar materials. In view of the significant role of residual stresses on the effect of prestressing on subsequent crack initiation, it is likely that the strain hardening characteristics of a material may be an extremely important factor in the consideration of prestress effects. It is highly possible that materials not normally susceptible to stress-corrosion cracking in a particular environment may in fact become susceptible as the result of prestressing.

In this investigation an attempt was made to characterize the effect of prestressing on subsequent stress-corrosion crack-initiation behavior in terms of a parameter that is applicable to actual design considerations. However, like any other design parameter, if the appropriate information associated with the structural component is not available, the parameter is of limited value. With regard to the application of the σ_{max}* concept to predicting crack initiation in potential aggressive environments, it is important that the loading conditions and appropriate stress levels associated with the application be well established. Often, developing such information is the most difficult aspect of any design analysis.

Summary and Conclusions

A preliminary evaluation of the effect of both tension and compression prestressing on subsequent stress-corrosion crack initiation behavior at blunt notches was conducted with two high strength AISI type 4340 steels. The prestressing was conducted in air, and the crack initiation testing was

conducted in 345-kPa (50 psig) gage H_2S gas. All testing involved edge-notched round tensile specimens with three different notch radii, the results expressed in terms of both applied net section and elastically calculated maximum notch stresses.

The pertinent conclusions associated with this investigation are summarized below.

1. Prestressing in air can have a significant effect on the subsequent stress-corrosion crack-initiation behavior at blunt notches in high strength steels.

2. Tension prestressing in air results in improved resistance to subsequent stress-corrosion crack initiation at blunt notches.

3. Compressive prestressing in air can have a severe detrimental effect on subsequent stress-corrosion crack initiation behavior. The maximum elastically calculated notch stress required to induce stress-corrosion cracking could be reduced by as much as a factor of 4 as the result of compressive prestressing.

4. Additional tests with specimens which permit net section prestressing beyond the yield strength of the materials are required to establish the maximum potential effect of prestressing in air on subsequent stress-corrosion crack initiation.

H. Riedel[1] *and J. R. Rice*[2]

Tensile Cracks in Creeping Solids

REFERENCE: Riedel, H. and Rice, J. R., **"Tensile Cracks in Creeping Solids,"** *Fracture Mechanics: Twelfth Conference, ASTM STP 700,* American Society for Testing and Materials, 1980, pp. 112-130.

ABSTRACT: The aim of the paper is to answer the question: which loading parameter determines the stress and strain fields near a crack tip, and thereby the growth of the crack, under creep conditions? As candidates for relevant loading parameters, the stress intensity factor K_I, the path-independent integral C^*, and the net section stress σ_{net} have been proposed in the literature. The answer, which is attempted in this paper, is based on the time-dependent stress analysis of a stationary crack in Mode I tension. The material behavior is modeled as elastic-nonlinear viscous, where the nonlinear term describes power law creep. At the time $t = 0$, load is applied to the cracked specimen, and in the first instant the stress distribution is elastic. Subsequently, creep deformation relaxes the initial stress concentration at the crack tip, and creep strains develop rapidly near the crack tip. These processes may be analytically described by self-similar solutions for short times t.

An important result of the analysis is that small-scale yielding may be defined. In creep problems, this means that elastic strains dominate almost everywhere except in a small "creep zone" which grows around the crack tip. If crack growth ensues while the creep zone is still small compared with the crack length and the specimen size, the stress intensity factor governs crack growth behavior.

If, however, the calculated creep zone becomes larger than the specimen size, the stresses become finally time-independent and the elastic strain rates can be neglected. In this limiting case, the stress field is the same as in the fully-plastic limit of power law hardening plasticity that has been treated in the literature. The loading parameter that determines the near tip fields uniquely is then the path-independent integral C^*.

It should be emphasized that K_I and C^* characterize opposite limiting cases. Which case applies in a given situation can be decided by comparing the creep zone size with the specimen size and the crack length. Criteria for small-scale yielding are worked out in several alternative forms. Besides several methods of estimating the creep zone size, a convenient expression for a characteristic time is derived also, which characterizes the transition from small-scale yielding to extensive creep of the whole specimen.

KEY WORDS: fracture mechanics, stress analysis, elevated temperature mechanical properties, creep, fractures (materials), crack propagation

[1] Visiting assistant professor, Division of Engineering, Brown University, Providence, R.I. 02912. Also a permanent affiliation with Max-Planck-Institut für Eisenforschung, 4000 Düsseldorf, Federal Republic of Germany.

[2] Professor, Division of Engineering, Brown University, Providence, R.I. 02912.

Under elevated temperature creep conditions in ductile solids, macroscopic cracks grow by local failure of the highly strained material near the crack tip due to the initiation and joining of microcavities, sometimes aided by local corrosion. These processes are often confined to a small fracture process zone near the crack tip. The aim of the present paper is to analyze the stress and strain fields that encompass the process zone and set boundary conditions on its behavior. In the analysis, the fracture process zone is assumed to be negligibly small. This kind of analysis is necessary to gain insight into the problem of which macroscopic loading parameter governs crack growth under creep conditions. As candidates for relevant loading parameters, the stress intensity factor K_I [*1*],[3] the net section stress σ_{net} [*2*], the path independent integral C^* [*3,4*], and the crack tip opening displacement rate $\dot{\delta}$ [*5*] have been proposed. For a more comprehensive survey of the recent literature, see Refs *6* through *8*. The question of the "right" loading parameter is far from being academic; if, from laboratory crack growth tests, growth rates in large structures are to be predicted, it may be too conservative to use the stress intensity factor as the correlating parameter. This is clearly demonstrated in the work of Koterazawa and Mori [*9*], where the crack growth rate drops by two orders of magnitude if the specimen size is chosen as 20 mm instead of 8 mm, although the nominal stress intensity factor is kept constant. On the other hand, the use of the net section stress as the correlating parameter between laboratory tests and large structures can lead to unconservative predictions in cases where the stress intensity factor should have been used.

Based on a Dugdale model, Riedel [*8*] and Ewing [*10*] have worked out conditions under which the stress intensity factor is the relevant parameter for creep crack growth. More recently, Riedel [*7*] has confirmed these results by the analysis of a stationary shear crack (Mode III) in an isotropic material that is capable of elastic and creep deformation everywhere. The key feature of the analysis is that "small-scale yielding" conditions may be defined. In creep problems, small-scale yielding means that elastic strains dominate almost everywhere in the specimen except in a small "creep zone," which grows around the crack tip. The creep zone boundary has been defined for stationary cracks as the locus where creep strain and elastic strain are equal. If crack growth ensues while the creep zone is still sufficiently small compared with the specimen size, the stress intensity factor governs crack growth.

In the present paper, the stress analysis of a stationary crack under creep conditions is worked out for tensile loading (Mode I). Both small-scale yielding as well as the case where the whole specimen creeps extensively ("fully yielded case") are considered. For small-scale yielding, the stress in-

[3] The italic numbers in brackets refer to the list of references appended to this paper.

tensity factor K_I governs crack growth initiation; whereas the path-independent integral C^* [*3,4*] is the relevant loading parameter for the case of extensive creep. Finally, it is pointed up that, for growing cracks, K_I and C^* remain the loading parameters, which determine the crack growth rate. But the relation between the crack growth rate and the loading parameter may become complicated, for instance, dependent on the previous history of loading and crack growth. The stress analysis of growing cracks will be further discussed in two forthcoming papers [*11,12*].

Constitutive Equations, Initial and Boundary Conditions

The authors will consider here the two-dimensional problems of plane-stress or plane-strain tension, known also as Mode I. A crack is embedded in a material that may be classified as a Maxwell-type elastic-nonlinear-viscous material, where the nonlinear behavior represents power law creep. Creep deformation is assumed to be incompressible. The deviatoric strain rate tensor, $\dot{\epsilon}'$ is related to the deviatoric stress and stress rate tensors, σ' and $\dot{\sigma}'$ by[4]

$$\dot{\epsilon}' = \frac{1}{2G}\dot{\sigma}' + \frac{3}{2}B\sigma'\sigma_e^{n-1} \tag{1}$$

Here, G is the elastic shear modulus. The creep exponent n and the temperature-dependent factor B are the parameters of the power law creep relation $\dot{\epsilon} = B\sigma^n$, measured in uniaxial tension creep tests. The equivalent tensile stress σ_e is given by (see footnote 4)

$$\sigma_e = \left(\frac{3}{2}\sigma' : \sigma'\right)^{1/2} \tag{2}$$

If elastic compressibility is admitted, the traces of stress and strain tensors are related via the bulk modulus κ

$$\operatorname{tr}\epsilon = \frac{1}{3\kappa}\operatorname{tr}\sigma \tag{3}$$

The material law stated in Eqs 1 to 3 is supplemented by the equilibrium condition

$$\nabla \cdot \sigma = 0 \tag{4}$$

[4] In the tensor notation used throughout this paper, boldface quantities are tensors. A dot between two tensors indicates summation over one index; a double dot indicates summation over two indexes. $\mathbf{I}$ is the two-dimensional unit tensor; that is, $\mathbf{I}:\mathbf{I} = 2$, ∇ is the three-dimensional gradient operator, and ∇^2 is the Laplace-operator. A prime indicates the deviant part of a three-dimensional tensor. Traces are the sum of the three diagonal tensor components.

and by the compatibility relation which, for plane problems, has the form

$$\nabla \cdot (\nabla \cdot \epsilon') = \frac{2}{3} \nabla^2 (\mathrm{tr}\, \epsilon) - \nabla^2 \epsilon_{33} \tag{5}$$

where $\nabla_3 = 0$ for plane problems. In the direction of the crack front (x_3-axis), we have an additional equation, either $\epsilon_{33} = 0$ (plane strain), or $\sigma_{33} = 0$ (plane stress).

The initial condition is that a load is applied suddenly to the cracked specimen at the time, $t = 0$. According to the material law stated in Eq 1, the instantaneous response of the material is elastic. Therefore, at time $t = 0$, the elastic stress distribution [*13*] prevails in the cracked body.

Boundary conditions are prescribed on the traction-free crack faces, $\mathbf{n} \cdot \sigma = 0$ ($\mathbf{n}$ = normal vector on crack face), and at infinity. For small-scale yielding (short time response), it suffices to regard the crack as being of semi-infinite extent, with the boundary condition at infinity being the requirement of asymptotic approach to the elastic singular field characterized by the stress intensity factor [*13*].

The problem stated in the preceding Eqs 1 through 5 will now alternately be formulated in terms of the Airy stress function, ϕ. It is related to the in-plane components of the stress tensor by

$$\sigma = -\nabla \nabla \phi + \mathbf{I} \nabla^2 \phi \tag{6}$$

thus automatically fulfilling the equilibrium condition (Eq 4). Inserting the stress tensor according to Eq 6 into the material law (Eqs 1 through 3) and inserting the resulting strain rate tensor into the compatibility condition (Eq 5), one arrives at an equation for the Airy stress function, ϕ.

For plane strain, the deviatoric stress component σ_{33}' cannot be expressed in terms of ϕ; the plane-strain condition $\epsilon_{33} = 0$ forms an additional equation. Thus, for plane strain we have two coupled equations for ϕ and σ_{33}'

$$2\frac{1-\nu}{E} \nabla^2 (\nabla^2 \dot{\phi} + \dot{\sigma}_{33}')$$

$$-B \nabla \cdot \{\nabla \cdot [(\mathbf{I}(\nabla^2 \phi - \sigma_{33}') - 2 \nabla \nabla \phi) \sigma_e^{n-1}]\} = 0 \tag{7}$$

$$\left(\frac{1-2\nu}{3E} \nabla^2 \dot{\phi} + \frac{1}{E} \dot{\sigma}_{33}'\right) + B \sigma_{33}' \sigma_e^{n-1} = 0 \tag{7a}$$

where

E = Young's modulus,
ν = Poisson's ratio, and
$\cdot$ = time derivative.

The equivalent stress σ_e is given in terms of ϕ and σ_{33}' as

$$\sigma_e = \frac{\sqrt{3}}{2}[2(\nabla\nabla\phi:\nabla\nabla\phi) - (\nabla^2\phi)^2 + 3\sigma_{33}'^2]^{1/2} \tag{8}$$

For incompressible material ($\nu \to 1/2$), Eqs 7 and 7*a* are simplified since $\sigma_{33}' = 0$.

For plane stress the governing equation for the Airy stress function has the form

$$\frac{2}{E}\nabla^4\dot{\phi} - B\nabla\cdot\{\nabla\cdot[(\mathbf{I}\nabla^2\phi - 3\nabla\nabla\phi)\sigma_e^{n-1}]\} = 0 \tag{9}$$

and the equivalent stress is

$$\sigma_e = \frac{1}{\sqrt{2}}[3(\nabla\nabla\phi:\nabla\nabla\phi) - (\nabla^2\phi)^2]^{1/2} \tag{10}$$

The authors use either a polar coordinate system (r, θ) with $\theta = 0$ directly ahead of the crack and the origin at the crack tip, or Cartesian coordinates (x, y) with the x-direction parallel to $\theta = 0$.

The equations for ϕ, (Eqs 7 and 9), together with the expressions for σ_e are nonlinear partial differential equations of fifth order with three independent variables, namely, r, θ, and t. Because of the complexity of the equations, no closed-form solutions can be expected, in general. On the other hand, numerical methods have particular stability problems with the rapid stress redistribution near crack tips in strongly nonlinear elasto-viscous materials. The authors show here, however, that an approximate but rather complete picture of the stress and strain fields can be achieved by analytical methods. In the following sections, first the asymptotic behavior near the crack tip is studied, which is common to the small-scale yielding and the fully yielded case and to intermediate cases. Then the fully yielded case follows, which is relatively simple, and finally the small-scale yielding case, which is more complicated, is treated by means of self-similar solutions.

The Asymptotic Field Near the Crack Tip

Near the crack tip ($r \to 0$), the elastic strain rates can be neglected in the material law, Eq 1, compared with the creep rates. The reason is that the creep exponent usually is greater than one ($n = 4$ to 6 is typical), which makes the creep rates ($\propto\sigma^n$) much larger than the elastic strain rates ($\propto\dot{\sigma}$), if the stress near the crack tip is unbounded. As a consequence, the linear terms in the partial differential Eqs 7 and 9 can be neglected for $r \to 0$. This

leads to exactly the same asymptotic problem which is known from the analysis of rate-insensitive "power law" strain-hardening materials. Hutchinson [*14*] and Rice and Rosengren [*15*] (referred to as HRR hereafter) have given the form of the stress and strain singularities

$$\sigma(r, \theta, t) = A(t)\tilde{\sigma}(\theta)r^{-1/(n+1)} \tag{11}$$

The creep strain and strain rate has an $r^{-n/(n+1)}$ singularity. The angular functions $\tilde{\sigma}(\theta)$ are given graphically in Refs *14* through *17*. Here, we understand $\tilde{\sigma}(\theta)$ normalized as in Ref *17*, such that the function, $\tilde{\sigma}_e(\theta)$, which belongs to the equivalent stress, is normalized to unity at its maximum value. The amplitude, A, of the HRR-stress field is a function of the time and of the applied load. It cannot be specified by analyzing the asymptotic problem alone. In the deformation theory of power-law hardening plasticity, the amplitude of the HRR-field could be specified by means of the J-integral [*14,15*]. Analogously, the amplitude of the HRR-field will be specified in terms of the C*-integral for the limiting case of extensive creep of the whole specimen (see next section). This case corresponds to steady-state creep, thus elastic strain rates vanish and the material responds as if it were purely viscous. For small-scale yielding, however, the elastic as well as the creep strain rates are important. Neither J nor C^* are then path-independent, and approximate methods must be applied to determine the amplitude $A(t)$.

Extensive Creep of the Whole Specimen

The material law stated in Eq 1 has the property that the stresses become time-independent ($\dot{\sigma} \to 0$) after long times ($t \to \infty$) if the load is kept constant and geometry changes can be neglected. This latter condition, in particular, implies that the crack must be effectively stationary. So, for $\dot{\sigma} = 0$, the constitutive Eqs 1 through 5 take the form of nonlinear elastic materials, if the strain rate is replaced by strain. The same nonlinear elastic material law also describes the fully plastic limit for power law hardening materials. This case has been studied extensively in the literature [*18–22*] and the results can immediately be used here by writing strain rate instead of strain, and the path-independent integral C^* [*3,4*] instead of the J-integral [*13*]. The C*-integral can be measured at the loading pins of cracked specimens [*3*]. Its relation to the applied load has also been calculated numerically, reading C^* instead of J in Refs *18* through *22*. On the other hand, C^* is related to the amplitude of the near tip singular field [*14,15*] by

$$A(t \to \infty) = \left[\frac{C^*}{BI_n}\right]^{1/(n+1)} \tag{12}$$

In plane strain, numerical values of the factor I_n range from 3.8 (for $n = \infty$)

to 6.3 (for $n = 1$) [*17*]. Plane-stress values of I_n are 2.87 (for $n = 13$) and 3.86 (for $n = 3$) [*16*].

According to Eq 12, C^* is the loading parameter that determines the near-tip singular field, and thereby the initiation of crack growth, if the whole specimen creeps extensively.

Small-Scale Yielding

In a previous paper [*7*] it has been shown that small-scale yielding can be defined under creep conditions. The small-scale yielding solution is valid as long as the creep zone is sufficiently small compared with the dimensions of the specimen. It may be also called a short-time solution, since it describes the development of stresses and strains shortly after the load is applied at $t = 0$.

The solution of the small-scale yielding problem is now shown to be possible in terms of self-similar functions. It follows the same lines as in the Mode III case [*7*], and also the nature of the time-dependence of stresses and strains is the same.

Observe that the stress field σ at any point r, θ at (short) time t after load application is a function of the following set of variables and material parameters

$$r, \theta, t, K_I, E, B, \nu, n$$

Further, from the form of the differential Eqs, 7 and 9, for ϕ, and hence for the stress field, it is clear that E, B, and t can enter only as the product EBt, and one notes that $(EBt)^{-1/(n-1)}$ has the same physical dimensions as does stress. Accordingly, from standard considerations of dimensional consistency, the stress field σ for small-scale yielding, or short times, has the form

$$\sigma = (EBt)^{-1/(n-1)}\mathbf{F}[(EBt)^{-2/(n-1)}r/K_I{}^2, \theta, n, \nu]$$

where $\mathbf{F}$ is a dimensionless function of its (dimensionless) arguments. In fact, for plane stress the function $\mathbf{F}$ is independent of ν, since ν appears in neither the differential Eq 9 nor the boundary conditions. The detailed formulation of a solution in the above "self-similar" form is discussed next, introducing notations paralleling those of Ref *7*.

Self-Similar Solutions

For plane strain, the self-similar stress function and stress component $\sigma_{33}{}'$ that satisfy Eq 7 as well as the initial and boundary conditions have the form

$$\phi(r, \theta, t) = \frac{E}{1 - \nu}\frac{1}{(2\pi)^2}\left(\frac{(1 - \nu)K_I}{E}\right)^4 \Phi(R, \theta)T^{3/(n-1)} \qquad (13a)$$

$$\sigma_{33}'(r, \theta, t) = \frac{E}{1-\nu}\Sigma_{33}'(R, \theta)T^{-1/(n-1)} \tag{13b}$$

The dimensionless time T and radial coordinate R are given by

$$T = \frac{n-1}{2}\left(\frac{E}{1-\nu}\right)^n Bt \tag{14}$$

$$R = \frac{r}{\frac{1}{2\pi}\left(\frac{(1-\nu)K_I}{E}\right)^2 T^{2/(n-1)}} \tag{15}$$

The dimensionless shape functions Φ and Σ_{33}' obey the following differential equations (where the operator ∇ is now understood to act in the dimensionless (R, θ) coordinate system)

$$-2\nabla^2\left(\frac{1}{2} + R\frac{\partial}{\partial R}\right)(\nabla^2\Phi + \Sigma_{33}') + \nabla\cdot\left\{\nabla\cdot\left[(2\nabla\nabla\Phi - \mathbf{I}(\nabla^2\Phi - \Sigma_{33}')\right.\right.$$

$$\left.\left.\left(\frac{3}{2}(\nabla\nabla\Phi:\nabla\nabla\Phi) - \frac{3}{4}(\nabla^2\Phi)^2 + \frac{9}{4}\Sigma_{33}'^2\right)^{(n-1)/2}\right]\right\} = 0 \tag{16a}$$

$$-\left(\frac{1}{2} + R\frac{\partial}{\partial R}\right)\frac{(1-2\nu)\nabla^2\Phi + 3\Sigma_{33}'}{3(1-\nu)}$$

$$+ \Sigma_{33}'\left[\frac{3}{2}(\nabla\nabla\Phi:\nabla\nabla\Phi) - \frac{3}{4}(\nabla^2\Phi)^2 + \frac{9}{4}\Sigma_{33}'^2\right]^{(n-1)/2} = 0 \tag{16b}$$

For plane stress the same form for ϕ as defined by Eqs 13*a*, 14, and 15 may be assumed, but with $1 - \nu$ replaced everywhere by 1. In this case, Eq 9 reduces to

$$-2\nabla^2\left(\frac{1}{2} + R\frac{\partial}{\partial R}\right)\nabla^2\Phi +$$

$$\nabla\cdot\left\{\nabla\cdot\left[(3\nabla\nabla\Phi - \mathbf{I}\nabla^2\Phi)\left(\frac{3}{2}(\nabla\nabla\Phi:\nabla\nabla\Phi) - \frac{1}{2}(\nabla^2\Phi)^2\right)^{(n-1)/2}\right]\right\} = 0 \tag{17}$$

The boundary condition at infinity is the elastic field. In dimensionless form

$$\Phi(R \to \infty) = \frac{4}{3}R^{3/2}\cos^3\frac{\theta}{2} \tag{18}$$

For plane strain, one also has the boundary condition

$$\Sigma_{33}'(R \to \infty) = -\frac{2}{3}(1 - 2\nu)R^{-1/2}\cos\frac{\theta}{2} \tag{19}$$

Once the shape functions Φ and Σ_{33}' are known by solving the differential Eqs 16 and 17, subject to traction-free crack surface boundary conditions, stresses and strains can be calculated. The stress tensor has the form

$$\sigma = \frac{E}{1 - \nu} T^{-1/(n-1)}\Sigma(R, \theta) \tag{20}$$

where the in-plane components of the dimensionless shape function Σ follow from Φ

$$\Sigma = -\nabla\nabla\Phi + \mathbf{I}\nabla^2\Phi \tag{21}$$

The factor $1 - \nu$ must be replaced by unity for plane stress. Further, from Eq 11 it is known that Σ must become infinite in the form $R^{-1/(1+n)}$ as $R \to 0$. The elastic strain, ϵ^{el}, follows from Eq 20 by Hooke's law. The creep strain, ϵ^{cr}, can also be expressed in terms of Σ, using Eq 1

$$\epsilon^{cr} = T^{-1/(n-1)}\mathbf{E}^{cr}(R, \theta) \tag{22}$$

with

$$\mathbf{E}^{cr}(R, \theta) = \frac{3}{2\sqrt{R}} \int_R^\infty \Sigma'\left(\frac{3}{2}\Sigma' : \Sigma'\right)^{(n-1)/2} \frac{d\rho}{\sqrt{\rho}} \tag{23}$$

Here, $\Sigma' = \Sigma'(\rho, \theta)$ is the deviatoric part of Σ and the integral on ρ is done with θ fixed. The total strain, ϵ, is given by the sum $\epsilon = \epsilon^{el} + \epsilon^{cr}$.

A precise graphical presentation of the stress and strain fields would require the numerical solution of the nonlinear partial differential Eqs 16 and 17, which will be attempted in future work, in analogy to the solutions obtained in Mode III [7].

Approximate Description of the Small-Scale Yielding Stress and Strain Fields

Presently, no numerical solutions of Eqs 16 and 17 are available, but a qualitative description of the stress and strain fields is possible. First the authors note that the time dependence of the stresses and strains (Eqs 20 through 23) is the same as in Mode III [7]: the initial elastic stress concentration at the crack tip is relaxed by creep deformation, and the stresses are dis-

tributed more homogeneously across the specimen, while creep strains develop preferably in a creep zone which grows around the crack tip.

Using Eqs 11 and 20, one knows the r and t dependence of the near-tip HRR-field, which can now be specified except for a numerical amplitude factor α_n. (This factor will be calculated approximately in the next subsection, where the authors show $\alpha_n \approx 1$.) Thus, the near tip stress and strain fields, for small-scale yielding, are

$$\sigma = \alpha_n \left[\frac{nK_I^2}{\pi(n+1)^2 EB}\right]^{1/(n+1)} \tilde{\sigma}(\theta)(rt)^{-1/(n+1)} \tag{24}$$

$$\epsilon = \frac{3}{2} B(n+1)\alpha_n{}^n \left[\frac{nK_I^2}{\pi(n+1)^2 EB}\right]^{n/(n+1)} \tilde{\sigma}'(\theta)[\tilde{\sigma}_e(\theta)]^{n-1} \frac{t^{1/(n+1)}}{r^{n/(n+1)}} \tag{25}$$

One now knows the asymptotic fields at infinity (linear-elastic field) and near the crack tip (HRR-field, Eqs 24 and 25). One can now assemble approximate solutions by simply extrapolating the asymptotic fields to the locus $r_1(\theta, t)$, which is defined by the equality of the equivalent stresses of the remote elastic and the near tip HRR-field. This definition leads to

$$r_1(\theta, t) = \frac{1}{2\pi}\left(\frac{K_I}{E}\right)^2 \left[\frac{(n+1)^2 E^n Bt}{2n\alpha_n{}^{n+1}}\right]^{2/(n-1)} F_1(\theta) \tag{26}$$

with the angular function

$$F_1(\theta) = \left\{\frac{\cos^2\frac{\theta}{2}\left[(1-2\nu)^2 + 3\sin^2\frac{\theta}{2}\right]}{[\tilde{\sigma}_e(\theta)]^2}\right\}^{(n+1)/(n-1)} \tag{27}$$

This form applies for plane strain; for plane stress, the expression $1 - 2\nu$ must be replaced by unity, and $\tilde{\sigma}_e(\theta)$ and α_n have their plane stress values.

The creep zone boundary has been defined by equating the equivalent creep strain $\epsilon_e{}^{cr}$ to the equivalent elastic strain $\epsilon_e{}^{el}$ [7]. If one uses this definition and calculates the strains from the assembled stress field described above, the result for the creep zone boundary $r_{cr}(\theta, t)$ has the same functional form as r_1 except for the angular function $F_{cr}(\theta)$:

$$r_{cr}(\theta, t) = \frac{1}{2\pi}\left(\frac{K_I}{E}\right)^2 \left[\frac{(n+1)^2 E^n Bt}{2n\alpha_n{}^{n+1}}\right]^{2/(n-1)} F_{cr}(\theta) \tag{28}$$

According to Eq 28 the creep zone expands in proportion to $t^{2/(n-1)}$. The angular functions $F_1(\theta)$ and $F_{cr}(\theta)$ are shown in Fig. 1. Within the accuracy of the present method, the creep zone boundary runs into the crack tip. More

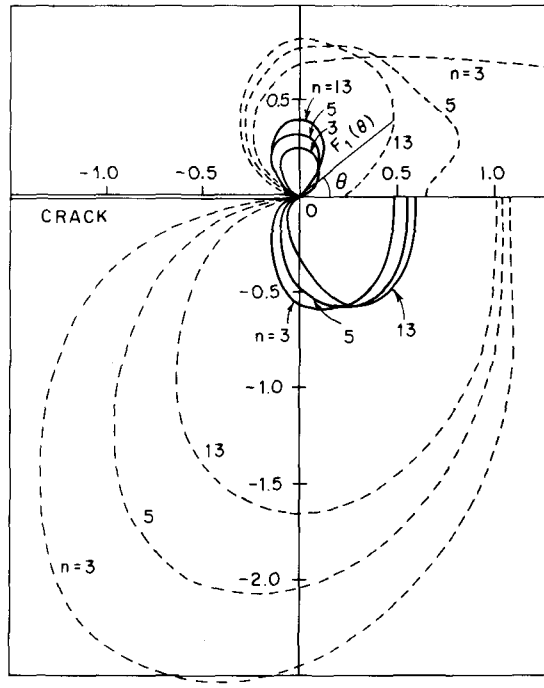

FIG. 1—*Polar diagrams of the angular functions* $F_1(\theta)$ (dashed lines) *and* $F_{cr}(\theta)$ (solid lines), *for plane strain* (upper half) *and plane stress* (lower half). *Creep exponent* n = *3, 5, 13. Poisson's ratio* $\nu = 0.3$.

accurate methods, however, might lead to a creep zone boundary which hits the crack faces behind the crack tip.

Approximate Calculation of the Factor α_n—The proper way to calculate the dimensionless factor α_n, which appears in the results of the preceding subsection, would be to solve the partial differential Eqs 16 and 17 numerically; the amplitude of the near tip singular field is then part of the result. In the present paper, however, the authors estimate the value of α_n by means of the path-integral J [*13*]. The quantity $W = \int \sigma : d\epsilon$, which appears in the J-integral, is understood as an integral over the deformation history at each material point. With this definition of W, the J-integral is, in general, path-dependent for creep problems. One assumes, however, that J is approximately path-independent. The reason why one regards this as a reasonable approximation is the following: creep straining takes place mainly in the creep zone. In this region, the HRR-field is a good approximation that becomes asymptotically exact as $r \to 0$. Further, one finds that it is possible to eliminate both coordinates (r, θ) from Eqs 24 and 25, thus showing that stresses and strains in the HRR-region behave as if there were a unique relationship $\epsilon(\sigma)$, independent of (r, θ) at any instant of time

$$\epsilon = \frac{3}{2} B(n+1) t \sigma' \sigma_e^{n-1} \tag{29}$$

The existence of a unique stress-strain relation, however, implies path-independence of J. For the stress-strain relation stated in Eq 29 the value of the J-integral has been calculated in Refs *17* and *18* as a function of the amplitude of the near tip field

$$J_o = (n+1) B t I_n [A(t)]^{n+1} \tag{30}$$

In the elastic field, J has the well-known value [*13*]:

$$J_\infty = \begin{cases} K^2(1-\nu^2)/E & \text{for plane strain} \\ K^2/E & \text{for plane stress} \end{cases} \tag{31}$$

Assuming approximate path-independence of J (that is, $J_o \approx J_\infty$), one obtains the amplitude of the singularity

$$A(t) \approx \left[\frac{K_I^2(1-\nu^2)/E}{(n+1) B I_n t} \right]^{1/(n+1)} \tag{32}$$

and, with the definition of α_n according to Eqs 11 and 24,

$$\alpha_n \approx \left[\frac{n+1}{n} \frac{\pi(1-\nu^2)}{I_n} \right]^{1/(n+1)} \tag{33}$$

This form is for *plane strain.* Numerical values are $\alpha_3 = 0.912$ and $\alpha_{13} = 0.975$ for $\nu = 0.3$. For *plane stress* the factor $(1-\nu^2)$ must be deleted, and the plane stress value for the integral I_n [*16*] must be inserted. Numerical values are $\alpha_n = 1.015$ independent of n, within 1/2 percent accuracy.

It is interesting to note that with this approximate value of α_n, Eq 33, the near tip fields of σ and $\dot{\epsilon}$ for small-scale yielding have the same form as for the extensive yielding case (Eqs 11 and 12), provided that C^*, which governs the amplitude of the latter case, is replaced in all formulas by $G/(1+n)t$ (here $G = (1-\nu^2) K_I^2/E$ for plane strain and K_I^2/E for plane stress).

Assessment of the accuracy—Unfortunately, the error of the approximations in the previous two subsections can be hardly estimated analytically. Therefore, one applies the approximate method to Mode III and compares the results with the numerical results, which are then available [*7*]. It turns out that the approximate method under-estimates the amplitude of the HRR-field by 5, 15, and 30 percent for $n = 4$, 3, and 2, respectively, whereas it gives the field amplitude exactly for $n \to \infty$ (elastic-perfectly plastic material) in Mode III. The practical range of creep exponents is $n = 4$ to 6 and

sometimes higher; in this range the approximation is very close to the exact Mode III result. On the other hand, as $n \rightarrow 1$ the concept of a growing creep zone becomes ill-defined, and this may result in the inaccuracy of the approximation at low n. Figure 2 shows a comparison between the numerically calculated stress and the approximately calculated stress which is composed of the HRR-field near the crack tip and the elastic field far from the crack tip. With the strains calculated from this stress field, one obtains a creep zone size which coincides within 20 percent accuracy with the value calculated numerically [7].

In conclusion, the approximate methods work well for Mode III, and the authors now proceed assuming their approximate validity for Mode I, too.

Criteria for Small-Scale Yielding versus Extensive Creep of Whole Specimen

From the preceding analysis it is clear that the stress intensity factor K_I and the integral C^* characterize the near tip field (and thereby crack growth behavior) in opposite limiting cases as follows: a description by K_I applies if the crack grows while the specimen behaves in a predominantly elastic manner except in a creep zone that is small compared with the specimen size (brittle failure); the C*-integral applies if crack growth is accompanied by extensive creep of the whole specimen (ductile behavior).

As an example, the initiation time for growth of a pre-existing sharp-tipped crack as a function of the loading parameter is calculated. One

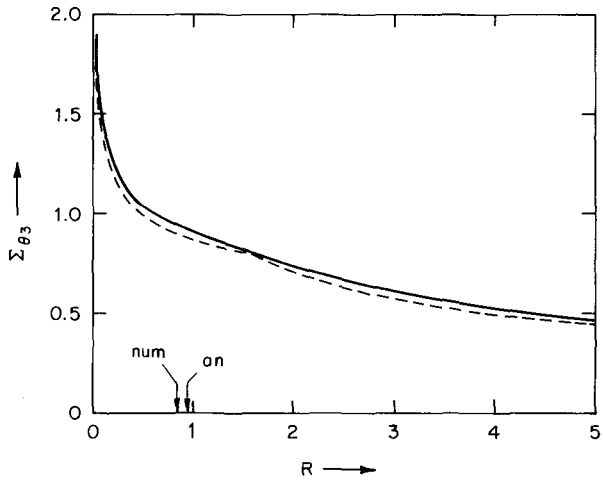

FIG. 2—*Stress component* $\Sigma_{\theta 3}$ *versus distance from crack tip,* R, *for Mode III, normalized as in Eqs* 13 to 15 *but with* 2 G *instead of* $E/(1 - \nu)$. *Comparison of approximate analytical result* (dashed line) *with numerical result* (solid line). *Analytical curve is given by* $\Sigma_{\theta 3} = R^{-1/2}$ *for* $R > 1.59$ *and* $\Sigma_{\theta 3} = 0.863\ R^{-1/5}$ *for* $R < 1.59$. *Arrows indicate creep zone boundary: num = numerical result; an = approximate analytical result. Creep exponent* $n = 4$.

assumes that the crack starts to grow once a critical equivalent strain, ϵ_c, is attained at a small structural distance, r_c, from the crack tip. For plane stress r_c is defined directly ahead of the crack ($\theta = 0$), and for plane strain it is measured in the direction where $\tilde{\sigma}_e(\theta)$ is a maximum. The near tip strains are given by Eq 25 for small-scale yielding. Inverting Eq 25, one obtains the crack growth initiation time, t_i, as a function of the stress intensity factor

$$t_i = {\epsilon_c}^{n+1} \frac{1}{E^n B(n+1)} \left[\frac{n+1}{2n{\alpha_n}^{n+1}} \frac{2\pi E^2 r_c}{{K_I}^2} \right]^n \tag{34}$$

If extensive creep of the whole specimen precedes crack growth initiation, the strains are given by inserting Eqs 11 and 12 into Eq 1. Then the initiation time depends on C^*

$$t_i = \epsilon_c B^{-1/(n+1)} \left[\frac{I_n r_c}{C^*} \right]^{n/(n+1)}. \tag{35}$$

Now some practical guidelines will be discussed as to how one can decide whether or not small-scale yielding conditions prevail in a given test situation:

1. A direct approach would be to estimate the creep zone size experimentally, for example, by observation of a polished specimen surface near the crack tip. Extensive creep of the whole ligament can be detected by measuring the displacement at the loading pins.

2. The second possibility would be to calculate the creep zone size from Eq 28 and compare it with the specimen size. Since the material parameters B and n play an important role in Eq 28, this formula is strictly limited to power law creep.

3. A formula for the creep zone size, which will be approximately valid for more general creep laws than pure power-law creep, is obtained if the time in Eq 28 is replaced by any one of the strain components, ϵ_{ij}. Using Eq 25 with Eq 28 leads to

$$r_{cr}(\theta, t) = \beta_n(\theta_o) \left[\frac{\sqrt{6\pi}\, \epsilon_{ij}(r, \theta_o, t) r^{n/(n+1)}}{(K_I/E)} \right]^{2(n+1)/(n-1)} F_{cr}(\theta) \tag{36}$$

with the numerical factor β_n

$$\beta_n = \left[\frac{n+1}{3^{3/2} n {\alpha_n}^{n+1} \tilde{\sigma}_{ij}'(\theta_o) {\tilde{\sigma}_e}^{n-1}(\theta_o)} \right]^{2(n+1)/(n-1)} \tag{37}$$

In Eqs 35, the strain component ϵ_{ij} is supposed to be measured at a position (r, θ_o) by means of a high-temperature strain gage. The position (r, θ_o) must

be within the creep zone; θ_o is an arbitrary angle and the result of Eq 36 is independent of θ_o. For plane stress, it will be convenient to measure $\epsilon_{\theta\theta}$ directly ahead of the crack tip ($\theta_o = 0$). For plane strain, larger tensile strains can be measured above the crack tip ($\theta_o = \pi/2$) with the axis of the strain gage oriented at an angle $\theta = 3\pi/4$. Then numerical values for β_n are $\beta_3 = 0.212$ and $\beta_{13} = 0.238$ for plane strain, and $\beta_3 = 0.074$ and $\beta_{13} = 0.067$ for plane stress. Thus, Eqs 36 and 37 provide a rough estimate for the creep zone size even if the creep exponent n is uncertain, since the result in this form is not strongly dependent of n, if n is large.

4. The creep zone size can also be expressed in terms of crack opening displacement (COD), δ, which is sometimes convenient to measure. The resulting relation depends on the definition of COD: one definition of COD is to measure the distance between the two crack faces at the point where the creep zone boundary hits the crack faces behind the crack tip. With the approximations of the present theory, this point cannot be determined (see Fig. 1), but the relation between r_{cr} and δ_{czb} (COD at the creep zone boundary) must have the form

$$r_{cr} = \beta_n' \left[\frac{E\delta_{czb}}{K_I}\right]^2 F_{cr}(\theta) \tag{38}$$

The factor β_n' can only be estimated by analogy with the Mode III case [7]. The result is $\beta_n' F_{cr}(\pi/2) \approx 0.3$. The advantage of Eq 38 is that it allows an estimate of the creep zone size independently of the creep parameters B and n. So it may be suspected that Eq 38 is approximately valid for more general creep laws than pure power-law creep. A practical drawback of Eq 38 is that COD at the creep zone boundary will be hard to measure precisely.

COD can also be defined at the point where the line $\theta = 135$ deg originating from the apex of the crack profile, intersects the crack profile [23]. This COD value will be denoted by δ_t. With this definition of COD, one obtains

$$r_{cr} = \beta_n'' \left[\frac{\delta_t}{8}\left(\frac{E}{K_I}\right)^2\right]^{2/(n-1)} \left(\frac{E\delta_t}{K_I}\right)^2 F_{cr}(\theta) \tag{39}$$

with

$$\beta_n'' = \frac{1}{16}\left[\frac{n+1}{n} \cdot \frac{(2\pi)^{1/2}}{|\tilde{u}_\theta(\pi)|\alpha_n{}^{n+1}}\right]^{2(n+1)/(n-1)} \tag{40}$$

The angular part, $\tilde{u}_\theta(\theta)$, of the displacement function is

$$\tilde{u}_\theta(\theta) = \frac{3}{2}\frac{n+1}{n}\left\{\frac{1}{2}(n+1)\frac{\partial}{\partial\theta}\left[\left(\tilde{\sigma}_{rr} - \tilde{\sigma}_{\theta\theta}\right)\tilde{\sigma}_e{}^{n-1}\right] - 2\tilde{\sigma}_{r\theta}\tilde{\sigma}_e{}^{n-1}\right\} \tag{41}$$

Typical numerical values are for plane strain: $\beta_3'' = 0.63$, $\beta_5'' = 0.40$, and $\beta_{13}'' = 0.32$; and for plane stress: $\beta_3'' = 0.127$, $\beta_5'' = 0.116$, and $\beta_{13}'' = 0.108$.

5. Finally, the characteristic time for the transition from small-scale yielding to extensive creep of the whole specimen can be estimated analytically. Figure 3 shows the time-dependence of the amplitude $A(t)$, of the near tip singular stress field. The short-time limit is given by the small-scale yielding result (Eq 32), and the long-time limit is given by Eq 12. The characteristic time, t_1, for the transition defined in Fig. 3, is

$$t_1 = \frac{K_I^2(1 - \nu^2)/E}{(n + 1)C^*} \tag{42}$$

for plane strain; for plane stress, replace $1 - \nu^2$ by 1. Small-scale yielding prevails if the time is sufficiently small compared with the characteristic time t_1. In Eq 42, C^* is considered as a quantity that is known from a numerical analysis of a nonlinear viscous (or, by analogy, small strain nonlinear elastic) problem [*18-22*]. For a center-cracked strip, for instance, Goldman and Hutchinson [*18*] give

$$C^* = a\sigma_\infty \dot{\epsilon}_\infty{}^{cr} \left(\frac{2}{\sqrt{3}}\right)^{n+1} \hat{J}\left(\frac{a}{b}, n\right) \tag{43}$$

The crack length is $2a$, the strip width is $2b$; $\hat{J}$ is given graphically in Ref *18* as a function of a/b and of the creep exponent n; σ_∞ and $\dot{\epsilon}_\infty{}^{cr}$ are the remotely

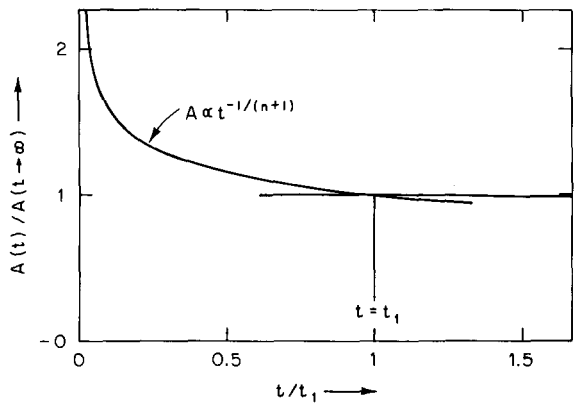

FIG. 3—*Time-dependence of the amplitude of the HRR-near tip stress field,* A(t). *The short-time (small-scale yielding) is described by Eq 32. After long times (extensive creep of the whole specimen) the value given in Eq 12 is approached. The characteristic time,* t_1, *is defined by equating long- and short-time solutions. Creep exponent:* $n = 4$.

applied stress and creep strain rate. With Eq 43 the transition time is given by

$$t_1 = \frac{\sigma_\infty}{E\dot{\epsilon}_\infty^{cr}} \frac{(\sqrt{3}/2)^{n-1}}{1+n} \frac{\hat{J}(a/b, 1)}{\hat{J}(a/b, n)} \tag{44}$$

The material parameter B does not appear in Eq 44, but the creep exponent n has a significant influence. According to Eqs 44 and 28, the creep zone size at the time t_1 is approximately 1/10 of the half crack length, a.

Discussion

Apart from the approximations which are involved in the analysis of the small-scale yielding case, further limitations of the present theory must be kept in mind.

Firstly, the theory has been worked out for a material law which, besides elastic deformation, allows for pure power-law creep only. However, the general conclusion, that a creep zone near the crack tip can be defined, will not be altered if more general creep laws are valid, as long as the creep rate increases stronger than linearly as a function of the stress. From the form of Eqs 36 through 42, it is expected that the size of the creep zone can be estimated even if the creep law is different from a pure power-law relation. In this connection, the authors remark in passing that the solution presented for small-scale yielding is also valid for creep laws which include, approximately, transient effects through a time-hardening expression of the form $\dot{\epsilon} = \dot{\sigma}/E + B(t)\sigma^n$, provided that the product Bt in our solution is everywhere replaced by $\int_o^t B(\tau)d\tau$.

Secondly, the theory is based on the assumption that the fracture process zone is always negligibly small compared with the creep zone and the specimen dimensions. In very ductile materials and small specimens, however, the fracture process zone may spread over the whole cross section of the cracked specimen. This situation can no longer reasonably be described by power law creep. The stress and strain distribution in the net section is likely to be more homogeneous in such a situation than predicted by the present theory. Under these conditions, the net section stress could be the loading parameter to determine the lifetime of cracked as well as uncracked specimens.

Thirdly, the theory does not cover the range between small-scale yielding and extensive creep of the whole specimen. One might expect that an interpolation between the two limiting cases is particularly doubtful for a large plate with a small center-crack under tension. In this case, the creep zone size at the transition time t_1 is about one-tenth of the half crack length. This first appears to be far away from extensive creep of the whole plate. However, if one estimates the strain rates at the transition time by simply adding the remotely applied creep rate $\dot{\epsilon}_\infty^{cr} = B\sigma_\infty^n$, to the creep rate obtained for

small-scale yielding, it turns out that the elastic strain rates are considerably smaller than the creep rates everywhere except near the creep zone boundary where they are of equal order of magnitude. The condition for the extensive creep limit to be valid is that the creep rates are much larger than the elastic rates everywhere. This starts being fulfilled at the transition time. Hence, there is no big gap between the validity of the small-scale yielding and the extensive creep case. Of course, if a higher degree of accuracy is required, the limiting cases are separated by a period of time where neither of them is accurate enough.

Finally, the analysis has been confined to stationary cracks. For growing cracks, the conclusions concerning the applicability of K_I and C^* are not fundamentally altered, but the situation becomes more complicated. The singular field immediately at the tip of a growing crack can no longer be the HRR-field when elastic effects are present [*11*]. As a consequence, the influence of the loading parameters on the near tip strains becomes more complicated than, for instance, the one given in Eq 25. In addition, the stress and strain fields become dependent on the prior history of the loading parameter and of the crack growth. This will be discussed in greater detail in a forthcoming paper [*12*].

Conclusions

An important result of the stress analysis is that a creep zone near the crack tip can reasonably be defined and calculated. The size in relation to specimen size and crack length determines which loading parameter governs crack growth initiation and growth rates. In large cracked specimens or structures (crack length and specimen size are large compared with the creep zone), the stress intensity factor is the loading parameter that correlates crack growth rates between specimens of different shape. In specimens that are small compared with the creep zone, but large compared with the fracture process zone, the path-independent integral C^* is the relevant loading parameter. If the ligament width of the specimen becomes comparable with the size of the fracture process zone (which has been neglected in the present analysis) the net section stress possibly determines the lifetime of a specimen. Excessive crack tip blunting will have a similar effect.

Criteria for small-scale yielding have been developed. They are either based on the comparison of specimen size and creep zone size or on the comparison of the test duration with a characteristic time that can be calculated analytically.

Acknowledgments

H. Riedel was supported in this work by the Max-Planck-Gesellschaft, Munich, and by a visiting appointment in the NSF Materials Research Labo-

ratory at Brown University; J. R. Rice was supported by Department of Energy Contract EY-76-S-02-3084 with Brown University. Helpful discussions with W. J. Drugan of Brown University are gratefully acknowledged. We would also like to thank C. F. Shih of General Electric Research Laboratory and C. Y. Hui of Harvard University who provided numerical tables of the functions $\tilde{\sigma}(\theta)$.

References

[1] Robson, K., "Crack Growth in Two Carbon Steels at 450°C," International Conference on Creep Resistance in Steel, Verein Deutscher Eisenhüttenleute, Düsseldorf, 1972.
[2] Harrison, C. B. and Sandor, G. N., *Engineering Fracture Mechanics*, Vol. 3, 1971, pp. 403-420.
[3] Landes, J. D. and Begley, J. A. in *Mechanics of Crack Growth, ASTM STP 590*, American Society for Testing and Materials, 1976, pp. 128-148.
[4] Nikbin, K. M., Webster, G. A., and Turner, C. E. in *Cracks and Fracture, ASTM STP 601*, American Society for Testing and Materials, 1976, pp. 47-62.
[5] Haigh, J. R., *Materials Science and Engineering*, Vol. 20, No. 2, 1975, pp. 213-224.
[6] Sadananda, K. and Shahinian, P., *Fracture Mechanics*, N. Perrone, H. Liebowitz, D. Mulville, and W. Pilkey, Eds., University Press of Virginia, Charlottesville, Va., 1978, pp. 685-703.
[7] Riedel, H., *Zeitschrift für Metallkunde*, Vol. 69, No. 12, 1978, pp. 755-760.
[8] Riedel, H., *Materials Science and Engineering*, Vol. 30, 1977, pp. 187-196.
[9] Koterazawa, R. and Mori, T., *Transactions* of the American Society of Mechanical Engineers, *Journal for Engineering Materials and Technology*, Vol. 99, Oct. 1977, p. 298.
[10] Ewing, D. J. F., *International Journal of Fracture*, Vol. 14, No. 7, 1978, p. 101.
[11] Hui, C. Y. and Riedel, H., submitted to *International Journal of Fracture*.
[12] Riedel, H. (research in progress).
[13] Rice, J. R., in *Fracture: An Advanced Treatise*, H. Liebowitz, Ed., Vol. 2, Academic Press, New York, 1968.
[14] Hutchinson, J. W., *Journal of Mechanics and Physics of Solids*, Vol. 16, No. 1, 1968, pp. 13-31.
[15] Rice, J. R. and Rosengren, G. F., *Journal of Mechanics and Physics of Solids*, Vol. 16, No. 1, 1968, pp. 1-12.
[16] Hutchinson, J. W., *Journal of Mechanics and Physics of Solids*, No. 5, Vol. 16, 1968, pp. 337-347.
[17] Shih, C. F. in *Fracture Analysis, ASTM STP 560*, American Society for Testing and Materials, 1974, pp. 187-210.
[18] Goldman, N. L. and Hutchinson, J. W., *International Journal of Solids and Structures*, Vol. 11, 1975, pp. 575-591.
[19] Parks, D. M. in *Numerical Methods in Fracture Mechanics*, A. R. Luxmoore and D. R. J. Owen, Eds., Department of Civil Engineering, University College of Swansea, Jan. 1978.
[20] Ranaweera, M. P. and Leckie, F. A. in *Numerical Methods in Fracture Mechanics*, A. R. Luxmoore and D. R. J. Owen, Eds., Department of Civil Engineering, University College of Swansea, Jan. 1978, pp. 450-463.
[21] Hutchinson, J. W., Needleman, A., and Shih, C. F. in *Fracture Mechanics*, N. Perrone, H. Liebowitz, D. Mulville and W. Pilkey, Eds., University Press of Virginia, Charlottesville, Va., 1978, pp. 515-528.
[22] *A Plastic Fracture Handbook*, C. F. Shih et al, Eds., General Electric Research Laboratory, in preparation.
[23] Tracey, D. M., *Transactions* of the American Society of Mechanical Engineers, *Journal of Engineering Materials and Technology*, Vol. 98, April 1976, pp. 146-151.

Ashok Saxena[1]

Evaluation of C^* for the Characterization of Creep-Crack-Growth Behavior in 304 Stainless Steel

REFERENCE: Saxena, Ashok, **"Evaluation of C^* for the Characterization of Creep-Crack-Growth Behavior in 304 Stainless Steel,"** *Fracture Mechanics: Twelfth Conference, ASTM STP 700,* American Society for Testing and Materials, 1980, pp. 131-151.

ABSTRACT: An experimental program to characterize the creep-crack-growth behavior of 304 stainless steel at several temperatures was conducted. Crack growth rates, da/dt, obtained from center crack tension and compact type specimens were correlated by the energy rate line integral, C^*. Experimental data indicate that minor differences in chemistry and microstructure do not significantly influence da/dt versus C^* relationship. Also, in the range of 538 to 705°C (1000 to 1300°F), the da/dt versus C^* relationship is not significantly affected by temperature. Simple analytical methods of estimating C^* are also evaluated.

KEY WORDS: creep, crack, propagation, 304 stainless steel, fracture mechanics, static loading, fractures (materials)

Several structural components of modern power plants operate in the elevated temperature regime where the possibility of creep deformation is an important design consideration. In addition, many of these components are of such large sizes that inspection and repair limitations preclude the assumption of a defect free structure. Consequently, the evaluation of the structural integrity of these components requires the capability to predict the subcritical crack growth behavior under creep conditions.

This paper attempts to establish an appropriate parameter for the characterization of creep crack growth behavior of American Iron and Steel Institute's (AISI) type 304 stainless steel. Although other parameters are

[1] Formerly, Westinghouse Research and Development Center, Pittsburgh, Pa. 15235; presently, reader, Department of Materials Science, Banaras Hindu University, Varanasi-221005, India.

discussed, the main thrust of the paper is directed towards evaluation of the energy rate line integral, C^*, proposed by Landes and Begley [*1*][2] and independently by Nikbin et al [*2*]. In addition, the influence of temperature, heat-to-heat variations, and microstructure, on creep-crack-growth behavior of 304 stainless steel is also explored.

Parameters for Characterizing Creep Crack Growth

Several field parameters have been proposed for characterizing the creep-crack-growth rate behavior of metals. These parameters include; stress intensity, K [*3*], contour integral, J [*4*], crack-tip opening displacement rate, $\dot{\Delta}$ [*5,6*], net section stress [*7*], and energy rate line integral, C^* [*1,2*]. These parameters are briefly evaluated in the subsequent discussion.

Stress Intensity, K

The relationship between creep crack growth rate, da/dt, and K was investigated by Siverns and Price [*3*] and also by Harrison and Sandor [*7*]. In these studies, even though only one specimen geometry was used, the success of K in describing da/dt was at best moderate. For more than one specimen geometry the correlation is expected to be worse. However, for Udimet 700 at 843°C (1550°F), Sadananda and Shahinian [*8*] reported good correlation between da/dt and K. These data were also obtained on one specimen geometry, but good correlation was reported among tests conducted at different loads. These apparently contradicting observations may be explained as below.

Figure 1 shows a schematic of the deformation zones ahead of a crack subjected to load in the creep regime. Upon loading, a plastic zone is formed instantaneously at the crack tip. The size of the plastic zone can be characterized in terms of K and the yield strength of the material. Also schematically shown is the K zone, of finite size, in which the near crack tip elastic stress and deformation fields apply. If the plastic zone size becomes comparable to the size of the K zone, K loses significance. Under such conditions, the crack tip stresses and strains can be characterized by J. With time, the stresses in the vicinity of the crack begin to relax due to creep deformation. The size of the relaxation zone increases as time accumulates. When the relaxation zone becomes comparable in size to the K zone size, neither K or J uniquely characterize the stresses and strains at the crack tip. Hence, these parameters are unsuitable for characterizing crack growth rate, da/dt, as was observed by Siverns and Price [*3*]. For creep resistant materials, such as Udimet 700, temperatures as high as 843°C (1550°F) are not sufficient to cause extensive creep deformation.

[2]Italic numbers in brackets refer to the list of references appended to this paper.

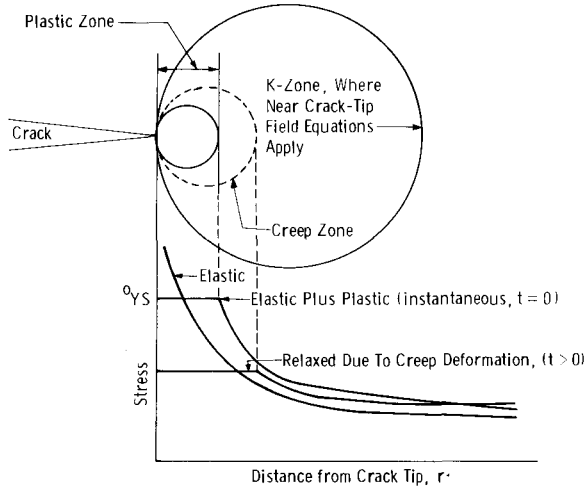

FIG. 1—*Schematic representation of the deformation zones ahead of the crack tip at elevated temperatures.*

Hence, stress relaxation at the crack tip is limited to a very local region, which is smaller compared to the K zone size. Under these circumstances, K will continue to characterize the crack growth rate behavior as it does for the small-scale yielding case. Thus good correlation of da/dt with K appears to exist as reported by Sadananda and Shahinian [*8*].

Net Section Stress

Experimental data for evaluating net section stress for characterizing creep crack growth rate are mixed. Harrison and Sandor [*7*] reported modest correlation between da/dt and net section stress in Cr-Mo-V steel using center crack tension specimens only. Other studies [*9*] involving various specimen geometries, including some with nonuniform stress fields, reported lack of correlation of da/dt with net section stress. Since net section stress does not describe the magnitudes of stress, strain, or strain rate in the crack-tip region, it is not expected to correlate with crack growth rate.

COD Rate, $\dot{\Delta}$

Some investigators have reported correlation between crack-tip opening displacement rate, $\dot{\Delta}$, and da/dt [*3,4*]. Estimation of $\dot{\Delta}$ involves determining the location of the plastic (or inelastic) hinge (point ahead of the crack tip where deflection is zero) and interpolating between the hinge point and load line deflection rate [*10*]. Also, $\dot{\Delta}$ and C^* (to be described in the following paragraph) may be related uniquely as K and Δ are related in linear-elastic-

fracture-mechanics [*11*] and, hence, may be conceptually equivalent. A more rigorous proof is not available at this time.

C* *Line Integral*

The C^* parameter is a path independent energy rate line integral defined by analogy to J [*1,2*]. It is given by

$$C^* = \int_\Gamma W^* \, dy - T_i \left(\frac{\partial \dot{u}_i}{\partial x} \right) ds \tag{1}$$

where

$$W^* = \int_0^{\dot{\epsilon}_{mn}} \sigma_{ij} d\dot{\epsilon}_{ij} \tag{2}$$

As illustrated in Fig. 2, Γ is the line contour taken from the lower crack surface to the upper crack surface. W^* is the strain energy rate density

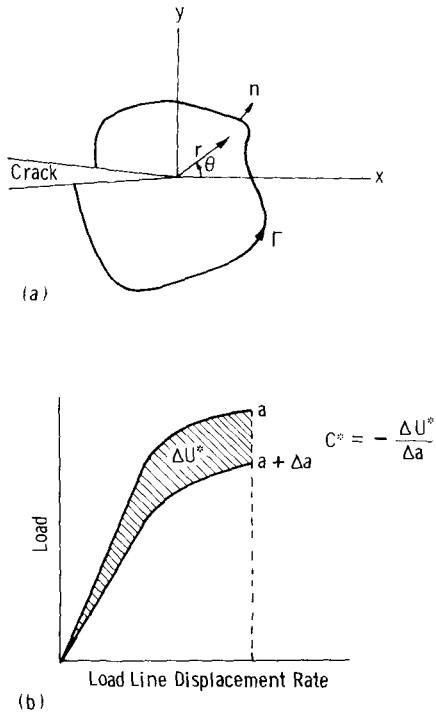

FIG. 2—(a) *Crack-tip coordinate system and arbitrary line integral contour* (b) *schematic illustration of the energy rate interpretation of* C*.

associated with point stress, σ_{ij}, and strain rate, $\dot{\epsilon}_{ij}$. T_i is the traction vector defined by outward normal, n_j, along Γ, $T_i = \sigma_{ij} \cdot n_j$. The displacement vector is denoted by u_i and s is the arc length along the contour.

The energy rate interpretation of C^* was given by Landes and Begley [*1*] also, by analogy to the J-integral. They defined C^* as the power difference between two identically loaded bodies having incrementally differing crack lengths, Fig. 2.

$$C^* = -\frac{dU^*}{da} \tag{3}$$

U^* is the power or energy rate per unit thickness defined for a load P and displacement rate $\dot{u}$. Based on an analogy to McClintock's [*12*] work on J describing the nature of the singularity in the crack-tip region, Goldman and Hutchinson [*13*] have shown that C^* characterizes the stress and strain rate in the vicinity of the crack tip in the secondary creep regime as follows

$$\sigma_{ij} \cdot \dot{\epsilon}_{ij} \propto \frac{C^*}{r} \tag{4}$$

For materials undergoing secondary creep deformation (steady state), the stress and strain rate is commonly related by

$$\frac{\dot{\epsilon}}{\epsilon_o} = \alpha \left(\frac{\sigma}{\sigma_o}\right)^n \tag{5}$$

where, $\dot{\epsilon}_o$ and σ_o are reference strain and stress, respectively, and α and n are material constants. Substituting Eq 5 in Eq 4 one obtains

$$\sigma_{ij} \propto \left(\frac{C^*}{r}\right)^{1/(1+n)} \tag{6}$$

$$\dot{\epsilon}_{ij} \propto \left(\frac{C^*}{r}\right)^{n/n+1} \tag{7}$$

where, r is the distance to the crack tip. Thus, C^* characterizes the crack-tip stress and strain rate field under conditions of local secondary creep behavior.

Experimental work on Discalloy [*1*], alloy 718 [*4*], and 1Cr-Mo-V steel [*14*] show that C^* correlates well with creep crack growth rate. However, there are still some questions about the ability of C^* for correlating crack growth rates obtained from different specimen geometries [*1*].

In this paper, C^* is used to characterize creep crack growth behavior of

304 stainless steel using two different specimen geometries. Simple methods of estimating C^* values are evaluated and recommendations for future work are provided.

Experimental Procedure

Material and Specimen Preparation

The test material used in this investigation was AISI type 304 stainless steel (heat 24348 of Jessop steel) supplied in the hot-rolled, annealed, and pickled condition in the form of a 64-mm (2.5-in.) thick plate. The chemical composition of the material is given in Table 1. Tensile properties of this material at room temperature and at 594°C (1100°F) are given in Table 2.

Center crack tension (CCT) and compact type (CT) specimens, Figs. 3 and 4, respectively, were machined with the notch oriented in the long transverse direction (TL) per ASTM Test For Plane-Stain Fracture Toughness of Metallic Materials (E 399-78). All specimens were precracked approximately 2.5 mm (0.1 in.) at room temperature prior to testing. The terminal value of ΔK for precracking was approximately 13.2 MPa$\sqrt{\text{m}}$ (12 ksi$\sqrt{\text{in.}}$).

Creep Crack Growth Tests

Creep crack growth tests were conducted under constant actuator deflection rate (approximately constant load-line deflection rate) using a servohydraulic test system. The test setup for compact specimen is shown in Fig. 5. The temperature in the test section was controlled to ± 2°C (± 36°F) of the desired value. The load, load-line displacement, and crack length were continuously monitored using load cell, linear voltage differential transformer (LVDT) and electrical potential system (described later in the section), respectively. A typical test record involving measurement of load, crack length, and load-line deflection against time is shown in Fig. 6.

The CCT specimens were each tested at a single constant displacement rate ranging between 0.075 to 0.3 mm/h. On the CT specimens, the displacement rate was changed three times in a step fashion between 0.025 and 0.15 mm/h (0.001 to 0.006 in./h) at crack extension intervals of approximately 5 mm (0.2 in.). This procedure was shown previously to yield more data points from each specimen [*1*]. To avoid any influence from the transient period following a displacement rate change, crack extension immediately following the change was not included while calculating growth rates. The tests were terminated when the crack had grown through 75 to 90 percent of the initial uncracked ligament. At this point, the specimen was cooled to room temperature and cyclically loaded until failure

TABLE 1—*Chemical composition of the 304 stainless steel tested, heat 24348.*

Chemical Composition, weight %										
C	Mn	P	S	Si	Ni	Cr	Mo	Co	Cu	Fe
0.058	1.48	0.035	0.012	0.38	8.90	18.15	0.44	0.17	0.57	balance

TABLE 2—*Room temperature and elevated temperature mechanical properties of the 304 stainless steel tested and for the material used in Ref* 20.

	Orientation	Temperature (deg C)	0.2% Yield Strength		Ultimate Strength		Elongation (%)	Reduction in Area (%)
			MPa	(ksi)	MPa	(ksi)		
Heat 24348	longitudinal	24	269.0	(39.0)	579.0	(84.0)	58.0	82.0
Heat 24348	transverse	24	283.0	(41.0)	586.0	(85.0)	58.0	80.0
Heat 24348	longitudinal	594	108.0	(15.7)	370.0	(53.6)	40.0	70.0
Ref *20*, quenched	longitudinal	24	242.8	(35.2)	603.0	(87.4)	78.0	79.0
Ref *20*, quenched	longitudinal	538	96.5	(14.0)	389.0	(56.4)	46.2	70.0
Ref *20*, quenched	longitudinal	705	86.2	(12.5)	266.9	(38.7)	37.8	60.0
Ref *20*, quenched	longitudinal	24	241.0	(34.9)	594.0	(86.1)	75.0	76.0
and sensitized 2 h	longitudinal	538	111.7	(16.2)	388.3	(56.3)	43.4	67.0
at 1450°F and 2 h	longitudinal	705	86.9	(12.6)	266.2	(38.6)	48.4	64.9
at 750°F								

Conversion factor—C = (°F−32)/1.8.

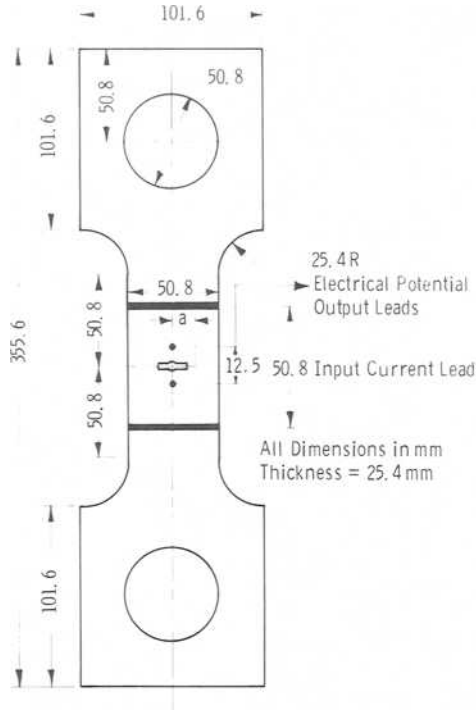

FIG. 3—*Schematic of a center crack tension specimen.*

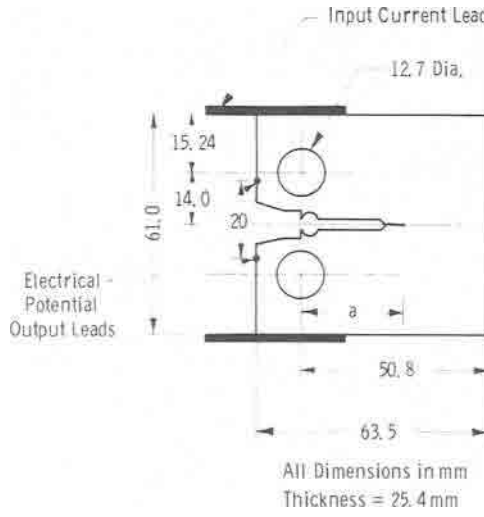

FIG. 4—*Schematic of a compact type (CT) specimen.*

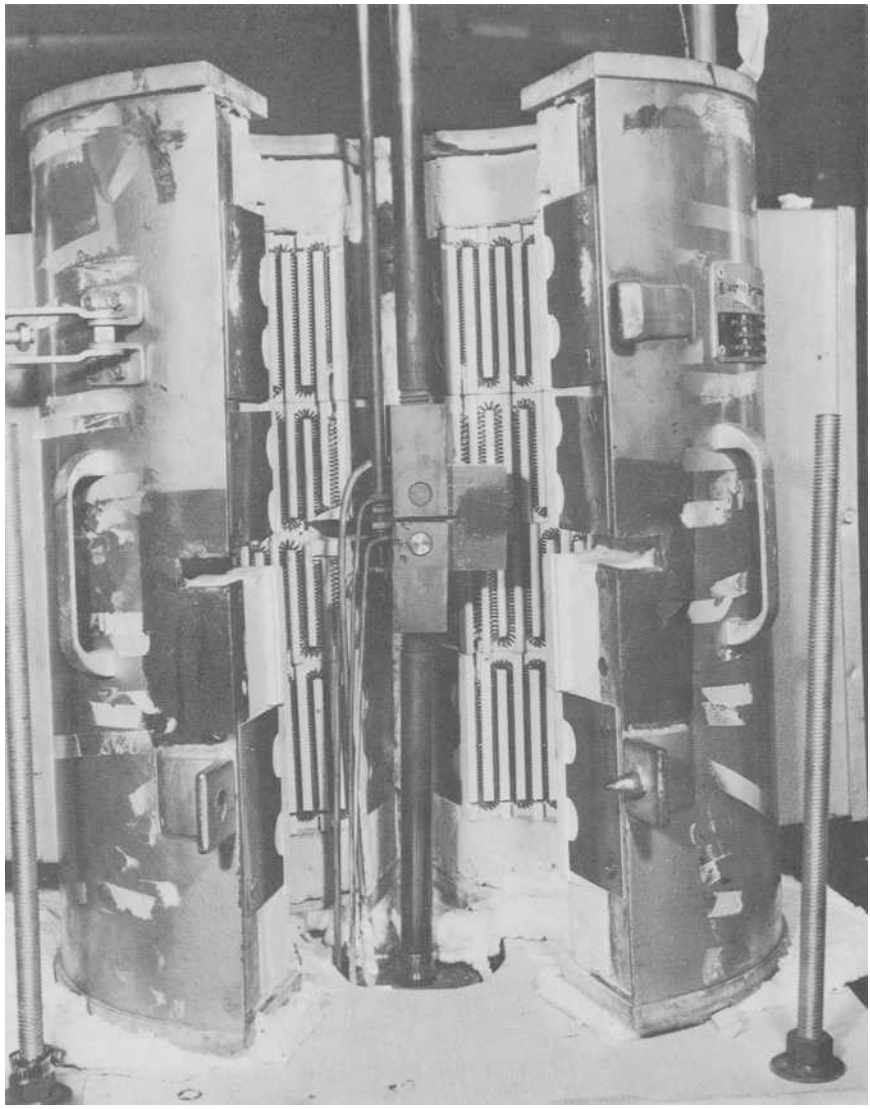

FIG. 5—*Test setup for compact specimen.*

occurred. Thus, an additional bench mark was created for comparing the crack length from electrical potential measurements.

Electrical Potential Technique for Monitoring Crack Extension

Crack length was monitored using a direct current, constant current

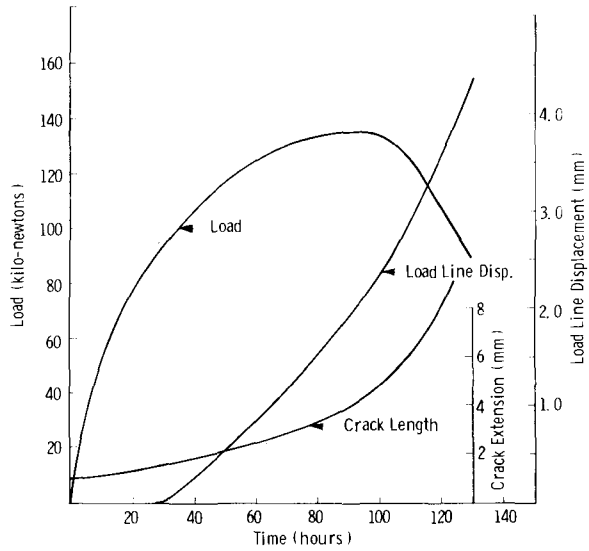

FIG. 6—*A typical test record obtained for a displacement rate controlled test on a CCT specimen.*

electrical potential system [*15*]. The location of the input and output current leads are shown in Figs. 3 and 4 for the two specimen geometries. These locations were found to provide optimum conditions for crack length measurements [*15,16*].

For CCT specimens, the percent change in output voltage was related to the percent change in uncracked ligament by rearranging the analytical calibration equation proposed by Johnson [*15*]. The analytical calibration was verified by comparing the predicted values of final crack length to those directly measured on the fracture surface. Correction factors were thus calculated for each individual test and applied to the electrical potential measurements.

For CT specimens, an experimental calibration curve, Fig. 7, was obtained between output voltage and crack extension by extending crack length under fatigue loading at 594°C (1100°F). Surface crack length was recorded at 1.25-mm (0.05 in.), intervals while a continuous record of electrical potential was obtained on a strip chart recorder. The specimens were also bench marked periodically (four to five times during a 2-cm (0.8 in.) crack extension) to assure that proper tunneling corrections were applied to the visual crack length measurements obtained on the surface. The starting crack length for the creep crack growth tests was between an a/W of 0.48 to 0.51, for which consistent calibrations in Fig. 7 were obtained.

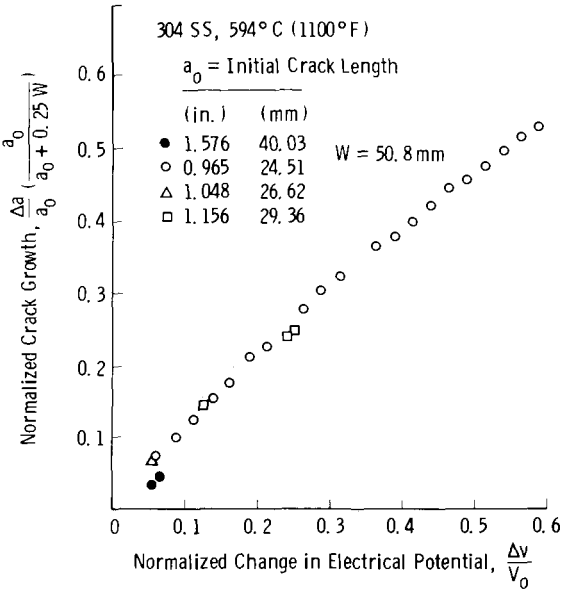

FIG. 7—*Crack extension versus change in electrical potential for 304 stainless steel, CT specimen at 594°C (1100°F).*

Data Reduction

Crack growth rate, *da/dt*, at various crack lengths was calculated by dividing two successive crack length measurements by the elapsed time. *C** was calculated by a multiple specimen graphical technique developed by Landes and Begley [*1*] and also by a simplified method developed from analogy to fully plastic solutions for the J-integral reported by Hutchinson et al [*17,18*]. In the subsequent discussion, the latter is referred to as single specimen analytical method. These methods of estimating *C** are described in detail in the following discussion.

Mulitple Specimen Graphical Procedure

A schematic illustration of the multiple-specimen graphical technique [*1*] used for reducing the data is shown in Fig. 8. The raw data consist of a plot of load, load-line displacement and crack length as a function of time. In Step 1, the load versus displacement rate is plotted for various crack lengths. The area under the load versus displacement rate plot is the energy rate, *U**, or power applied to the specimen. In Step 2, *U** is plotted as function of crack length at various displacement rates. By definition, Eq 7, *C** is the slope of the *U** versus "a" curve. In Step 3, the crack growth rate, *da/dt*, is plotted as a function of *C**.

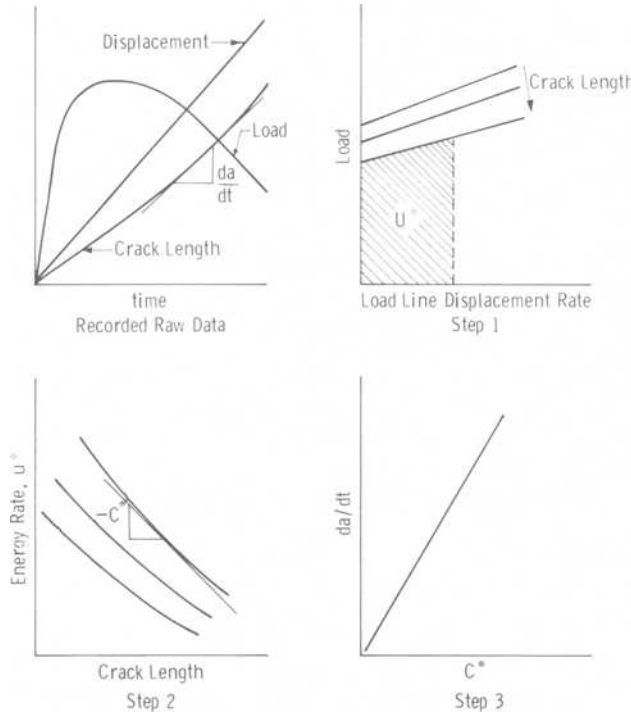

FIG. 8—*Various steps involved in reducing creep crack growth rate data for constant displacement rate test.*

This data reduction procedure requires that several specimens be tested in order to obtain only a few data points. Also, large errors can result during determination of the slope, dU^*/da, which will directly affect the accuracy of C^*. This error can be reduced by testing a large number of specimens at different displacement rates and using regression methods for calculating slopes. However, it would require longer test periods and extensive costs. Due to these disadvantages, an alternate procedure for estimating C^* was also used.

Single Specimen Analytical Method

Hutchinson et al [*17,18*] have proposed equations for estimating J under fully plastic conditions of loading for pure tension and pure bending conditions. These equations can be modified to estimate C^* provided the uncracked ligament of the specimen is undergoing secondary creep. For the CCT and CT specimens, C^* is given by Eqs 8 and 9, respectively

$$C^* = \alpha \dot{\epsilon}_o \sigma_o (1 - 2a/W) a g_1(2a/W, n)(P/P_o)^{n+1} \quad (8)$$

$$C^* = \alpha\sigma_o\dot{\epsilon}_o(W - a)h_1(a/W, n)(M/M_o)^{n+1} \tag{9}$$

where α, n, $\dot{\epsilon}_o$, and σ_o have been defined earlier in Eq 5; and g_1 and h_1 are functions of crack length and the strain rate hardening exponent, n. These functions will be further discussed later. P and M are the applied load and moments respectively. P_O and M_O are limit load and limit moment, respectively, and are given by

$$P_O \begin{cases} = 2(W - 2a)\sigma_o/\sqrt{3} \text{ plane strain} & (10a) \\ = (W - 2a)\sigma_o \quad \text{plane stress} & (10b) \end{cases}$$

$$M_O \begin{cases} = 0.364\ \sigma_o\ (W - a)^2 \quad \text{plane strain} & (11a) \\ = 0.2679\ \sigma_o\ (W - a)^2 \quad \text{plane stress} & (11b) \end{cases}$$

Equation 5 can be rewritten with fewer constants as follows

$$\dot{\epsilon} = A(\sigma)^n \tag{12}$$

where

$$A = \frac{\epsilon_o\sigma_o\alpha}{(\sigma_o)^{n+1}} \tag{13}$$

Substituting Eqs 10, 11, and 13 into Eqs 8 and 9 for plane strain, one obtains the following for CCT specimen

$$C^* = \frac{Aag_1(2a/W, n)}{(1 - 2a/W)^n}(\sqrt{3}\,P/2W)^{n+1} \tag{14}$$

for CT specimen

$$C^* = Ah_1(a/W, n)\cdot(W - a)\left(\frac{P(W + a)/2}{0.364(W - a)^2}\right)^{n+1} \tag{15}$$

Note that M has been replaced by $P\,(W + a)/2$ in Eq 15. The functions g_1 and h_1 were reported by Hutchinson et al [*17,18*] for plane-strain conditions for selected a/W-values and are plotted in Fig. 9 for n-values of interest in this study.

Constants A and n for 304 stainless steel at 594°C (1100°F) have been recently reported by Gowda et al [*19*]. These constants were obtained by testing under multiaxial conditions of loading. They subjected tubular specimens to internal pressure (using argon gas) and simultaneous axial

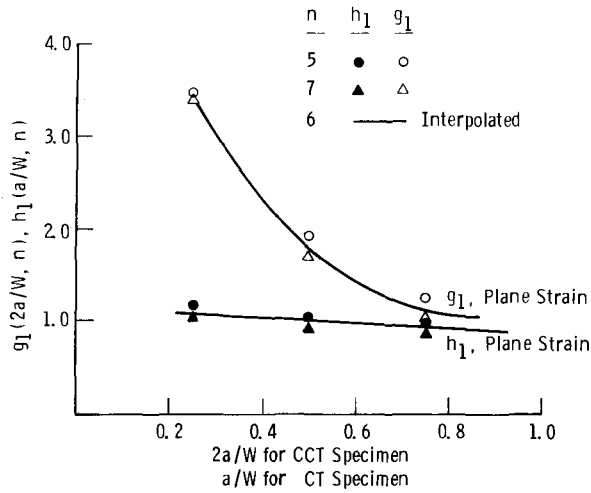

FIG. 9—*Nondimensional parameters* g_1 *and* h_1 *in Eqs 8 and 9 as a function of crack length for CCT and CT specimens, respectively* [18].

load. Creep rate data were obtained for principal stress ratios ($R = \sigma/\sigma_2$)[3] of 1.0, 1.5, and 2.0 and were plotted in the form of effective stress and effective strain rate to normalize the data for various R-values. For the values of R above, n and A were reported as 6.0 and 2.13 $\times$ 10^{-18}, respectively, when stress is expressed in mega pascals and strain rate in strain per hour. Substituting these constants along with values of g_1 and h_1, C^* was determined at various crack lengths for all specimens tested.

Values of C^*, estimated from the two techniques described previously, are compared in Table 3 for both specimen geometries. The discrepancies between the C^*-values calculated from the two techniques is between 8 to 40 percent. Several reasons that may explain this discrepancy are as follows. Firstly, the constants A and n in Eq 12 were developed for a different heat of 304 stainless steel than used in this study. The values of C^* are sensitive to these material parameters. Secondly, the calculations used plane-strain anlysis for the entire specimen. Although plane-strain conditions may prevail in the crack-tip region, the bulk of the specimen will be in plane-stress condition. Thirdly, for CT specimens, there is a tension component not accounted for in Eq 15 that was developed for pure bending. Finally, the estimates of C^* were obtained from a graphical method, which in itself may have scatter normally associated with experimental results.

Due to the approximate linear relationship between da/dt and C^* for 304

[3] σ_1 and σ_2 are the maximum and minimum values of the principal stresses.

TABLE 3—*Comparison of C* values estimated from the graphical technique to those obtained from eqs 8 and 9.*

Specimen Type	a/W or $2a/W$	C^* (J/m^2 · h)	
		Eq 8 or 9	Graphical Method
CCT	0.65	1.45×10^3	2.21×10^3
CCT	0.675	1.79×10^3	2.4×10^3
CT	0.595	2.05×10^3	3.48×10^3
CT	0.675	2.9×10^3	5.2×10^3
CT	0.740	8.4×10^3	7.8×10^3
CT	0.675	2.9×10^3	4.8×10^3
CT	0.800	10.8×10^3	7.3×10^3

Conversion factor—J/m^2·h = 5.70×10^{-3} in.·lb/in.^{2}·h.

stainless steel as shown in Fig. 10, an 8 to 40 percent discrepancy in estimating C^* implies a similar variability in growth rates. The scatter in growth rates from a single data reduction procedure itself is larger than the factor of 1.4. In view of this observation, the discrepancy in the C^* estimates mentioned above are not large enough to cast doubt on the more significant results of this study.

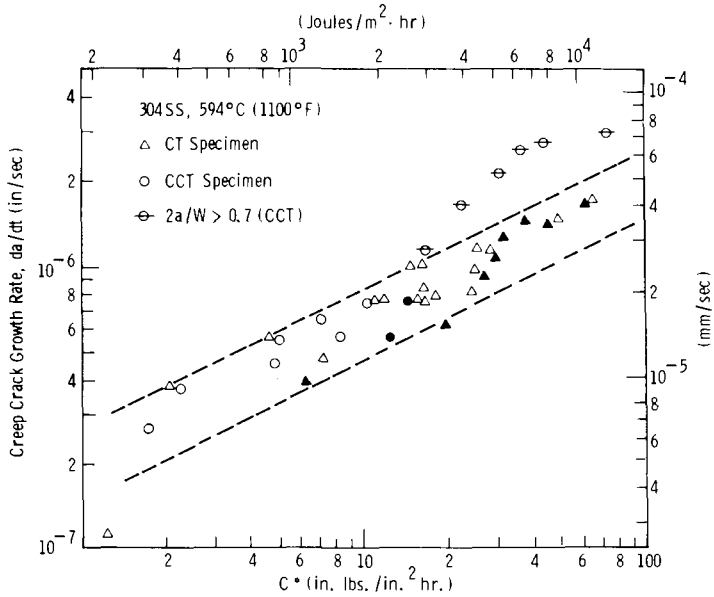

FIG. 10—*Creep crack growth rate of 304 stainless steel at 594°C (1100°F) as a function of C* for two specimen geometries. Filled points were obtained by multiple specimen data reduction technique and open points by fully plastic plane-strain solutions.*

Results and Discussion

In this section of the report, the influence of specimen geometry on *da/dt* versus *C** behavior is examined using data from heat 24348 of 304 stainless steel. Additional creep crack growth rate data on two microstructures in the temperature range of 538 to 705°C (1000 to 1300°F) on another heat of 304 stainless steel from the previous work of Begley [*20*] are also described. By comparing results from the two heats of 304 stainless steel, the influence of minor chemistry differences (heat-to-heat variations) on creep crack growth rate are characterized.

Effect of Specimen Geometry

The *da/dt* versus *C** behavior at 594°C (1100°F) is plotted in Fig. 10. Different symbols have been used to represent data from the two specimen geometries and the two procedures used for estimating *C**. At low *C**-values there is a good agreement between the crack growth rates obtained from the CCT and CT specimen geometries. For *C**-values above 2.9×10^3 J/m^2·h (16.5 in.·lb/in.^{2}·h), there is an upturn in growth rates obtained from CCT specimens. The upturn (deviation from CT data) began when the uncracked ligament became smaller than 7.5 mm (0.3 in.) or $2a/W > 0.7$, and may be explained as follows.

It is possible that a minimum size of uncracked ligament may be required to obtain geometry independent creep crack growth rate data. Such criteria are required in plane-strain, K_{Ic} fracture toughness testing (per ASTM E 399), in elastic-plastic J_{Ic} testing [*21*], and fatigue crack growth rate testing (per ASTM Test for Constant-Load-Amplitude Fatigue Crack Growth Rates Above 10^{-8}m/cycle (E 647-78T)). Further, the analytical results of McMeeking and Parks [*22*] have shown that for a *J*-controlled stress and strain field to hold in the crack tip region, a minimum ligament size proportional to J/σ_o should be maintained. They also show that the minimum ligament size requirements are considerably larger for CCT specimens compared to a bend type CT geometry. By analogy, these results imply that for maintaining a *C** dominated stress and strain rate field during creep crack growth testing, the ligament size required for CCT specimens will be larger than that for CT specimens at equal *C**-values. Hence, the upturn in the crack growth rates obtained on the CCT specimen may be attributed to the breakdown of *C** dominance of the stress and strain rate fields. More experimental data and analytical studies are needed to resolve this issue completely and to set specimen size limits for creep crack growth testing.

Despite the upturn in the crack growth rates under certain test conditions described previously, it can be tentatively concluded from the data of Fig. 10 that *C** provides a geometry independent characterization of creep

crack growth rates for 304 stainless steel. Demonstration of specimen geometry independence of test data is important in fracture mechanics testing because it substantiates the use of laboratory test data for making service life predictions of cracked components.

Influence of Temperature and Material Variables

Figure 11 shows creep crack growth rate data for a different heat of 304 stainless steel in as-quenched and quenched and sensitized conditions[4] at 538, 649, and 705°C (1000, 1200, and 1300°F) from tests conducted by Begley [*20*]. Standard 25.4-mm (1-in.) thick CT specimens were used to obtain the data, and a multiple specimen graphical technique was used for reducing the data. For comparison, the scatter band from Fig. 10 is also plotted.

All the data in Fig. 11 lie either within the scatterband obtained for

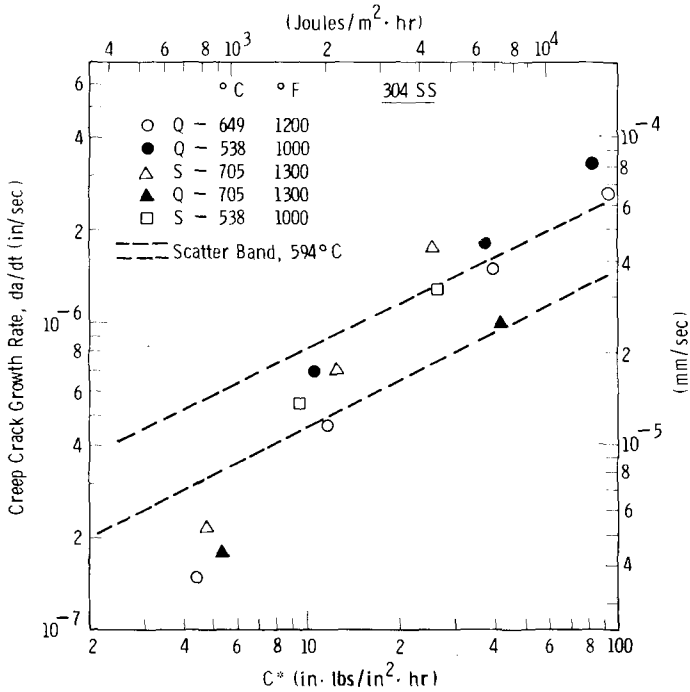

FIG. 11—*Creep crack growth rate as a function of temperature and heat treatment for 304 stainless steel. "S" refers to sensitized treatment and "Q" refers to an "as quenched condition."*

[4]The average tensile properties of the material for these two heat treatments are reported in Table 2 at three temperatures.

594°C (1100°F) or very close to it. This behavior is in contrast to the creep rupture life of 304 stainless steel obtained from smooth specimens, which is affected significantly by temperature and also by minor differences in chemistry [*23*].

The lack of significant temperature effect on da/dt versus C^* relationship can be rationalized as follows. During creep crack growth testing under constant displacement rate control or under constant load control, the increasing deformation is accommodated by: (*a*) crack growth and (*b*) additional inelastic creep deformation of the specimen. Now, consider two creep crack growth tests being conducted under constant displacement rate control in which only the test temperatures are different. The applied displacement rate, specimen geometry and size, and the crack lengths are identical. Since creep deformation rate will be higher for the specimen being tested at the higher temperature, the crack growth rate will have to be lower for that specimen to maintain equal displacement rate. Also, the load obtained for the higher temperature test at equal crack lengths is expected to be lower. Hence, a lower C^*-value is predicted for this test, which is consistent with the lower crack growth rate. If these tests were conducted under constant load, the C^* and, thus, the crack growth rate obtained would be higher for the higher temperature test. This would be due to the higher deflection rate obtained at the higher temperature under these conditions.

The above rationale is purely a mechanics based argument. In materials where fundamental mechanisms of cracking are different for various temperatures, more significant differences in da/dt versus C^* behavior are expected. Also, more significant differences may exist at growth rates lower than those for which data were obtained in this study.

Summary and Conclusions

Results of an experimental program to characterize the creep crack growth behavior of 304 stainless steel are described. The energy rate line integral, C^* is evaluated as a field parameter for geometry independent characterization of creep crack growth behavior. The following pertinent conclusions can be made from the results of this investigation.

1. C^* is a promising candidate parameter for characterizing creep crack growth rate, da/dt, in cracked members undergoing predominantly secondary creep. When da/dt was expressed as a function of C^*, data from CT and CCT specimen geometries collapsed on a single trend.

2. It was observed that, when $2a/W$ was greater than 0.7 for CCT specimens, an upturn in growth rates and deviation from CT data occurred. This is tentatively attributed to insufficient ligament size of the specimen.

3. Crack growth rates in 304 stainless steel as a function of C^* are

not significantly affected by temperature (in the range of 538 to 705°C (1000 to 1300°F)), heat treatment, or minor chemistry differences.

4. A single specimen analytical method was developed to calculate C^* using an analogy to the fully plastic J solutions. C^* estimates from this method were different by 8 to 40 percent from those obtained from the multiple specimen graphical procedure.

5. Recommendations for future work are provided.

Recommendations for Future Work

Specific areas that need more work in order to advance technology for predicting creep crack growth behavior, using C^* parameter are outlined below.

1. More creep-crack-growth data should be generated at various temperatures and on different materials to further evaluate C^* and understand its limitations. Tests covering lower growth rates should be performed.

2. Finite element techniques should be developed for obtaining numerical solutions to cracks in elevated temperature members. The feasibility of such analysis is clearly demonstrated by Wilson et al [*24*].

3. Single specimen analytical procedures for estimating C^* should be developed for other geometries. This is important for application of the data in life prediction schemes. The accuracy of the presently available expressions should be further verified. Also, these solutions should be modified to account for behavior under primary creep.

4. After establishing the C^* parameter for characterizing steady state creep crack growth rates, the problem of characterizing crack initiation at notches and that of characterizing incubation time should be approached. Incubation time is defined as the period between the application of the load and the onset of crack growth. This could account for a substantial portion of service life during creep loading.

Acknowledgments

The author wishes to express gratitude to several colleagues at Westinghouse Research and Development Center who contributed to the study. Several technical discussions with J. D. Landes, T. T. Shih, and W. K. Wilson were very helpful. P. J. Barsotti, R. B. Hewlett, and R. C. Brown provided assistance in conducting the tests. Part of the data used in this study were obtained under the direction of J. A. Begley currently with Ohio State University. The financial support for this work was provided by the Advanced Reactor Division and the Large Steam Turbine Division of Westinghouse Electric Corp.

References

[1] Landes, J. D. and Begley, J. A. in *Mechanics of Crack Growth, ASTM STP 590,* American Society For Testing and Materials, 1976, pp. 128-148.

[2] Nikbin, K. M., Webster, G. A., and Turner, C. E. in *Cracks and Fracture, ASTM STP 601,* American Society For Testing and Materials, 1976, pp. 47-62.

[3] Siverns, M. J. and Price, A. T., *International Journal of Fracture,* Vol. 9, No. 2, June 1973, pp. 199-207.

[4] Sadananda, K. and Shahinian, P., *Metallurgical Transactions A*, Vol. 8A, March 1977, pp. 439-449.

[5] McEvily, A. J. and Wells, C. H., "On Applicability of Fracture Mechanics to Elevated Temperature Design," International Conference on Creep and Fatigue in Elevated Temperature Applications, American Society of Mechanical Engineers, Philadelphia, Pa., 1973.

[6] Haigh, J. R., *Material Science Engineering,* Vol. 20, 1975, pp. 213-223.

[7] Harrison, C. B. and Sandor, G. N., *Engineering Fracture Mechs.*, Vol. 3, No. 4, Dec. 1971, pp. 403-420.

[8] Sadananda, K. and Shahinian, P., *Metallurgical Tansactions A,* Vol. 9A, Jan. 1978, pp. 79-84.

[9] Ellison, E. G. and Walton, D., "Fatigue Creep and Cyclic Creep Crack Propagation in 1CrMoV Steel," International Conference on Creep and Fatigue in Elevated Temperature Applications, American Society of Mechanical Engineers, Philadelphia, Pa., 1973.

[10] Ellison, E. G. and Harper, M. P., *Journal of Strain Analysis,* Vol. 13, No. 1, 1979, pp. 35-51.

[11] Robinson, J. N. and Tetleman, A. S. in *Fracture Toughness and Slow Stable Cracking, ASTM STP 559,* American Society for Testing and Materials, 1974, pp. 135-158.

[12] McClintock, F. A. in *Fracture,* H. Liebowitz, Ed., Vol. 3, Academic Press, pp. 47-225.

[13] Goldman, N. L. and Hutchinson, J. W., *International Journal of Solids and Structures,* Vol. 11, 1975, pp. 575-591.

[14] Harper, M. P. and Ellison, E. G., *Journal of Strain Analysis,* Vol. 12, No. 3, 1977, pp. 167-179.

[15] Johnson, H. H., *Materials Research and Standards,* Vol. 5, Sept. 1965, pp. 442-445.

[16] Ritchie, R. O., Garrett, G. G., and Knott, J. F., *International Journal of Fracture,* Vol. 7, No. 4, 1971, pp. 462-467.

[17] Shih, C. F. and Hutchinson, J. W., *Journal of Engineering Material Technology,* Series H, Vol. 98, 1976, pp. 289-295.

[18] Hutchinson, J. W., Needleman, A., and Shih, C. F., "Fully Plastic Crack Problems in Bending and Tension," MECH-6, Division of Applied Sciences, Harvard University, May 1978.

[19] Gowda, B. C., Daniels, C., and Thomas, K. C., "Creep Behavior of Type 304 SS Under Multiaxial Stresses," WARD-HT-3045-32, U.S. Energy Research and Development Administration, Oak Ridge, Tenn., June 1978.

[20] Begley, J. A., unpublished data, Westinghouse Research and Development Center, Pittsburgh, Pa., 1974.

[21] Landes, J. D. and Begley, J. A. in *Fracture Analysis, ASTM STP 560,* American Society for Testing and Materials, 1974, pp. 170-186.

[22] McMeeking, R. M. and Parks, D. M. in *Elastic-Plastic Fracture, ASTM STP 668,* J. D. Landes, J. A. Begley, and G. A. Clarke, Eds., American Society for Testing and Materials, 1979, pp. 175-194.

[23] Conway, J. B., Stenz, R. H., and Berling, J. T., "Fatigue, Tensile and Relaxation Behavior of Stainless Steel," TID-26135, Technical Information Center, U.S. Atomic Energy Commission, 1975.

[24] Wilson, W. K., Chan, S. K., and Swamy, S., "A Finite Element Analysis of a Cracked Body Subject to Creep," unpublished research, Westinghouse Research and Development Center, Pittsburgh, Pa., 1975.

[25] Riedel, H., "Creep Deformation at Crack Tips in Elastic-Viscoplastic Solids," Materials Research Laboratory Report MRL E-114, Brown University, Providence, R.I., June 1979.

Kuntimaddi Sadananda[1] *and Paul Shahinian*[1]

Elastic-Plastic Fracture Mechanics for High-Temperature Fatigue Crack Growth

REFERENCE: Sadananda, Kuntimaddi and Shahinian, Paul, **"Elastic-Plastic Fracture Mechanics for High-Temperature Fatigue Crack Growth,"** *Fracture Mechanics: Twelfth Conference, ASTM STP 700,* American Society for Testing and Materials, 1980, pp. 152-163.

ABSTRACT: Application of linear elastic and elastic-plastic fracture mechanics parameters to high-temperature fatigue crack growth is examined to determine which parameter provides a better correlation of crack growth data. It is concluded that the J-integral concept is applicable to fatigue, and methods of determination of J for both load-controlled and displacement-controlled fatigue are discussed. The J-integral parameter is shown to be better than the linear elastic parameter K in correlating fatigue crack growth, particularly so in materials that undergo metallurgical changes during test resulting in changes in flow properties. Application of the J-integral concept to time-dependent and combined cycle and time-dependent crack growth is discussed in detail.

KEY WORDS: fracture mechanics, fatigue, creep, crack growth, high temperature, J-integral, load-controlled, displacement controlled, time dependent, fractures (materials), crack propagation

Linear elastic fracture mechanics techniques have been used successfully to predict fatigue crack growth rates in many materials particularly at low or room temperature. This success is based on the fact that a single parameter, namely, stress intensity factor K [*1*],[2] can adequately describe the stress field around the crack tip provided the extent of plastic flow at the tip is small. Paris [*2*] has shown that a large body of fatigue crack growth data can be uniquely correlated on the basis of stress intensity factor range, ΔK, as

$$\frac{da}{dN} = B(\Delta K)^n \tag{1}$$

[1] Research metallurgist and supervisory metallurgist, respectively, Thermostructural Materials Branch, Material Science and Technology Division, Naval Research Laboratory, Washington, D.C. 20375.

[2] The italic numbers in brackets refer to the list of references appended to this paper.

where constants B and n depend on the material. The extent to which the linear-elastic parameter is applicable, however, is limited particularly when plasticity effects at the crack tip became appreciable. Dowling and Begley [*3,4*] have recently shown that in such cases the nonlinear parameter, J-integral, has a much broader range of applicability in terms of specimen dimensions or stress intensity values in predicting fatigue crack growth rates.

Since the limitation of linear-elastic fracture mechanics becomes more evident with increasing temperature, particularly because of decrease in yield stress of materials with temperature and because of incipience of nonlinear time-dependent effects such as creep and environmental interactions, use of nonlinear parameters such as J-integral for predicting crack growth at high temperatures becomes important. During the past few years there has been a significant amount of fatigue crack growth data generated at the Naval Research Laboratory on several thermostructural materials, and using this previously published data the authors examine in this report to what extent the J-integral concept is applicable for fatigue crack growth and what its limitations are.

J-Integral Concept for Fatigue

The concept of J-integral was orginally introduced by Rice [*5*] and its applicability as fracture criteria was proposed by Begley and Landes [*6*]. The value of J-integral can be experimentally determined for a cracked body from the load-displacement curve using a simple form of an equation as

$$J = -\frac{1}{B}\frac{\partial U}{\partial a}\bigg|_{\delta} \tag{2}$$

where B is the specimen thickness and J is proportional to the change in potential energy U due to infinitesimal crack extension da at a given crack deflection δ. Strictly the J-integral concept is valid only for monotonic deformation, and irreversible deformation during unloading would invalidate its applicability for fatigue. In fact, fatigue damage itself arises only because of the irreversibility of plastic flow during loading and unloading [*7*]. In spite of these arguments, initial attempts to use J-integral for fatigue were successful [*3*] and this may be explained by the following. It is known from several experimental investigations that a material develops a characteristic cyclic stress-strain behavior [*8*] under fatigue which is different from that under monotonic deformation and yet unique for a given set of experimental conditions such as temperature, environment, etc. At a microlevel this means that the material ahead of the crack tip acquires a characteristic plastic zone that is different from that under monotonic deformation and yet unique for a given crack length and loading condition [*9,10*]. This uniqueness of cyclic plastic zone implies that strain energy for a crack increment is unique for a

given crack length and load. Therefore, the J-integral concept is applicable under fatigue although its value at a given crack length differs from that under monotonic deformation. Experimental verification may be the only proof that can be provided at this stage for the validity of J-integral to fatigue crack growth.

Determination of J-Integral for Fatigue

Fatigue crack growth rates in fracture-mechanics type specimens can be determined either under displacement-controlled or load-controlled conditions although for some specimen geometries one may be more convenient than the other. For displacement-controlled fatigue, determination of J-integral is rather straightforward and follows directly from Eq 2. This is illustrated schematically in Fig. 1. In particular, the rising part of the load-displacement hysteresis loops in Fig. 1*a* for crack lengths a_1, a_2 are displaced to a common origin as in Fig. 1*b*. J-integral is then given by the hatched area [*3*].

For load-controlled fatigue, there is an ambiguity in terms of defining the proper limits of integration. It has been shown [*11*] that the following procedure ensures that J-integral is compatible to the ΔK-value, and it involves

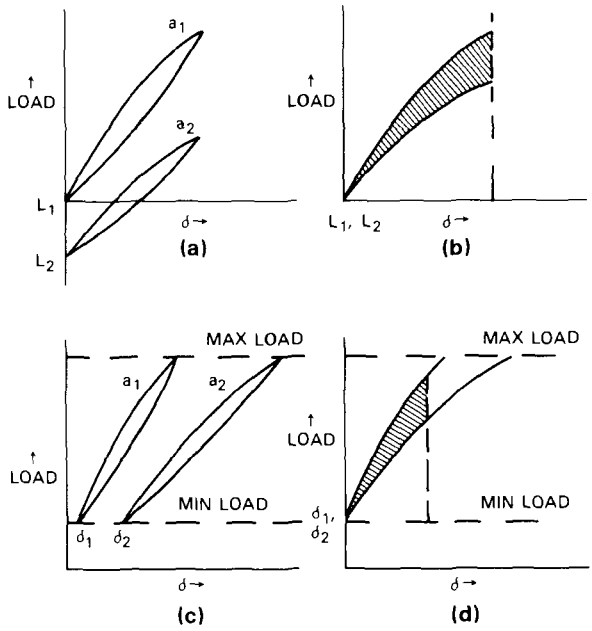

FIG. 1—*Methods of determination of J-integral for displacement-controlled* (a *and* b) *and load-controlled* (c *and* d) *fatigue.*

selecting minimum load as a reference point for the integral. In particular the rising parts of the load-displacement hysteresis loops in Fig. 1*c* for crack lengths a_1 and a_2 are displaced to a common origin as in Fig. 1*d*, and J-integral is determined from the hatched area. Thus, this definition of J-integral implies that in the load-controlled fatigue the cumulative cyclic strain such as δ_1, δ_2 (Fig. 1*c*) has no effect on the subsequent fatigue crack growth. In effect it is similar to the ΔK concept. Depending on minimum and maximum loads a proper J-integral can be determined which reflects R effects or mean stress effects, just as in da/dN versus ΔK plots.

Application of J-Integral for High-Temperature Fatigue

For displacement-controlled fatigue, Dowling and Begley [*3*] have shown that J-integral has a broader range of applicability in terms of ΔK or specimen geometry [*4*]. In particular, it was shown that the existence of Stage 3 in a da/dN versus ΔK plot disappears when the data are represented in terms of ΔJ-values for A533B steel at room temperature. On the other hand, correlation of crack growth data for load-controlled fatigue was unsuccessful and these authors attributed it to ratcheting. However, it was shown recently that ΔJ can be defined for load-controlled fatigue along the lines of Fig. 1*c* and *d*, and the data are consistent with those in terms of ΔK [*11*]. Figure 2 shows the applicability of J-integral for load-controlled fatigue with reference to high temperature fatigue crack growth in Udimet 700. The crack growth rate data are specifically represented in terms of $\sqrt{\Delta J \cdot E}$, where E is the Young's modulus so that the relative merits of linear and nonlinear parameters can be easily compared. The extent of spread in the data is less in terms of ΔJ than in terms of ΔK. These results along with Dowling and Begley's results [*3*] demonstrate that the J-integral concept is applicable for fatigue, in spite of the lack of any theoretical justification for this. Since nonlinear effects become more pronounced at high temperature, use of J-integral becomes important. Note that Stage 3 in Udimet 700 persists even in terms of ΔJ, and this is related to the change in the micromechanism of crack growth from transgranular to intergranular at high stress intensities. [*11*].

The superiority of J-integral over ΔK in correlating crack growth behavior becomes apparent when one considers cases where the metallurgical structure becomes unstable during the test. For example, if any time-temperature dependent transformations occur at test temperatures, the microstructure of the material ahead of the crack tip changes to a different extent in each specimen depending on the duration of the test. This in turn may cause a large spread in the da/dN versus ΔK plot for the same specimen geometry. Here the inapplicability of the linear-elastic parameter is not due to its limitation *per se* but due to its inability to take into consideration the changes in flow properties of the material ahead of the crack tip. On the other hand,

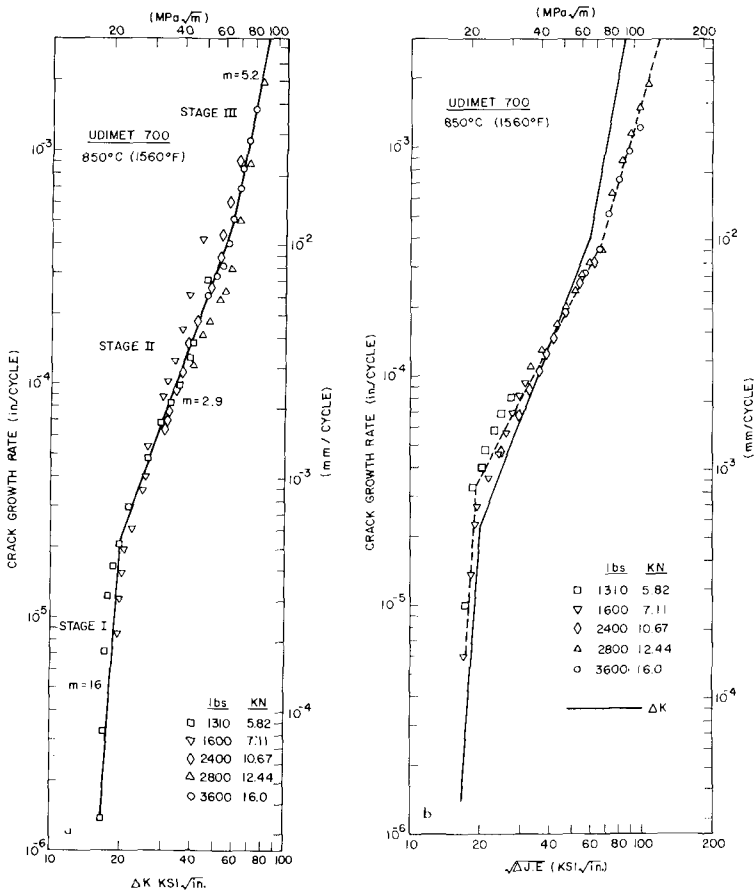

FIG. 2—*High-temperature fatigue crack growth data for Udimet 700 in terms of* (a) *stress intensity range and* (b) *J-integral parameter.*

since J-integral is determined using load-displacement curves, which reflect the *in situ* changes in flow properties of the material, it could be a better parameter to use to characterize crack growth in such materials. Thus, J as determined from the load-displacement curves is a kinematic parameter that takes into consideration kinematic changes in the flow properties of the material ahead of the crack tip.

Figure 3 shows the crack growth data [*12*] for 20 percent cold-worked Type 316 stainless steel which undergoes slow recovery at the test temperature 593°C (1100°F). In fact, because of this recovery, this material shows a significant enhancement in crack growth rates under creep-fatigue conditions [*13*]. There is a large spread in the crack growth data in terms of ΔK, particularly so at the lower load where the specimen was at the test

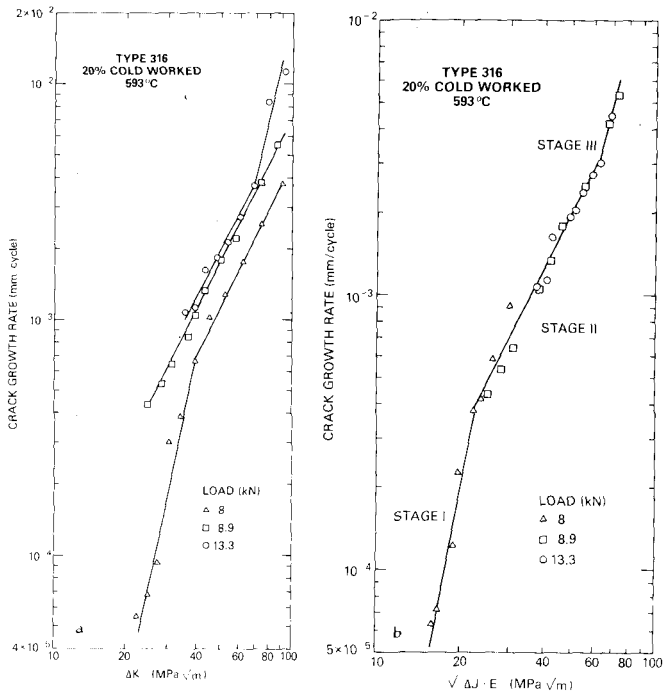

FIG. 3—*Crack growth data for 20 percent cold-worked stainless steel in terms of* (a) *stress intensity range and* (b) *J-integral parameter.*

temperature 20 to 40 times longer than those tested at higher loads. Clearly, the extent of spread in the crack growth data is less in terms of ΔJ than in terms of ΔK.

At high temperatures, in addition to recovery, there could be other types of time-temperature dependent transformations, such as precipitation, overaging, etc., that could occur which could alter the flow properties of structural material depending on the length of its service. For such cases the crack growth data in terms of ΔK cannot provide a reliable prediction of the component life. J-integral appears to be more suitable for such materials. It is reasonable to expect that a simple da/dN versus ΔJ plot may be sufficient to predict the fatigue crack growth rates in materials that differ to a small degree in chemistry or processing conditions, provided these differences do not contribute to large changes in flow properties or in their environmental sensitivity.

Of interest here is that crack growth rates in terms of ΔJ in each stage could be represented by

$$\frac{da}{dN} = B\ (\sqrt{\Delta J \cdot E})^n \tag{3}$$

where constants B and n are material properties. Clearly, in the limit of linear elastic behavior, this relation reduces to the Paris relation represented by Eq 1.

Time-Dependent Crack Growth

With increase in temperature, crack growth under cyclic load could become increasingly time-dependent and for such cases both ΔK and ΔJ parameters may not correlate crack growth rates. In the extreme case of purely time-dependent crack growth, linear parameter K_{max} or its nonlinear counterpart J_{max} may be better in correlating crack growth rates. J_{max} can be determined following the same procedure used for ΔJ except the load-displacement curves in Fig. 1 are now extrapolated back to zero load. Crack growth was found to be time dependent in Alloy 718 at 650°C (1200°F), where the combined effects of stress ratios, R and hold-times on fatigue crack growth rates were studied [*14*].

Figures 4 and 5 illustrate this case where crack growth rates in Alloy 718 are represented in terms of ΔK and ΔJ (Fig. 4) and K_{max} and J_{max} (Fig. 5). Although ΔJ parameter is better than ΔK, the spread in the data in terms of both parameters for different R-values is more than an order of magnitude. This spread is significantly less when plotted in terms of K_{max} or J_{max}, although crack growth rates for continuous cycling and for 1-min hold fall in separate bands. That crack growth in this alloy is predominantly time-dependent at 650°C (1200°F) for these test frequencies can be seen clearly in Fig. 6 where da/dt (da/dN times frequency) is represented in terms of K_{max}

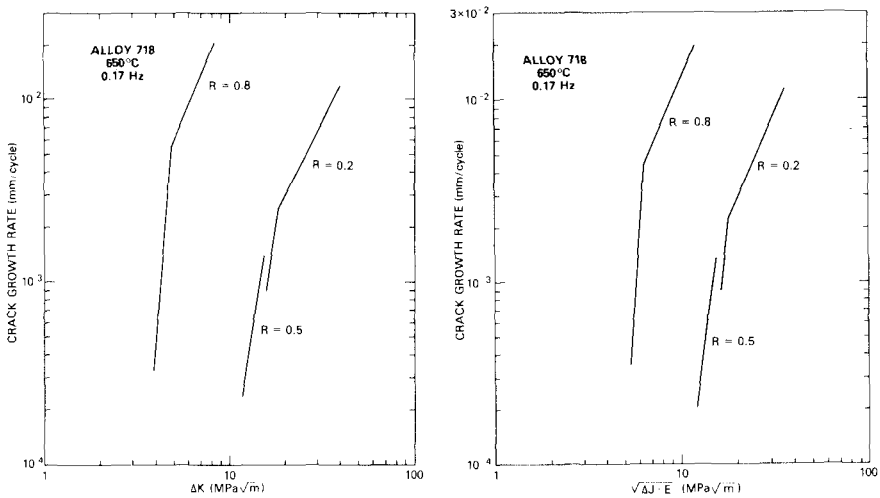

FIG. 4—*Crack growth rates in Alloy 718 in terms of* ΔK *and* ΔJ.

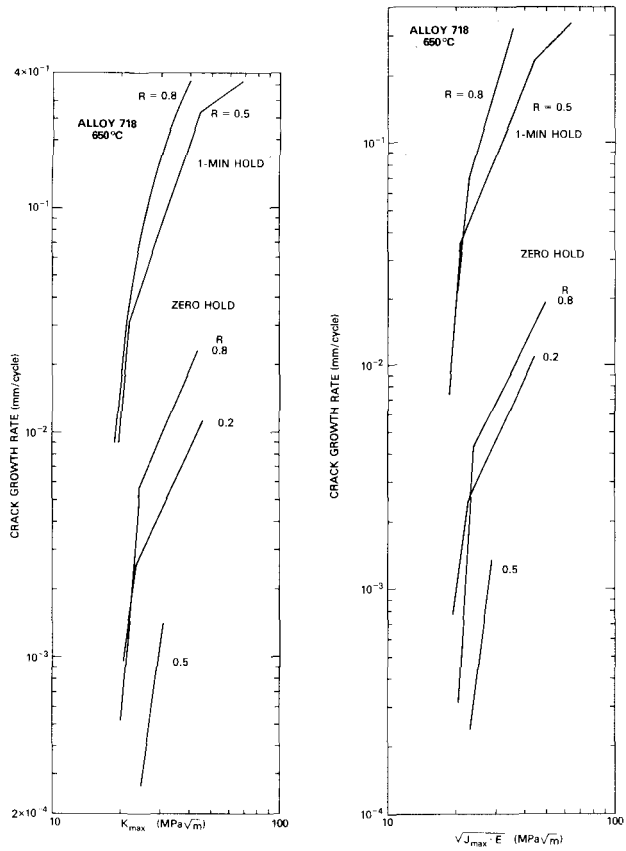

FIG. 5—*Crack growth rates in Alloy 718 in terms of* K_{max} *and* J_{max}.

and J_{max}. It is interesting to note that K_{max}- and J_{max}-values are nearly the same, and this is because crack growth in this alloy occurs essentially under elastic conditions. This is related to the high tensile and creep strengths of the alloy and its poor resistance to environmental interactions.

There is still some spread in the crack growth rate versus J_{max} (Fig. 6), and this could be related to the errors involved in extrapolating the load-displacement curves for high R tests to zero load in order to determine J_{max}-value. Also another reason for the spread could be the fact that crack growth in the alloy may not be completely time-dependent, and there is some contribution to crack growth from cycle-dependent processes, the extent of which varies with R.

The foregoing results raise two pertinent questions concerning the applicability of J-integral for high-temperature crack growth. First, can the

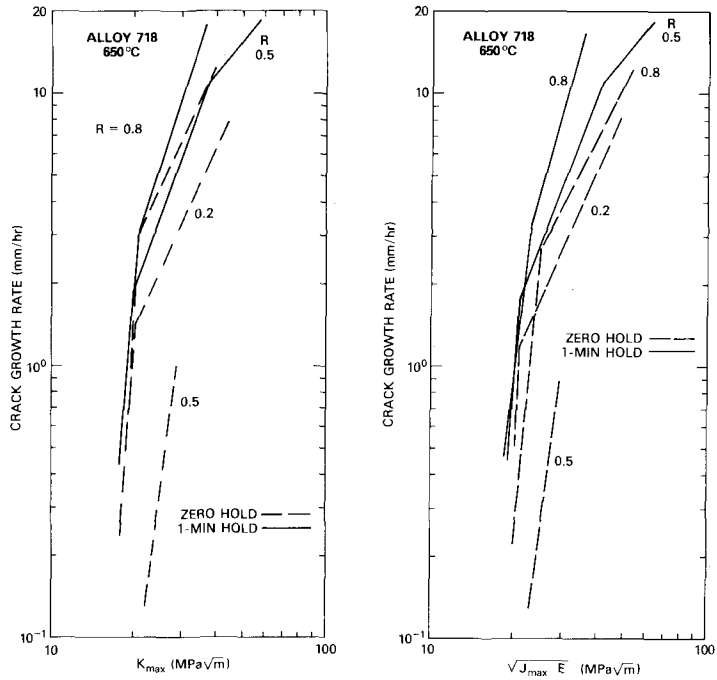

FIG. 6—*Crack growth rates,* da/dt, *in Alloy 718 in terms of* K_{max} *and* J_{max}.

J-integral concept be applicable to time-dependent crack growth or should one resort to the more complex rate-dependent integral, J^* [*15-18*]? (The authors favor the use of J^* instead of C^* for this integral since it is closely related to J-integral.) Second, what parameter is suitable for crack growth where both time-dependent and cycle-dependent processes occur simultaneously and when these processes interact with one another giving rise to creep-fatigue interaction or creep-fatigue-environmental interaction?

To answer the first question, it may be concluded on the basis of Fig. 6 that theoretically it is possible to define a characteristic J-integral value for time-dependent crack growth. There are, however, some experimental difficulties in determining J, characteristic of a crack length when crack growth occurs under static load. Here the difficulty is in obtaining a load-displacement curve characteristic of a given crack length without unloading the specimen and thus without introducing cyclic load effects. J-integral was determined for crack growth under static load in Alloy 718 [*17*] and Udimet 700 [*18*] using a lengthy data reduction scheme. It is not clear whether the large spread obtained in the crack growth data was due to the limitation of the parameter or due to incorrect J values. Turner and his coworkers [*20*] have determined J-integral for crack growth under static load, however, us-

ing a constitutive relation for creep deformation and assuming that the material ahead of the crack tip behaves similar to bulk material. Thus, J-integral may be applicable to time-dependent crack growth although it may be difficult to determine for crack growth under static load.

Referring to the second question, it is difficult to assess at this stage which fracture mechanics parameter is suitable when both time-dependent and cycle-dependent processess occur simultaneously, particularly so when there are synergistic effects. Figure 7 illustrates a case where crack growth in Udimet 700 [*20*] is represented in terms of ΔJ. Crack growth rate decreases and then increases with increase in ΔJ. A similar effect was noticed in terms of ΔK as well. Such crack retardation has been observed in several alloys [*14,21–23*], particularly when the stress intensities are less than the threshold stress intensity for creep-crack growth. The retardation occurs due to creep deformation which causes crack tip blunting, thereby contributing to stress relaxation at the crack tip. Since the extent of this relaxation depends independently on load, crack length, and specimen geometry the fracture mechanics parameters may not be useful in predicting the crack growth behavior. On the other hand, if crack growth occurs continuously by a com-

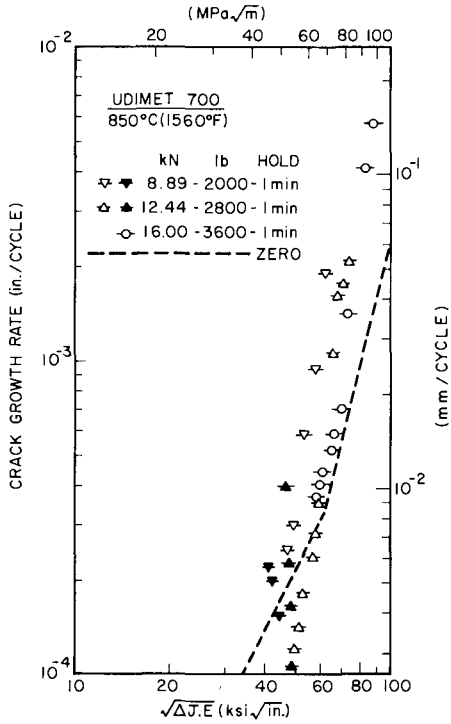

FIG. 7—*Crack growth rates in Udimet 700 under creep-fatigue conditions.*

bination of time- and cycle-dependent processes, fracture mechanics concepts may be applicable. Crack growth may then have to be correlated by a complex combination of both J_{max} and ΔJ-integral parameters depending on the relative ratio of cycle and time-dependent processes. The procedures may become more complex when there are synergistic effects.

Summary and Conclusions

Applicability of J-integral to high-temperature fatigue crack growth has been examined. Based on available experimental results it is concluded that the J-integral concept is applicable for fatigue conditions both at low and high temperatures, in spite of the fact such validity is not apparent from theoretical considerations.

The method of determination of J-integral for both load-controlled and displacement-controlled fatigue was discussed. It is shown that J-integral is better than linear parameter, K, particularly at high temperatures where nonlinear effects become more pronounced. For example, if metallurgical structural changes occur during test as a result of time-temperature dependent transformations, then J-integral provides much better correlation than linear elastic parameter K.

It is further concluded that the J-integral concept may be applicable even to time-dependent crack growth although conceptual problems exist in the experimental determination of J-values for crack growth under static load. A combination of both J_{max} and ΔJ-integral may be required to characterize crack growth under conditions where both time- and cycle-dependent processes occur simultaneously.

The present analysis shows that J-integral is a promising parameter for elastic-plastic fatigue crack growth. Additional work using different specimen geometries and materials is required before the limitations of the parameter can be fully ascertained.

Acknowledgment

The present research effort is supported by the Office of Naval Research.

References

[1] Irwin, G. R., *Journal of Applied Mechanics*, Vol. 24, 1957, pp. 361-364.
[2] Paris, P. C. and Erdogan, F., *Journal of Basic Engineering, Transactions*, American Society of Mechanical Engineers, Vol. 85, 1963, pp. 528-534.
[3] Dowling, N. E. and Begley, J. A. in *Mechanics of Crack Growth, ASTM STP 590*, American Society for Testing and Materials, 1967, pp. 82-102.
[4] Dowling, N. E. in *Cracks and Fracture, ASTM STP 601*, American Society for Testing and Materials, 1976, pp. 19-32.
[5] Rice, J. R. in *Fracture—An Advanced Treatise, Mathematical Fundamentals*, Academic Press, New York, Vol. 2, 1968, pp. 191-311.

[6] Begley, J. A. and Landes, J. D. in *Fracture Toughness, ASTM STP 514*, American Society for Testing and Materials, 1972, pp. 1-20.
[7] Laird,C. in *Fatigue Crack Propagation, ASTM STP 415,* American Society for Testing and Materials, 1967, pp. 131-168.
[8] Feltner, C. E. and Laird, C., *Acta Metallurgica,* Vol. 15, 1967, pp. 1621-1653.
[9] Rice, J. R. in *Fatigue Crack Propagation, ASTM STP 415*, American Society for Testing and Materials, 1967, pp. 247-309.
[10] Hahn, G. T., Hoagland, R. G., and Rosenfield, A. R., "Local Yielding Attending Fatigue Crack Growth," ARL-71-0234, Aerospace Research Laboratories, Wright-Patterson Air Force Base, Ohio, 1971.
[11] Sadananda, K. and Shahinian, P., *Engineering Fracture Mechanics,* Vol. 11, No. 1, 1979, pp. 73-86.
[12] Sadananda, K. and Shahinian, P., *International Journal of Fracture,* Vol. 15, No. 2, 1979, pp. R81-R84.
[13] Shahinian, P., *Journal of Pressure Vessel and Technology, Transactions,* American Society of Mechanical Engineers, Vol. 98, 1976, pp. 166-172.
[14] Shahinian, P. and Sadananda, K., *Engineering Materials and Technology,* Vol. 101, *Transactions,* American Society of Mechanical Engineers, July 1979, pp. 224-230.
[15] Hutchinson, J. W., *Journal of Mechanics and Physics of Solids,* Vol. 16, 1968, pp. 337-347.
[16] Landes, J. D. and Begley, J. A., in *Mechanics of Crack Growth, ASTM STP 590,* American Society for Testing and Materials, 1976, pp. 128-148.
[17] Sadananda, K. and Shahinian, P., *Metallurgical Transactions,* Vol. 8*a*, 1977, pp. 439-449.
[18] Sadananda, K. and Shahinian, P., *Metallurgical Transactions,* Vol. 9*a*, 1978, pp. 79-84.
[19] Nikbin, K. M., Webster, G. A., and Turner, C. E. in *Fracture 1977,* D. M. R. Taplin, Ed., Vol. 2, 1977, pp. 627-634.
[20] Sadananda, K. and Shahinian, P., *Journal of Materials Science,* Vol. 13, 1978, pp. 2347-2357.
[21] Shahinian, P. and Sadananda, K. in *Symposium on Creep-Fatigue Interaction,* ASME MPC-3, American Society of Mechanical Engineers, 1976, pp. 365-390.
[22] Haigh, J. R., *Engineering Fracture Mechanics,* Vol. 7, 1975, pp. 271-284.
[23] Scarlin, R. B., *Metallurgical Transactions,* Vol. 8*a*, 1977, pp. 1941-1948.

I. S. Abou-Sayed,[1] *P. Burgers,*[2] *and L. B. Freund*[3]

Stress Intensity Factor Due to Parallel Impact Loading of the Faces of a Crack

REFERENCE: Abou-Sayed, I. S., Burgers, P., and Freund, L. B., **"Stress Intensity Factor Due to the Parallel Impact Loading of the Faces of a Crack,"** *Fracture Mechanics: Twelfth Conference, ASTM STP 700,* American Society for Testing and Materials, 1980, pp. 164-173.

ABSTRACT: The plane-strain response of an unbounded elastic body containing a semi-infinite crack subjected to a pair of concentrated forces suddenly applied to the crack faces at some distance from the crack tip is determined. The forces act on opposite faces of the crack, in the plane of the crack, and in the same direction. An exact solution is obtained within the framework of linear elastodynamics using a fundamental solution obtained from dynamic elastic dislocation theory. If the loading is quasi-statically applied, then the stress intensity factor is zero. However, if the loads are suddenly applied, the stress intensity factor varies with time, and, for a short time, it takes on very large values. As time becomes large compared to the transit time of a Rayleigh wave from the load point to the crack tip, the stress intensity factor decays to zero. The same procedure may be applied for growing cracks subjected to the same type of loading.

KEY WORDS: fracture mechanics, dynamic fracture mechanics, stress intensity factor, dynamic stress intensity factor, impact loading, fractures (materials), crack propagation

In recent years, two analytical methods for determining the dynamic stress intensity factor for stationary and propagating cracks have been developed. In the first approach, the fracture process is viewed as the negation of traction arising from the applied loading on the prospective fracture plane. The traction at a particular point on the fracture plane is negated at the instant that the crack tip sweeps past that point. This viewpoint has been adopted by Freund [*1-4*][4] and Fossum [*5*] in the formulation and solution of several dy-

[1] Research scientist, Applied Solid Mechanics Section, Battelle Laboratories, Columbus, Ohio 43201.

[2] Post doctoral fellow, Department of Civil Engineering, Northwestern University, Evanston, Ill. 60201.

[3] Professor of engineering, Division of Engineering, Brown University, Providence, R.I. 02912.

[4] The italic numbers in brackets refer to the list of references appended to this paper.

namic crack propagation problems. A second method for determining the dynamic stress intensity factor, which has been found useful in some cases involving rapid loading, is based on the viewpoint that certain transient displacements arising from the applied loads must be negated to account for the presence of the crack. Taking this viewpoint, Freund [6] has shown that the notion of a fundamental solution for negating displacements, based on a moving elastic dislocation problem, is quite useful in obtaining solutions for a class of elastodynamic crack problems. Similar procedures have been followed by Achenbach and Tolikas [7], Freund [8], and Nilsson [9]. The same general procedure is applied here to yield some unusual results for a particular elastic crack problem.

The plane-strain problem under consideration is represented in Fig. 1. Two forces of magnitude T_o per unit length in the y-direction are applied to the crack faces at a distance, l, from the tip as shown. The forces are parallel and act in the same direction. It is a well-known result that if the loads are quasistatically applied then the stress intensity factor is identically zero [10]. However, if the loading is suddenly applied as in the case of impact, then the stress intensity factor exhibits a complicated transient behavior, and it takes on very large values for a short period of time. It is the purpose here to outline the analysis by means of which this transient behavior may be determined.

Formulation of the Problem

The body is stress free and at rest for time $t < 0$ and the crack face loading is suddenly applied at $t = 0$. The symmetry of the problem with respect to the x-axis makes possible a reduction to a half-plane problem in the region $z \geq 0$. The displacements are represented in terms of the displacement potentials ϕ and ψ, where ϕ is the longitudinal wave potential and ψ is the shear wave potential, and the displacement components are derived from the potentials according to

$$u = \phi_{,x} - \psi_{,z}, \qquad w = \phi_{,z} + \psi_{,x} \tag{1}$$

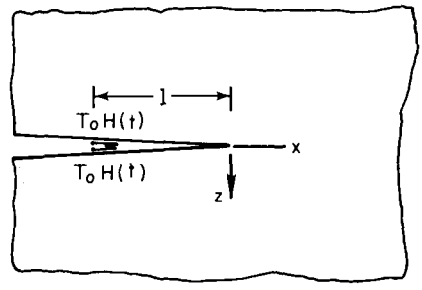

FIG. 1—*The plane-strain elastodynamic crack problem.*

where $u(x, z, t)$ and $w(x, z, t)$ are the components of displacement in the x- and z-directions, respectively, and commas denote partial differentiation. The boundary conditions for the problem at hand are

$$\sigma_{zz}(x, 0, t) = 0 \qquad x < 0 \tag{2}$$

$$\sigma_{xz}(x, 0, t) = -T_o H(t)\delta(x + l) \qquad -\infty < x < \infty \tag{3}$$

$$w(x, 0, t) = 0 \qquad x > 0 \tag{4}$$

where δ and H are the Dirac-delta function and the Heaviside-unit step function, respectively.

Direct application of integral transforms to the wave equations governing ϕ and ψ, along with the boundary and initial conditions, leads to a functional equation of the Wiener-Hopf type but one of nonstandard form; that is, one in which the transform of the kernel is not an algebraic function. Thus, the indirect approach introduced in Ref *6* is followed. The solution is constructed by superposition of the solutions of two separate problems. The first is a half-plane subjected to a tangential surface force, the dynamic version of Boussinesq's problem, and the normal component of surface displacement w_B is calculated. The second is the response of a body containing a crack to an edge dislocation climbing in the x-direction out of the crack tip. The solution of these two problems will be added in such a way as to recover the solution of the original problem.

Modified Boussinesq Problem

The problem considered in this section is the dynamic response of an elastic half-plane, $z \geq 0$, to a concentrated impact force, T_o, applied tangentially to the surface of the half plane, as shown in Fig. 2. The body is at rest for time $t < 0$, and the boundary conditions are

$$\sigma_{zz}(\xi, 0, t) = 0 \qquad -\infty < \xi < \infty \tag{5}$$

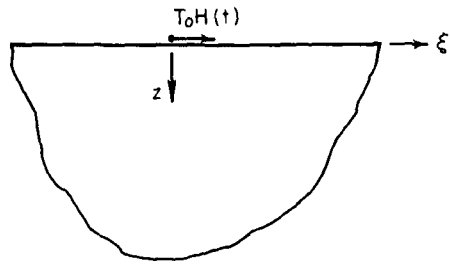

FIG. 2—*Suddenly applied tangential load on the edge of a half plane.*

$$\sigma_{xz}(\xi, 0, t) = -T_o\delta(\xi)H(t) \qquad -\infty < \xi < \infty \tag{6}$$

This problem may be solved by the following standard procedure [*11*]. First, displacement and stress components are expressed in terms of ϕ and ψ according to Eq 1. Then, the one-sided Laplace transform on time and the bilateral Laplace transform on ξ, defined by

$$F(\lambda, z, s) = \int_{-\infty}^{\infty} e^{-s\lambda\xi} \int_0^{\infty} e^{-st} f(\xi, z, t)dt\, d\xi \tag{7}$$

are applied to the governing equations, initial conditions, and boundary conditions. The solutions of the resulting ordinary differential equations for the double transforms of ϕ and ψ, denoted by Φ and Ψ, which satisfy all conditions are

$$\Phi(\lambda, z, s) = \frac{T_o}{\mu s^3} \frac{2\lambda\beta}{R(\lambda)} e^{-s\alpha z} \tag{8}$$

$$\Psi(\lambda, z, s) = -\frac{T_o}{\mu s^3} \frac{(\lambda^2 - \beta^2)}{R(\lambda)} e^{-s\beta z} \tag{9}$$

where μ is the elastic shear modulus, $\alpha = (a^2 - \lambda^2)^{1/2}$, $\beta = (b^2 - \lambda^2)^{1/2}$ and

$$R(\lambda) = 4\lambda^2\alpha\beta + (2\lambda^2 - b^2)^2 \tag{10}$$

The quantities a and b are the inverses of the longitudinal and shear wave speeds of the material, and c is the inverse of the Rayleigh wave speed, so that $R(\pm c) = 0$. Branch cuts are introduced in the complex λ-plane along $a, b < |\text{Re}\,\lambda| < \infty$, $\text{Im}\,\lambda = 0$ and branches of α, β with positive real parts everywhere in the cut plane are selected.

Once the transformed potentials are determined, as in Eqs 8 and 9, the transformed normal displacement of the surface $z = 0$, say $W_B(\lambda, 0, s)$, is known. The corresponding normal surface displacement in the physical plane is given in terms of the Laplace transform inversion integrals by

$$w_B(\xi, 0, t) = \frac{1}{2\pi i} \int_{B_1} \frac{1}{2\pi i} \int_{B_2} e^{s(\lambda\xi + t)} W_B(\lambda, 0, s)\, s d\lambda ds \tag{11}$$

where B_1 and B_2 are the usual inversion paths for the unilateral and bilateral Laplace transforms, respectively. Following the distortion of the contour B_2 and the mutual annihilation of the integrals, which is common in the Cagniard-deHoop scheme [*11*], it follows that, for $\xi > 0$

$$w_B(\xi, 0, t) = \frac{2T_o}{\mu\pi} \int_a^{t/\xi} \frac{\lambda|\alpha|\beta(2\lambda^2 - b^2)}{A(\lambda)} d\lambda + \frac{2c^2 - b^2 - 2|\alpha(-c)| \cdot |\beta(-c)|}{2\kappa S(-c)} H(t - c\xi) \tag{12}$$

where $\kappa = 2(b^2 - a^2)$, $S(\lambda) = R(\lambda)/\kappa(c^2 - \lambda^2)$, and $A(\lambda) = 16(a^2/b^2 - 1)\lambda^6 + 8(3b^2 - 2a^2)\lambda^4 - 3b^4\lambda^2 + b^6$. The first term in Eq 12 arises from a branch line integral, and the second term arises from a simple pole at $\lambda = -c$, which is crossed during distortion of the contour B_2. Equation 12 is the main result of this section, and it is subsequently used to calculate the required stress intensity factor for the stationary crack.

Fundamental Solution

In the previous section the z-component of the displacement w_B was calculated. To satisfy the boundary conditions of the original problem, an additional displacement w must be added to w_B such that the z-component of the displacement ahead of the crack tip will be identically zero, and then the stresses ahead of the crack tip can be calculated. For that purpose the following problem is considered. The entire plane containing the semi-infinite crack is taken to be at rest for time $\tau < 0$. At time $\tau = 0$, an edge dislocation with strength 2Δ starts to climb in the x-direction with constant velocity, v, as shown in Fig. 3. The faces of the crack are traction free. Again the problem considered is symmetric with respect to the x-axis, and it may be viewed as a half-plane problem in the region $z \geq 0$. Solution of the equations of motion is sought in this region, subject to the following boundary conditions

$$\sigma_{zz}(x, 0, \tau) = 0 \qquad x < 0 \tag{13}$$

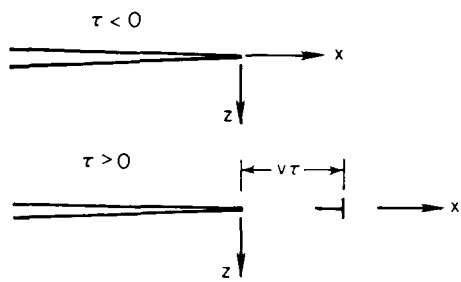

FIG. 3—*Moving dislocation problem that leads to the fundamental solution.*

$$\sigma_{xz}(x, 0, \tau) = 0 \qquad -\infty < x < \infty \tag{14}$$

$$w(x, 0, \tau) = \Delta H(v\tau - x) \qquad x > 0 \tag{15}$$

This is precisely the problem analyzed in the second section of Ref *6*, and therefore only the form of the solution is presented here. Following the same general procedure based on integral transforms that was outlined in the previous section, it can be shown that the normal stress on the line $z = 0$ is given by

$$\sigma_{zz}(x, 0, \tau) = -\frac{1}{\pi x} \operatorname{Im} G_+(-\tau/x) \tag{16}$$

for $\tau > ax$, where G_+ is a complicated function defined explicitly in Ref *6*. Equation 16 is that part of the fundamental solution that is required to find the dynamic stress intensity factor.

Stress Intensity Factor

The displacement $w_B(\xi, 0, t)$ given in Eq 12 can be rewritten as

$$w_B(\xi, 0, t) = \frac{T_o}{\mu}\left[\frac{2}{\pi}\int_a^{t/\xi} \lambda g(\lambda) d\lambda + f(c)H(t - c\xi)\right] \tag{17}$$

where the definitions of $g(\lambda)$ and $f(c)$ are obvious from Eq 12. The distance coordinates ξ in w_B and x in the fundamental solution are now related by $\xi = x + l$ and the corresponding time coordinates t and τ are related by $t = \tau + al$. Thus, the crack face loads are applied in the crack problem at time $t = 0$, place $x = -l$, and the stress intensity factor at the crack tip $x = 0$ is zero until $\tau = 0$ or $t = al$. The first wave arriving at the crack tip is the cylindrical longitudinal wave radiating out from the loading point; the time of arrival is $t = al$ or $\tau = 0$. It is observed that w_B is a homogeneous function of degree zero of ξ and t; that is, it depends on the ratio t/ξ only. Thus, any given displacement level radiates out along the x-axis at a constant speed. In particular, the displacement level $w_B(\xi/t)$ radiates out at speed ξ/t for $t > 0$. The speed varies between zero and the longitudinal wave speed. Consider a particular value of speed in this range, say v. The time at which the corresponding displacement level $w_B(v)$ arrives at $x = 0$ is $\tau_o = (1 - av)l/v$. As was observed before, the displacement level $w_B(a^{-1})$ arrives at $\tau_o = 0$. The speed of the displacement level arriving at $x = 0$ at any instant of time τ can be found by setting $\tau = \tau_o = (1 - av)l/v$ and solving for v, the result being $v = v_\tau = l(\tau + al)$. With this information, a superposition integral whose value is exactly equal but opposite to the normal displacement w_B for $x > 0$ may be determined.

Let $\Delta q(x, z, \tau; v)$ represent any scalar element of the fundamental solution, such as a stress component. Recall that in deriving the fundamental solution, it was assumed that a dislocation in the z-component of displacement of magnitude, 2Δ, began to extend from the crack tip at time $\tau = 0$ at speed v. If the dislocation began moving at $\tau = \tau_o$, instead of at $\tau = 0$, then the solution would be $\Delta q(x, z, \tau - \tau_o; v)$. Suppose further that the intensity of the dislocation is $2\, dw_B$, instead of 2Δ. The solution of this modified problem is $q(x, z, \tau - \tau_o; v)dw_B$. Finally, if w_B itself is some function of v, the result may be summed over an appropriate range of v, which is the case here. Letting Q^* and Q_B represent the corresponding elements of the solution of the impact loading problem of the crack and the impact loading of the half plane, respectively, the final result is

$$Q^*(x, z, t) = Q_B(x, z, t) + Q(x, z, t)H(t - al) \tag{18}$$

where

$$Q(x, z, t) = -\int_{a^{-1}}^{v_\tau} q(x, z, \tau - \tau_o; v \frac{dw_B(v)}{dv}\, dv \tag{19}$$

In particular, if the normal displacement of the surface is considered for $x > 0$, then $q = 1$ and $Q = -w_B(v)$. But $Q_B = w_B(v)$, so that $Q^*(x, 0, \tau) = 0$ for $x > 0$, as it should be according to boundary condition (Eq 4). Relation (Eq 19) actually represents the complete elastic field for the crack problem under consideration. As was stated in the beginning of this paper, however, the main interest is in the strength of the stress singularity at the crack tip as a function of time.

The total normal stress on the plane, $z = 0$, ahead of the crack can be determined by letting $\Delta q(x, z, \tau)$ in Eq 19 be $\sigma_{zz}(x, 0, \tau)$. The total stress will be $\sigma_{zz}{}^*(x, 0, t)$. The stress intensity factor, which is time dependent, is defined in terms of this stress component by

$$K(t) = \lim_{x \to 0^+} (2\pi x)^{1/2} \sigma_{zz}(x, 0, t) \tag{20}$$

The normal stress $\sigma_{zz}{}^B$ is not singular at $x = 0$, so that the stress intensity factor $K(t)$ is determined from Eq 19 alone. In working with the integral of Eq 19, it is more convenient to change the variable of integration from v to $\lambda = 1/v$. Then, after substituting the explicit expressions from Eqs 17 and 19, the normal stress component is

$$\sigma_{zz}(x, 0, t) = \frac{T_o}{\mu \pi x} \int_a^{(t+ax)/l} \frac{2}{\pi} \cdot g(\lambda) \cdot \mathrm{Im}\left[G_+\left(-\frac{\tau - \tau_o}{x}\right)\right] d\lambda$$

$$+ \int_a^{(t+ax)/l} f(c)\,\mathrm{Im}\left[G_+\left(-\frac{\tau - \tau_o}{x}\right)\right]\delta(\lambda - c)\,dc \quad (21)$$

Multiplying Eq 21 by $(2\pi x)^{1/2}$ and then letting $x \to 0^+$, the stress intensity factor is found to be

$$K(t) = \left(\frac{2}{\pi l}\right)^{1/2}\frac{T_o}{b^2}\left[\frac{2\kappa}{\pi}\int_a^{h^*}\frac{\lambda g(\lambda)}{(h^* - \lambda)^{1/2}}\frac{(c + \lambda)S_+(\lambda)}{\alpha_+(\lambda)}\,d\lambda + \frac{f(c)}{(h^* - c)^{1/2}}\frac{2c\cdot S_+(c)}{\alpha_+(c)}H(h^* - c)\right] \quad (22)$$

where $h^* = (\tau + al)/l = t/l$ and α_+, S_+ are defined in Eqs 13 and 14 of Ref *6*.

Equation 22 is the main result of this section. It should be observed in Eq 22 that h^* in the upper limit of integration does not exceed b, while h^* in the integrand is not limited. Therefore Eq 22 may be written in the form

$$K(t) = \left(\frac{2}{\pi l}\right)^{1/2}\frac{T_o}{b^2}\left[\frac{2\kappa}{\pi}\int_a^{m}\frac{g(\lambda)}{(h^* - \lambda)^{1/2}}\frac{(c + \lambda)S_+(\lambda)}{\alpha_+(\lambda)}\,d\lambda + \frac{f(c)}{(h^* - c)^{1/2}}\frac{2c\cdot S_+(c)}{\alpha_+(c)}H(h^* - c)\right] \quad (23)$$

where m is the smaller of t/l and b.

For numerical consideration Poisson's ratio, ν, was taken equal to 1/4. In this case, the ratios of the slowness are $b^2 = 3\,a^2$ and $c^2 = 3.549\,a^2$. The normal displacement, w_B, and the stress intensity factor, $K(t)$, have been evaluated numerically, and the results are shown in Figs. 4 and 5.

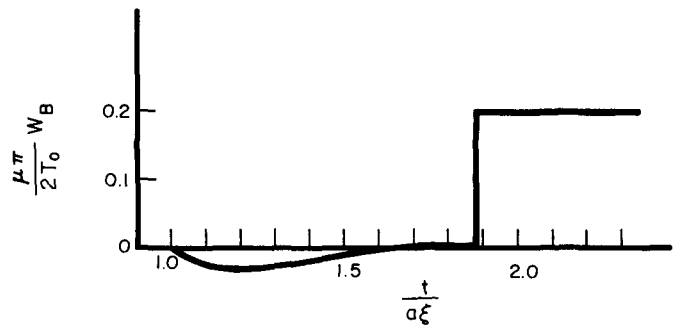

FIG. 4—*Nondimensional normal surface displacement for the problem in Fig. 3.*

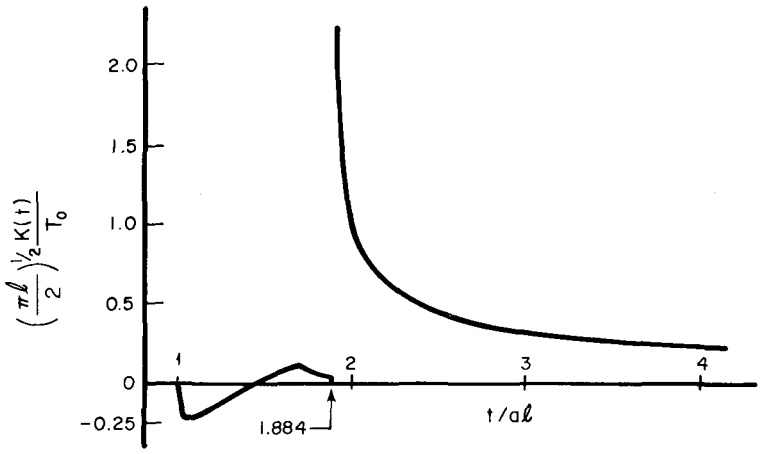

FIG. 5—*Nondimensional stress intensity factor versus time for the problem in Fig. 1.*

Figure 4 shows the component of the displacement w_B normal to the surface of a half plane $z \geq 0$. If attention is fixed on the point $\xi = l$, the eventual position of the crack tip, the initial motion of the surface is an outward displacement at $t = al$. At time $t = bl$ the surface will have moved inward, and it maintains the same value of normal displacement until $t = cl$, whereupon a large jump in displacement occurs and the displacement remains constant afterwards. If attention is fixed on fixed time t, then Fig. 4 shows the profile of the surface at time t where $\xi = 0$, the point of load application, will be represented in Fig. 4 by ∞ on the abscissa. As ξ increases the point $t/a\xi$ moves toward the origin on the abscissa. Figure 5 shows the stress intensity factor versus t/al. It is seen in Fig. 5 that the stress intensity factor takes on negative values upon the arrival of the first wave at $t = al$. It decreases until it reaches a minimum value at $t/al \simeq 1.05$ and then begins to increase, reaching zero at $t/al \simeq 1.44$. At time $t/al \simeq 1.69$, $K(t)$ reaches a small maximum. When the Rayleigh wave arrives at the crack tip, $t/al \simeq 1.884$, the stress intensity factor jumps to $+\infty$, and it starts to decrease in proportion to $(t - cl)^{-1/2}$. As the time increases to large values, $K(t)$ decays to zero, which is the exact value when the load T_0 is applied statically to the crack faces [*10*].

Conclusion

If symmetric tractions, acting in the plane of the crack and in the same direction on opposite faces (as in Fig. 1), are applied quasistatically to the faces of a crack, then the elastic stress intensity factor is zero. It has been shown here, however, that if such loading is rapidly applied then the stress

intensity factor is nonzero and it varies with time. Furthermore, for a short time, the stress intensity factor takes on large values, comparable to the values it would have if normal crack face tractions of the same magnitude were applied. Thus, in certain cases of impact loading, these crack face tractions, which act in the plane of the crack, may indeed be important. It is observed in Fig. 5 that the stress intensity factor is negative for a short time before it becomes positive. This may be interpreted as indicating that the crack faces near the tip, press against each other for a short time (with $K = 0$) before the crack begins to open.

Problems concerned with elastodynamic crack growth under the action of parallel impact loading of the crack faces have also been analyzed by means of the procedure outlined here [*12*]. The general features of the stress intensity factor dependence on time are similar to those for the stationary crack shown in Fig. 5. The more realistic case of a crack rapidly growing inward from the edge of an elastic half plane under the action of parallel impact loading, as well as other types of loading, has recently been analyzed by Burgers and Freund [*13*]. It appears that the presence of the free surface has a significant effect on the time dependence of the stress intensity factor.

Acknowledgment

The research support of the National Science Foundation, Solid Mechanics Program, through Grant ENG 77-15564 to Brown University is gratefully acknowledged.

References

[*1*] Freund, L. B., *Journal of the Mechanics and Physics of Solids,* Vol. 20, 1972, p. 129.
[*2*] Freund, L. B., *Journal of the Mechanics and Physics of Solids,* Vol. 20, 1972, p. 141.
[*3*] Freund, L. B., *Journal of the Mechanics and Physics of Solids,* Vol. 21, 1973, p. 47.
[*4*] Freund, L. B., *Journal of the Mechanics and Physics of Solids,* Vol. 22, 1974, p. 137.
[*5*] Fossum, A. F., "An Application of Numerical and Analytical Approximate Techniques in the Solution of Some Elastodynamic Problems with Free Surfaces," Ph.D. thesis, Brown University, Providence, R.I., July 1973.
[*6*] Freund, L. B., *International Journal of Engineering Science,* Vol. 12, 1974, p. 179.
[*7*] Achenbach, J. D. and Tolikas, P. K. in *Fast Fracture and Crack Arrest, ASTM STP 627,* American Society for Testing and Materials, G. Hahn and M. Kanninen, Eds., 1977, p. 59.
[*8*] Freund, L. B. in *Mechanics Today,* Vol. III, S. Nemat-Nasser, Ed., Pergamon, New York/London, 1976, p. 55.
[*9*] Nilsson, F. in *Fast Fracture and Crack Arrest, ASTM STP 627,* American Society for Testing and Materials, G. Hahn and M. Kanninen, Eds., 1977, p. 77.
[*10*] Tada, H., Paris, P. C., and Irwin, G. R., "The Stress Analysis of Cracks Handbook," Del Research Corp., Hellertown, Pa., 1973.
[*11*] Achenbach, J. D., *Wave Propagation in Elastic Solids,* North Holland, The Netherlands, 1973.
[*12*] Abou-Sayed, I. S., "Some Novel Problems in Dynamic Crack Propagation," Ph.D. thesis, Brown University, Providence, R.I., 1978.
[*13*] Burgers, P. and Freund, L. B., "Dynamic Growth of an Edge Crack in a Half Space," *International Journal of Solid Structures,* to be published.

L. Hodulak,[1] *A. S. Kobayashi,*[2] *and A. F. Emery*[2]

A Critical Examination of a Numerical Fracture Dynamic Code

REFERENCE: Hodulak, L., Kobayashi, A. S., and Emery, A. F., **"A Critical Examination of a Numerical Fracture Dynamic Code,"** *Fracture Mechanics: Twelfth Conference, ASTM STP 700,* American Society for Testing and Materials, 1980, pp. 174-188. pp. 000-000.

ABSTRACT: After upgrading the energy dissipation algorithm, numerical experiments were conducted to assess the reliability of the explicit dynamic finite element code, HCRACK. Two dynamic fracture specimens (that is, the wedge-loaded rectangular double cantilever beam (RDCB) specimen and the wedge-loaded tapered double cantilever beam (TDCB) specimen), which were studied experimentally by Kalthoff, Beinert, and Winkler, were then analyzed with this updated fracture dynamic code. Using the experimentally determined dynamic fracture toughness, K_{ID}, versus crack velocity, $\dot{a}$, relation, the RDCB specimen was analyzed first by the "propagation method" where good agreements between calculated and measured K_{ID} versus a relations were observed. The calculated a versus time, t, relation was then used as input data in the "generation method" where the resultant K_{ID} were virtually identical to those obtained in the propagation method. Error analyses of the generation method also were made first by using the experimentally determined a versus t relation and secondly by artificially perturbing this relation.

A TDCB specimen was then analyzed with both the propagation and generation methods by using the K_{ID} versus $\dot{a}$ relation established for this specimen and the measured a versus t relation, respectively. The computed K_{ID} obtained by both methods were in good agreement with the experimental results, showing that either approach can be used in analyzing fracture.

KEY WORDS: dynamic fracture, dynamic finite element analysis, dynamic fracture toughness, crack arrest stress intensity factor, fractures (materials), crack propagation

For the past three years, two of the authors have used a two-dimensional elasto-dynamic finite element code, which was based on HONDO [*1*],[3] to compute the dynamic stress intensity factor for a crack propagating with a prescribed velocity [*2-5*] by applying to each node a nodal force sufficient to

[1] Physicist, Fraunhofer-Institut für Werkstoffmechanik, Freiburg, West Germany.

[2] Professors, Department of Mechanical Engineering, University of Washington, Seattle, Wash. 98195.

[3] The italic number in brackets refer to the list of references appended to this paper.

release the node. This numerical procedure was later modified to include a startup procedure for computing dynamic stress intensity factor, dynamic energy release rate, fracture energy, kinetic energy and strain energy at each increment of crack advance [*6, 7*]. Also the impulse stress waves generated by the instantaneous application of a nodal force to model the release of a crack-tip node was reduced by varying the force over the time necessary for the crack tip to advance one nodal distance. Physically, this procedure models a more gradual transit of the crack-tip between two adjacent finite element nodes and is similar to that developed by Keegstra [*8–10*] with the exception that our restraining nodal force is completely eliminated when the crack-tip reaches its adjacent node. Other nodal force release mechanisms include those of Malluck and King [*11*] and Rydholm, Fredriksson, and Nilsson [*12*] with different postulated rates of nodal force release. The dissipated energy during a crack extension based on any of the above three nodal force release mechanisms is then computed from the nodal force versus nodal displacement relation during this incremental crack extension. In general this nodal force versus nodal displacement relation is nonlinear and is goverened by the dynamic state surrounding the propagating crack tip, thus requiring the monitoring of nodal force or nodal displacement or both at every incremental time in the dynamic finite element analysis. Interestingly enough, recent studies showed that the differences in the mechanism of nodal force release [*13, 14*] caused little changes in the resultant dynamic stress intensity factor. It is thus of no surprise that good to excellent agreements were claimed by all [*6, 11, 12*] when these three crack tip energy dissipation procedures for computing the dynamic stress intensity factor was checked by analyzing the Broberg problem [*15*].

The preceding procedure of computing dynamic stress intensity factor for a crack whose velocity is prescribed to be equal to measured one in a dynamically fracturing specimen was termed "generation calculation" by Kanninen [*16, 17*], who also expressed reservations on the accuracy of this numerical approach. The "propagation calculation" in contrast to the "generation calculation" is based on an assumed dynamic fracture toughness, K_{ID}, versus crack velocity, $\dot{a}$, relation which is then used to propagate a crack [*16–23*].[4] The assumed K_{ID} versus $\dot{a}$ relation is considered correct when the calculated crack propagation history coincides with the experimental data, and the K_{ID} at crack arrest, if any, is considered to be the crack arrest toughness, K_{Ia}, sought by some in predicting fracture arrest of a dynamically propagating crack.

While one can debate the merits of propagation versus generation calculations, only one study, which involved both propagation and generation calculation using the same numerical algorithm [*23*], has been published to

[4]Note that Keegstra in Refs *8–10* used the propagation calculation to compute K_{ID} versus a relations in fracturing specimens.

date. Since the limited study in Ref *23* did not provide a comprehensive error assessment of the two procedures, this paper will report on our comparative studies using two Araldite B fracture specimens which were analyzed by Kalthoff et al by the method of caustics [*24,25*].

Dynamic Finite Element Analysis

In the previous studies cited above [*6,26*], the dynamic fracture dynamic code HCRACK was shown to be an efficient and inexpensive method for simulating dynamic fracture problems. Numerical experiments proved that reasonable numerical accuracy can be obtained by using coarse meshes of conventional elements (see Figs. 1 and 2) and a moderate number of time steps; for example, about 150 steps for crack propagation and subsequent arrest in a RDCB specimen shown in Fig. 1. Unlike the implicit dynamic finite element codes used by others, however, it was difficult to accurately prescribe the rate of nodal force release since the input nodal force would not generally be in equilibrium with the dynamic state of stress in the adjoining finite elements in this explicit finite element code. As a result, an in-depth study on the performance of our fracture dynamic code was conducted for different crack tip force release rates, different calculation procedure for the dynamic stress intensity factor, and different finite element breakdown. A brief description of some of these findings are presented in the following.

As mentioned above, the algorithm for artificially prescribing an input nodal force at the crack tip for each time step for prescribed decrease in the resultant residual nodal force in the dynamic code is not straight-forward, and often a complete release of the nodal force cannot be achieved in the prescribed time period. The basis of the numerical method is to define the force, F_n^i which must be applied to a node at time step n such that the time variation of the stress follows the form shown in Fig. 3. In an implicit code,

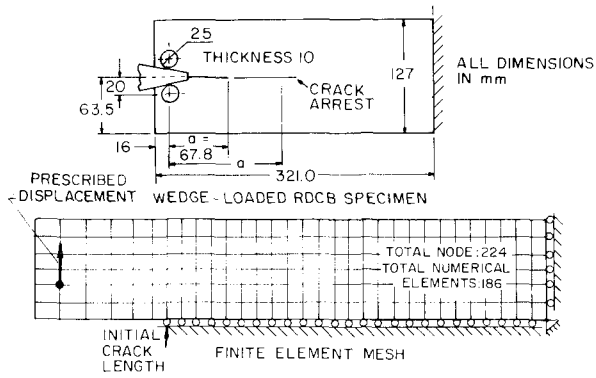

FIG. 1—*Wedge-loaded RDCB specimen.*

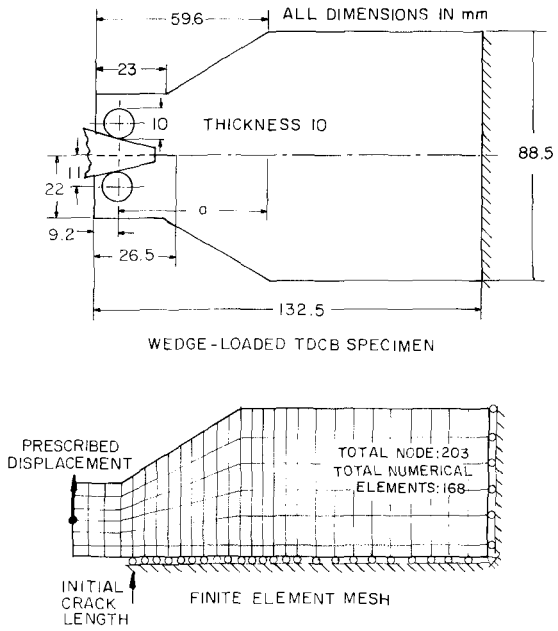

FIG. 2—*Wedge-loaded TDCB specimen.*

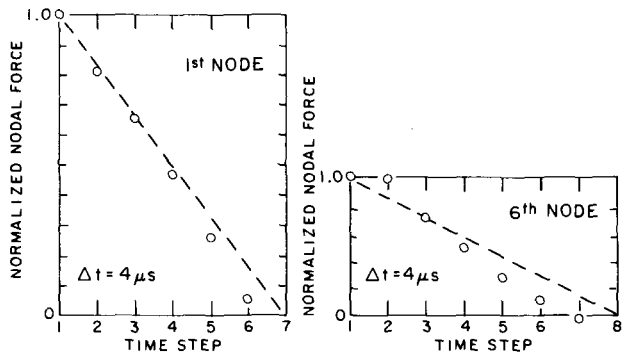

FIG. 3—*Gradual release of the nodal force at the crack tip.*

application of F_n would result in the same calculated force at the end of the time step. With the explicit code, however, the calculated force at the end of the increment, $F_n{}^0$, will rarely be equal to $F_n{}^i$. Accordingly, the force at the next time step, $F_{n+1}{}^i$, must be adjusted not only to compensate for the error, but also to yield the desired value at the end of the time step. The simplified method used in Ref *26* was replaced by the following equation and typical results are shown in Fig. 3.

$$F_{n+1}{}^{i} = F_n{}^{0} - F_{n+1}{}^{\text{prescribed}} - \sum_{j=1}^{n} \frac{F_j{}^{i}}{2^{n-j+1}} \tag{1}$$

At the beginning of the crack propagation history when the first crack tip node is released (see Fig. 3), excellent agreement between the prescribed (linear decrease in this case) and actually achieved nodal forces is noted; while for the sixth node that was released later (see Fig. 3), some deviations between both nodal forces are noted. Initial static equilibrium prior to crack propagation most likely contribute the excellent results in the former case.

Also noteworthy is the recent study by Malluck and King [*13*] who compared energy release rates for the two distinctly different functions of $F/F_0 = [1 - b/\Delta]^{3/2}$ and $F/F_0 = [1 - b/\Delta]^{1/2}$, where b is the distance between hypothetical crack tip location and the released crack tip node, Δ is the internodal distance, and F and F_0 are the instantaneous and original crack tip nodal forces, respectively. Their results showed no significant differences in the calculated dynamic stress intensity factors for crack speeds lower than 25 percent of the shear wave velocity; that is, $c < 0.25\, c_2$. Our use of a linearly decreasing nodal force, $F/F_0 = [1 - b/\Delta]$, with constant crack velocity between the two adjoining finite element nodes is thus justified.

The dynamic stress intensity factor was computed directly by the total strain energy released from an instantaneous balance of the total energy of the entire specimen [*7*] as

$$G_{\text{I}} = 2(E_n - E_{n+1})/(a_{n+1} - a_n) \tag{2}$$

where E_n, E_{n+1} are the total strain energies for crack lengths of a_n, a_{n+1}, respectively when the crack extended from node n to node $n + 1$. The dynamic stress intensity factor, K_{I}, was then computed from G_{I} using Freund's relation [*27*]. Alternatively, the value of G_{I} was computed by energy dissipated at the released node as

$$G_1 = [u_1 \Delta F_1 + \sum_{i=2}^{m} (u_i + u_{i-1}) \Delta F_i]/(a_{n+1} - a_n) \tag{3}$$

where m is the number of time steps between nodes n and $n + 1$, u_i and ΔF_i are displacement and decrease of force at the released node n, respectively.

Figure 4 shows the dynamic fracture toughness, K_{ID}, associated with crack propagation and arrest in one of Kalthoff's RDCB specimens [*24*] computed by both Eqs 2 and 3 using the "propagation method." Although details of this analysis are described in the following section, the results are shown in this section as an indication that little difference can be noted in the K_{ID} obtained by the two algorithms.

As shown in Fig. 4, the forced linear decrease in the crack tip nodal force improved the simulation of the smoothly propagating crack and eliminated

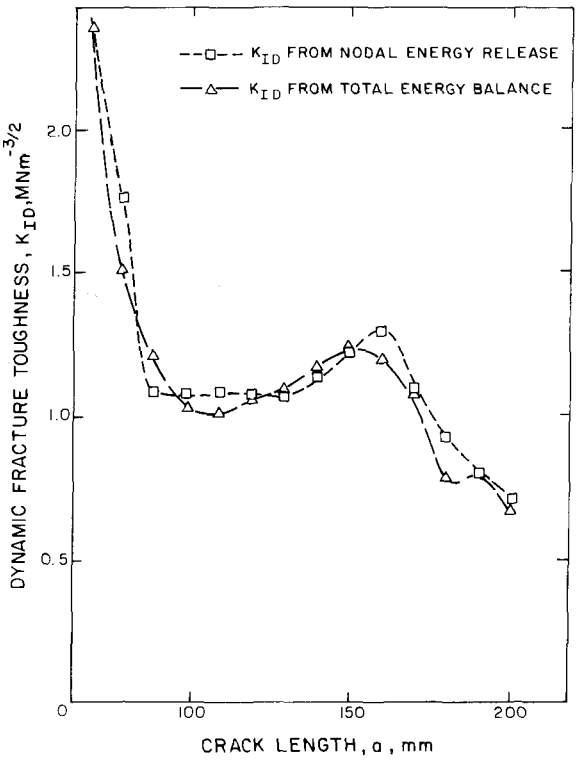

FIG. 4—*Dynamic fracture toughness in wedge-loaded RDCB specimen.*

the spurious oscillations in dynamic stress intensity factor observed previously [*2-5*]. It is uncertain, however, to what extent this smoothing procedure may hide the true oscillations of the dynamic stress intensity factor eventually induced by the reflected stress waves that emanated from the running crack.

Specimens and Material Data

The two specimens analyzed by the dynamic finite element code are the wedge-loaded, RDCB and TDCB specimens which were investigated experimentally by Kalthoff et al [*24,25*]. Specimen geometries of these Araldite B specimens and their finite element idealizations can be seen in Figs. 1 and 2.

Although the rigid loading wedge between the two loading pins will prevent any inward displacement of the loading pins, these pins are free to leave the wedge and travel outwards. The resultant dynamic stress intensity factors

in the presence of separating pins could vary significantly during crack propagation [*26*]. The smaller mass density and the two orders of magnitude larger compliance of the Araldite B specimens in comparison to the steel specimen studied in Ref *26* should have reduced the additional input energy due to any possible separation of the loading pins, and thus constant loading pin displacement were prescribed at the pin holes.

Material constants of Araldite B used for this dynamic finite element analysis after Ref *24* are modulus of elasticity $E = 3.38$ GPa, Poisson ratio of $\mu = 0.33$ and mass density, $\rho = 1047$ kg/m^3. The experimentally determined dynamic fracture toughness K_{ID}, versus crack velocity, $\dot{a}$, relations used in the propagation calculations of RDCB and TDCB specimens are both plotted in Fig. 5 [*24,25*], respectively. Crack length as a function of time used in the generation calculations of the RDCB specimen was taken from Fig. 5 in Ref *24* but is not reproduced in this paper.

For the dynamic crack initiation in the RDCB specimen, the dynamic crack initiation stress intensity factor, K_{IQ}, as reported in Ref *24*, was used and the subsequent dynamic stress intensity factors were computed from the energy released at the node adjacent to the reference crack tip node, except the set of K_{ID} data noted in Fig. 4. Since an experimentally determined K_{IQ} was not reported in Ref *25*, a statistically computed K_{IQ}, which was back calculated from the median of Kalthoff's measured oscillating K_{ID}-values [*25*] after crack arrest, was used in the analysis of the TDCB specimen.

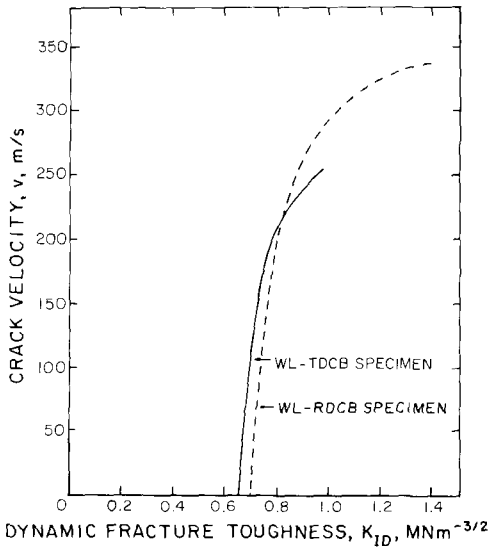

FIG. 5—*Crack velocity versus dynamic fracture toughness relations for Araldite B epoxy, from Ref* 24.

Results

RDCB Specimen

The first numerical analysis involved a propagation calculation for the RDCB specimen of Fig. 1 using the K_{ID} versus $\dot{a}$ relation of Fig. 5 and a $K_{IQ} = 2.32$ MN $m^{3/2}$. The resulting dynamic fracture toughness and crack tip motion of this propagation calculation are shown in Figs. 6 and 7, respectively. The "propagation" crack tip motion from Fig. 7 was then used as input data for the generation calculation. This result is not plotted in Fig. 6 since the K_{ID} versus $\dot{a}$ relations obtained by both the propagation and generation calculation were indistinguishable.

As an additional numerical experimentation, however, the measured crack length, *a*, versus time, *t*, relation of Ref *24* was used as input to the generation calculation, and the resultant K_{ID}-curves are also shown in Figs. 6 and 7. Despite the lack of complete agreement between the two K_{ID}-curves obtained

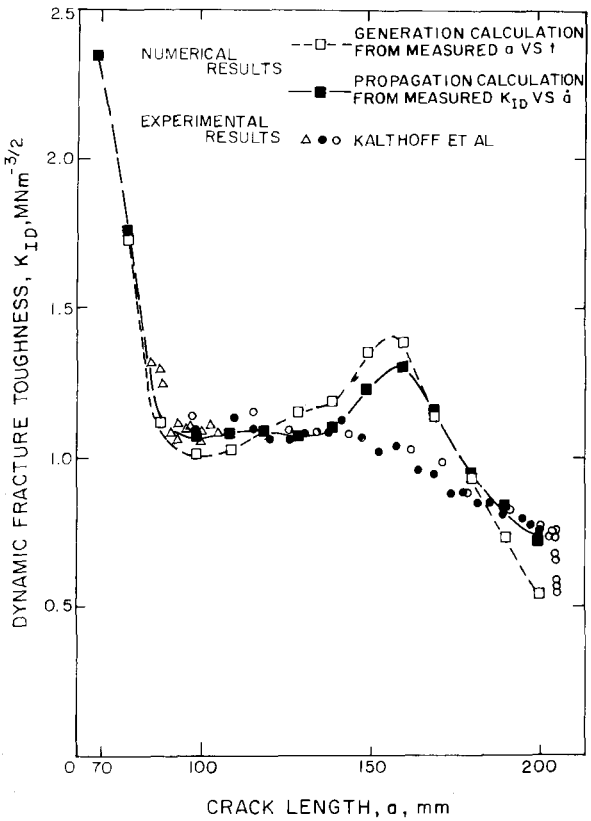

FIG. 6—*Dynamic fracture toughness in wedge-loaded RDCB specimen.*

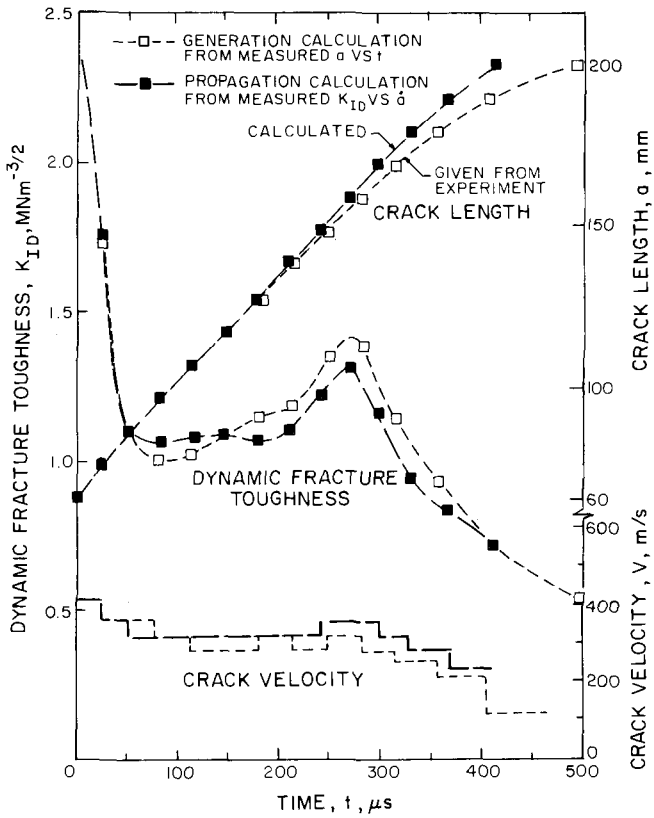

FIG. 7—*Crack length, dynamic fracture toughness, and crack velocity versus time in wedge-loaded RDCB specimen.*

by propagation and generation calculation, the shapes of these two curves are very close. Although both K_{ID}-curves agree well with experimental data during the first half of dynamic crack propagation as shown in Fig. 7, a distinct difference is noted by a second local maximum, which occurs in both propagation and generation calculations prior to crack arrest, but which does not occur in the experimental results. The similarity between the propagation and generation K_{ID}-curves is more apparent in Fig. 8 where the second maxima in the two calculations occur at the same time. The higher K_{ID}-values in the generation calculation at lower measured crack velocities during much of the crack propagation will result in a general shift of two K_{ID} versus $\dot{a}$ relations in Fig. 5.

Figure 6 also shows that the computed crack jump distance is 4 percent shorter of the measured one in the propagation calculation but by definition is equal to measured distance in the generation calculation. Although the

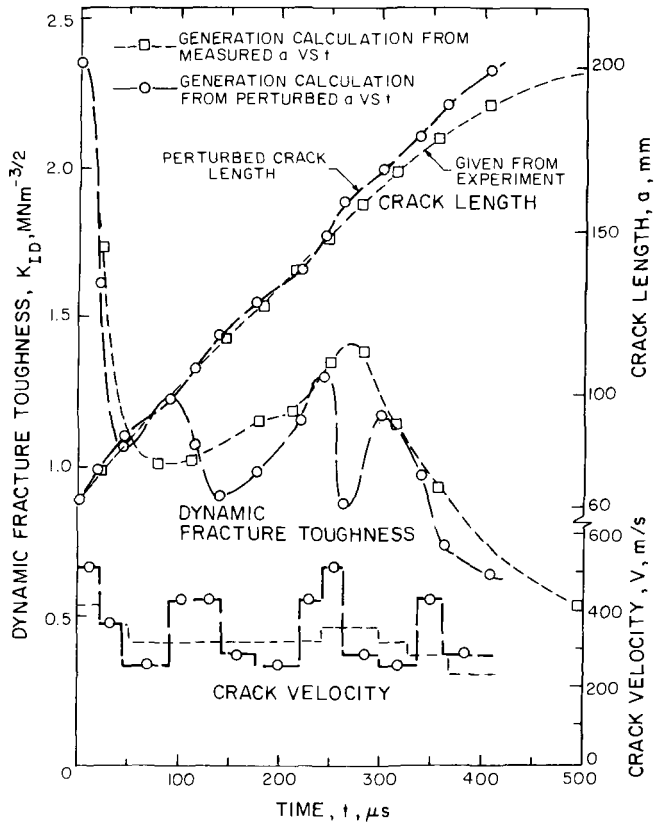

FIG. 8—*Crack length, dynamic fracture, and crack velocity versus time in wedge-loaded RDCB specimen.*

propagation calculation is terminated when the computed dynamic stress intensity factor falls below the minimum K_{ID}-value in Fig. 5, the generation calculation is continued up to the prescribed crack tip length and crack arrest time. Significantly lower dynamic stress intensity at the instant of crack arrest is noted.

The sensitivity of the dynamic stress intensity factor, which is calculated by the generation method, to the instantaneous crack velocity is further demonstrated in Fig. 8. In order to assess the sensitivity of K_{ID} obtained by the generation method to the input data, a numerical experiment was conducted by artificially perturbing the smooth experimental curve of the crack tip motion in Fig. 8. The result was a severely perturbed K_{ID} also shown in Fig. 8, where discrete increases and decreases in crack velocities are followed by local minima and maxima of K_{ID}, respectively.

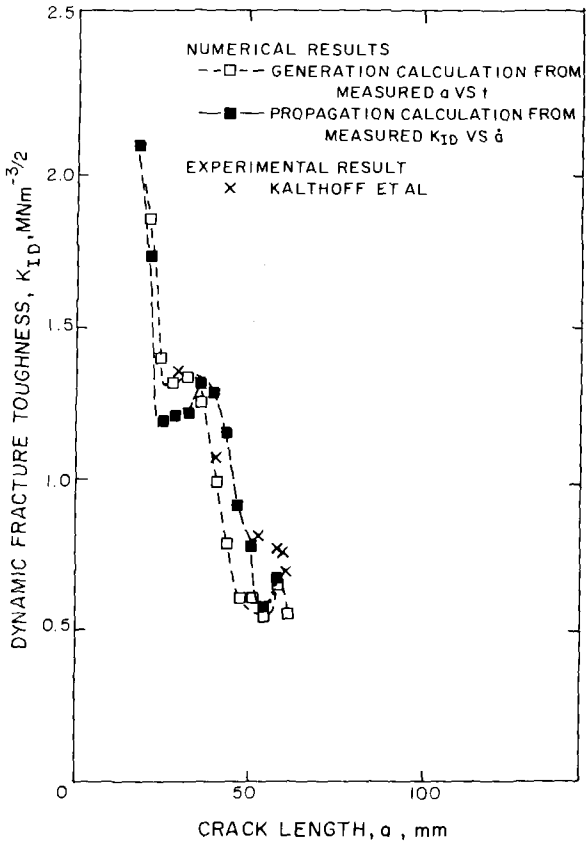

FIG. 9—*Dynamic fracture toughness in wedge-loaded tapered DCB specimen.*

TDCB Specimen

Figure 9 shows the K_{ID} as a function of a computed by the propagation method, using the K_{ID} versus $\dot{a}$ relation of Fig. 5 and by the generation method using experimentally determined a versus t relations for the TDCB specimen together with experimental data from Ref *25*. A second maximum, which resembles that found previously in the RDCB specimen, in K_{ID} can be observed. The computed crack jump distance obtained by the propagation method is shorter than the experimental one by 12 percent. In the propagation calculation, the computed K_{ID} increased again to a value approaching experimental K_{ID} after the initial crack arrest. Subsequently, computed K_{ID} oscillated around the few experimental points.

Figure 10 shows the K_{ID} versus t relations obtained by both propagation and generation calculations. Although the two calculated K_{ID} are in excellent

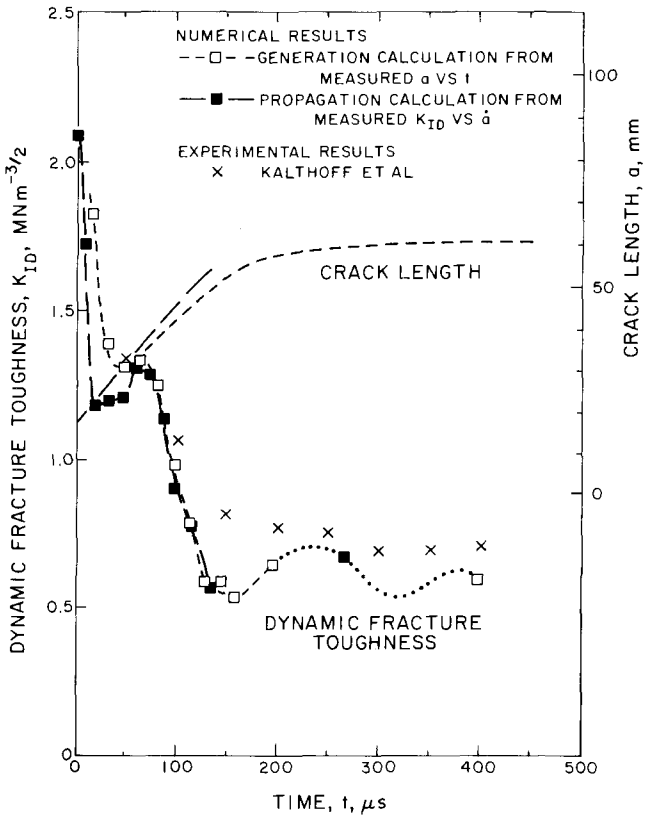

FIG. 10—*Dynamic fracture toughness and crack length versus time in wedge-loaded tapered DCB specimen.*

agreement with each other except for the initial phase of crack propagation in this TDCB specimen, the calculated K_{ID} are lower than the measured K_{ID} just prior to and after crack arrest. Previous experience with steel TDCB specimens [*4,5,26*] indicate that this small underestimate could be attributed to the possible separation of the loading pins from the loading wedge during crack propagation.

Conclusions

The results of the present and of the previous studies using HONDO II show that the dynamic stress intensity factor for a crack propagating in a finite two-dimensional body can be computed relatively inexpensively with an accuracy sufficient for many practical purposes. Very close agreements be-

tween the K_{ID} obtained by the generation and by the propagation calculations should dispel the reservations [*16,17*] about this dynamic fracture algorithm.

When used in conjunction with measured crack position versus time data, the generation method with proper care can be used to accurately calculate the dynamic stress intensity factor during the fast crack propagation and crack arrest.

On the other hand the uncertainty in the K_{ID} versus $\dot{a}$ relations, particularly in the region of very low velocities together with limitation in the finite element modeling of dynamic crack propagation, offers little chance for simulating the crack propagation and crack arrest event by the propagation method when the dynamic stress intensity factor oscillates in a narrow range about the crack arrest stress intensity factor as shown by some experimental results with the single edged notch specimens reported in Ref *25*.

Discussion

It has been a common practice by all, including the authors, to verify their fracture dynamic code by analyzing the Broberg problem [*15*] for which the dynamic solution is available. Good agreements in these studies cannot be construed as verification of numerical solutions generated for cracks propagating in finite specimens composed of real materials. The discrepancies between the computed and the experimentally determined K_{ID}-values shown in Figs. 6 and 9 could have arisen from the viscous damping in Araldite B which was not modeled in the elasto-dynamic analyses described in this paper. A study of the time-dependent energy balance during crack propagation and arrest suggests that the consistently appearing second maxima in the calculated K_{ID}-curves are real phenomena based on elastic analyses. It is interesting to note that the limited experimental K_{ID} versus a relation obtained for RDCB specimens machined from high-strength steel [*25*] is in qualitative agreement with our elastic analysis of the RDCB specimen.

Acknowledgment

The results of this investigation were obtained in a research contract funded by the Office of Naval Research (ONR) under Contract No. N00014-76-C-0060, NR 064-478. The authors wish to acknowledge the support and encouragement of N. R. Perrone of ONR during the course of this investigation. The first author, L. Hodulak, was supported by a postdoctoral fellowship from the Deutsche Forschungsgemeinschaft, FRG. The authors also wish to acknowledge the discussions with J. F. Kalthoff, Institut für Werkstoffmechanik.

References

[1] Key, S. W., "HONDO, A Finite Element Computer Program for the Large Deformation Dynamic Responses of Axisymmetric Solids," Sandia Laboratories.

[2] Kobayashi, A. S., Emery, A. F., and Mall, S., *Experimental Mechanics,* Vol. 16, No. 9, Sept. 1976, pp. 321-328.

[3] Kobayashi, A. S., Emery, A. F., and Mall, S. in *Fast Fracture and Crack Arrest, ASTM STP 627,* American Society For Testing and Materials, pp. 95-108.

[4] Urabe, Y., Kobayashi, A. S., Emery, A. F., and Love, W. J. in *Fracture Mechanics and Technology,* G. C. Sih and C. L. Chow, Eds., Sijthoff and Noordhoff International, Leyden, The Netherlands, 1977, Vol. II, pp. 1499-1512.

[5] Urabe, Y., Kobayashi, A. S., Emery, A. F., and Love, W. J., *Journal of Engineering Materials and Technology, Transactions,* American Society of Mechanical Engineers, Vol. 99, Series H, No. 4, Oct. 1977, pp. 324-328.

[6] Kobayashi, A. S., Mall, S., Urabe, Y., and Emery, A. F. in *Numerical Methods in Fracture Mechanics,* A. R. Luxmoore and D. R. J. Owens, Eds., University College of Swansea, Jan. 1978, pp. 673-684.

[7] Kanazawa, T., Kobayashi, A. S., Machida, S., and Urabe, Y. in *Numerical Methods in Fracture Mechanics,* A. R. Luxmoore and D. R. J. Owens, Eds., University College of Swansea, Jan. 1978, 709-720.

[8] Keegstra, P. N. R., *Journal of the Institute of Nuclear Engineers,* Vol. 17, No. 4, 1976, pp. 89-96.

[9] Keegstra, P. N. R., Head, J. L., and Turner, C. E. in *Proceedings of the 4th International Conference on Fracture,* University of Waterloo Press, Vol. 3, 1977, pp. 515-522.

[10] Keegstra, P. N. R., Head, J. L., and Turner, C. E., "The Interpretation of the Instrumented Charpy Test," *Transactions,* 4th International Conference on Structural Mechanics in Reactor Technology, Vol. G., CECA, CEE, CEEA Luxembourg, paper G 4/7, 1977.

[11] Malluck, J. F. and King, W. W., "Fast Fracture Simulated by a Finite Element Analysis which Accounts for Crack Tip Energy Dissipation," *Transactions,* 4th International Conference on Structural Mechanics in Reactor Technology, Vol. G., CECA, CEE, CEEA, Luxembourg, paper G 4/7, 1977, pp. 648-659.

[12] Rydholm, G., Fredriksson, B., and Nilsson, F., "Numerical Investigations of Rapid Crack Propagation," *Transactions,* 4th International Conference on Structural Mechanics in Reactor Technology, Vol. G., CEEA, CEE, CEEA, Luxembourg, paper G 4/7, 1977, pp. 660-672.

[13] Malluck, J. F. and King, W. W., "Finite Element Simulations of Fundamental Fast Fracture Problems," a paper presented at the ASTM Committee E-24 Symposium on Crack Arrest Methodology and Applications, Philadelphia, Pa., 6-7 Nov. 1978.

[14] Urabe, Y., private communication.

[15] Broberg, K. B., *Arkiv für Fysik,* Vol. 18, 1960, pp. 159-198.

[16] Kanninen, M. F., *Numerical Methods in Fracture Mechanics,* A. R. Luxmoore and D. R. J. Owens, Eds., University College of Swansea, Jan. 1978, pp. 612-633.

[17] Kanninen, M. F., Rosenfield, A. R., McGuire, P. M., and Barnes, R. C., "The Determination of Dynamic Fracture Toughness Values and Evaluation of Crack Arrest Concepts Using DCB Test Specimens," a paper presented at the ASTM Committee E-24 Symposium on Crack Arrest Methodology and Applications, Philadelphia, Pa., 6-7 Nov. 1978.

[18] Kanninen, M. F., *International Journal of Fracture,* Vol. 10, No. 3, Sept. 1974, pp. 415-431.

[19] Hahn, G. T., Hoagland, R. G., Kannen, M. F., and Rosenfield, A. R. in *Cracks and Fracture, ASTM STP 601,* American Society for Testing and Materials, June 1976, pp. 209-233.

[20] Hoagland, R. G., Gehlen, P. C., Rosenfield, A. F., and Hahn, G. T. in *Fast Fracture and Crack Arrest, ASTM STP 627,* American Society for Testing and Materials, July 1977, pp. 203-207.

[21] Hahn, G. T., Hoagland, R. G., and Rosenfield, A. R., "A Fracture Mechanics Practice for Crack Arrest," *Transactions*, 4th International Conference on Structural Mechanics in Reactor Technology, CECA, CEE, CEEA, Luxembourg, Paper G 1/6, 1977.

[22] Kanninen, M. F., Popelar, C., and Gehlen, R. C. in *Fast Fracture and Crack Arrest, ASTM STP 627*, American Society For Testing and Materials, July 1977, pp. 19–38.

[23] Hahn, G. T., Gehlen, R. C., Hoagland, R. G., Marshall, C. W., Kanninen, M. F., Pipelar, C., and Rosenfield, A. F., "Critical Experiments, Measurements and Analyses to Establish a Crack Arrest Methodology for Nuclear Pressure Vessel Steels," Task 62, Second Annual Report, Battelle Columbus Laboratories BMI-1959, Columbus, Ohio, Oct. 1976.

[24] Kalthoff, J., Beinert, J. and Winkler, S. in *Fast Fracture and Crack Arrest, ASTM STP 627*, American Society For Testing and Materials, July 1977, pp. 161–176.

[25] Kalthoff, J. F., Beinert, J., and Winkler, S., "Experimental Analysis of Dynamic Effects in Different Crack Arrest Specimen," a paper presented at the ASTM E-24 Symposium on Crack Arrest Methodology and Applications, Philadelphia, Pa., 6-7 Nov. 1978.

[26] Kobayashi, A. S., Urabe, Y., Emery, A. F., and Love, W. J., *Journal of Engineering Materials and Technology, Transactions*, American Society of Mechanical Engineers, Vol. 100, No. 4, Oct. 1978, pp. 402–410.

[27] Freund, L. B., *Journal of Mechanics and Physics of Solids*, Vol. 20, 1972, pp. 141–152.

J. R. Rice,[1] *W. J. Drugan,*[1] *and T-L. Sham*[1]

Elastic-Plastic Analysis of Growing Cracks

REFERENCE: Rice, J. R., Drugan, W. J., and Sham, T-L., **"Elastic-Plastic Analysis of Growing Cracks,"** *Fracture Mechanics: Twelfth Conference, ASTM STP 700,* American Society for Testing and Materials, 1980, pp. 189-221.

ABSTRACT: In an extension of earlier studies by Rice and Sorensen, a discussion is presented on the elastic-plastic stress and deformation fields at the tip of a crack which grows in an ideally plastic solid under plane strain, small-scale yielding conditions. The results of an asymptotic analysis suggest the existence of a crack-tip stress state similar to that of the classical Prandtl field, but containing a zone of elastic unloading between the centered fan region and the trailing constant stress plastic region. The near tip expression for the rate of opening displacement $\dot{\delta}$ at distance r from the growing tip is found to have the same form suggested by Rice and Sorensen

$$\dot{\delta} = \alpha \dot{J}/\sigma_o + \beta(\sigma_o/E)\,\dot{a}\,\ln(R/r)$$

but now the presence of the elastic wedge causes β to have the revised value of 5.08 (for Poisson ratio $\nu = 0.3$). Here, a = crack length, σ_o = yield strength, E = elastic modulus, and J denotes the far-field value, namely, $(1 - \nu^2)K^2/E$ for the small scale yielding conditions considered. The parameters α and R cannot be determined from the asymptotic analysis, but comparisons with finite element solutions suggest that, at least for small amounts of growth, α is approximately the same for stationary and growing cracks, and R scales approximately with the size of the plastic zone, being about 15 percent to 30 percent larger. For large scale yielding it is argued that a similar form applies with possible variations in α and β, at least in cases which maintain triaxial constraint at the crack tip, but in the fully yielded case R is expected to be proportional to the dimension of the uncracked ligament. The model crack growth criterion of Rice and Sorensen, requiring a critical δ at some fixed r from the tip, is reexamined in light of the more accurate solution. The results suggest that the J versus Δa relation describing growth will be dependent on the extent of yielding, although it is suggested that this dependency might be small for highly ductile materials, provided that a similar triaxial constraint is maintained in all cases.

KEY WORDS: elastic-plastic crack mechanics, stable crack growth, ductile tearing fracture, fractures (materials), crack propagation

[1]Professor and research assistants, respectively, Division of Engineering, Brown University, Providence, R.I. 02912.

The aim of this paper is to describe recent studies on the stress and deformation fields at growing plane strain crack tips in elastic-ideally plastic solids, and to interpret the results in terms of criteria for stable crack growth. In both respects the work is an extension of a recently published study by Rice and Sorensen [*1*].[2]

The next section presents the principal results of a recent analysis [*2*] of the asymptotic stress field at a growing crack tip where one finds, contrary to the assumption of Ref *1*, that a full Prandtl field cannot exist at the tip but, rather, its "centered fan" and trailing "constant stress" sectors are divided by an elastic unloading zone. The net stress triaxiality in front of the crack and, indeed, the entire near tip stress distribution differs little from that of the Prandtl field, which may explain why the effect was not revealed in previous finite element simulations of crack growth [*1,3*]. The authors find the same expression as in Ref *1* for the asymptotic form of the near tip openings, but with a revised value of their parameter β (see Eqs 19 and 21).

The following section analyzes recent finite element studies [*4*] of (limited amounts of) stable crack growth under small-scale yielding conditions, based on a refinement of mesh size as suggested in Ref *1* to more accurately determine parameters such as R and α (again, see Eqs 19 and 21) in their expression for the near-tip crack openings. The asymptotic and finite element results seem to be consistent with one another, and together they provide a reasonably complete understanding of the near tip field, at least for limited amounts of stable growth, although numerical results still leave some uncertainties in the determination of α and R.

Subsequent portions of the paper examine a criterion for crack growth, in the form suggested in Ref *1*, requiring that a fixed crack surface opening, δ_c, be maintained at a small characteristic distance r_m (intended to coincide approximately with a "fracture process zone" size) from the tip for continuing growth. Crack growth, under small-scale yielding, is discussed based on the criterion and, in addition, a discussion is included on some possible implications of the criterion for large-scale yielding (but in geometries like deeply-cracked bend specimens, maintaining a crack tip triaxial constraint similar to that of the Prandtl field even under fully yielded conditions).

The authors' considerations suggest a dependence of the J versus crack growth (Δa) relation on the extent of yielding, although for highly ductile materials (large values of the Paris tearing modulus T[*5,6*]) these dependencies might sometimes be relatively small. An Appendix to the paper compares some possible definitions of J for fully plastic specimens.

[2] The italic numbers in brackets refer to the list of references appended to this paper.

Asymptotic Near-Tip Fields for Stationary and Growing Cracks

Rice [*7,8*] and Hutchinson [*9*] have constructed asymptotic plane-strain crack-tip stress states for ideally plastic solids by slip line methods, and have analyzed the nature of the strain singularities within "centered fan" sectors for loading of a stationary crack. Similar methods have been adopted for growing cracks, where the nature of the elastic-plastic strain singularity in centered fan sectors moving with the tip has been discussed by Rice and Sorensen [*1*], Rice [*8,10*], and Cherepanov [*11*].

For the present discussion it is convenient to follow a development of Rice and Tracey [*12*] which analyzed directly, within conventional "small strain" assumptions, the stress state $\sigma_{ij} = \sigma_{ij}(\theta)$ resulting as $r \to 0$ at the tip of a crack in an ideally plastic solid under plane-strain conditions (r, θ are polar coordinates centered on the tip as in Fig. 1*a*). They observe first that since the stress at the tip must be bounded, terms of the form $r\,\partial\sigma_{ij}/\partial r$

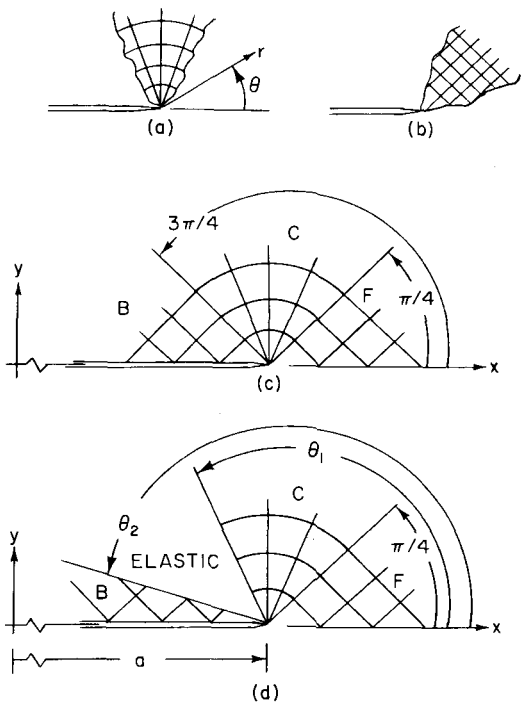

FIG. 1—*Stress field at crack tip consists, in yielded sectors, of either* (a) *centered fan or* (b) *constant stress regions. The full Prandtl field* (c) *results for a stationary crack, at least at small-scale yielding, but must be modified* (d) *with an elastic unloading sector for a growing crack.*

in the stress equilibrium equations must vanish as $r \to 0$, and hence the equilibrium equations reduce to the two ordinary differential equations

$$\sigma_{rr} - \sigma_{\theta\theta} + d\sigma_{r\theta}/d\theta = 0 \tag{1}$$

$$2\sigma_{r\theta} + d\sigma_{\theta\theta}/d\theta = 0 \tag{2}$$

Also, they assume that the plastic yield condition in highly strained material at the tip reduces to the form

$$(\sigma_{\theta\theta} - \sigma_{rr})^2/4 + \sigma_{r\theta}^2 = \sigma_o^2/3 \tag{3}$$

that is, that the maximum shear stress in the plane of straining is limited to the yield in shear, $\sigma_o/\sqrt{3}$ (where, using the Mises shear to tension conversion, σ_o is the tensile yield strength).

Equation 3 can either be accepted as an approximate criterion of plane-strain yielding or can be motivated in the following way. The three-dimensional Prandtl-Reuss-Mises theory is based on the plastic flow rule

$$D_{ij}^p = \Lambda s_{ij} \quad \text{where} \quad \Lambda = \sqrt{D_{ij}^p D_{ij}^p / s_{mn} s_{mn}} \geq 0 \tag{4}$$

and where

s_{ij} = the deviatoric part of σ_{ij}, and
D_{ij}^p = the plastic part of the strain rate tensor D_{ij}.

The latter is defined (relative to Cartesian coordinates x_1, x_2, x_3) by

$$2D_{ij} = \partial v_i/\partial x_j + \partial v_j/\partial x_i \tag{5}$$

where v_i is the velocity $\dot{u}_i$ (u_i is the displacement and the superposed dot means time derivative), and consists of elastic and plastic parts such that

$$D_{ij} = D_{ij}^e + D_{ij}^p = \frac{1+\nu}{E}\dot{\sigma}_{ij} - \frac{\nu}{E}\delta_{ij}\dot{\sigma}_{kk} + \Lambda s_{ij} \tag{6}$$

for isotropic elastic response. For elastic loading or unloading the term with Λ is deleted. In the ideally plastic case Λ is not determined directly by the stress rates, but variations in stress during plastic response must satisfy the yield condition

$$s_{ij}s_{ij}/2 = \sigma_o^2/3 \tag{7}$$

In plane strain, if $s_{zz} = 0$ (where the z axis is perpendicular to the x,y

plane of deformation), Eq 7 reduces to Eq 3. Now, by Eq 4 it is clear that whenever

$$D_{zz}^p / \sqrt{D_{ij}^p D_{ij}^p} = 0 \tag{8}$$

$s_{zz} = 0$, so that Eq 3 results. But since the plane-strain crack tip is expected to be the site of a plastic strain singularity, while the plastic strain in the z-direction is bounded (since total z strain and its elastic portions are bounded), Eq 8 is expected to be asymptotically valid as $r \to 0$, so that Eq 3 becomes the appropriate form of the yield condition at the tip. This argument is suggestive but not fully satisfactory because, as will be seen, the assumption of Eq 3 leads to the possibility of "constant stress" angular sectors at the tip, which do not produce unbounded plastic strain. Nevertheless, we continue by assuming that Eq 3 is valid within plastically deforming zones at the tip, noting that it must be valid within singular sectors and that the arguments based on it lead to fields in agreement with numerical finite element solutions [*12*] for the now well-documented case of loading of a stationary crack.

Rice and Tracey [*12*] showed that the only solutions of the equilibrium Eqs 1 and 2, valid within plastic regions at the tip for which Eq 3 is met, are of the following two types:

1. *Centered fan sectors,* in which

$$\sigma_{r\theta} = \pm \sigma_o / \sqrt{3}, \; \sigma_{rr} = \sigma_{\theta\theta} = \text{constant} \pm (2\sigma_o / \sqrt{3})\theta \tag{9}$$

and which have the interpretation in terms of slip lines shown in Fig. 1*a*; or

2. *Constant stress sectors,* in which stresses σ_{xx}, σ_{xy}, σ_{yy} (that is, referred to Cartesian coordinates) are independent of θ and meet Eq 3; these have the interpretation in terms of slip lines shown in Fig. 1*b*.

Hence, the crack-tip stress state consists of an array of plastic angular sectors of Type 1 and/or 2, among or between which there may be sectors that respond elastically (or currently respond elastically, but may previously have been yielded).

If we seek a solution of the equilibrium Eqs 1 and 2 corresponding to plastic response at all angles θ about the tip, then the only solution corresponding to Mode I loading for which all stresses are continuous (note: equilibrium considerations alone require continuity of $\sigma_{\theta\theta}$ and $\sigma_{r\theta}$, but not σ_{rr}) is that of the Prandtl field shown in Fig. 1*c*. This field was hypothesized by Rice [*7,8*] as the near tip solution for well-contained yielding; it is known to result as the nonhardening limit of the Hutchinson-Rice-Rosengren [*13,14*] singularities and seems to be well substantiated by numerical solutions for small-scale yielding at a stationary crack tip [*12*]. (On the

other hand, it is known that fully plastic solutions for nonhardening materials show a wide variety of crack tip stress fields, some of which involve discontinuities in σ_{rr} and angular sectors that are stressed below yield).

It was assumed in Ref *1* and previous studies of growth [*8,10,11*] that the same Prandtl field of Fig. 1*c* provides the stress state at a growing crack tip. However, as will be shown, this cannot be the case. It is still true that the stress field within plastic regions must consist of a combination of centered fan and constant stress sectors, but it is found that there must be a sector of elastic unloading between the fan and the trailing constant stress region as shown in Fig. 1*d*. The details of the analysis are complicated and, since the emphasis here is on the interpretation of results in terms of stable crack growth, they are reported separately [*2*]; only the major ideas and results are outlined here.

First, Rice and Sorenson [*1*] have presented the form of the velocity field in a centered fan stress field, of type in Eq 9, which moves with the crack. This is obtained by integration of the *rr* and $\theta\theta$ components of Eq 6, noting that $s_{rr} = s_{\theta\theta} = 0$ in a fan zone. For example, if a is crack length and the fan begins at $\theta = \pi/4$ as in Figs. 1*c* and *d* (it cannot begin at any smaller angle, nor at any larger angle, if the angular sector ahead of the tip is to be plastic, this due to the requirement of continuous shear stress), then [*1*] as $r \to 0$

$$v_r = \frac{2(2-\nu)}{\sqrt{3}} \frac{\sigma_o}{E} \dot{a} \sin\theta \ln\left(\frac{\bar{R}}{r}\right) + f'(\theta)$$

$$v_\theta = -\frac{2(2-\nu)}{\sqrt{3}} \frac{\sigma_o}{E} \dot{a} \left(\frac{1}{\sqrt{2}} - \cos\theta\right)\left[\ln\left(\frac{\bar{R}}{r}\right) - \frac{3\nu}{2-\nu}\right] - f(\theta) + g(r) \tag{10}$$

where the functions $f(\theta)$ and $g(r)$, and length $\bar{R}$, are undetermined by the asymptotic analysis, except that $g(0) = 0$. The functions f and g, in addition to being functions of θ and r, respectively, will be homogeneous functions of degree one (and possibly linear) in $\dot{a}$ and in the rate of whatever parameter describes the intensity of the applied load. One may compute the components of D_{ij} and, since the D_{ij}^e are known in terms of $\dot{\sigma}_{ij}$, of D_{ij}^p. The only nonvanishing component of D_{ij}^p referred to the polar coordinate system is, as $r \to 0$

$$D_{r\theta}^p = \frac{2-\nu}{\sqrt{6}} \frac{\sigma_o}{E} \frac{\dot{a}}{r} \ln\left(\frac{\bar{R}}{r}\right) + \frac{f''(\theta) + f(\theta)}{2r} \tag{11}$$

(Observe that since the rate quantities are referred to a moving polar

coordinate system, one cannot write $v_r = du_r/dt$, $D_{r\theta} = d\epsilon_{r\theta}/dt$, etc., although similar equations are valid for Cartesian components).

Owing to the path-dependence (in strain space) of plastic stress-strain relations, the nature of the near tip displacement and strain field is fundamentally different for a stationary versus a growing crack. For the stationary crack, $\dot{a} = 0$, under monotonic load increase the only nonvanishing plastic strain in the fan is $\epsilon_{r\theta}{}^p$, and this is given by an expression of the form

$$\epsilon_{r\theta}{}^p = F(\theta)/r, \qquad \text{as } r \to 0 \tag{12}$$

where $F(\theta)$ is undetermined by the asymptotic analysis. Further, the displacements at $r = 0$ vary with θ in the fan so that a discrete opening displacement results at the tip (the field on the size scale of this opening must be determined by a finite strain analysis). But when the crack length a is increasing continuously with the level of applied loading, asymptotic integration of Eq 11 in the manner described by Rice [*10*] (in the fan) and including the strain discontinuously accumulated by the velocity discontinuity at the leading edge of the fan leads to [*2*]

$$\epsilon_{ij}{}^p = \frac{2-\nu}{\sqrt{6}} \frac{\sigma_o}{E} G_{ij}(\theta) \ln\left(\frac{\bar{R}}{r}\right) + H_{ij}(\theta), \qquad \text{as } r \to 0, \tag{13}$$

where, referred to Cartesian coordinates as in Figs. 1*c* and *d*,

$$\begin{aligned} G_{xx}(\theta) &= -G_{yy}(\theta) = -2 \sin\theta \\ G_{xy}(\theta) &= G_{yx}(\theta) = \ln[\tan(\theta/2)/\tan(\pi/8)] \\ &\qquad + 2(\cos\theta - 1/\sqrt{2}) \end{aligned} \tag{14}$$

and where the functions $H_{ij}(\theta)$ are undetermined by the analysis but will depend, in a presumably monotonically increasing manner, on the ratio d(applied load)$/da$. Further, for the growing crack the displacements in the fan vanish at $r = 0$ and hence there is no discrete tip opening displacement.

Now, the difficulty with assuming the full Prandtl field of Fig. 1*c* for the growing crack is that there is a nonremovable discontinuity of velocity v_r at the boundary between the fan C and back constant stress zone B. Such discontinuities are permissible within an ideally plastic model, but only if they correspond to positive plastic work. Such is not the case here because, from Eq 10, $v_r \to +\infty$ as $r \to 0$ along the fan side and v_r is necessarily bounded along the constant stress side. Since $\sigma_{r\theta}$ is positive, it does negative work on this discontinuity.

Several possible remedies were explored [2]. One could try to continue the field beyond the back boundary of C, in Fig. 1*c*, by assuming an elastic zone throughout B and enforcing full continuity of velocities at the back boundary, but it is then found impossible to find a solution that does not violate yield and that meets crack surface boundary conditions. It was therefore attempted to terminate the fan at some initially unknown angle θ_1, as shown in Fig. 1*d*, necessarily bordering on an elastic sector, and to admit the possibility that there may be a trailing plastic region B as shown in Fig. 1*d*, necessarily a constant state region. Alternatively, it is easily shown that a plastic region *B* must exist, in the sense that the entire region $\theta > \theta_1$ cannot be elastic, since by Eqs 13 and 14 material points emerge from the fan with a negatively infinite $\epsilon_{xx}{}^p$ as $r \to 0$, requiring further yield to avoid unbounded "residual" stresses. The full details are given in Ref *2* where it is found, for $\nu = 0.3$, that

$$\theta_1 \approx 115°, \qquad \theta_2 \approx 163° \tag{15}$$

and Fig. 1*d* has been drawn to correspond to these angles. The corresponding angles are approximately 112 and 162 deg for $\nu = 0.5$.

The resulting Cartesian stress components $\sigma_{xx}(\theta)$, $\sigma_{yy}(\theta)$, $\sigma_{xy}(\theta)$ are plotted in Fig. 2 for this field and for the full Prandtl field of Fig. 1*c*. What is remarkable is how little they differ, σ_{yy} and σ_{xy} being barely distinguishable from the Prandtl values (the maximum value of σ_{yy}, occurring in the front constant stress sector *F*, is approximately 1 percent less than the Prandtl value of $(2 + \pi)\sigma_o/\sqrt{3}$), and σ_{xx} showing only a slight dip below the Prandtl value in the elastic sector. Presumably, this closeness has obscured the differences between the actual and the Prandtl fields for a growing crack in previous numerical simulations [*1,3,4*] where, to the accuracy expectable of such methods, the results were interpreted as verifying the presence of the Prandtl field.

The form of the crack opening rate $\dot{\delta}$ (here δ is the opening between upper and lower crack surfaces) very near the tip has been also obtained in Ref *2*. The result has the same form as in Ref *1*; namely

$$\dot{\delta} = \beta \frac{\sigma_o}{E} \dot{a} \ln\left(\frac{\bar{R}}{r}\right) + \dot{A}, \qquad \text{as } r \to 0 \tag{16}$$

where

$$\beta = 5.083 \qquad \text{for } \nu = 0.3 \tag{17}$$

The value is $\beta = 4.385$ for $\nu = 0.5$. (In Ref *1*, the value $\beta = 4(2 - \nu)/\sqrt{3} = 3.93$, for $\nu = 0.3$, was obtained based on the analysis of velocities within the unapplicable full Prandtl field of Fig. 1*c*). $\dot{A}$ is undetermined by the asymptotic analysis but is homogeneous of degree one in $\dot{a}$ and in the

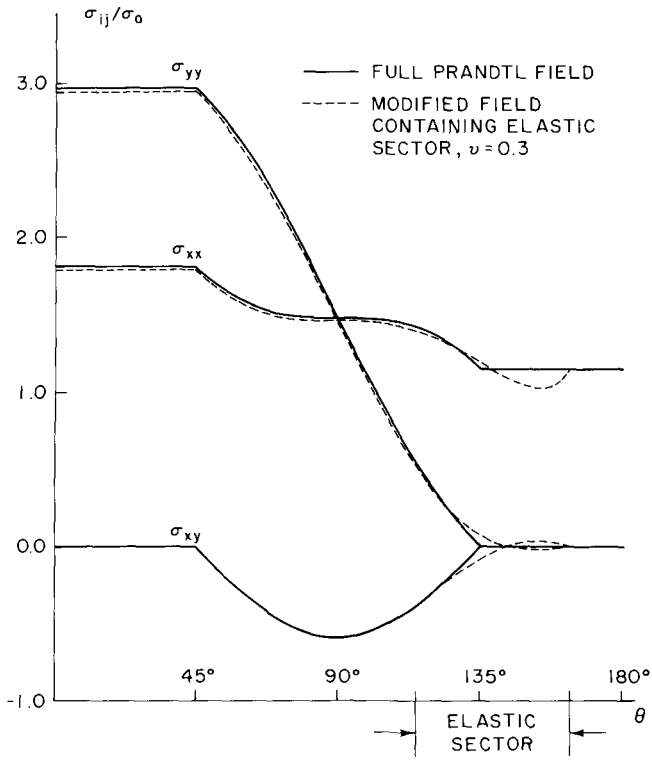

FIG. 2—*Comparison of crack-tip stress state for a growing crack (dashed lines, based on field of Fig. 1d) with the Prandtl field for a stationary crack (solid lines, based on field of Fig. 1c). Stresses are made dimensionless by tensile yield strength.*

rate of applied load increase. Indeed, for rates of applied load which do not finitely change the elastic-plastic boundary (for example, a negative load rate, inducing elastic response in large portions of the previously plastic zone), one expects $\dot{A}$ to be linear in $\dot{a}$ and the load rate. Any convenient parameter may be used to measure the applied load and, without loss of generality, one may use the far-field value of the J-integral, noting that it is well-defined for contained yielding (and may be essentially so for some general yielding cases) since the far-field is elastic, and that the use of J in this case carries no implication that it is path-independent or has any meaning whatever in the near-tip plastic region. Accordingly, one writes

$$\dot{A} = \alpha \dot{J}/\sigma_o + \mu \dot{a} \tag{18}$$

with α and μ undetermined by the asymptotic analysis, and then absorb μ into the first term of Eq 16 to write, finally

$$\dot{\delta} = \alpha \frac{\dot{J}}{\sigma_o} + \beta \frac{\sigma_o}{E} \dot{a} \ln\left(\frac{R}{r}\right), \qquad \text{as } r \to 0 \tag{19}$$

where now $\bar{R}$ has been replaced by a new length parameter R, also undetermined by the asymptotic analysis. In the next section the approximate determination of α and R is discussed, by fitting numerical results from finite element studies [*4*] to the theoretical results.

It is of interest to compare near tip crack openings for stationary versus growing cracks. Setting $\dot{a} = 0$ in Eq 19, one obtains for monotonic loading of a stationary crack

$$(\delta)_{r=0} = \int \alpha dJ/\sigma_o = \alpha J/\sigma_o \text{ for } \alpha \text{ constant} \tag{20}$$

(Note that by dimensional analysis α is constant in the small-scale yielding limit; it is thought to be approximately constant up to the general yielding range for geometries such as a deeply-cracked bend specimen). But when the crack is growing so that a increases continuously with J, asymptotic integration of Eq 19 in the manner of Rice and Sorenson [*1*] yields

$$\delta = \frac{\alpha r}{\sigma_o} \frac{dJ}{da} + \beta r \frac{\sigma_o}{E} \ln\left(\frac{eR}{r}\right), \qquad \text{as } r \to 0 \tag{21}$$

where e is the natural logarithm base. One sees that $\delta = 0$ at the tip, but a well-defined crack tip opening angle does not exist since $d\delta/dr \to \infty$ at $r = 0$.

With future discussion in mind, one may rewrite this expression as

$$\frac{E\delta}{\beta\sigma_o R} = \left[\frac{\alpha}{\beta} T + \ln\left(\frac{eR}{r}\right)\right] \frac{r}{R} \tag{22}$$

where $T = (E/\sigma_o^2)dJ/da$ is the Paris tearing modulus. Now, as will be seen in the next section, and as is suggested in Ref *1*, R is found to be comparable in size to the maximum plastic zone radius, at least under small-scale yielding conditions, and α/β is of the order 0.1. Hence in high T materials, where $0.1T$ greatly exceeds the logarithmic term everywhere except for values of r that are minute fractions of the plastic zone dimension, the near tip crack opening is almost linear in r and the concept of a crack opening angle has approximate validity. For example, if $T = 200$ (in the range of reported values [*5*] for the more ductile structural metals) the term $0.1T$ is more than 5 times the logarithmic term for all values of r greater than approximately 5 percent of the maximum plastic zone radius. At the other end of the ductility spectrum, say $T = 20$, the logarithmic

term exceeds $0.1T$ out to distances r of approximately 40 percent of the plastic zone radius (probably beyond the range of validity of the asymptotic result), and no meaningful definition of an opening angle could be given.

For purposes of illustration, near-tip crack opening profiles are compared in Fig. 3 for a stationary crack and for growing cracks with various values of T, taking for simplicity $\alpha = 0.65$, $\beta = 5$, and $R = 0.2\,EJ/\sigma_o^2$ (close to the value estimated in the next section for small-scale yielding), so that the left side of Eq 22 is just $\delta/(J/\sigma_o)$. Hence, Fig. 3 compares, approximately, the near tip profiles that would result at a given J level under small-scale yielding. The curve marked $T = 0$ might be thought of as a crack growing under environmental influences with negligible change in J.

Comparison with Finite Element Results for Growing Cracks

In Ref *1* an attempt was made to identify the parameters α and R appearing in Eqs 19 and 20 for the crack opening, by correlating the theoretical result against a finite element solution by Sorensen [*3*] for plane-strain crack growth under small-scale yielding conditions. It was remarked in Ref *1* that a numerical solution with a much finer mesh would be needed to determine more definitively the above parameters. But the tentative conclusions were reached that R scales approximately with the size of the plastic zone and that α is approximately the same for a growing crack as for monotonic loading of a stationary crack. Further, two attempts were made in Ref *1* to check the theoretical β value against values inferred from the numerical results. Both inferred values were too large compared

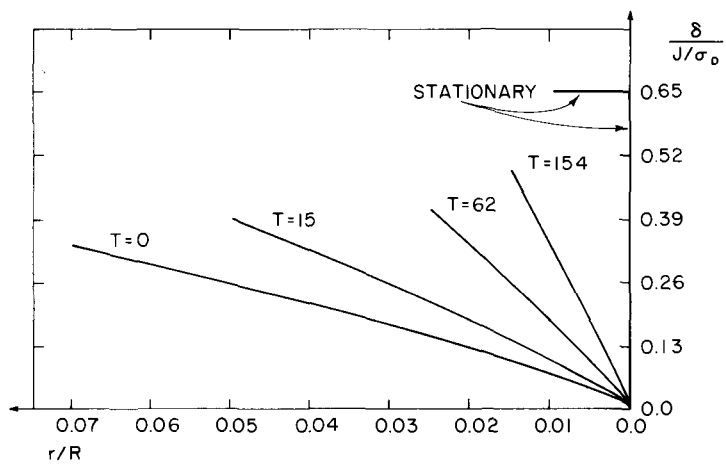

FIG. 3—*Opening profiles near the tips of growing cracks with various values of* $T \equiv (E/\sigma_0^2)dJ/da$, *and near a stationary crack tip; based on* $\alpha = 0.65$, $\beta = 5$, $R = 0.2\ EJ/\sigma_0^2$ ($\approx$ *plastic zone size*).

to what was then thought to be the theoretical value (3.93, for $\nu = 0.3$). However, as remarked, the true value of β based on the field of Fig. 1*d* is found to be 5.08 for $\nu = 0.3$, and this is not far from the inferred value of 4.8 in Ref *1*, based on displacement increments at the second node back from the tip.

A refined mesh finite element solution of the kind advocated in Ref *1* has now been carried out by Sham [*4*]. Some of the results are discussed here. The formulation of the small-scale yielding problem, type of elements used, and general features of the mesh layout are in all respects similar to those of [*3*] except the mesh is finer, so that the plastic zone size in the range for which crack growth is studied is of the order 50 times the side length of the smallest elements. These smallest elements are of uniform size along and adjacent to the path of crack growth, and consist of squares laid out in a rectangular array, with each square made up of four constant-strain triangular finite elements sharing a common node at its center. The material is an ideally plastic Mises solid with $\nu = 0.3$, and the loading, as appropriate for small-scale yielding, is specified in terms of the far field Mode I stress intensity factor, K. Some of Sham's results will be reported in terms of J, where it is to be understood that J has the "far-field" value appropriate for contours in the elastic region, namely $(1 - \nu^2)K^2/E$.

The load versus crack length history is shown in the inset diagram in Fig. 4, where K_o is the load required to yield the first element. The load is first increased without crack growth to slightly below 10 K_o, then 3 one-element crack growth steps are simulated (by incremental unloading of crack tip nodes at fixed K), each followed by an increase in K at fixed crack length, and then 8 further one-element crack growth steps are simulated at fixed K.

Sham [*4*] reported the near tip stress fields for both the stationary and growing crack cases to be consistent with the full Prandtl field of Fig. 1*c*. But as shown in Fig. 2, the differences between the full Prandtl field and its modification with the elastic sector of Fig. 1*d* are small. The numerical results for stresses are not accurate enough (presumably because they are based on a mesh with nonsingular elements at the tip; compare Ref *12*) to distinguish between the two, and can equally be regarded as being consistent with the field associated with Fig. 1*d* for the growing crack. Nevertheless, Sham reports that all crack growth steps are accompanied by elastic unloading of some elements behind the tip, of locations coinciding roughly with the location of the elastic sector in Fig. 1*d*. Further, elements adjoining the crack surfaces near the tip are found to yield in a direction corresponding to extension in the x-direction of Fig. 1*d*, as predicted within Region B, and which is expected since material points emerge from the fan with a value of ϵ_{xx}^p which becomes negatively infinite at the tip. Thus, these features as well as the element stresses near the tip are

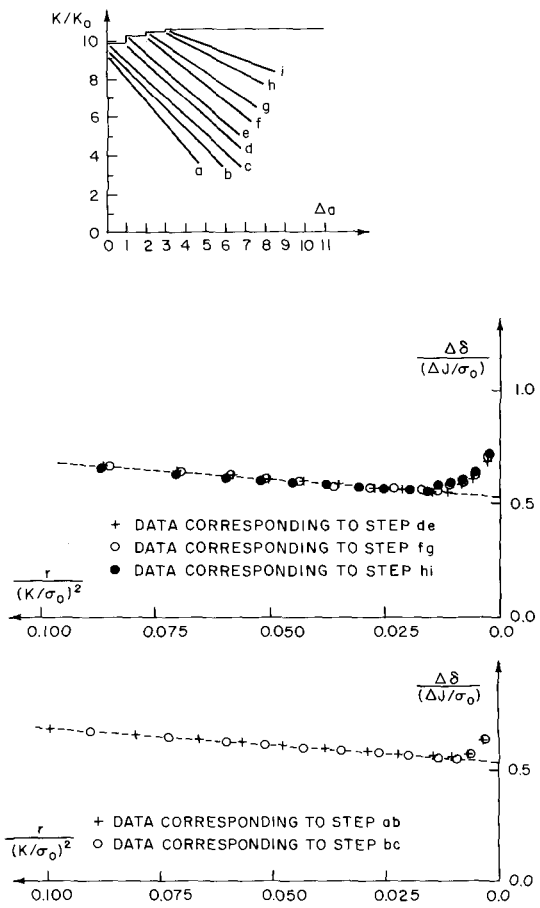

FIG. 4—*Finite element results for increments* $\Delta\delta$ *of crack surface opening due to load increase at fixed crack length, based on finite element solution for small-scale yielding with load history as shown.* (a) *Load increases following one-element steps of crack growth.* (b) *Last few increments of monotonic loading of stationary crack.*

consistent with the theoretical analysis [2] of the field at a growing crack tip.

For small load increase at fixed crack length, Eq 19 suggests a variation $\Delta\delta$ in crack tip opening displacement given by

$$(\Delta\delta)_{r=0} = \alpha \, \Delta J/\sigma_o \tag{23}$$

Thus, we are able to estimate the dependence of α on the amount of crack growth by estimating $(\Delta\delta)_{r=0}$ from the numerical results for the various

load increases at fixed crack length shown in Fig. 4. This is accomplished in Fig. 4*a* for the three load steps following growth, by plotting $\Delta\delta/(\Delta J/\sigma_o)$ at the crackline nodes as a function of $r/(K/\sigma_o)^2$. The results suggest that at least for the rather modest amounts of crack growth considered, the incremental openings for load increase at fixed crack length are unaffected by growth; that is, that α is essentially constant during growth. To determine the relation between δ and J for monotonic loading of a stationary crack, one observes that by dimensional considerations α is constant during monotonic loading under small-scale yielding conditions, but that its value is most accurately estimated from numerical solutions by using data from the range in which the plastic zone size is large compared to element size. Accordingly, in Fig. 4b $\Delta\delta/(\Delta J/\sigma_o)$ versus $r/(K/\sigma_o)^2$ is shown from data based on the last few increments of loading of the stationary crack, as indicated.

The points of Figs. 4*a* and *b* superpose on one another everywhere except in the region of upturn. If the upturn region is ignored and the data are extrapolated to the tip, as shown by the dashed line, $\Delta\delta/(\Delta J/\sigma_o) = 0.53$ is obtained in both cases; that is, $\alpha = 0.53$, the value being the same for both the stationary and growing crack. This value of α is somewhat smaller than the accepted value of approximately 0.65 for the stationary crack (see Ref *1* for a summary of results), whereas $\alpha \approx 0.65$ is consistent with the opening at the first node back from the tip in Fig. 4*b*. If we use similarly the opening at the first node in Fig. 4*a* to estimate α for the growing crack, then the values of α are higher (0.69, 0.71, 0.72 at the end of the three growth steps) than for the stationary crack; that is, by amounts ranging from 6 to 11 percent. The interpretation of these results is further clouded by the upturns in $\Delta\delta$, which occur within a region for which the finite element mesh of [*4*] undergoes a reduction by a factor of 2 in element size (starting three elements behind the original crack tip), and may indicate inadequacies of the numerical treatment.

The last 8 one-element steps of growth (Release Steps 4 to 11) at fixed K grow the crack away from the region of discontinuity in mesh size. Observing from Eq 21 that for growth at constant K (hence constant J) the near tip opening is

$$\delta = \beta \frac{\sigma_o}{E} r \ln\left(\frac{eR}{r}\right), \tag{24}$$

comparison of the finite element results for δ with this formula provides a means of estimating R and of seeing to what extent the numerical results are consistent with the theoretical value of β. To do so, the formula is rewritten as

$$\frac{E\delta}{\sigma_o r} = \beta \ln\left[\frac{R}{(K/\sigma_o)^2}\right] + \beta \ln\left[\frac{e(K/\sigma_o)^2}{r}\right] \tag{25}$$

and $E\delta/\sigma_o r$ is plotted against $\ln[e(K/\sigma_o)^2/r]$, so that β is given by the slope and R is determined from the axis intercept. This is done in Fig. 5 for the finite element openings along the path of growth at constant K, using data at the end of each of the Release Steps 6 to 11. The data for each release step form a straight line, confirming the logarithmic dependence in Eq 24, and the slopes are very close to one another; $\beta = 5.4$ can be taken as a representative value. This is close to, but somewhat larger than, the theoretical value of 5.08. The corresponding values of R as determined from axis intercepts are shown in Fig. 5, and these cluster about the value

$$R \approx 0.21\, K^2/\sigma_o^2 \approx 0.23\, EJ/\sigma_o^2 \tag{26}$$

which seems to be essentially independent of the amount of growth. Further, Sham [4] estimates a maximum plastic zone radius, which is approximately 0.16 $(K/\sigma_o)^2$ for stationary crack and which increases slightly with growth, to approximately 0.18 $(K/\sigma_o)^2$ at the end of the eleven growth

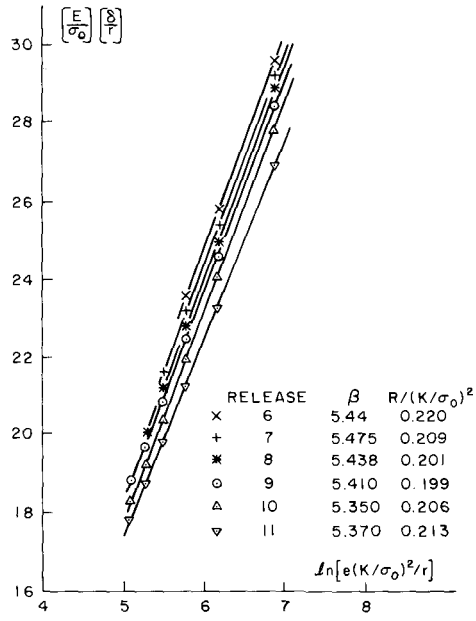

FIG. 5—*Correlation of finite element results for crack opening δ, in growth at constant* J, *with theoretical result. Each set of points corresonds to total δ-values, along the path of constant* J *growth, after a one-element growth step. Resulting estimates of* β *and* R *are shown.*

steps. Thus, the value estimated above for R essentially scales with the plastic zone size but is about 15 to 30 percent larger.

Again, however, the interpretation of numerical results is not unambiguous. For example, if lines with the theoretical slope $\beta = 5.08$ are fit to the data of Fig. 5, the value of R is found to decrease with crack growth, from $R \approx 0.35\,(K/\sigma_o)^2$ at Release Step 6 to $R \approx 0.21\,(K/\sigma_o)^2$ at Release Step 11.

Clearly, much remains to be done to determine expressions for the parameters α and R and for their dependence on crack growth, not only for the small-scale yielding case examined here but also for larger scale yielding. Lacking more definitive information, we will assume tentatively for the subsequent discussion of crack growth that α is approximately constant and that R scales with the plastic zone size (in the form $R \approx 0.2\,EJ/\sigma_o^2$ for small-scale yielding).

Speculations on Large-Scale Yielding

The numerical results just surveyed, as well as those in the original Rice and Sorensen study [*1*], were for the small-scale yielding limit, in which the plastic response is fully determined by the surrounding elastic K field. However, the results of the asymptotic analysis should be valid for larger scale contained yielding of ideally plastic solids, although R and α must then be expected to depend on the extent of yielding. For example, the tentative relation, $R \approx 0.2\,EJ/\sigma_o^2$, cannot be expected to persist at large-scale yielding because the dimensions of the plastic region no longer scale directly with J.

Finally, for fully yielded ideally plastic specimens, of a geometry that retains constraint comparable to that of the Prandtl field (for example, deeply-cracked bend specimens [*15*]), growth of the crack still requires that centered fan sectors of near tip stresses be moved through the material. This introduces logarithmic singularities of the type multiplying $\dot{a}$ in expressions like those of Eqs 10 for the near tip velocities, and leads, ultimately, to an expression in the form of Eq 16 for the near tip opening rates, namely

$$\dot{\delta} = \beta \frac{\sigma_o}{E} \dot{a} \ln\left(\frac{\bar{R}}{r}\right) + \dot{A}, \qquad \text{as } r \to 0$$

For a geometry like that of the tension specimen with deep double edge cracks, for which the full Prandtl field provides the near tip state for the stationary crack case, the construction of Fig. 1*d* is expected to apply during growth so that β has the same value as given earlier, Eq 17. For a geometry like that of the deeply cracked bend specimen, the stress field for a stationary crack is very close to that of the full Prandtl field [*15*], and

hence a similar value of β is expected in that case (we leave open the question of whether the value would be identical).

Regardless of the extent of yielding, $\dot{A}$ in Eq 16 will be homogeneous of degree one in $\dot{a}$ and in some loading parameter such as the imposed displacement (say, q) at the load point. For reasons discussed earlier, the authors believe it may be appropriate to regard the dependence as being linear in $\dot{a}$ and $\dot{q}$, say

$$\dot{A} = \xi \dot{q} + \bar{\mu} \dot{a}$$

where ξ and $\bar{\mu}$ are parameters undetermined by the asymptotic analysis. Now, suppose a quantity J, to be associated in an as yet imprecise way with the J-integral, is defined in some way, for all extents of yielding, such that $\dot{J}$ is linear in $\dot{q}$ and $\dot{a}$. Then one can write, analogously to Eq 18,

$$\dot{A} = \alpha \dot{J}/\sigma_o + \mu \dot{a}$$

where, again, α and μ are undetermined by the asymptotic analysis. In the Appendix the authors discuss two different ways of defining J: one (J_f) based on a far field contour; another (J_d) based on a "deformation theory" definition, that is, J_d is the same function of a and q as for monotonic loading to q with a fixed. Different definitions of J will lead to different values of μ (and perhaps α). Thus, when one follows the steps from Eqs 16 and 18 to Eqs 19 through 21, which are now seen to apply to all extents of yielding, it must be recognized that R will depend on the way that J is defined, since it incorporates the $\mu \dot{a}$ part of the expression for $\dot{A}$.

To apply dimensional considerations in order to understand the behavior of R, say, as a function of J, it is now necessary to be more precise about the definition of J at large-scale yielding. In particular, in the limit of a fully yielded specimen of rigid-ideally plastic material, it is obvious that $\dot{\delta}$ at the tip must take the form $\dot{\delta} = \omega \dot{q}$ where ω is some parameter (possibly dependent on the geometry of the cracked body). Further, one observes that for rigid-plastic materials this expression for $\dot{\delta}$ is equally valid for stationary or for growing cracks (that is, it is independent of $\dot{a}$). Now, if R is to remain well defined in the rigid-plastic limit, as $\sigma_o/E \to 0$, it is necessary that whatever expression one adopts for J be such that in this limit $\dot{J}$ depends only on $\dot{q}$ and not on $\dot{a}$. Otherwise the term R in Eq 19 would have to contain a factor $\exp[(\text{constant}) \times E/\sigma_o]$ to cancel out the σ_o/E in front of the ln term of Eq 19, and thus annul the $\dot{a}$ dependence of $\dot{J}$, as $\sigma_o/E \to 0$. It is shown in the Appendix, for the rigid-plastic bend specimen, that J_f, the value of the J-integral associated with an appropriate far field contour, has this property, whereas J_d does not. The authors do not, however, suggest that J_f will have this property for all specimen geometries, and, indeed, it

is found that J_d has the appropriate property in the case of a tension specimen with deep double edge cracks.

With the understanding that J has been appropriately defined so that R has no spurious dependence on a term like exp[(constant) $\times$ E/σ_o], one now observes that the terms containing R in Eqs 19 and 21 arise from moving a centered fan stress distribution through an elastic-plastic material. Thus, R should scale approximately with the size of the region over which such fan-like stress fields prevail. Hence, with reference to the deeply-cracked bend specimen of Fig. 6, R should saturate in size to some fraction of the ligament dimension b as fully plastic conditions are attained. Hence, as shown in Fig. 6, one expects R to increase linearly with J at first, as appropriate to the small-scale yielding regime, but then to saturate as J further increases. The saturation level of $R \approx b/4$ is only a guess and much further correlation of the asymptotic analysis against numerical results will be necessary to establish this level and, indeed, the full dependence of R on J.

There is, of course, already an approximation built into the notion that R should depend on J (and, of course, on geometric dimensions such as crack depth and ligament size): R should have at least some dependence on the amount of prior crack growth. However, as suggested by results for small-scale yielding, this dependence seems to be minor, probably because the shape and size of the currently active plastic zone is not strongly affected by prior growth. The point needs further clarification, but is neglected in our subsequent discussion of crack growth criteria.

Investigation of a Ductile Crack Growth Criterion

Here we investigate implications of the ductile crack growth criterion proposed in Ref *1*. This is based on the opening δ at a small characteristic distance from the tip, but, as will be seen, the criterion is similar in form

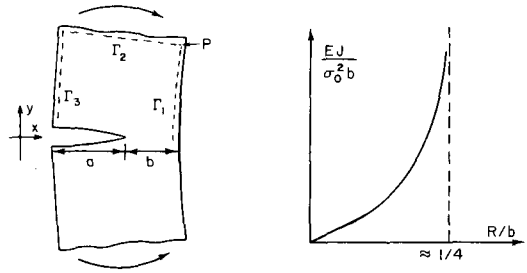

FIG. 6—*Speculation on the variation of* R *with* J *over the entire range of yielding. The linear variation at low* J *is expected to become nonlinear as shown and to finally saturate in value (the level* $\approx$ $^1/_4$ *is a guess) at general yielding.*

to other criteria which might be proposed based on other parameters of the near tip deformation field, for example, on local plastic strain.

It is important to remember, however, that the criterion is based on the deformation field, and makes no reference to the stress distribution. Such might be considered reasonable in the sense that the maximum tension immediately at the crack tip is always essentially the same (equal to the Prandtl value or a percent or so lower) for the highly constrained geometries that are considered, so that the only variable features of the near tip field are the levels of strain and opening displacement. But it is possible that the critical levels of deformation could, in some cases, be influenced by the "preconditioning" (for example, microcrack or cavity nucleation) of material elements by high stress levels experienced before the crack arrives. This preconditioning could be more severe when the region of triaxially elevated stresses extends over larger versus smaller size scales ahead of the crack. On the other hand, for cases of ductile rupture in which cavity nucleation is limited to the immediate vicinity of the crack tip (say, over a size scale comparable to the tip opening displacement for a stationary crack), the size scale over which the triaxially elevated stress state extends ahead of the crack is expected to be unimportant, and a growth criterion based on local deformations seems appropriate.

The model criterion of the Rice and Sorensen study [*1*] assumes that growth initiates by large plastic strains associated with opening at the stationary crack tip, and that once growth has thereby occurred over a distance comparable to the fracture process zone, subsequent growth continues in a mode for which a geometrically similar (in a sense to be made precise) profile of crack opening is maintained very near the tip. The criterion for growth is stated in Ref *1* as the requirement (Fig. 7) that a critical opening $\delta = \delta_c$ be maintained at a small characteristic distance r_m (called Δl in Ref *1*) behind the tip. Thus, from Eq 21, the criterion for continuing crack growth is

$$\frac{\delta_c}{r_m} = \frac{\alpha}{\sigma_o}\frac{dJ}{da} + \beta\frac{\sigma_o}{E}\ln\left(\frac{eR}{r_m}\right) \tag{27}$$

Since R is regarded as a function of J (though specimen dependent; that is, dependent also on a, at large-scale yielding (Fig. 6)), Eq 27 can be regarded as a first order differential equation which determines the manner in which J must vary with a in order to continue to meet the crack growth criterion. The initial condition is that $J = J_{Ic}$ (the initiation value) at $a = a_o$ (the initial crack length).

It seems appropriate to regard r_m as a size comparable to that of the "fracture process zone," although this is, of course, not a sharply defined size. It is tempting to identify δ_c with the crack-tip opening displacement, $\delta_{Ic} = \alpha J_{Ic}/\sigma_o$, at the onset of growth, but experimental observations are

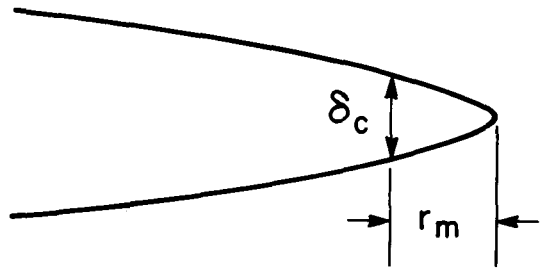

FIG. 7—*Crack growth criterion of Ref* 1 *requires that a critical opening* δ_c *be maintained at small distance* r_m *behind the tip. As discussed at the end of the paper, the criterion is similar qualitatively to others based on other deformation parameters (for example, plastic strain) of the near tip field.*

well-known to reveal crack profiles during growth that suggest much less near tip opening than at initiation. Thus, δ_c is regarded as an independent empirical parameter, sometimes much smaller than δ_{Ic}. Indeed, as discussed in Ref *1*, δ_{Ic} might more sensibly be regarded as a measure of the fracture process zone size, and hence of r_m.

Now, the solutions to Eq 27 show the manner in which J must vary with a, beyond the J_{Ic} point, to meet the crack growth criterion. In some cases, for example, sufficiently low δ_c/r_m and high σ_o/E, it may happen that the value of dJ/da calculated from Eq 27 at the J_{Ic} point is negative. In such cases, immediately unstable crack growth is expected. For more ductile materials (that is, sufficiently large δ_c/r_m and small σ_o/E), the calculated dJ/da is positive and integration of the equation leads to a J versus $a - a_o$ relation which must be followed for stable growth. It may happen, however, that the predicted dJ/da at some point in the growth history falls below what the loading system can supply, and at that point unstable crack growth occurs. Specifically, let $J_A(Q,a)$ be the "applied" J where Q is a monotonically increasing measure of the intensity of loading. In different cases Q may represent an imposed force or stress, or an imposed load-point displacement (or a displacement imposed on a compliant loading system attached to the cracked body). Then, if $J(a)$ represents the solution of Eq 27 for the given cracked body and initial conditions ($J = J_{Ic}$ when $a = a_o$), the variation of Q with a satisfies

$$J_A(Q, a) = J(a) \tag{28}$$

and instability ($dQ/da \rightarrow 0$) occurs when, simultaneously, this equation and

$$\partial J_A(Q, a)/\partial a = dJ(a)/da \tag{29}$$

are met. These equations have a well-known graphical solution in terms of tangential contact of the curves $J = J(a)$ and $J = J_A(Q,a)$, for fixed Q, on a J versus a diagram, although our work carries no implication that the "resistance" curve $J(a)$ is invariant to specimen geometry at large-scale yielding.

It is of interest to note, however, that the criterion of Ref *1* for crack growth can be rephrased in a manner which makes no reference to the "microscale" parameters r_m and δ_c. The authors develop this approach here noting that Eq 21 can be rephrased in the form

$$\delta = \beta r \frac{\sigma_o}{E} \ln \frac{\rho}{r}, \qquad \text{as } r \to 0 \tag{30}$$

where

$$\rho = R \exp(1 + \alpha T/\beta) \tag{31}$$

Thus, the criterion for crack growth with a geometrically similar profile very near the tip is that ρ remain constant during crack growth. One evaluates ρ in terms of the values of R and the tearing modulus T at the onset of crack growth under small-scale yielding conditions.

Since

$$R = \lambda EJ/\sigma_o^2 \quad \text{where, Eq 26,} \quad \lambda \approx 0.2 \tag{32}$$

for small-scale yielding, the corresponding value of R is

$$R = \lambda EJ_{Ic}/\sigma_o^2$$

and one defines a new fracture parameter T_o as the value of T at the onset of growth under small-scale yielding. Hence the critical value of ρ may be identified as

$$\rho = (\lambda EJ_{Ic}/\sigma_o^2) \exp(1 + \alpha_{ssy} T_o/\beta) \tag{33}$$

where α_{ssy} (≈ 0.65) is the value of α appropriate to small-scale yielding; one notes the possibility that $\alpha \neq \alpha_{ssy}$, for example, at general yielding.

Thus, the criterion for crack growth with a geometrically similar profile very near the tip is, by comparing Eqs 31 and 33, that

$$R \exp(1 + \alpha T/\beta) = (\lambda EJ_{Ic}/\sigma_o^2) \exp(1 + \alpha_{ssy} T_o/\beta)$$

This growth criterion may be rearranged to the form

$$T \equiv \frac{E}{\sigma_o^2}\frac{dJ}{da} = \frac{\alpha_{ssy}}{\alpha} T_o - \frac{\beta}{\alpha} \ln\left(\frac{R}{\lambda E J_{Ic}/\sigma_o^2}\right) \tag{34}$$

which is valid for all extents of yielding (assuming that conditions of plastic constraint remain such that a stress field like that of Figs. 1*d* and 2 results very near the tip). The new fracture parameter T_o which enters here can, of course, be expressed in terms of the microscale parameters δ_c and r_m, and the relation is

$$T_o = \frac{E}{\alpha_{ssy}\sigma_o}\frac{\delta_c}{r_m} - \frac{\beta}{\alpha_{ssy}} \ln\left(\frac{e\lambda E J_{Ic}}{r_m \sigma_o^2}\right)$$

However, as is clear from the form of Eq. 34, the growth criterion can be phrased entirely in terms of the macroscale parameters J_{Ic} and T_o.

For crack growth under small-scale yielding one identifies α as α_{ssy} in Eq 34 and uses Eq 32 for R. Hence, the growth criterion in this case is

$$T \equiv \frac{E}{\sigma_o^2}\frac{dJ}{da} = T_o - \frac{\beta}{\alpha_{ssy}} \ln\left(\frac{J}{J_{Ic}}\right) \tag{35}$$

This equation has been integrated by Rice and Sorenson [*1*] and the results are shown in Fig. 8 where the authors have set, in this paper, $\alpha = 0.65$, $\beta = 5.08$ and plotted

$$J/J_{Ic} \text{ versus } (a - a_o)/[0.2EJ_{Ic}/\sigma_o^2]$$

for a range of values of T_o. Here the crack growth $(a - a_o)$ has been made dimensionless by a quantity that is equal approximately to the maximum radius of the plastic zone at the onset of growth. All the curves in Fig. 8 exhibit a plateau, corresponding to steady state growth (that is, $dJ/da \rightarrow 0$), at J levels given by

$$J_{ss} = J_{Ic} \exp(\alpha_{ssy} T_o/\beta) = J_{Ic} \exp(0.128\, T_o)$$

For materials with large T_o-values, say $T_o > 25$, this level is so large (for example, $J_{ss} > 25\, J_{Ic}$) that in cracked bodies of practical sizes, large-scale and finally, fully-plastic yielding conditions will occur well before J approaches J_{ss}, invalidating the calculation. Of course, even for crack growth under small-scale yielding, the instability condition of Eqs 28 and 29 will usually be met before J reaches J_{ss}.

More generally, at large-scale yielding, the crack growth criterion takes the form of Eq 34 with $\alpha \neq \alpha_{ssy}$. Further, $R = \lambda EJ/\sigma_o^2$ at small-scale yielding but (Fig. 6) deviates from this at larger scale yielding and finally

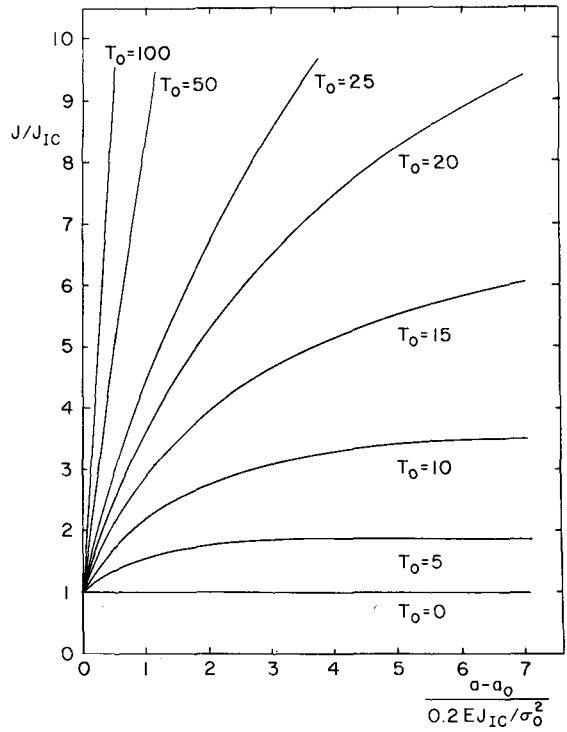

FIG. 8—*Predicted variation of* J *with* a − a_0 *for small-scale yielding. Curves are drawn for different values of* T_0, *which is the value of* $(E/\sigma_0^2)dJ/da$ *at the onset of growth under small-scale yielding conditions. Based on* $\alpha = 0.65$, $\beta = 5.08$. *Growth criterion of Ref* 1 *can be stated in terms of the "macroscopic" parameters* J_{Ic} *and* T_0, *rather than the "microscopic" parameters of Fig. 7. Note that* a − a_0 *is scaled by what is, approximately, the maximum plastic zone radius at the onset of growth.*

saturates in value at fully yielded conditions. The argument of the ln term in Eq 24 is the ratio of R to the value that it would have at the onset of growth under small-scale yielding conditions. It is this ln term which exhibits the sensitivity of the growth criterion at full plasticity to specimen size. For example, taking the numerical values of β and α_{ssy} as above, setting $\lambda = 0.2$ as suggested in Eq 32, and guessing as in Fig. 6 that the saturation value of R is approximately $b/4$, one has at fully yielded conditions

$$T \equiv \frac{E}{\sigma_0^2}\frac{dJ}{da} \approx \left[T_o - 7.8 \ln\left(\frac{b/4}{0.2EJ_{Ic}/\sigma_o^2}\right)\right]\frac{\alpha_{ssy}}{\alpha_{fy}}$$

$$\approx 1.3\, T_o - 10.0 \ln\left(\frac{b/4}{0.2EJ_{Ic}/\sigma_o^2}\right) \tag{36}$$

for the bend specimen, where α_{fy} (the value of α for fully yielded conditions) has been taken as 0.51 in the last version, so that $\alpha_{ssy}/\alpha_{fy} \approx 1.3$. This value of α_{fy} is suggested by the rigid-plastic solution (see Appendix).

Two observations can be made. First, if crack growth begins under fully yielded conditions the growth curve J versus $a - a_o$ (according to the ideally plastic model and other assumptions that have been made) is qualitatively different from that for small-scale yielding. The value of T is then essentially constant for amounts of growth that are small compared to ligament size (so that b in Eq 36 does not change significantly) and, if the formula is regarded as being accurate for large amounts of growth, T actually is predicted to increase with $a - a_o$ (since b diminishes), in marked contrast to the small-scale yielding behavior in Fig. 8.

Second, the (essentially constant) value of T for small, fully plastic growth will not be identical to T_o. The difference between the two arises in part because of the ratio α_{ssy}/α_{fy} in Eq 36. If this ratio were near to unity (as it seems to be for the deeply double edge-cracked tension specimen; see Appendix), then the difference between T and T_o would generally be negligible for high T_o materials, since the argument of the ln term in Eq 36 will seldom be very small or large compared to unity in practical cases. But for low T_o materials the differences could be significant. For example, the argument of the ln term is approximately equal to the ratio of the quarter-ligament size to the plastic zone size corresponding to onset of growth in a large specimen, sustaining small-scale yielding conditions. For a specimen that is sufficiently small that J_{Ic} conditions are attained only in the fully plastic regime, this ratio is expected to be less than unity, so that T exceeds T_o (or $T_o\ \alpha_{ssy}/\alpha_{fy}$ if variations in α are considered).

For example, consider a material that is tested in a specimen size at the limit of what is regarded as the permissible range for a valid fully plastic J_{Ic} test, namely, $b = 25\,J_{Ic}/\sigma_o$. Then Eq 36 predicts

$$T \approx [T_o + 7.8 \ln (E/31\sigma_o)]\alpha_{ssy}/\alpha_{fy}$$

$$= [T_o + 22]\alpha_{ssy}/\alpha_{fy} \approx 1.3\,T_o + 28, \qquad \text{for } \sigma_o/E = 0.002 \qquad (37)$$

$$= [T_o + 13]\alpha_{ssy}/\alpha_{fy} \approx 1.3\,T_o + 17, \qquad \text{for } \sigma_o/E = 0.006$$

where the last expressions given for each strength level are based on $\alpha_{ssy}/\sigma_{fy} = 1.3$, as for a bend specimen. Note that when the observed fully plastic T-value is sufficiently small, T_o would have to be negative. Such a material would be expected to show immediately unstable fracture when tested in specimens that are large enough to meet small-scale yielding conditions, although it exhibits stable crack growth in small, fully plastic specimens. On the other hand, if the fully plastic T-value is large,

say, greater than 100, the effect of the ln term can be disregarded and differences between T and T_o arise only because α_{fy} differs from α_{ssy}.

In fact in this latter case of high T materials, the ln terms in Eqs 34 and 36 are negligible, and, hence, the J versus $a - a_o$ relation, at least for small amounts of growth, is expected to show negligible dependence on specimen size in the fully yielded range. In this respect our conclusions are in partial agreement with those of Hutchinson and Paris [*6*], and this is of interest because the basic assumptions are very different in the two approaches. Hutchinson and Paris appeal to strain hardening of the material (whereas the authors have neglected hardening in the present approach) and assume that this hardening is sufficiently strong to create a Hutchinson-Rice-Rosengren (HRR) singular zone near a stationary crack tip, so that the near tip field is then uniquely characterized by J. Next, they consider crack growth under increasing imposed displacement on the specimen, and observe that if the imposed displacement increases rapidly enough with increasing a, effects of strongly nonproportional stressing are limited to a small neighborhood of the tip, whereas at greater distances the stress histories are such that the approximation of deformation plasticity theory is valid. Hence, they assume that a far field value of J is well-defined and path-independent everywhere except very near the tip, and this assumption has confirmation from the numerical studies of Shih [*16*], which are based on incremental plasticity and model observed crack growth in a high T material. Hence, for sufficiently large T, and degree of hardening, and for sufficiently limited amounts of crack growth, Hutchinson and Paris assume that the growth process takes place in a surrounding HRR singular field that is uniquely characterized by J, so that there is a universal relation of J to $a - a_o$. Further, their work carries the implication that this same relation would apply for small-scale yielding, although our work does not support this notion, even for high T materials, when the ratio α_{ssy}/α_{fy} of Eq 36 differs from unity. (We also note that Hutchinson and Paris [*6*] tacitly assume that this far field J-value, say, J_f, can be equated to the "deformation theory" function $J_d = J_d(q,a)$. We show in the Appendix that the two are definitely different in the rigid-plastic limit, although the differences between $\dot{J}_f$ and $\dot{J}_d$ will often be small for high T materials).

In comparison to the Hutchinson and Paris approach, our growth criterion is based on the actual structure of near tip fields as predicted for a material of the incremental plasticity type. Indeed, the near tip fields are strongly influenced by the path-dependent constitutive response of such a material. On the other hand, we have modeled the material as ideally plastic and this probably tends to overestimate dependences on the extent of yielding, particularly those arising from differences between α_{ssy} and α_{fy}, since, on the basis of the HRR fields, hardening is widely thought to lead to a lessened dependence of α on the extent of yielding than predicted from

ideally plastic solutions. Also, while it is clear that an incremental formulation of the plasticity equations is correct physically, there is reason to believe that models of the Prandtl-Reuss-Mises type, which assume invariant shapes of yield surfaces in stress space, may not be fully adequate for strongly nonproportional stress histories as experienced near a growing crack.

While it is of interest that the authors' approach and that of Hutchinson and Paris [6] are consistent, at least to the neglect of α variations, for high T materials, it is well to remember that both approaches rest on assumptions that require more study for full understanding of their range of validity. Also, enthusiasm over this concurrence of conclusions should be tempered by the recognition that the high T materials may be so resistant to crack growth that unstable crack propagation is seldom likely to be a practical problem. On the other hand, for low T materials, which are more prone to instability, the conditions which Hutchinson and Paris state for validity of a universal J versus $a - a_o$ relation are not met, and the authors' work suggests significant dependencies on the extent of yielding and specimen size.

The authors close this section by outlining an alternate crack growth criterion based on near tip plastic straining. The centered fan velocity field of Eq 10 includes the function $f(\theta)$, which is homogeneous of degree one in $\dot{a}$ and in the rate of applied load. If, analogously to the transition from Eq 16 to 19 in the expression for δ, one assumes this dependence to be linear in $\dot{a}$ and the load rate, then it is straightforward to show that the asymptotic integration leading to Eq 13 for $\epsilon_{ij}{}^p$ yields expressions of the form, as $r \to 0$,

$$\epsilon_{ij}{}^p = \frac{2 - \nu}{\sqrt{6}} \frac{\sigma_o}{E} G_{ij}(\theta) \ln\left[\frac{L_{ij}(\theta)}{r}\right] + \frac{1}{\sigma_o} M_{ij}(\theta) \frac{dJ}{da} \tag{38}$$

in the fan for a continuously growing crack (here no summation is implied by repeated indexes). The functions $G_{ij}(\theta)$ are given by Eqs 14, but the functions $L_{ij}(\theta)$, of length dimensions, and the dimensionless functions $M_{ij}(\theta)$ are undetermined by the asymptotic analysis.

Similarly, the equivalent plastic shear strain γ^p, with rate defined by

$$\dot{\gamma}^p = \sqrt{2 D_{ij}{}^p D_{ij}{}^p} = 2 D_{r\theta}{}^p \quad \text{in the fan} \tag{39}$$

is obtained by integration of Eq 11, adding on the γ^p accumulated discontinuously at the front boundary of the fan. This results in

$$\gamma^p = \frac{2(2 - \nu)}{\sqrt{6}} \frac{\sigma_o}{E} \left\{\sqrt{2} + \ln\left[\frac{\tan(\theta/2)}{\tan(\pi/8)}\right]\right\} \ln\left[\frac{L(\theta)}{r}\right] + \frac{M(\theta)}{\sigma_o} \frac{dJ}{da} \tag{40}$$

where the length function $L(\theta)$ and dimensionless function $M(\theta)$ are again undetermined by the asymptotic analysis. For example, setting $\theta = \pi/2$, γ^p represents the equivalent shear strain accumulated in the forward part of the fan and is given by

$$\gamma^p = 1.88\,(2 - \nu)\frac{\sigma_o}{E}\ln\left(\frac{L}{r}\right) + \frac{M}{\sigma_o}\frac{dJ}{da} \tag{41}$$

where $L = L(\pi/2)$, $M = M(\pi/2)$. Although verification would require detailed comparison with numerical solutions in a region where these have great inaccuracies, it seems reasonable to expect that L scales with the size of the plastic region (being approximately proportional to EJ/σ_o^2 for small-scale yielding) and that M is approximately invariant to growth. Hence, the features of the terms in this equation are expected to be similar to those of analogous terms in Eq 21.

Accordingly, if one requires as a criterion for continuing crack growth that all points closer than a certain small characteristic distance r_m above and below the tip have accumulated a plastic strain equal to or greater than a critical value $\gamma_c{}^p$ as the crack approaches, one obtains

$$\gamma_c{}^p = \frac{M}{\sigma_o}\frac{dJ}{da} + 1.88\,(2 - \nu)\frac{\sigma_o}{E}\ln\left(\frac{L}{r_m}\right) \tag{42}$$

as the differential equation governing growth. This is identical in form to the criterion studied here (compare Eq 27) and is expected to lead to qualitatively similar conclusions.

Acknowledgment

This study was supported by the Department of Energy under contract EY-76-S-02-3084 with Brown University. In addition, T-L. Sham was supported in part by an Electric Power Research Institute (EPRI) subcontract from the General Electric Company to Brown University, and the numerical results which we cite were obtained by computation at General Electric (Schenectady) under auspices of this subcontract. We are grateful to C-F. Shih of General Electric, A. Needleman of Brown, and E. P. Sorensen of Hibbitt-Karlsson, Inc. (Providence) for helpful discussions.

Authors' note: Since presentation of the paper we learned of the work of L. I. Slepyan ("Growing Crack During Plane Deformation of an Elastic-Plastic Body," Izv. AN SSR. *Mekhanika Tverdogo Tela,* Vol. 9, 1974, pp. 57-67). Using methods of asymptotic analysis similar to those of Ref *12* and, for the growing crack, Refs *8* and *10*, Slepyan determines the form of the near tip stress and deformation fields for a crack growing under steady-

state conditions in an ideally plastic Tresca material. He comes to the same conclusions as in Ref 2 on the necessity of an elastic unloading zone of the form shown in Fig. 1*d*. The results of Ref *2* have a slight dependence of the unloading zone boundary angles θ_1, θ_2 on the Poisson ratio, since Ref 2 is based on the Mises model; whereas Slepyan's work, based on the Tresca model, does not. But for $\nu = 1/2$ the results are identical.

APPENDIX

Interpretation of *J* at Full Plasticity

To clarify the interpretation of the term involving $\dot{J}$ in Eq 19, and dJ/da in Eq 21, for fully plastic specimens, consider the cracked bend specimen of Fig. 6 to consist of rigid-ideally plastic material. Let θ be the rotation of one end of the specimen relative to the other. Then the moment required to continue deformation is [*10*]

$$M = (0.63/\sqrt{3})\sigma_o b^2 \tag{42}$$

and the rate of opening at the tip is

$$\dot{\delta} = 0.37\, b\dot{\theta} \tag{43}$$

These formulas are valid for stationary or growing cracks, and when the latter is integrated for a continuously growing crack one obtains, for small r,

$$\delta = 0.37\, rb\, d\theta/da \tag{44}$$

As remarked in the text, if Eqs 19 and 21 are to reduce to Eqs 43 and 44 in the rigid-plastic limit ($\sigma_o/E \to 0$) with bounded ln R, it is necessary that the definition of J be such that in this limit it reduces to an expression for which $\dot{J}$ depends only on $\dot{\theta}$ and *not* on $\dot{a}$.

The authors examined two candidate definitions of J. First, the "deformation theory" definition takes J to be the same function of θ and a (or b) as it would be if the current rotation θ were imposed at a fixed value of b, namely the current b-value. This J, called J_d, is given in the rigid-plastic case by the well-known expression

$$J_d = \frac{2}{b} M\theta = [2(0.63)/\sqrt{3}]\sigma_o b\theta = 0.73\, \sigma_o b\theta \tag{45}$$

It does not have the desired feature, because

$$\dot{J}_d = 0.73\, \sigma_o(b\dot{\theta} - \theta\dot{a}) \tag{46}$$

An alternate definition is the far field contour J, called J_f, and for definiteness this is taken on the dashed line contour $\Gamma_1 + \Gamma_2 + \Gamma_3$ coinciding with the specimen boundary in Fig. 6. Thus

$$J_f = 2 \int_{\Gamma_1+\Gamma_2+\Gamma_3} (W\,dy - T_i\,\partial u_i/\partial x\,ds) \tag{47}$$

(the factor 2 appears because only one half of a complete contour is considered), where

$$W = \int \sigma_{ij} d\epsilon_{ij} \tag{48}$$

is the density of stress working, T_i the traction and u_i the displacement vector. The term with T_i vanishes on stress free surfaces Γ_1 and Γ_3, and it makes no net contribution on Γ_2 since each $\partial u_i/\partial x$ is uniform there (the boundary is rigid). The integrated value of each T_i on Γ_2 vanishes since the loading is pure bending. Also, W vanishes on the rigid boundaries Γ_2 and Γ_3, whereas on Γ_1 it has the value

$$W = -(2\sigma_o/\sqrt{3})\epsilon_{yy} = -(2\sigma_o/\sqrt{3})\partial u_y/\partial y \tag{49}$$

since those points along Γ_1 that yield do so in compression under stress $\sigma_{yy} = -(2\sigma_o/\sqrt{3})$. Hence

$$J_f = 2 \int_{\Gamma_1} W\,dy = (2\sigma_o/\sqrt{3})\,[-2u_y{}^P] \tag{50}$$

where $u_y{}^P$ is the vertical displacement at point P in Fig. 6. Now, the motion of the rigid portions of the rigid-plastic specimen is well-known to consist of rotation about a "hinge point" having an x coordinate that extends a distance $0.37\,b$ ahead of the tip [*10*], and hence

$$2\dot{u}_y{}^P = -(b - 0.37b)\,\dot{\theta} = -0.63b\dot{\theta} \tag{51}$$

Thus

$$J_f = [2(0.63)/\sqrt{3}]\sigma_o \int_0^\theta b\,d\theta = 0.73\sigma_o \int_0^\theta b\,d\theta \tag{52}$$

where the integral follows the history of crack growth (that is, b will in general vary with θ). It is obvious that $J_f = J_d$ of Eq 45 when the crack does not grow as θ is applied. But when the crack is growing J_f exhibits the desired feature

$$\dot{J}_f = 0.73\sigma_o b\dot{\theta} \tag{53}$$

(that is, independent of $\dot{a}$)

Hence, the symbol J, which is used when discussing the fully plastic case, can consistently be identified with a far field value like J_f, although not with the deformation theory value J_d. Further, Eq 43 yields in the rigid-plastic case

$$\dot{\delta} = 0.37\,b\dot{\theta} = 0.51\,\dot{J}_f/\sigma_o \tag{54}$$

This is the origin of the value $\alpha_{fy} \approx 0.51$ used in the text for the fully yielded bend specimen.

Also, one observes that since

$$\dot{J}_f = \dot{J}_d + J_d\,\dot{a}/b$$

or

$$dJ_f/da = dJ_d/da + J_d/b \tag{55}$$

for the rigid-plastic bend specimen, one expects the same to be approximately valid for a fully yielded elastic-plastic bend specimen. Hence, if

$$T_f = \frac{E}{\sigma_o{}^2}\frac{dJ_f}{da}$$

and

$$T_d = \frac{E}{\sigma_o{}^2}\frac{dJ_d}{da} \tag{56}$$

where T_f should be considered as the T of Eqs 36 and 37, then

$$T_d \approx T_f - EJ_d/\sigma_o{}^2 b \tag{57}$$

in this case. That is, the value of the tearing modulus is sensitive to the definition used for J, and T_d may turn negative with increasing growth while T_f remains positive. In particular, Eq 37 for the value of T (interpreted as T_f) at the onset of growth in a fully plastic bend specimen with $b = 25\,J_{Ic}/\sigma_o$ becomes, in terms of T_d,

$$\begin{aligned} T_d &\approx [T_o + 7.8\ln(E/31\sigma_o)]\alpha_{ssy}/\alpha_{fy} - E/25\sigma_o \\ &\approx 1.3\,T_o + 8, \quad \text{for } \sigma_o/E = 0.002 \\ &\approx 1.3\,T_o + 10, \quad \text{for } \sigma_o/E = 0.006 \end{aligned} \tag{58}$$

where α_{ssy}/α_{fy} has been set equal to $0.65/0.51 \approx 1.3$ again. Hence, even though J_d is fundamentally an incorrect parameter within the incremental, ideally plastic model, its use does seem under typical conditions to bring the fully plastic T-value somewhat closer to T_o. In fact, if the differences between α_{fy} and α_{ssy} were neglected, the difference between T_d and T_o in the foregoing expressions would be 2 and 6, respectively.

Finally, the authors remark that J_f does not seem to be the appropriate definition of J for all rigid-plastic specimens. For example, suppose the specimen in Fig. 6 is considered to represent one half of a double edge cracked tension specimen, with cracks deep enough to validate the Prandtl field over the uncracked ligament, and let U be the extension of one end of the specimen relative to the other. Then it is straightforward to show [*10*] that the deformation theory value is

$$J_d = [(2 + \pi)/\sqrt{3}]\sigma_o U = 2.97\sigma_o U \tag{59}$$

whereas J_f does not seem to have any unique value for the case of a growing crack (due to nonuniqueness of the stress field in rigid regions of the specimen) for the contour Γ shown. In this case it is J_d which exhibits the desired feature that $\dot{J}$ is independent of $\dot{a}$. Also, the rate of opening at the crack tip is [*10*]

$$\dot{\delta} = 2\dot{U} = 0.67\,\dot{J}_d/\sigma_o \tag{60}$$

Hence, $\alpha_{fy} \approx 0.67$ in this case, which is very close to what the authors estimated as the small-scale yielding value. Thus, lessened differences between T and T_o are expected for this type of specimen, particularly when T is based on J_d.

Finally, for the center-cracked, rigid-plastic plane strain tension specimen it is elementary to show that

$$J_d = J_f = (2\sigma_o/\sqrt{3})U \tag{61}$$

provided that J_f is evaluated on a contour similar to that in Fig. 6, and that the opening rate at the tip is

$$\dot{\delta} = \dot{U} = 0.87\,\dot{J}/\sigma_o \tag{62}$$

However, this specimen does not have a Prandtl-like stress state at its tip, and cannot be discussed in terms of the analysis in the body of the paper.

References

[1] Rice, J. R. and Sorensen, E. P., *Journal of the Mechanics and Physics of Solids,* Vol. 26, 1978, pp. 163-186.

[2] Drugan, W. J., and Rice, J. R., research in preparation for publication, Brown University, Providence, R.I., Spring 1979.

[3] Sorensen, E. P. in *Elastic-Plastic Fracture, ASTM STP 668,* American Society for Testing and Materials, 1979, pp. 151-174.

[4] Sham, T-L., "A Finite Element Analysis of Quasi-Static Crack Growth in an Elastic-Perfectly Plastic Solid," Sc.M. thesis, Brown University, Division of Engineering, Providence, R.I., March 1979.

[5] Paris, P. C., Tada, H., Zahoor, A. and Ernst, H., "A Treatment of the Subject of Tearing Instability," U.S. Nuclear Regulatory Commission Report NUREG-0311, Aug. 1977 (available through National Technical Information Service, Springfield, Va.).

[6] Hutchinson, J. W. and Paris, P. C., in *Elastic-Plastic Fracture, ASTM STP 668,* American Society for Testing and Materials, 1979, pp. 37-64.

[7] Rice, J. R. in *Fatigue Crack Propagation, ASTM STP 415,* American Society for Testing and Materials, 1967, pp. 247-311.

[8] Rice, J. R. in *Fracture: An Advanced Treatise,* H. Liebowitz, Ed., Vol. 2, Academic Press, New York, 1968, pp. 191-311.

[9] Hutchinson, J. W., *Journal of the Mechanics and Physics of Solids,* Vol. 16, 1968, pp. 337-347.

[10] Rice, J. R. in *Mechanics and Mechanisms of Crack Growth (Proceedings,* Conference at Cambridge, England, April 1973), M. J. May, Ed., British Steel Corporation Physical Metallurgy Centre Publication, 1974, pp. 14-39.

[11] Cherepanov, G. P., *Mechanics of Brittle Fracture* (in Russian), Nauka, Moscow, 1974, p. 271.

[12] Rice, J. R. and Tracey, D. M. in *Numerical and Computer Methods in Structural Mechanics,* S. J. Fenves et al., Ed., Academic Press, New York, 1973, pp. 585-623.

[13] Hutchinson, J. W., *Journal of the Mechanics and Physics of Solids,* Vol. 16, 1968, pp. 13-31.

[14] Rice, J. R. and Rosengren, G. R., *Journal of the Mechanics and Physics of Solids,* Vol. 16, 1968, pp. 1-12.

[15] McClintock, R. F. in *Fracture: An Advanced Treatise,* H. Leibowitz, Ed., Vol. 3, Academic Press, New York, 1971, pp. 47-225.

[16] Shih, C. F., deLorenzi, H. G., and Andrews, W. R. in *Elastic-Plastic Fracture, ASTM STP 668,* American Society for Testing and Materials, 1979, pp. 65-120.

Discussion

M. P. Wnuk[1] *(written discussion)*—The last slide shown by you gives an impression that the crack opening displacement (COD) criterion and the condition of attainment of a critical strain in the material element ahead of the crack front could be regarded as being equivalent. I would like to note that the latter criterion was first used by McClintock in 1958 and the equivalence of the "final stretch" (that is, a constant COD sustained at a fixed distance from the tip of a moving crack) was pointed out by Wnuk in 1972 and then again in 1974.

Your refined Prandtl slip line field associated with a quasi-static plane strain crack gives beautiful results, at least within the small-scale yielding range. In particular, your equation of a fracture resistance curve is so nice, since it is identical within an accuracy of a numerical constant with Wnuk's equation given in 1972 as derived from the final stretch model.

Your comments about possible solutions in the large-scale yielding range are rather speculative. It would appear to be a worthwhile project to compare these conjectures with the existing closed-form solutions based upon the final stretch concept (now in print in the *International Journal of Fracture Mechanics*). I agree, for example, with one of your conclusions that the tearing modulus of Paris is *not* a material property in a fully plastic situation.

J. R. Rice (author's closure)—Thank you for your comments. We are indeed aware of the relation of the crack growth criteria that we discuss (based on critical opening angle, and on critical accumulated strain, both referenced to a characteristic distance from the tip) to your "final stretch" interpretation of the Dugdale-Bilby-Cottrell-Swinden (DBCS) line plastic zone model. A mathematically similar form (see Eqs 27 and 42 of our paper) to that predicted by the "final stretch" criterion results, and this has been commented upon in the earlier work by Rice and Sorensen in Ref *1* upon which the present paper is based. I agree that comparisons of our fully plastic results with analogous results from the final stretch criterion would be interesting. But the DBCS model is of an *ad hoc* type and does not generate a field meeting accepted forms of the yield condition and plastic flow rule. Its divergence from more exact solutions is particularly marked in the plane strain case.

Further, the DBCS model does not show the sensitivity of fully plastic crack tip fields to specimen geometry (for example, bend versus center-cracked) that we discuss. Thus agreement or not with predictions of the

[1] Northwestern University, The Technological Institute, Department of Civil Engineering, Evanston, Ill. 60201.

final stretch model can hardly be taken as a condition for judging suitability of more exact analyses.

Finally, we do conclude that at least for materials which can be modeled with reasonable accuracy by the ideally plastic model that we adopt, the tearing modulus (T) will not be a universal material property. Differences between T-values for small, fully plastic bend specimens and large specimens, sustaining contained yielding would, we think be most marked for low T materials; that is, for those materials that are most readily fractured. For such materials the fully plastic T-values are expected to overestimate (in a predictable way, at least once present uncertainties with the fully plastic analysis are resolved) those prevailing for well-contained yielding.

J. A. Joyce,[1] *Hugo Ernst,*[2] *and P. C. Paris*[2]

Direct Evaluation of J-Resistance Curves from Load Displacement Records

REFERENCE: Joyce, J. A., Ernst, Hugo, and Paris, P. C., **"Direct Evaluation of J-Resistance Curves from Load Displacement Records,"** *Fracture Mechanics: Twelfth Conference, ASTM STP 700,* American Society for Testing and Materials, 1980, pp. 222-236.

ABSTRACT: The objective of this work was to experimentally develop a key curve for compact specimens of HY130 steel and to use this experimental function to generate the J-resistance curve from load displacement records alone using the analysis of Ernst et al. Eight 1/2T compact tension specimens with crack lengths from $a/W = 0.59$ to 0.94 were used to generate a series of load displacement records, which were assembled in a computer file as the key curve for geometrically similar compact specimens of this steel. Using this file, J-resistance curves (J-R curves) for 1T compact specimens were then obtained directly from the load displacement records and compared with unloading compliance J-R curves obtained for the same specimens. The critical J-values were found to be identical, but the new analysis gives much lower J-R curve slopes beyond the critical J for nonside grooved specimens. For side grooved specimens in which the crack does not tunnel, however, the J-R curves for the two methods were nearly identical. The J-R curves evaluated using the key curve method showed much less dependence on crack length than those obtained by the unloading compliance method. Agreement between the predicted and measured final crack length was excellent using the key curve method.

KEY WORDS: elastic-plastic fracture, J-integral, fracture toughness, slow crack growth, J-resistance testing, HY130 steel, unloading compliance, key curve method, tearing modulus, fractures (materials), crack propagation

The principal objectives of the work described herein are as follows:

1. To develop a "key curve" or $F1$ function following the work of Ernst et al [*1*][3] for an HY130 steel using a series of subsize compact specimens;

[1] Assistant professor of Mechanical Engineering, U.S. Naval Academy, Annapolis, Md. 21402.

[2] Graduate research assistant and professor of mechanics, respectively, Washington University, St. Louis, Mo. 63130.

[3] Italic numbers in brackets refer to the list of references appended to this paper.

2. To apply this function to determine the magnitude of corrections to the calculation of J and the subsequent calculation of the tearing modulus produced by crack growth;

3. To apply this function to determine J-R curves from load displacement records of a matrix of 1T compact specimens of HY130 steel reported by Gudas et al [2];

4. To compare the resulting J-R curves with the J-R curves obtained by Gudas et al [2] by their unloading compliance method as well as with physical measurements of crack extension obtained after each test; and

5. To compare the resulting J-R curves with multispecimen results available on this material.

This paper is an extension of recent work by Ernst et al [1] in which the authors show, among other things, that it is possible to construct J-R curves directly from load displacement records for simple specimen geometries if a "key curve function" is available for the material.

In the Ernst et al [1] analysis, dimensional analysis is used to show that for simple geometries in which the plasticity is confined to the uncracked ligament region, the load displacement relationship must have the form

$$\frac{PW}{Bb^2} = F1\left(\frac{\Delta}{W}, \frac{a}{W}, \frac{H}{W}, \frac{B}{W}, \text{material properties}\right) \tag{1}$$

where:

P = applied load,
Δ = total load line crack opening displacement,
a = crack length,
b = uncracked ligament,
B = specimen thickness,
$W = a + b$ = specimen width, and
H = specimen height.

It should be noted that in the work by Ernst et al [1], Δ/W was separated into elastic and plastic parts and the resulting J and crack extension expressions had elastic and plastic contributions. This separation was done only as an analytical convenience. In this experimental work it is more convenient to use the total load line displacement.

Assuming here the applicability of deformation plasticity theory, the formula for the path independent J-integral is given by [3]

$$J = \frac{-1}{W}\int_o^{\Delta}\left(\frac{\partial P}{\partial(a/W)_{\Delta}}\right)d\Delta \tag{2}$$

Substituting for P from Eq 1 into Eq 2 gives J as

$$J = -\int_o^{\Delta} \left(\frac{b^2}{W^2} \frac{\partial F1}{\partial (a/W)} - \frac{2b}{W} F1 \right) d\Delta \tag{3}$$

The differential of J can be written as

$$dJ = \frac{\partial J}{\partial \Delta} d\Delta + \frac{\partial J}{\partial a} da \tag{4}$$

Now evaluating from Eq 3 the terms of Eq 4 and substituting in Eq 4 gives

$$dJ = \left[\frac{2b}{W} F1 - \frac{b^2}{W^2} \frac{\partial F1}{\partial (a/W)} \right] d\Delta + \left[-\int_o^{\Delta} \frac{2}{W} F1 d\Delta + \int_o^{\Delta} \frac{4b}{W^2} \frac{\partial F1}{\partial (a/W)} d\Delta - \int_o^{\Delta} \frac{b^2}{W^3} \frac{\partial^2 F1}{\partial (a/W)^2} d\Delta \right] da \tag{5}$$

This differential expression can now be reintegrated along any convenient path in the $a/W - \Delta/W$ space to obtain J, at least if the partial derivatives $\partial F1/\partial(a/W)$ and $\partial^2 F1/\partial(a/W)^2$ and the differential crack extension da are somehow available. To obtain an expression for differential crack extension Ernst et al [*1*] take the differential of Eq 1 with Δ/W and a/W as variables to give

$$dP = \frac{\partial P}{\partial \Delta} d\Delta + \frac{\partial P}{\partial a} da \tag{6}$$

Evaluating the coefficients in terms of $F1$ gives

$$dP = \left[\frac{b^2}{W^2} \frac{\partial F1}{\partial (\Delta/W)} \right] d\Delta + \left[\frac{b^2}{W^2} \frac{\partial F1}{\partial (a/W)} - \frac{2b}{W} F1 \right] da \tag{7}$$

Solving for da gives

$$da = \frac{\frac{b^2}{W^2} \frac{\partial F1}{\partial (\Delta/W)} d\Delta - dP}{\frac{2b}{W} F1 - \frac{b^2}{W^2} \frac{\partial F1}{\partial \left(\frac{a}{W} \right)}} \tag{8}$$

Equations 5 and 8 together now allow calculation of dJ corrected for crack extension and the ratio dJ/da gives the Paris et al [*4*] tearing modulus from

$$T_{\text{mat}} = \frac{dJ}{da} \frac{E}{{\sigma_o}^2} \tag{9}$$

Terms involving $F1$ or dP in Eqs 5 and 8 can be evaluated from the load displacement record of the specimen. The terms involving

$$\frac{\partial F1}{\partial(a/W)}, \frac{\partial^2 F1}{\partial(a/W)^2}, \text{and} \frac{\partial F1}{\partial(\Delta/W)}$$

must be obtained from the key curve and cannot be obtained from the load displacement record of the test specimen.

The following sections describe the method used to evaluate an $F1$ function for the compact specimen geometry for a particular HY130 steel. Subscale (1/2T) specimens were used to obtain the $F1$ function experimentally so that load displacement values to larger Δ/W levels could be achieved in the 1T specimens without crack extension occurring. Blunt notched specimens were considered but fatigue cracked specimens were used in order to model as closely as possible the geometry of the 1T test specimens.

Experimental details of developing the experimental key curve function are given in the following section. In a later section the key curve is applied to a series of 1T compact specimens of the same material and J-R curves are developed and compared with results from the unloading compliance method and the multispecimen method.

Key Curve Function Development

Material

HY130 steel plate supplied in 25-mm thickness was used for all tests. The chemical composition of the plate is described in Table 1 and the mechanical properties are presented in Table 2.

Testing

Modified 1/2T compact specimens were produced according to Fig. 1, all with crack planes oriented in the T-L orientation. All specimens were machined from the center section of the 25-mm plate. A total of eight specimens were fatigue precracked to crack lengths between 0.59 and 0.94 a/W.

All tests were carried out at ambient temperature using computer data acquisition. A standard fracture mechanics clip on displacement gage was

TABLE 1—*Chemical composition of HY130 steel.*

Components, weight %												
C	Mn	P	Si	Ni	Cr	Mo	V	S	Cu	Al	Co	Ti
0.11	0.76	0.005	0.03	5.00	0.42	0.53	0.043	0.004	0.022	0.021	0.02	0.008

TABLE 2—*Tensile mechanical properties of HY130 steel.*

Yield Strength, 0.2% MPa	Ultimate Tensile Strength, MPa	Elongation, % in 2 in.	Reduction of Area, %
937	978	21	55

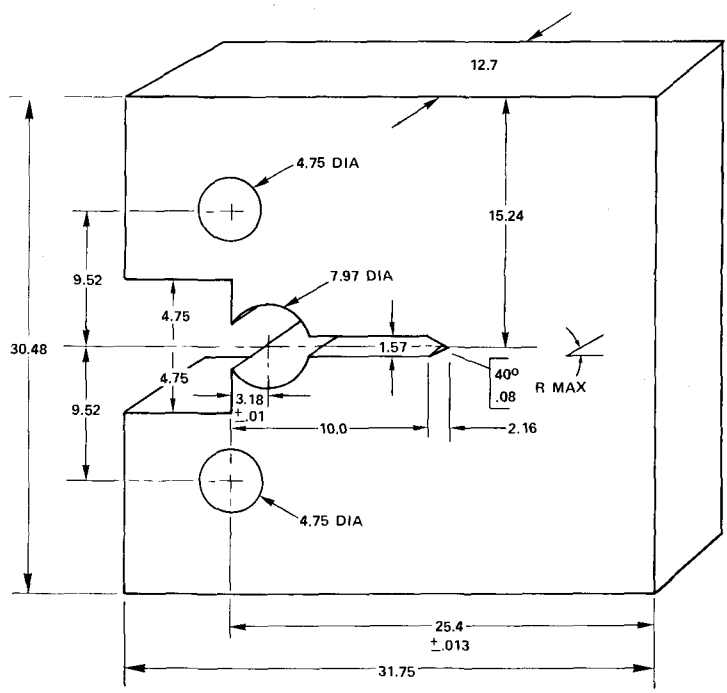

FIG. 1—*Compact specimen (1/2TCT) geometry* (measurements in millimetres).

mounted on the integral knife edges in the load line of each specimen. Using the computer interactive system for unloading compliance J-R curve determination described by Joyce and Gudas [5], the initial specimen compliance was carefully measured at loads below one half the expected limit load. Then starting from zero load, a load displacement record was run to a final crack opening displacement (COD) of 2.5 mm. In order to obtain as smooth a curve as possible, no unloadings were taken and no attempt was made to determine when crack extension initiated in these specimens. A uniform crosshead speed of 0.125 mm/min was maintained throughout each test. Data points were taken approximately every 0.002 mm of displacement and the load displacement file was stored on magnetic tape. After testing, each specimen was heat tinted at 370°C (698°F) for 20 min and broken open in

liquid nitrogen. The fatigue crack length was measured using a nine-point average technique.

Key Curve Assembly

The digital load displacement records for each of the eight subsize specimen tests were sent to the U.S. Naval Academy's time sharing system. For each file the load and displacement were normalized to give

$$P' = \frac{PW}{Bb^2}$$

$$\Delta' = \frac{\Delta}{W} \tag{10}$$

where

B = the specimen thickness, and
b = the uncracked ligament.

The displacement scale was then smoothed and reduced by an interpolation routine to contain evenly spaced displacement values at 0.0125-mm intervals, to facilitate numerical differentiation. The eight separate files were then assembled into a key curve file of x, y, z triples where

$$x = \frac{\Delta}{W}$$

$$y = \frac{a}{W} \tag{11}$$

$$z = \frac{PW}{Bb^2}$$

or

$$\frac{PW}{Bb^2} = F1\left(\frac{\Delta}{W}, \frac{a}{W}, C_1, C_2, C_3 \ldots\right) \tag{12}$$

where C_1, C_2, etc., are terms which are assumed to be identical for the 1/2T calibration specimens and the 1T specimens, test specimens to which the analysis is to be applied. Geometrical and material similarity were controlled as closely as possible between the two specimen sizes to assure, following

Rice, et al [6] and Ernst et al [1], that the $F1$ function of Eq 12 applies to both the 1/2T and 1T compact specimens of this plate of HY130 steel.

Discussion

The result of assembling normalized load displacement records of the eight 1/2 compact specimens gives the $F1$ function shown in the computer graphics drawing in Fig. 2. The eight grid lines intersecting the a/W axis are the normalized load displacement records for the eight 1/2T specimens. Crossing grid lines are shown at 0.0625-mm intervals. The $F1$ function was not used beyond $\Delta/W = 0.05$ because the load was approaching the maximum load in the shortest cracked specimens at this value of load line displacement, implying that crack extension was imminent or even occurring in these specimens. This cutoff limits the maximum load line crack opening displacement to 2.5 mm for a 1T specimen, but this is adequate in the material tested here to produce a J-R curve as specified by Clarke et al [7] in their J_{Ic} testing recommendation. The a/W-values used for each specimen were those obtained from the nine-point averaged measurements of the fatigue crack. In Fig. 3 a reduced view of the function is shown along the Δ/W axis to define clearly the dependence of the function on a/W. From this view it was noticed, that for this material, $F1$ is only a weak function of a/W, falling off linearly with a/W for a fixed Δ/W. For this reason terms of Eq 1 involving $\partial^2 F1/\partial(a/W)^2$ were set to zero.

Applications of the Key Curve Function

An application of the experimental key curve function to the determination of J-R curves directly from load displacement records was done by an

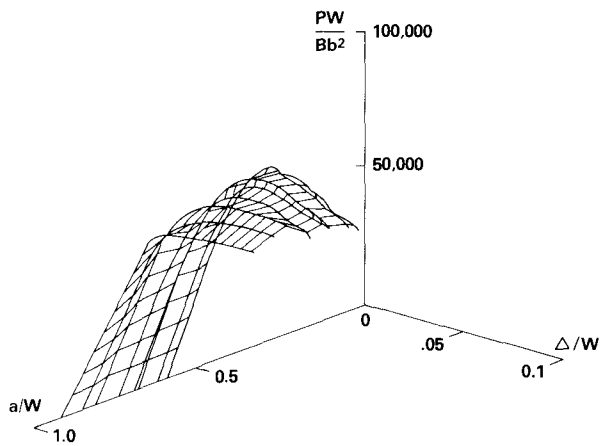

FIG. 2—*Computer graphics plot of experimental key curve for HY130 steel.*

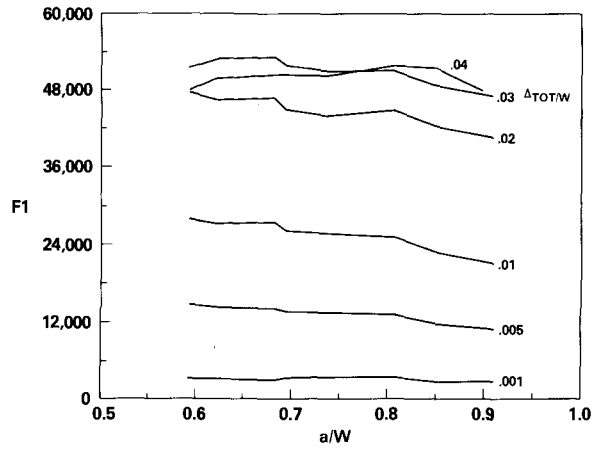

FIG. 3—*Selected Δ/W sections of the key curve function showing dependence of* F1 *on* a/W.

analysis of data reported previously by Gudas et al [*2*] on this same HY130 steel. In that work J-R curves for a matrix of specimens with a/W from 0.54 to 0.81 for 12 + 25 percent side grooved and nonside grooved specimens had been obtained using the computer interactive unloading compliance technique. Digital load displacement records were obtained for all of these specimens and recorded on computer files. Typical load displacement records are shown in Fig. 4 for these specimens.

The unloading compliance J-R curve results had shown that the average J_{1c} for all geometries was 153.5 KPa · m ± 10 percent. The tearing modulus, T, of Eq 9 was shown to be distinctly lower for side grooved specimens than for nonside grooved specimens. The tearing modulus was independent of a/W for side grooved specimens. For nonside grooved specimens, T was larger by a factor of two for specimens with $a/W = 0.81$ compared to specimens with $a/W = 0.54$. It was shown that the unloading compliance method underestimated crack extension when compared to a nine-point average of measured values obtained after heat tinting and breaking open the specimens whenever crack tunneling was present. If side grooves were used to straighten the crack front, the crack extension estimated by the unloading compliance method corresponded closely with the nine-point measured average.

To obtain J-R curves directly from the load displacement curves of these specimens, discrete versions of Eqs 5 and 8 were written; namely

$$\delta J_n = \left[\frac{2b}{W} F1_n - \frac{b^2}{W^2}\frac{\partial F1^*}{\partial(a/W)_n}\right]\delta\Delta_n + \left[-\frac{2}{W}\sum_{i=1}^{n} F1_i\,\delta\Delta_i + \frac{4b}{W^2}\sum_{i=1}^{n}\frac{\partial F1^*}{(a/W)_i}\delta\Delta_i\right]\delta a_n \tag{13}$$

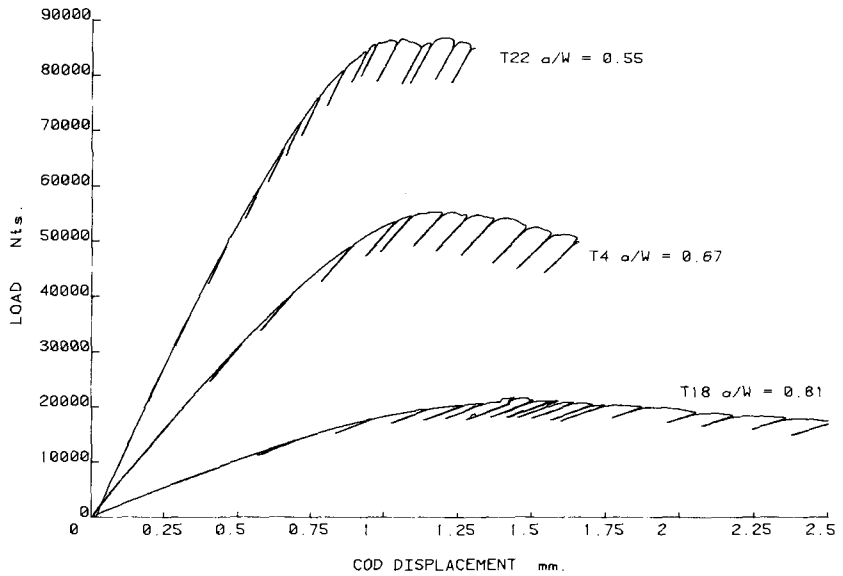

FIG. 4—*Plot of load displacement records of three HY130 1TCT compact specimens.*

and

$$\delta a_n = \frac{\dfrac{b^2}{W^2}\dfrac{\partial F1^*}{\partial(\Delta/W)_n}\delta\Delta_n - \delta P_n}{\dfrac{2b}{W}F1_n - \dfrac{b^2}{W^2}\dfrac{\partial F1^*}{\partial(a/W)_n}} \tag{14}$$

At each point on the load displacement record of a specimen the total J and Δa are

$$J = \sum_{n=1}^{m} \delta J_n \tag{15}$$

$$\Delta a = \sum_{n=1}^{m} \delta a_n \tag{16}$$

In foregoing equations the terms without asterisks are evaluated from the specimen load displacement curve. The terms with asterisks are evaluated from the $F1$ calibration curve file shown in Fig. 2. For the small amounts of crack extension considered here, the remaining uncracked ligament b was assumed to remain constant.

A small computer program was written on the U.S. Naval Academy's time sharing system that evaluates Eqs 12 through 16, generating for each point on the specimen's digital load displacement record a Δa–J pair on a J-R curve for the specimen. Each point, n, of the load displacement record gives $F1_n$ and δP_n directly. The specimens measured crack length-obtained by a heat-tint nine-point average measurement technique, and the Δ/W at each point of the specimens load displacement record locates a position on the $F1$ calibration function for the material shown in Fig. 2. Numerical differentiation techniques are used about this point to determine

$$\frac{\partial F1^*}{\partial (a/W)_n} \quad \text{and} \quad \frac{\partial F1^*}{\partial (a/W)_n} \tag{17}$$

These values give δa_n from Eq 14 and subsequently a δJ_n from Eq 13. Summation of these values using Eqs 15 and 16 gives running totals of J and Δa. Stepping through complete load displacement curves like those of Fig. 4, ignoring all data points on the unloadings, gives J-R curves like those shown in Figs. 5 through 7.

Discussion of Results

In the original plan for this work, it was felt that it was overly optimistic to expect to obtain J-R curves directly from load displacement records by using

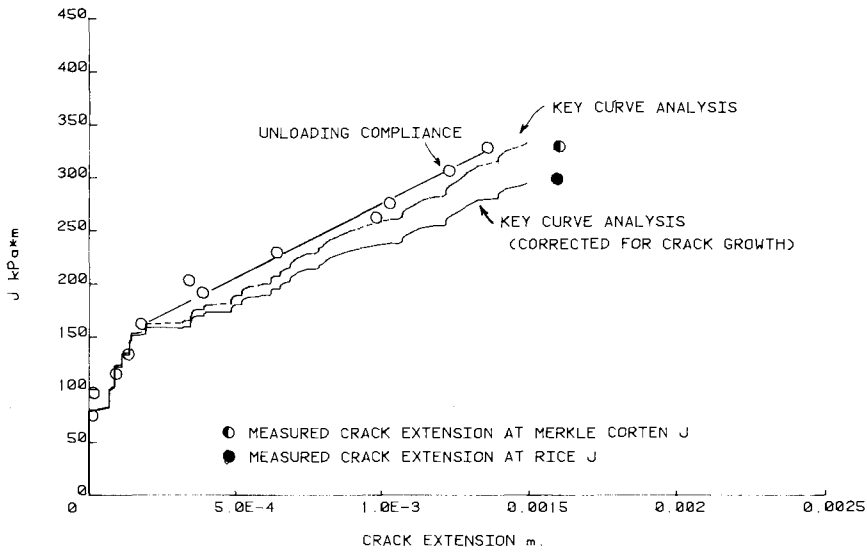

FIG. 5—*Comparison of the key curve J-R curve and unloading compliance result for a non-face grooved HY130 compact specimen with* a/W = *0.81.*

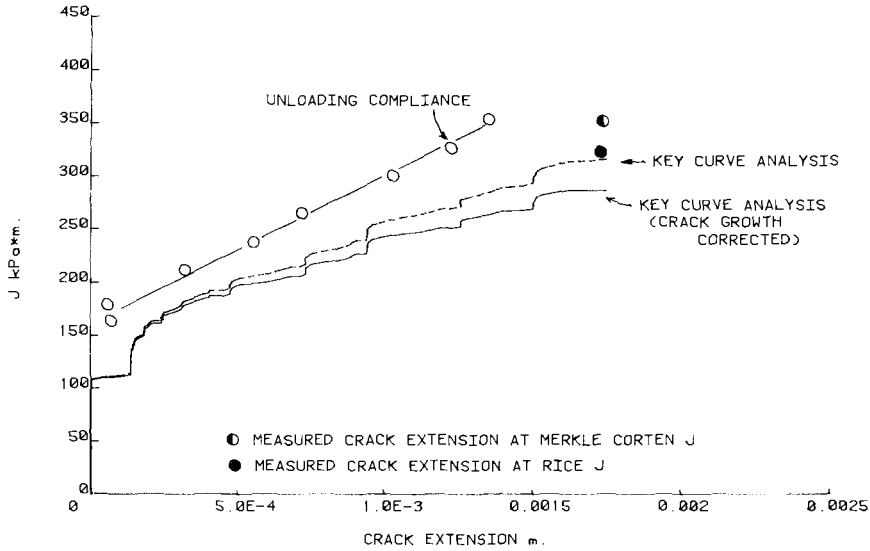

FIG. 6—*Comparison of the key curve J-R curve and unloading compliance result for a nonface grooved HY130 compact specimen with* a/W = *0.67.*

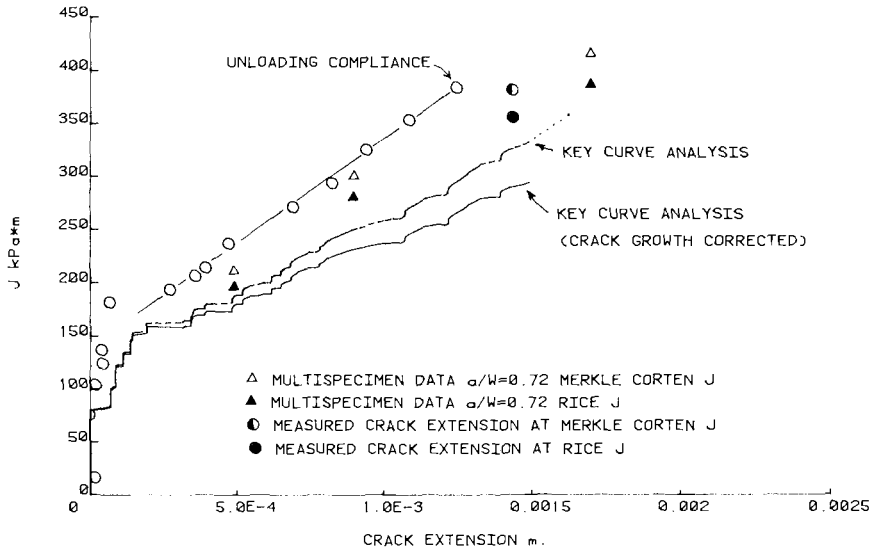

FIG. 7—*Comparison of the key curve analysis J-R curve and unloading compliance result for a nonface grooved HY130 compact specimen with* a/W = *0.81.*

the key curve method. Nonetheless, it appeared that the magnitudes of crack growth corrections to J could be evaluated, and that success in this would justify the effort involved in obtaining the key curve. The first analysis involved using Eqs 13 and 15 to evaluate the crack growth corrected J, obtaining the crack extensions from the unloading compliance results. When this was successful, calculation of crack extensions were added using Eqs 14 and 16, and it was found, somewhat surprisingly, to be very accurate. Only after these successes was the analysis of the side grooved specimens attempted because it was realized that the side grooves caused a degree of geometric dissimiliarity between the key curve specimens and the test specimens.

Figures 5 through 7 show J-R curves comparing the results of the key curve method to the unloading compliance J-R curves for nonside grooved specimen. Key curve results with and without the crack growth corrections are shown to demonstrate the magnitude of the corrections. (The crack growth correction terms are in the second bracket of Eq 13.) It should be noted also that the lumpiness in the J-R curves resulted from the unloadings present on the load displacement records, and if these were smoothed out more carefully (or did not exist), smoother J-R curves would have resulted.

Also plotted on these figures are the final measured crack extensions plotted at the final unloading compliance, Merkle-Corten [8] corrected, J-values; and at the J_{Rice}-values where

$$J_{\text{Rice}} = \frac{2A}{Bb} \tag{18}$$

is the value of J calculated from the area under the load displacement record, A, without an additional tensile correction.

The major component of J for both methods is this J_{Rice} value, and it is calculated by both methods in an identical fashion from the specimen load displacement record. The key curve method gives tensile corrections smaller by a factor of three or more than those predicted by the Merkle-Corten analysis. These corrections were also independent of crack length since $\partial F1^*/\partial(a/W)_n$ was found not to vary with crack length.

Corrections to J resulting from crack growth were on the order of a 25 percent reduction in J increments beyond J_{Ic}, resulting in an appreciable reduction in the material tearing modulus. Again little effect on these corrections could be attributed to specimen crack length.

The major difference between the key curve R-curve (without crack growth corrections) and the unloading compliance R-curve was derived from the crack extension predictions. For all specimens the key curve method predicted more crack extension than the unloading compliance method. The key curve method crack extensions agreed more closely with the measured nine-point average crack lengths found at the conclusions of the tests.

The combination of crack growth corrections, reduced tensile component

correction, and the increased crack extension predicted, means the key curve tearing modulus is about one half of that obtained with the unloading compliance method.

Figure 8 shows a comparison of the J-R curves resulting from the key curve analysis and the unloading compliance method for a 12 percent side grooved specimen. Here the two J-R curves without crack growth corrections are nearly identical by all measures. Similar results were found for all the side grooved specimens.

Also shown in Fig. 7 is the result of four multispecimen tests on this material that are plotted here with and without the Merkle-Corten correction. For these specimens $a/W = 0.72$. Good agreement is found between the multispecimen curve and the key curve result for the $a/W = 0.81$ specimen.

As crack extension takes place in the nonside grooved specimens of this material, crack tunneling occurs. This will eliminate the geometric similarity between the 1/2T specimens with straight fatigue cracks and the 1T specimens with the tunneled crack front and will introduce errors into the key curve analysis. This is possibly the reason the key curve method underestimates the crack extension for the $a/W = 0.55$ specimens, which tunnel dramatically, while overestimating the crack extension slightly for the deepest cracks, which tunnel only slightly.

For the side grooved specimens, geometric similarity does not exist at the

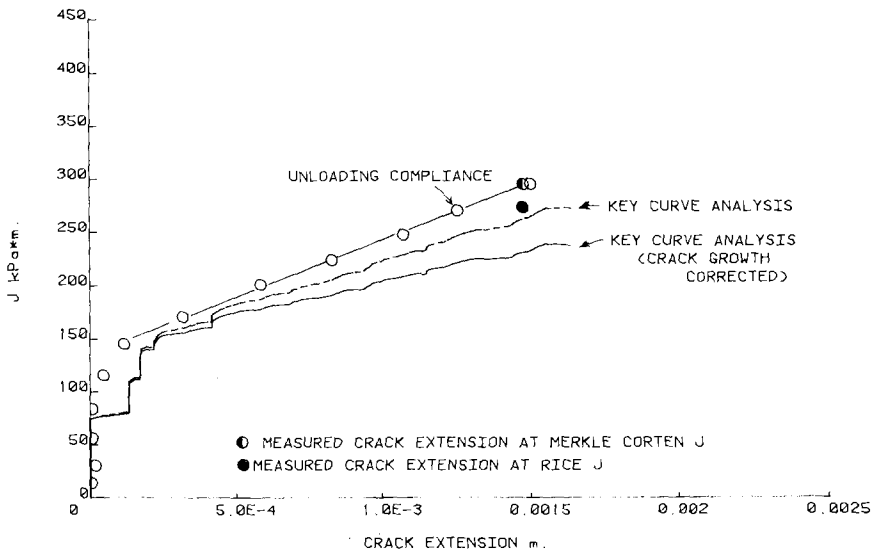

FIG. 8—*Comparison of the key curve analysis J-R curve and unloading compliance result for a 12 percent face grooved HY130 compact specimen with* a/W = *0.81. (Total cross section reduction was 12 percent using a 45 deg included angle Charpy notch cutter.)*

beginning of the test, but in these specimens the crack front remains straight as crack extension occurs so that there is no variation in the degree of geometric similarity during the test.

The key curve method as used here is a lengthy and complex method to evaluate the J-R curve for a material. The resulting J-R curve is, however, a considerable improvement over results obtained by unloading compliance methods or multispecimen methods. The key curve method adds a correction for crack extension and evaluates the tensile loading component without the fully plastic approximations used in the Merkle-Corten [*8*] analysis. Inaccuracies remain in the experimental evaluation of the $F1$ function and in the numerical differentiation of $F1$ to obtain the quantities used in Eqs 5 and 8 to evaluate the J-R curve. The key curve will, hopefully, act as a standard by which to evaluate the correctness of simpler methods.

Conclusions

The following conclusions can be drawn from this work:

1. An experimental $F1$ key curve can be obtained from subsize specimens, assembled in a computer file, and used to determine J-R curves from digitized load displacement records of geometrically similar specimens of the same material. The J-R curves that result from this analysis are complete in that a point on the J-R curve exists for each point on the digitized load displacement record. This is an improvement over previous methods that give J-R curves consisting of only a few discrete points through which curves must be fit.

2. The $F1$ function obtainable from fatigue cracked 1/2T compact specimens of this steel was restricted to Δ/W-values <0.05. This allowed analysis of 1T compact specimens to a load line COD of 2.54 mm in this HY130 steel, which was adequate to obtain 1.5 mm of crack extension.

3. For this range of crack extension, the crack extension corrections to J were on the order of 10 percent of the total J, but about 25 percent of the increments of J beyond J_{Ic}, resulted in an equivalent reduction in the tearing modulus.

4. The tensile correction term was found to be considerably smaller than that given in the Merkle-Corten equation. For this material, this correction was found to be independent of crack length, which was possibly due to the limited plasticity of the HY130 material tested.

5. J-R curves resulting from the key curve analysis of the HY130 matrix specimens were much more self-consistent with just a slight tendency to lower T-values for shorter crack lengths. Tearing modulus values from the key curve method agree well with those obtained for side grooved specimens using the unloading compliance method. Generally, the tearing moduli for nonside grooved specimens obtained by the unloading compliance appear to

be high due to effects of crack tunneling on crack length estimates obtained by a compliance technique.

6. Final crack length predictions from the calibration function method corresponded very accurately with final crack length measurements.

7. The J-R curves found using the key curve analysis agreed well with the results of multispecimen tests done on this alloy.

8. If the key curve method were to be extended to situations involving large amounts of crack extension, it would be necessary to use blunt notched, subscale specimens in order to have an accurate $F1$ function free of crack extension effects.

References

[1] Ernst, H., Paris, P. C., Rossow, M., and Hutchinson, J. W. in *Fracture Mechanics, ASTM STP 677,* American Society for Testing and Materials, 1979, p. 581.

[2] Gudas, J. P., Joyce, J. A., and Davis, D. A. in *Fracture Mechanics, ASTM STP 677,* American Society for Testing and Materials, 1979, p. 474.

[3] Rice, J. R., *Journal of Applied Mechanics,* Vol. 35, June 1968, pp. 379-386.

[4] Paris, P. C., Tada, H., Zahoor, A., and Ernst, H. in *Elastic-Plastic Fracture, ASTM STP 668,* American Society for Testing and Materials, J. D. Landes, J. A. Begley, and G. A. Clarke, Eds., 1979, pp. 5-36.

[5] Joyce, J. A. and Gudas, J. P. in *Elastic-Plastic Fracture, ASTM STP 668,* American Society for Testing and Materials, J. D. Landes, J. A. Begley, and G. A. Clarke, Eds., 1979, pp. 451-468.

[6] Rice, J. R., Paris, P. C., and Merkle, J. G. in *Progress in Flaw Growth and Fracture Toughness Testing, ASTM STP 536,* American Society for Testing and Materials, 1973, pp. 231-245.

[7] Clarke, G. A., Andrews, W. R., Begley, J. A., Donald, J. K., Embley, G. T., Landes, J. D., McCabe, D. E., and Underwood, J. E., *Journal of Testing and Evaluation,* Vol. 7, No. 1, Jan. 1979, pp. 49-56.

[8] Merkle, J. G. and Corten, H. T., *Journal of Pressure Vessel Technology,* Vol. 96, Nov. 1974, pp. 286-292.

D. E. Corman[1]

Estimation of J-Integral Uncertainty

REFERENCE: Corman, D. E., **"Estimation of J-Integral Uncertainty,"** *Fracture Mechanics: Twelfth Conference, ASTM STP 700,* American Society for Testing and Materials, 1980, pp. 237-250.

ABSTRACT: A method for determining the effect of random experimental error on the calculation of J and crack length extension Δa is presented. Predictor-corrector equations for determining Δa are also derived and their convergence properties studied. The application to a three-point bend specimen is considered and numerical results presented.

KEY WORDS: fractures (materials), J-integral, J-R curves, elastic plastic fracture mechanics, crack length extension, crack propagation

The J-integral has proven to be a useful parameter in describing the intensity of elastic-plastic deformation and the stress field near a crack tip [*1*].[2] Under elastic conditions or in cases where the deformation theory of plasticity is applicable [*2*], the J-integral is path independent. More recently Paris and Hutchinson [*3*] have obtained conditions, under the assumption of small-scale yielding, which guarantee J-controlled growth. Thus, information about near crack tip conditions can be obtained by taking a path sufficiently far away from the tip. The path independence of J in combination with stress-strain field data created by a finite element analysis provides an analytical method of determining J. Alternatively, a large number of experimental procedures have been developed for the determination of J from experimental data alone. Most recent among these methods is the "key curve" method for determining J and crack length extension, da, proposed by Ernst et al [*4*]. To be useful to the test engineer, however, some means must be provided for assessing the sensitivity of a given method to experimental error. For example, suppose two identical specimens are loaded to construct a J-R curve. Suppose further that the load cell and displacement gage are accurate to 1 percent. On the basis of each test, two different J-R curves are con-

[1] Formerly, research engineer, Center for Fracture Mechanics, Washington University, St. Louis, Mo. 63130; presently, research engineer, John Hopkins University, Applied Research Laboratories, Laurel, Md. 20510.

[2] *The italic numbers in brackets refer to the list of references appended to this paper.*

structed. The test engineer must then decide how much variation in the curves is due to the inaccuracy of load displacement measurements and how much variation is attributable to perhaps slight differences in material properties. This paper provides a first attempt to answer questions of this type. To accomplish this goal, a sensitivity analysis of the key curve method is presented. Here load and displacement are considered to be random variables. The idea now is to determine how calculations of J and crack length change depend on the random nature of the load-displacement measurements. Alternatively, a simple modification of the analysis presented here will give error estimates in *J-da* calculations which arise due to imperfect knowledge of the calibration function, $F_1(\Delta_{pL}/w, a/w)$, and its partial derivatives.

The major topics to be treated here are organized as follows. The section immediately following contains a brief review of the key curve method. The basic equations of the sensitivity analysis of this method are also presented here. The next section contains an application of the general equations formulated in the preceding section to a special case; a three-point bend specimen obeying a Ramberg-Osgood constitutive law. In the Appendix is found a description of a program developed to calculate J and crack length extensions, da, using load-displacement records alone.

Probabilistic Formulation of the J-Integral

In review the J-integral is defined as [5]

$$\int_T W dy - \mathrm{T} \frac{\partial \mathrm{u}}{\partial x} ds \tag{1}$$

where

W = strain energy density,
T = path of integration,
ds = increment of distance along the path,
T = traction vector on the contour, and
u = displacement vector on the contour.

Rice has also shown that J can be equivalently written as

$$J = \int_0^P \left(\frac{\partial \Delta}{\partial a}\right)_p dp = -\int_0^\Delta \left(\frac{\partial p}{\partial a}\right)_\Delta d\Delta \tag{2}$$

where Δ is the work producing component of load point displacement for the load, p.

Following [4] J is divided into elastic and plastic parts, J_{EL} and J_{pL}. Here J_{EL} is just defined as

$$J_{EL} = \int_0^P \left(\frac{\partial \Delta_{EL}}{\partial a}\right)_p dp \tag{3}$$

which is the familiar Griffith elastic energy rate $G(a, p)$. J_{pL} is simply

$$J_{pL} = -\int_0^{\Delta_{pL}} \left(\frac{\partial p}{\partial a}\right)_{\Delta_{pL}} d\Delta_{pL} \tag{4}$$

where

$$\Delta = \Delta_{EL} + \Delta_{pL} \tag{5}$$

$$J = J_{EL} + J_{pL} \tag{6}$$

with Δ_{EL} and Δ_{pL} the linear elastic and plastic components of load point displacement Δ respectively.

The Key Curve Method

In this section a brief description is presented of the key curve method. A more detailed treatment is found in Ref *4*.

The basic idea of Ref *4* is to utilize a dimensional analysis argument to obtain the following result

$$p = \frac{b^2}{W} F_1\left(\frac{\Delta_{pL}}{W}, \frac{a}{W}\right) \tag{7}$$

with

b = remaining ligament,
W = specimen width,
a = crack length, and
p = load per unit thickness.

When this equation is combined with the equations defining J_{pL} the result is

$$J_{pL} = 2b \int_0^{\Delta_{pL}} F_1 \, d\Delta_{pL} - \frac{b^2}{W} \int_0^{\Delta_{pL}} \frac{\partial F_1}{\partial (a/W)} d\Delta_{pL} \tag{8}$$

Taking differentials of Eq 7 and solving for da one gets

$$da = \frac{\frac{b^2}{W^2}\frac{\partial F_1}{\partial\left(\frac{\Delta_{pL}}{W}\right)}d\Delta_{pL} - dp}{\frac{2b}{W}F_1 - \frac{b^2}{W^2}\frac{\partial F_1}{\partial(a/W)}} \tag{9}$$

Finally combining Eqs 3 and 8 the equation

$$J = G(a, p) + 2b\int_0^{\Delta_{pL}} F_1\, d\Delta_{pL} - \frac{b^2}{W}\int_0^{\Delta_{pL}} \frac{\partial F_1}{\partial(a/W)}\, d\Delta_{pL} \tag{10}$$

is obtained. The two Eqs 9 and 10 represent the basis of the key curve method.

Before presenting a discussion of the sensitivity analysis of the key curve method, the problem of how to determine the calibration function, F_1, should be discussed. In general any method should have the following properties: (*a*) it must permit large plastic displacement prior to the initiation of crack growth, and (*b*) it must also be such that the basic geometry of the specimen, and in particular the structure of the *J*-field itself, should not be altered.

A first method for determining the calibration function, F_1, is to utilize sub-sized specimens. Suppose one desires to construct a J-R curve for a full-sized compact specimen. First a load-displacement test is performed on sub-sized specimens of the same material with exactly the same dimensional proportions as the full-sized specimen with one important difference. The sub-sized specimens are chosen with a/w values that vary slightly from the full-sized specimen to larger values. The load-displacement record for these sub-sized specimens and the full-sized specimen is plotted on the basis of pW/b_o^2 versus Δ/W as shown in Fig. 1*a*. The elastic displacement is then subtracted from the curve and a plot of pW/b_o^2 versus Δ_{pL}/W is obtained (Fig. 1*b*). The quantity pW/b_o^2 for the subsized (on crack-growth) specimens is the calibration function F_1. The slope of subsized specimen curves gives $\partial F_1/\partial(\Delta_{pL}/W)$ and the spacing of the curves gives $\partial F_1/\partial(a/W)$. One major advantage of using subsized specimens to "bracket" the load-plastic displacement curve of the full-sized specimen is that relatively long load-plastic displacement records are obtained. This permits greater accuracy in calculation of $\partial F_1/\partial(\Delta_{pL}/W)$ in the range of crack growth for the full-sized specimen.

A second method for determining the calibration function, F_1, involves the extrapolation of load-plastic displacement information from the region where no crack growth occurred into a region of large plastic displacement. This involves utilization of curve-fit techniques. The validity of this method depends to a great extent on the sensitivity problem and is discussed later.

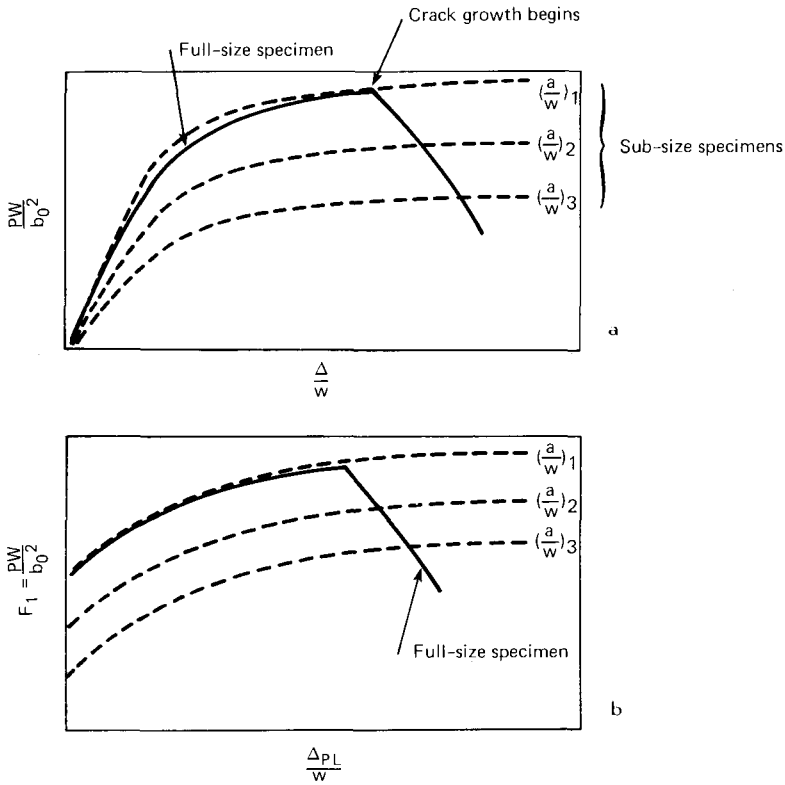

FIG. 1—*Evaluation of* F_1 *using sub-sized specimens.*

Calculation of the Δa

The sensitivity analysis of the key curve method will now be considered. As a first assumption suppose that the calibration function $F_1(\Delta_{pL}/W, a/W)$ is known. This information can take the form of either knowledge of the functional form, say $F_1 = 63\ 500\ (\Delta_{pL}{}^{0.08})$, or in a digitized version of load-plastic displacement records for various a/W's.

For simplicity the case of a continuous-time load-displacement test record is considered. The transformation to the discrete case is straight-forward. Suppose that the crack-length, a, is known. The elastic displacement can be written in terms of the compliance function $c(a)$ as follows

$$\Delta_{EL} = c(a)p \tag{11}$$

Solving for the plastic displacement using Eq 11 and substituting the result into Eq 9 there results

$$da = \frac{-dp\left[c\,\frac{b^2}{W^2}\,\frac{\partial F_1}{\partial\left(\frac{\Delta_{pL}}{W}\right)} + 1\right] + \frac{b^2}{W^2}\,\frac{\partial F_1}{\partial\left(\frac{\Delta_{pL}}{W}\right)}\,[d\Delta - pdc]}{\frac{2bF_1}{W} - \frac{b^2}{W^2}\,\frac{\partial F_1}{\partial(a/W)}} \tag{12}$$

For the case of small increments in total displacement, $d\Delta$, Eq 12 suggests two numerical schemes for determining da. First suppose that the function $c(a)$ is given. A simple Taylor expansion gives to second order

$$dc = c(a + da) - c(a) \sim c'(a)da \tag{13}$$

so that after some algebra, Eq 12 can be solved for da to give

$$da = \frac{-dp\left[c\,\frac{b^2}{W^2}\,\frac{\partial F_1}{\partial\left(\frac{\Delta_{pL}}{W}\right)} + 1\right] + \frac{b^2}{W^2}\,\frac{\partial F_1}{\partial\left(\frac{\Delta_{pL}}{W}\right)}\,d\Delta}{\frac{2bF_1}{W} + \frac{b^2}{W^2}\left(pc'(a)\,\frac{\partial F_1}{\partial\left(\frac{\Delta_{pL}}{W}\right)} - \frac{\partial F_1}{\partial(a/W)}\right)} \tag{14}$$

On first examination there appears to be a serious problem with the actual implementation of Eq 14. In order to use Eq 14, knowledge not only of the compliance function $c(a)$, but also its derivatives, $c'(a)$, is required. In practice $c(a)$ may be known only approximately [6] giving rise to the possibility of large error in the calculation of its derivative. A simple inequality can be derived which guarantees that Eq 14 is insensitive with respect to accuracy in the calculation of $c'(a)$. A material obeying a Ramberg-Osgood constitutive law is assumed. Under the assumptions of Ilyushins' theorem [7], the calibration function F_1 is separable into the form

$$F_1\left(\frac{\Delta_{pL}}{W}, \frac{a}{W}\right) = F\left(\frac{a}{W}\right)\left(\frac{\Delta_{pL}}{W}\right)^n \tag{15}$$

where typically $n \sim 0.1$.

Now from Eq 14 one has insensitivity with respect to accuracy in $c'(a)$ provided

$$\frac{2b}{W}F_1 \gg \frac{b^2}{W^2}pc'(a)\,\frac{\partial F_1}{\partial\left(\frac{\Delta_{pL}}{W}\right)} \tag{16}$$

Equation 16 can be rewritten using Eq 15 to give the simple inequality

$$2\Delta_{pL} \gg nbc'(a)p \tag{17}$$

Physically, Eq 17 can be interpreted as follows. Suppose that we are in the range of large plastic-displacement. Equation 17 then tells us that we can neglect terms containing $c'(a)$ provided the elastic displacement does not vary greatly with crack length.

An alternate numerical procedure can be developed for the determination of crack-length extension da. Here an iterative predictor-corrector method is used.

$$dc_p = c(a_p) - c(a) \tag{18}$$

$$da_p = a_p - a \tag{19}$$

$$da_c = a_c - a \tag{20}$$

where

a = crack-length at stage i,
a_p = predicted crack-length at stage $i + 1$, and
a_c = corrected crack-length at stage $i + 1$.

As a first assumption assume

$$dc = 0 \tag{21}$$

The idea here is to utilize Eq 12 to predict a crack-length extension da_p on the basis of zero compliance change. Using this predicted crack-length, a_p, the change in compliance, dc_p, can be estimated. Thus, the pair of equations obtained is

Predictor

$$da_p = \frac{-dp\left(c\frac{b^2}{W^2}\frac{\partial F_1}{\partial\left(\frac{\Delta_{pL}}{W}\right)} + 1\right) + \frac{b^2}{W^2}\frac{\partial F_1}{\partial\left(\frac{\Delta_{pL}}{W}\right)}d\Delta}{\frac{2bF_1}{W} - \frac{b^2}{W^2}\frac{\partial F_1}{\partial(a/W)}} \tag{22}$$

Corrector

$$da_c = \frac{-dp\left(c\frac{b^2}{W^2}\frac{\partial F_1}{\partial\left(\frac{\Delta_{pL}}{W}\right)} + 1\right) + \frac{b^2}{W^2}\frac{\partial F_1}{\partial\left(\frac{\Delta_{pL}}{W}\right)}(d\Delta - pdc_p)}{\frac{2bF_1}{W} - \frac{b^2}{W^2}\frac{\partial F_1}{\partial(a/W)}} \tag{23}$$

The predictor-corrector pair can then be repeated until a convergence criteria of the form is satisfied

$$|da_c - da_p| < \epsilon \tag{24}$$

Sensitivity Analysis

In this section the sensitivity analysis of the key curve method is now presented. It is this analysis that provides the means of determining the effect of random experimental error in measurements of load and displacement on the calculation of J and crack-length extension da. The method of solution is simple. Let $\{p_i\}$, $\{\Delta_i\}$ be the measured load displacement sequence. Define

$$\hat{\Delta}_i = \Delta_i + \eta_{\Delta_i} \tag{25}$$

$$\hat{p}_i = p_i + \eta_{p_i} \tag{26}$$

where

η_Δ = a Gaussian random variable with mean zero and variance $\sigma_\Delta{}^2$, and
η_p = a Gaussian random variable with mean zero and variance $\sigma_p{}^2$.

In this analysis then the size of the relative experimental error is intimately related to the relative size of σ_Δ and σ_p with respect to Δ and p. Now, suppose that the randomized load-displacement sequence is used to calculate J-da using Eq 10 and either Eqs 12 or 22 and Eq 23. The quantities J-da are then viewed as random variables. The size of the random error is J-da and is then expressed parametrically in terms of σ_p and σ_Δ minus the experimental error. The statistical correlation between the random variables η_Δ and η_p is an additional input parameter for the problem. Physically, the latter represents a coupling between errors in load-cell calibration and displacement gage calibration.

The method of solution to this problem is straight-forward. Given the load-displacement sequence $\{P_i\}$, $\{\Delta_i\}$ the equations presented are programmed on a digital computer and a Monte Carlo type simulation performed. The end result of this simulation is then the probability density and distribution functions of J and da. The latter furnishes confidence intervals for J-da which then reflect the uncertainty associated with the resulting J-R curve.

As stated before, the method described above treats load and displacement measurements as random variables. The calibration function, F_1, was assumed to be known. An alternate viewpoint may prove to be beneficial. Suppose that the load-displacement measurements are deterministic (non-random). The idea now is to place all the experimental uncertainty in the F_1 function. Thus, the calibration function, F_1, is treated as a random variable

with a specified distribution. The variance of this distribution then furnishes an estimate of the accuracy of the curve fit. The difference between these two viewpoints is indicated below. In the first case a two-dimensional random process is obtained. The load-displacement measurements are "smeared" out into a rectangle. Using the defining relationships for plastic displacement and the calibration function, F_1, it is seen that the two-dimensional distribution for load-displacement is transformed into a geometrically similar distribution in the F_1-plastic displacement space. Now in the second case where F_1 is treated as the random variable, a one-dimensional random process is obtained. Through use of the equation

$$p = \frac{b^2}{W} F_1 \left(\frac{\Delta_{pL}}{W}, \frac{a}{W} \right) \tag{27}$$

it is seen that the randomization of F_1, for a fixed crack-length, can be related to an equivalent randomization of load measurements. Thus, at least in the special case of no-crack growth, the case where the calibration function, F_1, is treated as a random variable can be treated as a special case of the more general problem discussed earlier.

In the case where crack growth is permitted, an order of magnitude analysis can be used to relate the randomization of F_1 to an approximate randomization in the load. To perform this analysis a first order difference type of argument is used. First, note that the remaining ligament b can be written

$$b = b_o + \Delta b \tag{28}$$

where

b_o = initial remaining ligament, and
Δb = random variable $\ll b_o$ (in the probability sense).

Similarly the calibration function can be written

$$\hat{F}_1 = F_1 + \Delta F_1 \tag{29}$$

so that

$$b^2 \hat{F}_1 = (b_o + \Delta b)^2 (F_1 + \Delta F_1) \tag{30}$$

or retaining terms at most linear in the Δ operator the approximate result

$$b^2 \hat{F}_1 = b_o^2 (F_1 + \Delta F_1) + 2 b_o \Delta b F_1 \tag{31}$$

is obtained. The first term corresponds to a randomization in the load at

fixed crack length, while the second term corresponds to a first order correction due to crack length change.

Application to Three-Point Bend Specimen

The application of the equations of the previous section to a specific example is now considered. Nine three-point bend specimens fabricated from tooled steel were tested at 250°C (482°F). The initial crack lengths tested ranged from 16.26 to 19.05 mm (0.64 to 0.75 in.). Precracking was done at room temperature. Using results generated by Ernst [7], the material was shown to obey a Ramberg-Osgood constitutive law defined in F_1 plastic displacement space by

$$F_1\left(\frac{\Delta_{pL}}{W}, \frac{a}{W}\right) = 63\,500\left(\frac{\Delta_{pL}}{W}\right)^{0.08}$$

In order to perform the sensitivity analysis discussed earlier, it is convenient to treat the growing and nongrowing crack cases separately.

The Nongrowing Crack

First, let us assume a nongrowing crack. The objective, then, is to determine the effects of random errors in load-displacement measurements on the calculation of the J-integral. A simple FORTRAN IV program was written to perform this analysis. The values of load and displacement obtained in the laboratory were treated as nominal values. Using a zero mean Gaussian number generator, the experimental measurements were randomized. As stated previously the variance of the Gaussian random variables was taken as an input parameter for the simulation. The degree of correlation between the randomized load and displacement was an additional input parameter. A Monte Carlo simulation was then performed to generate the probability density function for J. In the simulation conducted here displacements were sampled with an interval spacing of 0.0254 mm (0.001 in.). The simulation was conducted on the basis of a sample size of 200. Results of this simulation for the case of stochastic independence of load and displacement measurements are displayed in Fig. 2. It is to be noted that as $\sigma_\Delta{}^2$, $\sigma_p{}^2$ are decreased a proportional decrease is observed in $\sigma_J{}^2$. From Fig. 2 it is also noted that the J integral, based on Gaussian uncorrelated load-displacement measurements, is also of the Gaussian type. This is just the Central Limit Theorem. In the case where $\sigma_\Delta/\Delta = \sigma_p/p = 0.01$, the size of random error commonly occurring in a laboratory test [8], standard deviations of J on the order of 1 percent were observed.

In order to determine the effect of the degree of coupling between load-cell

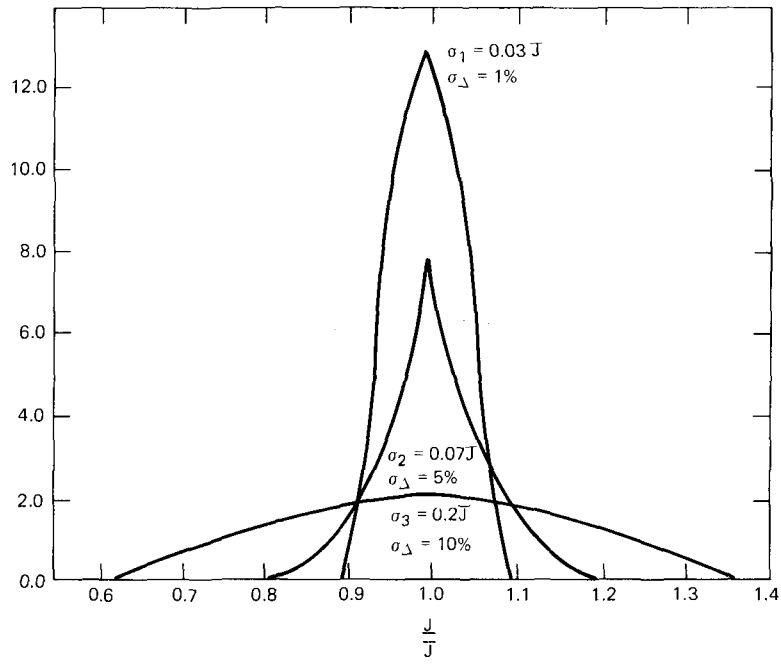

FIG. 2—*Probability density of* J-*based on Monte Carlo simulation.*

and displacement gage error on the uncertainty in J, a Monte Carlo simulation was performed for the extreme cases of independent errors and unity correlated errors. From the results illustrated in Fig. 3 it is evident that the degree of correlation in the experimentally important case discussed previously has negligible effect on the random error associated with J.

The Growing Crack

The growing crack problem is now considered. Using the method described earlier, digitized load-displacement records were randomized. Crack length extensions were calculated using the predictor-corrector equations developed previously. All tests conducted here were for the case of $\sigma_p = 0.01\,p$, $\sigma_\Delta = 0.01\,\Delta$. Monte Carlo results indicated that, as before, J is normally distributed with standard deviation $\sigma_J \sim 0.03\,J$. Crack length extensions calculated from the randomized data were comparable to those obtained for the determination check case. Additional results of the simulation indicate that for $\sigma_\Delta/\Delta = \sigma_p/p = 0.03$, standard deviation in J calculations on the order of 5 percent and variation in crack-length extension on the order of 8 percent are obtained.

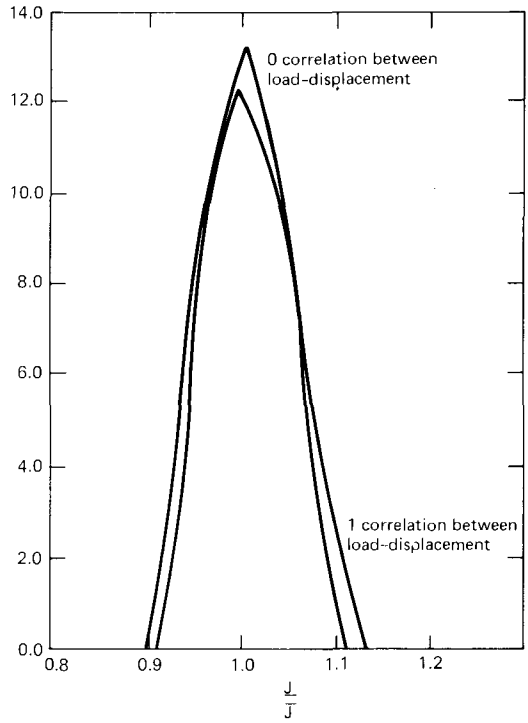

FIG. 3—*Effect of coupling on* J *distribution.*

TABLE 1—*Summary table of standard deviation of* J, Δa *based on Monte Carlo simulation.*

	Nongrowing, %	Growing, %	
σ_Δ, σ_P, %	σ_J	σ_J	$\sigma_{\Delta a}$
1	3	3.4	5
5	7	...	...
10	14	...	...
20	30	...	...

Discussion of Results

Qualitatively it is seen that the key curve method, at least for the case considered here, presents a reliable method for calculating J and crack-length change Δa. Small random errors in load displacement measurements on the order of those commonly occurring in laboratory tests lead to comparably sized error in determination of J and Δa. It is also noted that the effect of correlation of load-displacement errors is negligible for this important case.

In summary, a methodology for determining the effect of experimental random error in load-displacement measurements on J-R curve construction, based on the key curve method, has been presented. Although the numerical results presented here are limited to a specific type of specimen, the basic method is applicable to all two-dimensional configurations. Indeed, the general idea of a Monte Carlo simulation to determine confidence intervals in J-R curve construction could prove useful also for finite element based methods.

The predictor-corrector equations presented herein, in every case examined, were seen to converge within three iterations to six place accuracy. As stated before, these equations utilize only information available from a single test record and greatly facilitate the use of the key curve method.

APPENDIX

Simulation Procedure

A simple FORTRAN IV program was developed to perform the calculation necessary for computing J and Δa. This program is designed to operate in two phases. The first part deals with the creation of a data file for the calibration function, $F_1(\Delta_{pL}/W, a/W)$. As described in a previous section of this paper, load-displacement records are generated for the nongrowing cracked specimens at various a/W's. These analog records are then digitized for subsequent processing and storage either on magnetic tape or disk. Using the measured initial crack length and the compliance function, $c(a)$, a sequence of plastic displacements is calculated. Values of the calibration function, $F_1(\Delta_{pL}/W, a/W)$, are then generated using the equation

$$F_1\left(\frac{\Delta_{pL}}{W}, \frac{a}{W}\right) = \frac{pW}{b^2} \tag{32}$$

Schematically the procedure is shown in Fig. 4.

The second phase of the program deals with the calculation of J and Δa on the basis of a single load-displacement test. Here extensive use is made of the data files on the calibration function, $F_1(\Delta_{pL}/W, a/W)$, created in Part 1 of the program. Calcula-

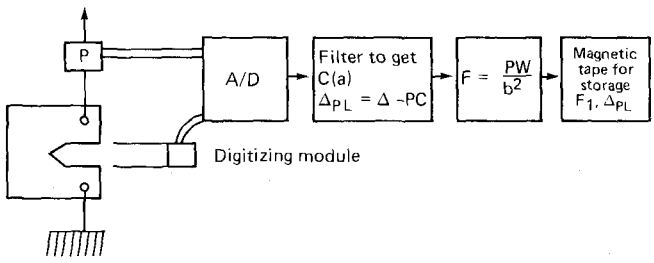

FIG. 4—*Schematic for calibration curve determination.*

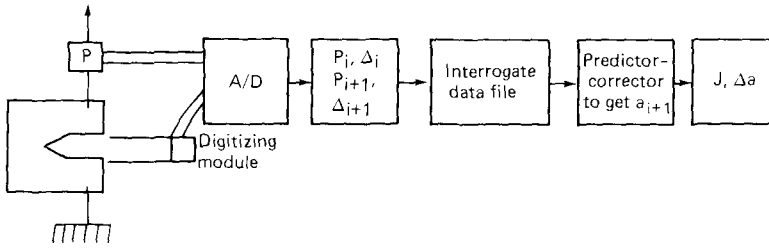

FIG. 5—*Procedure for determining* J, Δa.

tions are performed in an incremental manner. At Step i in the test the following quantities are available.

1. a_i
2. Δ_i, Δ_{i+1}
3. c_i
4. p_i, p_{i+1}
5. $(\Delta_{pL})_i$

Through interrogation of the data files created in Part 1 and Eq 32 the quantities $\partial F_1/\partial(\Delta_{pL}/W)$ and $\partial F_1/\partial(a/W)$ are evaluated.

The predictor-corrector equations are then used to obtain a_{i+1}. Using the computed value of a_{i+1}, it is simple to update the compliance and plastic displacements through the equations

$$c_{i+1} = c(a_{i+1}) \tag{33}$$

$$(\Delta_{pL})_{i+1} = \Delta_{i+1} - c_{i+1}p_{i+1} \tag{34}$$

This defines all the quantities necessary at step $i + 1$. The process is then repeated until the test is completed.

A block diagram of the procedure is illustrated in Fig. 5. It is noted that to perform the Monte Carlo simulation the basic structure of the program is unchanged. The only modification necessary is in the addition of a random input to the load-displacement measurements.

References

[1] Paris, P. C. in *Flaw Growth and Fracture, ASTM STP 631*, American Society for Testing and Materials, 1977, pp. 3-27.

[2] Rice, J. R., *Journal of Applied Mechanics, Transactions*, American Society of Mechanical Engineers, Vol. 35, 1968, pp. 379-386.

[3] Hutchinson, J. W. and Paris, P. C. in *Elastic-Plastic Fracture, ASTM STP 668*, American Society for Testing and Materials, 1979, pp. 37-64.

[4] Ernst, H., Paris, P. C., Rossow, M., and Hutchinson, J. W., "The Analysis of Load-Displacement Relationships to Determine J-R Curve and Tearing Instability Material Properties," to be published, 1978.

[5] Rice, J. R. in *Fracture*, Vol. 2, H. Liebowitz, Ed., Academic Press, New York, 1968, pp. 191-311.

[6] Tada, H. Paris, P. C., and Irwin, C. R., *The Stress Analysis of Cracks Handbook*, Del Research Corp., Hellertown, Pa., 1973.

[7] Ernst, H., to be published in Ph.D. dissertation, Mechanical Engineering Department, Washington University, St. Louis, Mo., 1978.

[8] Kirk, J., private communication.

M. G. Vassilaros,[1] *J. A. Joyce,*[2] *and J. P. Gudas*[1]

Effects of Specimen Geometry on the J_I-R Curve for ASTM A533B Steel

REFERENCE: Vassilaros, M. G., Joyce, J. A., and Gudas, J. P., **"Effects of Specimen Geometry on the J_I-R Curve for ASTM A533B Steel,"** *Fracture Mechanics: Twelfth Conference, ASTM STP 700,* American Society for Testing and Materials, 1980, pp. 251-270.

ABSTRACT: Two experiments were performed with ASTM A533B steel to evaluate effects of compact specimen geometry on the J_I versus crack growth resistance curve and evaluate validity limits for J-controlled crack growth. Side groove depth and crack length ratios were investigated with 1T compact tension specimens (1TCT) of HSST-02 plate. An investigation of thickness to ligament ratios over a broad range was conducted with 2T plan compact specimens using HSST-03 plate. All tests were performed at 150°C (302°F) using a computer-interactive unloading compliance test procedure.

Results showed that side grooves straightened the crack growth. With HSST-02 plate, total side groove depth of 20 percent is required to eliminate crack tunneling. With this steel, side grooves served to reduce J_{Ic} from nonside groove measurements and also resulted in less measurement variability. A change in slip mode from planar to cross-slip did not affect the tearing modulus measurement, which was shown to be insensitive to thickness to ligament ratios ranging from 0.63 to 3.89. The minimum ω required for J-controlled crack growth for this material was shown to be on the order of one when considering less than 6 percent crack extension.

KEY WORDS: elastic-plastic fracture, computer interactive testing, side grooves, crack extension, J-integral, A533B steel, B/b ratio, J_I-R curve, fractures (materials), crack propagation, J-controlled growth, tearing modulus

The use of the J-integral to characterize the fracture toughness of elastic-plastic materials has been shown to be valid and broadly applicable [*1*].[3] Substantial advances have been made in the development of routine single specimen J_{Ic} test procedures [*2,3*]. Importantly, the utilization of information from such testing has been expanded into the areas of crack growth beyond initiation [*4*] and instability of J-controlled crack growth [*5,6*].

[1]Metallurgist and head, respectively, Fatigue and Fracture Branch, David W. Taylor Naval Ship Research and Development Center, Annapolis, Md. 21402.

[2]Assistant professor, Department of Mechanical Engineering, U.S. Naval Academy, Annapolis, Md. 21402.

[3]The italic numbers in brackets refer to the list of references appended to this paper.

These concepts are directly related to the J_I versus crack growth resistance curve which, with HY 130 steel, has been shown to be dependent on ligament ratio and side groove geometry using compact specimens [7]. The objective of this investigation was to further explore the effects of specimen geometry using ASTM A533B steel to define possible validity limits for both J_{Ic} and J-controlled crack growth. The approach included a detailed investigation of side groove and crack length effects using 1T compact tension specimens (1TCT). An additional series of experiments was performed with 2TCT plan specimens to determine effects of the slip mode on J_{Ic} and the tearing modulus by varying the thickness to ligament ratio from 0.4 to 3.9.

Experimental Procedure

ASTM A533B steel was used for all tests. The side groove experiments were performed with material from HSST-02 plate, while the ligament ratio tests used HSST-03 plate. The chemical composition and mechanical properties of the respective plates are presented in Table 1.

For the side groove experiments, 24 modified compact specimens (1TCT) were produced according to Fig. 1. All cracks were placed in the T-L orientation. Specimens were fatigue precracked according to ASTM Test for Plane-Strain Fracture Toughness of Metallic Materials, (E 399-78) to crack lengths of 0.5, 0.6, 0.7, and 0.8 a/W, where a is the crack length and W is the specimen width. After precracking, side grooves were machined into some of the specimens with a standard Charpy cutter along the nominal crack plane to total section reductions of 10 or 20 percent. This test matrix is summarized in Table 2.

The ligament ratio tests were carried out with modified 2T compact specimens. In order to vary the ratio of specimen thickness to remaining

TABLE 1—*Chemical composition and room temperature mechanics properties of ASTM A533B steel (HSST-02 and HSST-03).*

	Chemical Composition						
	Element, weight %						
Plate	C	Mn	Ni	Mo	Si	S	P
HSST-02	0.22	1.48	0.68	0.52	0.25	0.018	0.012
HSST-03	0.20	1.26	0.56	0.45	0.25	0.018	0.011

	Room Temperature Mechanical Properties		
Plate	0.2% Yield Strength, MPa	Ultimate Tensile Strength, MPa	Total Elongation, %
HSST-02	448	621	19
HSST-03	462	613	24

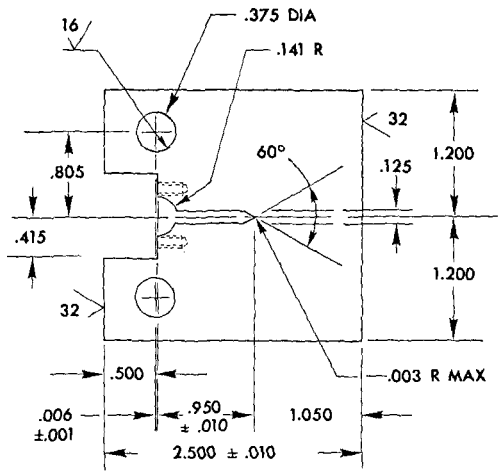

FIG. 1—*Drawing of 1T compact specimen used for side groove investigation (1 in. = 25.4 mm).*

TABLE 2—*Summary of test matrix for side groove investigation using ASTM A533B steel (HSST-02).*

	Side Groove, %		
a/W	0	10	20
0.5	2	2	2
0.6	2	2	2
0.7	2	2	2
0.8	2	2	2

[a]ASTM A533B steel, 150°C (302°F)

ligament (B/b), several specimens were produced with thicknesses of 50.8, 25.4, and 12.7 mm, respectively. Cracks were placed in the S-L orientation and fatigue cracks were produced according to ASTM E 399 criteria. Figure 2 presents the matrix of thickness to ligament ratios included in this study. It should be noted that these specimens were not side grooved.

All tests were carried out at 150°C (302°F) utilizing the computer interactive unloading compliance test facility of Joyce and Gudas [*3*]. A schematic of the test arrangement is shown in Fig. 3. This facility allows for on-line, real-time gathering and analysis of digitized load and displacement data. J_{Ic} tests are carried out by performing a series of approximately 10 percent unloading during the course of a normal fracture mechanics type test. From compliance measurements, instantaneous values of crack

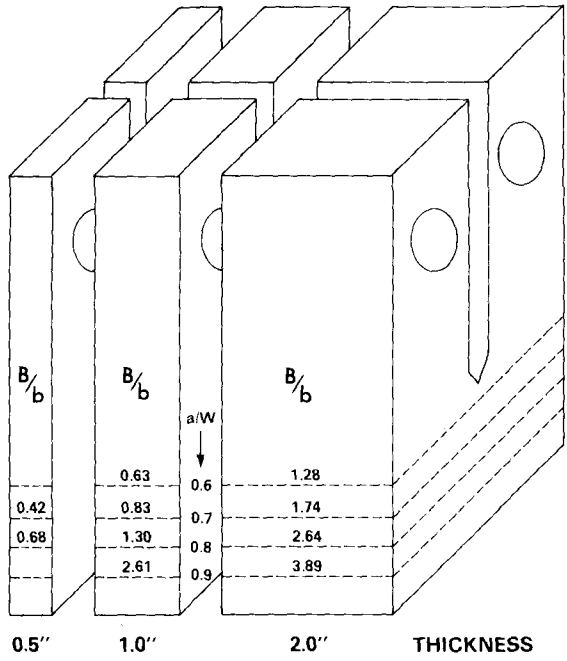

FIG. 2—*Test program for thickness to ligament ratio investigation using ASTM A533B steel (HSST-03).*

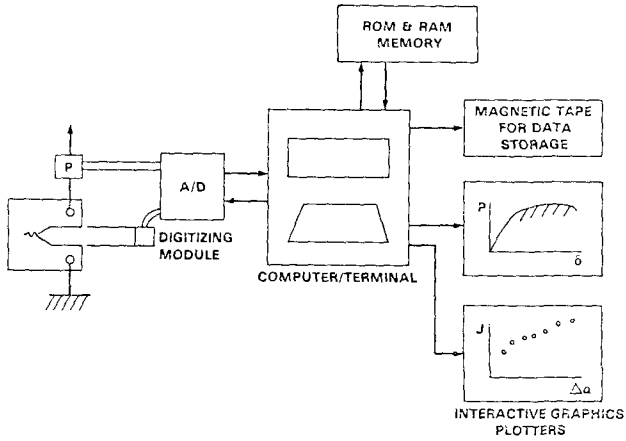

FIG. 3—*Schematic of computer interactive unloading compliance test arrangement.*

length and change in length are determined [3]. J_I is calculated according to the expression [8]

$$J_I = \frac{\beta A}{B_n(W - a)} \tag{1}$$

where

β = multiplicative factor ≈ 2 obtained from Merkle-Corten analysis of the compact specimen,
A = area under the load-displacement curve,
B_n = minimum specimen thickness,
W = specimen width, and
a = instantaneous crack length.

The compliance formula used for these calculations was that of Saxena and Hudak [9].

For 1TCT specimens, J_{Ic}-values were computed from the intersection of the crack opening stretch line ($J = 2\sigma_f \cdot \Delta a$) with the least squares fit of data points, which fell at least 0.15 mm beyond the blunting line and did not exceed 1.5 mm in crack growth from that point. For the 2TCT and 2T plan specimens, J_{Ic} was calculated from a range of total crack growth, which did not exceed 3.0 mm beyond the 0.15 mm offset of the blunting line. Tearing modulii were calculated according to the following expression [6]

$$T = \frac{E}{\sigma_o^2} \frac{dJ_I}{da} \tag{2}$$

where

T = tearing modulus,
dJ_I/da = slope of J_I versus crack extension curve,
E = elastic modulus, and
σ_o = flow stress (assumed 483 MPa).

At the conclusion of testing, specimens were heat tinted at 380°C (716°F) for 30 min to mark the extent of crack growth. After breaking open at liquid nitrogen temperature, the crack length and crack extension were measured at nine equally spaced points across the crack front including the two surfaces. An average value of the two surface measurements was used as a single point in computing crack dimension and crack growth.

Results and Discussion

Side Groove Geometry Study

The results of the 1T compact specimen tests with various side groove depths and crack lengths are described in Table 3. This table includes J_{Ic} and tearing modulus values, a summary of estimated and measured crack growth, multiples of J_{Ic}/σ_o for validity analysis, and the computed ω value at 6 percent crack extension. The ω factor has been defined by Hutchinson and Paris [*4*] as

$$\omega = \frac{b}{J}\frac{dJ_I}{da} \tag{3}$$

and the requirement that ω must be much greater than 1 was seen as sufficient criteria for J-controlled crack growth. Figures 4 through 7 are plots of J_I versus crack extension data for specimens where $a/W = 0.5$, 0.6, 0.7, and 0.8, respectively. Figure 8 is a plot of J_{Ic} versus the crack length ratio for all tests in this series, and Fig. 9 is a plot of the tearing modulii versus crack length ratio.

Several points can be made from examining these results. In the first place, the side grooves acted to eliminate crack tunneling for this material as shown previously with HY 130 steel [*7*]. Figure 10 is a photograph of specimens with a crack length ratio of 0.7. It can be seen that without side grooves, crack tunneling is substantial. However, 10 percent side grooves reduce crack tunneling, and 20 percent equalizes the crack extension across the specimen width. This degree of side grooving results in close correlation between compliance based crack growth prediction and the physical measurement as reported in Table 2.

From Fig. 8 it can be seen that the scatter of J_{Ic} data is reduced with side grooving, and J_{Ic}-values are generally below those measured with no side grooved specimens. The J_{Ic} data from 20 percent side grooved specimens is closely grouped in the range 200 to 247 KJ/m^2. Finally, it should be noted that several of the nonside grooved specimens do not meet postulated validity criteria based on requiring $B > 40\ J_{Ic}/\sigma_o$ [*1*]. These specimens demonstrated on elevation of J_{Ic} of about 50 percent when compared to side grooved specimens.

Figure 9 shows that tearing modulus measurements were generally affected by side groove depth. With this steel, specimens with 20 percent side grooves provide the lowest tearing modulus measurements at all but the largest a/W ratio. The difference in tearing modulus measurements between 10 and 20 percent side grooved specimens reflects the fact that crack front tunneling is not completely eliminated with 10 percent side grooves. Interestingly, Fig. 9 shows that tearing modulus measurements

TABLE 3—*Results of side groove investigation*[a].

Specimens	1-3[b]	1-2[b]	1-6[b]	1-1[b]	1-8[b]	1-7[b]	1-14[c]	1-15[c]	1-10[c]	1-11[c]	1-13[c]	1-12[c]
Side groove, %	0	0	10	10	20	20	0	0	10	10	20	20
J_{Ic}(kJ/m^2)	260	368	219	228	211	237	342	375	211	264	247	208
dJ_I/da	231	287	270	231	184	172	242	223	205	231	139	126
T	198	247	232	199	158	148	207	192	176	198	120	108
a_o/W	0.55	0.51	0.52	0.51	0.51	0.52	0.62	0.63	0.62	0.63	0.62	0.63
B/b	1.00	1.02	0.94	0.92	0.82	0.82	1.32	1.35	1.18	1.22	1.05	1.08
Δa predicted (mm)	1.24	...	1.37	1.78	1.35	2.62	1.12	1.57	2.01	2.06	2.44	2.29
Δa measured (mm)	1.57	2.66	1.70	2.05	1.63	2.85	1.70	2.31	2.36	2.64	2.64	2.39
$25\,J_{Ic}/\sigma_o$ (mm)	13.50	19.10	11.40	11.90	10.90	12.20	17.80	19.30	10.90	13.70	12.70	10.70
$40\,J_{Ic}/\sigma_o$ (mm)	21.60	30.50	18.00	19.10	17.50	19.60	28.20	31.00	17.50	21.80	20.60	17.30
ω(6% crack growth)	9.60	8.80	10.20	9.80	9.20	8.50	5.80	5.20	6.60	6.10	5.30	5.30
Specimen	1-18[d]	1-20[d]	1-22[d]	1-21[d]	1-23[d]	1-19[d]	1-30[e]	1-32[e]	1-26[e]	1-25[e]	1-27[e]	1-29[e]
Side groove, %	0	0	10	10	20	20	0	0	10	10	20	20
J_{Ic}/(kJ/m^2)	291	313	300	271	224	217	329	332	236	275	227	200
dJ_I/da	249	261	173	205	115	120	279	187	198	162	183	201
T	214	224	149	176	99	103	239	166	170	139	157	173
a_o/W	0.71	0.72	0.72	0.72	0.72	0.73	0.81	0.81	0.82	0.81	0.81	0.81
B/b	1.72	1.79	1.61	1.61	1.43	1.48	2.63	2.63	2.63	2.63	2.63	2.63
Δa predicted (mm)	1.96	1.96	1.35	1.73	1.83	1.85	1.45	1.88	1.96	1.78	1.75	1.78
Δa measured (mm)	2.51	2.59	1.78	2.01	2.18	2.34	2.13	2.57	2.39	2.01	2.08	2.16
$25\,J_{Ic}/\sigma_o$ (mm)	15.00	16.30	15.50	14.00	11.70	11.20	17.00	17.30	12.20	14.20	11.70	10.20
$40\,J_{Ic}/\sigma_o$ (mm)	24.10	25.90	24.90	22.40	18.40	18.00	27.20	27.40	19.60	22.90	18.80	16.50
ω(6% crack growth)	4.40	4.20	3.60	4.00	3.40	3.40	2.60	2.30	2.60	2.30	2.60	2.80

[a] ASTM A533B, HSST-02, 150°C (302°F)
[b] $a/W = 0.5$
[c] $a/W = 0.6$
[d] $a/W = 0.7$
[e] $a/W = 0.8$

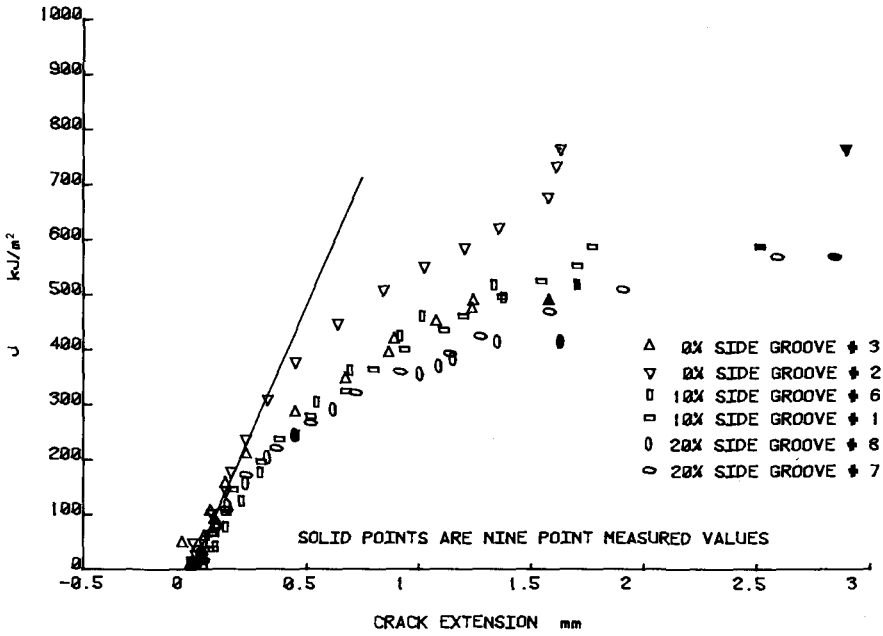

FIG. 4—J_I *versus crack extension data for, 1T compact specimens where* a/W = 0.5 *(ASTM A533B steel, HSST-02, 150°C (302°F)).*

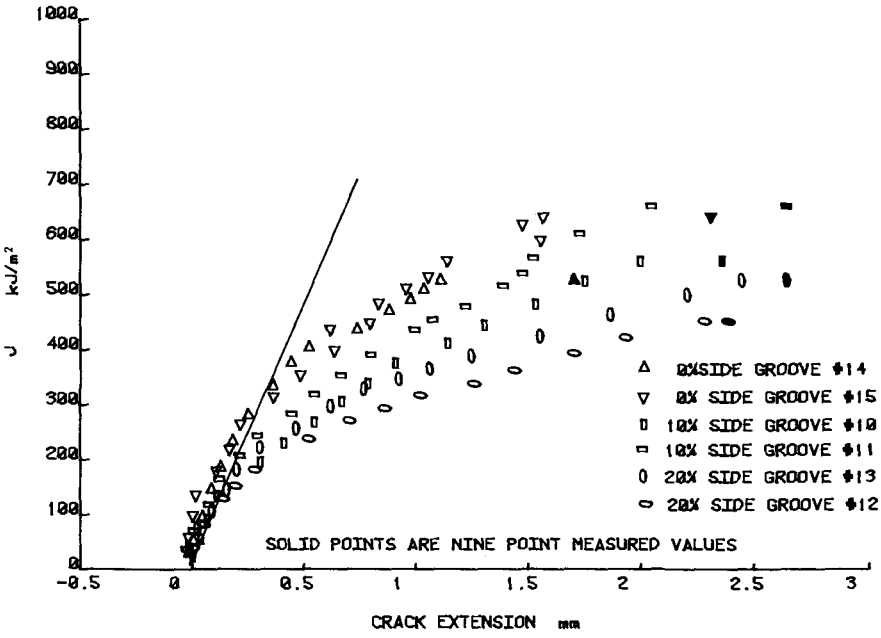

FIG. 5—J_I *versus crack extension data for 1T compact specimens where* a/W = 0.6 *(ASTM A533B steel, HSST-02, 150°C (302°F)).*

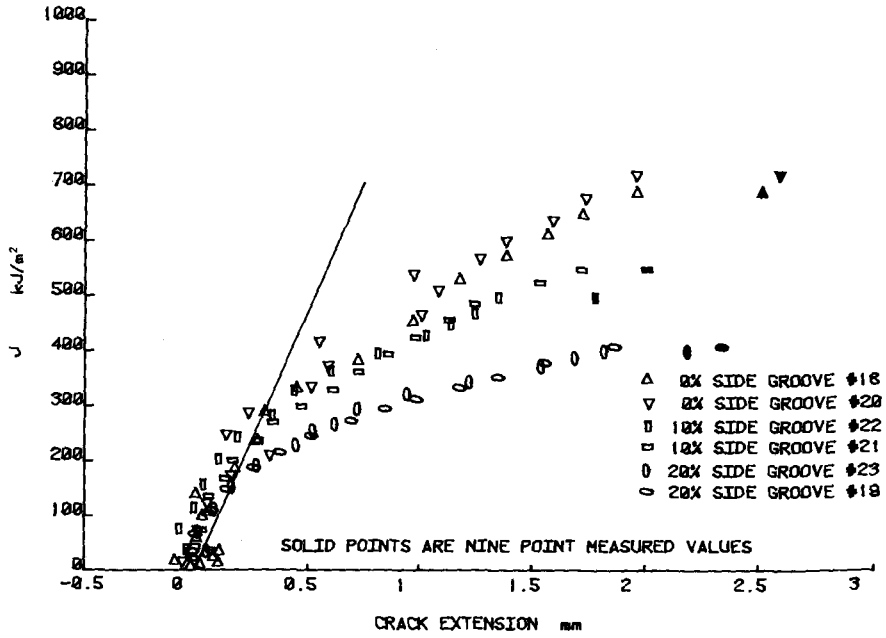

FIG. 6—J_I *versus crack extension data for 1T compact specimens where* a/W = 0.7 *(ASTM A533B steel, HSST-02, 150°C (302°F)).*

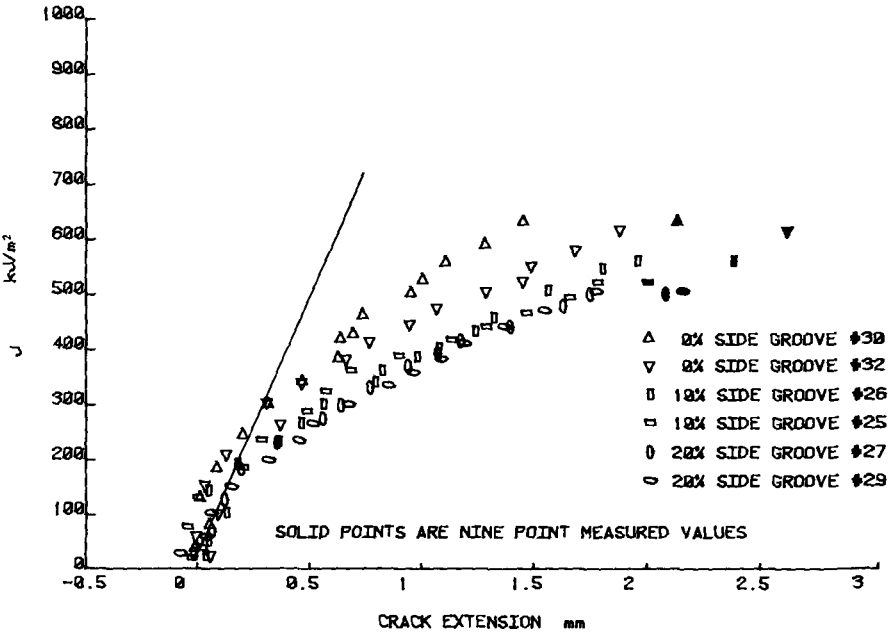

FIG. 7—J_I *versus crack extension data for 1T compact specimens where* a/W = 0.8 *(ASTM A533B steel, HSST-02, 150°C (302°F)).*

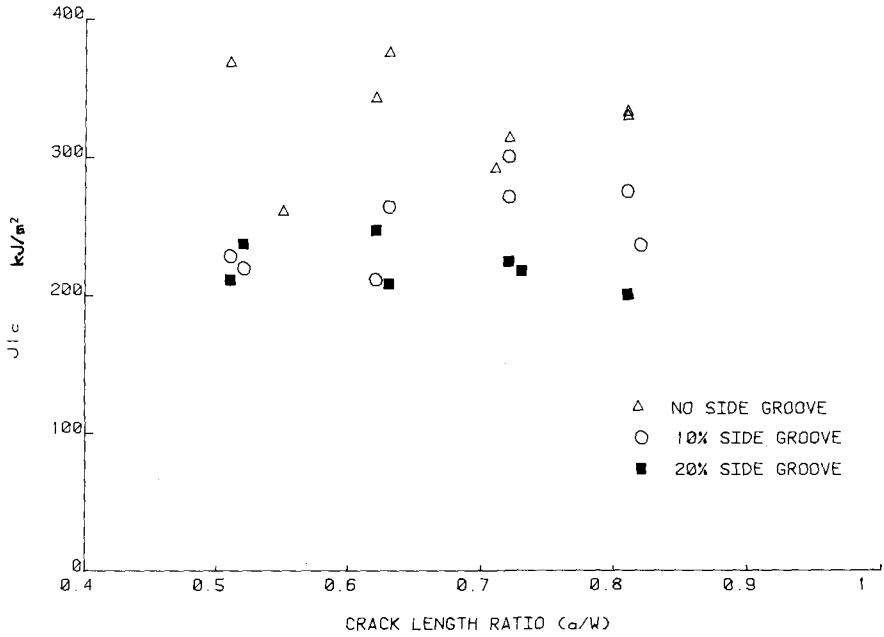

FIG. 8—J_{Ic} *versus crack length ratio for 1T compact specimens (ASTM A533B steel, HSST-02, 150°C (302°F)).*

for all specimen geometries are initially reduced with increasing crack length, then increased at the greatest crack length. The minimum tearing modulus measurements are produced in the range 0.6 to 0.7 a/W.

Thickness to Ligament Geometry Study

As stated earlier, the purpose of this experiment was to determine effects of varying slip mode on J_{Ic} and the tearing modulus of ASTM A533B steel. Figure 11 shows the type of crack growth developed in 25-mm-thick specimen with various crack lengths, and Fig. 12 shows the type of crack growth in 13, 25, and 50-mm specimens with a/W ratios of the order of 0.6. Substantial cross slip was developed in the thinnest specimens and a lesser degree of tunneling occurred in the thicker specimens. Figures 13 to 15 present the J_1 versus crack extension data for 13, 25, and 50-mm-thick specimens, respectively. Table 4 presents the results of all tests in this series in the same format as that of the side groove investigation.

As shown in the previous section, final crack extensions estimated from unloading compliance are smaller than the average from the nine-point measurement. This difference is reduced as specimen thickness increases and crack tunneling is reduced. Figure 16 is a plot of tearing modulus

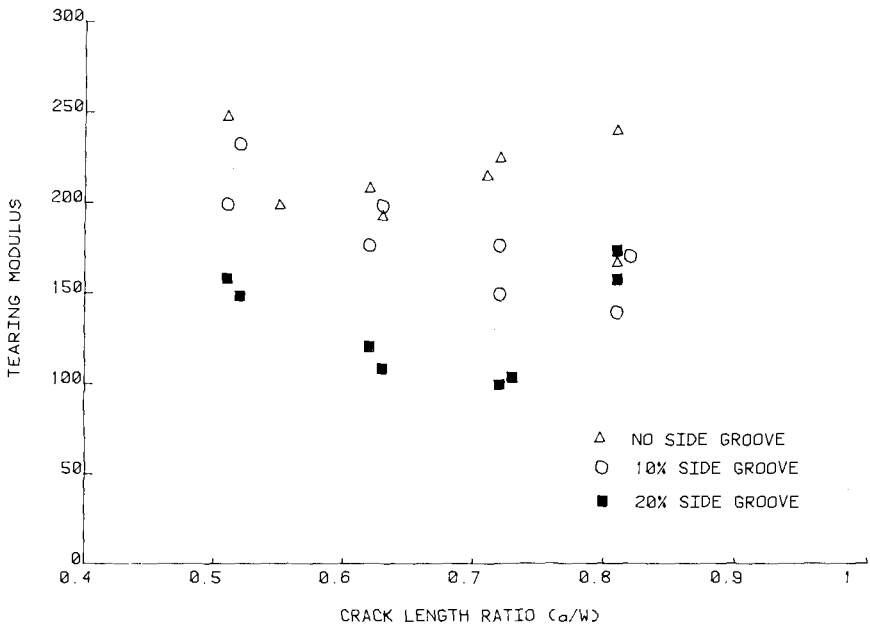

FIG. 9—*Tearing modulus measurements versus crack length ratio for 1T compact specimens (ASTM A533B steel, HSST-02, 150°C (302°F)).*

versus B/b for this test series. There is no strong dependence of T on the thickness to ligament ratio for these specimens where B/b ranged from 0.4 to 3.9. This same conclusion is reached in considering only the 50-mm specimens, which represented a B/b range of 1.5 to 3.9. Review of Table 4 shows that the tearing modulus measurements with these widely varying specimen geometries range from 97 to 128. There is no apparent pattern of T as a function of thickness and ω, where ω ranged from 1.35 to 7.87. This lack of J_I-R curve dependence on ω indicates that the minimum ω required for J-controlled crack growth may be of the order of one, and not substantially greater than one as suggested by Hutchinson and Paris [*4*]. This point is made from computations of ω for 6 percent crack growth which also coincided with the limits at which J_I - Δa data were gathered in these tests. The ω independence must be further explored with greater ranges of crack growth and with different materials.

From Table 4, it can be also seen that J_{Ic} as calculated here is apparently dependent upon specimen thickness. J_{Ic} from 50-mm specimens is consistently greater than J_{Ic} measured from 25 and 13-mm-thick specimens. This is at least partly due to the method of measuring J_{Ic} by fitting a straight line to a parabolic J_I-R curve. However, superposition of Figs. 14 and 15 shows that the J_I-R curves for thicker specimens are generally elevated

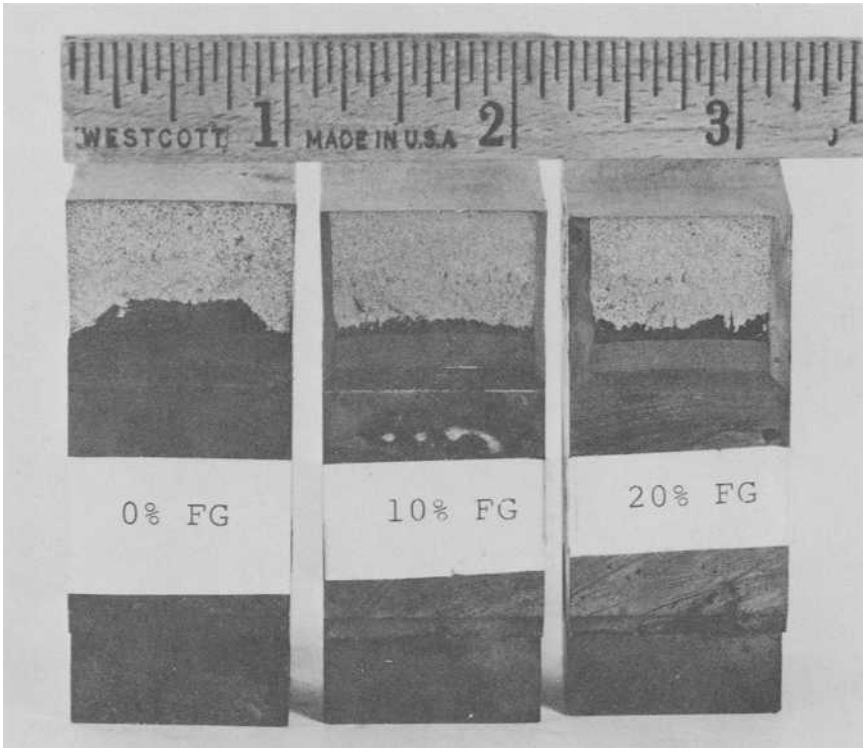

FIG. 10—*1T compact specimens of ASTM A533B steel, (HSST-02) where* a/W = *0.7.*

above those of thinner specimens along their complete length, and calculating J_{Ic} using only 1.5 mm of crack extension would give results similar to those presented in Table 4.

In this cross-slip investigation, one 2T specimen was tested with 20 percent side grooves. It is interesting to note that the J_{Ic}-value was reduced from other 2T specimens, and the dJ_I/da measurement was the lowest in this set of data. Figure 15 includes this specimen and as shown in the side groove experiment, crack growth was straight for this specimen geometry.

Conclusions

The objective of these two investigations was to explore the role of specimen geometry on the three parameters J_{Ic}, T, and ω at 6 percent crack growth. The principal variables included side groove depth, crack

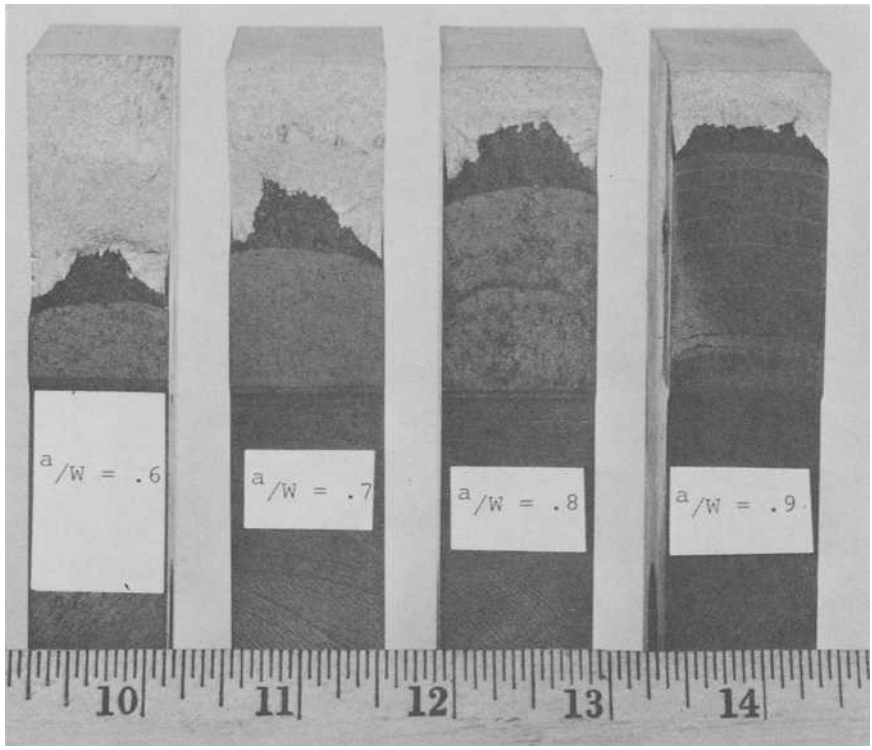

FIG. 11—*Twenty-five millimetre thick, 2T compact specimens of ASTM A533B steel (HSST-03) with various crack lengths.*

length, and thickness to ligament ratio. The following conclusions are warranted from these tests with ASTM A533B steel conducted at 150°C (302°F):

1. Side grooves in compact specimens serve to straighten the front of crack growth and result in lower J_1 versus crack growth resistance curves and resultant tearing modulus values than nonside grooved specimens;

2. Side groove depth on the order of 20 percent is required to fully straighten the crack front and result in agreement between unloading compliance and physical crack extension measurements;

3. J_{Ic}-values are somewhat reduced when side grooves were employed both for 1T and 2T specimen geometries, but less variability was present in the side groove results;

4. The mode of slip when varied from planar to cross slip does not effect the tearing modulus measurement. The tearing modulus is insensitive to

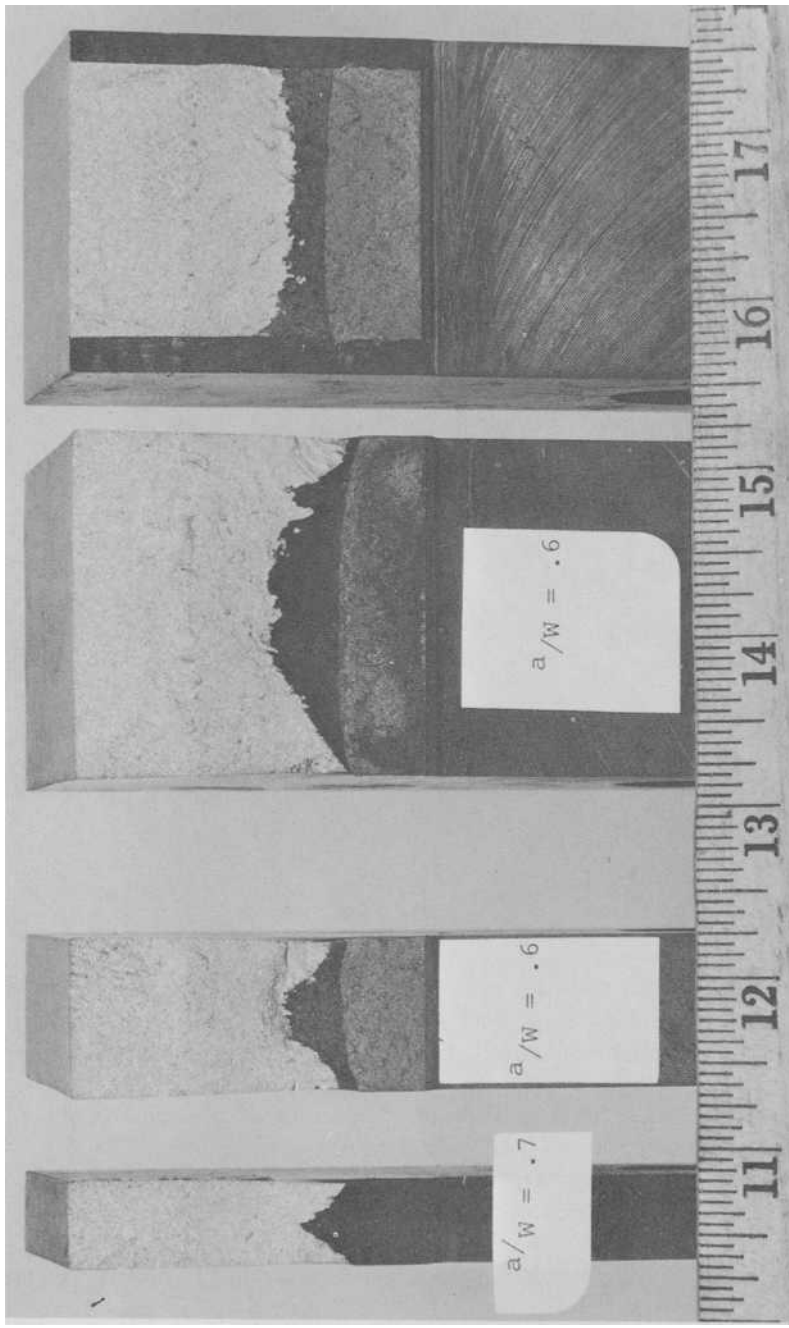

FIG. 12—*Thirteen, twenty-five, and fifty-one millimetre thick, 2T compact specimens of ASTM A533B steel (HSST-03) with a/W of the order of 0.6.*

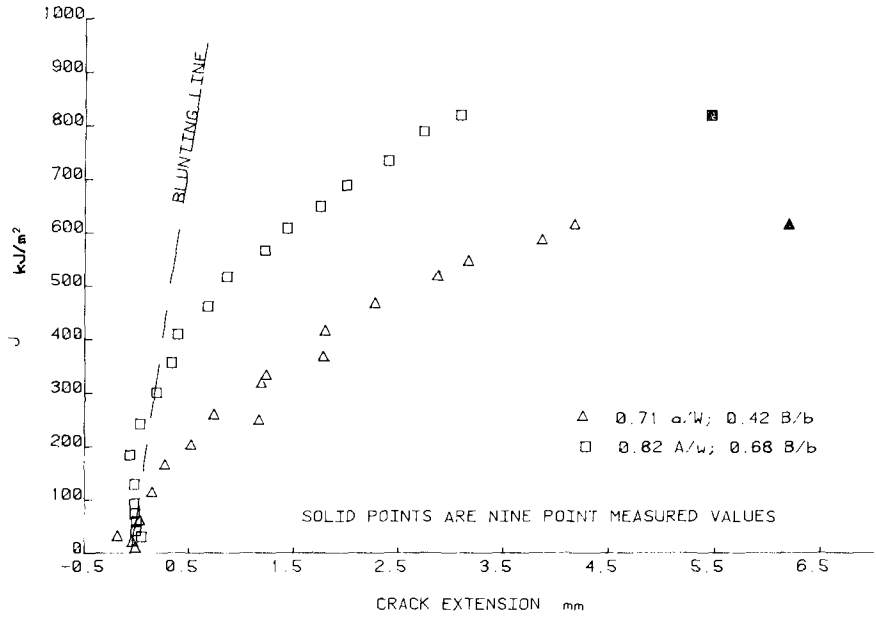

FIG. 13—J_I *versus crack extension data for 13-mm-thick 2T compact specimens (ASTM A533B steel, HSST-03, 150°C (302°F)).*

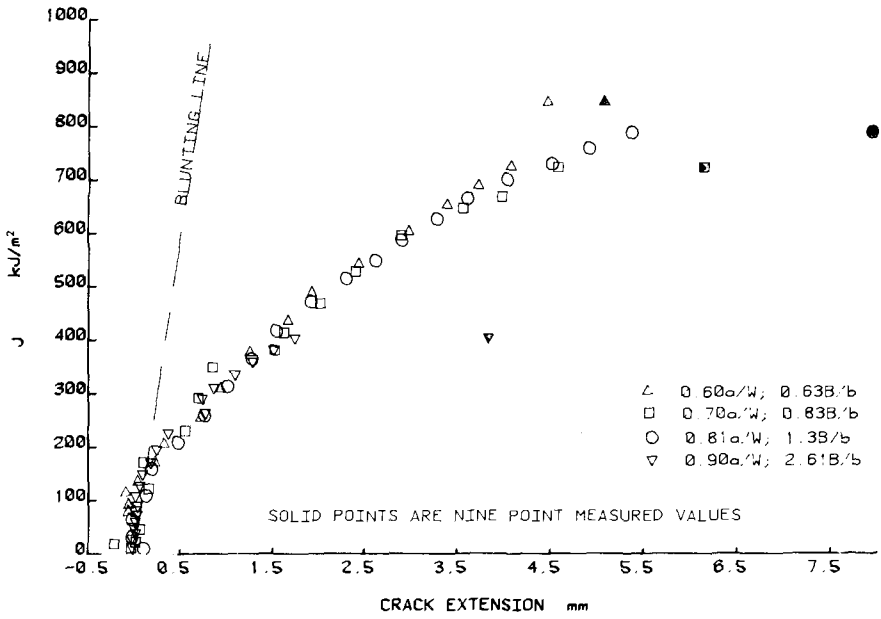

FIG. 14—J_I *versus crack extension data for 25-mm-thick 2T compact specimens (ASTM A533B steel, HSST-03, 150°C (302°F).*

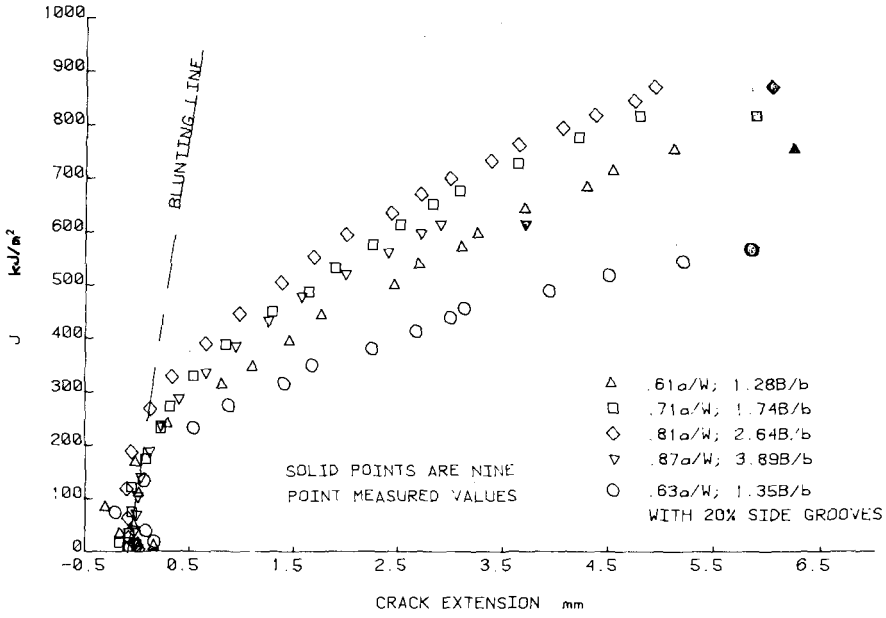

FIG. 15—J_I *versus crack extension data for 2T compact specimens (ASTM A533B steel, HSST-03, 150°C (302°F)).*

TABLE 4—*Results of thickness to ligament investigation.*

Specimen	FOE-6[b]	FOE-9[b]	FOE-1[c]	FOE-2[c]	FOE-4[c]	FOE-4[c]	FOC-2[d]	FOC-3[d]	FOC-5[d]	FOC-4[d]	FOC-1[d]
Side groove, %	0	0	0	0	0	0	0	0	0	0	20
J_{1c}(kJ/m^2)	166	440	208	211	187	216	251	303	332	286	213
dJ_1/da	130	146	144	141	149	126	113	135	139	126	82
T	112	125	124	121	128	108	97	116	120	109	70.60
a_o/W	0.71	0.82	0.60	0.70	0.81	0.90	0.61	0.71	0.81	0.87	0.63
B/b	0.42	0.68	0.63	0.83	1.30	2.61	1.28	1.74	2.64	3.89	1.35
Δa predicted (mm)	4.17	3.07	4.50	4.57	5.36	1.73	5.10	4.88	5.03	3.07	5.87
Δa measured (mm)	6.20	5.46	5.08	6.15	7.95	3.84	6.25	5.89	6.05	3.71	5.84
$25\,J_{1c}/\sigma_o$ (mm)	7.10	18.80	8.90	8.90	7.90	9.10	10.70	13.00	14.20	12.50	9.10
$40\,J_{1c}/\sigma_o$ (mm)	11.20	30.00	14.20	14.50	12.70	14.70	17.00	20.80	22.60	19.80	14.50
ω(6% crack growth)	5.40	2.40	7.90	5.30	3.20	1.35	6.70	4.40	2.60	1.71	5.80

[a] ASTM A533B, HSST-03, 150°C (302°F)
[b] B = 12.7 mm
[c] B = 25.4 mm
[d] B = 50.8 mm

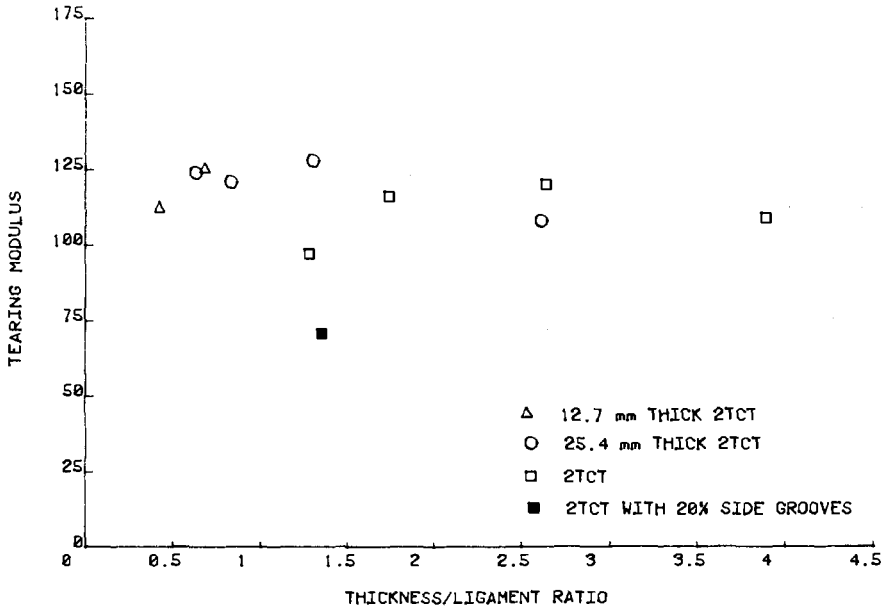

FIG. 16—*Tearing modulus measurements versus thickness to ligament ratio for 2T compact specimens (ASTM A533B steel, HSST-03, 150°C (302°F)).*

thickness to ligament ratios ranging from 0.63 to 3.89 in compact specimens;

5. The minimum ω required for J-controlled crack growth may be on the order of one when considering 6 percent or less crack extension.

Acknowledgments

The authors acknowledge the sponsorship of the U.S. Nuclear Regulatory Commission and the support of Pedro Albrecht in this research. Further, the contribution of Westinghouse Research Laboratory and J. D. Landes in preparing the 1TCT specimens is appreciated. The assistance of Edwin Hackett in performing the fracture mechanics tests is recognized.

References

[1] Begley, J. A. and Landes, J. D. in *Fracture Mechanics, ASTM STP 514,* American Society for Testing and Materials, 1972, pp. 1-20.

[2] Clarke, G. A., Andrews, W. K., Paris, P. C., and Schmidt, D. W. in *Mechanics of Crack Growth, ASTM STP 590,* American Society for Testing and Materials, 1976, pp. 27-42.

[3] Joyce, J. A. and Gudas, J. P. in *Elastic-Plastic Fracture, ASTM STP 668,* American Society for Testing and Materials, 1979, pp. 451-468.

[4] Hutchinson, J. W. and Paris, P. C. in *Elastic-Plastic Fracture, ASTM STP 668,* American Society for Testing and Materials, 1979, pp. 37-64.
[5] Paris, P. C., Tada, H., Zahoor, A., and Ernst, H. in *Elastic-Plastic Fracture, ASTM STP 668,* American Society for Testing and Materials, 1979, pp. 5-36.
[6] Paris, P. C., Tada, H., Zahoor, A., and Ernst, H. in *Elastic-Plastic Fracture, ASTM STP 668,* American Society for Testing and Materials, 1979, pp. 251-265.
[7] Gudas, J. P., Joyce, J. A., and Davis, D. A. in *Fracture Mechanics, ASTM STP 677,* C. W. Smith, Ed., American Society for Testing and Materials, 1979 pp. 474-485.
[8] Merkle, J. G. and Corten, H. T., *Journal of Pressure Vessel Technology, Transactions,* American Society of Mechanical Engineers, Vol. 96, Nov. 1974, pp. 286-292.
[9] Saxena, A. and Hudak, Jr., S. J., "Review and Extension of Compliance Information for Common Crack Growth Specimens," *International Journal of Fracture,* Vol. 14, No. 5, Oct. 1978, pp. 453-468.

S. J. Garwood[1]

Measurement of Crack Growth Resistance of A533B Wide Plate Tests

REFERENCE: Garwood, S. J., **"Measurement of Crack Growth Resistance of A533B Wide Plate Tests,"** *Fracture Mechanics: Twelfth Conference, ASTM STP 700,* American Society for Testing and Materials, 1980, pp. 271-295.

ABSTRACT: Nine 500-mm-wide, 110-mm-thick A533B Class I wide plates were tested at +70°C (158°F). Three crack types were used: (1) semi-elliptical, (2) surface notched, and (3) through-thickness center cracked. Various notch depths were employed. The progress of the stable propagating ductile tear resulting in the specimen from the use of the relatively stiff wide-plate rig was marked periodically using an unloading technique.

Estimates of the crack propagation resistance J_R-curves for these tests were made and compared to resistance curves obtained from small scale laboratory bend specimens.

The crack morphology exhibited by the surface notched wide-plate specimens, which propagate in the through-thickness direction, was essentially normal ductile rupture in contrast to the through-thickness crack, which showed mostly shear rupture.

Semi-elliptical notched specimens initially behaved in a similar fashion to the surface notched, and after penetration of the plate thickness, continuing propagation behaved as a center cracked plate.

Derivations of a simple estimation formula for the J_R-curves for the surface notched and semi-elliptical geometries have been made. Using these formulas, comparisons of all tests with the crack propagating in the L-T and L-S orientations were made.

The results of large-scale tension and large- and small-scale bend tests indicate that laboratory tests give reasonable lower bound estimates of the more structurally relevant tension situation in the L-T orientation where full-plate-thickness bend specimens are employed.

In the L-S orientation much more restrictive thickness requirements are necessary to achieve conservative estimates from laboratory bend tests and as an initial guideline the requirement $B > 25(J_R/\sigma_Y)$ is suggested for surface notched geometries although this may not be restrictive enough for very ductile materials.

KEY WORDS: ductile fracture, fracture toughness, steels, elasto-plastic analysis, crack initiation, crack propagation, geometry, shape, fracture (materials)

[1]Senior research engineer, The Welding Institute, Abington Hall, Abington, Cambridge, U.K.

Nomenclature

A Aspect ratio ($a_{max}/2c$)
a Crack length
a_{max} Maximum length, through thickness, of semi-elliptical notch.
a_o Initial crack length
B Specimen thickness
c Half-length of surface of semi-elliptical notch
D Specimen height
G_R G resistance (the value of crack extension force after some crack growth)
J The J-integral
J_R J resistance
L Constraint factor
L-T Specimen extracted in the rolling direction, notched in the transverse plane
L-S Specimen extracted in the rolling direction, notch through the thickness
P Load
q Displacement
R Resistance to fracture
S Span
U Energy under load displacement record
W Specimen width
Z Knife edge thickness
Δa Incremental crack extension
η Multiplication factor relating J and U
σ_u Ultimate tensile stress
σ_Y Yield stress
e Elastic
i Initiation
L Limit load value
n Current value
p Plastic
Y Yield value

The measurement and analysis of the crack growth resistance of structural steels has received much recent attention [*1-6*].[2] Ongoing studies have involved the adaptation of existing yielding fracture mechanics to attempt to characterize the behavior of a crack in structural steel extending by a ductile mechanism in the presence of large-scale plasticity [*5,6*]. The intention of this research is to solve the current problem concerning the determination of allowable flaw sizes, in particular for the nuclear industry.

[2]The italic numbers in brackets refer to the list of references appended to this paper.

Current assessment techniques tend to use the initiation of tearing as a measure of the material toughness. However, this seems an unduly conservative approach when viewed in the light of subsequent large toughness increases in crack growth resistance with crack extension often exhibited by these ductile materials.

The behavior of the material with crack extension can be measured in terms of the crack growth resistance or R-curve [*1,2,6*]. If a move is to be made away from the use of initiation of tearing as the characteristic toughness value, then the measure of toughness to be employed must be obtained from a consideration of the resistance curve of the material and the relevant driving force curve, which describes the applied loading conditions.

It would appear that the resistance curve is not a material parameter being dependent on test piece geometry [*6–8*]. The object of this test program is to evaluate the possibility of using laboratory test piece resistance curves to describe the behavior of the more structurally significant large-scale tension tests with through thickness, surface and semi-elliptical cracks.

Analysis

Recent work has concentrated on the use of the J-integral for describing the resistance of a stable tear. Initially any crack extension was considered by many to cause an invalidation of the theoretical justification of the use of the J-integral for elastic-plastic materials [*9,10*]. This argument was based on the fact that the nonlinear elastic analog, which is the premise upon which the J-integral is applied to elastic-plastic materials, can only be relevant to monotonic loading. Hence crack growth, with its accompanying relaxation of the original crack tip, invalidates this premise.

Recently, theoretical justifications have been made allowing the use of J-integral procedures for the description of crack growth, provided a "*J* dominant field" is maintained [*11*]. This condition is dependent on the parameter $\omega = (dJ)/(da)(W - a)/(J)$ which has to be $\gg 1$. Other investigations have intimated that crack growth should not exceed 6 percent of the remaining ligament for steels such as A533B [*5*], and for the center cracked tension geometry the size requirement of 25 to 50 J/σ_{flow} should be increased to 200 J/σ_{flow} [*12*].

Prior to these theoretical justifications, resistance curve measurements have been made with cracking extending beyond the now prescribed limits for *J* dominance [*2,6,8*]. This has been done on the basis that no theoretical claims have been made for J_R measurements. Instead the J_R techniques developed have been assumed to provide comparative estimates of the toughness that would be experienced in contained yielding structural situations; that is, the G_R resistance curve.

Evaluation of J_R for the standard test geometries is based on measurement of the area under the load displacement diagram. For extensive amounts of

tearing, corrections must be made to these area measurements to take account of the crack extension that has occurred. Initially, a method known as the "three-parameter technique" based on the *J-U* relationship developed by Rice, Paris, and Merkle [*13*] and Sumpter [*14*] was employed. However, a simpler estimation method has been developed based on the final load and displacement measurements [*15*]. The comparison of these methods was carried out in Ref *6*, and a good correlation obtained between the simple estimation and three-parameter techniques with the former technique providing conservative estimates.

This simple estimation method was originally developed for the three-point bend and center cracked tension (CCT) geometries in Ref *6*. However, the method is extended to compact tension (CT), single edge notched specimens (SENT), and semi-elliptical geometries in the Appendix.

To summarize, the formulas used for J determinations in this paper were as follows:

For bend with $0.4 < a_o/W < 0.7$ (Ref *16* sets these limits of applicability)

$$J_n = \frac{P_n q_n}{B(W - a_n)} + \frac{L\sigma_Y}{S}(W - a_n)q_p \tag{1}$$

L was assumed to be 1.3 for the geometry chosen.
For CCT

$$J_n = \frac{P_n q_p(1 - 2\eta_e) + 2\eta_e P_n q_n}{2B(W - 2a_n)} + \frac{L\sigma_Y q_p}{2} \tag{2}$$

L was assumed to be 1.155 for this geometry [*14*].
For single edge notch tension (see Appendix)

$$J_n = \frac{P_n q_n(1 - \eta_e) + \eta_e P_n q_n}{2B(W - a_n)} + \frac{L\sigma_Y q_p}{2} \tag{3}$$

L was also taken as 1.155
For semi-elliptical surface notched tension (see Appendix)

$$J_n = \frac{P_n q_n}{2B\left(\frac{WB}{\pi c_n} - \frac{a_{\max_n}}{2}\right)} + \frac{L\pi c_n}{2B}\,\sigma_Y q_p \tag{4}$$

For a conservative estimate L was assumed to be unity.

Experimentation

Specimen Design

Nine 508-mm-wide, 110-mm-thick, 915-mm-long tension specimens were tested in the wide-plate rig. All tests were on parent plate in the "as received" condition to A533B specifications. The chemical and mechanical properties are given in Table 1. Three types of notch were employed: (1) surface, (2) semi-elliptical, and (3) center cracked, see Fig. 1. Hence, crack propagation is through thickness for the surface notched (SENT) (that is, the L-S orientation), while the CCT geometry has a crack in the L-T orientation. The semi-elliptical notch behaves as a combination of SENT-CCT with propagation both through the plate thickness and along the width of the specimen. Three of each notch type were used with different a/W ratios.

Seven types of bend specimen were employed (see Table 2). Types 1, 4, 5, and 6 were extracted in the L-T orientation with 2, 3, and 7 in the L-S orientation. Full thickness (110 mm) specimens were used for Types 1, 2, and 6 with widths of 250, 125, and 500 mm, respectively. Types 3, 4, 5, and 7 were half thickness (53 mm) with widths of 65, 250, 125, and 125 mm, respectively. All specimens had an initial a_o/W of 0.4.

Experimental Details

All tests were carried out at +70°C (158°F) to ensure fully ductile behavior of the A533B employed.

All bend tests were conducted using a conventional 1800 kN hydraulic universal machine at a crosshead speed of 2 mm/min. Load was monitored against crosshead displacement, which was corrected for extraneous displacement by indenting the rollers into the broken halves of the specimen after the test, as described in Ref *17*.

For the wide-plate tension tests, load was monitored against the displacement of the clip gage mounted across the mouth of the notch in the center of the specimen with a knife edge spacing of 17.5 mm. Moveable knife edges were employed since periodic adjustments of the knife edge spacing was necessary due to the large displacement encountered in the tests. It was unnecessary to correct for extraneous displacement in these tests because of the use of a mouth opening mounted clip gage.

To remount the clip gage, periodic unloadings to zero of the wide place specimens were necessary. All tests in this program behaved in an entirely stable manner achieving a maximum load with stable tearing, via microvoid coalescence, continuing thereafter under a decreasing load. In the majority of the bend tests, initiation of tearing occurred after net section yield of the specimen but well before maximum load.

TABLE 1—*Properties of Steel to A533B Employed.*

Chemical Compositions, weight %

C	S	P	Si	Mn	Ni	Cr	Mo	V	Cu	Nb	Ti	Al	B	Pb	Sn	Co
0.20	<0.005	0.006	0.20	1.39	0.59	0.12	0.50	<0.01	0.10	<0.005	<0.01	0.023	<0.001	<0.01	0.01	0.01

Mechanical Properties at +70°C (158°F) of A553B

Yield Stress, N/mm^2, σ_Y	Tensile Strength, N/mm^2, σ_u	Elongation, %	Reduction of Area, %
465	600	30	65

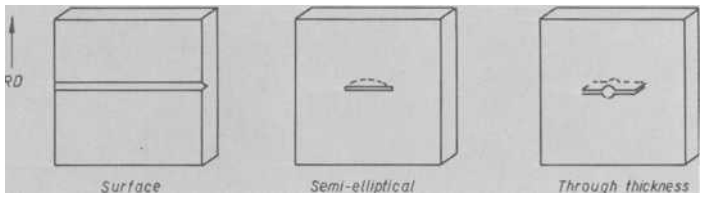

FIG. 1—*Crack types—wide plate specimens.*

Type 6 bend and the wide plate tests, however, experienced net section yield and initiation of tearing at very similar displacements.

Prior to testing, all specimens were fatigue precracked. The bend specimens were precracked according to British Standards Institute's (BSI) DD19 specifications [*18*]. The surface notched and semi-elliptical wide plates were fatigued in bending. Some difficulty was experienced in obtaining a fatigue crack in the latter specimens. Specimen 1006 with $D/W = 0.21$ had little or no fatigue propagation, and hence the initial notch diameter would approximate to the thickness of the abrasive slitting wheel used to cut the initial notch of 0.15 mm. Specimen 1007 also had a fatigue crack length of <1 mm in places along the crack front. The center cracked specimens were fatigued in two halves as three-point bend specimens, and the halves were electron beam welded to form the wide-plate specimens.

The Type 6 bend specimens had to be tested using a clamp and beam arrangement to double the effective load of the test machine since these specimens required a center point load of ~ 3000 kN.

To obtain crack growth resistance curves for the smaller bend specimens it was necessary to load a series of specimens to various displacements to achieve different amounts of crack extension. The specimens were then unloaded, cooled to below the transition temperature, and fractured to reveal the amount of stable tearing. This "break open" procedure was also used for the wide-plate specimens. However, it was found that the periodic unloadings during the test had left marks on the fracture surface presumably caused by the fracture faces coming together at the crack tip when complete unloading occurred (Fig. 2). Hence, it was possible to plot a number of points for these specimens and to obtain an approximate resistance curve from each individual specimen. This "unloading marking" method was also found to work on the larger bend tests (Types 1, 4, and 6). Test results involving repeated unloadings were compared with monotonically loaded specimens, and very similar values were obtained indicating little or no effect of the unloadings on the load, displacements, or amounts of stable crack growth experienced.

After final fracture of each specimen, average measurements of initial crack length and the amounts of stable tearing were taken.

TABLE 2—*Nominal Dimensions of A533B Bend Specimens.*

Type	*a/W*	*B*	*W*	Span	Notch Orientation	Comments
1	0.4	110	250	1000	L-T	three off each for *R*-curve determinations
2	0.4	110	125	500	L-S	
3	0.4	55	63	250	L-S	
4	0.4	55	250	500/1000	L-T	
5	0.4	55	125	500	L-T	nutcracker arrangement to give effective span width of 8:1
6	0.4	110	500	≡4000	L-T	
7	0.4	55	125	500	L-S	
5	0.4	55	125	500	L-T	four off each for initiation determinations
7	0.4	55	125	500	L-S	

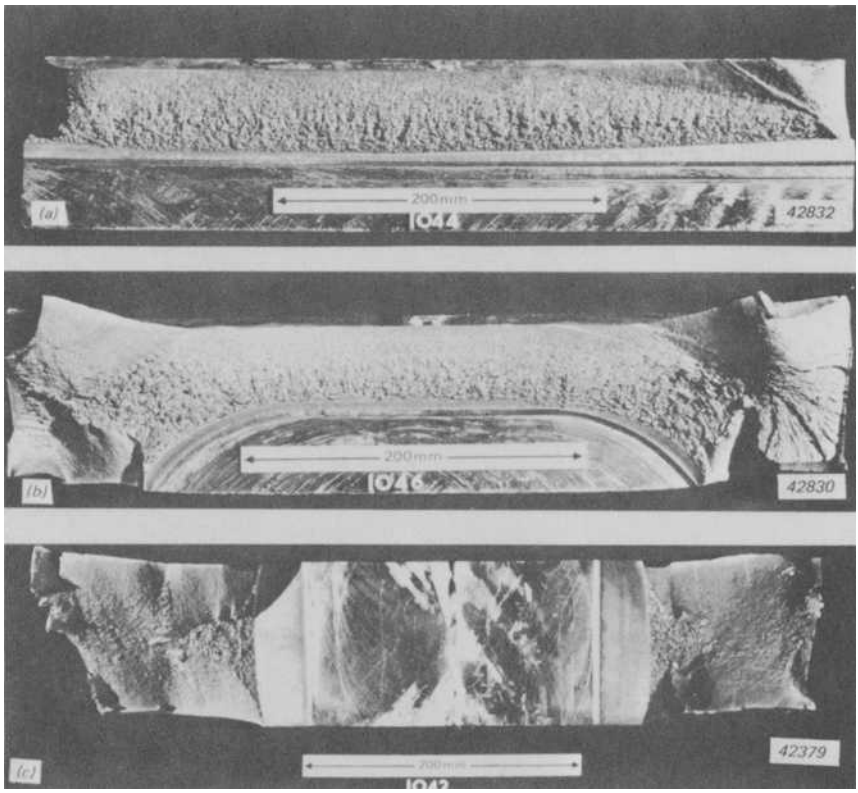

FIG. 2—*Wide plate fracture surfaces* (a) *surface notch,* (b) *semi-elliptical, and* (c) *center cracked.*

Alternating current potential-difference-monitoring of crack extension was carried out on all tests; however, determination of initiation and the accuracy of stable crack determinations were found to be inconsistent. Where potential measurements could be calibrated from unloading crack marks however, it was found possible to evaluate the shape of the resistance curve between these points by using crack extension measurements derived from the potential difference readings.

Results

Initiation Determination

The aim of this test program was to evaluate the geometric and orientation dependence of the R-curve in A533B. Since the entire resistance curves were being monitored, very few specimens were stopped with small amounts

of crack extension; therefore, the initiation of tearing value for the different geometries was not obtained directly. Values could be derived from the potential difference traces, but these results must be treated with extreme caution. In view of this, four Type 5 and Type 7 (100-mm-wide, 50-mm-thick) specimens in the L-T and L-S orientations were tested following ASTM Subcommittee E24.01 on Fracture Mechanics Test Methods, Task Group 9 recommendations [*19*] to evaluate initiation values in the two test orientations. The results of these tests are given in Fig. 3. Unlike Ref *19* specifications, this figure plots values of J against crack extension excluding stretch zone. This obviates the need for a blunting line construction and initiation values can be read off the figure at $\Delta a = 0$. These are 0.4 MJ/m^2 and 0.3 MJ/m^2 for the L-T and L-S orientations, respectively. The slope of the resistance curve was obtained employing a linear regression analysis.

Although, as stated previously, accurate initiation values were not obtained for the other specimen types the results obtained would indicate very similar values to those obtained in Fig. 3 for the relevant crack orientation.

Bend Resistance Curves

In all, seven specimen types were tested. Results for Types 1, 4 to 6 in the L-T orientation are given in Fig. 4, while Types 2, 3, and 7 in the L-S orientation are depicted in Fig. 5.

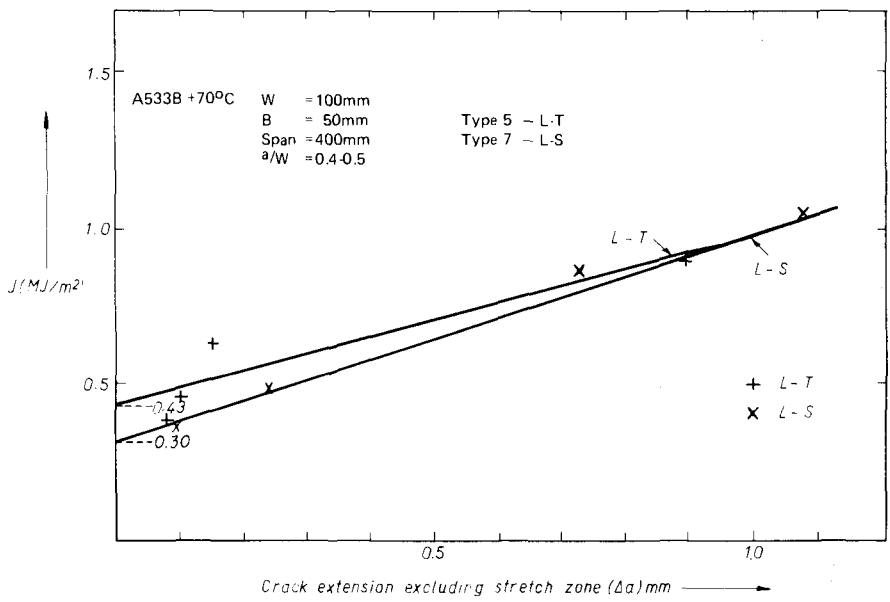

FIG. 3—*Initiation determination from bend specimens in the L-T and L-S orientations.*

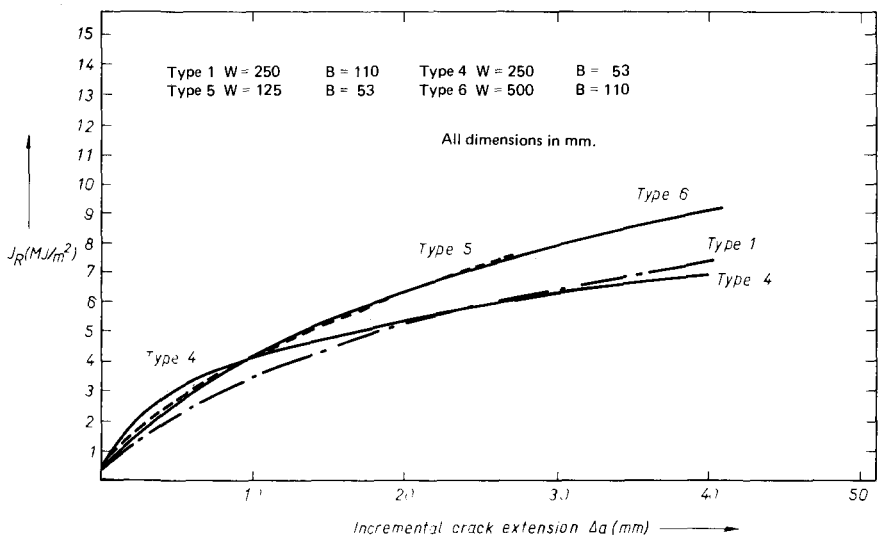

FIG. 4—*Bend resistance curves L-T orientation.*

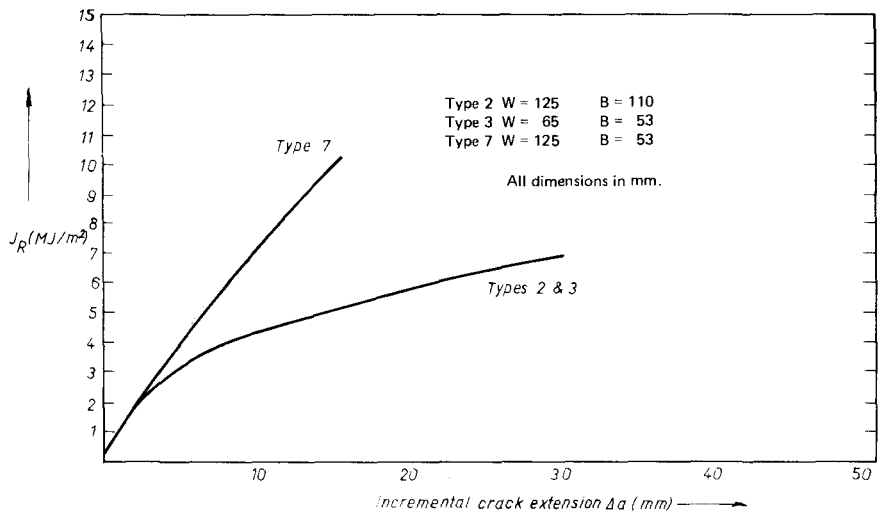

FIG. 5—*Bend resistance curves L-S orientation.*

In all cases J_R-values were calculated using the formula given in Eq 1 based on the final load, corrected total, and plastic displacements and final crack length.

Wide Plate Tension Tests

Three center cracked tests were carried out, the results from which are shown in Fig. 6. Three different $2a_o/W$ ratios were used (0.27, 0.42, and 0.52). Each point marked on the figure indicates an unloading position. J_R estimates were made using Eq 2 with the incorporation of the correct η_e factor based on the gage length of the measurement point to the width of specimen ratio (D/W), and the $2a/W$ ratio. In this instance D/W was the knife edge spacing divided by 508 mm, which was approximately 0.03. Although the knife edge spacing was altered during the test, the value of η_e was found to be insensitive to this change in the D/W when compared to the dependence on $2a/W$. Values of η_e were found to be in the range 2.0 to 0.5 for $2a/W$ between 0.3 and 0.8. Crack propagation in these specimens was in the L-T orientation.

Single edge notch tension specimens were tested with three a_o/W ratios (0.3, 0.34, and 0.47).

These specimens were surface notched along the 508-mm edge (see Fig. 1); hence, these tests had an effective width of 110-mm and thickness of 508-mm with crack propagation in the L-S orientation.

Results of these tests are given in Fig. 7. J_R calculations were carried out

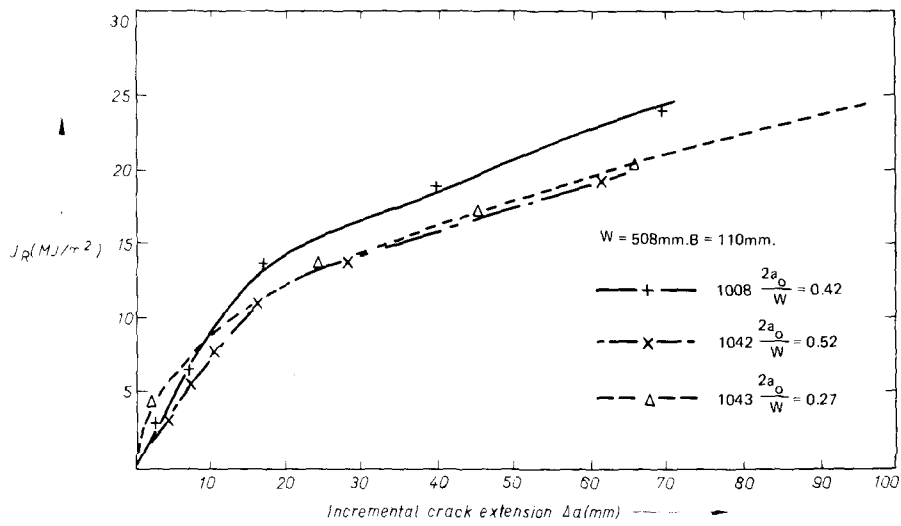

FIG. 6—*Crack propagation resistance, center crack tension.*

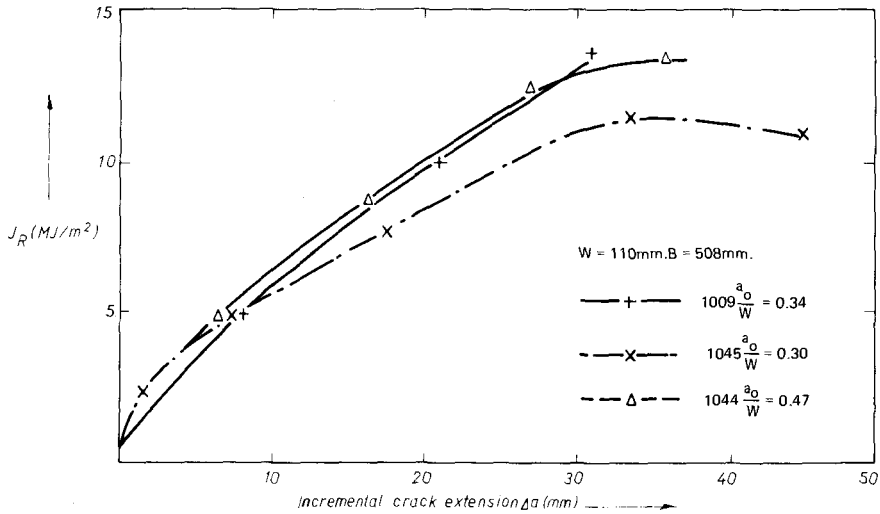

FIG. 7—*Crack propagation resistance, single edge notch tension.*

using Eq 3, which is derived in the Appendix. η_e values in this case were found to vary between 5 and 1.9 for a/W in the range 0.3 to 0.8.

The final three wide-plate specimens had semi-elliptical surface defects as shown in Fig. 1. All specimens had an $a_{max}/2c$ ratio of 0.16 with a_{max}/W ratios of 0.21, 0.34, and 0.5. As in the single edge notch tests, width was taken as 110 mm and specimen thickness as 508 mm. Crack propagation occurred in both through thickness (a) and width ($2c$) directions (see Fig. 2).

J_R calculations were made using Eq 4, as determined in the Appendix, for initial propagation of the crack, which is assumed to occur at a constant aspect ratio with a_{max} and $2c$ being defined by actual measurements at each unloading point. Once the crack had propagated through thickness, the CCT analysis was assumed to apply as given by Eq 2.

Values of J_R for this geometry are plotted against average crack extension in Fig. 8.

For the initial part of the curve this incremental crack extension is the average through-thickness extension, while for the final section, which behaves as a CCT specimen with two crack fronts, Δa refers to propagation along one crack front only.

Discussion

Bend Tests

The initiation of tearing toughness in the L-T orientation would appear higher than in the L-S direction as evident from Fig. 3 (which gives J_i's of 0.4

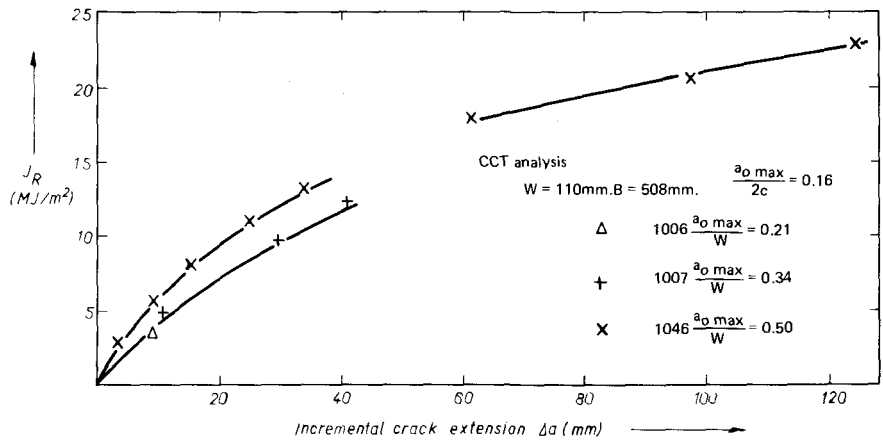

FIG. 8—*Crack propagation resistance, semi-elliptical notch tension.*

and 0.3 MJ/m^2, respectively). Subsequent propagation would indicate a steeper slope for the L-S orientation with the same value of toughness being obtained for both orientations after 1 mm of crack extension. When viewed in the light of the scatter, which is normally experienced with J_i determinations using the multispecimen technique, however, the results in Fig. 3 show very similar behavior between the orientations.

The effect of different specimen configurations in the L-T orientation can be seen in Fig. 4. A distinct geometric dependence is evident but there is a complicated relationship between width and thickness and their effect on the resistance curve. Generally the larger the B/W ratio the lower the resistance curve. In this orientation, however, there appears little effect of width on the full thickness plate results. Type 6 with a 500-mm width does give a higher resistance curve than the Type 1 with 250-mm width, but the difference is small compared to the effect of crack orientation in the wide plate tests.

Figure 5 depicts the geometric effect in the L-S orientation. Here a much larger effect is exhibited than in Fig. 4. Types 2 and 3, with similar B/W ratios, follow the same resistance curve, while Type 7 with a smaller ratio has a much steeper R curve.

Wide Plate Tests

The behavior of the center cracked wide plates is shown in Fig. 6. Similar curves are obtained for all three specimens. There would appear to be little effect of the $2a_o/W$ ratio.

A typical fracture face for the CCT geometry is shown in Fig. 2. Crack extension in this geometry starts with normal ductile rupture tunneling in the center of the specimen with 45 deg shear lips forming near the surfaces. As

extension proceeds so the shear lip width increases, until after 40 mm of crack extension full 45 deg shear occurs. The knee in the resistance curve would appear to coincide with the point on the fracture surface when the shear lips are almost fully formed.

The crack growth resistance curves relating to the surface (or single edge) notched specimen behavior are given in Fig. 7. As in the CCT case, no absolute effect of the a_o/W ratio can be ascertained. Since the crack is propagating through thickness these curves relate to the L-S orientation. A typical fracture surface is shown in Fig. 2 (the major portion of the fracture surface being normal rupture, small shear lips forming near the surface).

From Fig. 7 it can be seen that a peaking of the resistance curve appears to occur after 35-mm of crack extension. This phenomenon could be attributed to the reduction in the percent of shear fracture present due to the increasing bending component and hence constraint factor, as the crack approaches the back surface of the specimen.

The semi-elliptical surface notched specimens behaved in a similar fashion to the SENT test specimens, with the majority of the fracture surface being formed of normal ductile rupture. In this case however, the shear lips tended to form on the front surface of the specimen inhibiting crack extension in the thickness ($2c$) direction (see Fig. 2). In the center of the specimen however, the crack appears to propagate with an almost constant $a_{max}/2c$ ratio until the crack penetrates the back surface after which further extension occurs as if the specimen were center cracked.

This behavior makes analysis particularly difficult. As stated in the Appendix, a J_R analysis of the semi-elliptical crack can be approached in three ways. The conservative approach is to assume propagation through thickness only. The least conservative way assumes propagation with a constant $a_{max}/2c$ ratio. The most realistic assumption would seem to be assuming a constant $a_{max}/2c$ ratio but impose the actual value of a_{max} (which is incidentally the maximum through thickness value rather than the average as in the other geometries) and $2c$ which exist at each unloading position. This should still provide a conservative estimate since the resulting crack front geometry assumed will leave a larger remaining ligament than actually present in the test geometry. Once the crack becomes through thickness the CCT formulations apply.

Values of J_R using the constant aspect ratio with test a_{max} and $2c$ values are plotted in Fig. 8 for the three specimens tested. If any trend due to a_{max}/W ratio is to be interpreted from this figure it would be that the larger the ratio, and thus the nearer the specimen is to becoming a CCT geometry, the steeper the R-curve.

The resistance curve for specimen 1046 propagating as a through-thickness crack (L-T orientation) is also plotted in Fig. 8, which would appear to be remarkably consistent with prior propagation in the semi-elliptical mode (L-S orientation).

A comparison of results from the bend and tensile tests is made in Fig. 9. The entire bend result scatter band falls below the CCT scatter band enhancing confidence in the use of the bend geometry tests for the conservative prediction of structural resistance curves using full-thickness specimens.

In contrast, nonconservative estimates of more structurally relevant geometries result in the L-S orientation, particularly for the initial part of the curve, as can be seen from inspection of Fig. 10. Good correlation is obtained between semi-elliptical and surface notched defects, however, which is consistent with their similar fracture appearance.

The major reason for the steeper bend resistance curves in the L-S orientation is due to thickness effects. The wide plates had an effective thickness of 508 mm, while the maximum thickness of the bend specimens tested was 110 mm. Hence, the fracture surface of the bend tests contained a much larger shear lip proportion than did their tensile counterparts.

Therefore, to provide conservative estimates of through-thickness propagation (L-S orientation), some thickness criteria are obviously necessary. As a first approximation the plane strain requirements specified in British Standard (BS) 5447 [*20*] could be applied, that is

$$B > 2.5\left(\frac{K_{Ic}}{\sigma_Y}\right)^2 \tag{5}$$

in terms of J this converts to

$$B > 2.5\frac{EJ}{\sigma_Y{}^2} \tag{6}$$

For the specimens tested herein where $J_i = 0.3$ MJ/m^2, B would have to be greater than 720 mm and even thicker if more representative values of toughness after some crack extension occurred were used.

A more reasonable criterion would be to adopt the ASTM E24:01:09 Task Group recommendations [*19*] over the entire range of the resistance curve for plane strain validity; thus

$$B > 25\frac{J_R}{\sigma_Y} \tag{7}$$

Hence, on the basis of the results from the SENT geometry at initiation ($J_i = 0.3$ MJ/m^2) a thickness $B > 16$ mm would be required; after 10-mm crack extension ($J_R \simeq 6.5$ MJ/m^2) $B > 355$ mm; and after 20-mm extension ($J_R \simeq 10$ MJ/m^2) B would have to be >547 mm for continuation of plane-strain conditions.

These requirements would not be necessary, of course, if full-thickness

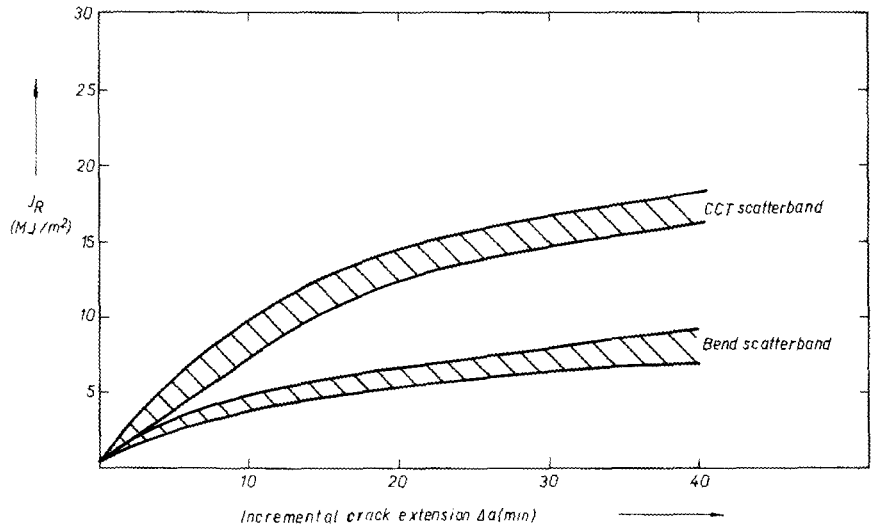

FIG. 9—*Resistance curve comparison, L-T orientation.*

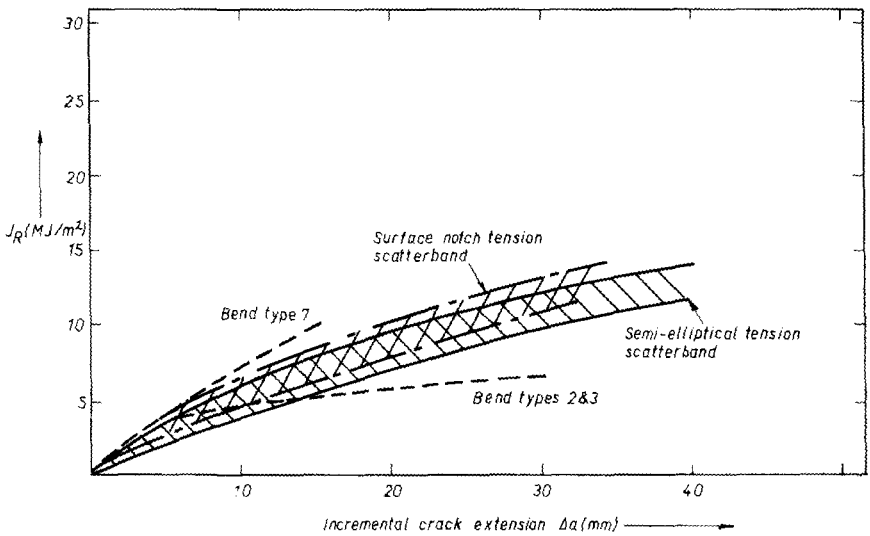

FIG. 10—*Resistance curve comparison, L-S orientation.*

plate specimens are employed for the description of crack propagation in the L-T orientation, since although they would not necessarily be plane strain curves they should still provide conservative estimates of the structural curve.

Conclusions

1. The initiation toughness of A533B plate tested in the L-T and L-S orientations was determined as 0.4 and 0.3 MJ/m^2, respectively. Although the initiation toughness was slightly lower in the L-S orientation, the initial resistance curve slope was steeper. Hence, generally similar behavior was exhibited by the two orientations.

2. Three-point bend specimen tests in the L-T and L-S orientations with variable width and thickness indicated distinct geometric effects on the crack propagation resistance curves. Generally the larger the thickness to width ratio the lower the resistance curve. However, the indications are that once a certain thickness is reached there is little effect of width on the resistance curve. The geometric effect which does exist indicates the smaller the width the more conservative the result.

3. Center-cracked wide plates form much larger shear lips than their equivalent thickness bend counterparts and exhibit much steeper resistance curves. Hence, provided full thickness bend specimens are employed conservative resistance curves should always be obtained for most structural applications with cracking in the L-T orientation.

4. Surface and semi-elliptical notched wide plate specimens having crack propagation in the L-S orientation behave in a very similar fashion for the initial period of crack propagation. However, once the semi-elliptical crack breaks through to the back surface of the specimen the test specimen behaves as a CCT with propagation in the L-T orientation.

5. In the L-S orientation conservative resistance curves are not necessarily obtained from bend specimens of thickness equivalent to the plate thickness. In this orientation the thickness must be governed by plane strain thickness requirements and as an initial guide it is suggested that the ASTM E24.01.09 Task Group guidelines are extended to R curve testing in this orientation. This gives the requirement

$$B > 25 \frac{J_R}{\sigma_Y}$$

to provide conservative estimates of tensile resistance curves in the L-S orientation. There is no evidence to suggest that such severe restrictions are necessary for crack length or width, and in fact it would appear that the smaller the width the lower the R-curve.

Acknowledgments

The views expressed in this paper are those of the author and do not necessarily represent the policy of the Nuclear Installations Inspectorate whose sponsorship of this work is gratefully acknowledged. The author wishes to thank B. A. Wakefield and the staff of the Brittle Fracture Laboratories of The Welding Institute for their assistance with the experimental work reported in this paper.

APPENDIX

The Determination of J_R (the Value of J for a Propagating Crack) from a Single Specimen for SENT and Semi-Elliptical Surface Notch Tension (SESNT) Geometries

The calculation of J_R for the three-point bend and center-cracked tension geometries was derived in Ref *6* and the relevant formulas stated in Eqs 1 and 2.

The method is based on a postulated loading curve of the crack length of interest (Fig. 11).

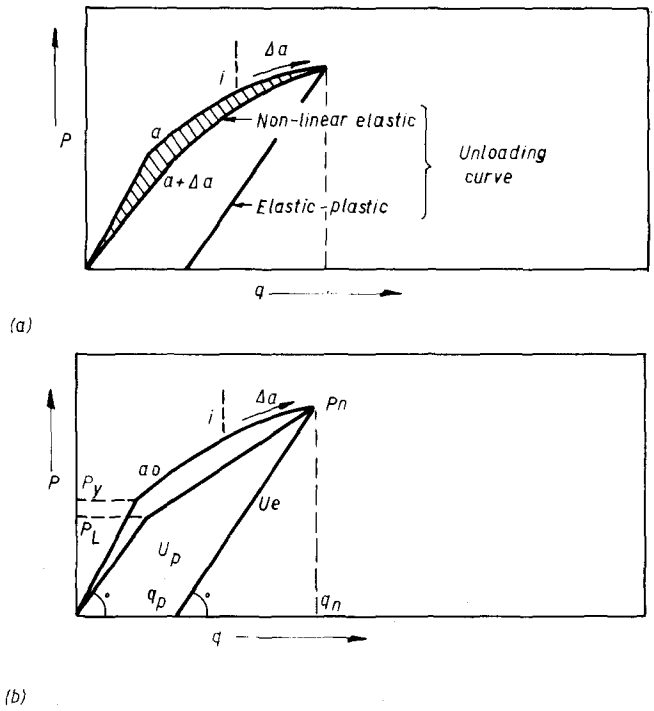

FIG. 11—*Postulated load-displacement diagrams:* (a) *actual load displacement record and postulated nonlinear elastic behavior,* (b) *an approximation to the nonlinear elastic curve.*

The area under this curve (U total) is given by

$$U \text{ total} = U_p + U_e \tag{8}$$

where

$$U_p = \frac{P_n + P_L}{2} q_p \tag{9}$$

$$U_e = \frac{P_n}{2}(q_n - q_p) \tag{10}$$

The plastic component of J can be derived from the equation

$$J_p = -\frac{d(U_p)}{Bda} |q_p \tag{11}$$

assuming rigid plastic behavior (that is, $P_n = P_L$ in Eq 9)
then

$$J_p = -\frac{1}{B} \frac{d(P_L)q_p}{da} |q_p \tag{12}$$

for the SENT geometry

$$P_L = L\sigma_Y B(W - a) \tag{13}$$

then

$$J_p = L\sigma_Y q_p \tag{14}$$

since for rigid plastic behavior

$$q_p = \frac{U_p}{P_L} \tag{15}$$

then

$$J_p = \frac{U_p}{B(W - a_n)} \tag{16}$$

The value of J after crack initiation can be related to the elastic and plastic areas under the postulated load displacement diagram by

$$J = J_e + J_p = \frac{\eta_e U_e}{B(W - a_n)} + \frac{\eta_p U_p}{B(W - a_n)} \tag{17}$$

from Eq 16

$$\eta_p = 1$$

Hence, by combining Eqs 9, 10 and 11

$$J = \frac{\eta_e P_n (q_n - q_p)}{2B(W - a_n)} + \frac{(P_n + P_L) q_p}{2B(W - a_n)} \tag{18}$$

and rearranging and substituting for P_L from Eq 13 gives, for the SENT geometry

$$J = \frac{P_n q_p (1 - \eta_e) + \eta_e P_n q_n}{2B(W - a_n)} + \frac{L\sigma_Y q_p}{2} \tag{19}$$

The semi-elliptical surface notched tension geometry is very difficult to analyze because of the curved crack front and propagation in both width and thickness directions.

To obviate the need for the lengthy and difficult calculation of η_e two approaches can be applied.

(1) For large plastic displacements the elastic contribution (U_e) could be ignored, or (2) For large plastic displacements since $U_e < U_p$, and, except for very deep cracks for the tension geometries $\eta_e > \eta_p$, a less conservative assumption than the first approach is to assume that $\eta_e = \eta_p$ hence

$$J = \frac{\eta_p U \text{ total}}{\text{remaining ligament area}} \tag{20}$$

If the crack is assumed to be semi-elliptical and limit load is based on the remaining ligament area then

$$P_L = L\sigma_Y \left(WB - \frac{\pi a_{\max} c}{2} \right) \tag{21}$$

To calculate J-values in this configuration three different assumptions can be applied:

(1) Assume propagation through thickness only, that is, in the a direction using actual $a_{\max}$ measurements;

(2) Assume propagation at a constant aspect ratio ($A = a_{\max}/2c$) measurements using actual $a_{\max}$; and

(3) Assume (2) with actual measurements of both $a_{\max}$ and c.

Assuming Propagation Through Thickness Only That is, constant c

from Eqs 12 and 21

$$J = \frac{L\sigma_Y \pi c}{2B} q_p \tag{22}$$

then substituting for q_p from Eq 15 and for P_L from Eq 21

$$J = \frac{\pi c}{2B} \frac{U_p}{\left(WB - \frac{\pi a_{\max} c}{2} \right)} \tag{23}$$

therefore

$$\eta_p = \frac{\pi c}{2B} \tag{24}$$

Hence, assuming $\eta_e \simeq \eta_p$ and since

$$U \text{ total} = \frac{P_n q_n}{2} + \frac{P_L q_p}{2} \tag{25}$$

therefore from Eq 20

$$J_{(c)} = \frac{\pi c}{2B} \frac{P_n q_n + P_L q_p}{2\left(WB - \frac{\pi a_{\max} c}{2}\right)} \tag{26}$$

substituting for P_L from Eq 21 in Eq 26 gives

$$J = \frac{\pi c}{4B} \frac{P_n q_n}{\left(WB - \frac{\pi a_{\max} c}{2}\right)} + \frac{\pi c}{4B} L\sigma_Y q_p \tag{27}$$

Assuming propagation at constant A ($= a_{\max}/2c$)

Rearranging Eq 21 with $A = a_{\max}/2c$

$$P_L = L\sigma_Y BW\left(1 - \frac{\pi a_{\max}^2}{4WBA}\right) \tag{28}$$

then from Eqs 12 and 21

$$J = \frac{2\pi a_{\max}}{4WBA} L\sigma_Y W q_p \tag{29}$$

that is

$$\eta_p = \frac{\pi a_{\max}}{2AB} = \frac{\pi c}{B}$$

then substituting for q_p from Eq 15 and for P_L from Eq 28

$$J = \frac{2\pi a_{\max}}{4WBA} \frac{U_p}{B(1 - \pi a_{\max}^2/4WBA)} \tag{30}$$

then assuming $\eta_e \simeq \eta_p$ from Eq 25 and substituting for P_L from Eq 28

$$J_{(A)} = \frac{P_n q_n}{2B\left(\dfrac{2WBA}{\pi a_{\max}} - \dfrac{a_{\max}}{2}\right)} + \frac{\pi a_{\max} L \sigma_Y q_p}{4AB} \tag{31}$$

Note that Eq 31 is exactly twice the numerical value of Eq 27.

Assuming propagation at constant A *with test values of* c *and* $a_{\max}$

If Eq 31 is used with current values of c and $a_{\max}$ it can be rearranged by substitution of $A = a_{\max}/2c$ to give

$$J = \frac{P_n q_n}{2B(WB/\pi c_n - a_{\max}/2)} + \frac{\pi c_n}{2B} L \sigma_Y q_p \tag{32}$$

For the CT geometry Merkle and Corten [*21*] give the η_p factor as

$$\eta_p = \frac{2(1 + \alpha)}{(1 + \alpha^2)} \tag{33}$$

where

$$\alpha = \sqrt{\left(\frac{2a_n}{W - a_n}\right)^2 + 2\left(\frac{2a_n}{W - a_n}\right) + 2} - \left(\frac{2a_n}{W - a_n} + 1\right) \tag{34}$$

therefore Eq 17 becomes for the CT geometry

$$J = \frac{\eta_e U_e}{B(W - a_n)} + \frac{2(1 + \alpha) U_p}{(1 + \alpha^2) B(W - a_n)} \tag{35}$$

Combining Eqs 9, 10, and 35 gives

$$J = \frac{\eta_e P_n (q_n - q_p)}{2B(W - a_n)} + \frac{(P_n + P_L) q_p}{B(W - a_n)} \frac{(1 + \alpha)}{(1 + \alpha^2)} \tag{36}$$

where P_L in Eq 36 is given by

$$P_L = L \sigma_Y B \alpha (W - a_n) \tag{37}$$

A simpler form of Eq 36 may be obtained using the analysis of Ref *22*, which is similar to the Merkle and Corten approach with the exception of an assumption that the CT specimen has a moment arm of $(a_n + 0.6(W - a_n))$. Using this expression the limit load equation becomes

$$P_L = \frac{L \sigma_Y B (W - a_n)^2}{4(0.4a_n + 0.6W)} \tag{38}$$

Using Eq 38 in the analysis described above (see SESNT section) gives

$$\eta_p = 1 + \frac{1}{0.6 + \dfrac{0.4a_n}{W}} \tag{39}$$

and the J estimation formula becomes

$$J = \frac{P_n q_p \left(1 + \dfrac{1}{0.6 + \dfrac{0.4a_n}{W}} - \eta_e\right) + P_n q_n \eta_e}{2B(W - a_n)} + \frac{L}{2}\left[1 + \frac{1}{0.6 + \dfrac{0.4a_n}{W}}\right] \frac{\left(1 - \dfrac{a_n}{W}\right)}{\left(0.6 + \dfrac{0.4a_n}{W}\right)} \sigma_Y q_p \tag{40}$$

References

[1] Novak, S. R., *Resistance to Plane-Stress Fracture (R-Curve Behavior) of A572 Structural Steel, ASTM STP 591,* American Society for Testing and Materials, 1974.

[2] Tanaka, K. and Harrison, J. D. "An R-Curve Approach to COD and J for an Austenitic Steel," Welding Institute Report 7/1976/E and *Welding Research Abroad,* Vol. 24, No. 3, March 1978, pp. 2-21.

[3] Paris, P. C., Tada, H., Zahoor A., and Ernst, H., "The Theory of Instability of the Tearing Mode of Elastic-Plastic Crack Growth," NUREG 0311, U.S. Nuclear Regulatory Commission, 1977; see also *Elastic Plastic Fracture, ASTM STP 668,* American Society for Testing and Materials, 1979, pp. 5-36.

[4] Hahn, G. T., Broek, D., Marshall, C. W., Rosenfield, A. R., Rybicki, E. F., Schmueser, D. W., Stonesifer, R. B., and Kannien, M. F., "Elastic-Plastic Fracture Mechanics for Nuclear Pressure Vessels: A Preliminary Appraisal—Tolerance of Flaws in Pressurised Components," International Mechanical Engineers' Conference, London, May 1978.

[5] Shih, C. F., de Lorenzi, H. G. and Andrews, W. R. in *Elastic Plastic Fracture, ASTM STP 668,* American Society for Testing and Materials, 1979, pp. 65-120.

[6] Garwood, S. J. in *Fracture Mechanics, ASTM STP 677,* American Society for Testing and Materials, 1979, pp. 511-532.

[7] Adams, N. J. I., Munro, H. F. and Neale, B. K., "The Influence of Specimen Configuration on Yield Zone Formation and Fracture Resistance," presented at the International Conference on Fracture, Waterloo, 1977.

[8] Garwood, S. J. and Turner, C. E., *International Journal on Fracture,* Vol. 14, No. (3), 1978, pp. R195-198.

[9] Begley, J. A. and Landes, J. D. in *Fracture Toughness, ASTM STP 514,* American Society for Testing and Materials, 1972, pp. 1-23.

[10] Turner, C. E. and Burdekin, F. M., *Energy Review,* Vol. 12, 1974, pp. 439-503.

[11] Hutchinson, J. W. and Paris, P. C. in *Elastic Plastic Fracture, ASTM STP 668,* American Society for Testing and Materials, 1979, pp. 37-64.

[12] McMeeking, R. M. and Parks, D. M. in *Elastic Plastic Fracture, ASTM STP 668,* American Society for Testing and Materials, 1979, pp. 175-194.

[13] Rice, J. R., Paris, P. C., and Merkle, J. G. in *Progress in Flaw Growth and Fracture Toughness Testing, ASTM STP 536,* American Society for Testing and Materials, 1973, pp. 231-245.

[14] Sumpter, J. D. G., "Elastic-Plastic Fracture Analysis and Design Using the Finite Element Method," PhD thesis, London, 1974.
[15] Garwood, S. J., *International Journal on Fracture,* Vol. 14, No. 1, 1978, pp. R21-24.
[16] Sumpter, J. D. G., Turner, C. E. in *Cracks and Fractures, ASTM STP 601,* American Society for Testing and Materials, 1976, pp. 3-18.
[17] Dawes, M. G., "A Method of Measuring Displacements and Rotational Factors in SENB Specimens," Welding Institute Report 6/1976/E, Cambridge, England, 1976.
[18] "Methods for Crack Opening Displacement (COD) Testing," Draft for Development DD19, British Standards Institution, London, 1972, now in revised form as BS 5762, 1979.
[19] Clarke, G. A., Andrews, W. R., Begley, J. A., Donald, K., Embley, G. T., Landes, J. D., McCabe, D. E., and Underwood, J. H., (ASTM E24.01.09 Task Group), *Journal of Testing and Evaluation,* Vol. 7, No. 1, 1979, pp. 49-56.
[20] "Methods of Test for Plane Strain Fracture Toughness (K_{Ic}) of Metallic Materials," BS 5447, British Standards Institute, London, 1977.
[21] Merkle, J. G. and Corten, H. T., *Journal of Pressure Vessel Technology,* Vol. 96, 1974, pp. 286-292.
[22] Towers, O. L. and Garwood, S. J., "Ductile Instability Considerations and the Prediction of Driving Force Curves for Six Test Geometries," to be published in *Welding Research International,* Vol. 9, No. 6, 1979.

H. Tada,[1] *P. C. Paris,*[1] *and R. M. Gamble*[2]

A Stability Analysis of Circumferential Cracks for Reactor Piping Systems

REFERENCE: Tada, H., Paris, P. C., and Gamble, R. M., **"A Stability Analysis of Circumferential Cracks for Reactor Piping Systems,"** *Fracture Mechanics: Twelfth Conference, ASTM STP 700,* American Society for Testing and Materials, 1980, pp. 296-313.

ABSTRACT: The high ductility and toughness of the stainless steel reactor piping system have made it virtually certain not to experience unstable crack extension. The present study attempts to provide theoretical assurance that the piping system will not suffer unstable crack extension even if severe circumferential cracking should occur. The analysis is based on the tearing instability concept and the tearing modulus criterion. Simplifications are conservatively made to facilitate the complicated analysis. The results are presented parametrically in graphical forms for convenience of general use. An application to a specific example is also discussed.

The results indicate that the ratio, L/R, is of major importance in consideration of crack stability, where L is the length of the pipe between supports and R is the radius of the pipe. It is shown that unstable crack extension would not occur in stainless steel piping systems designed in accordance with the American Society of Mechanical Engineers' (ASME) code even if severe circumferential flaws were present, provided that the values of L/R are less than about 200. Since the values of L/R for boiling water reactor (BWR) stainless steel piping systems are generally much smaller, large margins against unstable fracture are assured for these systems. When L/R exceeds 200, a more detailed analysis would be necessary to demonstrate crack stability.

KEY WORDS: stainless steels, reactor piping systems, stress corrosion cracking, J-integral, J-R curves, tearing instability, tearing modulus (T), fractures (materials), crack propagation

Circumferential cracks have been observed in some boiling water reactor (BWR) piping systems. These cracks normally initiate at the inner surface of the pipe wall and grow radially and circumferentially by stress corrosion (and

[1]Senior research associate and professor of mechanics, respectively, Center for Fracture Mechanics, Washington University, St. Louis, Mo. 63130.

[2]Section leader, Materials Integrity Section, Materials Engineering Branch, Division of Systems Safety, Office of Nuclear Reactor Regulation, U.S. Nuclear Regulatory Commission, Washington, D.C. 20555.

perhaps fatigue). Most of these intergranular stress corrosion cracks can be detected through inservice inspection before propagating through the wall. When cracks become through-the-wall, leak detection systems are capable of sensing the leaks. Further, materials used for the piping system, typically like Type 304 stainless steel, exhibit such high ductility and toughness that it is very unlikely to suffer sudden fracture even when relatively large flaws are present. In fact, all of the recent leaks due to stress corrosion cracking have been observed in stainless steel piping that did not fracture.

However, in order to provide assurance that piping subjected to stress corrosion cracking will leak before breaking, it is necessary to show that a through-wall crack, which leaks, grows in a stable manner and that it does not cause sudden pipe fracture. In the present study, a fracture mechanics analysis is performed to assess the stability of crack extension in the piping system. The analysis is based on the tearing stability concept and the tearing modulus stability criterion [*1*].[3] The criterion is valid for materials whose failure is characterized by gross yielding and subsequent plastic instability.

The concept of tearing modulus, T, has been developed on the basis of the J-integral resistance curve and the nondimensional quantities T_{mat} and T_{appl}. These quantities are defined by

$$T_{mat} = \frac{E}{\sigma_o^2}\frac{dJ_{mat}}{da} \quad \text{and} \quad T_{appl} = \frac{E}{\sigma_o^2}\frac{dJ}{da} \tag{1}$$

where

E = Young's modulus,
σ_o = an appropriate flow stress,
a = the relevant flaw size in the stability analysis,
J_{mat} = the value of J following the material resistance curve, and
J = the applied value of J.

The condition of stability of crack growth is given by

$$T_{mat} > T_{appl} \text{ stable} \tag{2a}$$

$$T_{mat} < T_{appl} \text{ unstable} \tag{2b}$$

When Eq 2*a* is satisfied with a substantial margin, the stable crack growth is assured. Rigorous accounts of the concept of T and its applicability are found in Refs *1* and *2*.

In this study, a simplified, conservative stability analysis is made parametrically. In the analysis the pipe is treated as a beam whose cracked cross section is subjected to plastic limit moment. Since segments of the

[3]Italic numbers in brackets refer to the list of references appended to this paper.

crack on the compressive side may close and carry the compressive load, the analysis is made for both cases with and without crack closure. Numerical results are presented graphically. The stability of cracks observed in actual reactor pipings is also discussed.

Method of Analysis

The fracture mechanics analysis of tearing stability based on the concept of tearing modulus, T, as defined by Eq 1, requires the knowledge of the applied value of J (or its differential form dJ) in terms of crack size and other geometric details and the loading system configuration and stiffness.

To facilitate the analysis, the pipe is treated as a beam subjected to bending and axial loads. For materials and operating conditions of interest, it is sufficient to examine the crack stability in ductile tearing. In the analysis, therefore, the following conditions are imposed:

1. The cross section containing a crack is fully yielded, while the other part of the pipe is elastic; and
2. The material is perfectly plastic (nonhardening).

That is, the cracked section of the pipe is subjected to the plastic limit moment, M_p.

Under these conditions, a conservative analysis is assured for the following reasons. The applied value of J calculated from an approximate formula, Eq 4, is an overestimate of J based on the definition, Eq 3. Also, it is known that the tearing portion of the J-integral resistance curve is in general an increasing function with decreasing slopes with respect to the crack extension. Therefore, the overestimated value of J corresponds to an underestimated value of T_{mat} on the J-resistance curve.

Then it is convenient to use the following definition of J [3]

$$J = -\int_0^{\phi} \left(\frac{\partial M}{\partial A}\right)_{\phi} d\phi \tag{3}$$

where

A = the crack area,
M = a bending moment applied on a cracked body, and
ϕ = the corresponding angle of rotation.

When perfectly plastic behavior is assumed and the limit moment is reached, Eq 3 is rewritten in the form (see Fig. 1)

$$J = -\frac{\partial M_p}{\partial A} \cdot \phi \tag{4}$$

It is noted that the axial force is normally a built-in load, such as internal pressure, and independent of flaw size, and that it is not usually expected to

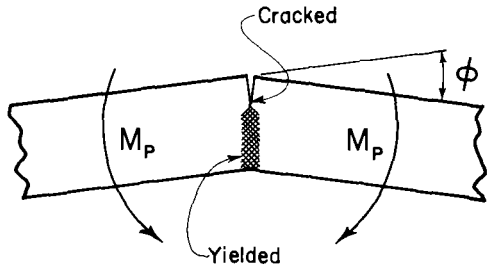

FIG. 1—*Limit moment,* M_p, *and angle of rotation,* ϕ.

be large enough to cause gross yielding of the net section. The influence of the axial force on the J-value is taken into account, in effect, as changes in the location of neutral axis and the limit moment, M_p. Thus, Eq 4 will provide a reasonable approximation. If J is known as a function of crack size and other variables, then the stability analysis may be performed for each specified loading system.

The geometry of the cracked section of the pipe is assumed to be as shown in Fig. 2, that is, the section contains an internal circumferential crack in addition to a through-wall crack. The following notation is used in the present analysis (Fig. 2):

R = radius of the pipe measured to the middle of the wall,
t = thickness of the pipe wall,
2θ = angle contained by the through-wall crack,
a = depth of the circumferential crack,
σ_o = flow stress, and
P = axial force.

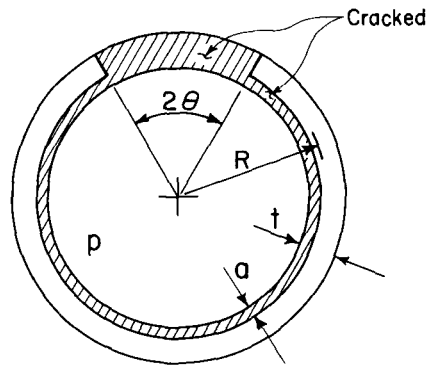

FIG. 2—*Cracked section of pipe.*

In addition, it is convenient to introduce the following nondimensional quantities

$$\bar{a} = \frac{a}{t} \tag{5}$$

$$\bar{P} = \frac{P}{(2\pi Rt)\,\sigma_o} \tag{6}$$

Since a part of the crack located on the compressive side may close and carry some compressive load, the analysis considers the two extreme cases; that is, (*a*) no crack closure occurs on compressive side, or (*b*) the crack closes completely on compression side and carry compressive load. These two situations are shown in Fig. 3.

It is readily seen that the location of neutral axis defined by angle α (Fig. 3), the limit moment, M_p, and the *J*-value, etc., are functions of four variables; that is, t/R, θ, a, and $\bar{P}$; and depend on condition (*a*) or (*b*) cited previously. However, for simplicity, one may assume that the pipe is a thin-walled cylinder, that is

$$t/R \ll 1 \tag{7}$$

Under this assumption, one of the parameters, t/R, is eliminated from the analysis. Also it should be noted that, when the axial force, P, is due to an internal pressure, p, $\bar{P}$ is related to p by

$$\bar{P} = \frac{1}{2}\left(\frac{R}{t}\right)\left(\frac{p}{\sigma_o}\right) \tag{8}$$

The expressions for the location of neutral axis, α, the limit moment, M_p, and the *J*-value are given below in terms of the remaining three parameters,

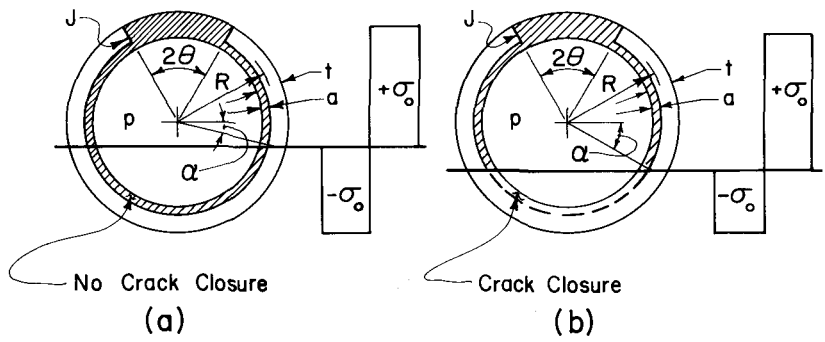

FIG. 3—*Location of neutral axis, α.*

θ, $\bar{a}$, and $\bar{P}$ for both cases (a) and (b). A simplified crack instability analysis follows.

Location of Neutral Axis

The location of the neutral axis is defined by an angle α as shown in Fig. 3; $\alpha = \alpha(\theta, \bar{a}, \bar{P})$ is readily written as follows.

(a) With no crack closure (Fig. 3a)

$$\alpha = \frac{1}{2}\theta + \frac{\pi}{2}\frac{\bar{P}}{1-\bar{a}} \tag{9}$$

(b) With crack closure (Fig. 3b)

$$\alpha = \frac{1-\bar{a}}{2-\bar{a}}\theta + \frac{\pi}{2-\bar{a}}\left(\bar{P} + \frac{\bar{a}}{2}\right) \tag{10}$$

Plastic Limit Moment, M_p

Now that the location of neutral axis is known, the limit moment, M_p, is also readily calculated by geometrical considerations. It is convenient to normalize M_p in the form

$$M_p = 4\,\sigma_o R^2 t\,\overline{M}_p(\theta, \bar{a}, \bar{P}) \tag{11}$$

Note that $4\,\sigma_o R^2 t$ is the limit moment of the gross section of the pipe ($\theta = \bar{a} = 0$) under pure bending ($\bar{P} = 0$). $\overline{M}_p$ is a nondimensional representation of the limit moment, which is given by

(a) With no crack closure

$$\overline{M}_p = (1-\bar{a})\left(\cos\alpha - \frac{1}{2}\sin\theta\right) + \frac{\pi}{2}\bar{P}\sin\alpha \tag{12}$$

where α is given by Eq 9.

(b) With crack closure

$$\overline{M}_p = (1-\bar{a})\left(\frac{1-\frac{1}{2}\bar{a}}{1-\bar{a}}\cos\alpha - \frac{1}{2}\sin\theta\right) + \frac{\pi}{2}\bar{P}\sin\alpha \tag{13}$$

where α is given by Eq 10.

The numerical values of $\overline{M}_p$ are plotted against θ in Figs. 4 and 5 for various values of each parameter and for both cases with and without crack closure.

The limit moment, M_p, increases slightly as the axial force, P, increases

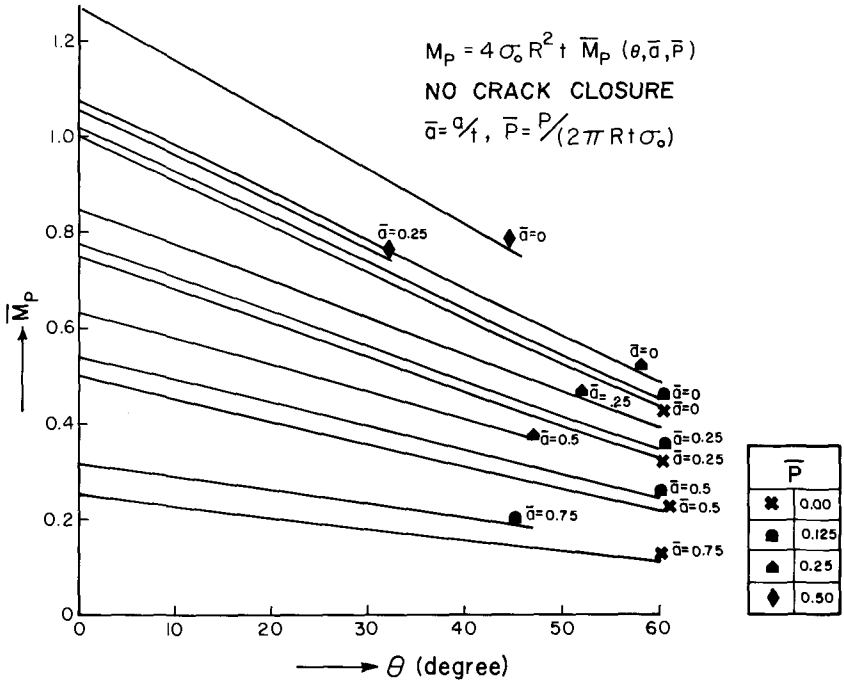

FIG. 4—M_p *versus* θ, *without crack closure.*

with other variables unchanged. However, it should be noted that the magnitude of bending moment, which can be externally applied on the cracked section, decreases due to the axial force. To obtain the applied value of J, the total magnitude, M_p, is used in Eq 4.

Expression of J

Since the stability of extension of the through-wall crack in the circumferential direction is sought, J should be calculated along the radial edge of the crack. Referring to Fig. 2, the increment of crack area, dA, is given by

$$dA = 2Rt(1 - \bar{a})\, d\theta \tag{14}$$

Substituting this into Eq 4 and combining with Eq 11, J is calculated as follows

$$J = -\frac{2\sigma_o R}{1 - \bar{a}} \cdot \frac{\partial \bar{M}_p}{\partial \theta} \cdot \phi \tag{15}$$

J is conveniently normalized in the form

$$J = (\sigma_o R)\bar{J} = (\sigma_o R) F_J(\theta, \bar{a}, \bar{P}) \cdot \phi \tag{16}$$

where $\bar{J} = F_J(\theta, \bar{a}, \bar{P}) \cdot \phi$ is a nondimensional representation of J and

$$F_J(\theta, \bar{a}, \bar{P}) = -\frac{2}{1-\bar{a}} \frac{\partial \bar{M}_p}{\partial \theta} \tag{17}$$

Combining Eqs 9, 10, 12, 13, and 17, $F_J(\theta, \bar{a}, \bar{P})$ is written in the following simple form.

(*a*) With no crack closure

$$F_J = \sin\alpha + \cos\theta - \frac{\pi}{2} \frac{\bar{P}}{1-\bar{a}} \cos\alpha \tag{18}$$

(*b*) With crack closure

$$F_J = \sin\alpha + \cos\theta - \frac{\pi}{2} \frac{\bar{P}}{1-\bar{a}/2} \cos\alpha \tag{19}$$

where α is given by Eqs 9 and 10, respectively.

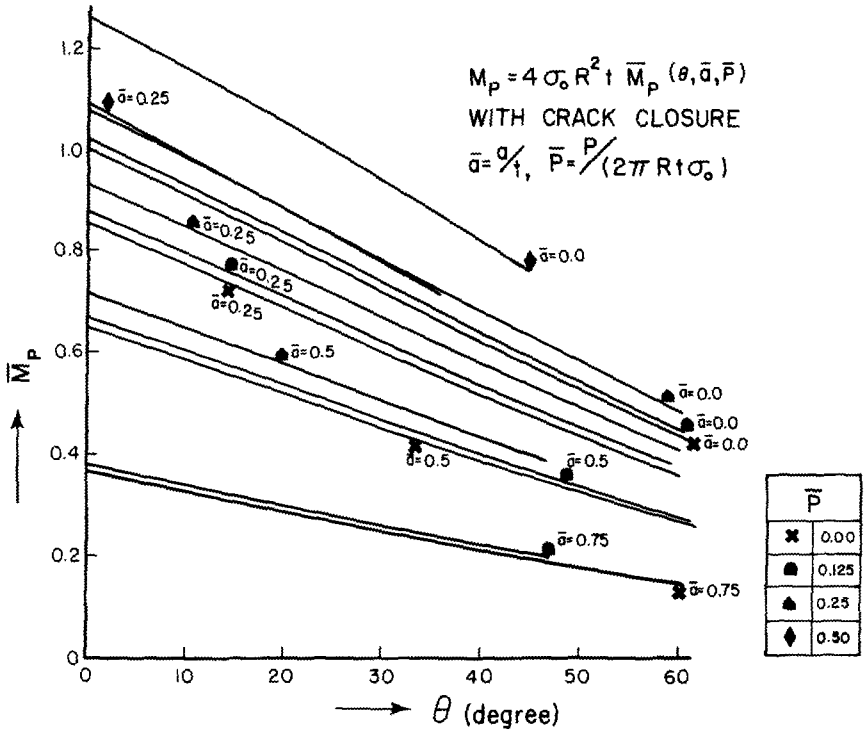

FIG. 5—M_p *versus* θ, *with crack closure.*

The numerical values of F_J are presented in Figs. 6 and 7 for various values of the parameters.

The preceding analysis of J and the subsequent stability analysis are readily generalized for a cracked beam with an arbitrary cross section subjected to the limit moment (Fig. 8). It is interesting to note that J is always given in the form

$$J = \left(\sigma_o h - \frac{1}{2}\frac{P}{B}\right)\phi$$

or

$$= \sigma_o\left(h - \frac{1}{2}\frac{A_p}{B}\right)\phi \tag{20}$$

where, referring to Fig. 6

h = vertical distance from the neutral axis to the crack edge,
B = width of the beam at the location of neutral axis,
P = axial force, and
A_p = area given by P/σ_o.

The expressions of J given by Eqs 16, 18, and 19 can be alternately obtained directly from Eq 20.

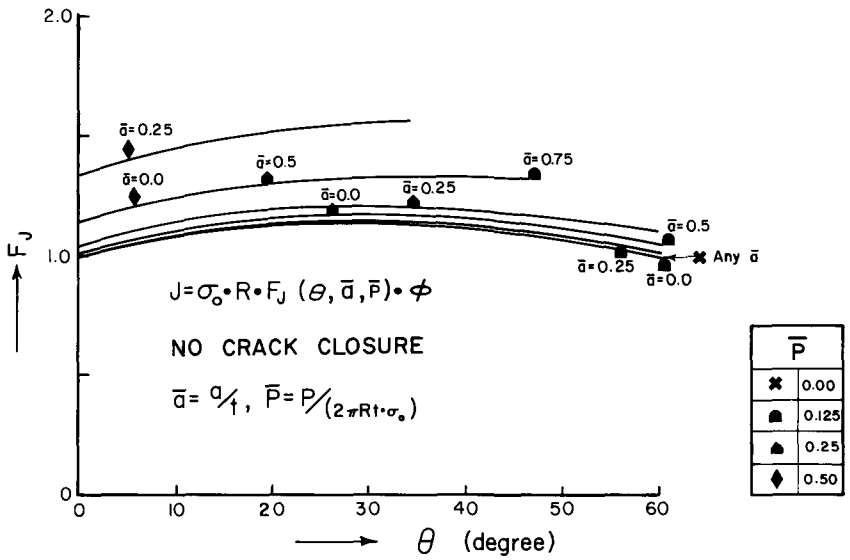

FIG. 6—F_J *versus* θ, *without crack closure.*

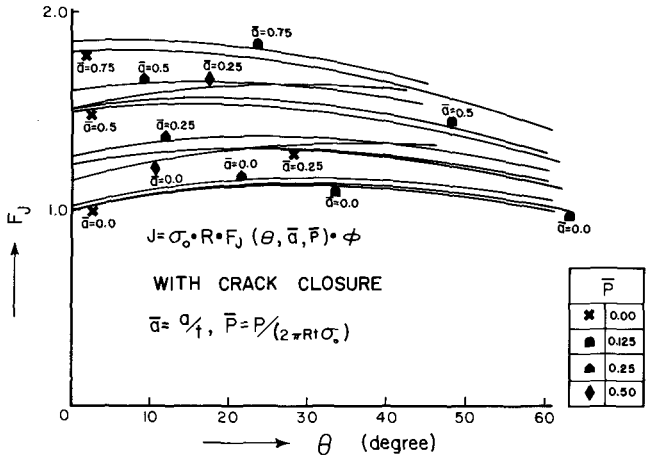

FIG. 7—F_J *versus* θ, *with crack closure.*

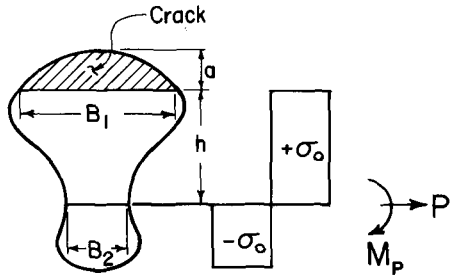

$$J = -\frac{\partial M_p}{B_1 \partial a}\phi = \sigma_o\left(h - \frac{1}{2}\frac{A_p}{B_2}\right)\phi$$

$$A_p = \frac{P}{\sigma_o}$$

FIG. 8—*Cracked beam with arbitrary cross section.*

Simplified Instability Analysis

It is now possible to make a conservatively simplified instability analysis of crack extension in the piping system. The analysis employs the similar procedure discussed in Ref *1*. That is, referring to Fig. 9, when a rotation $\bar{\phi}$, is imposed at the fixed ends of the beam, $\bar{\phi}$ is written in the following form considering separately the elastic part, ϕ_{el}, and the plastic part, ϕ_{pl}

$$\bar{\phi} = \phi_{el} + \phi_{pl} \tag{21}$$

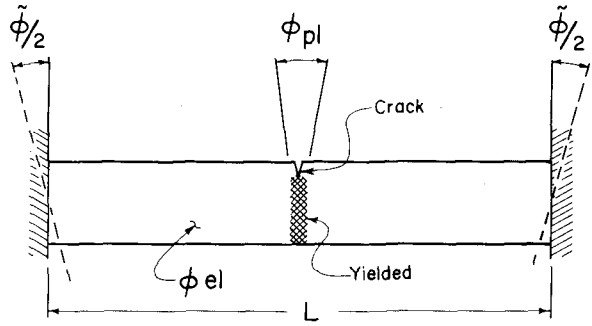

FIG. 9—*Fixed beam under uniform bending,* $\tilde{\phi}$ = constant.

The total rotation, $\tilde{\phi}$, remains constant during the examination of stability

$$d\tilde{\phi} = d\phi_{el} + d\phi_{pl} = 0 \tag{22}$$

The elastic part of rotation, ϕ_{el}, has the form

$$\phi_{el} = \frac{L}{\rho} = \frac{ML}{EI} \tag{23}$$

where

$M = M_p$ (limit moment, Eq 11)
$I = \pi R^3 t$

The plastic part of the rotation, ϕ_{pl}, is from Eq 16,

$$\phi_{pl} = \frac{J}{\sigma_o R} \cdot \frac{1}{F_J} \tag{24}$$

where F_J is given by Eqs 18 and 19.

Since the extension of the through-wall crack in the θ direction is sought, from Eq 23

$$d\phi_{el} = \frac{\partial M_p}{\partial \theta} \frac{L}{EI} d\theta \tag{25}$$

Combining Eqs 11 and 17, $d\phi_{el}$ is written in the form

$$d\phi_{el} = -\frac{2}{\pi} \frac{\sigma_o}{E} (1 - \bar{a}) \left(\frac{L}{R}\right) F_J(\theta, \bar{a}, \bar{P})\, d\theta \tag{26}$$

Also, from Eq 24, noting that both J and F_J contain θ

$$d\phi_{pl} = \frac{\partial \phi_{pl}}{\partial J} dJ + \frac{\partial \phi_{pl}}{\partial F_J} dF_J \tag{27}$$

For convenience, one writes this in the following form

$$d\phi_{pl} = \frac{1}{\sigma_o R F_J} dJ + \frac{J}{\sigma_o R} \left(- \frac{1}{F_J^2} \right) \frac{\partial F_J}{\partial \theta} d\theta \tag{28}$$

Substituting Eqs 26 and 28 into Eq 22 and noting that the crack increment in the θ direction is $R\, d\theta$, one has

$$\frac{dJ}{Rd\theta} \cdot \frac{E}{\sigma_o^2} = F_1(\theta, \bar{a}, \bar{P}) \cdot \frac{L}{R} + F_2(\theta, \bar{a}, \bar{P}) \cdot \frac{JE}{\sigma_o^2 R} \tag{29}$$

where F_1 and F_2 are related to F_J as follows

$$F_1 = \frac{2}{\pi} (1 - \bar{a}) F_J^2 \tag{30}$$

and

$$F_2 = \frac{1}{F_J} \cdot \frac{\partial F_J}{\partial \theta} \tag{31}$$

Thus, T_{appl} in the instability condition, Eq 2*b*, is given by

$$T_{appl} = F_1(\theta, \bar{a}, \bar{P}) \frac{L}{R} + F_2(\theta, \bar{a}, \bar{P}) \frac{JE}{\sigma_o^2 R} \tag{32}$$

From Eqs 18, 19, 30, and 31, F_1 and F_2 are written in the form

(*a*) With no crack closure

$$F_1 = \frac{2}{\pi} (1 - \bar{a}) F_J^2 \tag{33}$$

and

$$F_2 = \frac{1}{2} \frac{1}{F_J} (\cos\alpha - 2\sin\theta + \frac{\pi}{2} \frac{\bar{P}}{1 - \bar{a}} \sin\alpha) \tag{34}$$

where α and F_J are given by Eqs 9 and 18, respectively.

(*b*) With crack closure

$$F_1 = \frac{2}{\pi} (1 - \bar{a}) F_J^2 \tag{35}$$

and

$$F_2 = \frac{1}{2}\frac{1}{F_J}\cdot\frac{1-\bar{a}}{1-\bar{a}/2}\left(\cos\alpha - \frac{2-\bar{a}}{1-\bar{a}}\sin\theta + \frac{\pi}{2}\frac{\bar{P}}{1-\bar{a}/2}\sin\alpha\right) \quad (36)$$

where α and F_J are given by Eqs 10 and 19, respectively.

The numerical values of F_1 and F_2 are presented against θ in Figs. 10 through 13, for various values of parameters and conditions with and without crack closure.

Considering that the first term on the right-hand side of Eq 32, $F_1 \cdot (L/R)$, results from relaxation of the elastic deformation of the beam (or pipe) during the crack increment, one may reasonably expect that the uniform bending condition imposed in the present analysis is more severe than other loading conditions or pipe geometry provided the length of pipe, L, between the supports is equal. For example, consider a simply supported pipe subjected to a concentrate load that causes the maximum bending moment equal to M_p at the cracked section as shown in Fig. 14. When one imposes the condition that total vertical displacement at the load point remains constant ($d\Delta = 0$) during the instability analysis, T_{appl} is given by

$$T_{appl} = \frac{1}{3} F_1(\theta, \bar{a}, \bar{P}) \frac{L}{R} + F_2(\theta, \bar{a}, \bar{P}) \frac{JE}{\sigma_o^2 R} \quad (37)$$

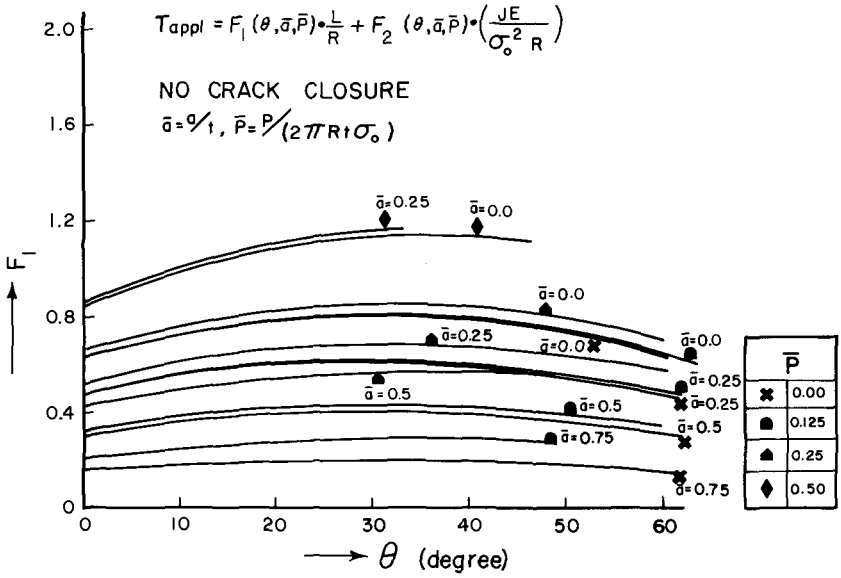

FIG. 10—F_1 *versus* θ, *without crack closure.*

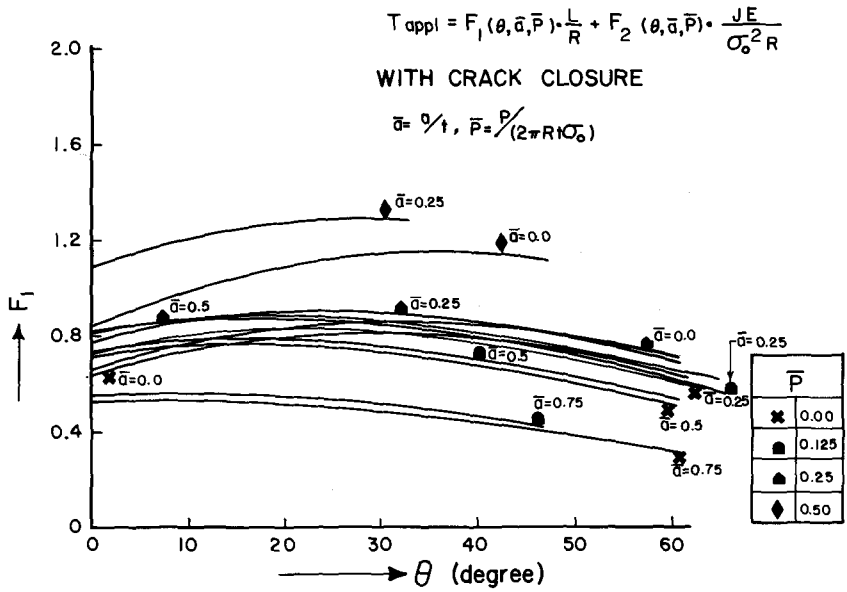

FIG. 11—F_1 *versus* θ, *with crack closure.*

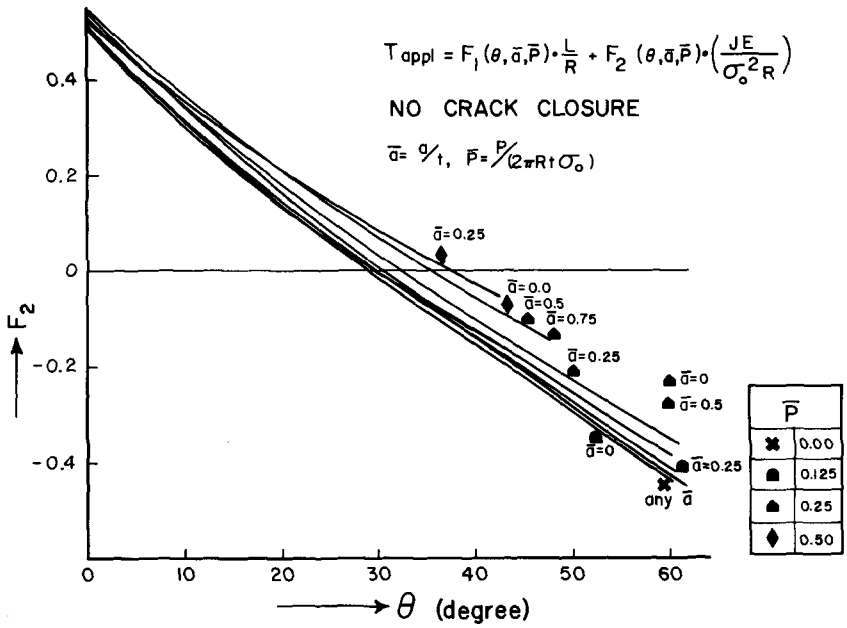

FIG. 12—F_2 *versus* θ, *without crack closure.*

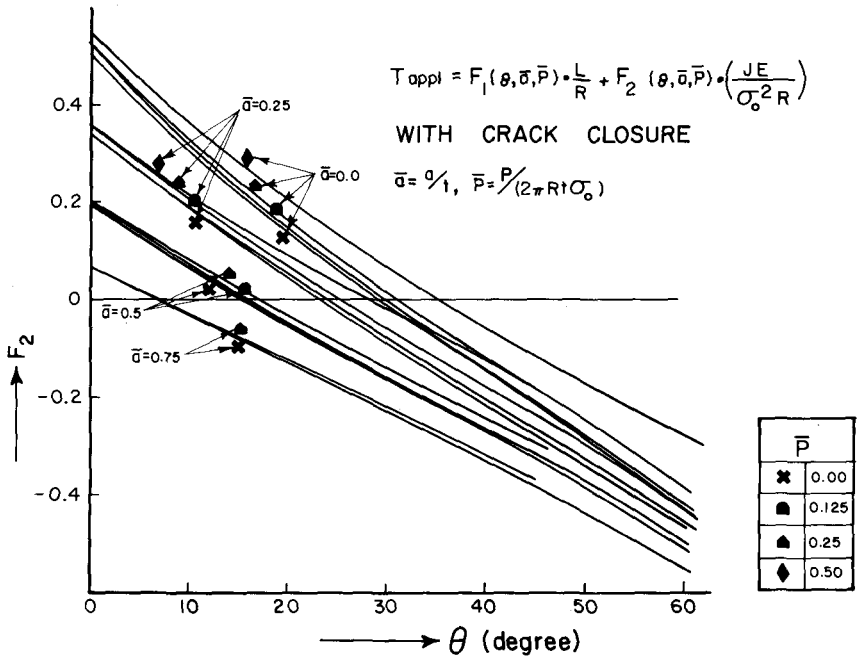

FIG. 13—F_2 *versus* θ, *with crack closure.*

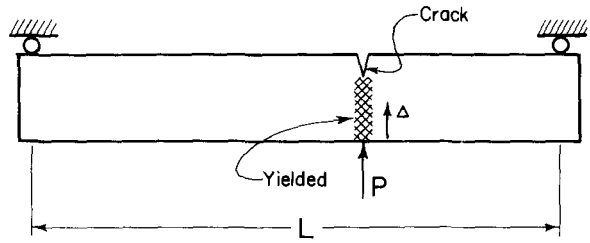

FIG. 14—*Simply supported beam,* Δ = *constant.*

where F_1 and F_2 are the same functions as in Eq 32. Note that the change in loading condition results in the change in the coefficient of the first term and does not change the second term. Thus, T_{appl} given by Eq 32 is expected to provide the upper bound of the T_{appl}-value in real structural situations.

Application

Consider a 711 mm (28 in.) BWR stainless steel recirculation outlet line, which might contain a large intergranular stress corrosion crack in its wall.

This line was selected because it is the largest in a BWR and has the largest possible coolant loss should a pipe rupture occur. The geometry of the cracked section is as follows (refer to Fig. 2):

R = 356 mm (14 in.)
t = 38 mm (1.5 in.)
$2\theta \simeq$ 100 deg (for example)
$\bar{a} = a/t \simeq 0.75$ (for example)

The applied pipe loading is assumed to be the BWR design pressure and a bending moment sufficient to produce a fully plastic bending moment in the remaining ligament of the cracked pipe section. The flow stress, σ_o, is assumed to be 345 MPa (50 ksi) accounting for hardening. Then, from Eq 8, the value of P is approximately 0.1.

$$\sigma_o = 345 \text{ MPa (50 ksi)}$$
$$\bar{P} \simeq 0.1$$

For these values of variables, the functions F_1 and F_2 in Eq 32 are read from Figs. 10 through 13. That is,

(*a*) With no crack closure (Figs. 10 and 12)

$$F_1 \simeq 0.24$$
$$F_2 \simeq -0.28$$

(*b*) With crack closure (Figs. 11 and 13)

$$F_1 \simeq 0.4$$
$$F_2 \simeq -0.44$$

Therefore, the T_{appl} is conservatively given by

$$T_{\text{appl}} = 0.4\left(\frac{L}{R}\right) + (-0.28)\frac{JE}{\sigma_o{}^2 R} \tag{38}$$

Using an experimental crack resistance curve for stainless steel [*4*] and assuming a significant crack extension, it is seen that the J-value is upward of 700 kJ/m^2 (4000 in.·lb/in.^{2}). Taking J = 700 kJ/m^2 (4000 in.·lb/in.^{2}) for conservativeness

$$T_{\text{appl}} \simeq 0.4\left(\frac{L}{14}\right) - 1.0$$

The value of T_{mat} for stainless steel is normally larger than 200 [*4*]. Assuming that $T_{mat} = 200$, Eq 2 requires

$$L \simeq 183 \text{ m (600 ft)}$$

for instability.

It should be noted that, from Figs. 10 through 13, for the range of variables considered in the present study

$$T_{appl} < 1.3 \frac{L}{R} + 0.5 \frac{JE}{\sigma_o{}^2 R}$$

Thus, the instability criterion, Eq 2*b*, always requires a very large value of L/R for instability.

This implies that the unstable crack extension cannot occur in the stainless steel reactor piping system designed in accordance with the American Society of Mechanical Engineers' (ASME) design code provided that its L/R is not too large.

Summary

It has been known that the stainless steel reactor piping system subjected to stress corrosion cracking is virtually sudden-fracture-proof because of its high ductility and toughness. The present study attempted to provide theoretical assurance that the piping system is in fact "fracture-proof."

The analysis is based on the tearing instability concept and the tearing modulus stability criterion. A conservative analysis successfully demonstrated that sudden fracture would not occur from circumferential cracks in the stainless steel piping system designed in accordance with the current design code, and limiting the L/R to values less than 200. The values of L/R for BWR stainless piping systems are generally substantially less. When L/R exceeds 200, a more detailed analysis would be necessary to assure crack stability.

Acknowledgments

The authors acknowledge the support of this work by the U.S. Nuclear Regulatory Commission, Contract Number NRC-03-78-135 with Washington University in St. Louis. The encouragement of the Regulatory Staff, especially R. E. Johnson is gratefully acknowledged.

References

[1] Paris, P. C., Tada, H., Zahoor, A., and Ernst, H., "A Treatment of the Subject of Tearing Instability," NUREG-0311, U.S. Nuclear Regulatory Commission, Aug. 1977; see also *Elastic-Plastic Fracture, ASTM STP 668,* American Society for Testing and Materials, 1979, pp. 5-36.

[2] Hutchinson, J. W. and Paris, P. C. in *Elastic-Plastic Fracture, ASTM STP 668,* American Society for Testing and Materials, 1979, pp. 37-64.

[3] Rice, J. R. in *Fracture,* H. Liebowitz, Ed., Vol. 2, Academic Press, New York, 1968, pp. 191-311.

[4] Bamford, W. H. and Bush, A. J., in *Elastic-Plastic Fracture, ASTM STP 668,* American Society for Testing and Materials, 1979, pp. 553-577.

C. E. Turner[1]

The Ubiquitous η Factor

REFERENCE: Turner, C. E., **"The Ubiquitous η Factor,"** *Fracture Mechanics: Twelfth Conference, ASTM STP 700,* American Society for Testing and Materials, 1980, pp. 314-337.

ABSTRACT: The η factor relates G or J to elastic or plastic work per unit ligament area rather than to the differential of work per unit crack advance. In principle this adds nothing to the understanding of fracture, but in practice it provides convenient relationships for the analysis of several fracture problems. The η factor can be expressed in terms of compliance, load or displacement, instead of work, and can be determined experimentally or analytically. Expressions are given for a selection of elastic, nonlinear, and plastic cases in some of which deep and shallow notch behavior differs markedly.

Application to elastic and plastic test analyses, a J based design curve including an approximate treatment of residual stresses, and both elastic and plastic instability problems are outlined.

KEY WORDS: fractures (materials), test methods, J-integral, plasticity, toughness, work to fracture, elastic-plastic fracture mechanics, crack propagation

When regarded as rate of change of potential energy with crack growth, G or J can be related to the rate of change $\partial w/\partial A$, of the area, w, under the load displacement curve with change of crack area A. Prior to initiation this area equals the mechanical work done so that by algebraic manipulation G or J can be related to work done in a given configuration. Such a relationship perhaps adds nothing to understanding but appears useful in certain practical circumstances. The relationship also allows a simple explanation of certain, sometimes puzzling, features; such as, the variation of (nominal) specific surface energy, w/Bb, with ligament width (where w is work done and Bb is the ligament area thickness B, breadth b); the radically different behavior of shallow notch and deep notch pieces and hence a derivation of the well-known crack opening displacement (COD) design curve or its related counterpart in terms of J; rationalization of the relationship between equivalent energy and various methods of estimating J; certain instability behavior and so on. Most of these problems have been

[1] Professor of Materials in Mechanical Engineering, Imperial College, London, U.K.

studied before. The object of the present paper is to bring them together and point up the essential unity of the term that arises in them all; that is, the relationship between G or J and work done, the η factor.

Some Common Uses of η Factors

In the development of linear fracture mechanics (LEFM) relationships have been stated between the energy release rate, G, and the elastic work done, w, in the form [*1*][2,3]

$$G = \eta_{el} w_{el}/Bb \tag{1}$$

A related expression was used by Marshall et al [*2*] and the same concept arose in Ref *3*. In a linear elastic system of compliance ϕ

$$w_{el} = Qq/2 = \phi Q^2/2 = q^2/2\phi \tag{2}$$

where Q is load and q is displacement of the loading points. Thus,

$$\eta_{el} = -\frac{b}{w}\frac{\partial w}{\partial a}\bigg|_q = \frac{b}{\phi}\frac{d\phi}{da} \tag{3}$$

where b is the ligament $W - a$, and if K is expressed in terms of the well-known LEFM shape factor Y (that is, $K = Y\sigma\sqrt{a}$ for other than crack-line loading) then

$$\eta_{el} = bY^2 a \Big/ \int Y^2 a\, da \tag{4}$$

The unnotched compliance, ϕ_u, is used in evaluating the integral in Eq 4 so that η_{el} is a function of absolute length, as well as of a/W. A useful expression for the notched to unnotched compliance ratio is

$$\phi_n/\phi_u = 2Y^2 ab/W\eta_{el} d \tag{5}$$

where d is either tensile gage length, D, or $S/9$, and S is the span in three-point bending. Some values of η_{el} are shown in Fig. 1 by way of example. A similar term has been used to relate J to work done in yielding mechanics. Tension and bending cases were discussed by Rice et al [*4*]. The relationship is of the form

$$J_{pl} = \eta_{pl} w_{pl}/Bb \tag{6}$$

[2] The italic numbers in brackets refer to the list of references appended to this paper.

[3] Reference *1* used the reciprocal notation for η and did not include shear deflection in evaluating η for three-point bending.

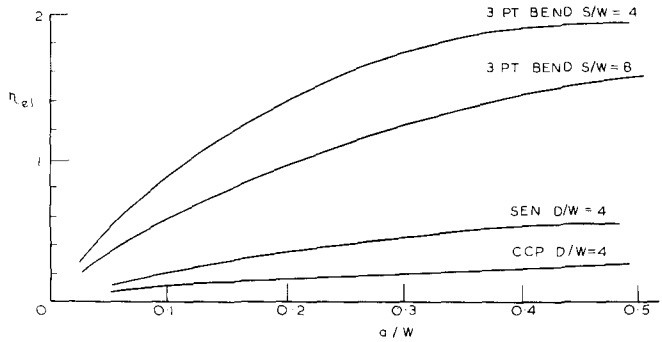

FIG. 1—*Some examples of the elastic factor* η_{el} [29].

where for the well-known case of deep notch bending (strictly, pure bending) $\eta_{pl} = 2$ for a/W greater than about 0.6. This was applied to three-point bending tests, but early use was restricted to cases where the elastic work was negligible or could be subtracted from the total.

Expressions for use with compact pieces have been described by Merkle and Corten [5]. Sumpter and Turner [6] suggested evaluating J in the two components

$$J = (\eta_{el} w_{el} + \eta_{pl} w_{pl})/Bb \tag{7}$$

for cases where η_{el} and η_{pl} were not closely similar. Dawes [7] and Chipperfield [8] have applied this method in bending down to $a/W \simeq 0.2$ with apparent success.

More recently the realization that $\eta_{el} \simeq 2$ for deep notch bending ($S/W = 4$, a/W greater than about 0.4) has led to the use of Eq 6 where J and η are overall terms, as discussed by Srawley [9], and w_t is the total work, elastic plus plastic. Thus

$$J = \eta_o w_t / Bb \tag{8}$$

For the limit state η_{pl} has been evaluated $w_{pl} = Q_L q$, where Q_L is the limit load, to give

$$\eta_{pl} = -\frac{b}{Q_L} \frac{\partial Q_L}{\partial a}\bigg|_q \tag{9}$$

writing

$$Q_L = L B (W - a)^N \sigma_Y / D^{N-1} \tag{10}$$

where L is the plastic constraint factor, and for tension $N = 1$, $D =$ gage length, or for three-point bending of beams of rectangular cross-section, $N = 2$, $D = S$ (the span), then

$$\eta_{pl} = N - \frac{b}{L}\frac{dL}{da} \tag{11}$$

If, as in many deep notch cases, the constraint factor does not vary significantly with crack length, then as commonly known

$$\eta_{pl} = N \text{ (1 for tension, 2 for bending)} \tag{12}$$

but clearly, the more general case is where both terms in Eq 11 are significant.

η Factor for Widespread Plasticity

Much of the foregoing is already known and has been summarized elsewhere [*10*] but is recounted here as a preamble to the further discussion. Two simple models of the η factor are outlined here for extensive plasticity.

The η factor has recently come to the fore in studies of stable crack growth [*11,12*]. Following the analysis of tearing by Paris et al [*13*], for which the use of the J theory was justified as rigorous by Hutchinson and Paris [*14*], a generalization of Eq 9 (that is, expressed for any load Q, not just the limit state) was evaluated experimentally [*12*] leading to the realization that this experimental term was indeed identical to the η factor of Ref *11*. This experimental evidence for η_{pl} and also the computational evidence for η_o described in Ref *10* (as discussed later here in connection with Figs. 2*a,b*) showed that at least for some configurations η was essentially independent of degree of deformation. A heuristic treatment leading to that result is given below. Another treatment in terms of J theory is offered in Ref *15*.

As a first model for nonlinear (nl) behavior, the load-displacement relation is expressed as a power law

$$Q = q^n/\Psi \tag{13}$$

where Ψ is a compliance function that depends on a/W but not on Q or q, then the work done w_{nl} is

$$w_{nl} = Qq/(n + 1) \tag{14}$$

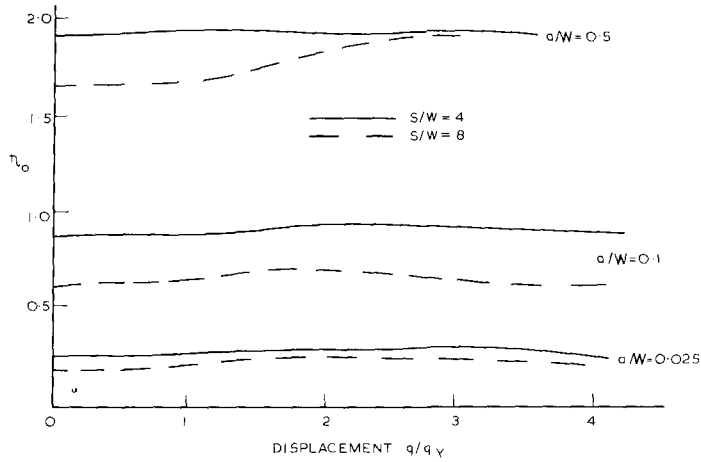

FIG. 2*a*—*The effect of extent of deformation on the overall factor,* η_o, *in three-point bending, from finite element computations in plane strain. NOTE:* q_Y *is the displacement at yield of the uncracked body.*

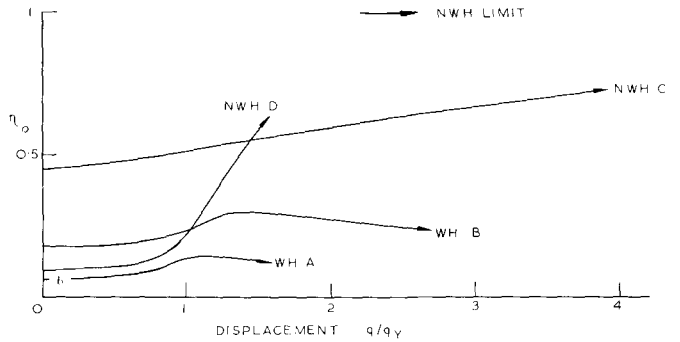

FIG. 2*b*—*The effect of extent of deformation on the overall factor,* η_o, *in tension. A, B = SEN with mild work hardening, deformed with ends kept parallel; for A,* D/W = *4,* a/W = *0.05; for B,* D/W = *4,* a/W = *0.1. C, D = CCP nonwork-hardening; for C,* D/W = *2,* 2a/W = *0.5; for D,* D/W = *2.5,* 2a/W = *0.0625.*

and

$$BJ_{nl} = -\partial w_{nl}/\partial a\,|_q = (w_{nl}/\Psi)\,(d\Psi/da) \tag{15}$$

whence using the form of Eq 6, but with the suffix, nl

$$\eta_{nl} = (b/\Psi)(d\Psi/da) \tag{16}$$

$$= -(b/Q)(\partial Q/\partial a)|_q \tag{16a}$$

$$= (nb/q)(\partial q/\partial a)|_Q \tag{16b}$$

Within the assumptions of this model, η_{nl} exists, Eq 16, as a constant for a given configuration. Note that Eq 1*a* is the form used for the experimental work of [*12*] although they are derived in a different way. Equation 16*a* reduces to Eq 9 for the limit state result, and if $n = 1$ all the above reduce to the LEFM cases. For real elastic-plastic materials it appears that Eq 13 can be interpreted either as an approximate fit to the whole load deflection diagram, in which case, *J*, *w*, η, etc., relate to the total (elastic plus plastic) behavior, or Eq 13 can be interpreted as the nonlinear part, additive to the separate linear elastic part as in Eq 7, in which case q must itself be divided into elastic and plastic components q_{el} and q_{pl}.

If Ψ is moreover independent of the exponent n of the load deflection diagram then $\Psi = \phi$ (that is, the LEFM value of compliance) and $\eta_{nl} = \eta_{el}$. The circumstances under which the variables are completely separable in this way are not clear and require further examination. The computational evidence suggests that although η_{pl} is independent of degree of plasticity for only a small range of configurations, Fig. 2*c* (the deep notch bending or related cases), the overall factor η_o is more nearly (though not entirely) independent of degree of plasticity for a much wider range of cases (Fig. 2*a*,*b*), for which there is by implication a near independence of η_o on n

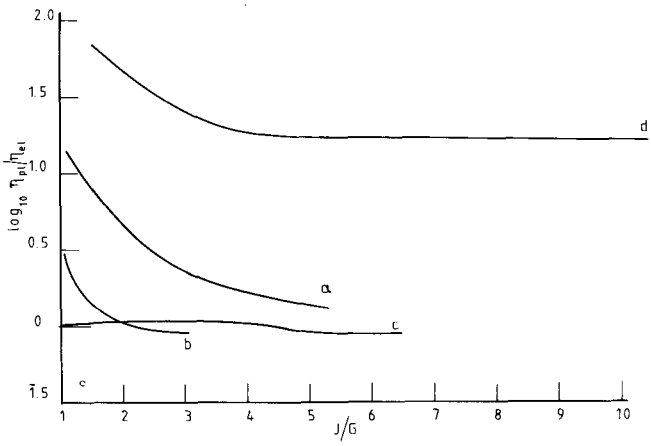

FIG. 2*c*—*The effect of degree of plasticity on the ratio of plastic to elastic factor* η_{pl}/η_{el}. *a*, *b*, = *mild work-hardening: for a, SEN,* D/W = 4, a/W = *0.1, for b, three-point bend,* S/W = *4,* a/W = *0.1. c, d.* = *nonwork hardening; for c, three-point bend,* S/W = *4,* a/W = *0.5, for d, CCP,* D/W = *2.5,* 2a/W = *0.0625.*

from the elastic case of $n = 1$ to the mildly work-hardening, for which $n \approx 0.1$ might be representative.

The second model of interest is the so-called shallow-notch work-hardening behavior, where yield of the gross section remote from the notch can occur if the inequality

$$\sigma_Y w^N < LM\sigma_{fl}\,(W - a)^N \tag{17}$$

is met. σ_{fl} is a work hardened flow stress notionally taken as the tensile strength, or some estimated average strength, $N = 1$ in tension, $N = 2$ in pure bending, L is the plastic constraint factor, and M is the plastic shape factor relating first yield of the section to the limit state ($M = 1.5$ for bending of beams of rectangular section). If the inequality, Eq 17, is not met, then yield is restricted to the slip field associated with the ligament ahead of the crack. This must be so for nonwork hardening and is often so for the deep notch configurations used in standard specimens unless there is a very high degree of hardening. For shallow notches (such as, $a/W < 0.1$) in tension (where $L = 1$, $M = 1$, $N = 1$), first yield of the gross section occurs for a very mild degree of hardening and is thus found in nearly all cases other than the ideal nonhardening behavior. This spread of yield to the "remote cross-sections" away from the notch region radically affects the relationships between the notch stress intensity as measured by J, and the overall work or displacement values as seen in the next section.

An approximate allowance for this behavior can be stated that helps understanding even if barely adequate for numerical purposes. Let suffix t denote "total" (that is, elastic plus plastic), and suffix o denote "overall" (that is, the whole component comprising notched region, n, and gross section remote from the notch, r), then write the work terms as two ratios, α and β

$$\begin{aligned} w_{plo} &= w_{pln} + w_{plr} \\ &= \alpha w_{pln} \end{aligned} \tag{18}$$

and

$$w_{to} = \beta w_{elo} \tag{19}$$

If for shallow notch tension the plastic deformation is assumed to be rather uniform along the gage length once the inequality, Eq 17 has been met, then approximately $\alpha \simeq D/D_n$ where D_n is identified with the gage length influenced by the notch (that is, the slip line region for nonhardening behavior); $D_n = 2(W - a)$ for single edge notch (SEN), or $D_n = W - 2a$

for double edge notch (DEN). For any given load-displacement diagram the ratio of overall to (linear) elastic work, β, can be estimated. For very shallow notch tension where the diagram approximates closely to an elastic triangle plus a plastic rectangle, $\beta \simeq (2qE/D\sigma_Y) - 1 = (2e/e_Y) - 1$. Thus, applying Eq 7

$$\eta_o \simeq [\eta_{el} + \eta_{pl}(\beta - 1)/\alpha]/\beta \tag{20}$$

Note even if elastic and plastic terms are not combined, the effective value of η_{pl} becomes

$$\eta_{pl}(\text{eff}) \simeq \eta_{pl}(\beta - 1)/\alpha\beta \tag{21}$$

As a very simple application of this approximation the following estimates are offered for comparison with a value extracted from an elastic-plastic finite element computation in which J was calculated from the contour integral and w from the total work done. The configuration is single edge notch, $D/W = 4$, $a/W = 0.1$ with mild hardening (not strictly power law) for which $n \simeq 0.12$ in Eq 13, up to $qE/D\sigma_Y \simeq 3$. As a first estimate for simple tension (nonhardening) $\eta_{pl} = N = 1$. As a better estimate (allowing for hardening) [*15*] $\eta_{pl} = 1 - n = 0.88$. Using Eq 20 with $\eta_{el} = 0.2$, $D/W = 4$, $D_n/W = 1.8$, then at a deformation $e/e_Y = 3$, η_o is evaluated as $\eta_o = 0.356$. This compares with the computed value of $\eta_o = 0.33$. According to the present simple estimate, as $e/e_Y \to \infty$ the upper limit of η_o (for n small) is $(1 - n)/\alpha \simeq 0.394$ here. Such an estimate is perhaps sufficient to show that the overall picture contains the correct features, although simple "back of envelope" estimates are hardly adequate. A weakness of the elastic plus plastic analysis is that for small amounts of plasticity there seems reason to suppose (Fig. 2*c*) that the η-value for the plastic component is not the same as the limit state value. The alternative of estimating η_{nl} from the power law hardening model requires a knowledge of Ψ, and if it is assumed $\Psi = \phi$ (the LEFM compliance) then $\eta_{nl} = \eta_{el}$. Some computed values of η_o, evaluated from J contour and work done in plane strain finite element computations are shown (Fig. 2*a*,*b*). The configurations include shallow and deep notches, bending, and tension. No data has been collected for a high degree of hardening. The broad trend of these results is that η_o is approximately independent of the degree of deformation, the more so for bending and rather less so for the tension cases. In no case studied is there the large variation that at first seemed likely when η_{el}-values were known and η_{pl} was taken as N. However, for the shallow notch where the absolute value of η is rather small there may be a significant increase from η_{el} to η_{pl} (take into account the previously cited example $\eta_{el} = 0.2$, $\eta_{pl} = 0.33$, as computed, where both are significantly less than $N = 1$, yet differ by 50 percent from each other), so that a

statement "η_o is approximately independent of deformation" requires careful interpretation according to circumstances.

Some Uses of the η Factor

Test Procedures

The original use of η in the author's previous analysis [*1*] was to show that the term w/Bb sometimes used in impact testing, where work is the only variable measured, is not equal to G, but can be related to it. If data are available for various notch depths (strictly with evidence that $w = Qq/2$, with no "tail" to the diagram) then from Eq 1 a plot of work to fracture against the "modified area" Bb/η_{el} will have a slope G_c, as seen in Fig. 3, Curve A. This method was used [*2*] for impact tests on brittle plastics. The unmeasured kinetic energy displaced the line from the origin (Fig. 3, Curve B) but appeared to give the slope substantially as required.

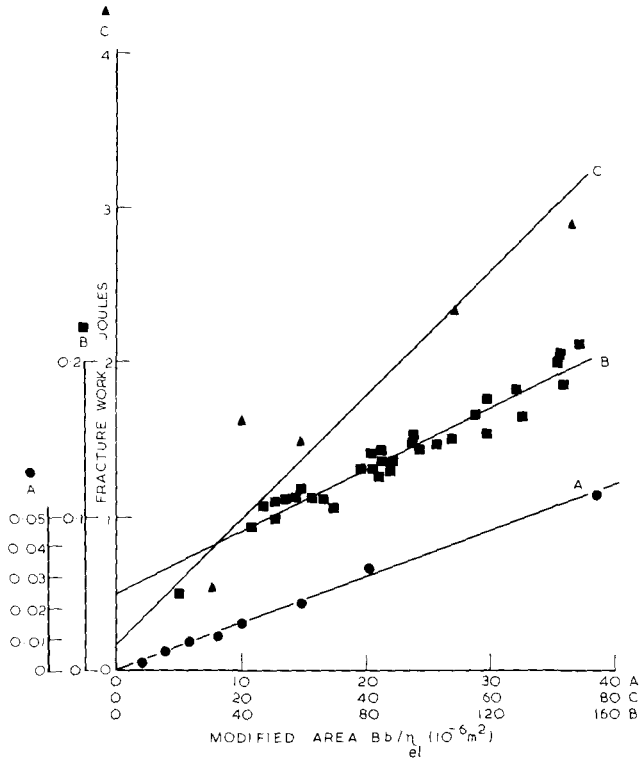

FIG. 3—*Determination of G_{Ic} by linear plots of work to fracture versus the modified area* Bb/η_{el}; *A—Poly-methyl-methacrylate (PMMA) static tests* [1]; *B—PMMA, impact tests* [2]; *and C—aluminum alloy L95WP, impact tests.*

Some recent data on a high-strength aluminum alloy are shown, Fig. 3, Curve C. The resulting value of G_c from the slope gives a toughness value in terms of K that compares favorably with conventional K_{Ic} tests. It is supposed that for this material there is a negligible effect of strain rate on toughness. Dynamic load-deflection records to picture more fully the work to fracture were not taken in this particular study, so that the near agreement in toughness value with that anticipated should not be regarded as definitive.

The direct relationship of toughness to work, extended to plasticity by Eq 6, is the basis of the one specimen technique for finding J_c. The requirement for detecting the onset of crack growth so that the work is measured up to that point only, parallels the requirement of "no tail" to the diagram in the LEFM use. Thus, use of Eq 6 overcomes the need for calibration using more than one crack length as originally introduced by Begley and Landes [*16*] but may still require the use of more than one specimen to determine the onset of growth. Following the experimental determination of η by Ernst et al [*12*] for a particular material and configuration, methods are now becoming available to determine both onset of growth and current crack length for the determination of the R-curve from a single test.

Other Estimates of J

A statement that η is independent of the degree of deformation clearly relates the concept of equivalent energy to the J theory. This statement implies nothing about the procedures that may be attached to the use of J or equivalent energy [*17*], or the absolute relevance of either, but merely points out that an equivalent G, G_{eq}, derived from an elastic diagram of equal area, w, will be numerically related to J by

$$G_{eq}/\eta_{el} = J/\eta_o = w/Bb \tag{22}$$

Clearly, if $\eta_{el} \simeq \eta_o$, as has been realized for some time for deep notch three-point bending, where for $S/W = 4$ both terms are approximately 2, then $G_{eq} \simeq J$. The evidence of Fig. 2 is that the near constancy of η_o with respect to deformation extends, at least approximately, over a wider range of configurations than was at one time realized. The relationship between J and work can be approximated in various ways. Thus

$$J = G(w_t/w_{el})(\eta_o/\eta_{el}) \tag{23}$$

where w_t is the total work done (OXAC), Fig. 4, and w_{el} is the actual elastic work (BAC). If a value for η_o is known then J is best estimated

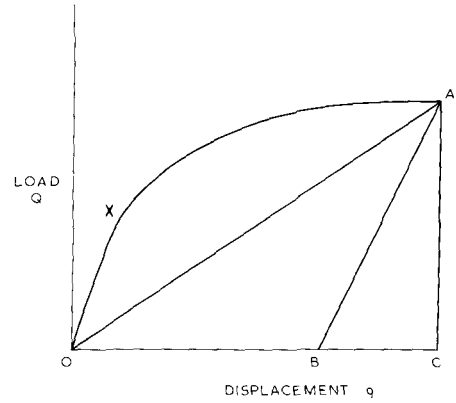

FIG. 4—*Load displacement diagram showing apparent compliance OA and actual elastic compliance BA (parallel to OX).*

from Eq 8. If a value for η_o is not known but the assumption $\eta_o \simeq \eta_{el}$ is nevertheless made, then an estimate for J is

$$J \simeq G(w_t/w_{el}) \tag{24}$$

As just noted, this would be reasonable for bending cases for all notch depths but less valid for tension beyond contained yield. J can also be expressed in terms of the apparent compliance OA (Fig. 4). Using the suffix (a) to denote the values associated with the apparent configuration for which OA is the compliance,

$$\begin{aligned} J &= G(\phi_a/\phi)(w_t/w_a)(\eta_o/\eta_{el}) \\ &= G_a(w_t/w_a)(\eta_o/\eta_{ela})(b_a/b) \end{aligned} \tag{25}$$

Data computed in bending with mild work-hardening show the term $(w_t/b) \approx (w_a/b_a)$ to within a few percent for shallow and deep notches (up to $J/G \simeq 2$). Although this relationship does not seem fundamental, it is quite plausible and allows the approximate statement

$$J \simeq G_a(\eta_o/\eta_{ela}) \tag{26}$$

If $\eta_o \simeq \eta_{el}$ and also η_{el} is independent of crack length in the range b to b_a, then

$$J \simeq G_a \tag{27}$$

This approximation would not be unreasonable for many cases of contained yield where it is analogous to $J \simeq G(a + r_p)/a$ but with the size of plastic zone, r_p, now evaluated by effective compliance rather than by the usual Irwin correction factor. It would also be reasonable for extensive yield in deep notch bending, $S/W = 4$, where $\eta_o \simeq \eta \simeq 2$ over a range of notch depths, but not for other circumstances where either $\eta_o > \eta_{el}$ or η_{el} varies significantly with crack length.

J-*Displacement Relationships and the* J *Design Curve*

If Eq 6 is differentiated for the limit case with $w_{pl} = Q_L q$ and η_{pl} constant, then

$$dJ_{pl}/dq = \eta_{pl} Q_L / Bb \tag{28}$$

The form of this expression was given by Bucci et al [*18*], but it is usually discussed for the case, Eq 12, where $\eta_{pl} = N$. The excellent agreement found [*19*] for both deep and shallow notch tension between computed data for center cracked panel (CCP) nonhardening cases (where inequality, Eq 17, is not satisfied) and Eq 28 with $\eta_{pl} = N = 1$ is shown in Fig. 5*a*, Curves A, B, and C. But with mild work hardening sufficient for inequality, Eq 17, to be satisfied (for SEN[4] with $a/W = 0.1$), the results, Fig. 5*a*, Curve D [*20*], require the insertion of η_{eff} from Eq 21.

Values for three-point bending are shown, Fig. 5*b*. Agreement with the simple theory is excellent for the deeper notches, A-a and B-b, but is inadequate for shallow notches, C-c, where yield breaks back to the front surface of the beam, requiring use of Eq 11 rather than Eq 12 for estimating η. If the abscissa of Fig. 5 is changed from displacement q to strain in the uncracked body, then the Curves C are representative of the J design curve [*20-22*]. Based on data computed in plane strain for shallow notch cases, $0.025 < a/W < 0.1$ in tension and bending and for certain other cases of cracks emanating from or buried beneath a hole in a plate in tension and at the bore of a thick cylinder under pressure (represented in two dimensions), it was shown [*22,23*], that the upper edge of the computed data could be represented by the three equations, as summarized [*10*] for $e/e_Y \leq 0.85$; that is, LEFM

$$JE/Y^2\sigma_Y{}^2 a = (e/e_Y)^2 \tag{29}$$

[4]It is clear from other data that the difference between the cases is not due to the change from CCP to SEN but from nonhardening to mildly hardening as judged in relation to Eq 17.

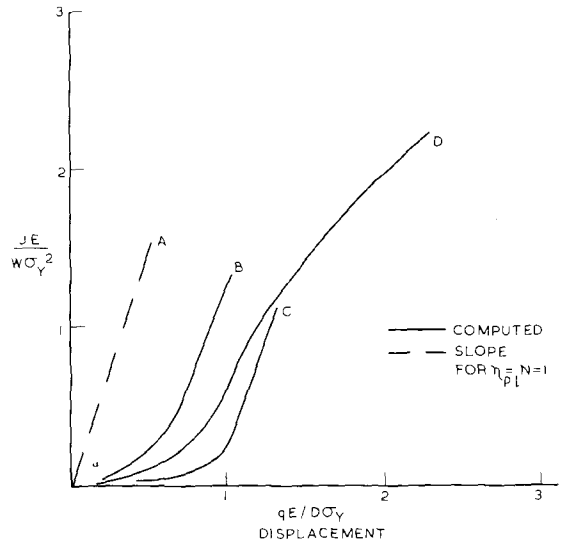

FIG. 5*a*—*Computed values of* J*-contour integral versus displacement showing comparison with slopes in the plastic regime as predicted by simple theory. Tension plane strain*—(A) *slope in plastic regime from simple theory* [18]; (*B*) *Nonwork hardening, CCP,* a/W = *0.5;* (*C*) *Nonwork hardening, CCP,* a/W = *0.0625; and* (*D*) *mild work hardening. SEN,* a/W = *0.1* [20].

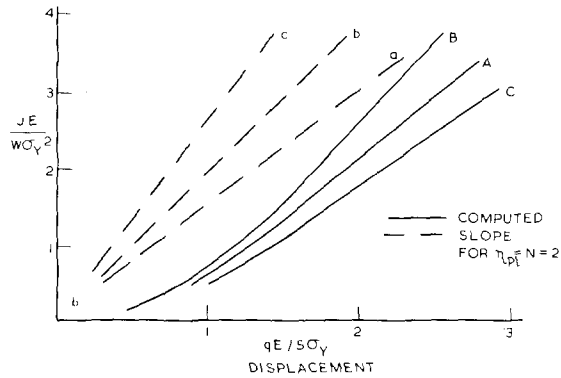

FIG. 5*b*—*Three-point bending, plane strain, mild work hardening. A, B, C computed; a, b, c, simple theory: A-a,* a/W = *0.5; B-b,* a/W = *0.3, and C-c,* a/W = *0.1.*

for $0.85 \leq e/e_Y \leq 1.2$; that is, contained yield

$$JE/Y^2\sigma_Y{}^2a < 5[(e/e_Y) - 0.7] \tag{30}$$

for $e/e_Y > 1.2$; that is, uncontained yield

$$JE/Y^2\sigma_Y{}^2a < 2.5[(e/e_Y) - 0.2] \tag{31}$$

The COD design curve [*24*] as now used [*25*], defines an equivalent crack, $\bar{a}$, such that $Y^2a = \pi\bar{a}$, by the equations

$$\delta E/\sigma_Y\bar{a} = (e/e_Y)^2 \qquad \text{for } e/e_Y \leq 0.5$$

$$\delta E/\sigma_Y\bar{a} = (e/e_Y) - 0.25 \qquad \text{for } e/e_Y \geq 0.5 \tag{32}$$

The COD and J design curves were compared in Refs *23, 24*. The $\bar{a}$ terminology is used in Fig. 6, where J is also translated to COD by $J = m\sigma_Y\delta$. It is usually found that $1 < m < 3$ and in extensive yield the slope of the COD curve agrees well with the J formulation if $m = 2$ (Fig. 6). In the LEFM regime the agreement is better if $m = 1$, but there are a number of

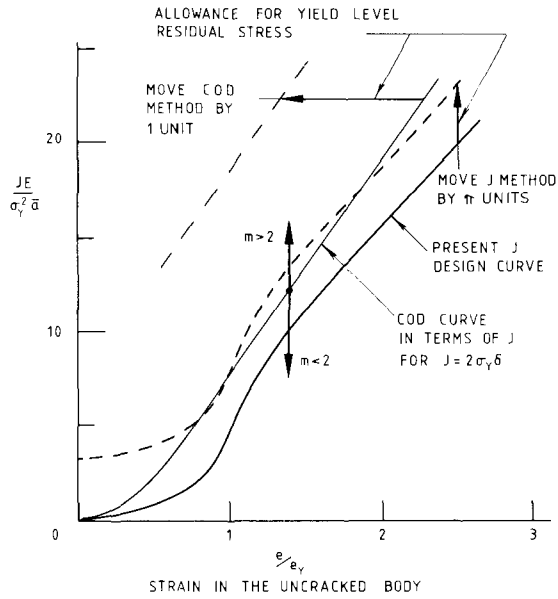

FIG. 6—*Comparison of proposed* J *design curve, with and without yield level residual stresses, and* J *derived from COD design curve using* $J = 2\sigma_Y\delta$ *(after* [24]*). NOTE:* _____ = *mechanical stress only, and* ---------- = *mechanical plus residual.*

other differences [*24*] that must be considered if close agreement is required. The point at issue is that the J analysis provides a curve that contains the η factor via Eq 28. The dependence of η on configuration (via Eqs 11, 20 and 21) allows the whole group ($JE/Y^2\sigma_Y{}^2a$) to be sufficiently independent of geometry (for shallow notches and mild work hardening) to permit the establishment of a simple one curve design concept when expressed against e/e_Y. This concept parallels in all general trends the COD design curve itself already supported by extensive experimental data, yet based on no firm theoretical formulation since the original Dugdale model did not allow the yield of the gross section or changes in constraint that determine the relevant value of η.

A further use of the η factor was incorporated into the J design curve [*24,27*] to allow for residual stresses. It is well-known that the J contour integral is not path-independent in the presence of residual stress but the close similarity between COD and J suggests that the satisfactory experience gained in using COD for residual stress cases [*28*] must have its counterpart in J theory, if rigor is dropped in favor of simplicity. It was therefore argued [*27*] that for rule of thumb purposes in which residual stress values are not known in detail, the effects could be allowed for in the following three steps: (1) effect of the procedure causing the residual stress (for example, welding, cold forming) on material toughness (including weld metal and heat affected zone (HAZ) if need be); (2) treatment of "long range" or "reaction" residual stress fields, if any, as conventional loads, probably displacement controlled, and (3) treatment of "short range" or equilibrium stress fields through the η factor. The maximum elastic strain energy, w, in the short range fields is $V\sigma_Y{}^2/2E$, where V is the volume affected, of order Blh where B is plate thickness, l is the length, and h is the width of the zone affected by high residual stress. Thus, applying Eq 1

$$G = \eta_{el}\sigma_Y{}^2 \frac{Blh}{2EB(W - a)} \tag{33}$$

Taking the shallow crack value of η_{el} for tensile loading, $\eta_{el} \approx 8a/D$, G is estimated for two cases: a transverse weld, $l = W$, $h = D$, in which a crack could sever the plate by running parallel to the weld line, and a longitudinal weld for which the effective width W is identified with the extent of the residual stress region h and for which the length l over which a crack would relax the stresses is identified as D. In both cases h is of order two or three B, as is l for the longitudinal weld, but the precise relationship is not required in the above approximations. Thus, in both cases, the effective G for residual stress is expressed by the relationship

$$GE/Y^2\sigma_Y{}^2a \simeq 1 \tag{34}$$

Expressing G as J_{el}, the design curve of Eqs 29-31 is moved by unity on the scale $JE/Y^2\sigma_Y{}^2a$ to allow for the combination of yield level residual stress and applied stresses that enter the plastic regime. On the ordinate of Fig. 6, the J-design curve is moved by π units. Although the procedure of adding G (or J)-values appears not to be conservative if the combined applied and residual stresses are elastic (and could therefore be treated by LEFM if the stress values were known), the present procedure offsets this by assuming the residual stresses to be of yield level. The concept is again heuristic. It acts in the same direction as the procedure in the COD design method, which adjusts the abscissa e/e_Y by unity for yield stress level residual stresses, but is less demanding. Further features relevant to the whole design diagram pertaining to notch depth and work-hardening in connection with inequality of Eq 17 and to the effect of the unnotched body (or remote parts of the component) being in plane stress or plane strain are discussed elsewhere [*23,27*] but are not directly associated with the present discussion on use of the η factor.

Instability

Since there are many expressions for K in terms of load, $\partial G/\partial a|_Q$ can be evaluated easily. Neglecting crack line loading cases the common form for K is $K = Y\sigma\sqrt{a}$ so that

$$\left.\frac{\partial G}{\partial a}\right|_Q = \frac{G}{a}\left[1 + \frac{2a}{Y}\frac{dY}{da}\right] \tag{35}$$

Various other quantities can then be expressed in terms of $\partial G/\partial a|_Q$ and η_{el}, perhaps more conveniently than in other ways [*29*]. Thus, from Eq 1 and for brevity, writing η_{el} as η

$$\frac{b}{G}\frac{dG}{da} = 1 + \frac{b}{\eta}\frac{d\eta}{da} + \frac{b}{w}\frac{dw}{da} \tag{36}$$

Using the notation

$$1 + \frac{b}{\eta}\frac{d\eta}{da} = f_1(\eta) \tag{37}$$

then

$$\frac{b}{G}\frac{dG}{da} = f_1(\eta) + \frac{b}{w}\frac{dw}{da} \tag{38}$$

and

$$\frac{b}{G}\frac{\partial G}{\partial a}\bigg|_Q = f_1(\eta) + \eta \tag{39}$$

$$= \frac{b}{a} + \frac{2b}{Y}\frac{dY}{da} \tag{39a}$$

From Eq 35, also

$$\frac{b}{G}\frac{\partial G}{\partial a}\bigg|_q = f_1(\eta) - \eta \tag{40}$$

Whence

$$\frac{\partial G}{\partial a}\bigg|_q = \frac{\partial G}{\partial a}\bigg|_Q - 2\eta\frac{G}{B} \tag{41}$$

For those cases where G is independent of gage length (that is, neglecting crack-line loading and short span beams where shear is significant), then $f_1(\eta) + \eta$ must be independent of gage length, although $f_1(\eta) - \eta$ is not, and this follows from Eq 4. The order of magnitude of some of the terms can be assessed for the common specimens. As seen Fig. 1, for deep notches η is about two (for bending) and one (for tension) though decreasing with increase of gage length or span, and tending to about $8a/d$ ($d = D$ for tension, $d = S/9$ for bending) for shallow notches. Values of (b/η) $(d\eta/da)$ lie between zero or slightly negative (deep-notch bending with $S/W = 4$) and about b/a, which is of order unity except for shallow notches. More precise values can, of course, be found from Eqs 3, 4, or 39. If fracture initiates at G_i and the toughness does not vary with crack growth or implied variables such as strain rate, then for unstable growth at constant displacement $\partial G/\partial a\,|_q$ must be positive, that is, the purely geometric relation

$$f_1(\eta) > \eta \tag{42}$$

must be fulfilled. For unstable growth at constant load the requirement is

$$f_1(\eta) + \eta > 0 \tag{43}$$

and since η is always positive this is nearly always so except for the crack-line loaded cases here excluded, in which $d\eta/da$ may be strongly negative. The effect of external compliance can be included by using an effective gage length or span. Thus, a structural or machine compliance can be

written $\phi_m = BEW/d_{\text{eff}}$ (where $d = D$ for tension and $S/9$ for bending). This term will greatly affect η and hence the constant displacement case, but not the constant load case, which as already noted is independent of length within certain restrictions.

The statements of unstable growth, Eqs 42 and 43, only ensure that on reaching $G = G_i$ growth will at first continue. There is no assurance that growth will continue to the extent that the ligament is completely severed. In short, the sign of $\partial G/\partial a$ even if initially positive may change to negative for certain configurations. If it is assumed that there is no dissipation other than by fracture, then the total work, w_f, to sever the ligament is (for constant toughness)

$$w_f = G_i B(W - a) \tag{44}$$

Thus, the condition for total severence is that when $G = G_i$ at the same time $w = w_f$. This condition is met for geometries where

$$\eta \leq 1 \tag{45}$$

The real problem is, of course, dynamic, and the preceding simple treatment implies that any kinetic energy generated when $G > G_i$ is returned to the fracture process as the crack spreads to regions where $G < G_i$ so that the elastic energy available (at constant displacement, with no further external work input) is just sufficient to provide the total work of fracture. The effect of gage length can again be included in estimating η so that the meaning of "external work" can be "external to the component" if the real gage length is taken or "external to the structure" if the effective gage length is taken, while still neglecting inertia for this static model. Clearly, if for reasons of material, temperature, or strain rate, some mean toughness, G_m, is known to be more relevant than G_i, then the statement for complete instability (after initiation at $G = G_i$) becomes

$$\eta \leq G_i/G_m \tag{46}$$

If, as may well be the case for some structural steels at low temperature, the mean toughness for propagation is perhaps only half of that for initiation, then since η is two or less for most of the conventional testpiece shapes (it is slightly in excess of two for compact tension (CT) specimens), complete separation is to be expected even in a stiff machine. If fracture toughness increases with crack growth as in the conventional picture of crack resistance or R-curves, then unstable growth requires not only $G \geq G_i$ but also $\partial G/\partial a \geq dR/da$. Crack-line load cases in which G decreases with crack length even at constant load are here neglected. The well-known

tangency condition for instability can be expressed in a simple way for either load or displacement control (including finite compliance within the latter case as an effective gage length, d_{eff}) by using Eqs 39 or 40 as appropriate. Thus, for unstable crack growth with finite compliance (with $d_{eff} = d_{actual}$ for "fixed grip")

$$\frac{G}{b}[f_1(\eta) - \eta] \geq \frac{dR}{da} \tag{47}$$

For fixed load, unstable growth requires

$$\frac{G}{b}[f_1(\eta) + \eta] \geq \frac{dR}{da} \tag{48}$$

With high compliance, represented by an effective gage length $d_{eff} \to \infty$ then $\eta_{el} \to 0$ so both expressions reduce to the same term. This formulation emphasizes that the applied term $\partial G/\partial a$ is but a simple multiple of G given by one of the geometry dependent expressions $(f_1(\eta) \pm \eta)/b$.

The problem of stable growth in the plastic regime has recently been described in terms of J [*30*] using the R-curve analysis of [*31*]. The relevance of η_{pl} is briefly recalled. The R-curve is seen as a measure of total dissipation of plastic work to which shear lips contribute a part but by no means the whole. Thus, a major component of the R-curve is gross plastic work not necessarily immediately adjacent to the crack surface. This dissipation of work is expressed in the form of a material property through dJ/da and appropriate size and configuration factors, $B(W - a)$ and η_{pl}, that in essence allow the original geometry dependent increment of work, dw, to be normalized in terms of J by differentiation of Eq 6. The argument was summarized in [*11*] and is not repeated here. Expressions similar in form to Eqs 36-41 have been written down [*32*] to relate dJ and η if the power law expression, Eq 13, is used. Additional terms in n arise (where $n \neq 1$) as given in the Appendix. Equation 39 does not, of course, apply unless $\eta_{nl} = \eta_{el}$, but subject to the uncertainties already discussed, estimates of η_{pl} or η_{nl} can be made and used for assessing the applied severity (T_{app} in the notation of Ref *13*) in problems of ductile tearing. It can be also noted that if $\omega \gg 1$ (where $\omega = (d/J)(dJ/da)$ as in Ref *14*) then the J_r curve for material tearing resistance (T_{mat} in the notation of Ref *13*) reduces to that found in conventional J testing. If a correction of the form $J_{corr} \simeq J(1 - (\Delta a/b))$ is introduced, it is relevant for deep notch bending, but not as a generality, since, as pointed up elsewhere [*33*], $J_{corr} = J + dJ_r$ only for that case, because the term $f_1(\eta) - \eta$ then has the value -1 which leads to the desired result.

The elastic energy release rate, I, available in the presence of plasticity,

was expressed [*11*] in terms of the elastic component of displacement, q_{el} and the η factor. For near limit load, Q_L, the expression was

$$BI = BG - \frac{q_{el}}{\eta_{pl}}(\eta_{pl} - \eta_{el})\frac{\partial Q_L}{\partial a} \tag{49}$$

The total work dissipation rate during crack growth also involved η, and was expressed (for the case $\omega \gg 1$) as

$$Bdw/da = B(b/\eta_{pl})(dJ_r/da) \tag{50}$$

Prediction of unstable growth was made when the available rate, Eq 49, exceeded the dissipation rate, Eq 50.

Although this analysis gives the same term $T_{mat} = (E/\sigma_Y{}^2)(dJ_r/da)$ for the measure of resistance to tearing as that found by Paris et al [*13*] and indeed the same dominant parameters in the applied term, nevertheless, the coefficient of T_{app} contains the term $(\eta_{pl} - \eta_{el})$ among others. It is relatively easy to show that for a tough material and with little external compliance, unstable growth is often impossible since $T_{mat} \gg T_{app}$, but if an actual prediction of instability is required (as T_{mat} is reduced by continued crack growth or if T_{app} is increased through compliance) then the numerical values are clouded by uncertainty over the term $(\eta_{pl} - \eta_{el})$ which, as seen from the data of Fig. 2, may in some cases become the small difference of similar quantities. More detailed discussion of the comparison between Refs *11* and *13* will be offered elsewhere [*33*], but for the prediction of the instability event it seems better estimates of η in contained yield and full plasticity are required. It was also suggested [*10*] that the combined term $\eta/B(W - a)$ accounts for size and configuration in a way that at least conceptually performs the role of Broberg's "screening function" [*34*], defining the fraction of overall work that reaches the tip.

Stress State

Two rather indistinct uses of η are noted with some reservations on validity. There is some computational evidence that the variation of η with extent of deformation reflects the change of constraint, if any, from elastic behavior to plastic behavior, but the evidence is not clear since the "far boundaries" which, of course, partly determine constraint, also affect the work done. The variation in η appears to arise from the constraint factor in Eq 10 being in effect a function of the extent of deformation (although the plastic constraint factor itself is defined only for the limit state), so that the effects of variation of constraint (Eq 11) and of degree of deformation (Eqs 18-21) combine. As discussed [*15*] this may mean that η_{pl} does not

exist in the strict sense in that the variables of deformation and configuration are no longer separable. The relation of fracture to stress state is uncertain. Despite a large amount of evidence there is still no agreement in the literature on whether J_i is a suitable criterion for all degrees of triaxiality. The writer inclines to the view that a one-parameter criterion should be a reasonable measure of crack-tip severity for a given degree of triaxiality. Insofar as the datum measure is usually taken as K_{Ic} (or G_{Ic}) (that is, plane-strain conditions in LEFM which is itself a condition of high triaxiality ($\sigma_{yy}:\sigma_{xx}:\sigma_{zz} = 1:1:2\nu$)), then other conditions of high triaxiality such as high work-hardening, contained yield (the Prandtl slip field) or extensive yield for those configurations that maintain high constraint (for example, bending and similar curved slip line fields) should all be relatable to the J analysis, which when used in plane strain, models high constraint. It may be argumentatively less relevant to the cases in extensive plasticity where low constraint is found even in plane strain, since these would not relate to the LEFM datum. Thus, a one parameter discussion of fracture initiation or instability may have to be restricted to constraint that closely matches the particular application or be accepted on a lower bound basis. For lower bound data the high constraint configurations of deep-notch bending or compact tension are usually deemed adequate although for a lower bound R-curve the appropriate direction of propagation and absence of shear-lip would also be necessary. The present discussion tentatively links the statements of the invariance or otherwise of η with degree of deformation, to maintenance of constraint so that the J dominated field continues to match the plane-strain LEFM field that is used as the datum.

A similar possible relevance of η also tentative as yet, arises in connection with creep cracking where relationships have been reported between crack growth rate and both a J-like term (called C^* in Ref *35* and $\dot{J}$ in Ref *36*) and work rate, Qdq/dt [*37*]. Insofar as both correlations are valid, a term corresponding to the η factor is implied linking C^* to work rate in analogy with J to work, although there is insufficient evidence to judge whether its value would match that of η_{el}. By analogy between power law hardening and secondary creep rate, it is likely to do so at least in those configurations where $\eta_{pl} \simeq \eta_{el}$.

Conclusions

The η factor provides a direct relationship between work per unit area, w/Bb, and crack tip deformation as measured by G in linear elastic, or J in nonlinear or plastic regimes. The relationship is complementary to and self consistent with the well-known definitions of G or J in terms of energy rate per unit crack advance. Analytical methods exist for evaluating the

term for simple cases when the variables of geometry and the degree of deformation are separable, and experimental, computational, or approximate methods can be used even when the use is not rigorous. Adoption of the factor to reexamine a range of fracture problems offers a certain insight, heuristic rather than rigorous, into test methods, design curves, effects of residual stress, instability, and so on that assists in the evaluation of approximate procedures and helps link together otherwise disparate problems.

Acknowledgments

The work described here was supported at Imperial College in part by the Science Research Council of the United Kingdom and developed through the help of several colleagues. It has been greatly stimulated by recent visits to the Center for Fracture Mechanics, Washington University, St. Louis, Mo., made possible by Paul Paris, his co-workers and sponsors.

APPENDIX

Relations Between dJ and η for Power Law Loading

If loading is described by Eq 13 and area under the loading deflection diagram by Eq 14, then subject to the restrictions on separation of variables, discussed [*15*], η_{nl} is defined by Eq 16, and relationships comparable to Eqs 36-41 are

$$\frac{b}{J}\frac{dJ}{da} = 1 + \frac{b}{\eta}\frac{d\eta}{da} + \frac{b}{w}\frac{dw}{da} \tag{51}$$

where here η implies η_{nl} whereas in Eq 36 it referred to η_{el}. Similarly, the $f_1(\eta)$ notation of Eq 38 here implies use of η_{nl} and

$$\frac{b}{J}\frac{\partial J}{\partial a}\bigg|_Q = f_1(\eta) + \frac{\eta}{n} \tag{52}$$

$$\frac{b}{J}\frac{\partial J}{\partial a}\bigg|_q = f_1(\eta) - \eta \tag{53}$$

whence

$$\frac{b}{J}\frac{\partial J}{\partial a}\bigg|_q = \frac{b}{J}\frac{\partial J}{\partial a}\bigg|_Q - \frac{n+1}{n}\eta\frac{J}{b} \tag{54}$$

References

[*1*] Turner, C. E., *Material Science Engineering*, Vol. 11, 1973, pp. 275-282.
[*2*] Marshall, C. P., Williams, J. G., and Turner, C. E., *Journal of Materials Science*, Vol. 8, 1973, pp. 949-956.

[3] Feddein, G. and Macherauch, E., "A New Method for Fracture Toughness Determination," Third International Conference on Fracture, Munich, Vol. 3, 1973, pp. 11-241.
[4] Rice, J. R., Paris, P. C., and Merkle, J. in *Progress in Flaw Growth and Toughness Testing, ASTM STP 536,* American Society for Testing and Materials, 1973, pp. 231-244.
[5] Merkle, J. G. and Corten, H. T., American Society of Mechanical Engineers' *Journal of Pressure Vessel Technology,* Vol. 96, No. 4, 1974, pp. 286-293.
[6] Sumpter, J. D. G. and Turner, C. E. in *Cracks and Fracture, ASTM STP 601,* American Society for Testing and Materials, 1976, pp. 3-15.
[7] Dawes, M. G., "*J* Estimation Procedures for Weldments," Welding Institute Research Report E 65/75, Welding Institute, Cambridge, U.K., 1975.
[8] Chipperfield, C. G. in *Dynamic Fracture Toughness,* Welding Institute/American Society for Metals, 1976, pp. 169-80.
[9] Srawley, J., *International Journal of Fracture,* Vol. 12, 1976, pp. 470-474.
[10] Turner, C. E. in *Post Yield Fracture Mechanics,* Chapter 2, D. G. H. Latzko, Ed., Applied Science, London, U.K., 1979.
[11] Turner, C. E. in *Fracture Mechanics, ASTM STP 677,* C. W. Smith, Ed., American Society for Testing and Materials, 1979, pp. 614-628.
[12] Ernst, H., Paris, P. C., Rossow, M., and Hutchinson, J. in *Fracture Mechanics, ASTM STP 677,* American Society for Testing and Materials, C. W. Smith, Ed., 1979, pp. 581-599.
[13] Paris, P. C., Tada, H., Zahoor, A., and Ernst, H. in *Elastic-Plastic Fracture, ASTM STP 668,* American Society for Testing and Materials, 1979.
[14] Hutchinson, J. and Paris, P. C. in *Elastic-Plastic Fracture, ASTM STP 668,* American Society for Testing and Materials, 1979.
[15] Ernst, H., Paris, P. C., and Turner, C. E., this publication, pp. 338-351.
[16] Begley, J. A. and Landes, J. D. in *Fracture Toughness, ASTM STP 514,* American Society for Testing and Materials, 1972, pp. 1-23.
[17] Witt, F. J. in *Practical Application of Fracture Mechanics to Pressure Vessel Technology,* Institution of Mechanical Engineers, London, 1971, pp. 163-167.
[18] Bucci, R. J., Paris, P. C., Landes, J. D., and Rice, J. R. in *Fracture Toughness, ASTM STP 514,* American Society for Testing and Materials, 1972, pp. 40-69.
[19] Sumpter, J. D. G., Hayes, D. J., Jones, G. T., and Turner, C. E., "Post-Yield Analysis and Fracture in Notch Tension Pieces," Third International Conference on Fracture, Munich, 1973, pp. 1-433.
[20] Sumpter, J. D. G. and Turner, C. E., "Design Using Elastic-Plastic Fracture Mechanics," *International Journal of Fracture,* Vol. 12, 1976, pp. 801-873.
[21] Begley, L. A., Landes, J. D., and Wilson, K. in *Fracture Analysis, ASTM STP 560,* American Society for Testing and Materials, 1974, pp. 105-109.
[22] Turner, C. E., "A *J* Design Curve Based on Estimates for Some Two-Dimensional Shallow Notched Configurations," Specialists Meeting on Elastic-Plastic Fracture Mechanics, United Kingdom Atomic Energy Authority/Organization for Economic Cooperation and Development—Nuclear Energy Authority, Committee for Safety of Nuclear Installation Report 32, Vol. 2, 1978.
[23] Dawes, M. G. in *Advances in Electro-Plastic Fracture Mechanics,* L. H. Larsson, Ed., 1980, Applied Science, London, U.K., pp. 279-300.
[24] Turner, C. E. in *Advances in Electro-Plastic Fracture Mechanics,* L. H. Larsson, Ed., 1980, Applied Science, London, U.K., pp. 301-318.
[25] Burdekin, F. M. and Dawes, M. G. in *Practical Application of Fracture Mechanics to Pressure Vessel Technology,* Institution of Mechanical Engineers, London, 1971, p. 28.
[26] Dawes, M. G., "Fracture Control in High Yield Strength Weldments," *Welding Journal Research Supplement,* Vol. 53, 1974, p. 369a.
[27] Turner, C. E., "Remarks on the Use of *J*-Integral for Yielding Fracture Mechanics," submitted to the *Journal of Strain Analysis,* 1980.
[28] Dawes, M. G. and Kamath, M. S., "The Crack Opening Displacement (COD) Design Curve Approach to Crack Tolerance," Conference on Tolerance of Flaws in Pressurised Components, Institution of Mechanical Engineers, London, 1978, pp. 27-42.
[29] Turner, C. E. in *Advances in Electro-Plastic Fracture Mechanics,* L. H. Larsson, Ed., 1980, Applied Science, London, U.K., pp. 91-108.

[30] Garwood, M. J., Pratt, P. L., and Turner, C. E., "Measurements of Slow Stable Crack Growth in Structural Steels and Prediction of Unstable Fracture," Specialists Meeting on Elastic-Plastic Fracture Mechanics, United Kingdom Atomic Energy Authority/ Organization for Economic Cooperation and Development—Nuclear Energy Authority, Committee for Safety of Nuclear Installation Report 32, Vol. 1, 1978.

[31] Garwood, S. J., Robinson, J. N., and Turner, C. E., *International Journal of Fracture,* Vol. 11, 1975, pp. 528-530.

[32] Turner, C. E. in *Advances in Electro-Plastic Fracture Mechanics,* L. H. Larsson, Ed., 1980. Applied Science, London, U.K., pp. 139-164.

[33] Turner, C. E., "Remarks on Unstable Crack Growth," Committee for Safety of Nuclear Installation Specialist Meeting on Plastic Tearing Instability, Organization for Economic Cooperation and Development—Nuclear Energy Authority and the U.S. Nuclear Regulatory Commission (to be presented Sept. 1979 at Washington University, St. Louis, Mo.).

[34] Broberg, K. B. in *Prospects in Fracture Mechanics,* Noordhoff, The Netherlands, 1974, pp. 125-138.

[35] Landes, J. D. and Begley, J. A., "A Fracture Mechanics Approach to Creep Crack Growth," Report 74-137-FES GT-P1, Westinghouse Research Laboratories, Pittsburgh, Pa., 1974.

[36] Nikbin, K. M., Webster, G. A., and Turner, C. E. in *Cracks and Fractures, ASTM STP 601,* American Society for Testing and Materials, 1976, pp. 47-62.

[37] Nikbin, K. M., Webster, G. A., and Turner, C. E., *Fracture 1974,* Fourth International Conference on Fracture, D. M. R. Taplin, Ed., University of Waterloo, Ont., Canada, Vol. 2, 1977, pp. 627-634.

P. C. Paris,[1] *Hugo Ernst,*[1] *and C. E. Turner*[2]

A J-Integral Approach to Development of η-Factors

REFERENCE: Paris, P. C., Ernst, Hugo, and Turner, C. E., **"A J-Integral Approach to Development of η-Factors,"** *Fracture Mechanics: Twelfth Conference, ASTM STP 700,* American Society for Testing and Materials, 1980, pp. 338-351.

ABSTRACT: Relating work done on a notched or cracked test piece directly to other fracture parameters, such as the J-integral, has been of interest at least since the development of the Charpy test. In this paper relationships between J and work are explored. The conditions for the existence of direct relationships are explained, and some cases where such relationships do not exist are observed. Moreover, these relationships are explored in terms of Turner's η-factors, which are useful both in J-integral test analysis methods and for structural analysis.

KEY WORDS: fractures (materials), J-integral, plasticity, elastic-plastic fracture mechanics, toughness, work to fracture, crack propagation

The η-factor is a factor relating J to the work per unit uncracked ligament area in loading a cracked body. An approach to provide the η-factor with a mathematical basis will be given here, which is based on the dimensional analysis of load-displacement relationships of Ernst, Paris, Rossow, and Hutchinson [*1*][3] and earlier such developments of Rice, Paris, and Merkle [*2*]. Following these works, [*1,2*], the J-integral may be written first in its alternative forms

$$J = \oint_\Gamma \left(W dy - T_i \frac{\partial u_i}{\partial x} ds \right)$$

or (1)

$$J = -\int \frac{\partial P}{\partial a} d\delta = \int \frac{\partial \delta}{\partial a} dP$$

[1] Professor of mechanics and research assistant, respectively, Washington University, St. Louis, Mo. 63130.

[2] Professor of mechanical engineering, Imperial College, London, U.K.

[3] The italic numbers in brackets refer to the list of references appended to this paper.

where the second of these forms with P, the load (per unit thickness) and δ, the work producing component of load point displacement is of most interest here. Now, it is always possible with elastic-plastic behavior to split the displacement, δ, into its elastic, δ_{EL}, and plastic, δ_{PL}, parts, so that

$$\delta = \delta_{EL} + \delta_{PL} \tag{2}$$

Making use of this separation, Eq 2, of elastic and plastic parts in Eqs 1 provides the separated form of J as in Refs *1* and *2*, and as previously used by Sumpter and Turner [*3*],

$$J = J_{EL} + J_{PL} \tag{3}$$

where

$$J_{EL} = -\int_0^{\delta_{EL}} \left.\frac{\partial P}{\partial a}\right|_{\delta_{EL}} d\delta_{EL} = \mathcal{G}$$

and

$$J_{PL} = -\int_0^{\delta_{EL}} \left.\frac{\partial P}{\partial a}\right|_{\delta_{PL}} d\delta_{PL}$$

Now, with these definitions in Eq 3, it is clear that J_{EL} is the Griffith energy rate, $\mathcal{G}$, computed as if no plasticity is present. It is therefore well defined, as well as already understood. Consequently, it shall be used to define the elastic η-factor, η_{EL}, and later attention will be given to J_{PL} and the plastic η-factor, η_{PL}.

Elastic η-Factor

The linear-elastic displacement, δ_{EL}, can be always written in terms of the elastic compliance, C, as

$$\delta_{EL} = C \cdot P \tag{4}$$

Moreover, $\mathcal{G}$ can be also always written in terms of the compliance derivative, $\partial C/\partial a$, as

$$J_{EL} = \mathcal{G} = \frac{P^2}{2}\frac{\partial C}{\partial a} \tag{5}$$

The elastic work (per unit thickness), W_{EL}, is defined as the work re-

covered by linear elastic unloading (with the crack length fixed) from any point on an elastic-plastic load-displacement record. Therefore

$$W_{EL} = \frac{P\delta_{EL}}{2} \tag{6}$$

Making use of Eq 4 to eliminate δ_{EL} in Eq 6 and rearranging it to substitute for P^2 in Eq 5 gives

$$J_{EL} = \frac{1}{C}\frac{\partial C}{\partial a} W_{EL} \tag{7}$$

Now defining the elastic η-factor by the relation [3]

$$J_{EL} = \eta_{EL}\frac{W_{EL}}{b} \tag{8}$$

where b is taken to be the uncracked ligament ahead of the crack. Comparing Eqs 7 and 8, it is noted that η_{EL} may be always written

$$\eta_{EL} = \frac{b}{C}\frac{\partial C}{\partial a} = -\frac{b}{P}\frac{\partial P}{\partial a}\bigg|_{\delta_{EL}} \tag{9}$$

This relationship, Eq 9, shows that η_{EL} always exists for converting the elastic work, W_{EL}, directly into J_{EL} by Eq 8.

Moreover, it is pointed up that stress intensity factor, K, formulas may be used to compute C and $\partial C/\partial a$ as follows. Noting that $\mathcal{G} = K^2/E'$ may be combined with Eq 5, then

$$\frac{\partial C}{\partial a} = \frac{2(K/P)^2}{E'} \tag{10}$$

This may be integrated to give

$$C = C_{NC} + \int_0^a \frac{2(K/P)^2}{E'}\,da \tag{11}$$

where C_{NC} is the elastic compliance with no crack present. Thus, Eqs 10 and 11 combined with Eq 9 show that η_{EL} can be found directly from no more information than elastic stress intensity factor formulas, as an alternative to making use of Eq 9 directly through experimental determinations of compliance.

Plastic η-Factors

In order to develop the plastic η-factor, η_{PL}, it is appropriate to begin by referring to the last term of Eq 3, J_{PL}, and its definition there. In order to evaluate J_{PL}, the functional relationship for load, P, in terms of crack size, a; plastic displacement, δ_{PL}; and other dimensional lengths, L, W, B, etc., must be known. Since in addition only the material's stress-strain properties also influence that functional relationship, the dimensional analysis arguments [*1,2*] lead to

$$\frac{PL}{b^2} = F_1\left(\frac{\delta_{PL}}{L}, \frac{a}{L}, \frac{W}{L}, \frac{B}{L}, \ldots, \text{etc.}\right) \tag{12}$$

or alternatively (equally appropriate) where both sides of Eq 12 are simply multiplied by b/L, noting $b = W - a$, to give

$$\frac{P}{b} = F_2\left(\frac{\delta_{PL}}{L}, \frac{a}{L}, \frac{W}{L}, \frac{B}{L}, \ldots, \text{etc.}\right) \tag{13}$$

In addition, other appropriate forms may be produced,[4] but F_1 and F_2 will be seen later to be most appropriate in those cases where predominately bending and tension, respectively, of the remaining uncracked ligament, b, occurs.

Proceeding by substituting Eqs 12 and 13 into the final term of Eq 3, noting $db = -da$, leads to

$$J_{PL} = \frac{2b}{L}\int_0^{\delta_{PL}} F_1 d\delta_{PL} - \frac{b^2}{L^2}\int_0^{\delta_{PL}} \frac{\partial F_1}{\partial\left(\frac{a}{L}\right)} d\delta_{PL} \tag{14}$$

and

$$J_{PL} = \int_0^{\delta_{PL}} F_2 d\delta_{PL} - \frac{b}{L}\int_0^{\delta_{PL}} \frac{\partial F_2}{\partial\left(\frac{a}{L}\right)} d\delta_{PL} \tag{15}$$

Resubstituting for F_1 and F_2 in the first terms of the right sides of Eqs 14 and 15 gives

$$J_{PL} = \frac{2}{b}\int_0^{\delta_{PL}} P d\delta_{PL} - \frac{b^2}{L^2}\int_0^{\delta_{PL}} \frac{\partial F_1}{\partial\left(\frac{a}{L}\right)} d\delta_{PL} \tag{16}$$

[4] Substituting $P/b(L/b)^m$ with any m for the left side of Eq 12 or 13 and using δ_{PL}/b, instead of δ_{PL}/L, etc., in the functions produces other forms.

and

$$J_{PL} = \frac{1}{b}\int_0^{\delta_{PL}} P d\delta_{PL} - \frac{b}{L}\int_0^{\delta_{PL}} \frac{\partial F_2}{\partial\left(\frac{a}{L}\right)} d\delta_{PL} \tag{17}$$

Now in Eqs 16 and 17 the first term of the right side of each contains the plastic work, W_{PL}, (per unit thickness) which is

$$W_{PL} = \int_0^{\delta_{PL}} P d\delta_{PL} \tag{18}$$

Thus, the plastic work, W_{PL}, so defined is the total work, W, minus the elastic work, W_{EL}, as defined by Eq 6. In addition, the plastic η-factor, η_{PL}, is defined in a manner consistent with its elastic counterpart in Eq 8 by [3]

$$J_{PL} = \eta_{PL}\frac{W_{PL}}{b} \tag{19}$$

Moreover, it is specified that η_{PL} may depend on crack length, a/L, but that it will not depend on the extent of plastic deformation δ_{PL}/L, by definition. At this point it is readily seen that Eqs 16 and 17 can be reduced to the form of Eq 19 with Eq 18 inserted, only if the second integrals on the right sides of Eqs 16 and 17 can be reduced to $\int_0^{\delta_{PL}} P d\delta_{PL}$ forms. Since this reduction will occur only under special additional conditions, as defined here η_{PL} (Eq 19) does not always exist for all structural and specimen configurations and material combinations. On the other hand, for many configurations they do indeed exist and are of great computational convenience.

In general, the plastic η-factors only exist where the crack length dependence, a/L, and plastic displacement dependence, δ_{PL}/L, can be separated in F_1 and F_2 (or alternative functions of their form). Let us assume that this is possible, then and only then

$$F_1\left(\frac{\delta_{PL}}{L}, \frac{a}{L}, \ldots\right) = G_1\left(\frac{\delta_{PL}}{L}, \ldots\right)\cdot H_1\left(\frac{a}{L}, \ldots\right) \tag{20}$$

or

$$F_2\left(\frac{\delta_{PL}}{L}, \frac{a}{L}, \ldots\right) = G_2\left(\frac{\delta_{PL}}{L}, \ldots\right)\cdot H_2\left(\frac{a}{L}, \ldots\right) \tag{21}$$

Under such conditions, Eqs 20 or 21, the second integrals of Eq 16 or 17 would become

$$\int_0^{\delta_{PL}} \frac{\partial F_1}{\partial\left(\frac{a}{L}\right)} d\delta_{PL} = \frac{\partial H_1}{\partial\left(\frac{a}{L}\right)} \int_0^{\delta_{PL}} \mathcal{G}_1 d\delta_{PL}$$

$$= \frac{\partial H_1}{\partial\left(\frac{a}{L}\right)} \cdot \frac{1}{H_1} \int_0^{\delta_{PL}} F_1 d\delta_{PL}$$

$$= \frac{\partial H_1}{\partial\left(\frac{a}{L}\right)} \cdot \frac{L}{b^2 H_1} \int_0^{\delta_{PL}} P d\delta_{PL} \tag{22}$$

or (similarly)

$$\int_0^{\delta_{PL}} \frac{\partial F_2}{\partial\left(\frac{a}{L}\right)} d\delta_{PL} = \frac{\partial H_2}{\partial\left(\frac{a}{L}\right)} \frac{1}{bH_2} \int_0^{\delta_{PL}} P d\delta_{PL} \tag{23}$$

Substituting Eq 22 or 23 into Eq 16 or 17 gives

$$J_{PL} = \frac{1}{b} \int_0^{\delta_{PL}} P d\delta_{PL} \left[2 - \frac{b}{L} \frac{\partial H_1}{\partial\left(\frac{a}{L}\right)} \frac{1}{H_1}\right] \tag{24}$$

or

$$J_{PL} = \frac{1}{b} \int_0^{\delta_{PL}} P d\delta_{PL} \left[1 - \frac{b}{L} \frac{\partial H_2}{\partial\left(\frac{a}{L}\right)} \frac{1}{H_2}\right] \tag{25}$$

Finally, comparing these results with Eqs 18 and 19, it is seen that

$$\eta_{PL} = \left[2 - \frac{b}{L} \frac{\partial H_1}{\partial\left(\frac{a}{L}\right)} \frac{1}{H_1}\right] \tag{26}$$

or

$$\eta_{PL} = \left[1 - \frac{b}{L} \frac{\partial H_2}{\partial\left(\frac{a}{L}\right)} \cdot \frac{1}{H_2}\right] \tag{27}$$

In addition, other forms may be possible or as noted earlier, it may be that η_{PL} does not exist for some configuration-material combinations. As perplexing as this result may be, let the discussion proceed to cases where η_{PL} clearly does exist and provides useful results.

A General Condition for the Existence of η_{PL}

In general, η_{PL} will exist if a separation of variables can be found in the form of Eq 20 or 21 (or alternate form). This separation may be viewed as shown in Fig. 1.

Now, plotting $P/b(L/b)^m = F$ with the appropriate m as with Eq 12 or 13 versus δ_{PL}/L, if all of the curves for each constant a/L-value are of heights F in constant scale to each other, then the separation exists. Further, if this scaling exists for some range of a/L-values from $\delta_{PL} = 0$ to some limiting values of δ_{PL}^{limit}, then the separation of variables exist over that region. That is to say, if the condition

$$\frac{F\left[\frac{\delta_{PL}}{L}, \left(\frac{a}{L}\right)_i \cdots\right]}{F\left[\frac{\delta_{PL}}{L}, \left(\frac{a}{L}\right)_j \cdots\right]} = C_{ij}(\text{constant}) \tag{28}$$

for any values of $(a/L)_i$, and $(a/L)_j$, and for all δ_{PL}/L-values for the region

$$\left(\frac{a}{L}\right)_1 \leq \frac{a}{L} \leq \left(\frac{a}{L}\right)_2$$

and

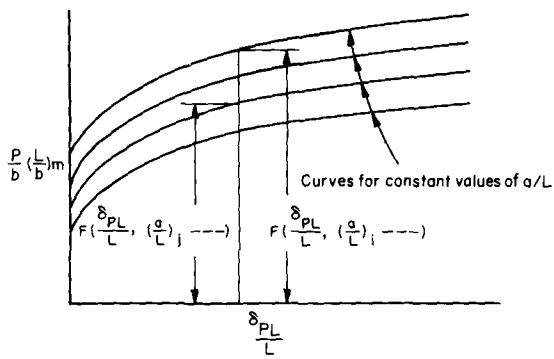

FIG. 1—P *versus* δ_{PL} *records are plotted.*

$$0 \leq \frac{\delta_{PL}}{L} \leq \frac{\delta_{PL}{}^{limit}}{L} \tag{29}$$

then within that region the separation of variables will exist and therefore η_{PL} will exist for the region. It has been proven [4] that η_{PL} does not exist if this condition is not met, and indeed it can be seen that the η_{PL} approach will give approximately correct results sufficiently accurate to be practically useful if the condition is only slightly violated (by small amounts or for small parts of the region).

Taking a more practical view, the condition of Eq 28 for the region, Eq 29, may be tested experimentally by testing identical configurations with identical material differing only in their (a/L)-values to produce P versus δ_{PL} records, which can be plotted as in Fig. 1 and tested numerically. Subsized (or blunt notch) specimens of the configuration-material combination may be utilized for this purpose which will avoid having crack growth occur prior to the $\delta_{PL}{}^{limit}/L$ of applicability. In this way the existence of η_{PL} can be directly and experimentally determined, and indeed the idea of the separation of variables was first noted by Ernst [4] from this behavior of experimental data.

On the other hand, Turner [3] and subsequent work [5] has observed the existence of the η_{PL} approach through finite element computations. However, subsequent attention here will be directed to specific analytical conditions for which the η_{PL} approach is possible.

Examples of Specific Conditions for which η_{PL} Exists

Power Hardening Materials

Ernst [4] has also shown for power hardening material, characterized by

$$\frac{\epsilon}{\epsilon_0} = \left(\frac{\sigma}{\sigma_0}\right)^N \tag{30}$$

that Ilyushin's theorem may be invoked to show that the condition for existence of η_{PL}, through Eq 28 with unlimited region (Eq 29), is met for any two-dimensional configuration. This is very significant. First, the elastic case, $N = 1$, where it was previously shown that η_{EL} always exists, is a limiting case of this proof. Therefore, for nearly elastic behavior, $N \to 1$, including small-scale yielding and highly hardening materials, the method should be practical for almost all configurations.

Further, for the tendency towards rigid-perfectly-plastic materials, $N = \infty$, the other limiting case, η_{PL} always exists. That is to say that for situations where a limit load has been attained considerably prior to a point

at which J is to be computed, then the η-factor method should work very well. For moderate amounts of hardening, $\infty > N >$ say 10 (or perhaps lower) it is seen that the method should work very well. Indeed power hardening, for all values of N, is usually a fair approximation for developing load-displacement relations whenever displacements are very large, compared to elastic displacements, so existence of η-factors for power hardening shows a strong tendency toward existence for very many practical cases.

Pure Bending of a Small Remaining Ligament

Rice's case [*2*] of pure bending moment, M, (per unit thickness) on a small remaining ligament, b, ahead of a crack approaching perpendicular to a free boundary is one where η_{PL} can be shown to exist for any elastic-plastic material (with a monotonic stress-strain relation). For such a case, dimensional considerations lead to

$$\theta = f\left(\frac{M}{b^2}\right) \tag{31}$$

where θ is the relative work producing rotation of the applied moments, M. Now, θ may be split into its elastic and plastic parts where

$$\theta = \theta_{EL} + \theta_{PL} = \alpha \frac{M}{b^2} + f_{PL}\left(\frac{M}{b^2}\right) \tag{32}$$

hence

$$\theta_{PL} = f_{PL}\left(\frac{M}{b^2}\right) \tag{33}$$

which may be inverted

$$\frac{M}{b^2} = F(\theta_{PL}) \tag{34}$$

This result may be compared directly with Eq 12 by noting that it is appropriate to substitute $M = PL$ and $\theta_{PL} = \delta_{PL}/L$, then

$$\frac{PL}{b^2} = F\left(\frac{\delta_{PL}}{L}, \text{ material properties}\right) \tag{35}$$

where the variables are already separated as in Eq 20, since a/L is absent, or

H_1 is simply a constant. Thus, referring to Eq 26, since $\partial H_1/\partial(a/L) = 0$, then

$$\eta_{PL} = 2 \tag{36}$$

and it always exists for arbitrary material properties for this configuration.

Similarly, the elastic parts of Eq 32 may be separated and using Eq 9, the result is

$$\eta_{EL} = 2 \tag{37}$$

for this configuration. Also referring to Eqs 3, 8, and 19, if $\eta_{EL} = \eta_{PL} = \eta$ as in Eqs 36 and 37 for a given configuration, then

$$\begin{aligned} J &= \frac{\eta_{EL} W_{EL}}{b} + \frac{\eta_{PL} W_{PL}}{b} \\ &= \frac{\eta}{b}(W_{EL} + W_{PL}) = \frac{\eta W}{b} \end{aligned} \tag{38}$$

where η can now be interpreted as a total work, W, η-factor. Of course, all of these results were available in Rice et al [2], but the repetition gives some new prospective on η-factors.

Deeply Cracked Beams

For example, for the bending of a deeply cracked beam, where the plasticity is confined to the remaining ligament (uneffected by other boundaries) then it is clear that

$$\eta_{PL} = 2 \tag{39}$$

with the remainder of the beam such as its length and loading arrangement unspecified (except that no appreciable beam shear shall exist at the ligament). Now on the other hand, from Eqs 9, 10, and 11, it is clear that η_{EL} is not in general equal to two. However, η_{EL} can be altered by simply changing the compliance of the beam away from the cracked section, that is, C_{NC} changes, so that η_{EL} can be often adjusted to two. This is precisely the case of the three-point bend specimen with $s/W = 4$, so that both η-factors are two. For that specific configuration, Eq 38 may be again invoked, simplifying the determination of J. Moreover, it is clear that other beam configurations could be designed to have this same advantage.

Now, the advantage just illustrated is unusual since from Eq 9 and from Eqs 26 and 27 it is clear that η_{EL} and η_{PL} are not only usually not equal but indeed both may be dependent on the crack size, a/L. However, specimens could be designed so that η_{EL} and η_{PL} exist and are equal at least at one convenient value of crack size, so that very simple relations such as Eq 38 could be used to determine J. It is suggested here that a modified compact specimen might well be specifically designed for optimum J-integral testing convenience.

Tension of a Small Remaining Ligament

Rice et al [2] also considered the case of a small remaining ligament, b, subject to a remote tension force, P (per crack tip and unit thickness). The more general modified form of F_2 is adopted here to accommodate finiteness of the tension specimen. It is

$$\frac{P}{b} = F_{\bar{2}}\left(\frac{\delta_{PL}}{b}, \frac{a}{L}, \frac{W}{L}, \cdots\right) \tag{40}$$

In a fashion similar to the previous discussion this form leads to

$$J_{PL} = \frac{2}{b}\left[\int_0^{\delta_{PL}} P d\delta_{PL} - \frac{P\delta_{PL}}{2}\right] - \frac{b}{L}\int_0^{\delta_{PL}} \frac{\partial F_{\bar{2}}}{\partial\left(\frac{a}{L}\right)} d\delta_{PL} \tag{41}$$

Now if the separation of $F_{\bar{2}}$ is possible in the usual form

$$F_{\bar{2}} = G_{\bar{2}}\left(\frac{\delta_{PL}}{b}\right) H_{\bar{2}}\left(\frac{a}{L}\right) \tag{42}$$

Then Eq 41 may be reduced to

$$J_{PL} = \frac{1}{b}\int_0^{\delta_{PL}} P d\delta_{PL}\left[2 - \frac{P\delta_{PL}}{\int_0^{\delta_{PL}} P d\delta_{PL}} - \frac{b}{L}\frac{\partial H_{\bar{2}}}{\partial\left(\frac{a}{L}\right)}\frac{1}{H_{\bar{2}}}\right]$$

For such conditions

$$\eta_{PL} = 2 - \frac{P\delta_{PL}}{\int_0^{\delta_{PL}} P d\delta_{PL}} - \frac{b}{L}\frac{\partial H_{\bar{2}}}{\partial\left(\frac{a}{L}\right)}\frac{1}{H_{\bar{2}}} \tag{43}$$

For tension of a small remaining ligament, the a/L dependence of $F_{\bar{2}}$ disap-

pears, and then the last term in Eq 43 goes to zero. Hence, for tension it should always be small compared to one. Moreover, it is observed that the middle term on the right side of Eq 43 is slightly greater than one and tends to one as deformations, δ_{PL}, increase. Therefore, if η_{PL} exists for tension, its value will tend to one or will be a bit less than one. Finally, if η_{PL} is to exist in the strict sense for tension, then in addition to separation, Eq 42, the middle term of Eq 43 must be constant (independent of the extent of deformation, δ_{PL}).

Again, it is clear here that Turner's observation, for example, Ref *3*, of $\eta_{PL} = 1$ (or slightly less) for tension of a ligament is sound. Moreover, if a tension specimen can be designed so that $\eta_{EL} = \eta_{PL} = 1$, then again the most convenient form, Eq 38, would be appropriate and useful for evaluating J directly from total work, W, done in loading.

Other examples of conditions for the existence of η_{PL} can be found, but those provided above are sufficient to illustrate the argument to be made here. Therefore, the discussion will proceed to examples of situations where η_{PL} does not exist.

Examples of Conditions Where η_{PL} Does Not Rigorously Exist

If the nature or location of plasticity present changes radically during loading, then η_{PL} may not exist (with specific exceptions or approximations).

An example of such a case is where plasticity at a location remote from the uncracked ligament region occurs at some stage of deformation. The effect of remote plasticity can be viewed in terms of the existence condition, Eqs 28 and 29, with reference to Fig. 1 to observe the effects. Suppose for a compact specimen of low a/L (that is, a/W) that yielding near the loading pins occurs, whereas it does not for high a/L. Moreover, for low a/L and hardening, the commencement of remote yielding would occur at different values of δ_{PL}/L. Then it is clear their load versus plastic displacement curves, as on Fig. 1, cannot meet the condition, Eq 28 for existence of η_{PL}, except for a/L and δ_{PL}/L-values, that is, the region of Fig. 1, where no remote plasticity has occurred. Therefore, in general, the η-factor method should not be used where plasticity has occurred remote from the uncracked ligament region, except where further justification is given.

However, from a practical point of view, if the effects of the remote plasticity can be removed, then an η_{PL} may be found for computation of J_{PL} from plastic work, W_{PL}, as in Eq 19. For example, for a long uniaxially loaded tension specimen, if plasticity at loading pins (or grips) occurs, gage length points between the pins and crack location can be selected (remote from both) so that measurement of displacements appropriately evaluates work within the gage length excluding effects of the remote plasticity.

On the other hand, where hardening causes the gradual spread of plasticity throughout the length of a tension specimen, no precise η-factor evalua-

tion method is present. Nevertheless, Turner [5] reports some success with approximate evaluation of J through η-factors, where the plastic work is adjusted by subtracting the remote plastic work (outside the perfectly plastic slip field) in an approximate way.

Another example of a situation where η_{PL} does not rigorously exist is the case where the plasticity at the remaining uncracked ligament changes form substantially as it develops from small-scale yielding into the fully plastic state. This would cause the early portion of the load-displacement curves of Fig. 1 to be nonsimilar according to Eq 28. Under such conditions, evaluations of J_{PL} by Eq 19 would not be correct, but as deformations proceed well into the fully plastic state, applying the η-factor method via Eq 19 etc., would become an increasingly better approximation.

Therefore, the preceding examples illustrate conditions where the η-factor method is not strictly or rigorously applicable, but it is also made clear that certain modifications or approximations may be possible to permit practical evaluations of J by the η-factor method for some special cases in violation of rigorous conditions for applicability.

Summary and Discussion

The existence of the η-factor method is not necessary for the evaluation of J, which alternately can be found by other means directly from its definitions, Eq 1. However, the η-factor method is a great simplification in finding J, both in specimens and in structural components for circumstances where it is applicable either in a rigorous or approximate way.

Indeed, although the previous discussion here has been formulated on the basis of computations of J using equations employing η-factors, such as Eq 19, which were written as if no crack growth has occurred, they can be easily adapted for growing cracks. For previous discussion of such adaptation see Refs *1* and *6*. However, a correct method for determining J for any point on Fig. 1 is to take the load-displacement record with no crack growth for the a/L, which passes through the point and makes the computation according to Eq 19, etc. The computation will be correct provided that the point is in the region of applicability of η-factors, Eqs 28 and 29, and if the conditions for "strict deformation theory" apply [*6*]. Therefore, the η-factor method can be adopted whether or not crack growth occurs.

It is also noted here that this work on J, especially using η-factor methods, impacts directly on the conditions for which the so-called "equivalent energy method" may be applied. In particular, it is shown here that Eq 38 is applicable only under severely limited conditions (η_{PL} exists and $\eta_{EL} = \eta_{PL}$), and it is observed that "equivalent energy" is not applicable unless Eq 38 applies, exactly or at least approximately. Moreover, crack growth prior to instability [*7*] may interfere and thus can in addition invalidate "equivalent energy" even for those few cases where Eq 38 does apply.

Finally, some examples of configuration material combinations and conditions have been given here where the η-factor method is rigorously applicable or approximately applicable. On the other hand, some combinations and conditions have been identified where η_{PL}, as defined here, does not exist. This work is not a full clarification of conditions where η-factors can be usefully applied, but hopefully it is a fair beginning in that direction.

Acknowledgments

The work contained herein was made possible and motivated by a series of visits between C. E. Turner and the Washington University Center for Fracture Mechanics group from late 1977 to beyond midyear 1978. All of these visits were at least in part supported by the U.S. Nuclear Regulatory Commission (NRC) contracts at Washington University and encouraged in essential ways by NRC personnel, especially R. Gamble and the late E. K. Lynn.

References

[1] Ernst, H., Paris, P., Rossow, M., and Hutchinson, J. in *Fracture Mechanics, ASTM STP 677,* American Society for Testing and Materials, 1979, p. 581.

[2] Rice, J., Paris, P., and Merkle, J. in *Progress in Flow Growth and Fracture Toughness Testing, ASTM STP 536,* American Society for Testing and Materials, 1973, p. 231.

[3] Sumpter, J. P. G., and Turner, C. E., *International Journal of Fracture,* Vol. 12, No. 6, 1976, p. 861.

[4] Ernst, H., "Techniques of Analysis of Load-Displacement Records by J-Integral Methods," Ph.D. thesis, Department of Mechanical Engineering, Washington University, St. Louis, Mo., Sept. 1979; see also NUREG/CR-1222, U.S. Nuclear Regulatory Commission, Jan. 1980.

[5] Turner, C. E., private communication of results of finite element studies of η-factors, 1978.

[6] Hutchinson, J. and Paris, P. in *Elastic-Plastic Fracture, ASTM STP 668,* American Society for Testing and Materials, 1979, pp. 37–64.

[7] Paris, P., Tada, H., Zahoor, A., and Ernst, H., "A Treatment of the Subject of Tearing Instability," NUREG 0311, U.S. Nuclear Regulatory Commission, Aug. 1977; see also *Elastic-Plactic Fracture, ASTM STP 668,* American Society for Testing and Materials, 1979, p. 5 and p. 251.

Heikki Kotilainen[1]

Temperature Dependence of the Fracture Toughness and the Cleavage Fracture Strength of a Pressure Vessel Steel

REFERENCE: Kotilainen, Heikki, **"Temperature Dependence of the Fracture Toughness and the Cleavage Fracture Strength of a Pressure Vessel Steel,"** *Fracture Mechanics: Twelfth Conference, ASTM STP 700,* American Society for Testing and Materials, 1980, pp. 352-367.

ABSTRACT: A new model for the temperature dependence of the fracture toughness has been sought. It is based on the yielding processes at the crack tip, which are thought to be competitive with fracture. Using this method a good correlation between measured and calculated values of fracture toughness has been found for a Cr-Mo-V pressure vessel steel as well as for A533B. It has been thought that the application of this method can reduce the number of surveillance specimens in nuclear reactors.

A method for the determination of the cleavage fracture strength has been proposed. It can be measured either with low temperature tensile tests or with slow bend tests of Charpy V-notch specimens.

KEY WORDS: temperature dependence, cleavage fracture, cleavage strength, fracture toughness, fractures (materials), crack propagation

There have been many efforts to correlate the ordinary tensile properties with the fracture toughness K_{Ic} [*1-8*].[2] Most of these attempts fail, however, to give a proper temperature dependence for the fracture toughness. This is mostly due to a lack of material data over a sufficient temperature range. The starting point in the calculations is usually the plastic zone at the crack tip. Using the stress concentration inside the plastic zone, it has been possible to calculate a microstructural unit X_o over which the stress has to exceed the critical cleavage fracture strength σ_{fc} needed to cleave the material. This then poses the following questions: What is the distance X_o, how is σ_{fc} mea-

[1]Head of Materials Testing Section, Valtion Teknillinen Tutkimuskeskus, Technical Research Centre of Finland, Metals Laboratory, Espoo 15, Finland.

[2]The italic numbers in brackets refer to the list of references appended to this paper.

sured, what is the yield strength and its temperature dependence? In the following there will be a thorough analysis of these problems.

Experimental

The steel studied experimentally was a low-carbon low-alloy pressure vessel steel with a bainitic microstructure. The analysis of the steel was 0.15C-2.7Cr-0.6Mo-0.3V, and has been heat-treated to three different conditions (see Table 1).

The yield strength (0.2 percent proof strength) has been determined over the temperature range 12 to 300 K for each heat treatment condition. The results are given in Fig. 1.

The fracture toughness, K_{Ic}, has been measured using 25-mm thick three-point bend and compact tension (CT) specimens. Because the thickness of the specimens was insufficient, the real value of K_{Ic} (Fig. 2) has been estimated using Chell and Milne's [*10*] method. The validity of the estimated fracture toughness values has been checked by testing a 75-mm-thick specimen at the temperature of 185 K. The result was 3105 $Nmm^{-3/2}$, and it is marked with a dark dot in Fig. 2. The measured value meets all requirements of ASTM Test for Plane-Strain Fracture Toughness of Metallic Materials (E 399-78). Thus, the curve drawn in Fig. 2 seems to be justified.

In spite of the small thickness, all specimens showed a cleavage type fracture surface at all testing temperatures. The measured and estimated fracture toughness values are also given in Table 2.

For the determination of the cleavage fracture strength σ_{fc} for the Cr-Mo-V steel in condition T, a set of V-notched specimens were tested in three-point bending. The general yield strength and the fracture strength coincide at 100 K as can be seen from Fig. 3.[3]

The general yielding has been analyzed in two different ways using the methods proposed by Clausing [*13*]. The third method utilizes the log F versus log D_p plot, in which F is the force and D_p is the plastic part of the displacement. The first deviation from the linearity in this plot has been taken as the point of general yielding (σ_{GY}^2).

TABLE 1—*Heat treatment, yield strength* σ_Y, *and lath packet size* d_b. *The steel A533B (HSSTP Plate 2) has been taken from* Ref 9.

Steel	T_γ, °C	T_t, °C	σ_Y, Nmm^{-2}	d_b, μm
K	980	760	380	2.4
T	980	670	600	2.4
M	950	610	960	2.4
A533B	870	660	480	...

[3]Here, the general yield strength must be understood as equivalent to the uniaxial yield strength, because the influence of the constraint factor (1.26) was removed in calculation.

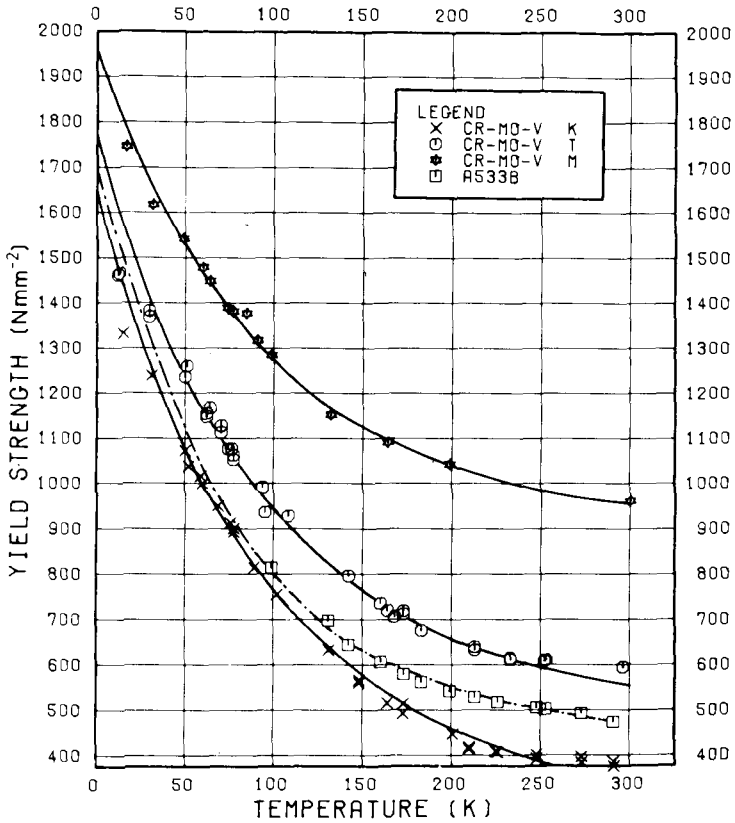

FIG. 1—*Yield strength (0.2 percent) as a function of temperature for Cr-Mo-V and A533B steels. Note: Condition M—18650 tempering parameter, condition T—20100 tempering parameter, and condition K—22000 tempering parameter.*

Discussion

The yield strength of a steel can be generally divided into two parts, the temperature independent part σ_μ and the temperature dependent part σ_θ. It has been proven that for many materials the yield strength obeys the law given by Yaroshevich and Ryvkina [*14*]

$$\sigma_Y = \sigma_\mu + [\sigma_Y(0) - \sigma_\mu]e^{-mT} \tag{1}$$

where

σ_Y = yield strength,
$\sigma_Y(0)$ = yield strength at 0 K,
σ_μ = temperature independent part of the yield strength,

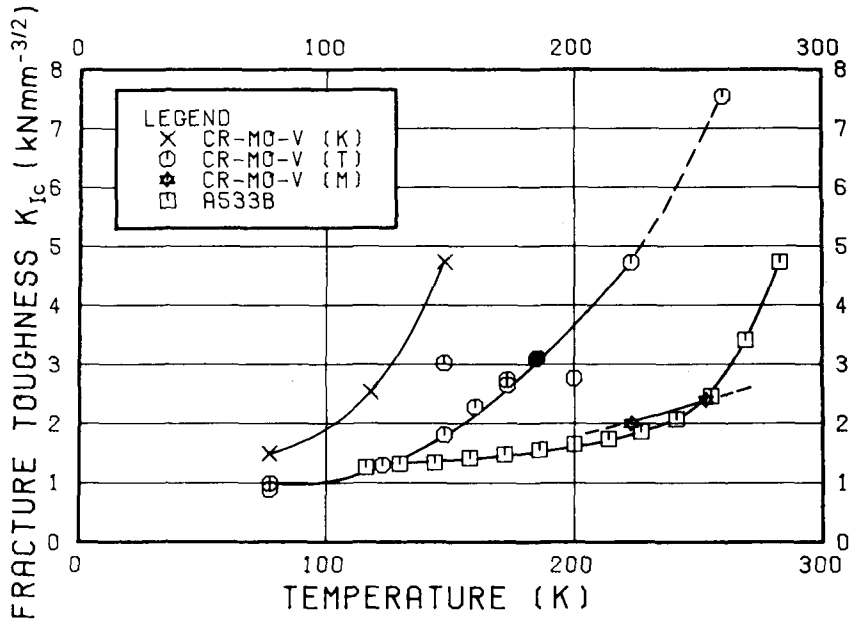

FIG. 2—*Measured and estimated fracture toughness.*

TABLE 2—*Measured and estimated fracture toughness.*

Steel	T, K	K_Q, Nmm$^{-3/2}$	K_J, Nmm$^{3/2}$	K_δ, Nmm$^{-3/2}$	K_{Ied}, Nmm$^{-3/2}$	K_{Qp}, Nmm$^{-3/2}$	Type of Specimen
K	78	1490	...	...	...	...	CT
	118	2440	2530	...	...	...	CT
	148	3710	4725	...	...	...	CT
T	77	990	...	935	...	...	3-p
	77	885	...	695	...	...	3-p
	123	1300	...	1525	...	...	3-p
	148	2760	3025	2435	2840	3185	3-p
	148	1805	...	...	...	...	CT
	160	2070	2280	2150	2060	2240	3-p
	173	2440	2645	...	...	...	CT
	173	2540	2740	...	...	...	CT
	185	3105	...	...	...	...	CT
	200	2370	2760	2290	2415	2750	3-p
	223	3035	4715	3635	4120	5905	3-p
	260	2830	7535	5500	6285	8360	3-p
M	223	1995	...	...	...	...	CT
	253	2390	...	...	...	...	CT

NOTE: 3-p = three point; $K_J = K_{Ic}$ estimated after Ref *10*; $K_\delta = K_{Ic}$ estimated from COD; $K_{Ied} = K_{Ic}$ estimated from the equivalent energy method [*11*]; $K_{Qp} = K_{Ic}$ estimated by making a plane stress plastic zone correction [*12*].

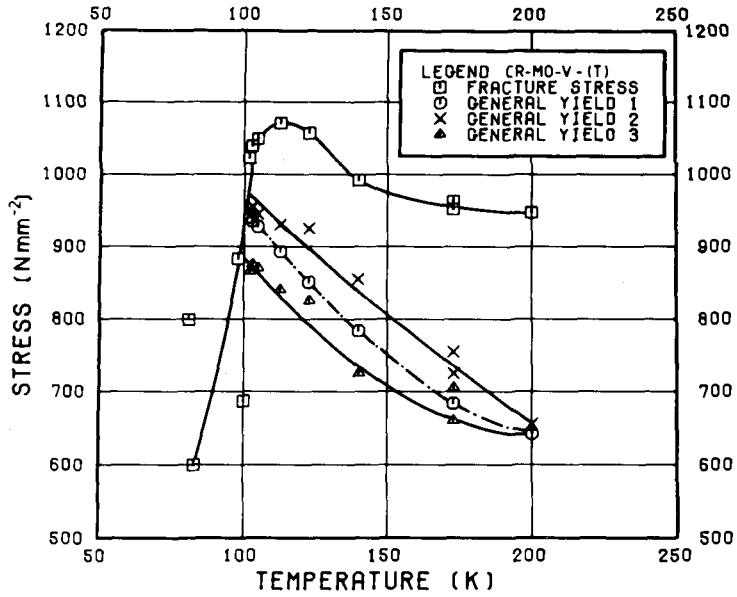

FIG. 3—*General yield stress and fracture stress as function of temperature for Cr-Mo-V steel in condition T. Note: General yield 1—19.68* σ_Y, *general yield 2—LogF-LogD*$_P$ *deviation of linearity, and general yield 3—*$D_P = 0.0254$ *mm displacement.*

m = constant, and
T = absolute temperature.

For the steels studied the factors in Eq 1 can be solved [*15*] and they are given in Table 3.

It is now possible to estimate the cleavage fracture stress. Assuming that the cleavage fracture stress σ_{fc} is equal to the yield stress $\sigma_Y(0)$ at 0 K, the specimen breaks when the maximum stress σ_{yy}^{max} at the tip of the notch has reached the cleavage fracture strength, ($\sigma_{fc} = \sigma_Y(0) = \sigma_{yy}^{max}$). The maximum stress σ_{yy}^{max} can be calculated using the method of Hill [*16*] and Green and Hundy [*17*]. The calculation gives a value $\sigma_{yy}^{max} = \kappa\sigma_{GY}$, where κ is the plastic stress concentration factor and equals 2.18 for the 45 deg inclined angle of the notch using Tresca's yield criterion. However, a more detailed study by Ewing [*18*] gives $\kappa = 1.94$.

Now it is possible to solve the critical temperature at which the fracture and general yield strength are equal, that is, by putting $\sigma_{yy}^{max} = \sigma_Y(0) = \kappa\sigma_{GY}$

$$T_c = \frac{1}{m} \ln \frac{\sigma_Y(0) - \sigma_\mu}{\frac{\sigma_Y(0)}{\kappa} - \sigma_\mu} \tag{2}$$

TABLE 3—*Values of the constants in Eq 1.*

Steel	σ_μ, Nmm^{-2}	$\sigma_Y(0)$, Nmm^{-2}	m, 1/K
K	285	1630	0.0104
T	500	1755	0.0104
M	905	1955	0.0104
A533B	450	1677	0.0126

where

T_c = critical temperature at which $\sigma_f = \sigma_{GY}$, and
κ = plastic stress concentration factor.

For the Cr-Mo-V steel, Eq 2 gives a value T_c = 109 K. From Fig. 3 one can see that the measured value is 100 K, which is in close agreement with the calculated temperature.

The cleavage fracture strength can be now calculated using the σ_{GY} (100) values and κ. Depending on the method used to obtain the general yield stress, a cleavage fracture strength between 1736 Nmm^{-2} and 1891 Nmm^{-2} can be calculated. This calculated value is very close to the measured $\sigma_Y(0)$ value in uniaxial tension. For this reason the yield strength at 0 K is taken as the cleavage fracture strength in the following.

Methods for the Estimation of the Temperature Dependence of K_{Ic}

The first attempt to correlate K_{Ic} with tensile properties was made by Krafft [*19*] using the Equation

$$K_{Ic} = E \cdot n\sqrt{2\pi d_T} \tag{3}$$

where

E = Young's modulus,
n = strain hardening exponent, and
d_T = the size of a process zone in which the fracture process is taking place.

Hahn and Rosenfield [*4*] have used a semi-empirical dependence between K_{Ic} and the tensile ductility similar to Krafft's equation, that is

$$K_{Ic} = (2/3E\sigma_Y n^2 \epsilon_f)^{1/2} \tag{4}$$

where

n = strain hardening exponent, and
ϵ_f = true strain at fracture of a smooth tensile bar.

However, this equation does not give a correct temperature dependence of K_{Ic} for the steels under consideration, because the yield strength increases much faster than ϵ_f decreases with decreasing temperature.

A second approach of Hahn et al [*3*] gives an empirical solution

$$\frac{\sigma_{fc}}{\sigma_Y} = \alpha \left(\frac{K_{Ic}}{\sigma_Y} \right)^{\beta} \tag{5}$$

where

α, β = empirical constant, and
σ_{fc} = cleavage fracture strength.

A similar kind of solution has been given by Irwin et al [*20*], by postulating a temperature dependent fracture toughness

$$K_{Ic} = \frac{\sigma_Y(T_o)}{\sigma_Y} K_{Ic}(T_o) \tag{6}$$

where T_o = critical temperature. Rosenfield et al [*21*] have also found experimentally that in a limited temperature range K_{Ic} is inversely dependent on the yield strength.

Krafft and Sullivan [*22*] have postulated a correlation between the yield strength and the fracture toughness

$$K_{Ic} = M\sigma_Y{}^{-1.5} \tag{7}$$

where M = constant. The same result has been obtained later [*6, 7*].

An attempt to correlate the yield strength, cleavage fracture strength, and fracture toughness has been made also by Malkin and Tetelman [*23*]. They proposed a formula in which K_{Ic} is given as a function of the notch root radius ρ

$$K_{Ic}(\rho) = 2.89\sigma_Y(\exp[\sigma_{fc}/\sigma_Y - 1] - 1)^{1/2}\sqrt{\rho} \tag{8}$$

For some materials they have found a limiting value of $\rho = \rho_o$, below which the fracture toughness is independent of ρ. Knowing ρ_o, a dependence between σ_Y and K_{Ic} can be found.

Application of the Methods

Hahn et al [*3*] have found for a number of steels that Eq 5 can be written as

$$K_{Ic}\sigma_Y{}^2 = \left(\frac{\sigma_{fc}}{2.35} \right)^3 \tag{9}$$

This means that the left hand side of Eq 9 should be constant over a temperature range in which the fracture is essentially cleavage type. This applies, of course, when assuming a temperature independent σ_{fc}. The results of this can be seen in Fig. 4 for A533B and for the Cr-Mo-V steel in the heat-treated condition *T*.

The curve of the Cr-Mo-V steel swings up at the temperature of 140 K, but the fracture appearance of the specimens is still of plane strain (cleavage) type at a temperature of 223 K as can be seen in Fig. 5. The specimen tested at 260 K showed also a cleavage type fracture, but it was initiated by 0.3 mm stable growth.

The reason for this could be the temperature dependence of σ_{fc}, or that Eq 9 fails to describe the behavior of mechanical properties correctly. In fact by plotting σ_{fc}/σ_Y against K_{Ic}/σ_Y, the factors α and β in Eq 5 can be obtained and the results are given in Table 4 and Fig. 6.

Hahn et al [*3*] give $\alpha = 2.35$ to 2.82 and $\beta = 0.36$ to 0.43 for A533B. If for the best fit the temperature range is limited, and only K_{Ic}/σ_Y-values below 3.6 $mm^{1/2}$ are considered, then $\alpha = 1.75$ and $\beta = 0.5$ are obtained for A533B. As a consequence, Eq 5 has to be rewritten for the different steels as follows

$$\text{Cr-Mo-V(T)}: K_{Ic}\sigma_Y{}^3 = \left(\frac{\sigma_{fc}}{1.79}\right)^4 \tag{10a}$$

$$\text{A533B}: K_{Ic}\sigma_Y = \left(\frac{\sigma_{fc}}{1.75}\right)^2 \tag{10b}$$

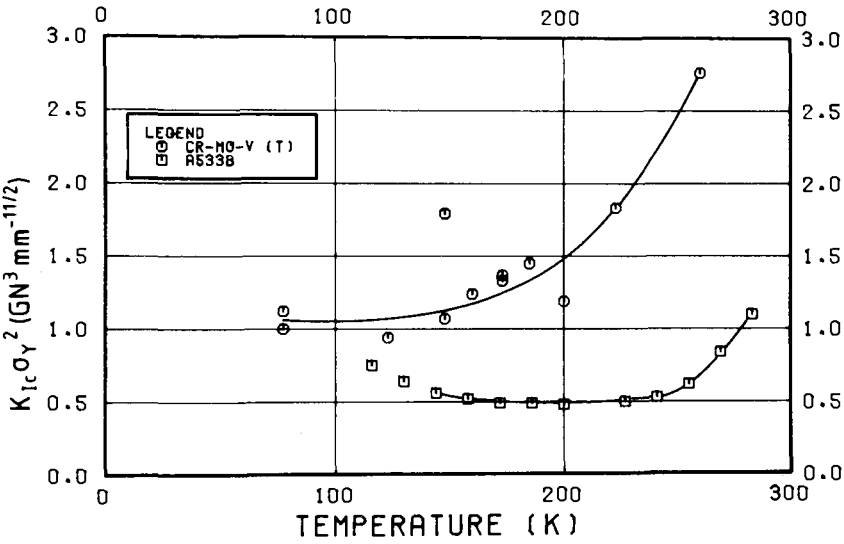

FIG. 4—*Temperature dependence of* $K_{Ic}\,\sigma_Y{}^2$.

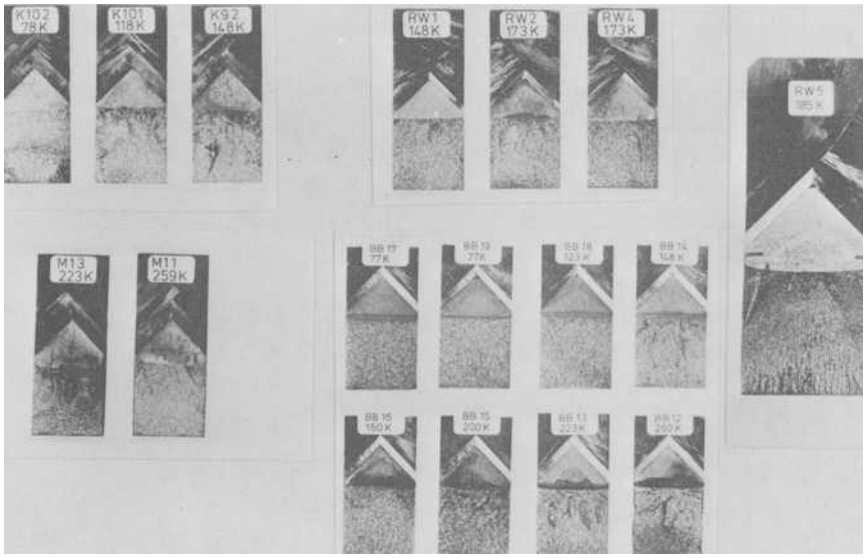

FIG. 5—*Fracture appearance of the specimens (three-point bend specimens are marked BB).*

TABLE 4—*Calculated Constants α and β of Eq 5.*

Steel	α	β
K	1.63	0.27
T	1.79	0.23
A533B	2.21	0.24

As one can see there is a remarkable difference between these two steels. As a conclusion one can claim that the procedure presented by Hahn et al [*3*] is not a universal one, but the procedure can be used as an experimental search for the temperature dependence of the fracture toughness. The procedure can also be used for estimating the cleavage fracture strength.

The cleavage fracture strength of the steel A533B is appreciably higher than given Hahn et al [*3*], who give a value of 1035 Nmm^{-2}. It is interesting to note that Parks [*24*] has given a value of 1690 Nmm^{-2}, which is very close to the value found in this work.

Equations 6 and 7 give approximately the same behavior as Hahn et al [*3*] (Eq 9, Fig. 4). Equations 6, 7, and 10 could be given in a general form

$$K_{Ic} = M\sigma_Y^{-p} \tag{11}$$

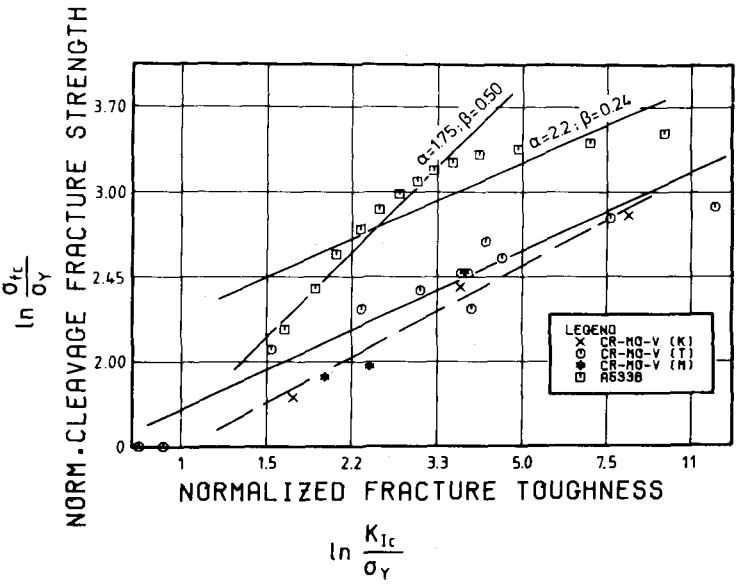

FIG. 6—*Normalized cleavage fracture strength as a function of the fracture toughness.*

where M, p = constant. Equation 11 can describe the fracture toughness properly within a certain temperature range when the constants M and p are determined experimentally.

The validity of Eq 8 can be checked if a constant value for notch root radius ρ is found. If one calculates the ρ value using the results given in Figs. 1 and 2 and Table 2, assuming again that $\sigma_Y(0) = \sigma_{fc}$, one does not get a constant ρ for the whole temperature range. This is true for both steels under consideration. However, the cleavage fracture strength given in Table 3 has been used in Eq 8, but the cleavage fracture strength is not necessarily the same as that "critical tensile stress" used by Malkin and Tetelman [*23*]. The fracture stress can be estimated when the ρ_o-value is assumed to be 50 μm for A533B steel [*23*]. The calculation using Eq 8 gives a value 2200 Nmm^{-2}. This value is very close to the value 2130 Nmm^{-2}, which was given by Malkin and Tetelman [*23*] and is exactly the same value as given by Knott [*25*]. However, these values differ markedly from the values given in this work and by Parks [*24*]. The difference between the fracture stresses in the various works could be the reason for the poor correlation between K_{Ic} and σ_Y. It should be remembered that the ρ_o-value has not been measured for the A533B steel, but only assumed. To check the existence of ρ_o for the Cr-Mo-V steel, a set for Charpy size specimens with varying notch root radii has been tested at liquid nitrogen temperature. The results are given in Fig. 7.

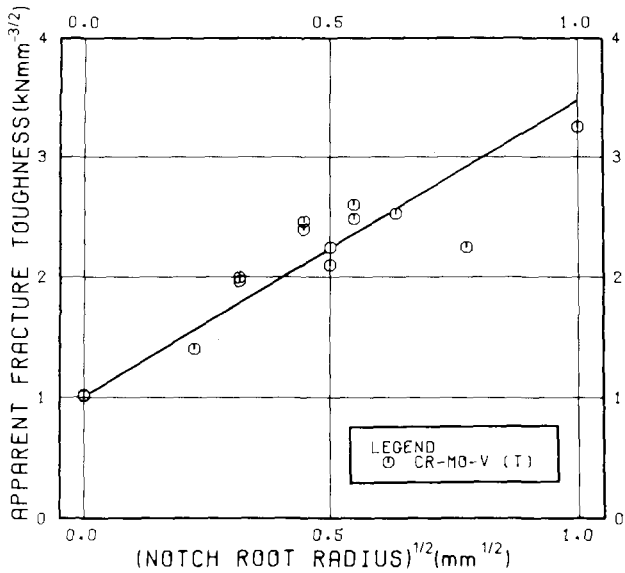

FIG. 7—*Apparent fracture toughness as a function of notch root radius.*

As one can see, there does not seem to be any constant ρ_0-value. This experimental result is consistent with the calculation of the root radius.

Knowing the cleavage fracture strength, the method for revealing the temperature dependence of the fracture toughness proposed by Ritchie et al [*2*] can be applied. In this method the stress distribution at the crack tip can be used for estimating a critical distance X_0. When the stress is higher than the cleavage fracture strength over the length X_0, the critical condition for cleavage has been reached. Ritchie et al [*2*] used the Rice-Johnson [*26*] stress distribution, which takes crack tip blunting into account. However, a drawback of the stress distribution is that the curves are given for certain values of σ_Y/E and for certain strain hardening exponents. Therefore, a sufficiently accurate stress distribution for the whole temperature range cannot be found. In spite of this a calculation has been carried out using the values $\sigma_Y/E = 0.0025$ and $\sigma_Y/E = 0.0050$ with a strain hardening exponent $n = 0.1$. The results can be seen in Fig. 8.

In this figure the calculated values for X_0, using the stress distribution given by Tracey [*27*], are also plotted. As one can see there is no constant value of X_0, but the curves tend to approach a minimum at low temperatures. For the Cr-Mo-V (T) steel the X_0^{min} is about 65 μm for both the Rice-Johnson and Tracey distributions, and for A533B the minimum value is about 100 μm using the Rice-Johnson's solution and about 70 μm for Tracey's solution. This minimum value corresponds fairly well with Parks' [*24*] result of 75 μm.

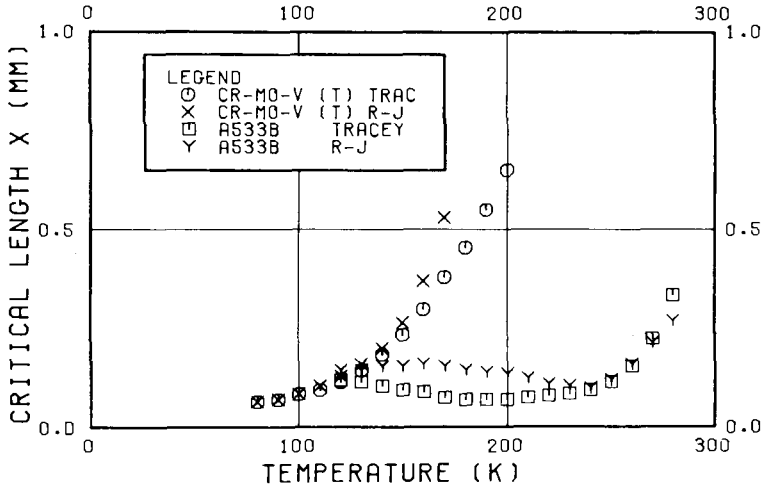

FIG. 8—*Critical length* X *as a function of temperature.*

The reason for the nonconstant value of X in the case of the Cr-Mo-V steel might be that the σ_{fc}/σ_Y ratio is fairly small being between 1.6 and 3.0. In the case of A533B the ratio varies between 2.2 and 3.4. At low σ_{fc}/σ_Y-values the stress distribution is very flat and also large errors in the estimates can be made. For the Cr-Mo-V steel the $X_o^{\min}$-value does not correspond to any microstructural unit, for example, as found by Ritchie et al [*2*].

Due to the varying X_o-value no reasonable K_{Ic} versus T curve can be estimated for the Cr-Mo-V steel. however, for A533B an estimate in the temperature range of 140 K to 240 K could be made, because X_o is approximately constant.

In summary it can be stated that the Krafft and Sullivan [*22*], the Malkin and Tetelman [*23*], the Hahn et al [*3*] and the Ritchie et al [*2*] methods can give satisfactory results in certain cases, but they do not give any universal solution and are material dependent.

A New Approach for the Temperature Dependence of the Fracture Toughness

The toughness of a material depends on its ability to yield. That means that if the plastic zone at the crack tip is small the yielding cannot relax the stresses and the cleavage fracture strength is exceeded. At very low temperatures near to the absolute zero, the very first slip causes fracture due to the undisturbed singularity of the stress at the crack tip. At these extreme temperatures the toughness may not depend on the critical distance [*2*], but merely on the strain energy stored in the sample. The toughness

may not be determined by plastic flow only, but also by adiabatic effects at possible crack tips and by the probability of the crack initiation.

When the temperature increases, more and more plastic flow occurs. At some temperature a homogeneous plastic flow occurs, and a proper plastic zone forms at the crack tip. With further temperature increase, the toughness depends on the possibility of plastic flow that is, on the activation energy of yielding. The activation energy and volume of yielding increase with both temperature and the plastic zone size. However, this is due to the decrease of the temperature dependent part of the yield strength. One can conclude that there is a small fracture volume, the size of which is inversely dependent on the temperature dependent part of the yield strength. The size of the process volume is directly related to the plastic zone size and to the fracture toughness. One can now write

$$r_Y \sim K_{Ic} \sim \frac{A}{\sigma_\theta} \tag{12}$$

where A is a factor depending on the yield strength, because the size of the plastic zone is a function of the yield strength. Above a certain temperature, K_{Ic} can be given as

$$K_{Ic} = K_o + k\frac{\sigma_Y}{\sigma_\theta} \tag{13}$$

where k, K_o = constant. Combining Eqs 1 and 13 one can obtain an exponential dependence between the fracture toughness and the temperature. Basically the same kind of dependence, but without any theoretical explanations, has also been obtained by Nakamura et al [*28*] for a number of iron and iron alloys.

The fracture toughness K_{Ic} has been plotted as a function of σ_Y/σ_θ in Fig. 9. There seems to be a linear relationship and the straight lines converge at $\sigma_Y/\sigma_\theta = 1.5$ to 2 and at $K_{Ic} \approx 1000$ Nmm$^{-3/2}$. The values of the steel A533B deviate from the linear relationship probably because the fracture mode changes from cleavage to ductile tear at higher temperatures.

Using the data of Fig. 9 the constants K_o and k can be deduced, and a correlation between the measured and calculated values of the fracture toughness can be obtained Fig. 10. The points lie very close to the 1:1 correlation.

Application of the Method

The proposed method can be applied to estimate the fracture toughness shift after irradiation. The increase of the yield strength can be attributed

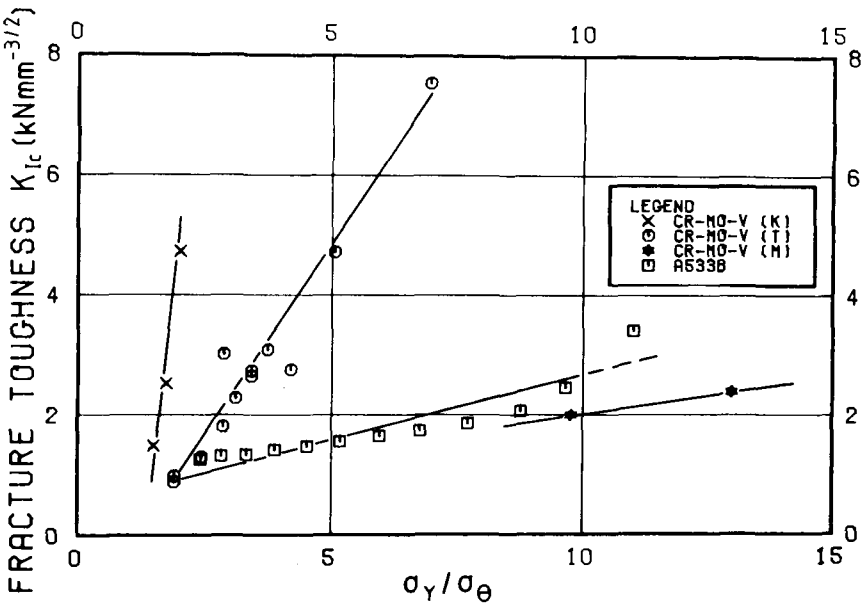

FIG. 9—*Fracture toughness as a function of the normalized yield strength.*

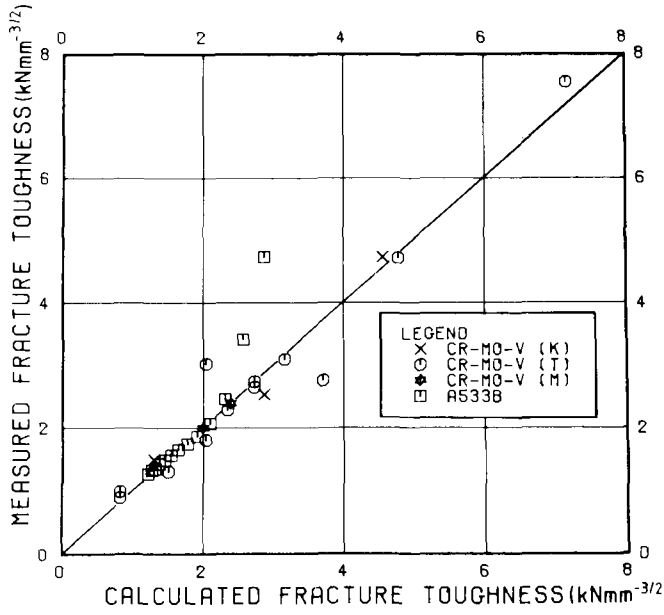

FIG. 10—*Correlation between measured and calculated fracture toughness.*

to the temperature independent part only. Then the temperature T_c can be calculated using Eq 2, and the temperature shift due to the irradiation can be estimated. New values of fracture toughness can be calculated after Eq 13 assuming that constants K_o and k are the same. The validity of the calculation can be checked with one or two irradiated specimens. The advantage of this method is to reduce the number of surveillance specimens.

Summary

The cleavage fracture strength of the Cr-Mo-V steel has been determined by means of slow bend tests as well as tensile tests. A good agreement between the results of the tests has been found. A new theory for the determination of the temperature dependence of the fracture toughness has then been presented. It is based on the competition of plastic flow and fracture at the crack tip. The determining factor is the temperature dependent part of the yield strength, as well as the size and homogeneity of the plastic zone.

References

[1] Tetelman, A. S., Wilshaw, T. R., and Rau Jr., C. A., *International Journal of Fracture Mechanics*, Vol. 4, No. 2, June 1978, pp. 147-157.
[2] Ritchie, R. O., Knott, J. F., and Rice, J. R., *Journal of the Mechanics and Physics of Solids*, Vol. 21, 1973, pp. 395-410.
[3] Hahn, G. T., Hoagland, R. G., and Rosenfield, A. R., *Metallurgical Transactions*, Vol. 2, Feb. 1971. pp. 537-541.
[4] Hahn, G. T. and Rosenfield, A. R. in *Applications Related Phenomena in Titanium Alloys, ASTM STP 432*, American Society for Testing and Materials, 1968, pp. 5-32.
[5] Burns, S. J. and Bilek, Z. J., *Metallurgical Transactions*, Vol. 4, April 1973, pp. 975-984.
[6] Pisarenko, G. S. and Krasowsky, A. J., *Proceedings*, First International Conference on Mechanical Behavior of Materials, Kyoto, Japan, 1971, pp. 421-432.
[7] Pisarenko, G. S. and Krasowsky, A. J. in *Proceedings*, Second International Conference on Mechanical Behavior of Materials, Boston, Mass., 16-20 Aug. 1976, pp. 348-376.
[8] Ivanova, V. S. and Maslov, L. I. in *Proceedings*, Second International Conference on Mechanical Behavior of Materials, Boston, Mass. 16-20 Aug. 1976, pp. 377-414.
[9] Wessel, E. T. in *Practical Fracture Mechanics for Structural Steel*, M. O. Dobson, Ed., United Kingdom Atomic Energy Authority, Chapman and Hall, Risley, 1969, Paper H.
[10] Chell, G. G. and Milne, I., *Material Science and Engineering*, Vol. 2, 1976, pp. 249-253.
[11] Witt, F. J. and Mager, T. R., Fifth National Symposium on Fracture Mechanics, University of Illinois, 31 Aug.-2 Sept. 1971.
[12] Gray, T. G. F. in *Fracture Mechanics in Engineering Practice*, P. Stanley, Ed., Applied Science Publishers, London, 1976, pp. 123-147.
[13] Clausing, D. P., *International Journal of Fracture Mechanics*, Vol. 6, No. 1, March 1970, pp. 71-85.
[14] Yaroshevich, V. D. and Ryvkina, D. G., *Soviet Physics-Solid State*, Vol. 12, No. 2, Aug. 1970, pp. 363-370.
[15] Törrönen, K., Kotilainen, H., and Nenonen, P., *Proceedings*, International Conference on Strength of Metals and Alloys, ICSMA 5, Aachen, Germany, 27-31 Aug., 1979, Vol. 2, pp. 1431-1435.
[16] Hill, R., *Plasticity*, Clarendon Press, Oxford, 1950, p. 245.

[17] Green, A. P. and Hundy, B. B., *Journal of the Mechanics and Physics of Solids,* Vol. 4, 1956, pp. 128-144.
[18] Ewing, D. J. F., *Journal of the Mechanics and Physics of Solids,* Vol. 16, 1968, pp. 205-213.
[19] Krafft, J. M., *Applied Material Research,* Vol. 3, April 1964, pp. 88-101.
[20] Irwin, G. R., Krafft, J. M., Paris, P. C., and Wells, A. A. in *Technology of Steel Pressure Vessels for Water-Cooled Nuclear Reactors,* G. D. Whitman, G. C. Robinson Jr., A. W. Savolainen, Eds., U.S. Atomic Energy Commission, Report ORNL-NSIC-21, 1967, Chapter 7, pp. 430-538.
[21] Rosenfield, A. R., Votava, E., and Hahn, G. T. in *Ductility,* American Society for Metals, Metals Park, Ohio, Chapter 3, 1968, pp. 63-85.
[22] Krafft, J. M. and Sullivan, A. M., *Transactions,* American Society for Metals, Vol. 56, 1963, pp. 160-175.
[23] Malkin, J. and Tetelman, A. S., *Engineering Fracture Mechanics,* Vol. 3, No. 2, Aug. 1971, pp. 151-167.
[24] Parks, D. M., *Journal of Engineering Materials and Technology,* Vol. 98, No. 1, Jan. 1975, pp. 30-36.
[25] Knott, J. F., *Fracture 1977,* Vol. 1, International Conference on Fracture 4, Waterloo, Canada, 19-24 June 1977, pp. 61-92.
[26] Rice, J. R. and Johnson, M. A. in *Inelastic Behavior of Solids,* M. F. Kanninen et al, Eds., McGraw-Hill, New York, 1970, pp. 641-670.
[27] Tracey, D. M., *Journal of Engineering Materials and Technology, Transactions,* American Society for Mechanical Engineers, April 1976, pp. 146-151.
[28] Nakamura, H., Naiki, T., Okabayashi, H., Kuribayashi, M. and Morishige, N., *Engineering Fracture Mechanics,* Vol. 7, No. 3, 1975, pp. 541-549.

J. D. Landes[1] *and D. H. Shaffer*[1]

Statistical Characterization of Fracture in the Transition Region

REFERENCE: Landes, J. D. and Shaffer, D. H., **"Statistical Characterization of Fracture in the Transition Region,"** *Fracture Mechanics: Twelfth Conference, ASTM STP 700,* American Society for Testing and Materials, 1980, pp. 368-382.

ABSTRACT: Fracture toughness results are measured in the transition region for an ASTM A471 Ni-Cr-Mo-V steel on two specimen sizes 1T compact tension (CT) and 4T-CT. The results are typical for steels in the transition in that the smaller specimen toughness values are greater than the larger specimen results. Two explanations are given for this behavior. One explanation, based on loss of constraint, suggests that small specimens cannot be used to characterize the toughness of a large structure in the transition region. A second explanation, based on a statistical model, suggests that small specimen results when properly analyzed can be used to characterize the toughness of large structures.

The results of these tests and others support the statistical model as the proper explanation for the observed difference in toughness between small and large specimens in the transition. The model gives a method for analyzing small specimen results to properly predict the toughness of a large structure.

KEY WORDS: fracture toughness, J-integral, Ni-Cr-Mo-V steel, transition effects, Weibull statistics, specimen size effects, cleavage fracture, fractures (materials), crack propagation

The fracture toughness of steels used in large structural components has in the past been determined from tests of very large specimens using K_{Ic} as a toughness characterizing parameter [*1,2*].[2] Developments in elastic-plastic fracture methodology, using the J-integral as a characterizing parameter [*3*], have provided a technique for determining these same toughness results from smaller specimens [*4,5*]. For steels that exhibit a fracture mode transition, an apparent problem exists with the small specimen fracture toughness evaluation. Toughness values obtained in the tran-

[1] Advisory engineer, Structural Behavior of Materials Department and manager, Mathematics Department, respectively, Westinghouse Research and Development Center, Pittsburgh, Pa. 15235.

[2] The italic numbers in brackets refer to the list of references appended to this paper.

sition region from small specimens may greatly overestimate the equivalent toughness measured on larger specimens [*6, 7*], implying that small specimen results are not suitable for characterizing the toughness of large structures.

This observation is usually explained in terms of a loss of constraint [*7*]. The smaller specimen has less thickness than the larger specimen and less crack-tip constraint is developed during loading causing higher measured toughness in the small specimens. The loss of constraint explanation implies that small specimens cannot be used to characterize the toughness of large structural steel components in the transition region. The British method for crack opening displacement (COD) testing (DD19) requires that test specimens have the full thickness of the component being characterized [*8*].

The loss of constraint explanation is not completely consistent with the observed fracture toughness results for small specimens. In this paper a different rationale is proposed to explain the difference in toughness between small and large specimen test results. This explanation is based on a statistical distribution of toughness properties. Fracture toughness data is generated in the transition to illustrate typical transition toughness properties. A model based on extremal statistics is presented. This model suggests that small specimen toughness results can be used to characterize the toughness of large structures if these results are properly analyzed and applied.

Transition Behavior

The problem with transition toughness characterization is illustrated by the schematic in Fig. 1. Toughness determined from small specimens in the transition exhibits considerable scatter but on the average is higher in value than the toughness determined from larger specimens. This implies a lower transition temperature for the small specimens and suggests that the small specimen toughness results may not adequately predict the toughness of a larger and thicker structure.

An explanation based on loss of constraint in the smaller specimens offers one rationale for this difference. The smaller specimens that have less thickness do not develop triaxial constraint equivalent to the larger, thicker specimens and therefore exhibit higher toughness. This explanation suggests that small specimens should never be used to characterize the toughness of large structures in the transition region. The constraint explanation is questionable in two respects. Small specimens, which are of the deeply cracked bend type (compact or bend bar), do develop a good deal of geometric constraint. Also the loss of constraint model is not consistent with observed toughness behavior as will be illustrated in later discussion. A statistical explanation can be proposed which is more consistent

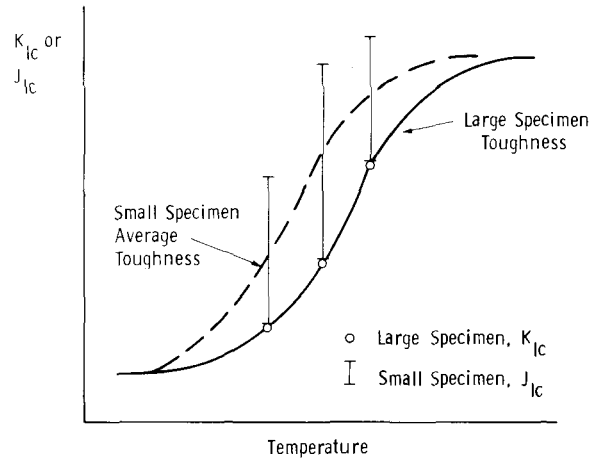

FIG. 1—*Schematic of small specimen fracture toughness data in the transition region. Small specimen has toughness data scatter that makes the transition temperature appear lower, and the toughness appear higher than the large structural toughness.*

with the observed behavior and provides a method for estimating the toughness of a large structure from small specimen results.

Experimental Details

The material used in the test program is an ASTM A471 Ni-Cr-Mo-V rotor steel (Heat 388). It has a yield strength of 765 MPa (111 ksi) and an ultimate tensile strength of 1007 MPa (146 ksi) [*9*]. The Charpy impact energy test results for this material are shown in Fig. 2. The 50 percent ductile fracture appearance transition temperature (FATT) is approximately 294 K (70°F).

Test specimens of the compact geometry were machined in two sizes, a 1T compact tension (CT) specimen, 1-in.-thick (small specimen) and a 4T-CT specimen, 4-in.-thick (large specimen). The material was in the form of a large disk. Previous results showed that there was a variation in Charpy impact properties from the inside diameter to the outside diameter of the disk [*9*], implying that the fracture toughness properties may also show this variation. Therefore specimens were carefully taken so that the crack tip after precracking were all a constant distance from the inside diameter of the disk. This was done to eliminate any variation in toughness due to the specimen location.

The specimens were tested by loading monotonically until a cleavage fracture occurred. Tests were conducted at a number of temperatures going through the transition. The majority of the tests were conducted at three temperatures—294, 311, and 325 K (70, 100, and 125°F). In some

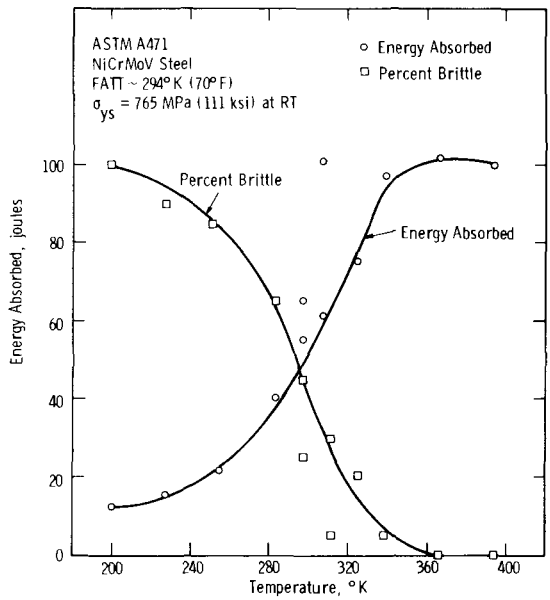

FIG. 2—*Charpy impact data for ASTM A471 steel (Ni-Cr-Mo-V heat 388).*

cases no cleavage was observed after a considerable amount of loading, and the specimen was unloaded without cleavage. Nearly all of the tests exhibited some plasticity before cleaving, and the toughness was characterized by the J-integral using the method of J-calculation proposed by the ASTM working group [5]. The value of J for cleavage was labeled J_c; toughness for specimens that were unloaded before cleavage was characterized at the point of maximum load and displacement.

Results and Model Rationale

The toughness results for the ASTM A471 steel were plotted as a function of temperature, Fig. 3. A total of 31 specimens were tested, 26 1T-CT specimens and 5 4T-CT specimens. At each of the three principal test temperatures, eight 1T specimens and one or more 4T-CT specimens were tested. The data further illustrate the problem associated with small specimen testing in the transition in that the 1T specimens show a good deal of scatter for a given temperature and have higher toughness on the average than the 4T specimens. As the temperature is increased in the transition range, the scatter becomes greater, and the difference between the 1T specimen average and 4T specimen lower bound becomes greater.

An explanation for this behavior can be given in terms of a statistical

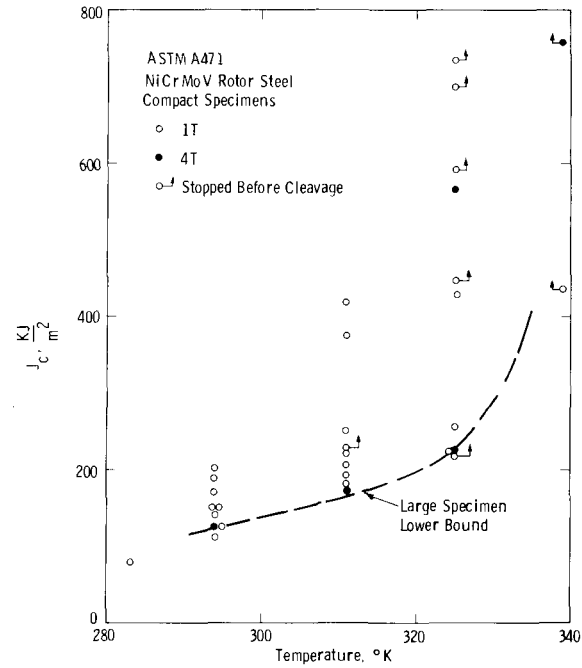

FIG. 3—*Fracture toughness* (J) *for cleavage versus temperature for an ASTM A471 steel.*

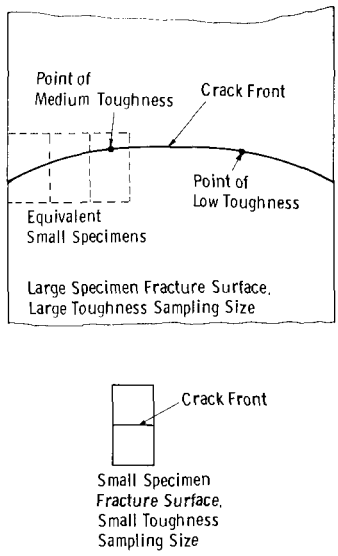

FIG. 4—*Schematic showing the difference in fracture toughness sampling size between large and small specimens.*

model [*4*]. The rationale for this model is given in Fig. 4. The toughness of a given heat of material is proposed to be variable, differing throughout the material and particularly along the crack front. Additionally, the fracture toughness of any specimen is proposed to be governed by the point or region of lowest toughness along the crack front. Larger specimens contain a greater sampling of these variable toughness points or regions and are more likely to contain a low toughness region. Smaller specimens, correspondingly, sample less of the variation in toughness and on the average should exhibit higher toughness. However, when a large number of smaller specimens are tested, the toughness should show a good deal of scatter ranging from values near the large specimen toughness to values much greater than the large specimen toughness. This is exactly the behavior exhibited by the results from the Ni-Cr-Mo-V steel shown in Fig. 3.

The explanation given by Fig. 4 is not the statistical model itself (this will be given later); rather it gives a rationale for the model. The two important points from this rationale are that toughness varies along the crack front, and that the point or region of lowest toughness controls the fracture toughness of the specimen. This rationale suggests that extremal statistics can be used to both characterize the scatter in the smaller specimen toughness results and predict a distribution of toughness for larger specimens.

Additional support for the rationale given in Fig. 4 can be taken from two sources. First, the fracture surfaces of specimens tested in the transition suggest a controlling region of lowest toughness. Figure 5 shows the fracture surfaces of three 1T-CT specimens. The first was tested at 227 K (51°F) below the transition. It shows a fairly homogeneous fracture surface with no clear region of fracture initiation, suggesting that the fracture event was initiated at many points along the crack front. The other two specimens were tested in the transition and show distinct regions along the crack front where the fracture originated. This suggests that the fracture was initiated by a region of low toughness. Figure 6 shows a fracture surface for a 4T-CT specimen tested at 294 K (70°F) in the transition range. This fracture surface shows two regions where the fraction appears to have originated, again suggesting a region of lower toughness that causes the fracture.

Additional support for a statistical explanation is given in Figs. 7 and 8. Figure 7 shows fracture toughness results for an A533B steel [*10*]. A large specimen was tested that gave a valid K_{Ic}-value. Small specimens (1/2T, 1T, and 2T-CT) were tested and evaluated by J-integral techniques, which showed results similar to those in Fig. 3. The smaller specimens had a great deal of scatter ranging from below the K_{Ic}-value to much higher values. Figure 8 shows results for an A216 cast steel [*11*] where again small specimens evaluated by J showed a good deal of scatter ranging from values near valid K_{Ic}-results to much higher values.

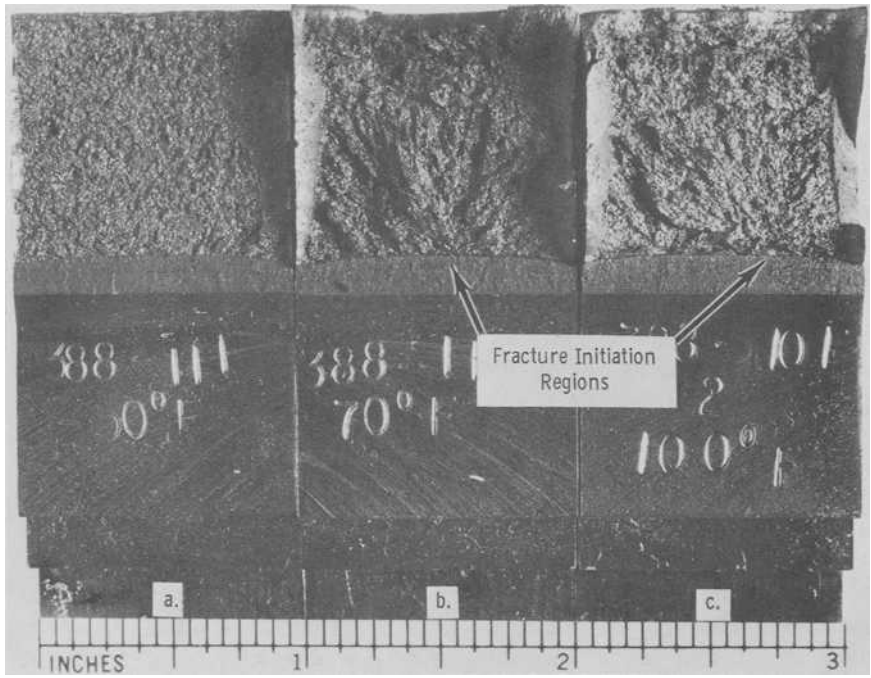

(*a*) Tested at 227 K below the transition, no single fracture initiation point (J_c = 19.3 KJ/m^2).
(*b*) Tested at 294 K in the transition, fracture initiation near center (J_c = 172 KJ/m^2).
(*c*) Tested at 211 K in the transition, fracture initiation to the right of center (J_c = 206 KJ/m^2).

FIG. 5—*Fracture surfaces for 1T-CT specimens of Ni-Cr-Mo-V steel showing regions of fracture initiation.*

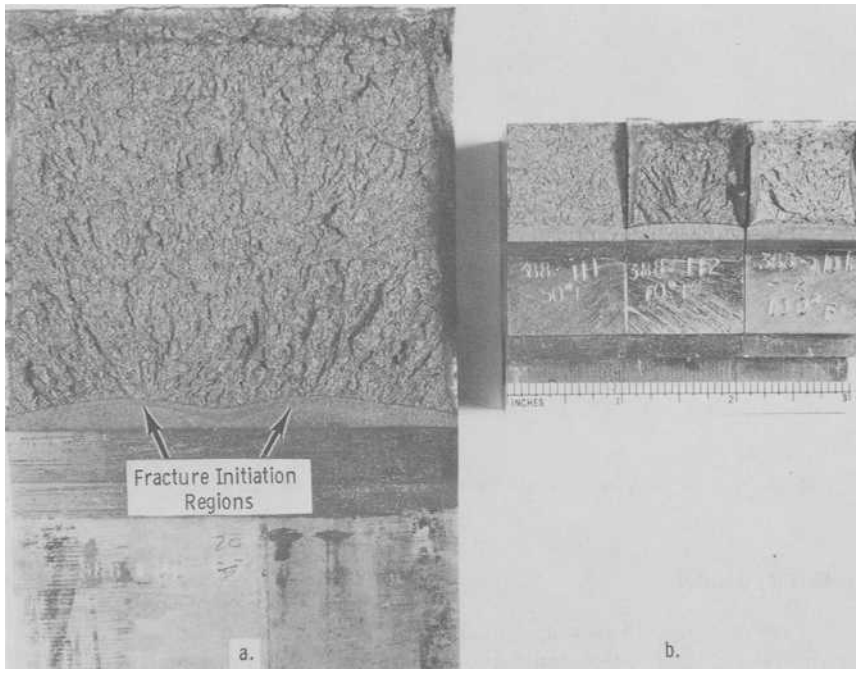

(*a*) 4T-CT tested at 294 K in the transition, two apparent regions of fracture initiation (J_c = 126 KJ/m^2).
(*b*) 1T-CT specimens from Fig. 5.

FIG. 6—*Fracture surface of the 4T-CT specimen of Ni-Cr-Mo-V steel compared with the 1T specimen of Fig. 5.*

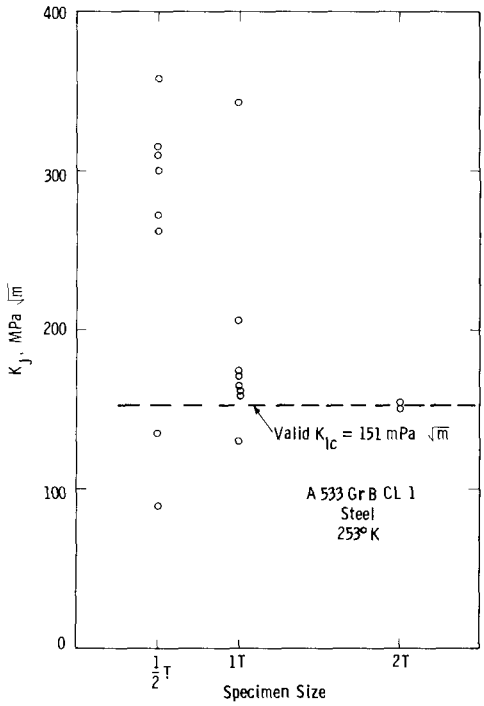

FIG. 7—K *for fracture calculated from* J *versus specimen size, A533B, CL1 steel.*

Statistical Model

The rationale given in Fig. 4 suggests that the fracture toughness results for the Ni-Cr-Mo-V steel could be correlated with a statistical model such as a Weibull distribution. The toughness results for the 1T-CT specimens tested at 294 K (70°F) are plotted on a Weibull graph in Fig. 9. The linear distribution of data points indicates that the Weibull model was an appropriate one for this data. The form of the Weibull distribution function can be given by

$$F_1(x) = 1 - e^{-(x/b)^c}, \qquad x > 0 \tag{1}$$

where $F_1(x)$ is the Weibull distribution function, b is a scale parameter, and c is the shape parameter also called the Weibull slope since it is the slope of the straight line in Fig. 9. The slope for the results at 294 K (70°F) is approximately five. The 1T-CT toughness results for the Ni-Cr-Mo-V steel at 311 K and 325 K (100 and 126°F) were also plotted on a Weibull graph. These plots are not shown here, but they also gave accept-

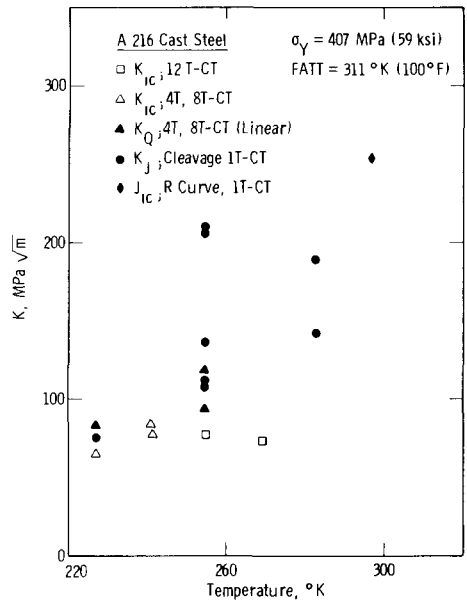

FIG. 8—K *at fracture versus temperature for an A216 WCC grade cast steel.*

able linearity although not as good as for the 294 K (70°F) results. The slopes for these cases were approximately four and two, respectively.

Using the constants from the Weibull distribution function, the mean and standard deviation of the distribution can be analytically determined. The purpose for developing a statistical model is to use the 1T-CT results to predict what the 4T-CT results (or any other specimen size) should be. If the Weibull model holds for these larger sized specimens, than a Weibull distribution function can be developed for them from the 1T-CT distribution. From this a mean and standard deviation can also be analytically determined.

Using the rationale given in Fig. 4 the distribution function for 4T-CT results can be developed by the following steps. $F_1(x)$ is the probability that a given 1T-CT specimen has a fracture toughness value less than x. The probability that the toughness is greater than x is $1 - F_1(x)$ or $e^{-(x/b)^c}$. The distribution function for the 4T-CT specimen is taken from the probability that four 1T-CT specimens have toughness greater than x or equivalently the minimum toughness for four 1T-CT specimens is greater than x. This probability is $[1 - F_1(x)]^4$ or $[e^{-(x/b)^c}]^4$. This can be written as

$$\exp - \left[\frac{(4)^{1/c}x}{b}\right]^c$$

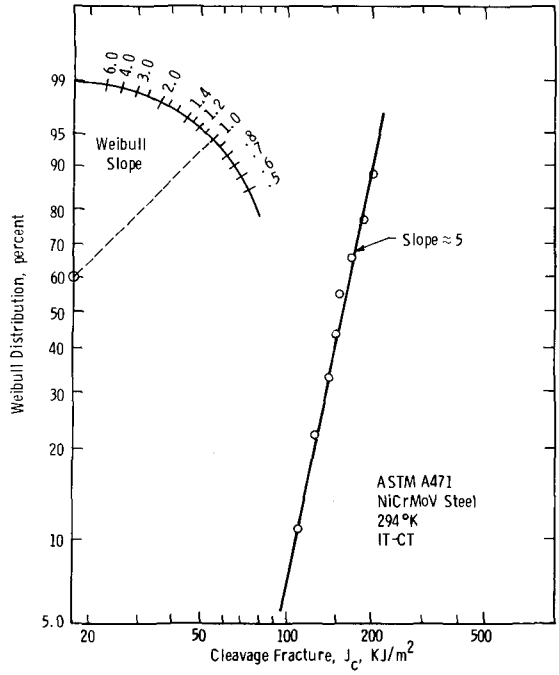

FIG. 9—*Weibull distribution versus* J_c *plotted on Weibull paper—Ni-Cr-Mo-V results at 294 K.*

The Weibull distribution function for the 4T-CT specimen, $F_4(x)$, is then

$$F_4(x) = 1 - \exp - \left[\frac{(4)^{1/c}x}{b}\right]^c \tag{2}$$

The mean value of the distribution for the 1T-CT specimens is approximately given by the scale parameter b. It can be seen from Eq 2 that the mean for the 4T-CT distribution would be $b/4^{1/c}$. Using a similar argument, the distribution function for any size of specimen can be determined, and the mean would be reduced by a corresponding factor (that is, for size N the mean is reduced by $1/N^{1/c}$).

Using this factor, values of the mean toughness for the 4T-CT can be calculated to compare with the experimentally observed value. Table 1 gives values of the mean and standard deviation for the 1T-CT specimens. Calculated mean values for the 4T-CT specimens are compared with the observed values in Table 2. Figure 10 compares the observed mean for the 1T-CT results, the calculated mean for the 4T-CT, and the observed 4T-CT results. For each of the three temperatures, the calculated mean falls very close to the lowest observed value for the 4T-CT results.

TABLE 1—*Mean and standard deviation for the 1T-CT toughness results.* [a]

Temperature, K	Mean Toughness, KJ/m^2	Standard Deviation, KJ/m^2
294	156	31
311	259	89
325	451	209

[a] ASTM A471 steel, eight tests at each temperature.

TABLE 2—*Calculated mean from the Weibull distribution for the 4T-CT specimen compared with the experimentally observed value.*

Temperature, K	Calculated Mean, KJ/m^2	Observed Value, KJ/m^2
294	118	126
311	183	175
325	225	229,566

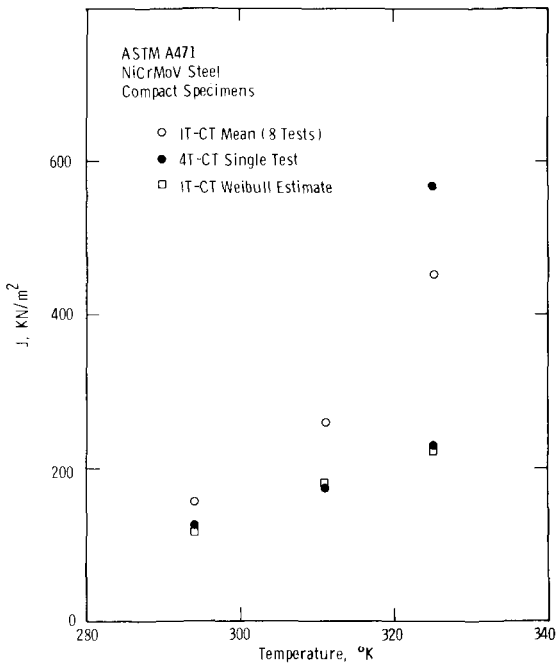

FIG. 10—*Fracture toughnes for cleavage, J_c, versus temperature comparing 1T-CT mean and Weibull estimates with 4T-CT values.*

Discussion

The close agreement between the predicted mean for the 4T and the lowest observed toughness value may be partly fortuitous; however, it does illustrate how the statistical model should work. The results at 294 and 311 K (70 and 100°F) were probably more representative of how the Weibull model should work. At 325 K (125°F) the Weibull slope is only two; this is fairly close to a slope of one where the Weibull model becomes meaningless. It appears that the toughness at 325 K (125°F) is very close to being controlled by a ductile fracture mode; at 339 K (150°F) tests on both 1T and 4T specimens were completely ductile. It is realistic to assume that this model works only for cleavage fracture in the transition region.

The results presented for the Ni-Cr-Mo-V rotor steel and the other supporting data appear to affirm the statistical model rather than a loss of constraint explanation. Two points are worth noticing relative to loss of constraint. The 1T-CT specimens of Ni-Cr-Mo-V steel exhibit toughness results that in a few cases are as low or lower than the 4T-CT specimen results. This behavior is very often observed in the transition. Because the specimens are all identical, it would be hard to explain why some of the 1T specimens lose constraint while others do not. One of the 4T-CT specimens of Ni-Cr-Mo-V steel at 325 K (125°F) showed a very high toughness level. This is hard to explain by loss of constraint because this would indicate that the 4T specimen had lost constraint while some of the smaller 1T specimens did not. It is much easier to explain this result from a statistical model. The 4T specimen with the high toughness value simply did not contain a region of low toughness as did the other 4T specimen and several of the 1T specimens.

The statistical explanation for the observed fracture toughness behavior in the transition is easier to accept than the loss of constraint argument in that it suggests that small specimens can be used to characterize the toughness of large structures. The loss of constraint argument not only suggests that full thickness fracture toughness specimens should be tested but could also suggest that full thickness results are questionable. A compact specimen that has the same thickness as the component may not give adequate toughness characterization because that specimen could have a different crack tip constraint than a structural component with a flaw, such as a partial thickness crack. The loss of constraint argument might suggest that only full sized component structures can be tested to determine toughness in the transition region.

The results presented here do not imply that small specimens never lose constraint; there are many possible small specimen geometries that could have less constraint than larger specimens. However, deeply cracked specimens of the bend type, such as a compact specimen with crack length to specimen width ratio of greater than 0.5 and full proportional thickness

to width ratio, 0.5, have a geometric constraint that should give them a constraint nearly equivalent to that of a larger specimen.

A statistical model that is based on the Weibull distribution may only be one of many that would adequately characterize the transition toughness behavior. The approach taken here should be treated as a first attempt to describe the observed toughness behavior. This approach may have many areas for improvement, but as a first attempt it looks very promising. The problem of dealing with small specimen toughness results in the transition is an important one. It is hoped that the approach given here will encourage other workers to consider possible approaches to this problem.

Conclusions

1. For steels that exhibit a fracture mode, transition fracture toughness results measured on small specimens in the transition region generally overestimate the results obtained from larger specimens, implying that small specimens may not be appropriate for characterizing the toughness of large structures.

2. Two explanations have been discussed in this paper. One is that the smaller specimens have less crack tip constraint than the larger specimens causing higher toughness. The second is that the material has a variable toughness, and fracture is controlled by the region of lowest toughness along the crack front. A statistical model based on a Weibull distribution can explain the difference in toughness.

3. Results from an ASTM A471 Ni-Cr-Mo-V steel and other steels support the statistical model rather than the loss of constraint explanation.

4. With a proper application of the statistical model, transition fracture toughness results from small specimens can be used to characterize the toughness of large structures.

Acknowledgment

The authors would like to acknowledge the assistance of their colleagues at Westinghouse Research and Development Center. W. H. Pryle assisted with the preparation of the test specimens; R. B. Hewlett, W. H. Halligan, and L. W. Burtner conducted the experimental part of this work; and R. R. Hovan and Donna Gongaware helped with the preparation of the manuscript.

References

[1] Begley, J. A. and Toolin, P. R., *International Journal of Fracture,* Vol. 9, No. 3, Sept. 1973, pp. 243-253.

[2] Wessel, E. T., Clark, W. G., Jr., and Pryle, W. H. in *Fracture 1969,* Proceedings of the Second International Conference on Fracture, Brighton, April 1969, pp. 825-850.

[3] Rice, J. R., *Journal of Applied Mechanics, Transactions,* American Society of Mechanical Engineers, June 1968, pp. 379-386.
[4] Landes, J. D. and Begley, J. A. in *Developments in Fracture Mechanics Test Methods Standardization, ASTM STP 632,* W. R. Brown, Jr., and J. G. Kaufman, Eds., American Society for Testing and Materials, 1977, pp. 57-81.
[5] Clarke, G. A. et al in *Journal of Testing and Evaluation,* Vol. 7, No. 1, Jan. 1979, pp. 49-56.
[6] Sumpter, J. D. G., *Metal Science,* Vol. 10, 1976, p. 359.
[7] Milne, I. and Chell, G. G. in *Elastic-Plastic Fracture, ASTM STP 668,* J. D. Landes, J. A. Begley, and G. A. Clarke, Eds., American Society for Testing and Materials, 1979, pp. 358-377.
[8] "Methods for Crack Opening Displacement (COD) Testing," Draft for Development DD19, British Standards Institution, 1972, p. 5.
[9] Logsdon, W. A., unpublished results, 1972.
[10] Sunamoto, D., Satoh, M., Funato, T., and Tominatsu, M., *Fracture 1977,* Vol. 3, Proceedings of the Fourth International Conference on Fracture, Waterloo, Canada, June 1977.
[11] Landes, J. D. and Begley, J. A. in *Fracture Analysis, ASTM STP 560,* American Society for Testing and Materials, 1974, pp. 170-186.

R. H. Dean[1] *and J. W. Hutchinson*[2]

Quasi-Static Steady Crack Growth in Small-Scale Yielding

REFERENCES: Dean, R. H. and Hutchinson, J. W., **"Quasi-Static Steady Crack Growth in Small-Scale Yielding,"** *Fracture Mechanics: Twelfth Conference, ASTM STP 700,* American Society for Testing and Materials, 1980, pp. 383–405.

ABSTRACT: A numerical analysis of quasi-static, steady-state crack growth under small-scale yielding conditions has been carried out for antiplane shear (Mode III) and plane strain, Mode I. In addition to results for an elastic-perfectly plastic solid, the study includes results relating to the influence of strain hardening on stable crack growth. Limited results based on a corner theory of plasticity give some indication of the extent to which stable crack growth predictions are sensitive to the type of plasticity theory used.

KEY WORDS: elastic-plastic crack growth, plane strain, Mode III, steady crack growth, small scale yielding, fractures (materials), crack propagation

Crack-tip plasticity is primarily responsible for the phenomenon of stable crack growth in metals under monotonically increasing load or displacement conditions. As the crack advances, a material element just above or below the plane of the crack experiences a distinctly nonproportional history of straining; that is, the relative proportions of the strain components vary strongly as the tip passes beneath or above the element. By contrast, a material element in the vicinity of a stationary crack experiences predominantly proportional plastic loading. An elastic-plastic solid offers considerably more resistance to nonproportional strain histories than to proportional ones, and this is the main source of stable crack growth. In small-scale yielding the strain at a given distance from the tip in the plastic zone is larger in the stationary problem than it is in the steady growth problem at the same value of the stress intensity factor K.

[1] Assistant professor of engineering mechanics, Department of Engineering Mechanics, Ohio State University, Columbus, Ohio 43210.

[2] Professor of applied mechanics, Division of Applied Sciences, Harvard University, Cambridge, Mass. 02138.

For a stationary crack in an elastic-perfectly plastic solid the strains increase as $1/r$ as the distance from the tip r is diminished. For a growing crack the strain singularity is the weaker, $\ln(1/r)$, as has been discussed by Rice [*1*][3]. The character of the singular behavior at the tip of a growing crack in a hardening material has been found for linear strain hardening by Amazigo and Hutchinson [*2*]; but for more realistic hardening characterizations, such as power law hardening, the near-tip singularity fields have remained elusive.

In carrying out a numerical analysis of a growing crack starting from its stationary state it is necessary to specify a near-tip fracture criterion or some relation between the crack advance and the applied load or displacement parameter. Various techniques have been proposed for such analyses and some of the most recent papers pursuing this approach are included in Ref *3*. As the crack advances, the increment in applied load or displacement needed to achieve a given increment of growth diminishes. In small-scale yielding the crack approaches nominally steady-state growth conditions, with an unchanging stress intensity factor K, following a crack advance which is one or two times the plastic zone size associated with the steady-state K. It is this steady-state problem which is studied in the present paper. Small-scale yielding is invoked, and all traces of the transient growth period are assumed to have been left far behind the current crack tip. As seen in Fig. 1, the crack is semi-infinite with a wake of residual plastic strains trailing behind the advancing tip. The formulation and solution of the steady-state problem does not require the specification of a fracture criterion. Instead, K plays the role of a scaling parameter to which all stress and strain quantities are related. Studies of the steady-state problem in Mode III have been published by Chitaley and McClintock [*4*] and by Andersson [*5*], who also considers plane stress in Mode I.

The present paper begins by reexamining the Mode III problem. Some

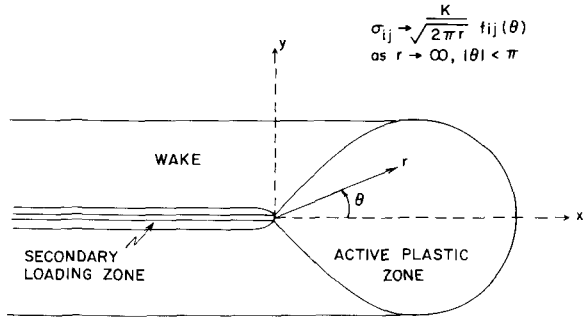

FIG. 1—*Steady-state crack growth in small-scale yielding.*

[3]The italic numbers in brackets refer to the list of references appended to this paper.

modification of the Chitaley-McClintock solution for elastic-perfectly plastic materials is noted. The effects of strain hardening and of corner development on the yield surface are also taken into account, and an attempt is made to assess their influence on the level of K required for steady-state growth compared to the K needed to cause crack growth initiation. The second part of the paper deals with plane-strain crack growth in Mode I for hardening and nonhardening materials. Contact with the recent results of Rice and Sorensen [6] and Rice, Drugan, and Sham [7] is made in the steady-state limit.

Numerical Analysis of Steady Growth

In the small-scale yielding limit, the elastic singularity field is imposed as the far field limit via a semi-infinite crack as depicted in Fig. 1. Thus, as $r \to \infty$

$$\sigma_{ij} = \frac{K}{\sqrt{2\pi r}} f_{ij}(\theta) \tag{1}$$

where the θ-variations depend on the symmetry of the field with respect to the crack plane $y = 0$. The material is elastically isotropic and the standard definition of K is employed throughout. It is imagined that the crack has grown from the left in Fig. 1 under steady-state conditions at constant K. The stress and strain fields around the moving crack tip will appear unchanging to an observer moving with the tip. At any fixed material point an increment of any quantity such as the stress is given by

$$\dot{\sigma}_{ij} = -\dot{a}\, \partial\sigma_{ij}/\partial x \tag{2}$$

where $\dot{a}$ is the increment of crack advance.

It is convenient to nondimensionalize the equations. In Mode III the dimensionless quantities are

$$\bar{w} = \frac{G\tau_0 w}{K^2} \qquad \bar{r} = \left(\frac{\tau_0}{K}\right)^2 r$$
$$\bar{\gamma}_\alpha = G\gamma_\alpha/\tau_0 \qquad \bar{\tau}_\alpha = \tau_\alpha/\tau_0 \tag{3}$$

where

τ_0 = the yield stress in shear,
G = the elastic shear modulus,
w = the displacement in the z-direction,
$\tau_\alpha = \sigma_{\alpha 3}$, and $\gamma_\alpha = 2\epsilon_{\alpha 3}$.

The dimensionless problem is independent of K. A similar nondimensionalization will be used for the Mode I problem.

A displacement-based finite element method is employed in the analysis. In a standard vector notation, the variational equation of equilibrium is

$$\int \sigma^T \, \delta\epsilon \, dA = \int \mathbf{F}^T \, \delta\mathbf{u} \, ds \tag{4}$$

where dA is an area element and tractions $\mathbf{F}$ from Eq 1 are applied on a circuit with line element, ds, far from the tip. The strains and displacements are given in terms of the nodal displacements $\mathbf{U}$ by

$$\epsilon = \mathbf{BU} \quad \text{and} \quad \mathbf{u} = \mathbf{RU} \tag{5}$$

where small-strain theory is assumed. The stresses are given by

$$\sigma = \mathbf{D}^e(\epsilon - \epsilon^p) \tag{6}$$

where $\mathbf{D}^e$ is the elastic constitutive matrix and ϵ^p is the plastic strain. With $\mathbf{K}^e = \int \mathbf{B}^T\mathbf{D}^e\mathbf{B} \, dA$ as the elastic stiffness matrix, the nodal displacements must satisfy

$$\mathbf{K}^e\mathbf{U} = \int \mathbf{R}^T\mathbf{F} \, ds + \int \mathbf{B}^T\mathbf{D}^e\epsilon^p \, dA \tag{7}$$

The iterative procedure for solving Eq 7 is as follows:

1. Given the estimate of ϵ^p from the $i - 1^{\text{th}}$ iteration, use it in Eq 7 to compute the i^{th} estimate of $\mathbf{U}$, $\mathbf{U}^{(i)}$.
2. Compute $\gamma^{(i)}$ everywhere from $\mathbf{U}^{(i)}$.
3. Compute $\sigma^{(i)}$ in the elastic region ahead of the plastic zone using $\sigma^{(i)} = \mathbf{D}^e\epsilon^{(i)}$.
4. Using the steady-state relation

$$\partial\sigma_{ij}/\partial x = D^{ep}_{ijkl} \, \partial\epsilon_{kl}/\partial x \tag{8}$$

integrate in the negative x-direction through the elastic-plastic elements to obtain $\sigma^{(i)}$, where $\partial\epsilon_{kl}\partial x$ is obtained by taking appropriate differences in $\epsilon^{(i)}$ between elements. Here $\mathbf{D}^{ep}$ is the instantaneous tangent moduli from the elastic-plastic constitutive relation. In the active plastic zone where the yield condition is currently met, $\mathbf{D}^{ep}$ is the matrix of the loading moduli, while $\mathbf{D}^{ep}$ takes on elastic values where the stress falls within the yield surface. A technique similar to that in Rice and Tracey [*8*] was used to compute the normal to the yield surface for the current iteration.

5. Compute the i^{th} estimate of the plastic strain everywhere using

$$\epsilon^p = \epsilon - (\mathbf{D}^e)^{-1}\sigma$$

6. Repeat Steps 1 through 5 until convergence is achieved.

The basic element used was the constant strain triangle. The finite element mesh, shown schematically in Fig. 2, is composed of triangles and quadrilaterals, the latter being formed from four triangles with the center node condensed out. A mesh consisting of 1609 degrees of freedom before condensation was used in the Mode III calculations, while twice that number was used in the Mode I calculations. In Mode III the size of the smallest quadrilateral element was 0.4 percent of the distance to the elastic-plastic boundary directly ahead of the crack on the x-axis, while the corresponding figure in plane strain Mode I was 3 percent or about 1 percent of the height of the plastic zone in the y-direction.

A form of parameter tracking was used to facilitate convergence of the iteration scheme. The elastic solution ($\epsilon^p = 0$) was used to produce the first iteration for a high hardening case. When this case had converged the hardening parameter (either the tangent modulus for the linear straining hardening or the hardening exponent for power hardening) was decreased and the distribution of ϵ^p in the previous case was used to start the new iteration. The elastic-perfectly plastic cases required the most iterations to achieve satisfactory convergence and 50 to 100 iterations were used. The elastic stiffness matrix $\mathbf{K}^e$ in Eq 7 remained unchanged during all the computations, and therefore was formed and decomposed only during the initial elastic solution.

Steady Growth in Mode III

Elastic-Perfectly Plastic Material Behavior

Results for the elastic-perfectly plastic case will be discussed first to show the relationship with the previous work on this problem by Chitaley and

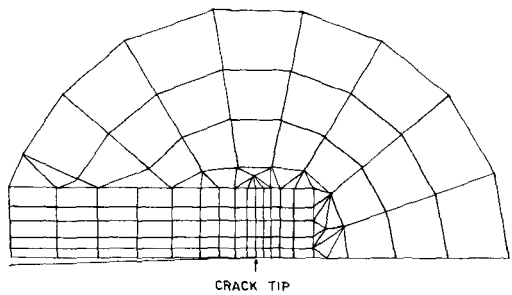

FIG. 2—*Coarse representation of finite element grid.*

McClintock [4]. In Mode III the Mises and Tresca yield conditions both reduce to

$$\tau_x^2 + \tau_y^2 = \tau_0^2 \tag{9}$$

Prandtl-Reuss equations (J_2 flow theory) were assumed in conjunction with Eq 9.

The plastic zone is shown in Fig. 3 using the nondimensional coordinates as axes. For comparison, the plastic zone for the corresponding stationary problem in small-scale yielding is also shown. The elastic-plastic boundary of the stationary problem is circular and extends a distance $\pi^{-1}(K/\tau_0)^2$ ahead of the tip. The position of the elastic-plastic boundary for the growing crack was interpolated from the numerical results. Its distance ahead of the tip at the plane of the crack is about 10 percent greater than for the stationary problem at the same K, that is

$$r_p \cong 0.36(K/\tau_0)^2 \tag{10}$$

The zone computed by Chitaley and McClintock extended about 5 percent beyond the stationary zone ahead of the crack. However, the main difference between the zone of Fig. 3 and that computed by Chitaley and McClintock is that their active zone was confined between two radial lines emanating from the tip at about 20 deg on either side of the plane of the crack. The active zone of Fig. 3 extends to almost ± 60 deg from the plane of the crack. The numerical scheme employed by Chitaley and McClintock appears to have involved the built-in assumption that the slip lines (that is, the straight lines along which the resolved shear stress equals τ_0) all pass

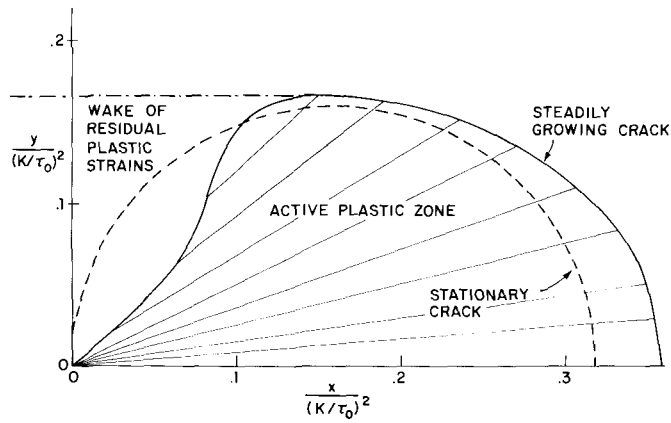

FIG. 3—*Active plastic zone for steady-state crack growth in an elastic-perfectly plastic material in Mode III small-scale yielding.*

through the crack tip. In other words, they assumed the plastic zone could be characterized by a centered fan of slip lines. Numerical results presented here indicate that this is not the case as can be seen from the lines of maximum shear stress shown in Fig. 3. For lines making an angle less than about 20 deg with $y = 0$ it does appear that the lines focus at the tip, but for angles greater than this the lines would intersect the plane of the crack behind the tip if extended out of the active plastic zone. The greater the angle with the x-axis, the further back the point of intersection.

In light of these findings we have reexamined the asymptotic analysis of Chitaley and McClintock for the stress field at the crack tip in Mode III. In particular, the possibility of a wedge shaped sector of nonfocused slip lines was considered, as suggested by the above results, in addition to the sectors containing a centered fan and elastic unloading considered by Chitaley and McClintock. The authors were unable to find an asymptotic stress field different from that of Chitaley and McClintock which was consistent with the requirement that the plastic work rate of the near-tip stresses be everywhere positive. Even though the smallest quadrilateral element at the tip used in calculating the results of Fig. 3 was less than 0.4 percent of the size of the active plastic zone, there is no evidence in the results to suggest that the asymptotic stress field, with its ± 20 deg focused fan and elastic unloading outside the fan, is approached. Assuming that the asymptotic field of Chitaley and McClintock is correct, it would appear that it is attained only at distances that must be less than 1 percent of the plastic zone size.

The strain ahead of the tip on the x-axis can be obtained by integrating the slip line equations with the result for $r \leq r_p$

$$\gamma_y = \gamma_0 \left[1 + \ln (r_p/r) + \frac{1}{2} \ln^2 (r_p/r) \right] \tag{11}$$

where $\gamma_0 = \tau_0/G$ is the yield strain in shear. Since the estimate of r_p (Eq 10) is only about 5 percent larger than that of Chitaley and McClintock, the authors' findings for the strain ahead of the crack are in fairly close agreement with theirs. To give some indication of the accuracy of the present numerical results for the strains, one notes that the computed results for γ_y agreed closely with Eq 11 for values of γ_y/γ_0 less than 15, corresponding to r/r_p greater than 0.01, as will be seen in a subsequent figure.

Curves of the crack opening displacement, $\delta = w(x, y = 0^+) - w(x, y = 0^-)$, behind the tip are shown in Fig. 4. Included in that plot for comparison purposes are curves for the stationary problem for an elastic material and for an elastic-perfectly plastic material; namely, the curve for the growing crack in an elastic-perfectly plastic material and

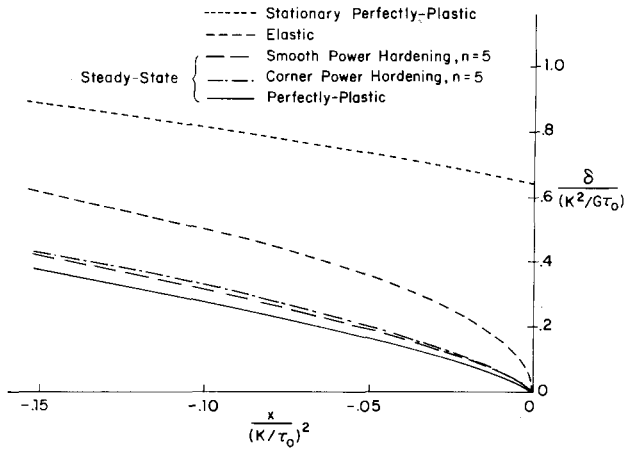

FIG. 4—*Comparison of crack opening (shearing) displacements in Mode III for stationary and growing cracks.*

curves for two hardening materials, which will be discussed below. In steady growth in an elastic-perfectly plastic material, the crack opening displacement goes to zero like $r \ln (1/r)$ as $x = -r$ goes to zero. A numerical fit to the finite element results for δ, which is displayed in Fig. 5, gives

$$\frac{\delta G \tau_0}{K^2} = 0.83 \frac{r\tau_0^2}{K^2} \ln \left(\frac{2.17K^2}{r\tau_0^2} \right) \tag{12}$$

Linear Strain Hardening

With

$$\tau = (\tau_x^2 + \tau_y^2)^{1/2} \tag{13}$$

the incremental flow law for plastic loading of a linear strain hardening material in antiplane shear is

$$G_t \dot{\gamma}_\beta = \alpha \dot{\tau}_\beta + (1 - \alpha) \tau_\beta \dot{\tau}/\tau \qquad \text{for } \dot{\tau} > 0 \tag{14}$$

where G_t is the constant tangent modulus of the shear stress-strain curve and $\alpha = G_t/G$. For elastic unloading or within the yield surface, $\dot{\tau}_\beta = G\dot{\gamma}_\beta$.

Amazigo and Hutchinson [2] have determined the crack-tip singularity fields for steady-state growth in the linear hardening material (Eq 14). Asymptotically as $r \to 0$, they find

$$\tau_\beta \sim r^s \tilde{\tau}_\beta(\theta), \qquad \dot{\gamma}_\beta \sim r^{s-1} \tilde{\dot{\gamma}}(\theta), \qquad w \sim r^{s+1} \tilde{w}(\theta) \tag{15}$$

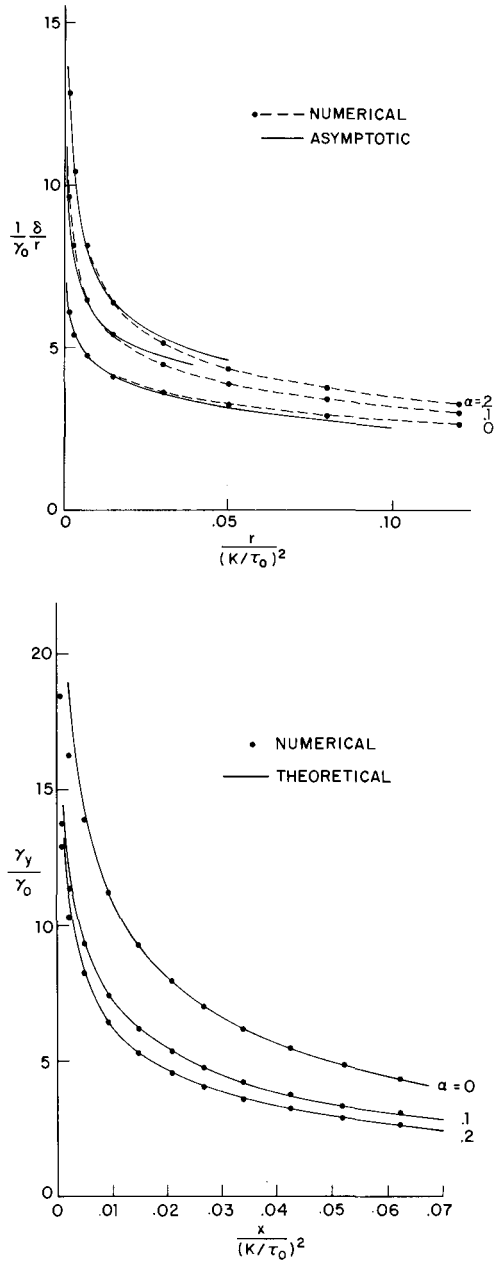

FIG. 5—*Comparison of numerical results with theoretical results chosen to give best fit as discussed in the text for Mode III.*

where s and the θ-variations depend on α. With $\bar{r}$ as the nondimensional radial distance defined in Eq 3, Eq 15 implies that the strain just ahead of the crack on $y = 0$ and the crack opening displacement just behind the crack should be of the form

$$\gamma_y/\gamma_0 = c_1\bar{r}^s + c_2 \tag{16}$$

$$\frac{\delta G\tau_0}{K^2} = c_3\bar{r}^{s+1} \tag{17}$$

where c_1, c_2, and c_3 are undetermined constants. (It is possible that there are additional singular terms, of lower order than r^s, which should appear in Eq 16. These have not been determined and are not taken into account here.) The coefficients in Eqs 16 and 17 were chosen to fit to the finite element results. Solid line curves in Fig. 5 are from Eqs 16 and 17 with the coefficient values shown in Table 1. The finite element values are shown as solid dots. The s-values in Table 1 are taken from Ref *2*, Table 1. Included in Fig. 5 are the elastic-perfectly plastic finite element results, together with curves from Eqs 11 and 12.

The strain hardening parameter α has relatively little influence on the location of the elastic-plastic boundary as can be seen in Fig. 6. The angular extent of the active zone near the tip on either side of $\theta = 0$ increases as α increases in approximate agreement with the predictions of the asymptotic analysis of Ref *2*. The present numerical results reveal a very small reversed zone of plastic yielding in the wake behind the tip. But this secondary zone extended less than 2 percent of the height of the plastic zone above and below the crack flank. The effect of this secondary zone, which was taken into account in Ref *4* but not in Ref *2*, appears to play a negligible role in Mode III.

These results can be used to obtain some insight into the role of strain hardening as it affects stable crack growth in small-scale yielding. First, consider a strain-based fracture criterion similar to the one proposed by McClintock and Irwin [*9*] where crack growth can initiate or continue if ahead of the crack in the plastic zone

$$\gamma_y = \gamma_c \quad \text{at} \quad r = r_c \tag{18}$$

TABLE 1—*Coefficient values.*

α	s	c_1	c_2	c_3
0.1	−0.207	5.25	−6.35	2.30
0.2	−0.277	2.61	−3.06	2.02

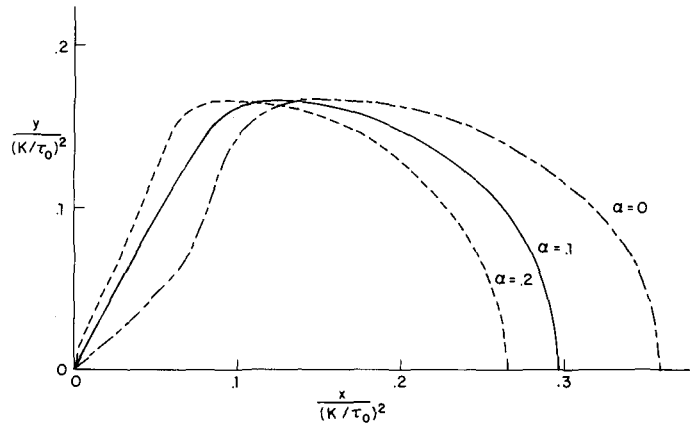

FIG. 6—*Effect of linear hardening parameter α on active plastic zone shape in Mode III.*

Reviewing quickly for the elastic-perfectly plastic case ($\alpha = 0$), one uses the strain ahead of the crack in the stationary problem

$$\gamma_y/\gamma_0 = r_p^s/r \quad \text{where} \quad r_p^s = \pi^{-1}(K/\tau_0)^2 \tag{19}$$

together with γ_y from Eq 11 for the steadily growing crack and the growth criterion from Eq 18 to determine the ratio of K_{ss} needed to drive the crack in steady-state to K_c needed to initiate growth. If one approximates r_p in Eqs 10 and 11 by r_p^s in Eq 19, as McClintock and Irwin did, one obtains

$$(K_{ss}/K_c)^2 = (\gamma_0/\gamma_c) \exp\left[\sqrt{2(\gamma_c/\gamma_0) - 1} - 1\right] \tag{20}$$

showing that K_{ss}/K_c may be very large if the "fracture strain," γ_c, is many times the yield strain, γ_0.

For the linear hardening material the strain ahead of the crack in the plastic zone of the small-scale yielding stationary problem can be shown from Ref *10* to satisfy

$$\bar{r} = \frac{1}{\pi(1-\alpha)}\left[\frac{\gamma_0}{\gamma_y} + \frac{\alpha}{1-\alpha} \ln\left(\frac{\alpha\gamma_y}{\alpha\gamma_y + (1-\alpha)\gamma_0}\right)\right] \tag{21}$$

where $\bar{r}$ is again given by Eq 3. For $\alpha \to 0$, Eq 21 yields Eq 19; and for $\alpha \neq 0$, Eq 21 gives $\gamma_y/\gamma_0 \to (2\pi\alpha\bar{r})^{-1/2}$ as $\bar{r} \to 0$. The full relation (Eq 21) was used in the following calculation. Using Eq 21 for the stationary problem and Eq 11 or 16 for the steady-state problem, together with the imposed growth criterion (Eq 18), the ratio K_{ss}/K_c for $\alpha = 0$, 0.1 and 0.2

was calculated. The ratio, which depends only on γ_c/γ_0, is plotted in Fig. 7. Note that the curve for the elastic-perfectly plastic case ($\alpha = 0$) is not exactly as indicated by Eq 20, since in Fig. 7 the more accurate result for r_p from Eq 10 has been used. Although linear hardening does not provide a very realistic representation of most stress-strain behavior, the trend with increasing hardening in Fig. 7 is clearly a decrease in the potential for stable crack growth. The exponential-type dependence of K_{ss}/K_c on large γ_c/γ_0, as typified for the zero hardening case by Eq 20, results from the weak logarithmic strain distribution (Eq 11) ahead of the growing crack. Hardening leads to a more robust singularity in the strains (see Eq 16 and Table 1) and consequently to smaller values of K_{ss}/K_c at large γ_c/γ_0.

An alternative growth criterion, which will be used later in the Mode I analysis, is based on a critical crack opening displacement (COD) a given distance behind the crack, as has been employed by Rice and Sorensen [*6*] in their Mode I analysis, that is

$$\delta = \delta_c \quad \text{at} \quad r = r_c \tag{22}$$

For the stationary problem in Mode III small-scale yielding [*10*]

$$\bar{r} = \begin{cases} -\dfrac{\alpha}{1-\alpha}\left\{\dfrac{1}{2}\bar{\delta} + \dfrac{1}{(1-\alpha)\pi}\ln\left[1 - \dfrac{\pi}{2}(1-\alpha)\bar{\delta}\right]\right\} & \bar{\delta} < \dfrac{2}{\pi} \\ \dfrac{\pi}{8}\bar{\delta}^2 - \dfrac{\alpha}{\pi(1-\alpha)^2}(1 - \alpha + \ln\alpha) - \dfrac{1}{2\pi} & \bar{\delta} \geq \dfrac{2}{\pi} \end{cases} \tag{23}$$

where $\bar{\delta} = \bar{w}(r, \pi) - \bar{w}(r, -\pi)$ and $\bar{r}$ and $\bar{w}$ are given in Eq 3. The growth criterion (Eq 22) was used in conjunction with the numerical data for the growing crack and for the stationary crack (Eq 23) to generate K_{ss}/K_c as a function of $\delta_c/(\gamma_0 r_c)$ for $\alpha = 0$, 0.1 and 0.2. The results are shown in Fig. 8. Again one sees a decrease in the potential for stable crack growth with an increase in hardening.

Power Hardening with Smooth and Cornered Yield Surfaces

A limited study was made for a power hardening material that deforms in monotonic shearing according to

$$\begin{aligned} \gamma/\gamma_0 &= \tau/\tau_0 \qquad \tau \leq \tau_0 \\ &= (\tau/\tau_0)^n \qquad \tau > \tau_0 \end{aligned} \tag{24}$$

The asymptotic form of the singularity fields is not known for a growing

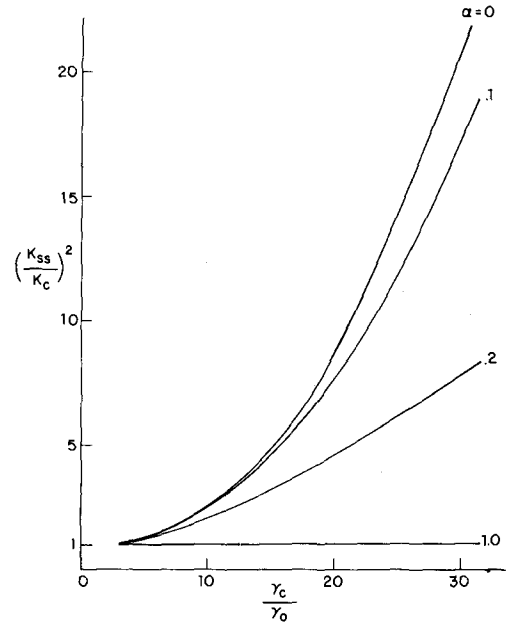

FIG. 7—*Dependence of* K_{ss}/K_c *on hardening in Mode III as predicted from a near-tip growth criterion based on attainment of a critical strain* γ_c *a distance* r_c *ahead of the tip.*

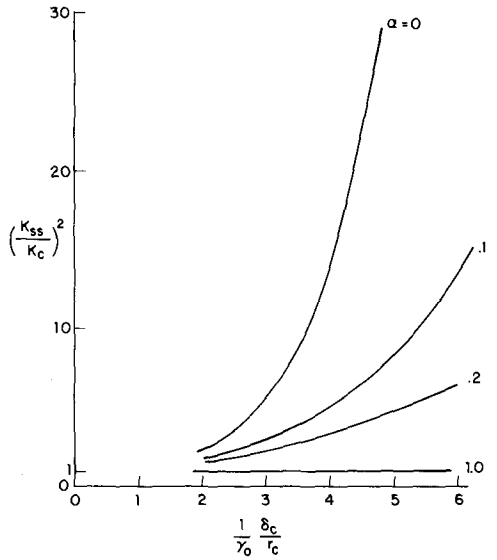

FIG. 8—*Dependence of* K_{ss}/K_c *on hardening in Mode III as predicted from a growth criterion based on attainment of a critical shearing displacement* δ_c *a distance* r_c *behind the tip.*

crack in a power law material, as has already been mentioned. Our main concern here will be to contrast the results from two different flow theories, both of which satisfy Eq 24 in pure shear. One employs the classical smooth isotropic hardening surface based on Eq 13 (that is, J_2 flow theory), and the other is a recently proposed [*11*] law, called J_2 corner theory, in which a corner develops on the yield surface at the loading point. Subsequent yield surfaces for the two theories in antiplane shear are shown in Fig. 9.

Plastic loading according to the classical J_2 flow theory requires

$$\dot{\gamma}_\alpha = G^{-1}\dot{\tau}_\alpha + (G_t^{-1} - G^{-1})\tau_\alpha \dot{\tau}/\tau \tag{25}$$

where G_t is the current tangent modulus whose dependence on τ is obtained from Eq 24.

The plastic strain-rate given by the second term in Eq 25 is constrained to lie along the normal to the yield surface. In a nonproportional stress history, such as that shown in Fig. 9 where the ratios of the stress components change, the stiffness associated with the component of stress increment, which is tangent to the yield surface, is necessarily the elastic value. Crack growth inherently involves strongly nonproportional stressing in material elements lying above and below the plane of the crack, as mentioned in the beginning of this paper. Isotropic hardening based on the smooth Mises yield surface tends to overestimate the resistance of an elastic-plastic material to nonproportional deformation. A corner theory of plasticity, by contrast, probably underestimates somewhat the resistance to nonproportional deformation, although perhaps not significantly. Thus, a comparison of results based on the two theories may give some indication as to whether the extensive stable crack growth predicted by classical flow theory (as indicated by the large values of K_{ss}/K_c) is realistic.

Full details of J_2 corner theory are given in the paper by Christoffersen and Hutchinson [*11*]. In their notation, the angle between the axis of the corner (see Fig. 9) and the stress-rate is given by

$$\cos\beta = \tau_\alpha \dot{\tau}_\alpha/(\tau\sqrt{\dot{\tau}_\mu \dot{\tau}_\mu}) \tag{26}$$

The total strain-rate is given by $\dot{\gamma}_\alpha = \partial W/\partial \dot{\tau}_\alpha$ where W is the stress-rate potential defined by

$$W = \frac{1}{2G} Q(\beta)\dot{\tau}_\alpha \dot{\tau}_\alpha \tag{27}$$

The strain-rate is

$$G\dot{\gamma}_\alpha = \left(Q + \frac{1}{2} Q' \operatorname{cotan}\beta\right)\dot{\tau}_\alpha - \frac{1}{2} Q' (\sin\beta \cos\beta)^{-1}\tau_\alpha \dot{\tau}/\tau \tag{28}$$

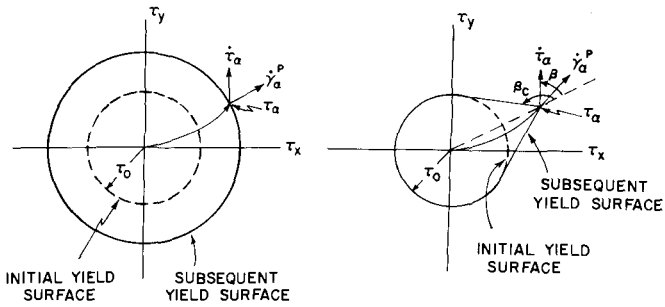

FIG. 9—*Two yield surfaces employed in the Mode III power hardening calculations.*

where $Q' = dQ/d\beta$. The function $Q(\beta)$ provides a smooth transition from a proportional loading increment ($\beta = 0$) to elastic unloading for $\beta \geq \beta_c$. For proportional loading the predictions of Eq 25 and 28 are identical, and for nearly proportional loading the strain-rates from Eq 28 coincide with the predictions of the J_2 deformation theory of plasticity. The function $Q(\beta)$ used in the calculations reported below is specified by the function $g(\phi)$ defined in Ref *11*, Eq 2.46 (with $m = 3$ and $\theta_0 = 0$).

The active plastic zones for the smooth theory and corner theory with $n = 5$ are shown in Fig. 10. Ahead of the crack the plastic boundaries are essentially coincident. The corner theory unloading boundary trails the isotropic hardening unloading boundary. The corner theory active zone is somewhat larger than that for isotropic hardening, reflecting the diminished resistance of the corner theory material to nonproportional stress histories.

Curves of COD behind the tip for the classical flow theory and the corner

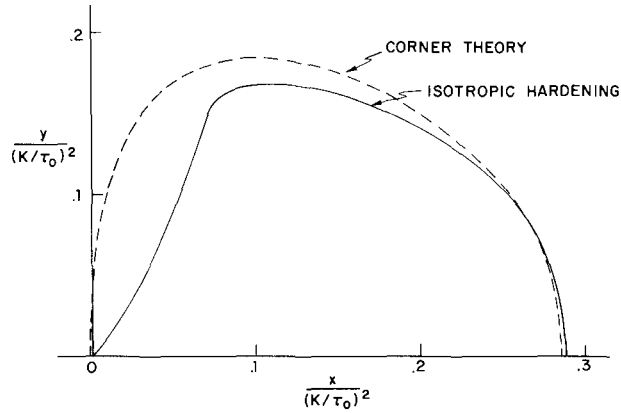

FIG. 10—*Comparison of active plastic zones in Mode III for power hardening* (n = 5) *for two yield surface characterizations.*

theory for $n = 5$ are included in Fig. 4. Over the portion of the plastic zone in which the present results are accurate (that is, to within about 1 percent of the plastic zone size from the tip), there is rather little difference in the results for the two theories. The COD, a given distance behind the tip, is slightly larger for the corner theory material than for the smooth yield surface material. This small difference again reflects the lowered resistance that the corner theory material offers to nonproportional plastic deformation.

The strain ahead of the crack from the two theories is shown in Fig. 11. Here again the difference is small but now the strain from the smooth yield surface solid is slightly larger than the other, at least for strains less than 15 γ_0 for which the authors' results are accurate. This somewhat surprising interchange can be rationalized by noting that the deformation on the line ahead of the crack is exactly proportional ($\tau_x = 0$), while nonproportional deformation takes place above and below the plane of the crack. Examination of the numerical results indicates that the standard flow theory solid tends to concentrate the straining in the region ahead of the crack, compared to the corner theory solid. Although the effect is not large, the corner theory solid shows relatively more straining above and below the line of the crack, consistent with what one would expect and consistent with its slightly larger opening displacement.

Our study of the influence of reduced resistance to nonproportional flow

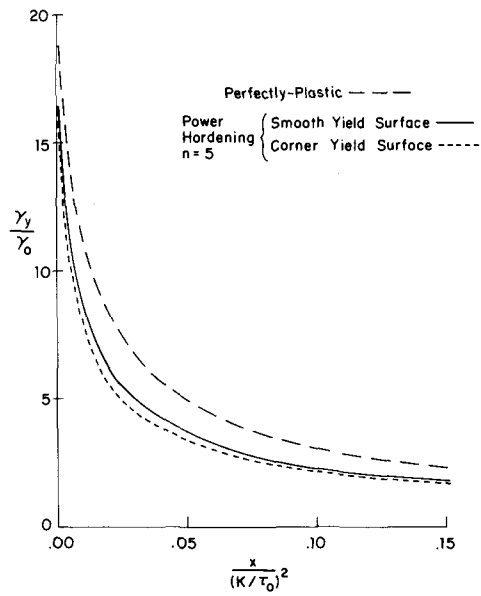

FIG. 11—*Strain ahead of crack in Mode III for power hardening theories and comparison with elastic-perfectly plastic distribution.*

as modeled by the corner theory has not been sufficiently extensive to warrant the apparent conclusion that the effect is not very large. It is possible that larger discrepancies will emerge closer to the tip at higher strain levels. One also notes that use of the corner theory results, as opposed to the standard flow theory results, with the critical strain criterion (Eq 18) would yield slightly higher estimates of K_{ss}/K_c. On the other hand, use of the corner theory results for the opening displacement with Eq 22 would give slightly lower estimates of this ratio, at least over the range considered here. Nevertheless, it does appear that the influence of strain hardening may be more significant than the corner effect.

Steady Growth in Plane Strain Mode I

In the plane strain study a piecewise-power law material was assumed whose uniaxial stress-strain curve is given by

$$\begin{aligned} \epsilon/\epsilon_0 &= \sigma/\sigma_0 \qquad \sigma < \sigma_0 \\ &= (\sigma/\sigma_0)^n \qquad \sigma > \sigma_0 \end{aligned} \tag{29}$$

where

σ_0 = the uniaxial yield stress,
$\epsilon_0 = \sigma_0/E$ = the yield strain, and
E = Young's Modulus.

The classical incremental theory (J_2 flow theory) was used to generalize Eq 29 to multiaxial states. This theory assumes isotropic hardening based on the Mises surface (that is, $J_2 = 1/2\ s_{ij}s_{ij}$ = constant, where s_{ij} is the stress deviator). The material was taken to be elastically isotropic with Poisson's ratio, ν. Included in Eq 29 for $n \to \infty$ is elastic-perfectly plastic behavior.

Amazigo and Hutchinson [*2*] obtained singularity fields for the plane strain, Mode I problem for linear strain hardening. However, they neglected the effect of reversed plastic loading along the flank of the crack behind the tip. The present numerical results indicate that substantial reversed loading occurs in plane strain, and therefore its omission in Ref *2* is likely to render those results inaccurate. For this reason no attempt was made to use the linear hardening material in the present plane strain study.

The elastic-plastic boundary of the active plastic zone is shown in Fig. 12 for the elastic-perfectly plastic material ($n = \infty$) and for $n = 3$ and 10. Poisson's ratio was taken to be $\nu = 0.3$ in all cases. The zone in which "reversed" plastic flow occurs, trails behind the tip as shown with a width that is approximately 15 percent of the vertical extent of the plastic zone for $n = 10$ and ∞.

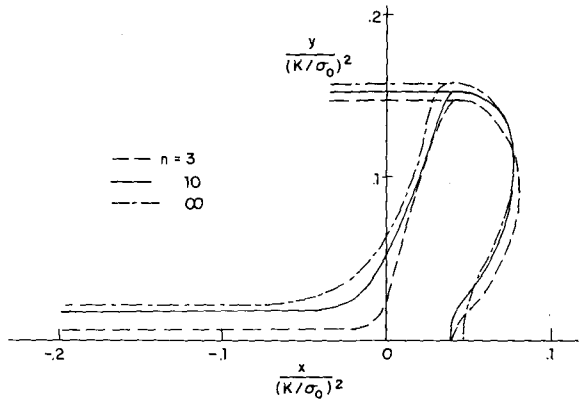

FIG. 12—*Active plastic zone in plane strain Mode I small-scale yielding for two levels of power hardening and elastic-perfectly plastic behavior.*

Stresses near the tip as determined from the finite element results for the elastic-perfectly plastic material are shown in Fig. 13. The numerical results are compared with the asymptotic near-tip stress field recently determined by Rice et al [7]. These new asymptotic stresses differ only by about 1 percent from the stresses of the Prandtl field, except in the neighborhood of $\theta = 135$ deg, where the differences are on the order of 10 percent. The main difference between the new asymptotic field and the Prandtl field is

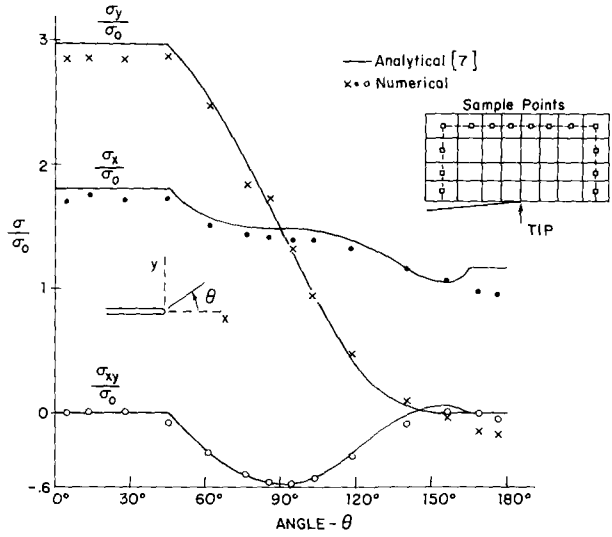

FIG. 13—*Comparison of the near-tip numerical stress results with asymptotic field of Ref 7 for plane strain Mode I.*

the presence of a wedge of elastic unloading extending from approximately $\theta = 115$ deg to $\theta = 163$ deg, whereas yield is satisfied for all θ in the Prandtl field. There is no evidence in the authors' numerical results of elastic unloading near the tip. As can be seen in Fig. 12, the active plastic zone appears to fully surround the tip. It is quite likely that the mesh refinement used in the present calculations is not sufficient to reveal the wedge shaped unloading region. In Mode III it was noted that the mesh used indicated a substantially smaller wedge of elastic unloading near the tip than that predicted by the Chitaley-McClintock asymptotic field. In plane strain, the mesh used in this analysis is relatively coarser (the smallest quadrilateral element is about 3 percent of the distance to the elastic plastic boundary ahead of the crack) and this may explain the authors' failure to observe any elastic unloading near the tip.

Curves of the nondimensional COD behind the crack for the steady growth problem are shown in Figs. 14*a* and *b*. The linear elastic curve ($n = 1$) is shown in Fig. 14*a*. The numerical values from the finite element calculations for the elastic-perfectly plastic case ($n = \infty$) are shown as solid dots in Fig. 14*b*. As the tip is approached the opening displacement goes to zero as

$$\delta = \beta \frac{\sigma_0}{E} r \ln \left(\frac{eR}{r} \right) \tag{30}$$

where, following the notation of Rice and Sorensen [6], β is a numerical constant (with no relation to the angle β used in the corner theory), $e = 2.7183$ and $R = c(K/\sigma_0)^2$ where c is another numerical constant. The best least-square fit of Eq 30 to the four computed values of δ nearest the tip (see Fig. 14*b*) gives

$$\beta = 4.28 \quad \text{and} \quad c = 0.71 \tag{31}$$

The analysis of Rice et al [7], which employs the asymptotic near-tip field mentioned above, gives the theoretical value $\beta = 5.08$. Fixing β at 5.08 and choosing c to give a best least-square fit of the same four values of δ, one finds

$$\beta = 5.08 \quad \text{and} \quad c = 0.28 \tag{32}$$

This latter estimate of c is in reasonable agreement with the value obtained in Ref 7 from a fit of numerical data for the transient growth of a crack. Curves from Eq 30, using Eq 31 and 32, are shown in Fig. 14*b*. There is relatively little difference between the two curves for $x/(K/\sigma_0)^2$ in the range -0.001 to -0.02.

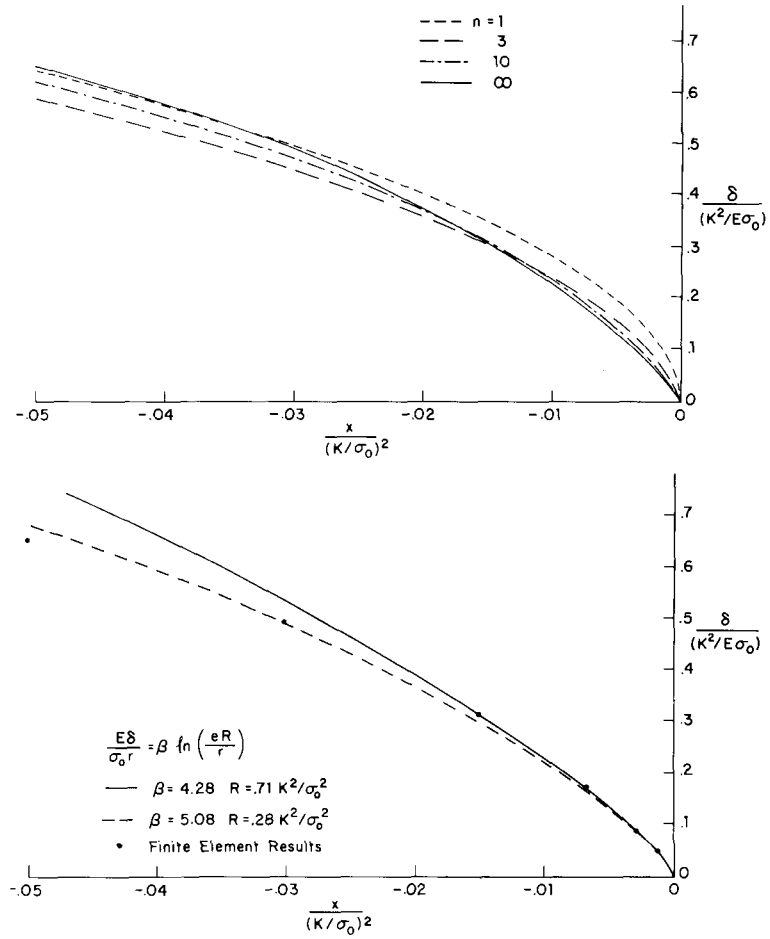

FIG. 14—*Crack opening displacement in plane strain Mode I* (a) *effect of hardening, and* (b) *numerical values for elastic perfectly plastic case* (n = ∞) *and comparison with asymptotic formula.*

The results for δ for $n = 3$, 10 and ∞ have been replotted as $\delta/(\epsilon_0 r)$, where $\epsilon_0 = \sigma_0/E$, as a function of $r/(K/\sigma_0)^2$ in Fig. 15. It is in this form that the results are most convenient for predicting K_{ss}/K_c from a near-tip fracture criterion based on a critical δ.

Following Rice and Sorensen [*6*], and also Ref *7*, one again adopts the near-tip criterion (Eq 22) for initiation and continuation of crack growth. For a given value of $\delta_c/(\epsilon_0 r_c)$ and n, the value of $r_c/(K_{ss}/\sigma_0)^2$ for steady-state growth can be read off the abscissa of Fig. 15. The value of $r_c/(K_c/\sigma_0)^2$ for initiation of growth can be read from the corresponding curve for the stationary problem. These two values supply the ratio $(K_{ss}/K_c)^2$ for a given

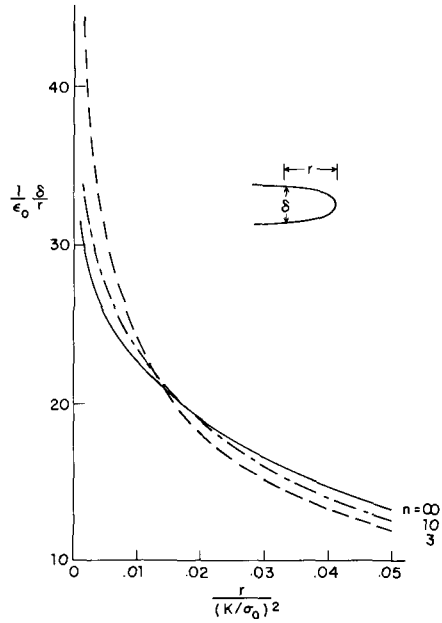

FIG. 15—*Normalized crack opening displacement in plane strain Mode I.*

pair $\delta_c/(\epsilon_0 r_c)$ and n. Curves obtained in this manner are plotted in Fig. 16 for $n = 3$, 10 and ∞. For the stationary problem the authors derived curves of $\delta/(\epsilon_0 r)$ versus $r/(K/\sigma_0)^2$ from Ref *12* for $n = 3$ and ∞ and from Ref *6* for $n = 10$. However, the n-dependence of the stationary solution for δ plays a relatively minor role in determining the influence of hardening on the variation of K_{ss}/K_c with $\delta_c/(\epsilon_0 r_c)$ in Fig. 16. Primarily, the influence of hardening on the curves in Fig. 16 is due to the dependence of the steady growth solution of Fig. 15 on the hardening index n.

The strong dependence of K_{ss}/K_c on hardening is qualitatively similar to what was found in Mode III for linear hardening. The curves in Fig. 16 were not extrapolated to values of $\delta_c/(\epsilon_0 r_c)$ beyond about 32, corresponding to the limit to which the numerical results are felt to be accurate. Rice and Sorensen [6] suggest that values of $\delta_c/(\epsilon_0 r_c)$ larger than 100 may be appropriate for certain intermediate strength pressure vessel steels with unusually high tear resistance. Then, values of K_{ss}/K_c will be enormous for light to moderate strain hardening ($10 \leq n \leq \infty$, say) as can be seen from the trends of Fig. 16. But it is also clear from these trends that the elastic-perfectly plastic result for a given $\delta_c/(\epsilon_0 r_c)$ appears to significantly overestimate the potential for stable crack growth in a hardening material. It seems reasonable to assume that the same conclusion holds for the entire transient growth process. That is, one expects that the normalized resistance

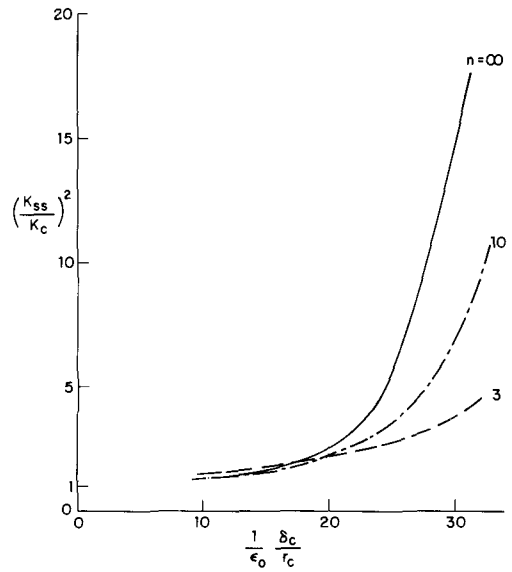

FIG. 16—*Effect of hardening on* K_{ss}/K_c *in plane strain Mode I as predicted by a criterion based on the attainment of a critical opening displacement* δ_c *a distance* r_c *behind the current tip.*

curve in small-scale yielding (that is, K_R/K_c as a function of Δa), as predicted using a near-tip fracture criterion such as the one employed here, will be strongly influenced by small to moderate amounts of hardening. Predictions for elastic-perfectly plastic solids will tend to be unconservative when strain hardening is present.

Acknowledgments

We are indebted to D. M. Parks and his colleague P. S. Lam for making available for comparison purposes some of their results for the Mode III problem, which were obtained using a similar numerical method to that employed here. We also acknowledge receipt of an early version of Ref *7* from J. R. Rice and helpful discussions with him in connection with the asymptotic near-tip fields. This work was supported in part by the National Science Foundation under Grant NSF-ENG78-10756, and by the Division of Applied Sciences, Harvard University. In addition, R. H. Dean acknowledges support in the initial stages of the work from a National Science Foundation Graduate Fellowship.

References

[*1*] Rice, J. R. in *Mechanics and Mechanisms of Crack Growth,* British Steel Corp., 1973.
[*2*] Amazigo, J. C. and Hutchinson, J. W., *Journal of the Mechanics and Physics of Solids,* Vol. 25, 1977, pp. 81-97.

[3] *Elastic-Plastic Fracture, ASTM STP 668,* American Society for Testing and Materials, 1979.

[4] Chitaley, A. D. and McClintock, F. A., *Journal of the Mechanics and Physics of Solids,* Vol. 19, 1971, pp. 147-163.

[5] Andersson, H., *Journal of the Mechanics and Physics of Solids,* Vol. 22, 1974, pp. 285-308.

[6] Rice, J. R. and Sorensen, E. P., *Journal of the Mechanics and Physics of Solids,* Vol. 26, 1978, pp. 163-186.

[7] Rice, J. R., Drugan, W. J., and Sham, T. L., "Elastic Plastic Analysis of Growing Cracks," Technical Report No. 65, Division of Engineering, Brown University, May 1979.

[8] Rice, J. R. and Tracey, D. M. in *Numerical and Computer Methods in Structural Mechanics,* Academic Press, New York, 1973, pp. 585-623.

[9] McClintock, F. and Irwin, G. R. in *Fracture Toughness Testing and Its Applications, ASTM STP 381,* American Society for Testing and Materials, 1965, pp. 84-113.

[10] Rice, J. R., *Journal of Applied Mechanics,* Vol. 34, 1967, pp. 287-298.

[11] Christoffersen, J. and Hutchinson, J. W., *Journal of the Mechanics and Physics of Solids,* Vol. 27, 1979, pp. 465-487.

[12] Shih, C. F., Andrews, W. R., German, M. D., VanStone, R. H., and Wilkinson, J. P. D., "Methodology for Plastic Fracture," Report No. SRD-78-116, Combined Seventh and Eighth Quarterly Report by General Electric Company to Electric Power Research Institute, Inc., July 1978.

Virendra Kumar[1] *and C. F. Shih*[1]

Fully Plastic Crack Solutions, Estimation Scheme, and Stability Analyses for the Compact Specimen

REFERENCE: Kumar, Virendra and Shih, C. F., **"Fully Plastic Crack Solutions, Estimation Scheme, and Stability Analyses for the Compact Specimen,"** *Fracture Mechanics: Twelfth Conference, ASTM STP 700,* American Society for Testing and Materials, 1980, pp. 406-438.

ABSTRACT: This paper presents the fully plastic solutions for the compact specimen and an estimation scheme that exploits these solutions to generate crack driving force diagrams under contained and large-scale plasticity conditions.

Plane-strain and plane-stress fully plastic solutions for compact specimens are obtained for a wide range of crack length to width ratios and for hardening exponent n of up to 20. The calculations are based on deformation plasticity theory and use the finite element method for incompressible deformation developed by Needleman and Shih. Relevant crack parameters like the J-integral, crack opening displacement, mouth opening displacement, and load-line displacement are appropriately normalized and tabulated. Simple formulas are given for estimating the relevant crack parameters from contained yielding to fully plastic situations using the elastic and the tabulated fully plastic solutions. The results thus obtained are compared with accurate finite element solutions for stationary and extending cracks based on flow theory of plasticity.

Crack driving forces in terms of the J-integral and crack opening displacement are computed for A533B compact specimens using the above estimation scheme. Assuming that the conditions for J-controlled growth are satisfied, the load-displacement behavior, stable crack extension, and the point of instability can be determined from the crack driving force diagrams if the material J-resistance curve is known. Comparisons of the predictions with actual test measurements for several different sized compact specimens show good agreement.

KEY WORDS: compact specimen, plane strain, plane stress, fully plastic solutions, elastic-plastic estimation scheme, crack growth, instability, creep crack growth, limit load, J-integral, crack opening displacement, resistance curve, tearing modulus, fractures (materials), crack propagation

[1]Mechanical engineers, Corporate Research and Development, General Electric Co., Schenectady, N.Y. 12301.

In two earlier publications Shih [*1*][2] and Shih and Hutchinson [*2*] proposed a relatively simple procedure for estimating solutions to contained and large-scale yielding crack problems where the load is monotonically increased and the crack is stationary. The essential ingredients for the estimation procedure are the linear elastic solutions as tabulated by Tada [*3*] and the fully plastic solutions as tabulated by Shih, Hutchinson, Goldman, Needleman [*1,2,4-6*], Ranaweera and Leckie [*7*] and Parks [*8*]. The estimation procedure exploits the scaling laws associated with linear elastic and fully plastic solutions to interpolate over the range from small-scale yielding to large-scale yielding. The method also accounts for strain hardening and the stress strain representation of material behavior. In [*1,2*] the simple estimates were compared with full numerical calculations; the interpolation formulas for the J-integral, crack opening displacement δ, and other relevant crack parameters were found to be fairly accurate.

Subsequent to the investigation by Begley and Landes [*9,10*] and Green and Knott [*11*], which led to the characterization of the onset of crack growth by the critical value of J and δ, denoted by J_{Ic} and δ_{Ic} respectively, experimental data on stable crack extension became available. The data from Clarke et al [*12*], Griffis and Yoder [*13*], Clark et al [*14*], and Shih and Andrews [*15,16*] suggest that limited amounts of crack growth is characterizable by the J or δ resistance curve. The latter experimental studies [*15,16*] were complemented by analytical and finite element studies of the growing crack based on measured crack growth behavior. Simultaneously, Paris et al [*17*] initiated an approach for analyzing crack growth stability based on the concept of a J-integral resistance curve. Pursuing similar lines, Hutchinson and Paris [*18*] and Zahoor and Paris [*19*] employed formulas based on the deep crack approximation in Ref *20* and the interpolation formulas in Refs *1* and *2* to examine the stability of small amounts of crack growth under J-controlled growth conditions.

In this paper the plane-strain and plane-stress fully plastic solutions for the compact specimen are presented. These solutions are appropriately normalized and comparisons with the deep crack approximations are made. Improved interpolation formulas for J-integral and other relevant crack parameters are compared with experimental data and full numerical calculations for the growing crack. Crack driving force diagrams in terms of J and the tearing modulus are computed for A533B steel compact specimens. The load-displacement behavior of the specimen, amount of stable crack extension, and the maximum load are determined directly from these diagrams. These predictions are compared with test measurements for a number of compact specimens. The J-integral resistance curve may be obtained directly from the crack driving force diagrams in conjunction with the measured

[2]The italic numbers in brackets refer to the list of references appended to this paper.

load-displacement record. Examples that illustrate this feature and sensitivity analyses are reported.

Fully Plastic Solutions for Compact Specimens

Considered here is a class of small strain fully plastic crack problems for incompressible power law materials as in Refs *1,2,4,* and *5*. In simple tension, the strain is related to the stress by

$$\epsilon/\epsilon_o = \alpha(\sigma/\sigma_o)^n \tag{1}$$

where σ_o and ϵ_o are some reference stress and strain (the connection $\sigma_o = E\epsilon_o$ can always be made, but is not necessary), n is the hardening exponent, α is a material constant, and E is the Young's modulus. At one limit given by $n = 1$, (1) represents linear elastic behavior while at the other limit of $n \to \infty$, (1) gives rigid-perfectly plastic behavior. Generalizing this uniaxial relationship by J_2 deformation theory of plasticity leads to

$$\frac{\epsilon_{ij}}{\epsilon_o} = \frac{3}{2}\,\alpha\left(\frac{\sigma_e}{\sigma_o}\right)^{n-1}\frac{S_{ij}}{\sigma_o} \tag{2}$$

where S_{ij} is the deviator stress and σ_e is the effective stress defined by $\sigma_e^2 = 3/2\, S_{ij}S_{ij}$.

As first noted by Ilyushin [*21*], a solution to a boundary value problem involving a single load or displacement parameter, which is increased monotonically, has two important properties. First, the field quantities including crack parameters like the J-integral and crack opening displacement increase in direct proportion to the load or displacement parameter raised to some power dependent on n. For example, if P is the load parameter, the stress at every point is proportional to P while the strain is proportional to P^n. The second property follows from the first. Since the stress and strains at every point increase in exact proportions, the fully plastic solution based on Eq 2 is also the exact solution to the same problem posed for flow theory of plasticity.

For fully plastic crack problems of the type described by Eq 2, the material is fully nonlinear and incompressible. In anti-plane shear or plane stress problems examined in Refs *1,* and *2*, the incompressible deformation do not introduce any additional complexity on the finite element method. Thus, fully plastic solutions were obtained for a number of crack configurations using a modified Newton-Raphson scheme coupled with parameter tracking for solving the fully nonlinear system of equations. The iterative scheme is discussed in the Appendix of Ref *1*. In plane-strain problems, the enforcement of the incompressibility constraints complicates the displacement finite element method.

Incompressible deformation can be accommodated within the framework of the finite element method in a variety of ways and these are briefly discussed elsewhere [6]. In this paper the authors employ the finite element method developed in Ref 6 to obtain the plane strain fully plastic solutions. The method is formulated from the virtual work equation based on deviatoric quantities. The incompressibility constraint is imposed directly on the admissible displacement field by direct elimination of nodal displacements. This leads to a stiffness matrix that is symmetric and positive definite. A modified Newton-Raphson iterative scheme [1] is employed to solve the nonlinear system of equations. Once a convergent solution for the displacement is obtained, the hydrostatic stress is determined using the principle of virtual work.

Fully Plastic Plane-Strain Solutions

Plane-strain fully plastic analyses were carried out for the standard ASTM compact specimen for $a/b = 1/4, 3/8, 1/2, 5/8$, and $3/4$ and for $n = 1, 2, 3, 5, 7, 10, 13, 16$, and 20. As illustrated in Fig. 1*a*, a is the crack length and b the specimen width. Because of symmetry along the crack, only the upper half of

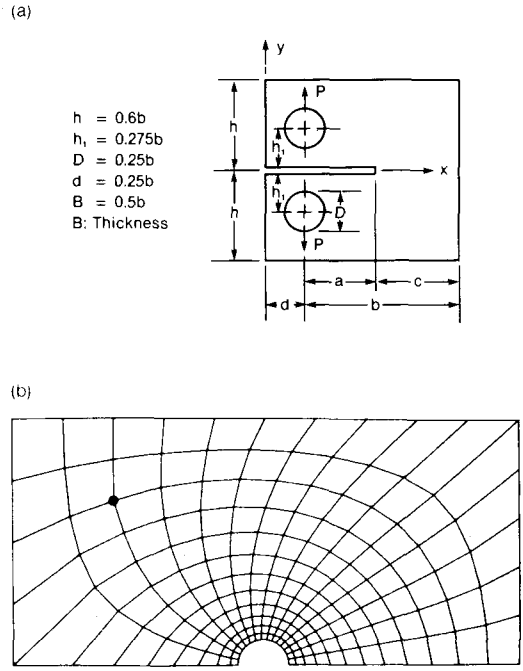

FIG. 1—(a) *Geometry of ASTM standard compact specimen; and* (b) *finite element mesh for upper half of compact specimen with* a/b = 3/8 *(within the semicircular hole are eight rings of elements; the load is applied at the node shown by the dot).*

the specimen was modeled. A typical finite element mesh for the case $a/b = 3/8$ is shown in Fig. 1*b*. The quadrilateral consists of four constant strain triangles; the former are grouped in substructures in which all linearly independent incompressibility constraints are satisfied. As discussed in Ref *6* these substructures are employed as the basic building blocks of the finite element grid. The loading pin hole could not be conveniently accommodated using the substructures and therefore was not included in the present model; the effect of not including the hole will be discussed subsequently.

As shown in Fig. 1, the model had 15 quadrilaterals in the circumferential direction about the crack tip (from $\theta = 0$ to π) and 20 elements in the radial direction from the tip to the external boundaries. The meshes used for the other values of a/b also had the same number of elements and were similar to the one shown here. In these analyses the singular crack tip element was not used because of the associated convergence problems for large n-values. Instead, the mesh had a small hole at the crack tip with radius equal to 1 to 2 percent of the crack length or the remaining ligament, whichever was the smaller dimension. This circumvented some of the numerical difficulties at the crack tip and the solution converged fairly rapidly. The hole was very small in size, and numerical experimentation showed that it had virtually no effect on the J-integral, mouth opening displacement, and the load-line displacement for the range of n examined. In most cases, the difference amounted to less than 1 percent.

Following the procedure in Refs *1* and *6*, linear or modified Newton-Raphson interations were employed to obtain the fully plastic solution. The parameter tracking technique was used by which the appropriately scaled solution corresponding to $n = 1$ was taken as the initial guess to obtain the $n = 2$ solution, and which in turn is used as the starting point for $n = 3$ and so on. For $n > 5$, the Newton's iterations did not always converge, and it seemed necessary to employ several linear iterations typically before using the Newton's method. For $n > 10$, direct application of Newton's iterations could lead to numerical instability, and, therefore, mostly linear iterations were employed. It typically took three Newton's iterations for $n < 5$, five linear iterations plus three Newton's iterations for $5 \leq n \leq 10$ and eight linear iterations for $n > 10$. The computations were performed in single precision (about 14 digits) on the CDC 7600. In similar calculations for a center-cracked plate (CCP), Newton's iterations worked well for the entire range of n investigated [*22*]. It is suspected that the numerical difficulties with the compact specimen is partially due to the high stress gradient across the ligament.

The present results for the linear elastic case corresponding to $n = 1$ were compared with the results of Newman [*23*] without the pin hole. For all a/b ratios, the average value of the J-integral computed over a wide range of contours using the line-integral definition given by Rice [*24*] is within 2 percent of the value given in Ref *23*. The variation from path to path is less than 1

percent from the average value. The mouth opening displacement, δ, at the outer edge was also within 2 percent of Ref *23* for all the values of a/b considered here. The load line displacement, Δ_L, is of similar accuracy except for the extreme a/b ratios where it differed from Ref *23* by 4 percent.

As mentioned earlier, the present results do not include the effect of a pin hole. Newman [*23*] has investigated the effect of a pin hole on K (or J), δ, and Δ_L. He found that for $n = 1$, the effect is negligible for $a/b \geq 0.4$. For nonlinear materials ($n \geq 3$) and under fully plastic conditions, the deformation concentrates along the uncracked ligament; that is, the ligament is much more compliant than the remaining body. Thus, it is argued that for n ranging from 7 to 20, which is the case for most structural steels, the error associated with ignoring the pin hole is negligible. The comparison of the fully plastic results with the deep crack formulas in a later section also supports the above inference.

As discussed in the previous section, an important characteristic feature of the fully plastic solutions is that they are scalable. The results obtained here for various a/b and n-values were normalized using the following scheme [*1,2,4*]

$$J = \alpha\sigma_o\epsilon_o c h_1(a/b, n)(P/P_o)^{n+1} \tag{3}$$

$$\delta = \alpha\epsilon_o a h_2(a/b, n)(P/P_o)^n \tag{4}$$

$$\Delta_L = \alpha\epsilon_o a h_3(a/b, n)(P/P_o)^n \tag{5}$$

where

P = the load per unit thickness, and

$c = b - a$ = the uncracked ligament.

It is noted that h_1, h_2, and h_3 in the above equations are functions of a/b and n alone. P_o is the limit load per unit thickness and is given by (see Appendix 1)

$$P_o = 1.455\,\eta c\sigma_o \tag{6}$$

where η is defined as

$$\eta = \left[\left(\frac{2a}{c}\right)^2 + 2\left(\frac{2a}{c}\right) + 2\right]^{1/2} - \left(\frac{2a}{c} + 1\right) \tag{7}$$

This limit load is obtained by using the procedure of Merkle and Corten [*25*]. An upper bound limit load for the compact specimen in plane strain can also be calculated by using the Rice's method [*26*] or the Green and

Hundy field [*27*]. A comparison of the limit load derived by these different procedures is discussed in Appendix 1.

In Eq 4, δ is the mouth opening displacement of the crack at the outer edge (that is, $\delta = U_y(0, 0^+) - U_y(0, 0^-)$. In Eq 5 the crack opening displacement at the load line is given by $\Delta_L = U_y(d, 0^+) - U_y(d, 0^-)$.

The calculated values of h_1, h_2, and h_3 for the plane-strain compact specimen are presented in Table 1 for $a/b = 1/4, 3/8, 1/2, 5/8, 3/4$, and 1 and for $n = 1, 2, 3, 5, 7, 10, 13, 16$, and 20.[3] The h's for $n = 1$ were taken from the elastic solution [*23*] with the pin hole effect included and using the normalization scheme, Eqs 3 to 5. Poisson's ratio ν was taken to be 0.5 for the $n = 1$ situation to indicate the elastic limit of the incompressible fully plastic formulation. For $a/b = 1/2, 5/8$, and $3/4$, the plots of h_1, h_2, and h_3 versus $1/n$ are shown in Figs. 2 and 3, respectively. These plots are useful for interpolating and extrapolating the h's corresponding to various values of n and a/b. Similar plots of h_1, h_2, and h_3 versus a/b for fixed values of n can be also constructed.

Fully Plastic Plane Stress Solutions

Fully plastic plane-stress analyses based on Eq 2 were also carried out for the compact specimen using a conventional displacement finite element method [*2,22*]. The same iterative scheme as discussed in the previous section was employed to solve the nonlinear system of equations associated with the plane stress formulation.[4] The meshes for the plane-stress analyses were identical to the corresponding plane strain meshes.

The plane-stress fully plastic solutions are normalized in the same form (Eqs 3 through 5) as for the plane-strain case, except that the limit load appropriate to the plane-stress situation as discussed in Appendix 1 and given by

$$P_o = 1.072\eta c\sigma_o \tag{8}$$

is used in the normalization and η is as in Eq 7. The plane-stress solutions require less iterations to converge[5] when compared to plane-strain solutions. The values of h_1, h_2, and h_3 are tabulated in Table 2. For purposes of interpolation and extrapolation, the h's can be plotted in the format of Figs. 2 and 3.

[3]Values for $a/b \to 1$ are obtained by extrapolation—see Appendix B.

[4]To check out the plane-stress computer code, the center cracked panel was analyzed. The fully plastic solutions for a wide range of n were within 1 to 2 percent of the earlier results tabulated in Ref *2*.

[5]Measured by the error norm based on L_2.

TABLE 1—h_1, h_2, *and* h_3 *for plane-strain compact specimen.*

		$n = 1$	$n = 2$	$n = 3$	$n = 5$	$n = 7$	$n = 10$	$n = 13$	$n = 16$	$n = 20$
$a/b = 1/4$	h_1	2.227	2.048	1.783	1.475	1.334	1.248	1.258	1.325	1.566
	h_2	17.883	12.481	11.675	10.788	10.538	10.745	11.460	12.570	14.563
	h_3	9.852	8.506	8.170	7.774	7.706	7.942	8.517	9.371	10.887
$a/b = 3/8$	h_1	2.148	1.716	1.392	0.970	0.693	0.443	0.276	0.176	0.098
	h_2	12.644	8.176	6.521	4.319	2.970	1.794	1.102	0.686	0.370
	h_3	7.944	5.760	4.643	3.103	2.139	1.292	0.793	0.494	0.266
$a/b = 1/2$	h_1	1.935	1.509	1.242	0.919	0.685	0.461	0.314	0.216	0.132
	h_2	9.327	5.846	4.304	2.747	1.912	1.199	0.788	0.530	0.317
	h_3	6.406	4.268	3.157	2.024	1.413	0.888	0.585	0.393	0.236
$a/b = 5/8$	h_1	1.763	1.449	1.237	0.974	0.752	0.602	0.459	0.347	0.248
	h_2	7.612	4.572	3.423	2.359	1.810	1.319	0.983	0.749	0.485
	h_3	5.521	3.431	2.583	1.787	1.373	1.000	0.746	0.568	0.368
$a/b = 3/4$	h_1	1.709	1.424	1.263	1.033	0.864	0.717	0.575	0.448	0.345
	h_2	6.370	3.948	3.179	2.337	1.876	1.441	1.124	0.887	0.665
	h_3	4.857	3.048	2.456	1.807	1.450	1.114	0.869	0.686	0.514
$a/b \to 1$	h_1	1.568	1.450	1.350	1.180	1.080	0.950	0.850	0.730	0.630
	h_2	5.388	3.738	3.093	2.433	2.121	1.795	1.573	1.333	1.136
	h_3	4.310	2.990	2.474	1.946	1.697	1.436	1.258	1.066	0.909

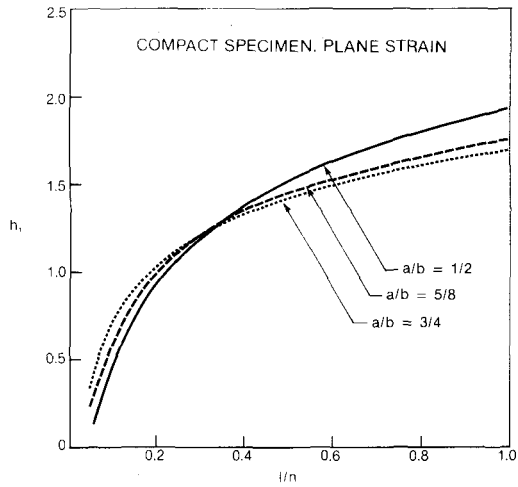

FIG. 2—h_1 *versus* $1/n$ *for a compact specimen in plane strain.*

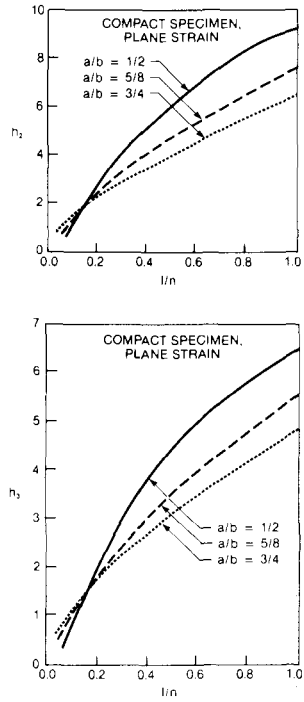

FIG. 3—h_2 *and* h_3 *versus* $1/n$ *for a compact specimen in plane strain.*

TABLE 2—h_1, h_2, *and* h_3 *for plane-stress compact specimen.*

		$n = 1$	$n = 2$	$n = 3$	$n = 5$	$n = 7$	$n = 10$	$n = 13$	$n = 16$	$n = 20$
$a/b = 1/4$	h_1	1.609	1.464	1.284	1.060	0.903	0.729	0.601	0.511	0.395
	h_2	17.552	12.042	10.706	8.736	7.316	5.744	4.629	3.746	2.916
	h_3	9.670	7.996	7.205	5.944	5.000	3.945	3.191	2.591	2.023
$a/b = 3/8$	h_1	1.552	1.249	1.047	0.801	0.647	0.484	0.377	0.284	0.220
	h_2	12.410	8.203	6.538	4.563	3.447	2.442	1.830	1.360	1.019
	h_3	7.800	5.734	4.615	3.253	2.475	1.765	1.330	0.990	0.746
$a/b = 1/2$	h_1	1.398	1.084	0.901	0.686	0.558	0.436	0.356	0.298	0.238
	h_2	9.155	5.673	4.212	2.801	2.123	1.571	1.245	1.026	0.814
	h_3	6.288	4.149	3.107	2.087	1.590	1.181	0.938	0.774	0.614
$a/b = 5/8$	h_1	1.274	1.031	0.875	0.695	0.593	0.494	0.423	0.370	0.310
	h_2	7.471	4.483	3.347	2.367	1.923	1.539	1.292	1.116	0.928
	h_3	5.419	3.375	2.536	1.804	1.468	1.176	0.988	0.853	0.710
$a/b = 3/4$	h_1	1.234	0.977	0.833	0.683	0.598	0.506	0.431	0.373	0.314
	h_2	6.252	3.780	2.893	2.135	1.775	1.437	1.204	1.030	0.857
	h_3	4.767	2.922	2.242	1.657	1.379	1.116	0.936	0.800	0.666
$a/b \to 1$	h_1	1.133	1.010	0.775	0.680	0.650	0.620	0.490	0.470	0.420
	h_2	5.288	3.536	2.412	1.905	1.734	1.592	1.232	1.166	1.029
	h_3	4.231	2.829	1.930	1.524	1.387	1.274	0.985	0.933	0.824

Evaluation of Fully Plastic Solutions

An expression for J in terms of the load-displacement record has been obtained by Merkle and Corten specifically for the compact specimen [*25*][6]

$$J_{MC} = \frac{2}{c}\left(\frac{1+\eta}{1+\eta^2}\right) \int_0^{\Delta_L} P d\Delta_L \tag{9}$$

One can evaluate Eq 9 using the fully plastic results and see how closely J_{MC} agrees with J for various values of n. Using Eq 5 in Eq 9, one has

$$J_{MC} = 2\alpha\epsilon_o \left(\frac{n}{n+1}\right) \left(\frac{1+\eta}{1+\eta^2}\right) \left(\frac{a}{c}\right) P_o \left(\frac{P}{P_o}\right)^{n+1} h_3 \tag{10}$$

Dividing Eq 10 by Eq 3 gives the ratio in terms of η and h_3 and h_1

$$\frac{J_{MC}}{J} = \frac{2P_o}{\sigma_o c}\left(\frac{a}{c}\right) \left(\frac{n}{n+1}\right) \left(\frac{1+\eta}{1+\eta^2}\right) \frac{h_3}{h_1} \tag{11}$$

An expression by Rice et al [*20*] valid for deep cracks in bending, is given by

$$J_{RPM} = \frac{2}{c} \int_0^{\Delta_L} P d\Delta_L \tag{12}$$

In terms of the fully plastic results

$$J_{RPM} = 2\alpha\epsilon_o \left(\frac{n}{n+1}\right) \left(\frac{a}{c}\right) P_o \left(\frac{P}{P_o}\right)^{n+1} h_3 \tag{13}$$

The ratio J_{RPM}/J is

$$\frac{J_{RPM}}{J} = \frac{2P_o}{\sigma_o c}\left(\frac{a}{c}\right) \left(\frac{n}{n+1}\right) \frac{h_3}{h_1} \tag{14}$$

The ratios, Eqs 11 and 14, for the plane-stress problem using Eq 8 for P_o, were computed from the numerical values of h_1 and h_3 in Table 2. Plots of Eqs 11 and 14 against $1/n$ for a/b equal to 1/2 and 3/4 are shown in Fig. 4. From the graphs it is clear that the accuracy of formulas expressed in Eqs 9 and 12 increases with larger crack length (for fixed crack width) and n values. The Merkle-Corten expression also appears to be better suited for compact specimens. For $n \geq 3$, J_{MC} is within 3 percent of J-value for $a/b \geq$

[6]The second term to J_{MC} may be ignored for a/b ratios greater than 0.45 [*25*].

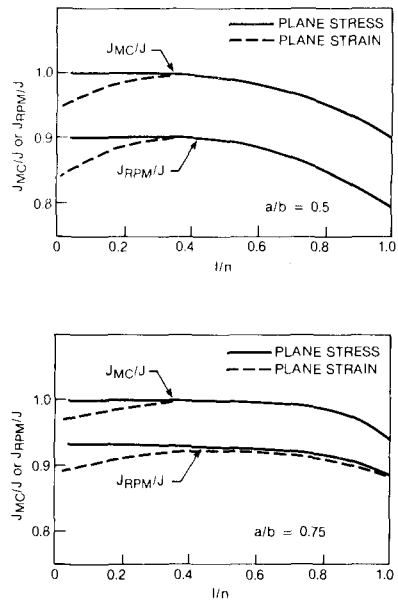

FIG. 4—*Values of* J_{MC}/J *and* J_{RPM}/J *from Eq 11 and 14 under plane strain and plane stress condition.*

3/8. The authors interpret this as indicating that Eqs 9 and 10 are appropriate for purposes of calculating J for a wide range of hardening materials as long as the remaining ligament is fully yielded. The trend and consistency of the approach to the deep crack limit also attests to the numerical accuracy of the fully plastic solutions.

Equations 9 and 12 were also evaluated using the fully plastic plane-strain solutions tabulated in Table 1. The ratios thus obtained are shown by dashed curves in Fig. 4 for $a/b = 1/2$ and $3/4$. Generally the trends of the plane-strain results are similar to the plane-stress results. However at higher n-values, the ratio deviates from unity by about 5 percent or so. This is probably due to the numerical errors in h_1, h_2, and h_3 at large values of n and do not suggest a departure of J_{MC} and J_{RPM} from the true J.[7] Based on these checks, one expects errors of up to 7 percent in the plane-strain values of h_1, h_2, and h_3 at the larger n-values. Using the same reasoning, the plane-stress values should be considerably more accurate.

In Tables 1 and 2, h_1, h_2, and h_3 are tabulated at several values of a/b and n. Procedures for the purpose of extrapolating the h's for the complete range of a/b and n, especially for the limit of $a/b \to 0$, are discussed in Ref *2*. To

[7]In the plane strain calculations, the iterations converge rather slowly for the larger n-values. The errors noted may be partially attributed to the techniques employed to improve the rate of convergence.

carry out the estimation schemes, crack analyses, and the examination of crack growth stability to be discussed subsequently, it is desirable to express h_1, h_2, and h_3 as analytic functions of a/b. For this purpose, the h's at any paticular n-value are expressed as a polynomial in a/b where the coefficients of the polynomials are obtained by least square analyses of the tabulated values in Tables 1 and 2.

Estimation Scheme for Elastic-Plastic Specimens

Consider the Ramberg and Osgood stress strain law, which in uniaxial tension has the form

$$\frac{\epsilon}{\epsilon_o} = \frac{\sigma}{\sigma_o} + \alpha \left(\frac{\sigma}{\sigma_o}\right)^n \tag{15}$$

For materials that may be approximated by Eq 15, the J-integral, mouth opening displacement, δ, and the load line displacement is given by the sum of the adjusted linear elastic and fully plastic contributions. In abbreviated notation, the elastic-plastic formulas are of the form [*1,2*]

$$\begin{aligned} J &= J(a_e, n = 1) + J(a, n) \\ \delta &= \delta(a_e, n = 1) + \delta(a, n) \\ \Delta_L &= \Delta_L(a_e, n = 1) + \Delta_L(a, n) \end{aligned} \tag{16}$$

where a_e is the adjusted or effective crack length that will be defined later.

Elastic-Plastic Interpolation Formulas

In the linear elastic range, the parameters J, δ and Δ_L are given by

$$J = \frac{aF_1^2(a/b)}{E'b^2} P^2 \tag{17}$$

$$\delta = \frac{1}{E'} V_1(a/b)P \tag{18}$$

$$\Delta_L = \frac{1}{E'} V_2(a/b)P \tag{19}$$

where P is the load per unit thickness, the functions F_1, V_1, and V_2 are given in Ref *3*, and $E' = E$ for plane stress or $E' = E/(1 - \nu^2)$ for plane strain. These expressions are rewritten as

$$J = f_1(a) \frac{P^2}{E'} \tag{20}$$

$$\delta = f_2(a) \frac{P}{E'} \tag{21}$$

$$\Delta_L = f_3(a) \frac{P}{E'} \tag{22}$$

where $f_1 = aF_1^2/b^2, f_2 = V_1$, and $f_3 = V_2$. In the fully plastic state, J, δ, and Δ_L are given by Eqs 3, 4, and 5, respectively.

Using the quantities defined in Eqs 3 through 5 and 20 through 22, the estimation scheme Eq 16 can be written in the following form for the entire range of elastic-plastic deformation

$$J = f_1(a_e) \frac{P^2}{E'} + \alpha \sigma_o \epsilon_o c h_1(a/b, n) (P/P_o)^{n+1} \tag{23}$$

$$\delta = f_2(a_e) \frac{P}{E'} + \alpha \epsilon_o a h_2(a/b, n) (P/P_o)^n \tag{24}$$

$$\Delta_L = f_3(a_e) \frac{P}{E'} + \alpha \epsilon_o a h_3(a/b, n) (P/P_o)^n \tag{25}$$

The crack length adjustment employed in this paper is slightly different from the effective crack length of the earlier papers [*1,2*]. To ensure continuity of the partial derivatives of J and Δ_L with respect to applied load at $P = P_o$[8], the authors have chosen to use an adjusted crack length given by

$$a_e = a + \phi r_y \tag{26}$$

where

$$r_y = \frac{1}{\beta \pi} \left(\frac{n-1}{n+1}\right) \left(\frac{K}{\sigma_o}\right)^2 \tag{27}$$

and $\beta = 2$ for plane stress and $\beta = 6$ for plane strain. The length r_y is based on Irwin's idea of a plastically adjusted crack length, but modified to account for strain hardening [*1*]. As an additional simplification, r_y is taken as an explicit function of the elastic stress intensity factor K [*1,2*].

Edmund and Willis [*28*] have shown that the asymptotic correction using

[8]The crack driving force or the tearing modulus involve such partial derivatives.

r_y alone (Eq 27) is rigorously correct for the antiplane shear problem ($\beta = 2$ in this case). The appropriate correction for the plane-strain situation, based on the leading term of their asymptotic analyses, is about a third of Eq 27. The additional crack length adjustment based on the higher order terms will involve details of the overall geometry and loading beyond that supplied by K; but these corrections will slightly increase the adjusted length. The ϕ factor in Eq 26 attempts to reduce the overadjustment under conditions of contained plasticity, while at the same time restrains the plasticity adjustment r_y in the fully plastic regime where the contributions to J, δ, and Δ_L must be dominated by the second term in Eqs 23 through 25. Motivated by the above arguments, and without any further justifications, the authors choose to define ϕ by

$$\phi = \frac{1}{1 + (P/P_o)^2} \tag{28}$$

Comparison of Estimation Scheme with Full Numerical Calculations and Experimental Measurements

In this section, the estimation formulas (Eqs 23 through 25) are compared with the full numerical calculations and the experimental data for several compact specimens reported in [*15,16,29*]. Coefficients of the Ramberg-Osgood law (Eq 15) appropriate to A533B steel at 93°C (199.7°F) were obtained by the least square fit of the uniaxial stress strain data. Values of the coefficients are $\alpha = 1.115$ and $n = 9.7$, and ν, E, and σ_o are taken to be 0.3, 29×10^6 lb/in.^{2} and 60×10^3 lb/in.^{2}, respectively.

The J-integral crack driving force diagrams are computed for a 4T compact specimen in plane strain using Eqs 23 through 25 and the material properties given above. Figure 5 shows the crack driving force for two limiting situations; the solid line indicates the variation of J with crack length with the applied load held fixed, and the dashed line corresponds to displacement held fixed. To determine the load-deformation behavior of a 4T compact specimen with initial crack length of 4.615 in., the experimentally measured J resistance curve denoted by J_R [*16,29*], which is indicated by the heavy solid line, is superimposed on the diagram at an initial crack length of 4.615 in. Equilibrium of crack growth requires that the applied J equals the material resistance J_R. Thus the values of P and Δ_L associated with the respective solid and dashed lines that intersect at a particular point on the J_R curve is the set required to maintain crack growth. By repeating the process at different points along the J_R curve, the complete load-deformation behavior is obtained. Alternatively, the P-Δ_L curve can also be obtained by solving numerically, for example by the Newton's method, the nonlinear set of equations (Eqs 23 and 25) for values of J and a given by the J_R curve.

Figure 6 shows the load-deflection behavior obtained by the foregoing pro-

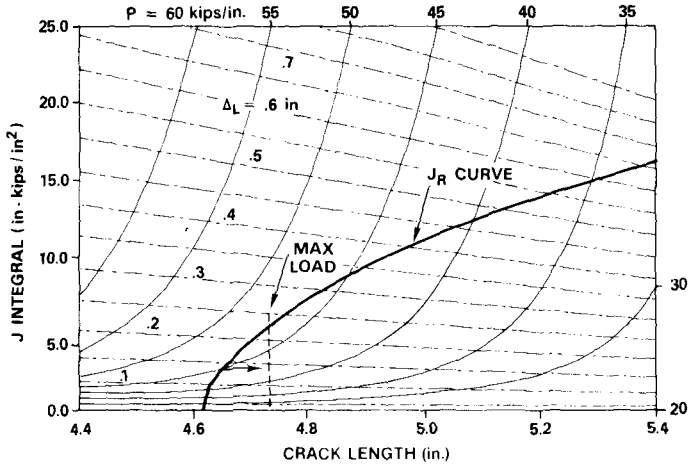

FIG. 5—*J-integral crack driving force diagram for a 4T, T-52 compact specimen in plane strain with 25 percent side groove—A533B steel at 93.3°C (200°F),* E = 29 × 10^3 *ksi,* ν = 0.3, σ_0 = 60.1 *ksi,* α = 1.115, n = 9.708 *(1 ksi* = 6.89 *MPa).*

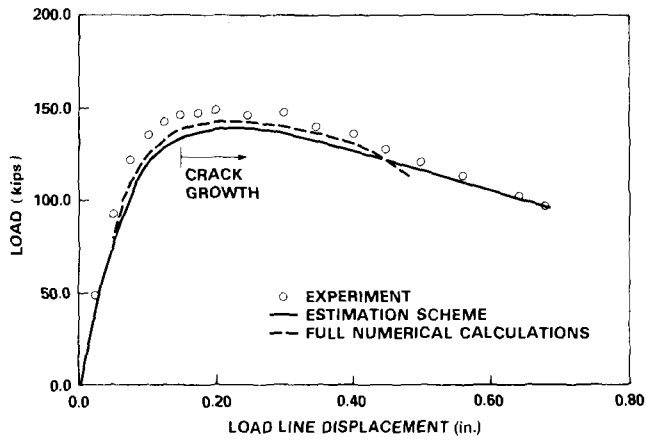

FIG. 6—*Comparison of predicted and experimentally measured load-displacement relationship for 4T, T-52, 25 percent side groove compact specimen in plane strain with* a_0/b = 0.577, b = 8 *in. Results from full numerical calculations based on* J_2 *flow theory of plasticity are shown by the dashed line.*

cedure, the measured load-deflection record for the A533B steel 4 T compact specimen with an initial crack length of 4.615 in., and the finite element crack growth calculations for the configuration based on J_2 flow theory of plasticity. The agreement between all three results is very good, in fact the estimated curve follows completely the trend of the experimental data and the full numerical calculations. Details concerning the experimental data

and the crack growth calculations based on flow theory are given in Refs *15* and *29*.

Following the above procedure, the load-displacement behavior of several compact specimens are determined. Comparisons of the results from the estimation scheme, the full numerical calculations, and the experimental data [*29*] are shown in Figs. 7 through 9 for plane-strain and in Fig. 10 for plane-stress conditions. In all cases, the estimated curves follow the measured data fairly accurately.

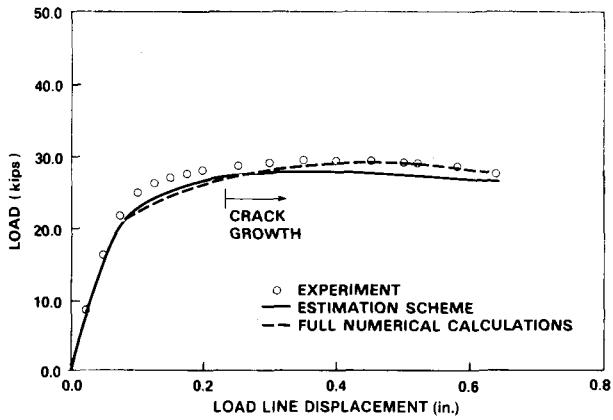

FIG. 7—*Comparison of predicted and experimentally measured load-displacement relationship for 4T, T-61, 25 percent side grooves, plane-strain compact specimen with* $a_0/b = 0.8$, $b = 8$ *in. Results from full numerical calculations based on* J_2 *flow theory of plasticity are also included.*

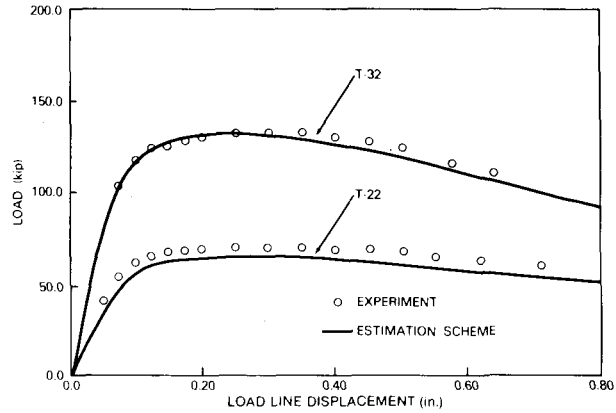

FIG. 8—*Comparison of predicted and experimentally measured load-displacement relationship for two 4T compact specimens in plane strain with 12.5 percent side grooves.* $a_0/b = 0.615$ *for T-32 and* $a_0/b = 0.718$ *for T-22.*

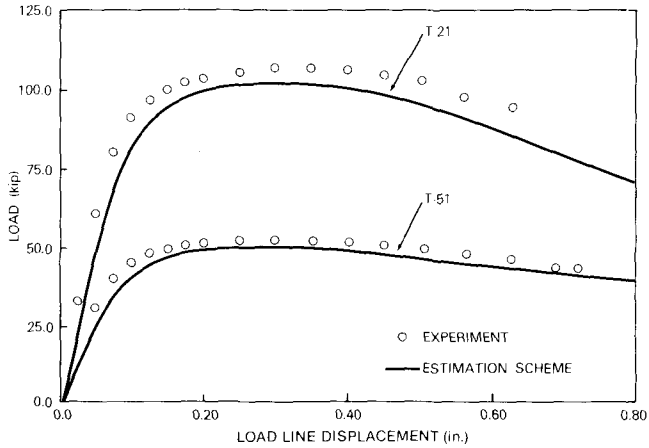

FIG. 9—*Comparison of predicted and experimentally measured load-displacement relationship for two 4T compact specimens in plane strain. T-21 has* $a_0/b = 5.274$ *and 12.5 percent side grooves, and T-51 has* $a_0/b = 0.736$ *and 25 percent side groove.*

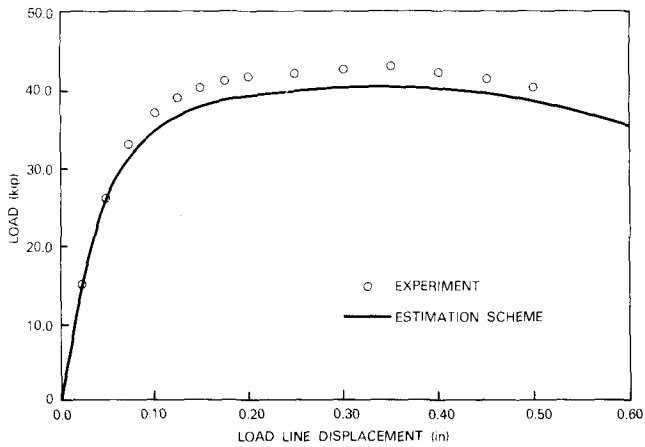

FIG. 10—*Comparison of predicted and experimentally measured load-displacement relationship for compact specimen in plane stress—4T plane, 1 in. thick,* $a_0/b = 0.553$. *Predictions employ plane stress fully plastic results.*

Predicting J_R *Curve from Load-Displacement Record*

There exists considerable experimental data in the form of load-displacement curves for several materials, particularly for irradiated specimens, and it would be of some interest to infer the material J_R curve from this data. Next, it is illustrated how the estimation scheme can be used to obtain the J_R curve from P-Δ_L record.

Using the appropriate deformation properties, the J-integral crack driving forces are computed according to Eqs 23 through 25 for the specific crack configuration under consideration. On the J-integral diagram identify the solid line and the dash line (for example, Fig. 5) corresponding to the respective measured pair of load and load line displacement (that is, the values of P and Δ_L for a point on the P-Δ_L record). The intersection of these two lines give the value of J and crack length a that satisfy the given P and Δ_L for this particular crack configuration. By repeating the process for other measured pairs of load and load line displacement (that is, other points on the P-Δ_L record), the J_R curve may be constructed. Alternatively, given the P-Δ_L data and the initial crack length a_o, the nonlinear equation (Eq 25) can be solved numerically by the Newton's method to obtain a and thus Δa. Knowing P and a, J can be obtained from Eq 23. This procedure would give the material J_R-Δa curve from the given P-Δ_L data.

In Fig. 11, the J_R curve determined from the J-integral diagrams in conjunction with the load-displacement record are compared with actual experimental data from two specimens under plane strain conditions. The

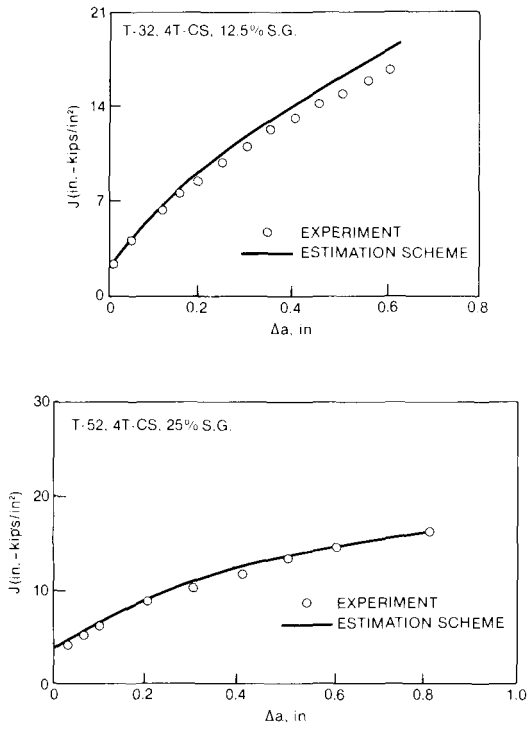

FIG. 11—*Predicted J_R curve using the J-integral crack driving force diagram in conjunction with the measured load-displacement records for compact specimen T-52 and T-32. The experimentally measured J_R curve from T-52 and T-32 are included.*

authors noted good agreement between the predicted and actual curve. The comparison clearly suggests that the J_R curve can be estimated to a fair degree of accuracy using Eqs 23 through 25 and the load-displacement record.

Effect of Variation of J_R *Curve on Structural Deformation Behavior*

The experimentally determined J_R curves are subject to varying amounts of scatter depending on the technique employed for measuring crack extension; for example, heat tinting or unloading compliance. It is certainly affected by the procedure for defining the amount of crack extension in situations where the leading edge of the crack has a thumbnail shape. The sensitivity of load-displacement record or the deformation behavior to variations in the J_R curve is examined here for the plane strain situations. Details of this analysis are given in Ref *22*.

Figure 12 illustrates the situation where J_{Ic} is either 30 percent too high or 30 percent too low. The deformation behavior of the compact specimen determined by the procedure discussed in a previous section, for the respective J_R curves are included. For this specimen configuration and the a/b ratio, it appears that moderate variation in J_{Ic} has little influence on the deformation behavior.

Figure 13 illustrates the situation where the slope of the J_R curve is either 30 percent too high to 30 percent too low. The figure suggests that the slope of the J_R curve has a greater influence on the specimens deformation behavior.

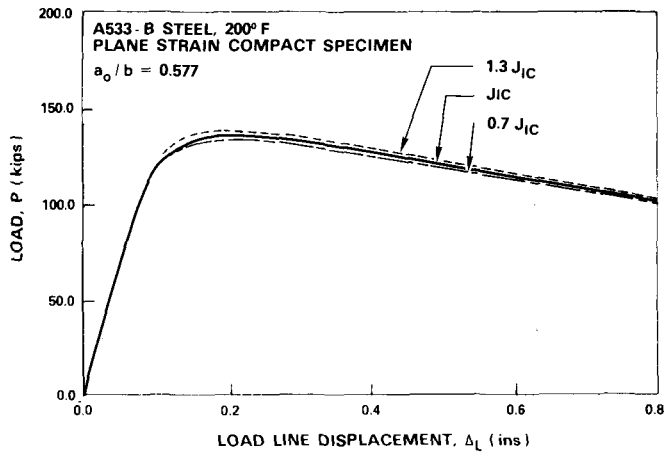

FIG. 12—*Effect of variation in* J_{Ic} *on load-displacement behavior for T-52 compact specimen. For A533B steel, the mean* J_{Ic} *was taken to be 1825 in. lb/in.*^{2} *and* dJ/da *to be 2.50* $\times$ 10^4 *in. lb/in.*^{3}.

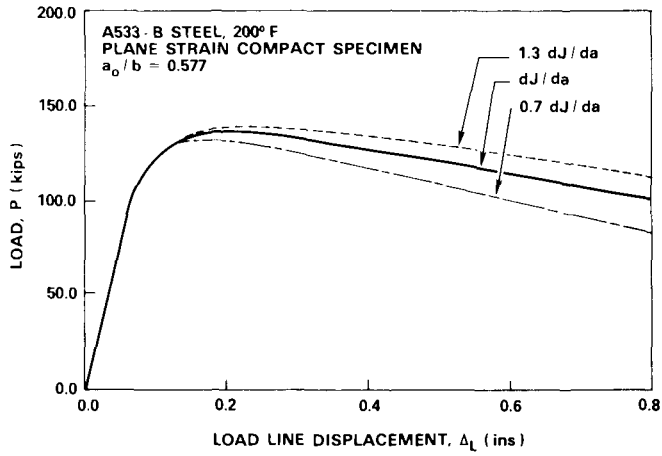

FIG. 13—*Effect of variation in slope of* J_R *curve on load-displacement behavior for compact specimen T-52.*

Finally, the cases where both the J_{Ic} and the slope of the J_R curve are 30 percent too high or 30 percent too low are examined. The effect of these variations on the deformation behavior is shown in Fig. 14.

These analyses suggest that the deformation behavior of a flawed structure is relatively more sensitive to variations in the slope of the material J_R curve than to variations in J_{Ic}. This means that experimental measurements of the slope of the J_R curve should be carried out with relatively greater care and precision. It also appears that in the context of crack growth stability and

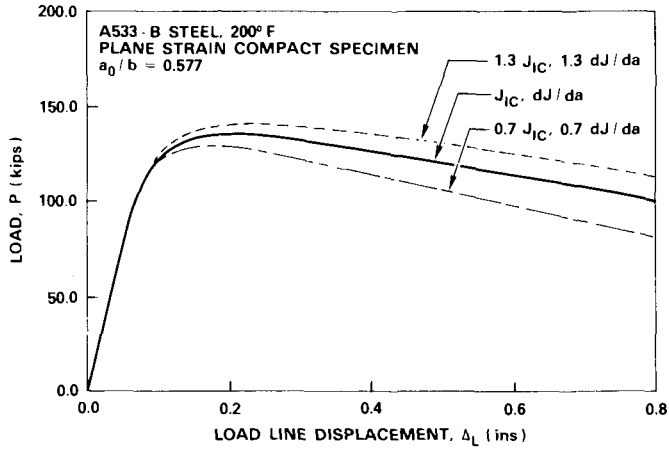

FIG. 14—*Effect of variation in* J_{Ic} *and slope of* J_R *curve on load-displacement behavior for compact specimen T-52.*

overall deformation behavior, the manner of definition of J_{Ic} (that is, whether it be based on onset of crack extension of some fixed or relative amount of crack extension) is not important so long as the J_R curve is correctly measured.

On the whole, the load-deformation behavior is not very sensitive to variations in the J_R curve. This is probably due to two factors; namely, the low strain hardening of the material and the fully plastic condition of the specimen under evaluation. Under contained plasticity conditions, the load deformation behavior of a cracked body will be more strongly dependent on the J_R curve.

Crack Growth Stability Analyses

The resistance curve approach, based on K, for treating crack growth stability under conditions of linear elastic fracture mechanics or small-scale plasticity is fairly well-known and is discussed in detail in an ASTM publication [*30*]. The extension of this approach to deal with fully plastic situations have been described by Paris et al [*17*] and by Hutchinson and Paris [*18*]. The following discussion follows the treatment in Ref *18*.

At any applied load, P, and crack length, a, the condition for continued crack growth is

$$J(a, P) = J_R(\Delta a) \tag{29}$$

where J_R is a function of the amount of crack growth only. Crack growth is unstable if

$$\left(\frac{\partial J}{\partial a}\right)_{\Delta_T} \geq \frac{dJ_R}{da} \tag{30}$$

The subscript in Eq 30 denotes a partial derivative with Δ_T held fixed; Δ_T the total displacement is defined by

$$\Delta_T = \Delta + C_M P \tag{31}$$

where C_M is the compliance of a linear spring placed in series with the cracked body. In this and subsequent sections Δ and Δ_L are used interchangeably.

Paris et al [*17*] introduced the nondimensional quantities

$$T_J = \frac{E}{\sigma_o^2}\left(\frac{\partial J}{\partial a}\right)_{\Delta_T} \quad \text{and} \quad T_{JR} = \frac{E}{\sigma_o^2}\frac{dJ_R}{da} \tag{32}$$

The instability criterion (Eq 30) can be phrased in terms of the tearing modulus

$$T_J \geq T_{JR} \tag{33}$$

The crack driving force can be expressed more conveniently through

$$\left(\frac{\partial J}{\partial a}\right)_{\Delta T} = \left(\frac{\partial J}{\partial a}\right)_P - \left(\frac{\partial J}{\partial P}\right)_a \left(\frac{\partial \Delta}{\partial a}\right)_P \left[C_M + \left(\frac{\partial \Delta}{\partial P}\right)_a\right]^{-1} \tag{34}$$

The stability of crack growth can also be analyzed through the use of the crack opening displacement parameter [*15,31*]. As in the previous situation, equilibrium of crack growth requires

$$\delta(a, P) = \delta_R(\Delta a) \tag{35}$$

and instability develops if

$$\left(\frac{\partial \delta}{\partial a}\right)_{\Delta T} \geq \frac{d\delta_R}{da} \tag{36}$$

The quantity $d\delta_R/da$ is sometimes called the crack opening angle and is a measure of the material resistance to crack growth. The crack driving force and the crack growth resistance can be expressed again in terms of respective dimensionless parameters

$$T_\delta = \frac{E}{\sigma_o}\left(\frac{\partial \delta}{\partial a}\right)_{\Delta T} \quad \text{and} \quad T_{\delta R} = \frac{E}{\sigma_o}\frac{d\delta_R}{da} \tag{37}$$

and condition (Eq 36) can be restated as

$$T_\delta \geq T_{\delta R} \tag{38}$$

Stability Diagrams for Compact Specimen

The estimation scheme (Eqs 23 through 25) was employed with the expression of Eq 34 to compute the crack driving force for the compact specimen. The material deformation behavior is assumed to be governed by Eq 15.

For a typical structural steel, the tearing modulus "applied" T_J is shown in Fig. 15 as a function of J normalized by $c\sigma_o^2/E$ by solid and dashed lines for plane stress and plane strain conditions respectively. The specimen has an a/b ratio of 0.75 and the wide range of $\overline{C}_M(\overline{C}_M = EC_M)$ is intended to span a wide range of system compliance ranging from a typical rigid grip test

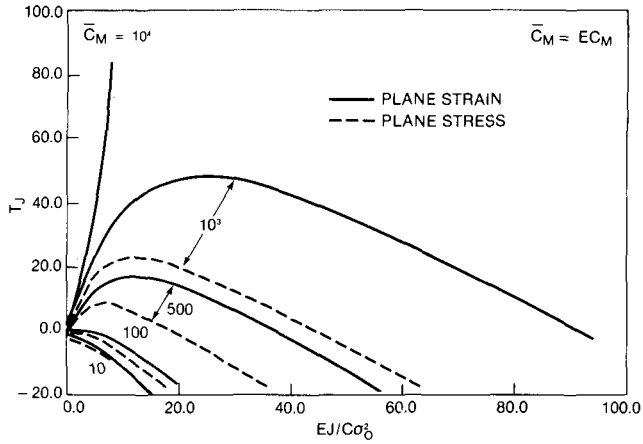

FIG. 15—*Numerical results for* T_J *versus* $EJ/(\sigma_0^2 c)$ *for A533B steel compact specimen with* $a_0/b = 0.75$ *for various values of* $\bar{C}_M$. *Typical test machine compliance* $\bar{C}_M = 10$.

machine and a soft loading machine. For a typical test machine with C_M ranging from 10 to 100, T_J will always be less than five. Now T_{JR} for most structural steels ranges from 20 to 200 [*17,15*]. Thus it is apparent that stable crack extension will almost always be observed in compact specimens tested in a typical rigid or displacement controlled machine. However it can be seen that the driving force T_J increases fairly rapidly with compliance.

A consistent difference was noted between plane-strain and plane-stress driving force. With all quantities being equal (that is, the in-plane dimensions, material deformation properties, etc.), T_J associated with plane-strain condition is larger than that for plane stress condition. This was also noted in Ref *18*.

The variation of T_J with crack length at several constant load levels for a soft testing system ($\bar{C}_M = 1000$) is shown in Fig. 16. The dependence of T_J on applied load, crack length, and system compliance is clearly illustrated.

Discussion

The estimation procedure (Eqs 23 through 25) coupled with a crack initiation criteria, based either on J or crack tip opening displacement δ_t, could be employed to assess the combination of load and crack length that will cause the onset of crack growth in a structure. Such analyses assumes that the so-called Hutchinson-Rice-Rosengren (HRR) singularity [*33,34*] dominates over a microstructurally meaningful distance at the crack tip. The conditions and the minimum size requirements essential to the validity of a one parameter crack initiation criterion based on J or δ_t (J and δ_t are the amplitudes of the

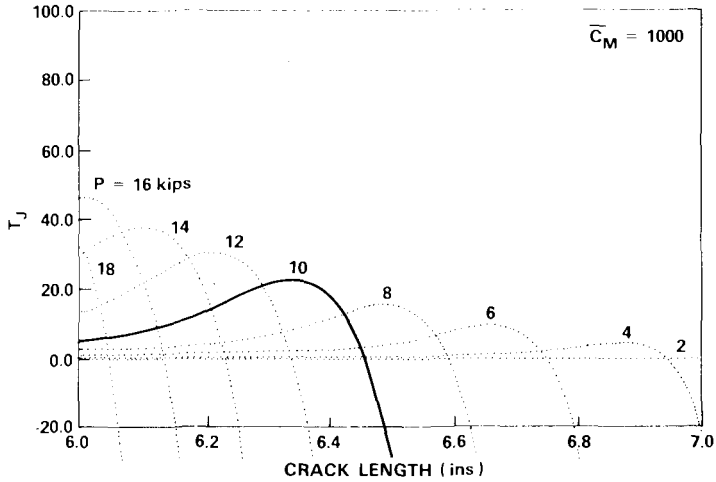

FIG. 16—*Variation of plane strain* T_J *with crack length at several levels of applied load for* $\bar{C}_M$ = *1000—A533B steel, 4T compact specimen.*

HRR singularity) have been discussed by McMeeking and Parks [*34*] and Shih and German [*35*]. In essence, the uncracked ligament must be larger than some multiple of J_{Ic}/σ_o or δ_{Ic}.

Similarly continued crack growth and growth instability can be examined using Eqs 23 through 25 coupled with Eqs 29 and 30. The conditions for J controlled growth have been discussed by Hutchinson and Paris [*18*] and Shih and Dean [*36*]. It appears that the J approach is valid for growth up to 6 percent of the uncracked ligament that has fully yielded.

It is also noted that with a slightly different interpretation of Eq 2, the fully plastic results (Tables 1 and 2) are directly applicable to a stationary crack in a material undergoing steady state power law creep [*4*]. Landes and Begley [*37*] successfully correlated creep crack growth data by the C^* parameter. They employed a rather complex experimental technique to obtain C^*. If the steady-state creep properties are known, then C^* is readily determined from Eq 3 (replace J by C^* in Eq 3). Haigh [*38*] proposed to use $\dot{\delta}_t$ as a creep crack growth parameter. It is noted that the C^* or $\dot{\delta}_t$ approach are equivalent (as J and δ_t are both equivalent in time independent plastic fields [*31*]), and both may be computed using the fully plastic results of Tables 1 and 2. The regimes of applicability of the K parameter and the C^* or $\dot{\delta}_t$ parameters are discussed in a recent paper by Riedel and Rice [*39*].

Summary and Conclusions

In this study a catalog of fully plastic solutions for the compact specimen

was developed, and the estimation procedure to analyze crack growth and instability was employed. The following summarizes the present study:

1. Fully plastic plane strain and plane stress solutions were obtained for the compact specimen over a wide range of crack length to width ratio and hardening exponent. The solutions were appropriately normalized and are tabulated in Tables 1 and 2.

2. The estimation scheme was refined to ensure the continuity of the crack driving forces during the transition from contained plasticity to large-scale yielding. Crack driving force diagrams were generated for the compact specimen. These diagrams together with the material J_R curves were employed to obtain load-displacement behavior of several compact specimens with different crack lengths. In all the cases examined, the load displacement relationships thus determined are in good agreement with the experimentally measured load-displacement record. The estimated loads are generally about 5 percent lower than the measured loads, but the estimated load deflection curve follows the trend of the experimental curve completely.

3. The load-displacement records for specific compact specimens together with the J-integral diagrams for the configurations under consideration, were successfully employed for obtaining the material J_R curve.

4. The tearing modulus, T_J, was computed for the compact specimen and displayed as a function of applied load, crack length, and systems compliance. The diagrams illustrate the role of system compliance and clearly suggest that very soft systems are necessary to induce unstable crack growth in compact specimens.

5. Preliminary investigations show that all things being equal, the crack driving forces assuming plane strain conditions are larger than the corresponding forces assuming plane stress condition. This factor coupled with the general observation that the material resistance to continued crack growth is larger for nonplane-strain conditions than for plane strain conditions suggests that stability analyses based on plane strain assumption will be conservative.

6. The fully plastic results show that the Merkle-Corten formula for J for the compact specimen is accurate as long as $a/b \geq 0.4$ and $n > 2$. The expression by Rice, Paris and Merkle is suited for deep cracks $a/b > 0.75, n > 2$.

Acknowledgment

The authors are grateful to M. D. German for coding the estimation formulas and developing the interactive graphic display of the crack driving force diagrams. This work was sponsored by the Electric Power Research Institute (EPRI), Palo Alto, Calif. The encouragement and support of R. L. Jones and T. U. Marston of EPRI is gratefully acknowledged.

APPENDIX I

Limit Load Analysis of the Compact Specimen

Limit load analyses of the compact specimen are presented here. Both plane-strain and plane-stress conditions are considered. A comparison of the limit load values obtained by using different procedures is also discussed.

First, a perfectly plastic compact specimen (CS) under plane strain is considered. The applied limit load P_o imposes an axial force and a moment on the uncracked ligament. If the effect of axial force is ignored, which would be a reasonable assumption for deep cracks, the Green and Hundy analysis [*27*] of a deeply cracked beam in pure bending can be also applied to the CS. The corresponding slip line field under this assumption is shown in Fig. 17*a*. It is noted that the center of rotation, Q, is at a distance of $(a + 0.369c)$ from the load line and, therefore, the moment about Q due

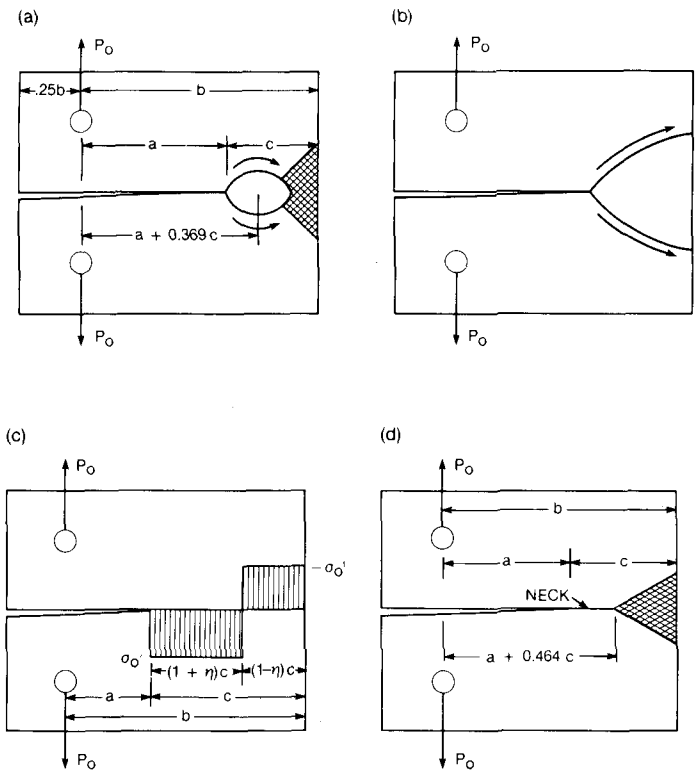

FIG. 17—*Various deformation mechanisms for a deeply cracked compact specimen*—(a) *Green and Hundy slip line field for plane strain,* (b) *slip line field corresponding to the Rice's model for plane strain, and* (c) *lower bound stress distribution at the plastic collapse without considering the stress redistribution due to crack. For plane stress* $\sigma_o' = \sigma_o$ *and* $\sigma_o' = (2/\sqrt{3})\sigma_o$ *for plane strain and* (d) *Ford and Lianis slip line field for plane stress condition.*

to P_0 is $(a + 0.369\,c)P_0$, and this should be equal to the Green and Hundy limit moment of $0.364\,\sigma_0 c^2$ under the collapse conditions. This gives

$$P_0 = \frac{0.364\,\sigma_0 c^2}{a + 0.369\,c} \tag{39}$$

Rice [*26*] obtained an upper bound limit load solution for an edge cracked panel with the uncracked ligament subjected to both an axial force and a moment based on the slip line field as illustrated in Fig. 17*b*. Following Rice's procedure, P_0 can be readily obtained as

$$P_0 = \frac{2}{\sqrt{3}}\,\sigma_0 c\,\left[\frac{0.3 + \sqrt{0.9 + 0.4\,\zeta}}{\zeta}\right] \tag{40}$$

where

$$\zeta = 1 + 1.1025\left[\frac{1 + a/b}{1 - a/b}\right]^2 \tag{41}$$

and the factor of $2/\sqrt{3}$ accounts for plane-strain condition. Bucci et al [*40*] employed this solution in their J-integral estimation procedure.

An alternate analysis was proposed by Merkle and Corten [*25*], which introduces the effect of axial force into the deep crack formulas for the J-integral. Following their procedure, which assumes the stress field as shown in Fig. 17*c*, and multiplying the net section limit load by the Green and Hundy constraint factor of 1.26, yields the following expression for P_0

$$P_0 = 1.26\,\frac{2}{\sqrt{3}}\,\eta c\sigma_0 \tag{42}$$

where

$$\eta = \sqrt{\left(\frac{2a}{c}\right)^2 + 2\left(\frac{2a}{c}\right) + 2} - \left(\frac{2a}{c} + 1\right) \tag{43}$$

The limit load values calculated by the methods discussed above is plotted in the form of $P_0/(2/\sqrt{3})\sigma_0 b$ versus a/b in Fig. 18. The experimental data shown in this figure is taken from Shih et al [*29*]. The experimental P_0 is taken as the maximum load reached in a test, a/b corresponds to the ratio at the maximum load, and σ_0 was taken to be 413.7 MPa (60 ksi), which is the yield stress for A533B steel at 93.3°C (200°F). As a/b increases, the effect of axial force decreases and, therefore, as expected, the three curves approach one another. The experimental data are in good agreement with the calculated values for $a/b > 0.6$, the regime where all three approaches give almost the same values. Experimental data are not available for $a/b < 0.5$, and it is not clear which of the three is the most appropriate curve. The trends suggest that Eq 42 may represent a lower bound solution to the problem. Nevertheless, the three approaches discussed here do provide solutions that are in reasonably good agreement in the range of practical interest. For the calculations

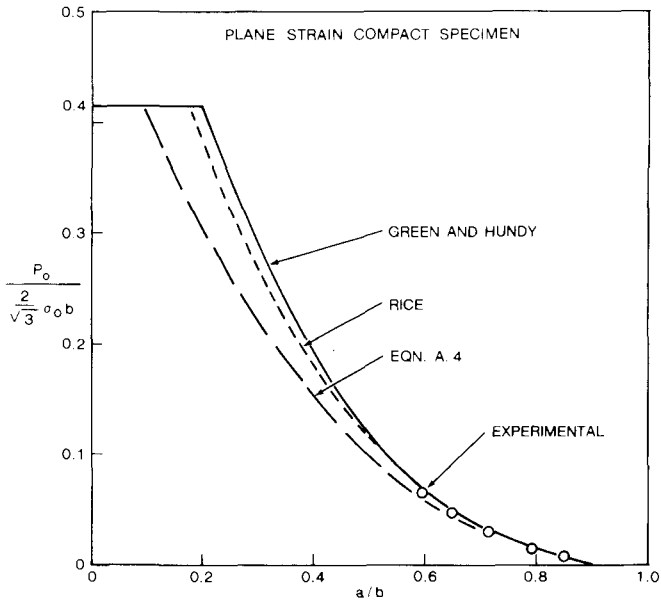

FIG. 18—*Limit load for a compact specimen in plane strain.*

discussed in the section on crack growth stability, the limit load given by Eq 42 was used that gave values of h functions within a range convenient from the viewpoint of interpolation and extrapolation.

A similar analysis is carried out for plane stress. Here one cannot directly employ the solutions due to Green and Hundy and Rice as they are basically derived for plane strain condition. Instead, the analysis by Ford and Lianis [*41*] for the case of the deeply cracked beam under pure bending is employed to obtain the limit load for the deeply cracked compact specimen. Their slip line field [*41*] is depicted in Fig. 17*d*. By equating the applied moment with the limit moment, one obtains

$$P_o = \frac{0.268\,\sigma_o c^2}{(a + 0.464\,c)} \tag{44}$$

To account for the effect of axial force in the plane-stress compact specimen, one follows the procedure used in the plane-strain problem. In other words, the net section limit load, which corresponds to the stress distribution shown in Fig. 17*c*, is multiplied by the Ford and Lianis constraint factor of 1.072, and this gives the following expression for P_o

$$P_o = 1.072\,\eta c \sigma_o \tag{45}$$

where η is still given by Eq 43.

The plot of $P_o/\sigma_o b$ versus a/b obtained from Eqs 44 and 45 is shown in Fig. 19. Equation 45 is employed in the normalization scheme to obtain the h functions for the plane-stress compact specimen.

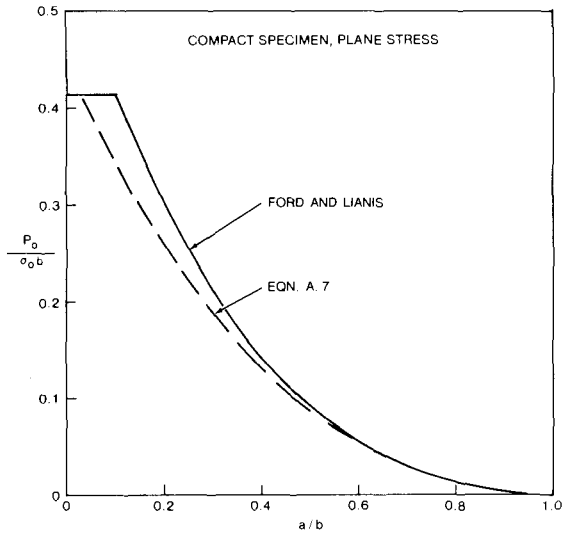

FIG. 19—*Limit load for a compact specimen in plane stress.*

APPENDIX II

Calculations of h Functions for the Limit a/b → 1

First consider the plane strain situation for which the limit load expressions are derived in Appendix 1. As $a/b \to 1$ the applied load approaches the pure bend situation; therefore the various slip line fields will approach the Green and Hundy solution. Moreover, J_{MC}/J and J_{RPM}/J, discussed in the section on the evaluation of fully plastic solutions, will approach unity for $a/b \to 1$. Substituting Eq 39 for P_o in Eq 14, one obtains the following expression for J_{RPM}/J

$$\frac{J_{RPM}}{J} = 0.728 \frac{a}{a + 0.369\,c} \frac{n}{n+1} \frac{h_3}{h_1} \tag{46}$$

As $a/b \to 1$, $c/a \to 0$ and therefore $a/(a + 0.369\,c) \to 1$. Also, $J_{RPM}/J \to 1$ for this limit. Using these in Eq 46, one obtains

$$h_3(a/b \to 1, n) = 1.374 \left(\frac{n+1}{n}\right) h_1(a/b \to 1, n) \tag{47}$$

Since h_1 is approximately linear in a/b for large n, the values of h_1 for $a/b \to 1$ can be obtained rather easily by extrapolating to the limit using the values at $^1/_2$, $^5/_8$, and $^3/_4$. Equation 47 is then used to calculate h_3 for $a/b \to 1$ and for various values of n.

Knowing h_1 and h_3, one next evaluates h_2 using the following procedure. From Eqs 4 and 5 one has

$$\frac{\delta}{\Delta_L} = \frac{h_2}{h_3} \tag{48}$$

which is valid for all a/b and n values. Using the Green and Hundy slip line field, shown in Fig. 17*a*, and assuming that the crack opening profile is linear for deep cracks, it follows that δ/Δ_L is also related by

$$\frac{\delta}{\Delta_L} = \frac{a + 0.369\,c + 0.25\,b}{a + 0.369\,c} \tag{49}$$

In Eq 49 the term $0.25\,b$ comes from the distance between the points at which δ and Δ_L are measured according to the ASTM specimen as illustrated in Fig. 1. For $a/b \to 1$, Eq 49 reduces to

$$\frac{\delta}{\Delta_L} = 1.25 \tag{50}$$

Equating Eqs 48 and 50 gives the following expression for h_2 in terms of h_3

$$h_2(a/b \to 1, n) = 1.25\,h_3(a/b \to 1, n) \tag{51}$$

Similar results for the plane stress case are obtained by using the Ford and Lianis expression (Eq 44) in place of the Green and Hundy solution. Carrying out the details, one readily obtains

$$h_3(a/b \to 1, n) = 1.866 \left(\frac{n+1}{n}\right) h_1(a/b \to 1, n) \tag{52}$$

$$h_2(a/b \to 1, n) = 1.25\,h_3(a/b \to 1, n) \tag{53}$$

The plane stress values of h_1 for $a/b \to 1$ are also obtained by extrapolating from the values for $a/b = 1/2$, $5/8$, and $3/4$.

References

[1] Shih, C. F. in *Mechanics of Crack Growth, ASTM STP 590,* American Society for Testing and Materials, 1976, pp. 3-22.

[2] Shih, C. F. and Hutchinson, J. W., *Transactions* of the American Society of Mechanical Engineers, *Journal of Engineering Materials and Technology,* Series H. Vol. 98, No. 4, Oct. 1976, pp. 289-295.

[3] Tada, H., Paris, P. C., and Irwin, G. R., *The Stress Analysis of Cracks Handbook,* Del Research Corp., Hellertown, Pa., 1973.

[4] Goldman, N. L. and Hutchinson, J. W., *International Journal of Solids and Structures,* Vol. 11, 1975, pp. 575-591.

[5] Hutchinson, J. W., Needleman, A., and Shih, C. F. in *Fracture Mechanics,* N. Perrone et al, Eds., University Press of Virginia, Charlottesville, Va., 1978, pp. 515-527.

[6] Needleman, A. and Shih, C. F., *Computer Methods in Applied Mechanics and Engineering,* Vol. 15, 1978, pp. 223-240.

[7] Ranaweera, M. P. and Leckie, F. A. in *Proceedings,* First International Conference on Numerical Methods in Fracture Mechanics, A. R. Luxmore and D. R. J. Owens, Eds., Swansea, U. K., 1978, pp. 450-463.
[8] Parks, D. M. in *Proceedings,* First International Conference on Numerical Methods in Fracture Mechanics, A. R. Luxmore and D. R. J. Owens, Eds., Swansea, U. K., 1978, pp. 464-478.
[9] Begley, J. A. and Landes, J. D. in *Fracture Toughness, ASTM STP 514,* American Society for Testing and Materials, 1972, pp. 1-23, 24-39.
[10] Begley, J. A. and Landes, J. D., *International Journal of Fracture,* Vol. 12, 1976, pp. 764-766.
[11] Green, G. and Knott, J. F., *Journal of the Mechanics and Physics of Solids,* Vol. 23, 1975, pp. 167-183.
[12] Clarke, G. A., Andrews, W. R., Paris, P. C., and Schmidt, D. W. in *Mechanics of Crack Growth, ASTM STP 590,* American Society for Testing and Materials, 1976, pp. 27-42.
[13] Griffis, C. A. and Yoder, G. R., *Transactions* of the American Society of Mechanical Engineers, *Journal of Engineering Materials and Technology,* Vol. 98, 1976, pp. 152-158.
[14] Clark, G., El Soudani, S. M., Ferguson, W. G., Smith, R. F., and Knott, J. F. in *Tolerance of Flaws in Pressurized Components,* International Mechanical Engineers' Conference Publication, Vol. 10, 1978, pp. 105-116.
[15] Shih, C. F., deLorenzi, H. G., and Andrews, W. R. in *Elastic-Plastic Fracture, ASTM STP 668,* American Society for Testing and Materials, 1979, pp. 65-120.
[16] Andrews, W. R. and Shih, C. F. in *Elastic-Plastic Fracture, ASTM STP 668,* American Society for Testing and Materials, 1979, pp. 426-450.
[17] Paris, P. C., Tada, H., Zahoor, A., and Ernst, H. in *Elastic-Plastic Fracture, ASTM STP 668,* American Society for Testing and Materials, 1979, pp. 5-36.
[18] Hutchinson, J. W. and Paris, P. C. in *Elastic-Plastic Fracture, ASTM STP 668,* American Society for Testing and Materials, 1979, pp. 37-64.
[19] Zahoor, A. and Paris, P. C., "General Instability Analysis of a Center Cracked Strip of an Elastic-Plastic Strain Hardening Material," presented at the Eighth U. S. National Congress of Applied Mechanics, 1978, to be published.
[20] Rice, J. R., Paris, P. C., and Merkle, J. G. in *Progress in Flaw Growth and Fracture Toughness Testing, ASTM STP 536,* American Society for Testing and Materials, 1973, pp. 231-245.
[21] Ilyushin, A. A., *Prikadnaia Matematika i Mekhanika,* P. M. M., Vol. 10, 1946, p. 347.
[22] Shih, C. F. and Kumar, V., "Estimation Technique for the Prediction of Elastic-Plastic Fracture of Structural Components of Nuclear Systems," First Semiannual Report, SRD-79-101, General Electric Co., Schenectady, N.Y., June 1979.
[23] Newman, J. C., Jr., in *Fracture Analysis, ASTM STP 560,* American Society for Testing and Materials, 1974, pp. 105-121.
[24] Rice, J. R., *Journal of Applied Mechanics,* Vol. 35, 1968, pp. 379-386.
[25] Merkle, J. G. and Corten, H. T., *Journal of Pressure Vessel and Technology, Transactions* of the American Society of Mechanical Engineers, Vol. 96, 1974, pp. 286-292.
[26] Rice, J. R. in *The Surface Crack: Physical Problems and Computational Solutions,* J. L. Swedlow, Ed., American Society of Mechanical Engineers, New York, 1972, pp. 171-186.
[27] Green, A. P. and Hundy, B. B., *Journal of the Mechanics and Physics of Solids,* Vol. 4, 1956, pp. 128-144.
[28] Edmunds, T. M. and Willis, J. R., *Journal of the Mechanics and Physics of Solids,* Vol. 24, 1976, pp. 205, 225, Vol. 25, 1977, p. 424.
[29] Shih, C. F. et al, "Methodology for Plastic Fracture," First through Eighth Quarterly Reports to Electric Power Research Institute, Inc., Contract No. RP601-2, Corporate Research and Development, General Electric Co., Schenectady, N.Y., Sept. 1976—Jan. 1979; also Electric Power Research Institute's Ductile Fracture Review Document, T. U. Marston, Ed., EPRI NP-701-SR, Feb. 1978.
[30] *Fracture Toughness Evaluation by R-Curve Methods, ASTM STP 527,* American Society for Testing and Materials, 1973, pp. 1-118.
[31] Shih, C. F., "Relationships Between the J-Integral and the Crack Opening Displacement for Stationary and Extending Cracks," TIS Report No. 79CRD075, General Electric Co., April 1979, submitted for publication.

[32] Hutchinson, J. W., *Journal of the Mechanics and Physics of Solids,* Vol. 16, 1968, pp. 13-31; pp. 337-47.
[33] Rice, J. R. and Rosengren, G. F., *Journal of the Mechanics and Physics of Solids,* Vol. 16, 1968, pp. 1-12.
[34] McMeeking, R. M. and Parks, D. M. in *Elastic-Plastic Fracture, ASTM STP 668,* American Society for Testing and Materials, 1979, pp. 175-194.
[35] Shih, C. F. and German, M. D., "Requirements for a One Parameter Characterization of Crack Tip Fields by the HRR Singularity," TIS Report No. 79CRD076, General Electric Co., 1979; also *International Journal of Fracture,* to be published.
[36] Shih, C. F. and Dean, R. H., "On J-Controlled Crack Growth: Evidence, Requirements and Applications," TIS Report, General Electric Co., 1979, to be published.
[37] Landes, J. D. and Begley, J. A. in *Mechanics of Crack Growth, ASTM STP 590,* American Society for Testing and Materials, 1976, pp. 128-148.
[38] Haigh, J. R., *Materials Science and Engineering,* Vol. 20, 1975, pp. 213-224.
[39] Riedel, H. and Rice, J. R., "Tensile Cracks on Creeping Solids," Brown University Report E(11-1) 3084/64, Feb. 1979; also presented at the ASTM Twelfth National Symposium on Fracture Mechanics, St. Louis, Mo., May 1979.
[40] Bucci, R. J., Paris, P. C., Landes, J. D., and Rice, J. R. in *Fracture Toughness, ASTM STP 514,* American Society for Testing and Materials, 1972, pp. 40-69.
[41] Ford, H. and Lianis, G., *Zeitschrift für Angewandte Mathematik und Physik,* 1957, Vol. 8, pp. 360-382.

Genki Yagawa,[1] *Tatsuhiko Aizawa,*[1] *and Yoshio Ando*[1]

Crack Analysis of Power Hardening Materials Using a Penalty Function and Superposition Method

REFERENCE: Yagawa, Genki, Aizawa, Tatsuhiko, and Ando, Yoshio, **"Crack Analysis of Power Hardening Materials Using a Penalty Function and Superposition Method,"** *Fracture Mechanics: Twelfth Conference, ASTM STP 700,* American Society for Testing and Materials, 1980, pp. 439-452.

ABSTRACT: Crack analysis is performed for plates characterized by the power hardening material law. A new superposition method of the analytical and the finite element models is proposed with the use of the penalty function, which is frequently adopted to solve the optimization problems. The characteristic distributions of the stress and strain around the crack tip are calculated and compared with the analytical results. Numerical discussion is also made regarding the effects of the crack length to plate width ratio and the power exponent in the hardening law on the nondimensional values of the J-integral, the crack opening displacement, and the residual load point displacement.

KEY WORDS: crack analysis, power hardening material, penalty function, superposition method, finite element method, J-integral, crack opening displacement, residual load point displacement, fractures (materials), crack propagation

Various numerical formulations based on the finite element methods have been developed in order to calculate the stress intensity factor, K, in the linear fracture mechanics [*1-3*].[2] Among these techniques, Yamamoto et al [*4,5*] and Yagawa et al [*6-9*] have proposed the independent superposition methods of the analytical and the finite element methods in a variety of linear fracture mechanics problems. As is well known, however, the fracture and the fatigue behaviors of most engineering materials under loadings clearly depend on the elastic-plastic stress and deformation states in the vicinity of the crack tip. In connection with this problem, the dominant singularity has been obtained by Hutchinson [*10,11*] and Rice and Rosengren [*12*] for a power law hardening material in which the plastic strain is proportional to the stress raised to a power n. This singularity in the form of the asymptotic

[1]Associated professor, graduate student, and professor, respectively, Department of Nuclear Engineering, University of Tokyo, Hongo, Bunkyo-ku, Tokyo, Japan.

[2]The italic numbers in brackets refer to the list of references appended to this paper.

solution shows that the stress components at the crack tip have the form, $r^{-1/(n+1)}$ (r = distance from the crack tip), for the plane-stress as well as the plane-strain conditions. Incorporating the singularity in the crack-tip element, the singular element methods have been reported by several researchers [*13–16*] to study the effectiveness of the numerical fracture mechanics in this case.

With the use of the penalty function method, one of the powerful procedures in the optimization problems under nonlinear constraints, the present authors propose in this paper a new superposition method, which allows us to analyze rather straightforwardly both linear and nonlinear crack problems with any complex boundary conditions. With the Fourier expansion, which is adopted as the analytical term with the singularity, the characteristic distributions of the stress and strain around the crack tip are calculated and compared with the Hutchinson's results obtained by eigen-value analysis [*10,11*]. Further discussion is made on the effects of the crack length to plate width ratio and the power n on the nondimensional values of the J-integral, the crack opening displacement, and the residual load point displacement.

Basic Formulation—Linear Elastic Case

In order to avoid the complexity in deriving the basic solution technique, the formulation is limited to the linear elastic case in this section.

The usual form of the potential energy, π, for the finite element displacement model becomes the quadratic one as follows [*17*]

$$\pi = \frac{1}{2} \lfloor d \rfloor [K]\{d\} - \lfloor d \rfloor \{f\} \tag{1}$$

where

$\{d\}$ = the nodal displacement vector,
$[K]$ = the stiffness matrix, and
$\{f\}$ = the nodal force vector.

As is well known, the minimization of π with respect to $\{d\}$ yields the simultaneous equations that are solved for $\{d\}$. Considered here is the case where the equality constraint is additionally provided as follows

$$[A]\{d\} = \{b\} \tag{2}$$

where $[A]$ and $\{b\}$ are, respesctively, a proper matrix and a vector. According to the external method of the optimization problem, the minimization problem of Eq 1 under the constraint of Eq 2 can be transformed into the unconstrained minimization problem of the following functional

$$\pi^* = \frac{1}{2} \lfloor d \rfloor [K]\{d\} - \lfloor d \rfloor \{f\} + \frac{1}{2} (\lfloor d \rfloor [A]^t - \lfloor b \rfloor)[\tilde{K}]([A]\{d\} - \{b\}) \quad (3)$$

where t denotes the transpose of matrix, and $[\tilde{K}]$ is the penalty coefficient matrix with the diagonal elements being α, which is called the penalty coefficient, and the other elements null. The penalty coefficient α has the property that as α tends to infinity, the minimization problem of π^* is equivalent to that of π with the constraint of Eq 2 under the appropriate condition, that is, the Kuhn-Tucker's condition [*18*].

Next, the superposition technique is explained with the aid of Eq 3 and its application to the two-dimensional crack analysis (Fig. 1). As the figure depicts, the finite element displacement, $\{d^F\}$, and the analytical one, $\{d^A\}$, including singular function are superposed in the near crack tip region $V^{(1)}$, and the usual finite element model is used in the surrounding region $V^{(0)}$. The virtual boundary between these two regions are designated as $S^{(01)}$, where the appropriate continuity conditions must be satisfied. The traction forces $\bar{T}_i^{(0)}$ and $\bar{T}_i^{(1)}$ are prescribed on the boundaries $S_\sigma^{(0)}$ of $V^{(0)}$ and $S_\sigma^{(1)}$ of $V^{(1)}$, respectively, and the boundary displacements $\bar{u}_i^{(0)}$ and $\bar{u}_i^{(1)}$ on $S_u^{(0)}$ of $V^{(0)}$ and $S_u^{(1)}$ of $V^{(1)}$, respectively.

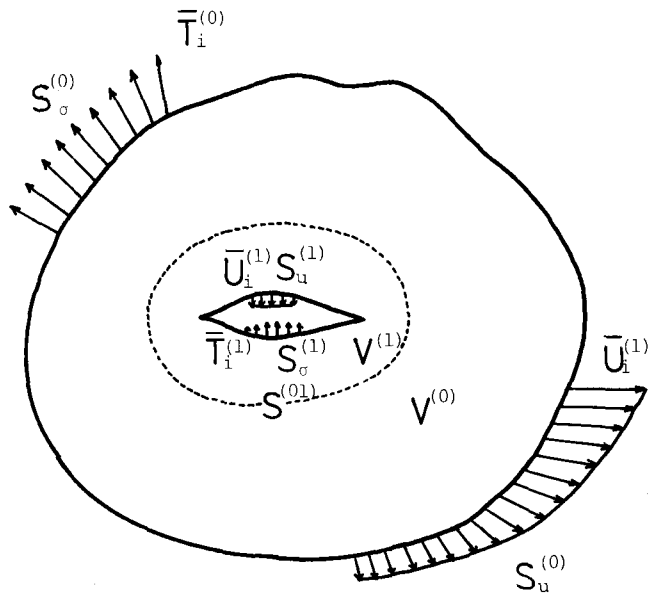

FIG. 1—*Continuum with crack that is fictitiously divided into the regular region* $V^{(0)}$ *and the singular region* $V^{(1)}$.

As is already shown by Yagawa et al [6], Eq 1 in this case can be written as follows

$$\pi = \frac{1}{2} \lfloor d^F d^A \rfloor \begin{bmatrix} K^{FF} & K^{AF} \\ K^{FA} & K^{AA} \end{bmatrix} \begin{Bmatrix} d^F \\ d^A \end{Bmatrix} - \lfloor d^F d^A \rfloor \begin{Bmatrix} f^F \\ f^A \end{Bmatrix} \tag{4}$$

where

$$[K^{FF}] = \int_{V^{(0)}+V^{(1)}} [B]^t[D][B]\, dV \tag{5a}$$

$$[K^{AA}] = \int_{V^{(1)}} [Q]^t[D][Q]\, dV \tag{5b}$$

$$[K^{AF}] = [K^{FA}]^t = \int_{V^{(1)}} [B]^t[D][Q]\, dV \tag{5c}$$

Here $[B]$ and $[Q]$ are defined as

$$\{\epsilon^F\} = [B]\{d^F\} \tag{6a}$$

$$\{\epsilon^A\} = [Q]\{d^A\} \tag{6b}$$

where $\{\epsilon^F\}$ and $\{\epsilon^A\}$ denote the strains pertinent to the finite element and the analytical displacements, respectively. The matrix $[D]$ in Eqs 5*a* to 5*c* is the usual stress-strain matrix. The vectors $\{f^F\}$ and $\{f^A\}$ are the forces relating, respectively, to $\{d^F\}$ and $\{d^A\}$. The subsidiary conditions in this case are the geometrical boundary conditions on $S_u{}^{(0)}$ and $S_u{}^{(1)}$, and the continuity condition on $S^{(01)}$, which can be written formally as follows

$$[A] \begin{Bmatrix} d^F \\ d^A \end{Bmatrix} = 0 \tag{7}$$

where $[A]$ is a proper matrix.

The present constrained problem can be transformed into the unconstrained one as Eq 3. Incorporating Eq 7 in Eq 4, one has the functional to be minimized as follows

$$\pi^* = \frac{1}{2} \lfloor d^F, d^A \rfloor \begin{bmatrix} K^{FF} & K^{AF} \\ K^{FA} & K^{AA} \end{bmatrix} \begin{Bmatrix} d^F \\ d^A \end{Bmatrix} - \lfloor d^F, d^A \rfloor \begin{Bmatrix} f^F \\ f^A \end{Bmatrix}$$

$$+ \frac{\alpha}{2} \lfloor d^F, d^A \rfloor [A]^t [A] \begin{Bmatrix} d^F \\ d^A \end{Bmatrix} \tag{8}$$

The formulation mentioned above is extended to the nonlinear crack problems in what follows.

Nonlinear Crack Problems

Though the stress singularity of the crack in linear elasticity is given by $1/\sqrt{r}$, it is usually difficult to determine the singularity with consideration of the nonlinear behavior of materials. Hutchinson [*10,11*] and Rice and Rosengren [*12*] have obtained the singularity in full plasticity, where the constitutive equation is given as follows

$$\bar{\epsilon} = \kappa \bar{\sigma}^n \tag{9}$$

where

$\bar{\epsilon}$ = the equivalent strain,
$\bar{\sigma}$ = the equivalent stress,
n = the strain hardening exponent, and
κ = the proportional coefficient.

Employing the J_2 deformation theory, the multiaxial stress-strain law becomes as

$$\{\epsilon\} = \frac{3}{2} \kappa \bar{\sigma}^{n-1} \{\sigma'\} \tag{10}$$

where $\{\sigma'\}$ is the stress deviation.

According to eigen-value analysis by Hutchinson [*10,11*], the singularity of stress is represented in the form $r^{-1/(n+1)}$, and the distributions of the displacement, strain and stress near the crack tip are given, respectively, as follows

$$\{u\} = \kappa K_\sigma{}^n r^{1/(n+1)} \{\tilde{u}(\theta)\} = \kappa K_\epsilon r^{1/(n+1)} \{\tilde{u}(\theta)\} \tag{11}$$

$$\{\epsilon\} = \kappa K_\sigma{}^n r^{-n/(n+1)} \{\tilde{\epsilon}(\theta)\} = \kappa K_\epsilon r^{-n/(n+1)} \{\tilde{\epsilon}(\theta)\} \tag{12}$$

$$\{\sigma\} = \kappa K_\sigma r^{-1/(n+1)} \{\tilde{\sigma}(\theta)\} \tag{13}$$

where K_σ is the plastic stress intensity factor, K_ϵ is the plastic strain intensity factor, and $\{\tilde{u}(\theta)\}$, $\{\tilde{\epsilon}(\theta)\}$, and $\{\tilde{\sigma}(\theta)\}$ are the characteristic functions of θ with (r, θ) being the polar coordinates around the crack tip. Rice and Rosengren [*12*] have obtained this singularity based on the fact that the strain energy density of cracked continuum has $1/r$ singularity and that the J-integral value must be finite even at the crack tip. Yagawa and Miyazaki [*19*] have calculated the characteristic function by combination of the superposition method and the Lagrange multiplier's method. According to their result of Mode I crack analysis of a square plate, the characteristic functions obtained by Yagawa and Miyazaki [*19*] and Hutchinson [*10, 11*] agree qualitatively well. Special element methods have also been applied to the similar problems by several investigators [*13–16*].

In this paper, the authors first take up the Mode I crack analysis of the rectangular plate with a center-notched crack as shown in Fig. 2. Here, it is assumed that $V = V^{(1)}$ in Eqs 5*a* through 5*c* and the analytical displacement (u^A, v^A) is superposed on the finite element displacement over the whole region. As the former, the expansions used are as follows

$$u^A = r^{1/(n+1)} \sum_{m=1}^{N_1} a_m \cos \frac{m}{2}\theta \tag{14}$$

$$v^A = r^{1/(n+1)} \sum_{m=1}^{N_2} b_m \sin \frac{m}{2}\theta \tag{15}$$

where a_m and b_m are unknown coefficients to be determined, and N_1 and N_2

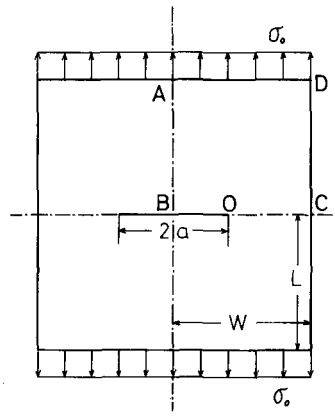

FIG. 2—*Rectangular plate with a center crack.*

are numbers of Fourier terms adopted in the calculations. From the symmetrical geometry and the boundary conditions of the structure, only a quarter of the plate *ABOCD* in Fig. 2 is analyzed under the following boundary conditions

$$u = u^F + u^A = 0, \qquad \tau_{xy} = 0 \text{ on } AB \tag{16}$$

$$\sigma_y = 0, \qquad \tau_{xy} = 0 \text{ on } BO \tag{17}$$

$$v = v^F + v^A = 0, \qquad \tau_{xy} = 0 \text{ on } OC \tag{18}$$

$$\sigma_x = 0, \qquad \tau_{xy} = 0 \text{ on } CD \tag{19}$$

$$\sigma_y = \sigma_0, \qquad \tau_{xy} = 0 \text{ on } DA \tag{20}$$

The functional in this case corresponding to Eq 8 in the linear case can be written as follows

$$\pi^* = \frac{n}{n+1}\int_V \bar{\sigma}\,\bar{\epsilon}\,dV - \int_{S(AD)} \lfloor u \rfloor \{\mathrm{f}\}\,dS + \frac{\alpha_1}{2}\int_{S(AB)} (u^{\mathrm{F}} + u^{\mathrm{A}})^2\,dS$$

$$+ \frac{\alpha_2}{2}\int_{S(BO)} \sigma_{\mathrm{y}}{}^2\,dS + \frac{\alpha_3}{2}\int_{S(BO)} \tau_{xy}{}^2\,dS \tag{21}$$

where α_1, α_2, and α_3 are penalty coefficients, and $\int_{S(AB)} dS$ and $\int_{S(BO)} dS$ denote, respectively, the line integrals on *AB* and *BO* in Fig. 2. Equations 16*a*, 17*a*, and 17*b* are taken into account in Eq 21 as the penalty terms. Especially, the stress free requirement on *BO*, which is considered important to obtain accurate results, is enforced by the last two terms of the right hand side of Eq 21, although this is the natural boundary condition without these two terms. Equation 18*a* is satisfied by adopting Eqs 14 and 15 as the analytical displacement and constraining v^F to be zero on *OC*. The other boundary conditions, Eqs 16*b*, 18*b*, 19*a* and *b*, and 20*a* and *b* are usual natural boundary conditions in Eq 21.

The combination of Eq 21 with the nonlinear constitutive law, Eq 10 yields the authors' functional, from which one obtains the nonlinear simultaneous equations with respect to the nodal displacement vector $\lfloor d \rfloor = \lfloor d^F\, d^A \rfloor$. In order to solve the nonlinear equations, the Newton-Raphson method was employed. As for the convergence of the solution in the case of $n = 3$, six iterations are found enough to have the difference of the potential energies

between two succeeding iteration steps to be less than 1 percent of the total potential energy. Also, the central processing unit's time per an iteration in this case is about 16 s with the HITAC 8700/8800 system employed in the University of Tokyo.

Based on the test in linear analysis of cracked plate [*20*], the authors set α_1, α_2, and α_3 in Eq 21 to be 10^5 with the word length of 64 bits.

Singular Characteristic Functions in Nonlinear Crack Problems

Figures 3 and 4 show, respectively, the calculated distributions of $\tilde{\sigma}_{ij}{}^A$ and $\tilde{\epsilon}_{ij}{}^A$ for the plate of L/W = 2.0, $\lambda = a/W = 0.25$ and $n = 3$. In this case, $N(= N_1 + N_2)$ is set to be 20 and a quarter of the plate is idealized as is depicted in Fig. 5. The strain distributions in Fig. 4 are obtained from the following relations

$$\tilde{\epsilon}_r{}^A = (\tilde{\sigma}^A)^{n-1}\left(\tilde{\sigma}_r{}^A - \frac{1}{2}\tilde{\sigma}_\theta{}^A\right) \tag{22a}$$

$$\tilde{\epsilon}_\theta{}^A = (\tilde{\sigma}^A)^{n-1}\left(\tilde{\sigma}_\theta{}^A - \frac{1}{2}\tilde{\sigma}_r{}^A\right) \tag{22b}$$

$$\tilde{\gamma}_{r\theta}{}^A = \frac{3}{2}(\tilde{\sigma}^A)^{n-1}\tilde{\tau}_{r\theta}{}^A \tag{22c}$$

Comparing the present results with the solutions by Hutchinson [*10, 11*] as given in Figs. 6 and 7, it can be seen that the strain distributions are nearly the same with each other except $\tilde{\epsilon}_\theta{}^A$ at small value of θ. As for the stress distributions, both results agree well at least qualitatively.

The relation between n and the characteristic function at the crack tip is

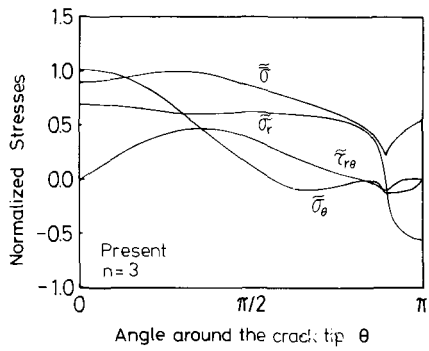

FIG. 3—*Normalized stress distributions around the crack tip.*

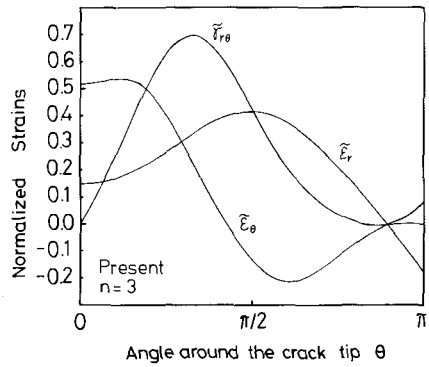

FIG. 4—*Normalized strain distributions around the crack tip.*

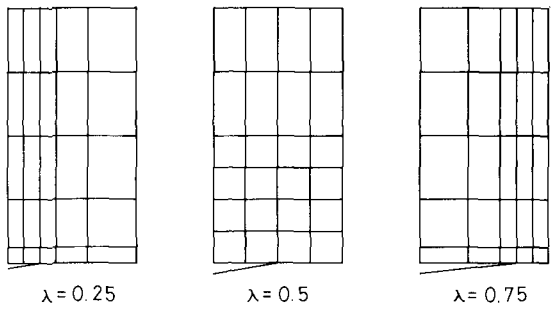

FIG. 5—*Examples of the finite element mesh for a quarter of the plate.*

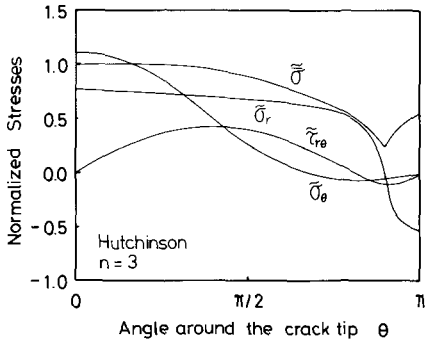

FIG. 6—*Normalized stress distributions around the crack tip.*

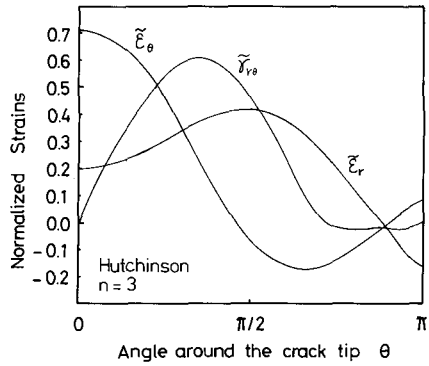

FIG. 7—*Normalized strain distributions around the crack tip.*

studied in what follows. Substituting Eqs 11 through 13 into the definition of the J-contour-integral which is given as [*21*]

$$J = \int_{-\pi}^{\pi} r \left[\frac{n}{n+1} \kappa \tilde{\sigma}^{A^{n+1}} \cos\theta - (\sigma_x{}^A \cos\theta + \tau_{xy}{}^A \sin\theta) \frac{\partial u^A}{\partial x} \right.$$

$$\left. - (\tau_{xy}{}^A \cos\theta + \sigma_y{}^A \sin\theta) \frac{\partial v^A}{\partial x} \right] d\theta \tag{23}$$

one obtains the relation as follows

$$J = \kappa K_\sigma{}^{n+1} I_n \tag{24}$$

where

$$I_n = \int_{-\pi}^{\pi} \left\{ \frac{n}{n+1} \tilde{\sigma}_e{}^{n+1} \cos\theta - \left[\sin\theta \left(\tilde{\sigma}_r \left(\tilde{u}_\theta - \frac{\partial \tilde{u}_r}{\partial \theta} \right) \right. \right. \right.$$

$$\left. \left. \left. - \tilde{\tau}_{r\theta} \left(\tilde{u}_r + \frac{\partial \tilde{u}_\theta}{\partial \theta} \right) \right) + \frac{1}{n+1} (\tilde{\sigma}_r \tilde{u}_r + \tilde{\tau}_{r\theta} \tilde{u}_\theta) \cos\theta \right] \right\} d\theta \tag{25}$$

Table 1 shows the comparison of I_n for several values of n between the present solution and Hutchinson's one [*11*]. It can be seen from the table that both results are in good agreement for the whole range of n compared.

Evaluation of Nonlinear Fracture Parameters

In the continuum with the crack that has the $r^{-1/(n+1)}$ type singularity, the J-contour-integral is defined as the invariant path integral around the crack tip and is determined, uniquely corresponding to the singularity, as a function of the crack geometry, the geometry of specimen as well as the loading condition.

According to Shih and Hutchinson's definition [*16*], the authors represent the nondimensional parameters of the J-integral, the crack opening displacement δ, and the residual load point displacement Δ, respectively, in the following form

$$J = a\kappa (1 - \lambda) g_1 (\lambda, n) \sigma_{net}{}^{n+1} \tag{26}$$

$$\delta = a\kappa g_2 (\lambda, n) \sigma_{net}{}^{n} \tag{27}$$

$$\Delta = a\kappa g_3 (\lambda, n) \sigma_{net}{}^{n} \tag{28}$$

where σ_{net} is the net section stress, g_1, g_2, and g_3 are the nondimensional representations of J, δ, and Δ, respectively, which are only dependent on λ and n, and Δ is defined as

$$\Delta = \Delta_{crack} - \Delta_{no\ crack} \tag{29}$$

Here, Δ_{crack} is the load point displacement of cracked plate and $\Delta_{no\ crack}$ is that of uncracked plate. Δ_{crack} and $\Delta_{no\ crack}$ can be, respectively, written as follows

$$\Delta_{crack} = \frac{1}{2W} \int_{-W}^{W} [v(x,L) - v(x,-L)]\, dx = \frac{2}{W} \int_{0}^{W} v(x,L)\, dx \tag{30}$$

TABLE 1—*Variation of* I_n *with the values of the strain hardening exponent* n.

n	1.0	3.0	5.0	7.0	9.0
Present ($\lambda = 0.25$)	4.76	3.85	3.41	3.10	2.86
Hutchinson	4.71	3.86	3.41	...	3.03

TABLE 2—*Nondimensional nonlinear fracture parameters* g_1, g_2, *and* g_3 *with the values of the strain hardening exponent* n *and the crack length to plate width ratio* λ.

		1.0		1.5		2.0		3.0	
λ	*n*	Present	Ref *16*	Present	Ref *16*	Present	Ref *16*	Present	Ref *16*
1/8	g_1	2.821	2.800	3.222	3.231	3.552	3.543	4.052	4.00
	g_2	3.500	3.532	3.874	3.867	4.134	4.107	4.435	4.464
	g_3	0.344	0.347	0.496	0.491	0.651	0.640	0.944	0.949
1/4	g_1	2.564	2.544	2.798	2.820	2.964	2.972	3.145	3.140
	g_2	3.111	3.116	3.255	3.235	3.318	3.286	3.337	3.304
	g_3	0.611	0.611	0.827	0.820	1.026	1.010	1.373	1.352
1/2	g_1	2.223	2.211	2.198	2.242	2.173	2.195	2.046	2.056
	g_2	2.365	2.382	2.204	2.182	2.026	2.003	1.724	1.703
	g_3	0.930	0.924	1.097	1.085	1.198	1.180	1.273	1.254
3/4	g_1	2.073	2.073	1.887	1.893	1.710	1.703	1.457	1.458
	g_2	1.573	1.611	1.225	1.215	0.982	0.970	0.692	0.685
	g_3	0.936	0.933	0.894	0.886	0.813	0.802	0.650	0.642

$$\Delta_{\text{no crack}} = 2L\epsilon_\infty = 2L\kappa\sigma_\infty{}^n \tag{31}$$

where ϵ_∞ and σ_∞ are the uniform strain and stress at the far end of plate, respectively.

In order to study the effect of λ as well as n on the nondimensional nonlinear fracture parameters g_1, g_2, and g_3, the authors analyze the rectangular plate of $L/W = 2.0$ with a center-notched crack of length $2a$ as is shown in Fig. 2. With the use of the same element mesh which is depicted in Fig. 5 for a quarter of the plate, one obtains the J-value as the half-circle path integral at the adjacent elements to the crack tip, δ as the crack opening displacement in the tensile direction at the center of the crack, and Δ as the displacement in the tensile direction at the loading end. Table 2 shows the nondimensional parameters g_1, g_2, and g_3 for various values of λ and n corresponding, respectively, to J, δ, and Δ.

Table 3 also shows the nondimensional parameters g_1 and g_2 for the same plate but here $\lambda = 1/2$ and n is up to 7. As seen from these tables, the differences between the present results and those of Shih and Hutchinson [*16*] are very small; whereas, the solutions by Ranaweera and Leckie [*22*] underestimate the parameters.

Summary and Conclusions

1. A superposition method coupled with the penalty function method is proposed and found effective for the nonlinear crack analysis with complex boundary conditions.

2. The characteristic distributions of displacement, strain, and stress for the cracked plate with $r^{-1/(n+1)}$ stress singularity are determined using the superposed Fourier expansion with the singularity.

3. Through the nonlinear crack analysis of the cracked rectangular plate,

TABLE 3—*Nondimensional nonlinear fracture parameters* g_1 *and* g_2 *with the values of the strain hardening exponent* n *(*$\lambda = 1/2$*).*

	n	1.0	3.0	5.0	7.0
Present	g_1	2.223	2.046	1.817	1.597
	g_2	2.365	1.724	1.291	1.097
Ref *16*	g_1	2.212	2.056	1.812	1.644
	g_2	2.382	1.703	1.307	1.084
Ref *22* (Coarse mesh)	g_1	2.192	1.994	1.608	1.222
	g_2	2.355	1.668	1.166	0.864
Ref *22* (Fine mesh)	g_1	2.198	2.016	1.750	1.382
	g_2	2.367	1.682	1.263	0.904

such nondimensional nonlinear fracture parameters as g_1, g_2, and g_3 are found to be in excellent agreement with Shih and Hutchinson's results.

4. The present analysis considers only the problem of plane stress condition. The special formulation is necessary for the problem of plane strain condition, and a relating work will be reported in a forthcoming paper. In the latter case, the incompressibility of plastic strain is to be taken into account by adding the additional penalty term to the right hand side of Eq 21.

References

[1] Gallagher, R. H. in *Numerical Methods in Fracture Mechanics,* A. R. Luxmoore and D. R. J. Owen, Ed., University College Swansea, Swansea, U.K., 1978, pp. 1-25.

[2] Apostal, M. C., Jordan, S., and Marcal, P. V., "Finite Element Techniques for Postulated Flaws in Shell Structures," EPRI SR-22 Special Report, Electric Power Research Institute, 1975.

[3] Benzley, S. B. and Parks, D. M. in *Structural Mechanics Computer Programs,* W. Pilkey, K. Saczalski and H. Schaeffer, Eds., University Press of Virginia, Charlottesville, Va., 1974, pp. 81-102.

[4] Yamamoto, Y. and Tokuda, N., *International Journal of Numerical Methods in Engineering,* Vol. 6, 1973, pp. 427-439.

[5] Yamamoto, Y. and Sumi, Y., *International Journal of Fracture,* Vol. 14, 1978, pp. 17-38.

[6] Yagawa, G., Nishioka, T., Ando, Y., and Ogura, N. in *Computational Fracture Mechanics,* E. Rybicki and S. Benzley, Ed., *American Society of Mechanical Engineers,* Special Publication, 1975, pp. 21-34.

[7] Yagawa, G. and Nishioka, T., *International Journal of Numerical Methods in Engineering,* Vol. 12, 1978, pp. 1295-1310.

[8] Yagawa, G. and Nishioka, T., *International Journal of Numerical Methods in Engineering,* Vol. 14, 1979, pp. 727-740.

[9] Nishioka, T. and Yagawa, G., *Proceedings,* Japan Society of Mechanical Engineers, No. 770-11, 1977, p. 1-3.

[10] Hutchinson, J. W., *Journal of the Mechanics and Physics of Solids,* Vol. 16, 1968, pp. 13-31.

[11] Hutchinson, J. W., *Journal of the Mechanics and Physics of Solids,* Vol. 16, 1968, pp. 337-347.

[12] Rice, J. R. and Rosengren, G. F., *Journal of the Mechanics and Physics of Solids,* Vol. 16, 1968, pp. 1-12.

[13] Goldmann, N. L. and Hutchinson, J. W., *International Journal of Solids Structures,* Vol. 11, 1975, pp. 575-591.

[14] Barsoum, R. S., *International Journal of Fracture,* Vol. 12, 1976, pp. 463-466.

[15] Atluri, S. N., Nakagaki, M., and Chen, Wen-Hwa in *Flaw Growth and Fracture, ASTM STP 631,* American Society for Testing and Materials, 1977, pp. 42-61.

[16] Shih, C. F. and Hutchinson, J. W., *Journal of Engineering Materials and Technology,* 1976, pp. 289-295.

[17] Zienkiewicz, O. C., *The Finite Element Method in Engineering Science,* Third Ed., McGraw-Hill, New York, 1977.

[18] Jacoby, S. L. S., Cowalik, J. S., and Pizzo, J. T., *Iterative Methods for Nonlinear Optimization Problems,* Prentice-Hall, New York, 1972.

[19] Yagawa, H. and Miyazaki, N., *Nuclear Engineering Design,* to be published.

[20] Yagawa, G., Aizawa, T., and Ando, Y., *Proceedings,* Japan Society of Mechanical Engineers, No. 780-12, 1978, pp. 164-171.

[21] Rice, J. R., *Transactions,* American Society of Mechanical Engineers, Series E 35-2, 1968, pp. 379-386.

[22] Ranaweera, M. P. and Leckie, F. A., *Proceedings,* First International Conference on Numerical Methods in Fracture Mechanics, 1978, pp. 450-463.

S. Mall[1]

Dynamic Finite Element Analysis of Cracked Bodies with Stationary Cracks

REFERENCE: Mall, S., **"Dynamic Finite Element Analysis of Cracked Bodies with Stationary Cracks,"** *Fracture Mechanics: Twelfth Conference, ASTM STP 700,* American Society for Testing and Materials, 1980, pp. 453-465.

ABSTRACT: A dynamic finite element analysis utilizing a simple singular element (obtained from a degenerate eight-node isoparametric element) was used to investigate three elastodynamic problems with stationary cracks. The first problem, involving a centrally cracked rectangular bar (subjected to uniaxial tension with Heaviside-function time dependence) was analyzed in order to compare the present simple singular element formulation with previously developed higher order singular element formulations. In the second problem, a three-point bend specimen of birefringent material (under drop-weight testing) was analyzed to compare the dynamic stress intensity factors obtained from the present analysis with the experimental counterpart. Excellent agreement between the present results and those from previous investigations (both numerical as well as experimental) demonstrates the capability and reliability of this simple singular element formulation for solving fracture dynamics problems with stationary cracks. The third problem, involving a three-point bend specimen of A533B steel, suggests a potential application of the present method in instrumented impact tests.

KEY WORDS: fracture dynamics, instrumented impact test, dynamic finite element method, fractures (materials), crack propagation

For the last few years, the author and his colleagues have investigated the transient response of three-point notched bend specimens in the drop weight testing mode [*1-3*].[2] In these investigations [*1,2*] dynamic tear test specimens machined from brittle and ductile photoelastic polymers, that is, Homalite-100 and polycarbonate, were analyzed for dynamic fracture response before and after rapid crack propagation using combined dynamic photoelastic and dynamic finite element methods. Subsequently,

[1]Assistant professor, Department of Mechanical Engineering, University of Maine, Orono, Me. 04469.

[2]The italic numbers in brackets refer to the list of references appended to this paper.

this finite element method was employed to determine the dynamic initiation fracture toughness, K_{Id} in notched bend specimens of A533B steel and 6061 aluminum alloy [3]. The dynamic finite element method utilized the HONDO code [4], which is a two-dimensional solid finite element program, to calculate the time-dependent displacements, velocities, accelerations and stresses. The HONDO code employs the four-node isoparametric quadrilateral element with an explicit time integration scheme. On the other hand, Aberson et al [5] have solved several stationary crack elastodynamic problems with the help of special crack tip singular elements. They have formulated singular elements of eight-nodes for the opening mode and ten-nodes for the mixed-mode problems based on William's eigenfunctions [6]. These very high order elements have been shown to perform well in analysis of fracture dynamic problems with stationary cracks; however, their use in modeling the running crack was not encouraging [7]. Another application of the special singular element in stationary crack problems under dynamic loading was demonstrated by Glazik [8]. Glazik employed the singular element formulation of Benzley [9] where the singularity at the crack tip is modeled by supplementing the first order term in bilinear displacement field of a quadrilateral element. This special singular element was employed in conjunction with special transition elements to ensure compatibility between singular and regular elements.

The purpose of this paper is to present results of dynamic finite element analyses of fracture dynamic problems with stationary cracks using an alternate but a very simple singular crack tip element. A simple singular element can be formulated from an eight-node isoparametric element either by placing the mid-side nodal coordinate on any side (connected to the crack tip) at the quarter point of that side adjacent to the crack or by collapsing one side [10,11]. This distorted eight-node isoparametric element is attractive to users since regular eight-node elements are already available in many widely distributed finite element computer programs, and thus saves the user the effort of incorporating a special singular element in existing programs. This simple singular element has received a fair deal of attention in static fracture problems (for example, see Ref 12) and the present study is thus its natural extension in fracture dynamics. The present paper deals with three problems. The first problem is a theoretical problem that involves a centrally cracked strip whose ends are subjected to suddenly applied and maintained tension and is usually referred to as Chen's problem [13]. Chen's problem has almost become the benchmark problem for a fracture dynamic problem with a stationary crack, and was selected to compare the results obtained from this simple singular element formulation with that obtained from special singular elements of Aberson et al [5] and Glazik [8]. The second problem is the analysis of a three-point bend specimen whose dynamic stress intensity

factors from instant of impact up to rapid crack propagation were obtained with the help of a dynamic optical method. It provides a further check of the present dynamic finite element analysis. The third problem deals with the application of the present analysis to determine the dynamic initiation fracture toughness, K_{Id} of an instrumented impact specimen of A533B steel. Results of these investigations are summarized here.

Distorted Eight-Node Singular Element

Barsoum [*10*] and Henshell and Shaw [*11*] have independently shown that the eight-node isoparametric, planar element can be slightly modified to incorporate the required inverse square root singularity characteristics of linear fracture mechanics. (This concept has also been extended in case of three-dimensional, plate and shell formulation.) This singularity can be achieved in two manners. In the first approach, the singularity can be obtained by placing the mid-side node of the side connected to the crack tip at quarter position adjacent to the crack tip. In the second approach, one side of an eight-node element is collapsed to form a triangular quadratic isoparametric element, and the mid-side node is then placed near the crack tip at the quarter point. Reference *10* gives the complete discussion of the reason this element behaves in this unique way, so no theory of this element is mentioned here. It has also been shown that the collapsed eight-node triangular element possesses the same $(1/\sqrt{r})$ singularity in the interior as on the boundary; while the rectangular element has the $(1/\sqrt{r})$ singularity only on its boundary. Furthermore, Barsoum [*14*] has shown that total strain energy of an eight-node triangular element remains bounded, while that of the distorted eight-node rectangular element is unbounded. The collapsed triangular element was, therefore, employed in the present work with nine-point Gaussian integration quadrature as recommended by previous investigators [*10–12,14*].

Dynamic Finite Element Analysis

The finite element NONSAP code [*15*] was employed in the present investigation. This program can handle both static and dynamic problems and has built-in capability of using four- to eight-node isoparametric quadrilateral elements. The time integration schemes available are both Wilson's θ- and Newmark's β methods with both consistent and lumped mass formulations. In the present investigation, Newmark's method (with parameters α and δ equal to 0.25 and 0.5, respectively) was utilized due to two following reasons: (1) this method is unconditionally stable for this choice of parameters in linear problems, and (2) Rydholm et al [*16*] have successfully employed these values for rapid crack propagation studies.

Chen's Problem

One of extensively treated (numerically) stationary crack problems is a rectangular bar with a central crack loaded dynamically by a uniform tension $\sigma_0 H(t)$, where $H(t)$ is the Heaviside step function. Chen [*13*] solved this problem with the help of finite-difference method (The Hemp Code). Later, Aberson et al [5] analyzed this problem extensively with a finite element method employing the special crack tip singular element. Recently, Glazik [*8*] has investigated this problem with Benzley's special crack tip element [*9*] as well as with a regular isoparametric element. The author with his colleagues [*3*] have also solved Chen's problem with regular isoparametric elements. Obviously, the present dynamic finite element analysis incorporating a singular eight-node quadratic triangular element was first assessed with the help of Chen's problem.

Figure 1 shows the finite element breakdown of one quadrant of the rectangular bar of Chen's problem [*13*]. A plane strain condition of deformation is assumed. The material of the bar is a linear elastic with Young's modulus of 200 GPa, Poisson's ratio of 0.3 and density of 5 g/cm^3 [*13*]. In Fig. 1, elements marked "A" are singular eight-node quadratic triangular elements, those marked "B" are regular eight-node quadratic elements, those marked "C" are regular five-node quadratic elements and unmarked are four-node regular isoparametric elements. One important consideration in the dynamic finite element method is the size of time step for the integration scheme. It has been suggested that the time step should be equal to d/c, where d is the characteristic dimension of the element and c the wave velocity [*17*]. Three time steps of 0.148, 0.074 and 0.037 μs corresponding to the transit time of longitudinal wave across the two end-nodes, end- and mid-nodes, and end- and quarter-nodes of the collapsed triangular element were used. These three time steps yielded the dynamic stress intensity factors within $\pm$ 0.5 percent of each other; thus, the time step based on transit time of wave across the smallest size of element can be employed without any noticeable gain over the accuracy due to small time steps based on mid-point or quarter-point dimensions. Figure 2 shows the normalized dynamic stress intensity factor versus time relationship with 0.148 μs time step and lumped-mass formulation along with Chen's result obtained from finite difference method [*13*]. The dynamic stress intensity factors were calculated by simply comparing the dynamic crack opening displacement (COD) of the node close to the crack tip to its static value. This ratio of dynamic and static COD is also the ratio of dynamic stress intensity factor to the static value. This simple procedure for computing the dynamic stress intensity factor was successfully employed in the previous investigations by the author with his colleagues [*1-3*] and also by Glazik [*8*]. Figure 2 shows that the present finite element results are in excellent agreement with Chen's finite difference analysis

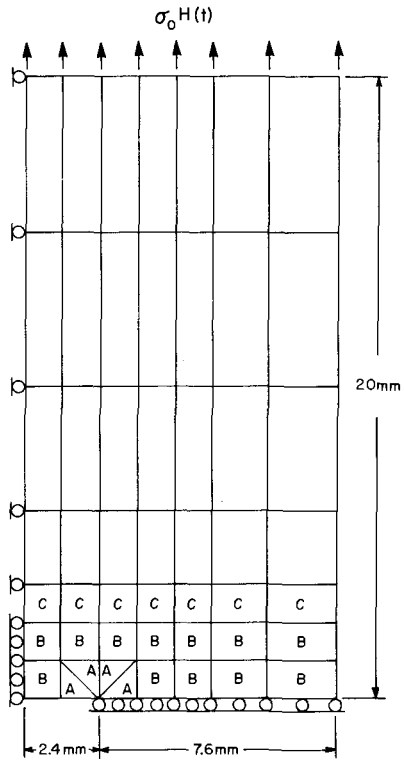

FIG. 1—*Finite element breakdown of Chen's problem.*

[*13*] except over two time periods. These two regions correspond to the arrival times of the Rayleigh surface wave at the crack tip from the other tip and its subsequent reflection as marked by R_1 and R_2 in the Fig. 2. This deviation in the results obtained from finite element and finite difference analysis in the vicinity of R_1 and R_2 was also observed by Aberson et al [*5*], Glazik [*8*] and Mall et al [*3*].

To demonstrate further the validity of the present analysis, a comparison of results (for Chen's problem), obtained from special singular elements by Aberson et al [*5*] and Glazik [*8*] with present simple singular element formulation, are shown in Figs. 3 and 4. Figure 3 compares results with lumped mass formulation, while Fig. 4 is for a consistent mass formulation. The results of Figs. 3 and 4 are in excellent agreement with each other. The deviation among these three results occurring near instants of arrival of Rayleigh surface wave (R_1 and R_2) at the crack tip, in Figs. 3 and 4, can be attributed to the character of different singularity formulations. In the present analysis, the lumped mass model yields the max-

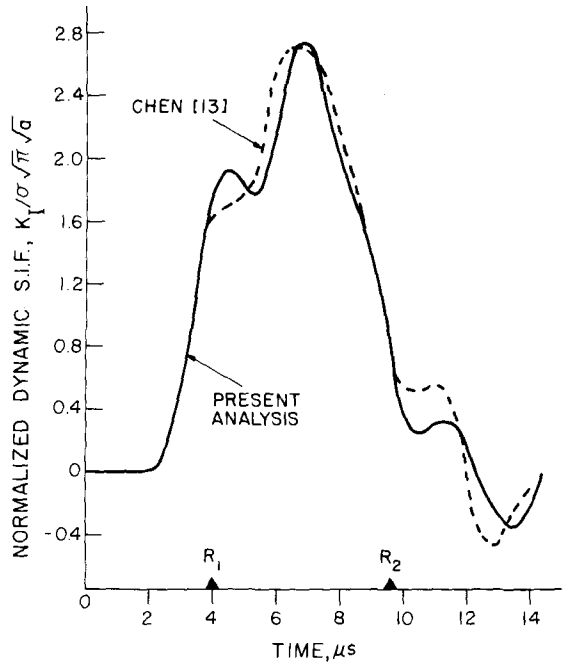

FIG. 2—*Dynamic stress intensity factors for Chen's problem obtained by finite element and finite difference methods.*

imum value of stress intensity factor 2 percent higher than reported by Chen [*13*], while the consistent-mass model yields a value 2 percent lower than that of Chen. The lumped-mass formulation, thus, provides the conservative peak value and also results a substantial saving in computation time. It seems, therefore, that excellent results could be expected in solving fracture dynamics problems of stationary crack with lumped-mass formulation in the present analysis. The following two analyses endorse this statement.

Kalthoff's Specimen

Kalthoff et al [*18*] have reported results of drop weight impact testing of notched-bend specimen where the instantaneous dynamic stress intensity factors were measured directly by utilizing the method of shadow pattern (caustics). The notched bend specimens with dimensions 550 by 100 by 10 mm, nominal crack length of 20 mm and support length of 400 mm, were machined from an epoxy resin, Araldite B. Twenty-four shadow spots at successive time intervals were recorded with the help of a high speed camera that provided the history of directly measured dynamic stress

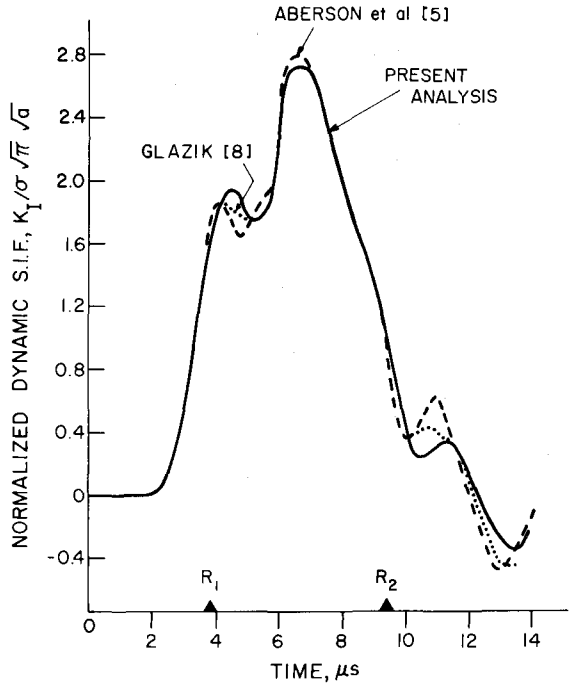

FIG. 3—*Dynamic stress intensity factors for Chen's problem with lumped-mass formulation.*

intensity factor from the instant of impact to the time of crack initiation. They have published these results for three specimens with different sharpness of the starter notch [*18*]. The impact (tup) load-time history and also the dynamic stress intensity factor-time history of the three reported specimens closely correspond to each other except for the time of crack initiation (and thereby critical dynamic stress intensity factor), which depends on the sharpness of the starter crack. In the present analysis, all three specimens are treated as a single specimen.

Figure 5 shows the finite element breakdown of half of Kalthoff's specimen. The material properties of Araldite B were as follows: (*a*) Young's modulus of 3660 MPa, (*b*) Poisson's ratio of 0.392, and (*c*) density of 1.15 g/cm^3 [*18*]. Figure 6 shows the idealized tup load-time history, which is the average of the three experimental curves of Fig. 2 of Ref *18*. This load-time history was input as the time dependent boundary condition at the node corresponding to the impact point, which was also given an initial (experimental) impact velocity of 5 m/s. Since the specimen is relatively thin (10 mm), the plane stress condition was assumed in the finite element analysis. The results of this computation are shown in Fig. 6, where the numerically obtained dynamic stress intensity factor is

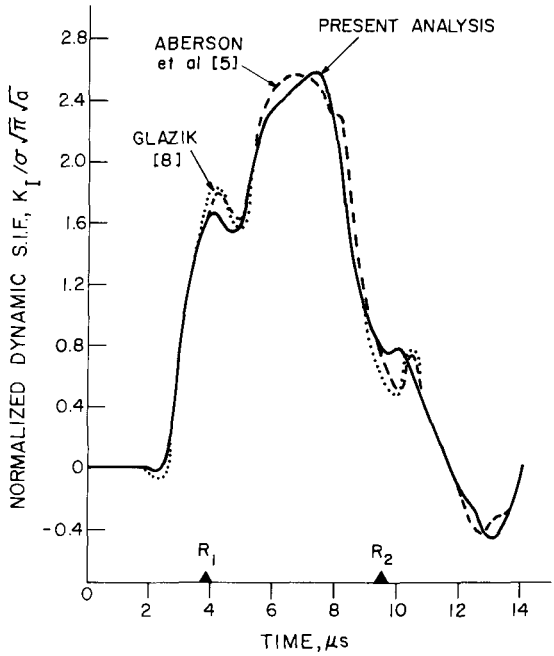

FIG. 4—*Dynamic stress intensity factors for Chen's problem with consistent-mass formulation.*

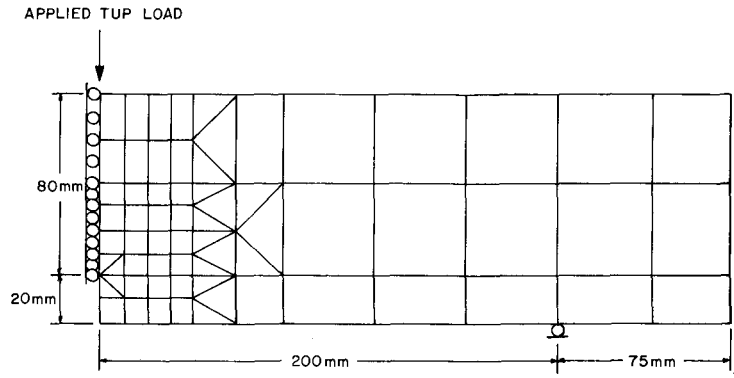

FIG. 5—*Finite element breakdown of Kalthoff's specimen.*

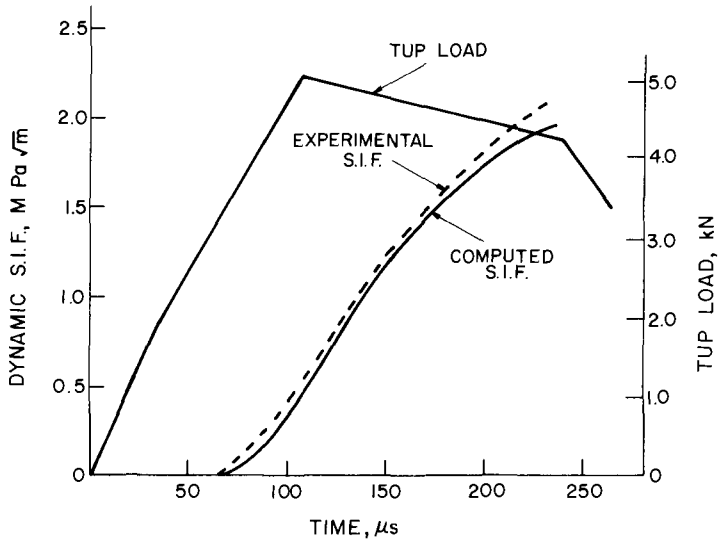

FIG. 6—*Dynamic stress intensity factors for Kalthoff's specimen.*

compared with its experimental counterpart. The curve representing the experimental dynamic stress intensity factor in Fig. 6 is again the average of experimental data for three specimens shown in Fig. 2 of Ref *18*. Figure 6 shows an excellent agreement between the experimentally and numerically obtained dynamic stress intensity factors, and thus endorsing the validity of present dynamic finite element analysis utilizing the simple singular element. The time-phase difference between dynamic stress intensity factor and load-time curve correspond to the time taken by the plate-wave from the impact point to the other side of the specimen and then back to the crack tip. This closely corresponds to recorded experimental results. This dynamic analysis further confirms that crack initiation in the instrumented impact test need not necessarily correspond to the recorded peak tup load, a phenomenon also observed by the author and his colleagues [*1-3*] in their experiments.

Loss' Specimen

Loss has conducted a series of instrumented drop-weight impact tests of 25.4-mm thick specimen of A533B steel at various temperatures [*19*]. These specimens, possessing dimensions of 228.6 by 50.8 mm, support length of 203 mm, and with nominal crack length of 25.4 mm, were fatigue precracked. With the objective of developing a simple procedure to compute the dynamic initiation fracture toughness, K_{Id} without any dynamic

analysis, Loss [*19*] instrumented these specimens with a 3.2 by 3.2 mm strain gage near the crack tip as indicated in Figs. 7 and 8. Prior to impact testing, a static calibration was established between the strain gage near the crack tip and tup load. During the actual impact test, the dynamic strain of the same gage was recorded. The recorded dynamic strain in conjunction with static calibration was used to compute dynamic bending moment. The dynamic initiation fracture toughness (K_{Id}) was, then, obtained from this dynamic bending moment from expression of fracture toughness (K_{Ic}) for a three-point bend specimen given in ASTM Test for Plane-Strain Fracture Toughness of Metallic Materials (E 399-74), with the assumption that dynamic bending moment so measured is proportional to the instantaneous stress intensity factor as computed under static loading. Here the present dynamic analysis with simple singular element of one of Loss' specimen tested at −18°C (−0.4°F) is presented, and Loss' simple procedure to obtain K_{Id} is discussed.

Figure 7 shows the finite element breakdown of half of Loss' specimen. The material properties of A533B steel were as follows: (*a*) Young's modulus of 207 GPa, (*b*) Poisson's ratio of 0.3, and (*c*) density of 7.9 g/cm^3 [*19*]. The dynamic finite element analysis was conducted under plane stress condition. Figure 8 shows the idealized (tup) load-time history of its experimental counterpart that was obtained with the help of strain gages located on the tup (50 mm from the tup tip), and was used as input in the dynamic finite element analysis. The node corresponding to impact was also given the experimental impact velocity of 2.4 m/s as initial condition in finite element analysis. Figure 8 shows the reasonable agreement between the experimental and numerically computed dynamic strain at the location marked "strain gage" of this figure. The precipitous drop in the

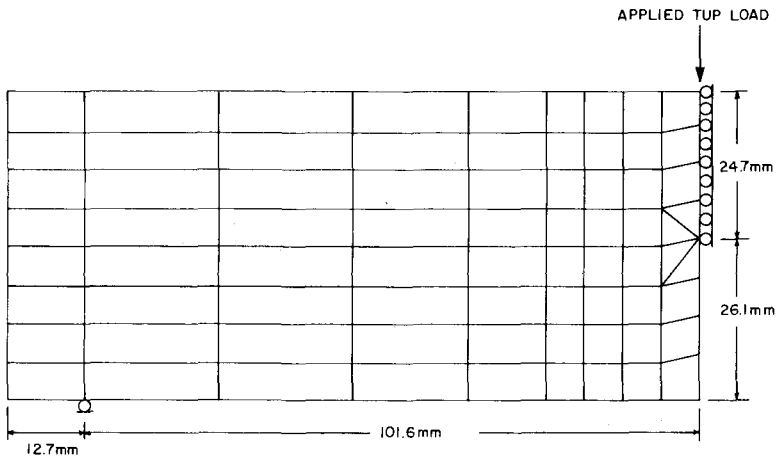

FIG. 7—*Finite element breakdown of Loss' specimen.*

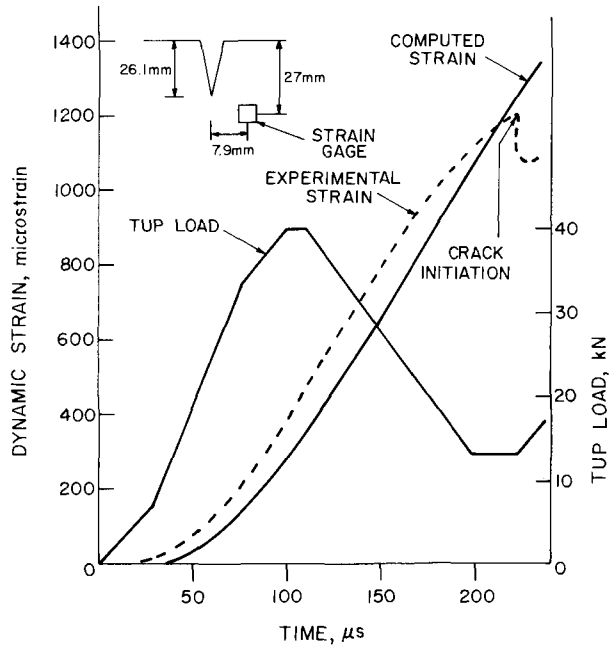

FIG. 8—*Dynamic strains at a location in Loss' specimen.*

experimental dynamic strain depicted in Fig. 8 represents the rapid crack propagation that was not modeled in the dynamic finite element analysis. The computed dynamic strain with assumed stationary crack, thus, continues to increase even after experimentally observed crack propagation.

Figure 9 shows the development of dynamic stress intensity factor obtained from the COD from the instant of impact to the time of crack initiation, as well as the dynamic stress intensity factor obtained from numerically computed dynamic strain at the gage location as per Loss' procedure. The excellent agreement between dynamic stress intensity factors obtained from dynamic finite element analysis and from Loss' procedure, as shown in Fig. 9, suggests that dynamic analysis (to compute K_{Id}) can be replaced by this simple analysis. However, it should be emphasized here that the success of Loss' procedure depends on the suitable location of strain gage, which has been previously demonstrated in Refs *1* and *2*.

Conclusions

The results presented herein clearly demonstrate that the simple singular element obtained from a degenerate eight-node isoparametric element is

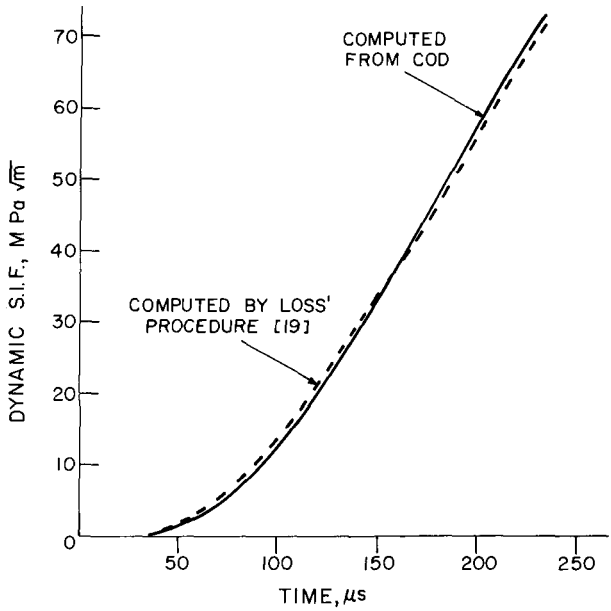

FIG. 9—*Dynamic stress intensity factors for Loss' specimen from two procedures.*

a viable alternative to special crack tip elements for the dynamic finite element method in case of fracture dynamic problems with stationary crack. The simplicity, wide availability, and saving in extra effort of formulation are undoubtedly advantages of this simple eight-node triangular singular element over the special crack tip singular elements. A straightforward procedure in conjunction with this singular element resulted in dynamic stress intensity factors that are in excellent agreement with their counterparts, obtained either numerically by previous investigators or computed directly through experimental measurements. Furthermore, a demonstration of the present analysis indicates that there is a potential application of this method in augmenting the instrumented impact tests, such as Loss' procedure.

Acknowledgments

The author would like to thank F. J. Loss and J. F. Kalthoff for providing various details of their experimental work and to A. S. Kobayashi for many helpful discussions with regard to the paper.

References

[*1*] Mall, S., Kobayashi, A. S., and Urabe, Y., *Experimental Mechanics*, Vol. 18, No. 12, Dec. 1978, pp. 449-456.

[2] Mall, S., Kobayashi, A. S., and Urabe, Y. in *Fracture Mechanics, ASTM STP 677*, American Society for Testing and Materials, 1979, pp. 498–510.

[3] Mall, S., Kobayashi, A. S., and Loss, F. J. in *Crack Arrest Methodology and Applications, ASTM STP 711*, American Society for Testing and Materials, 1980.

[4] Key, S. W., "HONDO—A Finite Element Computer Program for the Large Deformation Dynamic Responses of Axisymmetric Solids," Report SLA-74-0039, Sandia Laboratories, April 1974.

[5] Aberson, J. A., Anderson, J. M., and King, W. W. in *Elastodynamic Crack Problems*, G. C. Sih, Ed., Noordhoff International Publishing, Leyden, The Netherlands, 1977, Chapter 5, pp. 249–292.

[6] Williams, M. L., *Journal of Applied Mechanics*, Vol. 24, No. 1, March 1957, pp. 109–114.

[7] Aberson, J. A., Anderson, J. M., and King, W. W. in *Fast Fracture and Crack Arrest, ASTM STP 627*, American Society for Testing and Materials, 1977, pp. 123–134.

[8] Glazik, J. L., Jr., ASME Preprint 78-PVP-94, The American Society of Mechanical Engineers, New York, 1978.

[9] Benzley, S. E., *International Journal for Numerical Methods in Engineering*, Vol. 8, No. 3, 1974, pp. 537–545.

[10] Barsoum, R. S., *International Journal for Numerical Methods in Engineering*, Vol. 10, No. 1, 1976, pp. 25–37.

[11] Henshell, R. D. and Shaw, K. G., *International Journal for Numerical Methods in Engineering*, Vol. 9, No. 3, 1975, pp. 409–507.

[12] Gallagher, R. H. in *Numerical Methods in Fracture Mechanics*, A. R. J. Luxmoore and D. R. J. Owens, Eds., University College Swansea, U.K., 1978, pp. 1–25.

[13] Chen, Y. M., *Engineering Fracture Mechanics*, Vol. 7, No. 4, 1975, pp. 653–660.

[14] Barsoum, R. S., *International Journal for Numerical Methods in Engineering*, Vol. 11, No. 1, 1977, pp. 85–98.

[15] Bathe, K. J., Wilson, E. L., and Iding, R. H., "NONSAP—A Structural Analysis Program for Static and Dynamic Response of Nonlinear Systems," Report No. UC SESM 74-3, Structural Engineering Laboratory, University of California, Berkeley, Calif., Feb. 1974.

[16] Rydholm, G., Fredriksson, B., and Nilsson, F. in *Numerical Methods in Fracture Mechanics*, A. R. J. Luxmoore and D. R. J. Owens, Eds., University College Swansea, U.K., 1978, pp. 660–672.

[17] Bazant, Z. P., Glazik, J. L., and Achenbach, J. D., *Journal of Engineering Mechanics Division*, American Society of Civil Engineers, Vol. 102, No. EM3, 1976, pp. 479–496.

[18] Kalthoff, J. F., Winkler, S., and Beinert, J., *International Journal of Fracture*, Vol. 13, No. 4, Aug. 1977, pp. 528–531.

[19] Loss, F. J., "Structural Integrity of Water Reactor Pressure Boundary Components," Progress Report ending 29 Feb. 1976, Naval Research Laboratory Report 8006 (also NRL NUREG 1), 26 Aug. 1976.

Bernard Gross [1]

Mode I Crack Surface Displacements and Stress Intensity Factors for a Round Compact Specimen Subject to a Couple and Force

REFERENCE: Gross, Bernard, **"Mode I Crack Surface Displacements and Stress Intensity Factors for a Round Compact Specimen Subject to a Couple and Force,"** *Fracture Mechanics: Twelfth Conference, ASTM STP 700,* American Society for Testing and Materials, 1980, pp. 466-477.

ABSTRACT: Mode I displacement coefficients along the crack surface and stress intensity coefficients are presented for a radially cracked round compact specimen, treated as a plane elastostatic problem, subjected to two types of loading; a uniform tensile stress and a nominal bending stress distribution across the net section. By superposition the resultant displacement coefficient or the corresponding stress intensity coefficient can be obtained for any practical load location. Load line displacements and stress intensity coefficients are presented for A/D ratios ranging from 0.40 to 0.95, where A is the crack length measured from the crack mouth to the crack tip and D is the specimen diameter. Through a linear extrapolation procedure, crack mouth displacements are also obtained. Experimental evidence and comparisons with other investigators shows that the results of this study are valid over the range of A/D ratios analyzed for a practical pin loaded round compact specimen.

KEY WORDS: crack propagation, fracture tests, stress intensity factors, crack surface displacements, boundary collocation analysis, fractures (materials)

Nomenclature

A	Crack length measured from crack mouth to crack tip
$a = A + W - D$	Crack length measured from load line to crack tip
B	Specimen thickness

[1] Materials engineer, Structural Materials, National Aeronautics and Space Administration, Lewis Research Center, Cleveland, Ohio 44135.

D	Disk diameter
E	Young's modulus
E'	Effective modulus, equals $E/(1 - \nu^2)$ for plane strain or E for plane stress
$E'Bv/P$	Influence coefficient
$K_I = K_{IP} + K_{IM}$	Mode I stress intensity factor $K_I = K_{IM}$ when $\sigma_P = 0$, and $K_I = K_{IP}$ when $\sigma_M = 0$
L	Distance measured from load line to centerline of disk
M	Resultant moment at nominal neutral axis position
P	Applied pin load
$v = v_P + v_M$	Resultant vertical displacement at location z across the crack surfaces
v_P	Vertical displacement across the crack surfaces at z resulting from a fictitious uniform net section tension
v_M	Vertical displacement across the crack surfaces at z resulting from a fictitious nominal net section bending
W	Distance measured from load line to circumference of specimen $(L + D/2)$
x, y	Cartesian coordinates (Fig. 1)
$z = [(A + W) - (x + D)]/(A - 0.15D)$	Dimensionless location along the crack surface for $0.3 < z < 1$
$\Gamma = K_I/(\sigma_P + \sigma_M)\sqrt{A(1 - A/D)}$	Stress intensity coefficient $\Gamma = \Gamma_P$ when $\sigma_M = 0$, and $\Gamma = \Gamma_M$ when $\sigma_P = 0$.
$\delta z = (D - W)/(A - 0.15D)$	Dimensionless distance from load line to crack mouth
$\Delta_P(z) = E'v_P/\sigma_P A$	Displacement coefficient as a function of z due to σ_P
$\Delta_M(z) = E'v_M/\sigma_M A$	Displacement coefficient as a function of z due to σ_M
$\Delta(z) = E'v/(\sigma_P + \sigma_M)A$	Resultant displacement coefficient as a function of z
ν	Poisson's ratio
$\sigma_M = 6M/B(D - A)^2$	Component of fictitious linear net section bending stress at crack tip resulting from moment, M
$\sigma_P = P/B(D - A)$	Component of fictitious uniform net section tensile stress resulting from applied load, P

M Value associated with net section bending

P Value associated with net section tension

ASTM Committee E24 on Fracture Testing is currently considering the round compact specimen (edge-cracked disk) for incorporation into ASTM Test on Plane Strain Fracture Toughness of Metallic Materials (E399-78). Pursuant to this task, a program to evaluate the round compact specimen was initiated by ASTM Task Group E24.01.12.

The objective of this paper is to aid in the establishment of the round compact specimen as an alternate standard for the determination of the plane strain fracture toughness (K_{Ic}) in international testing and certification standards. The round compact specimen geometry, when compared to existing standard specimens, is most efficient in testing round bar stock because of the low cost of fabrication. Displacement and stress intensity coefficients were obtained herein for the range of ratio of crack length-to-specimen diameter, A/D, from 0.40 to 0.95 (where A is the distance from the crack tip to the circumference). Displacement coefficients Δ_P and Δ_M and stress intensity coefficients Γ_P and Γ_M apply to two types of specimen loading; Δ_P (or Γ_P) to a uniform distribution of stress across the net section, and Δ_M (or Γ_M) to a nominal bending stress distribution across the net section (Fig. 1). While these types of load are in themselves impractical, the two coefficients can be combined to represent any practical case of loading by a pair of equal and opposite forces normal to the crack (pin loading). The appropriate displacement (or stress intensity) coefficient Δ (or Γ) is obtained from a linear combination of displacement coefficients Δ_P and Δ_M (or Γ_P and Γ_M).

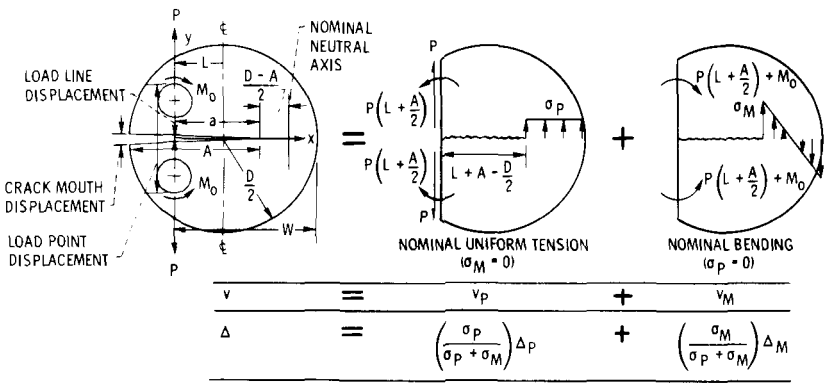

FIG. 1—*Application of superposition principle to obtain the resultant displacement at a given location, L, along the crack surface of a round compact specimen.*

In obtaining the crack surface displacement solution, the same boundary conditions on the stress function and its derivative given in Ref *1* were used. Through a linear extrapolation of the displacement coefficient function at the load line, the crack mouth displacement coefficient is obtained.

For small A/D ratios the differences between the actual distribution of loading forces in a pin-loaded specimen and the distribution assumed in the analytical model may be significant. Crack displacements often become sensitive to these differences as the pin hole nears the crack tip or the crack surface. To verify the applicability of the present results to the smallest A/D ratios of practical interest, calculated displacements are compared with experimental measurements. Fisher and Buzzard [*2*][2] experimentally obtained the influence coefficients across the crack surfaces along the load line and crack mouth for a given load line location ($W/D = 0.7407$) with A/D ratios varying from 0.398 to 0.909 (Fig. 1). Comparisons of load point and load line displacements were made at $A/D = 0.398$ and 0.909. In addition, comparison is made with displacement coefficients for the standard rectangular compact specimen. These results were obtained assuming a parabolic shear distribution along the load line. The boundary conditions on the stress function and its derivative are given in Ref *3*. Further comparisons are made with analytical results of other investigators for the round compact specimen given in Refs *4* and *5*.

Displacement coefficients Δ_P and Δ_M and stress intensity coefficients Γ_P and Γ_M are presented in tabular form, and as least squares best fit polynomials. An example is provided illustrating the use of coefficients Δ_P and Δ_M to obtain load line and crack mouth displacements. Examples are given in Ref *1* illustrating the use of coefficients Γ_P and Γ_M.

Approach

For a given A/D ratio and at a given z location, the displacement coefficients are defined as follows

$$\Delta_P(z) = E' n_P(z)/\sigma_P A \tag{1}$$

$$\Delta_M(z) = E' v_M(z)/\sigma_M A \tag{2}$$

$$\Delta(z) = E' v(z)/(\sigma_P + \sigma_M)A \tag{3}$$

Applying the superposition principle as shown in Fig. 1, $v = v_P + v_M$, one obtains

$$\Delta(z) = [\sigma_P/(\sigma_P + \sigma_M)]\Delta_P(z) + [\sigma_M/(\sigma_P + \sigma_M)]\Delta_M(z) \tag{4}$$

[2]The italic numbers in brackets refer to the list of references appended to this paper.

Since $\sigma_M = 6M/B(D - A)^2$ where $M = M_o + P(2L + A)/2$ and $\sigma_P = P/B(D - A)$. Substitution into Eq 4 together with some algebraic manipulation results in

$$\Delta(z) = \frac{PD(1 - A/D)\Delta_P(z) + 3[2M_o + PD(2L/D + A/D)]\Delta_M(z)}{PD(1 + 6L/D + 2A/D) + 6M_o} \quad (5)$$

The influence coefficient $E'Bv/P$ can be obtained directly from Eq 3 and 4 as

$$E'Bv/P = \frac{(A/D)(1 - A/D)\Delta_P(z) + 3(A/D)(2M_o/PD + 2L/D + A/D)\Delta_M(z)}{(1 - A/D)^2} \quad (6)$$

To obtain the crack mouth displacement coefficient, the slope of $\Delta(z)$ is assumed constant at and beyond the load line location $x = 0$, hence $zo = (A + W - D)/(A - 0.15D)$. Thus

$$d\Delta/dz|_{zo} = [\sigma_P/(\sigma_P + \sigma_M)]d\Delta_P/dz|_{zo} + [\sigma_M/(\sigma_P + \sigma_M)]d\Delta_M/dz|_{zo}$$

and it follows that

$$\Delta_{mo} = \Delta|_{zo} + d\Delta/dz|_{zo}\delta z \quad (7)$$

where

$\delta z = (D - W)/(A - 0.15D)$
mo = mouth and
zo = load line location.

Similarly, the crack mouth influence coefficient is

$$E'Bv/P|_{mo} = E'Bv/P|_{zo} + d(E'Bv/P)/dz|_{zo}\delta z \quad (8)$$

For a given A/D ratio stress intensity coefficient Γ_P, Γ_M, and Γ are defined as

$$\left.\begin{aligned} \Gamma_P &= \frac{K_{IP}}{\sigma_P\sqrt{A(1 - A/D)}} \\ \Gamma_M &= \frac{K_{IM}}{\sigma_M\sqrt{A(1 - A/D)}} \\ \Gamma &= \frac{K_I}{(\sigma_P + \sigma_M)\sqrt{A(1 - A/D)}} \end{aligned}\right\} \quad (9)$$

By superposition one has

$$K_I = K_{IP} + K_{IM} \tag{10}$$

Applying Eq 9 and 10 one obtains

$$\Gamma = \left(\frac{\sigma_P}{\sigma_P + \sigma_M}\right)\Gamma_P + \left(\frac{\sigma_M}{\sigma_P + \sigma_M}\right)\Gamma_M \tag{11}$$

If at load line L, a load P is applied through pins and the moment $M_o = 0$, after algebraic manipulation of Eq 11 one obtains a more common form

$$\frac{KB\sqrt{D}}{P} = \sqrt{\frac{A/D}{1 - (A/D)}}\left\{\Gamma_P + \frac{3[(A/D) + (2L/D)]}{1 - (A/D)}\Gamma_M\right\} \tag{12}$$

Results and Discussion

The resultant displacement solution of the cracked disk problem is obtained by superposition of two types of loading as shown in Fig. 1. The first type of loading is based on a constant net section stress $\sigma_P = P/[B(D - A)]$ resulting in the displacement coefficient Δ_P as a function of σ_P and A/D. The second solution is based on a nominal pure bending stress where $\sigma_M = 3[P(A + 2L) + 2M_o]/[B(D - A)^2]$ at the crack tip from which the displacement coefficient Δ_M as a function of σ_M and A/D is obtained. The values of Δ_P and Δ_M, Table 1, are obtained using the boundary collocation method and stress function boundary conditions described in Ref *1*.

Table 2 contains comparisons of the present influence coefficient results (Eqs 6 and 8 with $M_o = 0$) with those of Refs *2* through *5*. The results in Ref *4* are for a point load at location $L = 0.25$ D and $y = 0.2$ D (Fig. 1 and Table 2), thus, $W/D = 0.75$. The influence coefficient values obtained herein along the load line are in very good agreement with those published in Ref *4*. For the influence coefficient at the crack mouth, good agreement was obtained for A/D ratios greater than 0.7.

For $W/D = 0.7407$, which is the value being considered for standardization, good agreement among the present results, those of Ref *5*, and the experimental results of Ref *2* at the crack mouth and load line is obtained over the whole range of A/D ratios. The experimental results were obtained on a specimen geometrically similar to the proposed standard round compact specimen. The test specimen had the following dimensions: $D = 20.42$ cm, $B = 2.73$ cm, and $W = 15.12$ cm. The material used, 6061-T651 aluminum, had a modulus $E = 689.48 \times 10^9$ N/m^2. A least squares best fit polynomial of sixth degree, $\ln(E'Bv/P) = C_0 + C_1X + C_2X^2 + C_3X^3 + C_4X^4 + C_5X^5 + C_6X^6$ (where $X = 1 + A/W - D/W$) is fitted to the

TABLE 1—*Coefficients of three degree polynomial least squares best fit for crack surface displacement coefficients.*

	$\Delta_P(z) = C_0 + C_1z + C_2z^2 + C_3z^3$				$\Delta_M(z) = B_0 + B_1z + B_2z^2 + B_3z^3$			
A/D	C_0	C_1	C_2	C_3	B_0	B_1	B_2	B_3
0.40	0.63259	−2.79804	3.14766	−5.82857	0.52340	4.65676	−1.72455	1.73955
0.45	0.81814	−3.67342	5.39112	−7.34770	0.43518	4.36949	−1.70006	1.73346
0.50	0.97526	−4.57193	7.38877	−8.56467	0.36390	4.09767	−1.60570	1.63752
0.55	1.10031	−5.38109	8.96387	−9.41258	0.30182	3.85332	−1.46881	1.48341
0.60	1.18337	−5.99026	9.94839	−9.82094	0.25308	3.60392	−1.26286	1.27581
0.65	1.22402	−6.38020	10.35781	−9.82159	0.21419	3.35430	−1.01423	1.03953
0.70	1.21929	−6.52059	10.15645	−9.40042	0.18281	3.10465	−0.72847	0.78052
0.75	1.16734	−6.40654	9.36121	−8.57212	0.14603	2.92152	−0.53120	0.57055
0.80	1.07257	−6.07930	8.06399	−7.38548	0.12054	2.71632	−0.29821	0.35624
0.85	0.93559	−5.57558	6.34743	−5.87687	0.08993	2.56627	−0.15371	0.19946
0.90	0.75158	−4.94125	4.33777	−4.15626	0.05776	2.45278	−0.07881	0.09642
0.95	0.49699	−4.20252	2.14393	−2.11343	0.03195	2.30750	0.00978	0.00863

NOTE—Δ_P and Δ_M for range of $0.3 \leq z \leq 1$.

TABLE 2—*Comparison of analytical results with those of other investigators* [a/W = (A/D + W/D − 1)/(W/D)].

	$E'Bv/P$						
	Analytical Results Collocation Method		Newman (Ref 4)		Gregory (Ref 4)		Analytical Results Using Collocation Method for Standard Rectangular Compact Specimen Across Crack at Load Line
A/D	Across crack at load line	At crack mouth	Across crack at load line	At crack mouth	Across crack at load line	At crack mouth	
0.400	8.437	18.29	7.602	13.35	9.335	14.10	8.36
0.450	12.02	23.33	...	...	12.88	...	...
0.475	...	...	...	...	...	...	14.17
0.500	16.77	30.15	15.86	25.51	17.62	26.40	...
0.550	23.32	39.55	...	...	24.16	...	22.78
0.600	32.68	52.92	31.76	48.44	33.53	49.36	...
0.625	...	...	...	...	...	...	36.89
0.650	46.67	72.74	...	...	47.53	...	...
0.700	68.81	103.8	67.90	99.38	69.67	100.3	63.2
0.750	106.5	156.1	...	...	107.4	...	...
0.775	...	...	...	...	...	...	122.6
0.800	177.8	254.3	176.9	250.3	178.6	250.8	...
0.850	335.9	470.3	...	...	336.8	...	304.7
0.900	800.0	1099	...	...	801.1	...	...
0.950	3356	4536	...	...	3379	...	...

NOTE—$W/D = 0.750$

experimental displacement data sets (*a*) measured at the crack mouth, and (*b*) measured across the load line. The experimental influence coefficient values in Table 3 are then obtained using this fitting function for interpolation.

On comparing the load line experimental results with the present values, the percent variations ranged from −0.3 to +4.0 over the whole range of A/D ratios. At the crack mouth, the percent variation ranged from +2.3 to +6.8 over the whole range of A/D ratios. While the experimental specimen approached plane stress conditions, the specimen thickness was 2.73 cm and a thinner test specimen should reduce these variations.

It should be appreciated that there can be a limitation on the applicability of the present results to the practical pin loaded cracked disk. When the crack tip is very close to the load line (small A/D ratios), differences in displacement coefficient values can occur since there is a significant difference between the actual distribution of loading forces and that assumed in the model.

As described earlier, the influence coefficients of Table 2 and 3 were obtained by application of the superposition principle to those computed

TABLE 3—*Comparison of analytical results with those of other investigators* [a/W = (A/D + W/D − 1)/(W/D)].

	$E'Bv/P$					
	Experimental Results (Ref 2)		Analytical Results Collocation Method		Specimen Modeled with Loading Pin Hole (Ref 5)	
A/D	Across crack at load line	At crack mouth	Across crack at load line	At crack mouth	Across crack at load line	At crack mouth
0.400	7.91	17.03	7.89	17.89	...	...
0.407	8.34	17.65	...	...	7.90	17.54
0.450	11.17	21.61	11.35	22.78	...	...
0.482	13.72	25.14	...	...	13.51	25.32
0.500	15.46	27.57	15.94	29.46	...	...
0.550	21.38	36.06	22.28	38.69	...	...
0.556	22.18	37.22	...	...	22.45	38.29
0.600	30.07	48.75	31.34	51.83	...	...
0.630	37.28	59.26	...	...	37.95	60.72
0.650	43.50	68.24	44.91	71.33	...	...
0.700	65.11	98.92	66.39	101.9	...	...
0.704	67.18	101.8	...	...	67.72	103.2
0.750	101.7	149.7	103.0	153.5	...	...
0.778	133.6	193.7	...	...	134.8	197.5
0.800	169.5	243.0	172.3	250.3	...	...
0.850	319.0	448.8	326.2	463.4	...	...
0.852	327.7	460.9	...	...	334.6	474.6
0.900	760.2	1050	778.0	1083	...	...
0.950	...	...	3269	4477	...	...

NOTE—$W/D = 0.7407$

functions given in Table 1, with load line $L/D = 0.2407$ and 0.2500. The results of Table 1 are limited to an L/D maximum of 0.35 (Ref *1*). The lower bound on L/D for crack load line displacements depends on the length of the crack and the lower bound of z, which is 0.3; for example, $A/D = 0.40$ and $z = 0.30$, since $x = 0$, L/D minimum = 0.175, and for $A/D = 0.95$ and $z = 0.30$, since $x = 0$, L/D minimum = −0.21. Here the negative value indicates that L (Fig. 1) is measured to the right of the disk centerline.

Fitting functions for Γ_P and Γ_M, Table 4 (Ref *1*), were obtained by linear and nonlinear least squares best fit regression analyses, respectively. These functions are

$$\Gamma_M = 5.611 - 21.246\,\frac{A}{D} + 38.149\left(\frac{A}{D}\right)^2 - 32.169\left(\frac{A}{D}\right)^3 + 10.320\left(\frac{A}{D}\right)^4$$

and

$$\Gamma_P = 0.501 + \frac{0.02104[(A/D) - 0.525]}{[(A/D) - 0.525]\,[(A/D) - 0.0798] + 0.0625}$$

These functions are considered to be accurate to less than a percent of the computed solution in the range $0.40 < A/D < 1$. Clearly, the accuracy of application is dependent upon how well the assumed model boundary conditions approximate the real boundary conditions. Examples illustrating the use of these functions are given in Ref *1*. The limit values for Γ_P and Γ_M as $A/D \rightarrow 1$ were obtained from Ref *6*.

Summary and Conclusions

The solution obtained provides crack displacements and stress intensity coefficients for any combination of bending moment and normal forces acting on the round compact specimen. These combinations of loads are not restricted to a single load line to specimen diameter ratio. The loading of the specimen is characterized by the statically equivalent combination of resultant forces and moment chosen to act through the mid-net section. The advantage of this approach is that the influence coefficient and stress intensity coefficient for any reasonable load line location can be obtained efficiently by superposition of two complementary fictitious cases; namely, net section tension where the value of the moment is zero and net section bending where the value of the resultant normal force is zero.

On comparing the load line experimental influence coefficient results with the present values, very good agreement was obtained over the whole range of A/D ratios (0.40 to 0.95); thus, verifying the accuracy of the mathematical model. Comparison of the crack mouth experimental in-

TABLE 4—*Values of stress intensity coefficients* Γ_P *and* Γ_M *for the edge cracked disk.*

A/D	Γ_P	Γ_M
0.40	0.3857	1.4172
0.45	0.4538	1.2695
0.50	0.4901	1.1551
0.55	0.5090	1.0637
0.60	0.5184	0.9885
0.65	0.5228	0.9255
0.70	0.5246	0.8717
0.75	0.5251	0.8252
0.80	0.5251	0.7845
0.85	0.5249	0.7487
0.90	0.5242	0.7168
0.95	0.522	0.682
1.00[a]	0.521	0.663

[a] Limit values obtained from Ref *6*.

fluence coefficient results with the analytical results of this investigation showed good agreement over the whole range of A/D ratios. Comparisons of stress intensity coefficients with those of other investigators are given in Ref *1*.

Example

The results in Table 2 and 3 are for a round compact specimen with load P at load line location L (or equivalent location $x = 0$), $M_0 = 0$ and $\sigma_P = P/B(D - A)$ and $\sigma_M = 3P(2L + A)/B(D - A)^2$.

For the following geometry, where $L = D/4$ ($W/D = 0.75$) and $A/D = 0.55$, to obtain the displacement across the crack at the load line and at crack mouth, it follows that $W/D = 0.75$ and $zo = 0.75$.

From Eq 6 and Table 1

$$E'Bv/P = \frac{0.55(0.45)\Delta_P|_{zo} + 1.65(0.5 + 0.55)\Delta_M|_{zo}}{(1. - 0.55)^2}$$

$$\Delta_P|_{zo} = 1.10031 - 5.38109\,zo + 8.96387\,zo^2 - 9.41258\,zo^3 = -1.86426$$

$$\Delta_M|_{zo} = 0.30182 + 3.85332\,zo - 1.46881\,zo^2 + 1.48341\,zo^3 = 2.99142$$

Thus, at the load line $E'Bv/P = 23.315$.

To obtain the crack mouth influence coefficient, differentiating Eq 6 and evaluating the derivative at the load line one obtains

$$d(E'Bv/P)/dz|_{zo} = \frac{0.55(0.45)d\Delta_P/dz|_{zo} + 1.65(0.5 + 0.55)d\Delta_M/dz|_{zo}}{(0.45)^2} = 25.978$$

$$d\Delta_P/dz|_{zo} = -7.8190 \text{ and } d\Delta_M/dz|_{zo} = 4.1534$$

For this case $\delta z = 0.625$, and from Eq 8 one obtains the crack mouth influence coefficient.

$$E'Bv/P = 23.315 + 25.978\,(0.625) = 39.55$$

References

[*1*] Gross, B. in *Developments in Theoretical and Applied Mechanics*, Vol. 9, R. M. Hackett, Ed., Plenum, New York, pp. 195-203.

[2] Fisher, D. and Buzzard, R., proposed NASA Technical Memorandum.

[3] Gross, B. and Srawley, J. E., "Stress-Intensity Factors By Boundary Collocation for Single-Edge-Notch Specimens Subject To Splitting Forces," NASA TN D-3295, National Aeronautics and Space Administration, Washington, D.C., Feb. 1966.

[4] Gregory, R. D., "The Edge-Cracked Circular Disk Under Symmetric Pin-Loading," Technical Report No. 78-36, University of British Columbia, Vancouver, Canada, Oct. 1978.

[5] Newman, J. C., private communication from NASA Langley Research Center, Hampton, Va.

[6] Srawley, J. E. and Gross, B. in *Fracture Analysis, ASTM STP 560,* American Society for Testing and Materials, 1974, pp. 559-579.

T. W. Orange[1]

On the Equivalence Between Semi-Empirical Fracture Analyses and R-Curves

REFERENCE: Orange, T. W., **"On the Equivalence Between Semi-Empirical Fracture Analyses and R-Curves,"** *Fracture Mechanics: Twelfth Conference, ASTM STP 700,* American Society for Testing and Materials, 1980, pp. 478-499.

ABSTRACT: This paper examines the relationship between several semi-empirical fracture analyses (SEFA) and the R-curve concept of fracture mechanics. The conditions for equivalence between a SEFA and an R-curve are derived. A hypothetical (imaginary) material is employed to study the relationship analytically. Equivalent R-curves (ERC) are developed for real materials using data from the literature.

For each SEFA there is an ERC whose magnitude and shape are determined by the SEFA formulation and its empirical parameters. If the R-curve is indeed unique, then the various empirical parameters cannot be constant, and vice versa. However, for one SEFA the differences are small enough that they may be within the range of normal data scatter for real materials.

KEY WORDS: fracture properties, crack growth, resistance curves, residual strength, semiempirical analyses, crack propagation, fractures (materials)

Nomenclature

- a Length of single-tip crack or half-length of double-tip crack, equals $a_o + \Delta$
- E' Effective modulus, equals E for plane stress or $E/(1 - \nu^2)$ for plane strain, where E is Young's modulus and ν is Poisson's ratio
- G_A Strain energy release rate
- G_R Crack extension resistance
- G_c Strain energy release rate or crack extension resistance at instability
- K_I Opening-mode stress intensity factor
- n Number of crack tips (one or two)

[1] Research engineer, National Aeronautics and Space Administration-Lewis Research Center, Cleveland, Ohio 44135.

W Specimen width
Y Stress intensity calibration factor, $K_I/\sigma\sqrt{a}$, a dimensionless function of λ
α Sensitivity factor, Eq 1
Δ Effective crack extension (sum of physical crack extension plus a plastic zone correction)
λ Relative crack length, na/W
σ Stress normal to crack
σ_u Ultimate tensile strength
σ_{ys} Yield strength
$_c$ At critical or instability condition
$_o$ Original value prior to loading

This paper examines the relationships between several semi-empirical fracture analyses (SEFA) and the R-curve concept of fracture mechanics. These relationships may explain why a semi-empirical fracture analysis will yield good results with one set of data and poor results with another. They may also indicate which analyses deserve further consideration.

Over the past decade a number of SEFA have been presented [*1-5*].[2] These analyses all attempt to correlate failure stresses for precracked tension specimens with initial crack length over a range of crack lengths. The correlations involve the determination of one [*1-3*] or two [*4,5*] empirical parameters from test data. The parameters are treated as material properties, which are independent of the specimen and crack configuration but which are functions of specimen thickness and such variables as heat treatment and test temperature. The analyses do not always provide good correlations using data sets other than those chosen by the original authors. To date these analyses have only been formulated for and applied to test specimen configurations. Thus their applicability to the design of complex structural configurations is uncertain.

The progressive development of the R-curve concept has been reviewed in Ref *6*. The concept postulates that, for a given material and thickness, there is a unique relationship between the amount of stable crack growth under rising load and the crack-tip stress intensity factor. This relationship is called the crack-extension resistance curve, or R-curve, and represents the response of the material in the vicinity of the crack tip to externally imposed loading. If the R-curve is known, both failure load and critical crack length can be predicted (as functions of initial crack length) for any specimen or structural configuration for which an appropriate stress intensity analysis is available. Thus, the R-curve concept appears to be a more useful method than any of the semi-empirical analyses.

If the R-curve for a given material and thickness is available, one can

[2]The italic numbers in brackets refer to the list of references appended to this paper.

calculate fracture stress as a function of original crack length for any test specimen configuration. The converse should also be true. That is, if a relationship between fracture stress and original crack length is available, one should be able to calculate the corresponding R-curve. This observation was the impetus for the present study, which was undertaken to test the following hypotheses:

1. For each SEFA there is an equivalent R-curve (ERC) whose magnitude and shape are determined by the SEFA formulation and its empirical parameters. The ERC is equivalent in that it predicts exactly the same relationship between fracture stress and original crack length as the SEFA.

2. A SEFA will correlate residual strength data (fracture stress against original crack length) closely if its ERC closely matches the actual R-curve of the material in question, and will correlate poorly if the match is poor.

This paper first reviews some characteristics of the R-curve concept when applied to finite-width specimens. Next the conditions for equivalence between a semi-empirical analysis and an R-curve are derived. A hypothetical material is employed to study the relationship between R-curves and semi-empirical analyses. Finally, equivalent R-curves are developed for real materials using data from the literature.

R-Curve Concept

The R-curve concept and its historical development are reviewed in Ref *6*. A general representation of the concept is shown in Fig. 1*a*. The strain energy release rate is given by the expression

$$G_A = Y^2\sigma^2 a/E'$$

and represents the driving force (per unit thickness) tending to cause crack propagation. The material's resistance to crack propagation, G_R, is a function of crack extension, Δ. At the critical stress σ_c the driving force curve and the R-curve are tangent. Beyond the point of tangency the driving force increases faster with crack length than does the material's resistance. This instability condition represents the failure of the body. The point of tangency defines the fracture toughness, G_c, and the critical crack length, $2\,a_c$. For an infinite body, Y is a constant and the driving force curve is a straight line. Thus, both the fracture toughness, G_c, and the amount of crack extension at instability, Δ_c, increase with increasing original crack length.

For cracks in simple finite bodies and test specimens, the trends are somewhat different. If one defines a dimensionless sensitivity factor as

$$\alpha \equiv \frac{\lambda}{Y}\frac{dY}{d\lambda} \tag{1}$$

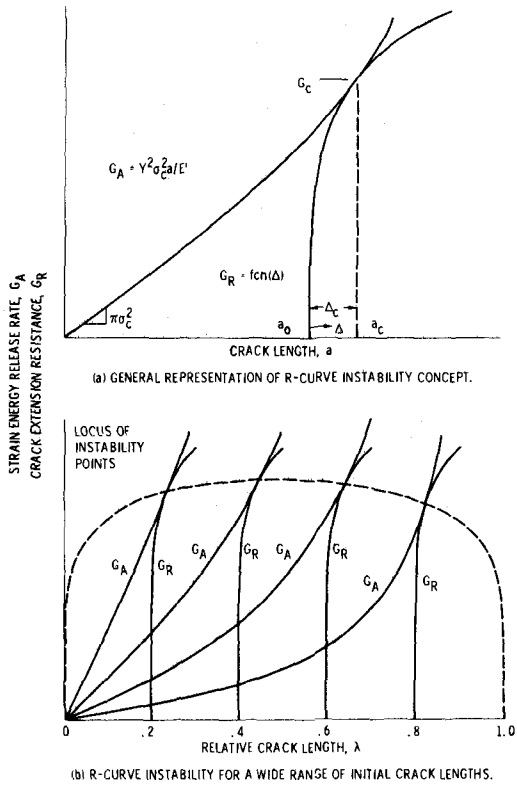

FIG. 1—*R-curve instability concepts.*

then the crack driving force curve and its slope (for constant stress) are

$$E'G_A = Y^2\sigma^2 a$$

$$E'\frac{dG_A}{da} = Y^2\sigma^2(1 + 2\alpha)$$

For convenience, the crack extension resistance curve and its slope are written here as

$$g(\Delta) \equiv E'G_R$$

$$g'(\Delta) \equiv E'dG_R/d\Delta$$

At the instability point, $G_A = G_R$ and $dG_A/da = dG_R/d\Delta$ (see Fig. 1*a*). If

$g(\Delta)$ and $g'(\Delta)$ are mathematically describable, the instability point is determined by the simultaneous solution of two equations

$$E'G_c = Y_c^2 \sigma_c^2 (a_o + \Delta_c) = g(\Delta_c) \tag{2}$$

$$E' \frac{dG_A}{da}\bigg|_{a_c} = Y_c^2 \sigma_c^2 (1 + 2\alpha_c) = g'(\Delta_c) \tag{3}$$

The coefficients Y and α are usually expressed as trigonometric or polynomial functions of the relative crack length λ. As a result, a closed-form simultaneous solution is seldom possible, and numerical methods must be used to solve for Δ_c. Then $G_c = g(\Delta_c)/E'$ and the fracture stress σ_c is determined from Eq 2.

As the initial crack length is increased from zero, both G_c and Δ_c increase. However, due to the fact that $dY/d\lambda$ continually increases with λ, both G_c and Δ_c reach maximum values, which depend on the specimen width, W, and the forms of both the driving force curve and the R-curve. As a_o is increased still further, both G_c and Δ_c begin to decrease. This behavior is shown schematically in Fig. 1*b* where instability curves are shown for a wide range of initial crack lengths. The locus of all instability points is shown by the dotted line. From Fig. 1*b* it is also apparent that there are pairs of original crack lengths, say $(a_o)_1 = 0.2\ W$ and $(a_o)_2 \approx 0.7\ W$, which will have the same critical crack extension, $(\Delta_c)_{1,2}$, and fracture toughness, $(G_c)_{1,2}$. From Eq 2, the fracture stresses for these original crack lengths are related by

$$\frac{(\sigma_c)_2}{(\sigma_c)_1} = \frac{(Y_c)_1}{(Y_c)_2} \sqrt{\frac{(a_o)_1 + (\Delta_c)_{1,2}}{(a_o)_2 + (\Delta_c)_{1,2}}}$$

Thus, there is a relationship between fracture stresses for short cracks and long cracks that is implicit in the R-curve concept, and this relationship is a function of the specimen type and the shape of the R-curve.

It should be noted that, in this paper, Δ is the "effective" crack extension. It is the sum of the physical crack extension plus an adjustment to account for the effect of crack-tip plasticity.

Equivalency Analysis

In the preceding section it was shown that, if a mathematical formulation of the R-curve is available, fracture stress can be determined as a function of original crack length. In this section it will be shown that, if an equation for fracture stress as a function of original crack length is available, the equiv-

alent R-curve can be determined. In this paper, only the case where specimen width, W, is constant is considered. Parallel derivations for the cases where a_o is constant and where a_o/W is constant are given in Ref 7, which contains a more complete treatment of this same subject.

Differentiating both sides of Eq 2 with respect to Δ_c

$$\frac{d}{d\Delta_c} EG_c = Y_c^2 \sigma_c^2 \cdot 2\alpha_c \left[\frac{da_o}{d\Delta_c} + 1\right] + Y_c^2 (a_o + \Delta_c)$$

$$\times \frac{d}{d\Delta_c} (\sigma_c)^2 + Y_c^2 \sigma_c^2 \left[\frac{da_o}{d\Delta_c} + 1\right] \equiv g'(\Delta_c)$$

and substituting Eq 3, results in

$$0 = \sigma_c^2 \left[(1 + 2\alpha_c) \frac{da_o}{d\Delta_c}\right] + (a_o + \Delta_c) \frac{d}{d\Delta_c} (\sigma_c^2) \tag{4}$$

Assume that there is a function, f, such that one can define

$$\left.\begin{aligned} f(a_o) &\equiv \sigma_c^2 \\ f'(a_o) &\equiv d(\sigma_c^2)/da_o \end{aligned}\right\} \text{for } W = \text{constant}$$

Then Eq 4 becomes

$$0 = \frac{da_o}{d\Delta_c} \left[(1 + 2\alpha_c) f(a_o) + (a_o + \Delta_c) f'(a_o)\right]$$

and since $da_o/d\Delta_c \neq 0$, one has

$$0 = (1 + 2\alpha_c) f(a_o) + (a_o + \Delta_c) f'(a_o) \tag{5}$$

For cracks in infinite bodies, $\alpha = 0$ and Eq 5 becomes

$$\Delta_c = \frac{f(a_o)}{-f'(a_o)} - a_o \tag{6}$$

which, after substituting the infinite-body formulations for $f(a_o)$ and $f'(a_o)$ from the Appendix, gives Δ_c for any a_o in terms of the empirical parameters. Then terms can be rearranged to give a_o as a function of Δ_c, say

$$a_o = F(\Delta_c)$$

Substituting this function into Eq 2 yields

$$E'G_c = Y_c^2[F(\Delta_c) + \Delta_c] \cdot f[F(\Delta_c)] \tag{7}$$

Since Eq 6 gives Δ_c for any value of a_o, Eq 7 must give $E'G_c$ for any and all values of Δ_c, which is a definition of the R-curve. Thus, after writing the function F in terms of the empirical parameters, it is appropriate to write Eq 7 in the general terms of $E'G_R$ and Δ, rather than $E'G_c$ and Δ_c. The end result is an explicit ERC formulation in terms of the empirical parameters.

To determine the ERC for cracks in finite bodies, an indirect method is required. First, the finite-body formulations for $f(a_o)$ and $f'(a_o)$ from the Appendix are substituted into Eq 5. Because of the more complicated nature of the finite-body formulations, it is unlikely that an explicit function $F(\Delta_c)$ will be obtainable. But for any given value of Δ_c, a_o is a root of Eq 5, which may be found by standard numerical methods and which represents a single value of $F(\Delta_c)$. Substituting this value into Eq 7 yields a discrete point on the ERC. By incrementing Δ_c and repeating the calculation, the ERC can be determined point by point.

Analytical Comparisons

Dimensionless Equivalent R-Curves

It is helpful and more efficient to first compare SEFA and ERC on an analytical basis. This is most easily done using the problem of a crack in an infinite plate as a baseline.

The infinite-body ERC for Kuhn's analysis [*1*] is obtained using the method described in the paragraph containing Eqs 6 and 7. Substituting Eqs 21 and 22 from the Appendix into Eqs 6 and 7 with $Y_c^2 = \pi$ yields

$$\Delta_c = \sqrt{a_o}/C_m \tag{8}$$

$$E'G_R = \frac{\pi\sigma_u^2\Delta}{1 + C_m^2\Delta} \tag{9}$$

where C_m is an empirical parameter having units ($L^{-1/2}$). Equation 9 is plotted in dimensionless form in Fig. 2*a*. This curve obviously resembles an R-curve and might be expected to closely match some (but not all) experimental R-curves.

The infinite-body ERC for Orange's analysis [*2*] is obtained in the same manner. Using Eqs 23 and 24 (Appendix) results in

$$\Delta_c = (K_u/\sigma_u)^2/\pi \tag{10}$$

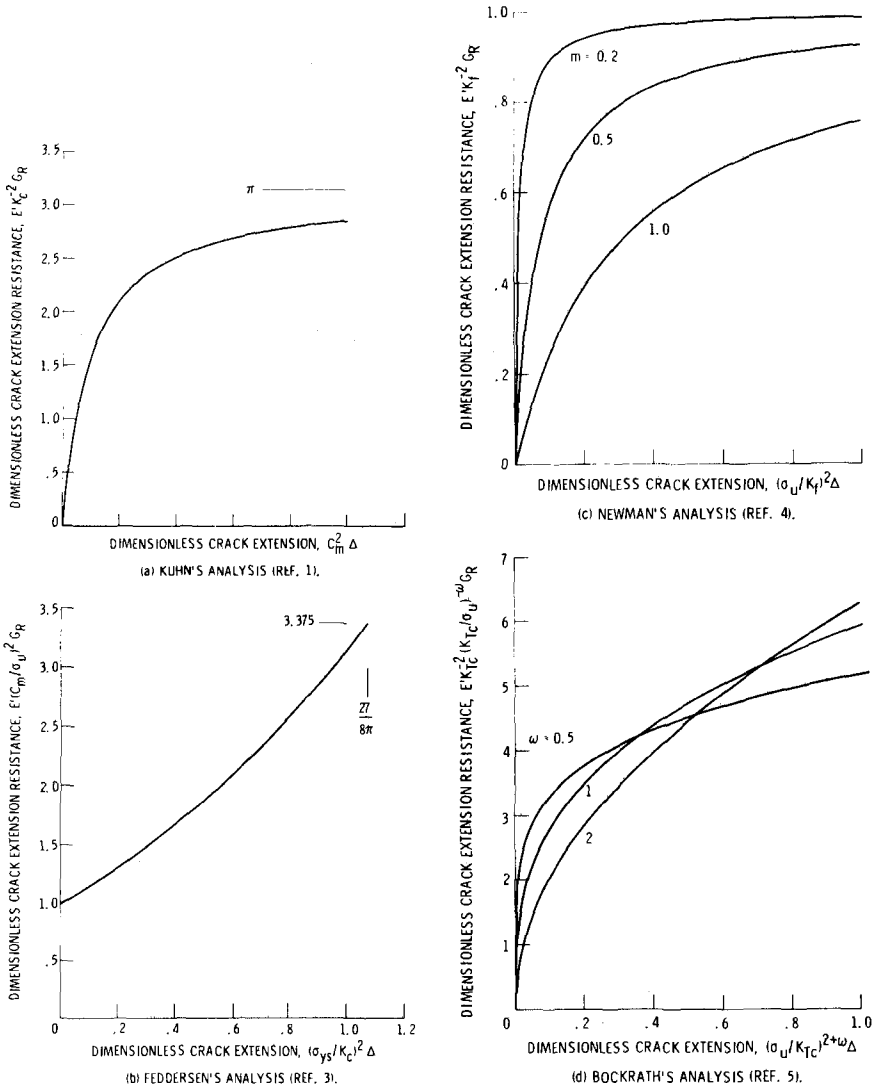

FIG. 2—*Dimensionless R-curves equivalent to various semi-empirical fracture analyses for a crack in an infinite plate.*

$$E' G_R = K_u^2 \tag{11}$$

where K_u is an empirical parameter having units $(FL^{-3/2})$. These equations define a single point. In order to relate this single point to the R-curve concept, the point may be thought of as the corner of a step-function, and that step-function might in turn be considered as a very simple approximation of an actual R-curve.

The infinite-body ERC for Feddersen's analysis [3] is obtained by substituting Eqs 25 and 26 (Appendix) into Eqs 6 and 7 as before, yielding

$$\Delta_c = \frac{27}{8\pi} \left(\frac{K_c}{\sigma_{ys}}\right)^2 - \frac{3}{2} a_o \tag{12}$$

$$E' G_R = K_c^2 \left\{1 + \left[\frac{4\pi}{9} \left(\frac{\sigma_{ys}}{K_c}\right)^2 \Delta\right] + \frac{1}{3}\left[\frac{4\pi}{9} \left(\frac{\sigma_{ys}}{K_c}\right)^2 \Delta\right]^2 + \frac{1}{27}\left[\frac{4\pi}{9} \left(\frac{\sigma_{ys}}{K_c}\right)^2 \Delta\right]^3\right\} \tag{13}$$

for $a_o \leq (9/4\pi)(K_c/\sigma_{ys})^2$ where K_c is an empirical parameter having units $(FL^{-3/2})$. Equation 12 requires that critical crack extension decrease as original crack length increases from zero. This is in direct opposition to the R-curve concept and is not supported by any data known to this author. Equation 13, which is plotted in Fig. 2*b*, does not look at all like an R-curve but does satisfy the requirements of coincidence and tangency. For $a_o = 0$, the point of tangency is the right-hand terminus of the curve. As a_o increases, the point of tangency moves downward and leftward along the curve. Finally, at $a_o = (9/4\pi)(K_c/\sigma_{ys})^2$, the point of tangency is the left-hand terminus.

The infinite-body ERC for Newman's analysis [4] is obtained by substituting Eqs 31 and 32 (Appendix) into Eqs 6 and 7 as before, yielding

$$\Delta_c = \frac{mK_f}{\sigma_u} \sqrt{\frac{a_o}{\pi}} \tag{14}$$

$$E' G_R = \frac{\sigma_u^2 \Delta}{m^2/\pi + (\sigma_u/K_f)^2 \Delta} \tag{15}$$

where K_f is an empirical parameter having units $(FL^{-3/2})$ and m is a dimensionless empirical coefficient which is not greater than unity. Equation 15 is plotted in dimensionless form in Fig. 2*c*. This ERC is asymptotic to $E' G_R = K_f^2$, and the coefficient m determines the rapidity of the approach. As m decreases from unity to near-zero, the ERC develops a progressively sharper

knee. The flexibility of this two-parameter ERC should allow it to match R-curves for a wide range of real materials.

The infinite-body ERC for Bockrath's analysis [5] is obtained by substituting Eqs 33 and 34 (Appendix) into Eqs 6 and 7 as before, resulting in

$$\Delta_c = (\omega/2)a_o \tag{16}$$

$$E'G_R = \frac{\pi}{2}(2+\omega)K_{Tc}^2\left(\frac{2}{\omega}\Delta\right)^{\omega/(2+\omega)} \tag{17}$$

where

ω = a dimensionless empirical coefficient, and
K_{Tc} = an empirical parameter having irrational units (FL^{ω}).

Equation 17 is plotted in Fig. 2*d*. This ERC has no asymptote, and its slope is infinite at $\Delta = 0$. Except for notation, it is identical to the R-curve model proposed by Broek (Ref *8*, Eq 10). Broek's model was derived using R-curve concepts and the experimental observation that for small cracks in wide specimens, the critical crack length is often proportional to the initial crack length.

At this point we can state the following. For each SEFA, in its infinite-body form at least, there is indeed an ERC. For four of the analyses considered, the ERC resembles or approximates an actual R-curve. The ERC for Feddersen's analysis [*9*] does not resemble an R-curve and will not be considered further.

Comparisons Using Synthetic Data

Hypothesis (2), introduced earlier in this paper, postulates that a SEFA will correlate residual strength data closely if its ERC closely matches the actual R-curve and will correlate poorly if the match is poor. To test this hypothesis one would need, as a minimum, both residual strength data (for several specimen sizes having a wide range of crack lengths) and R-curve data for two materials having significantly different R-curve shapes. Since no such body of data is known to this author, it was necessary to synthesize one. This was done by formulating two R-curve equations using the following guidelines. First, to avoid exact fits, neither equation should be mathematically equivalent to one of the ERC formulations previously derived. Second, one R-curve should have a definite knee, the other should be gently curving. Using these equations, synthetic test data can be generated by instability analysis for any specimen size and type. An advantage of this approach is the total absence of data scatter.

"Unobtainium" is assumed to be a heat-treatable material. Since the material is imaginary, the units will be left to the reader's imagination. In the

annealed condition, its ultimate tensile strength is 150 and its R-curve is given by

$$E'G_R = 8000\ \sqrt{10\Delta - \Delta^2} \tag{18}$$

In the aged condition, its ultimate tensile strength is 200 and its R-curve is given by

$$E'G_R = \frac{50\ 000}{\pi} \arctan(10\Delta) \tag{19}$$

These are shown in Fig. 3. The coefficients in Eqs 18 and 19 were selected so that the significant features of both curves would lie within the ranges $0 \leq E'G_R \leq 25\ 000$ and $0 \leq \Delta \leq 1$.

The pseudo-test data points are calculated using conventional instability analysis as follows. Dividing Eq 2 by Eq 3 and rearranging terms gives

$$0 = \frac{g(\Delta_c)}{g'(\Delta_c)} - \frac{a_o + \Delta_c}{1 + 2\alpha_c} \tag{20}$$

The functions $g(\Delta_c)$ and $g'(\Delta_c)$ are given by either Eq 18 or 19 and their derivative. The factor α_c is determined using Eq 1 and the secant stress intensity calibration factor for uniformly-loaded center-crack specimens [9].

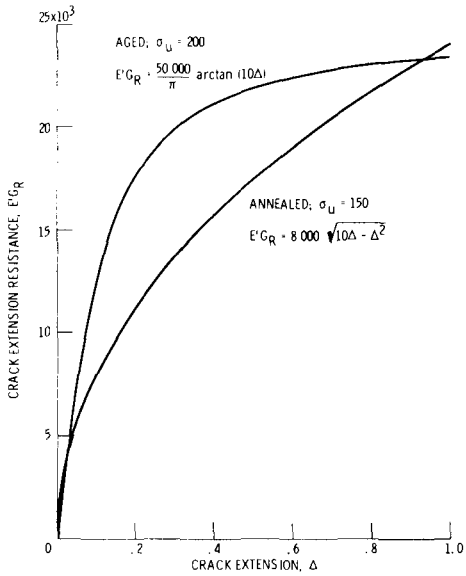

FIG. 3—*R-curves for hypothetical material "unobtainium."*

Then, for prescribed values of a_o and W, Δ_c is the least positive root of Eq 20. This root can be found by any of several numerical methods. Next, Δ_c is substituted back into Eq 18 or 19 to calculate $E' G_c$. Finally, the fracture stress σ_c is obtained from Eq 2.

The "specimens" that are studied here were sized as follows. For the infinite-width pseudo-tests, the initial crack half-lengths a_o were chosen (by trial and error) to give Δ_c-values, well distributed over the entire R-curve. For the finite-width pseudo-tests, the specimen widths were fixed at eight times (first series) and four times (second series) the largest initial crack half-length in the infinite-width series. The calculated values of stress and crack extension at instability are given in Table 1. The values of stress and initial crack length were then used as inputs to the various semi-empirical analyses.

The empirical parameters were determined as follows. Kuhn's parameter [*1*] C_m was calculated for each specimen in the infinite-width series using Eq 21. The simple average of seven values, $\overline{C_m}$, is given in Table 1. The bar is used here to denote the average value for one data set. Orange's parameter [*2*], K_u, was also calculated for each specimen in the infinite-width series using Eq 23. The average value $\overline{K_u}$ given in Table 1 is a weighted average determined in the same manner as that of Ref *2*, Eq 6. Newman's parameters [*4*] $\overline{K_f}$ and $\overline{m}$ were determined using the least-squares procedure given in Ref *4*, Appendix C. Bockrath's parameters [*5*] $\overline{K_{Tc}}$ and $\overline{\omega}$ were determined by a least-squares fit of Eq 33 (Appendix). Since Bockrath's method is restricted to cases where the crack area is less than 10 percent of the gross area, specimens having $a_o > W/20$ were excluded from the least-squares fit.

The equivalent R-curves were calculated as follows. For the infinite-width series, the empirical parameters from Table 1 were simply substituted into the appropriate one of Eqs 9, 11, 15, or 17. For the finite-width series, the indirect method (described in the paragraph containing Eq 7) was used. Specifically, Eqs 29 and 30 or Eqs 33 and 34 (Appendix) were used along with Eqs 5 and 7 and the appropriate empirical parameters.

The residual strength of the infinite-width "unobtainium" is shown in Fig. 4. For the annealed condition, Bockrath's SEFA provides a nearly perfect fit to the pseudo-data. When ranked according to the sum of the squares of deviations, Newman's SEFA, Kuhn's, and Orange's follow in that order. For the aged condition, the ranking is quite different. Here Newman's SEFA provides a nearly perfect fit, with Orange's, Kuhn's, and Bockrath's following in that order. The equivalent R-curves (ERC) are shown in Fig. 5. For the annealed condition, the Bockrath ERC matches the actual R-curve almost perfectly. When ranked according to the integral of the square of the deviation, the Newman ERC, the Kuhn ERC, and the Orange ERC follow in that order. For the aged condition, the Newman ERC is the best match to the actual R-curve; the Bockrath ERC, the Kuhn ERC, and the Orange ERC follow in that order. The Orange ERC, although crude, is a better approximation for the aged material than for the annealed.

TABLE 1—*Pseudo-test data for hypothetical material "unobtainium" and fitted empirical parameters.*

	$W = \infty$		$W = 8.8$		$W = 4.4$	
a_o	Δ_c	σ_c	Δ_c	σ_c	Δ_c	σ_c
0.10	0.0980	112.56	0.0971	112.42	0.0945	112.00
0.21	0.2015	93.25	0.1939	92.75	0.1757	91.36
0.32	0.3008	83.70	0.2773	82.71	0.2313	80.08
0.44	0.4044	77.08	0.3529	75.43	0.2692	71.29
0.56	0.5036	72.36	0.4137	69.98	0.2901	64.26
0.80	0.6897	65.82	0.4996	61.79	0.2986	52.84
1.10	0.9016	60.36	0.5580	54.09	0.2713	41.02
$\overline{C_m}$	1.355		not computed			
$\overline{K_u}$	111.8					
$\overline{K_{Tc}}$	62.13		60.76		59.52	
$\overline{\omega}$	1.853		1.727		1.642	
$\overline{K_f}$	165.7		172.8		159.6	
$\overline{m}$	0.8549		0.8497		0.7800	

NOTE—Annealed Condition; $\sigma_u = 150$.

	W = ∞		$W = 96$		$W = 48$	
a_o	Δ_c	σ_c	Δ_c	σ_c	Δ_c	σ_c
0.05	0.0953	162.93	0.0953	162.93	0.0953	162.92
0.36	0.2014	100.08	0.2014	100.07	0.2013	100.05
1.0	0.3067	69.77	0.3064	69.74	0.3055	69.64
2.0	0.4135	52.91	0.4121	52.82	0.4081	52.58
3.2	0.5093	43.37	0.5054	43.21	0.4942	42.73
6.4	0.6978	31.93	0.6791	31.50	0.6286	30.21
12.0	0.9346	23.95	0.8566	22.87	0.6760	19.60
$\overline{C_m}$	1.820		not computed			
$\overline{K_u}$	140.7					
$\overline{K_{Tc}}$	63.80		66.57		68.38	
$\overline{\omega}$	0.838		1.151		1.310	
$\overline{K_f}$	163.3		166.0		168.4	
$\overline{m}$	0.7266		0.7378		0.7469	

NOTE—Aged Condition; $\sigma_u = 200$.

Since the Orange ERC is rather crude and since Kuhn's SEFA is equivalent to a special case of Newman's (see Appendix, following Eq 32), these two were not considered further. The Newman and Bockrath ERCs for the finite-width center-crack series are shown in Figs. 6 and 7. Here the same trends are seen as in the infinite-width series. The Bockrath ERC is the better match for the annealed condition, while the Newman ERC is the better match for the aged condition. Note in Table 1 that the empirical parameters $\overline{K_{Tc}}$, $\overline{\omega}$, $\overline{K_f}$, and $\overline{m}$ all vary slightly with specimen width. The ERCs shown in

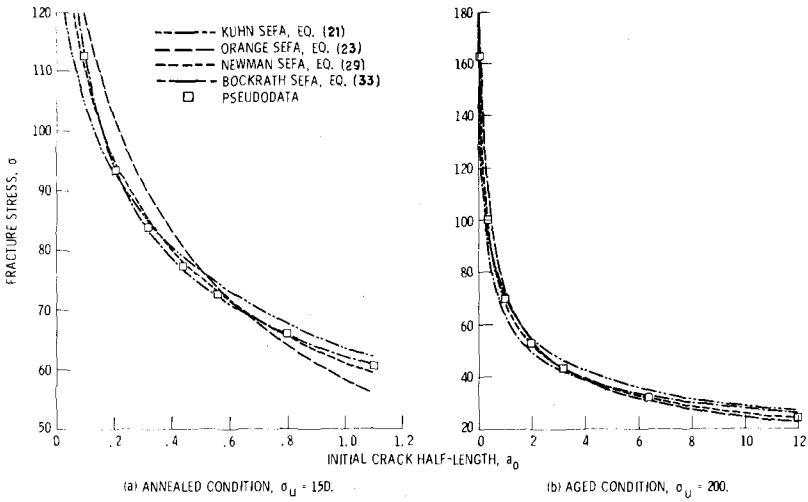

FIG. 4—*Residual strength of hypothetical material "unobtainium," infinite-width series; various SEFA fit to pseudo-test data.*

Figs. 5 through 7 are also distinctly different for different specimen widths, but the differences are slight.

The results of this exercise using synthetic data can be summarized as follows. Hypothesis (2), presented at the opening of this discussion, postulates that an SEFA will correlate residual strength data closely if its ERC closely matches the actual R-curve and will correlate poorly if the match is poor. Strictly speaking, this hypothesis cannot be proven, since the ERC magnitude and shape depend on empirical parameters that must be obtained from residual strength data. However, the converse appears to be true. That is, if a SEFA correlates residual strength data closely, its ERC will closely match the actual R-curve. Furthermore, it is apparent that if for a given material and thickness the R-curve is unique, the various empirical parameters are not, and vice versa.

Comparisons Using Actual Test Data

As mentioned earlier, experimental studies containing both residual strength and actual R-curve data are relatively few in number. Nevertheless, enough were found in the literature to allow some comparisons to be made using actual data obtained from real materials.

NASA Data for 2014-T6 Aluminum Alloy

In Ref. *10* this author presented test data for 2014-T6 aluminum alloy specimens 1.5-mm (0.06-in.) thick, tested at 77 K (−320°F). Figure 14 of

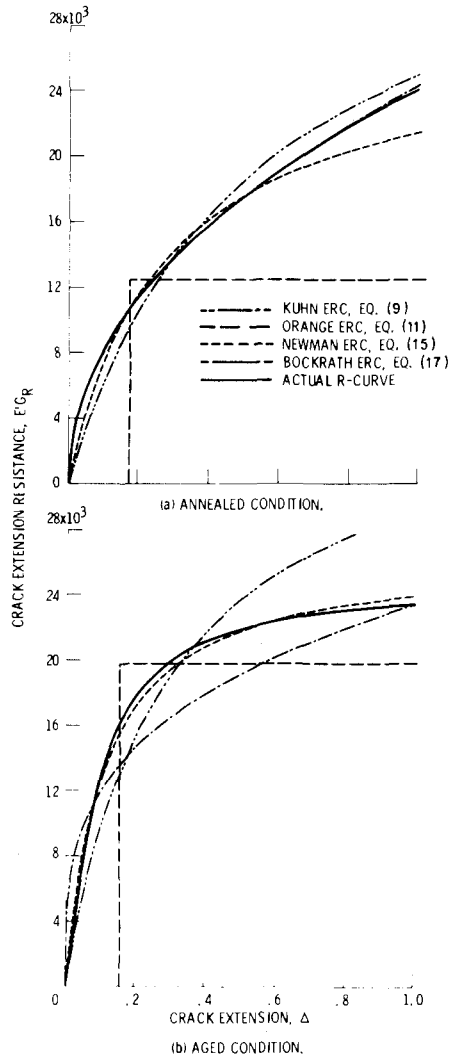

FIG. 5—*Actual R-curves and ERCs for hypothetical material "unobtainium," infinite-width series.*

that reference presented typical curves of crack growth against applied stress for notches of six initial lengths in 30-cm (12-in.) wide specimens. Those curves were developed by plotting individual crack growth data points for replicate specimens, then drawing a smooth curve to give a good visual average. For the present report, those data were reanalyzed. The crack extension resistance and effective crack length were computed for each data point as

$$E'G_R = \sigma^2 \pi a_{\text{eff}} \text{ secant } (\pi a_{\text{eff}}/W)$$

$$a_{\text{eff}} = a + (E'G_R/2\pi\sigma_{ys}^2)$$

respectively. Since these equations are transcendental, an iterative solution was required. A total of 176 data points were obtained from 17 specimens with initial crack lengths ($2a_o$) ranging from 3 to 100 mm (1/8 to 4 in.). The empirical parameters for the Newman and Bockrath SEFAs were determined in the manner described earlier. As before, only specimens with $a_o \leq W/20$ were included in the Bockrath analysis. The fitted empirical parameters are listed in Table 2.

Residual strength is shown in Fig. 8*a*. Newman's SEFA gives a good fit over the entire range. Bockrath's SEFA fits the short-crack data fairly well, but the fit would be poor if extrapolated to longer cracks. The R-curve data points and the equivalent R-curves are shown in Fig. 8*b*. Both ERCs fit the data rather well, with Bockrath's somewhat better at small crack extensions and Newman's somewhat better for larger extensions. These results suggest that the ERC concept applies to real data as well as to synthesized data.

Boeing Data for 2219-T87 Aluminum Alloy

Earlier it was shown using synthetic data that, if the actual R-curve is unique, one obtains slightly different values of the empirical parameters from data sets for specimens having different widths. Data from the Boeing Company for 2219-T87 aluminum alloy specimens have the same charac-

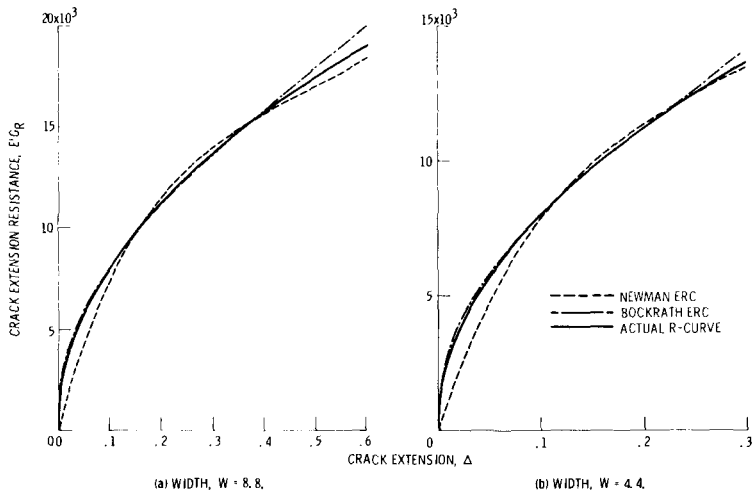

FIG. 6—*Actual R-curve and ERCs for hypothetical material "unobtainium," finite-width, annealed condition.*

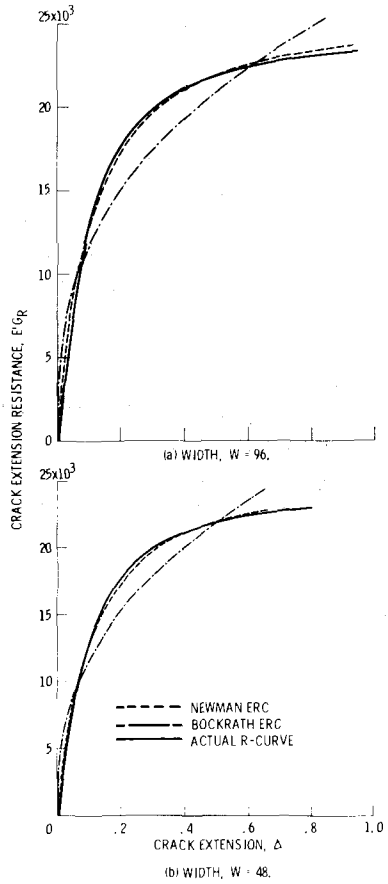

FIG. 7—*Actual R-curve and ERCs for hypothetical material "unobtainium," finite width, aged condition.*

teristics. These data originally appeared in an internal report [*11*] but are also tabulated in Ref *1*. Center-crack specimens 2.5-mm (0.10-in.) thick were tested. The data for specimens 60 and 120 cm (24 and 48 in.) wide are used here because they cover a wide range of initial crack lengths.

Bockrath's analysis was not applied since only one of the wider specimens had $a_o \leq W/20$. Newman's parameters were determined separately for each specimen width, and somewhat different values were obtained as can be seen in Table 2. The residual strength curves fit the data quite well, as can be seen in Fig. 9*a*, with the average error being less than 3½ percent. Using a method that is outside the scope of this paper, it was found that the actual R-curve for this material could be estimated by

$$E'G_R = 8.07 \times 10^{15}\,\Delta^{0.554}$$

TABLE 2—*Empirical parameters for test data from the literature.*

Data Source	Alloy	Specimen Constant, (cm)	Empirical Parameters, Ref 4			Empirical Parameters, Ref 5[a]		
			$\overline{K_f}$			$\overline{K_{Tc}}$		$\bar{\omega}$
			MN $m^{-3/2}$	ksi $\sqrt{in}$	$\overline{m}$	SI Units	English Units	
10	2014-T6	$W = 30$	89.9	81.8	0.8094	99.70 MN $m^{-1.761}$	34 790 lb $in^{-1.761}$	2.188
		$W = 60$	183.1	166.6	0.8841			
1	2219-T87	$W = 120$	210.2	191.3	1.0	not computed		

[a] Only specimens having $a_o \leq W/20$ were included in least squares fit.

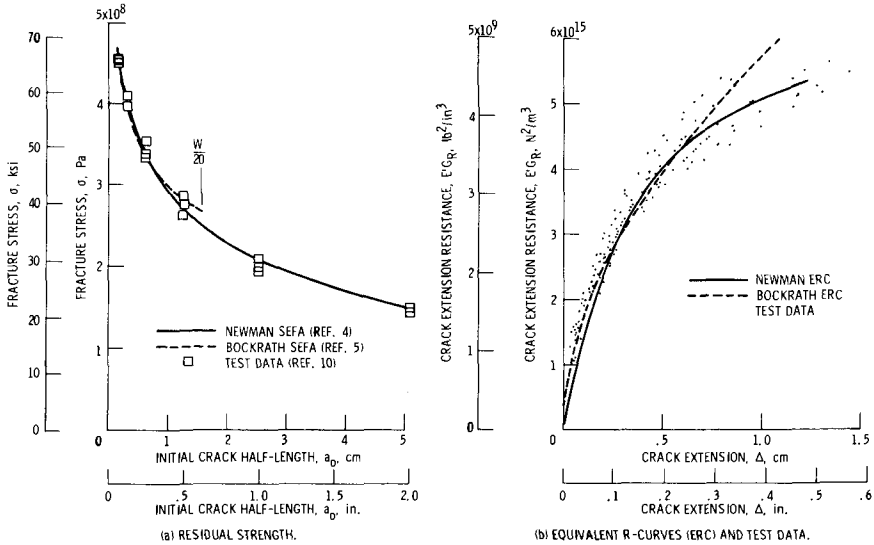

FIG. 8—*Residual strength, ERCs, and R-curve data points for 2014-T6 aluminum alloy sheet at 77 K (Ref* 10).

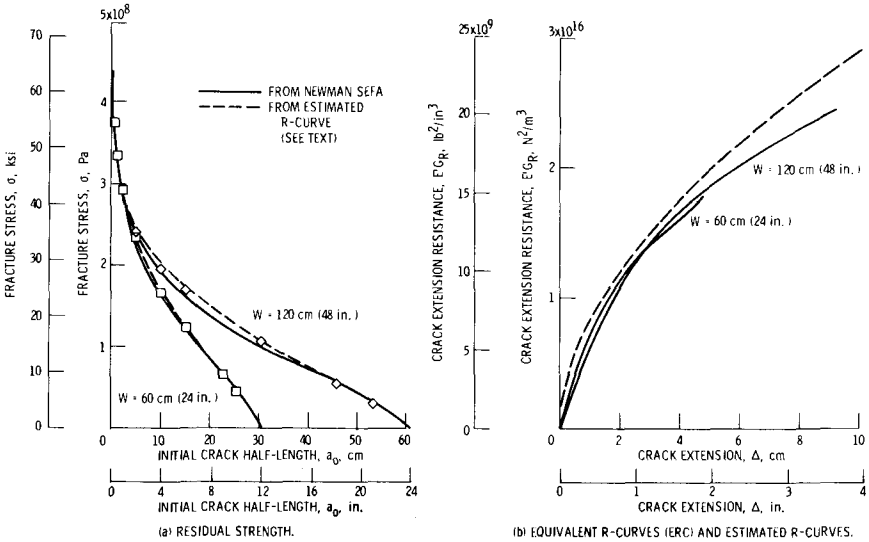

FIG. 9—*Residual strength, ERCs, and estimated R-curve for 2219-T87 aluminum alloy sheet (Ref* 1).

where $E'G_R$ is in Newtons squared per cubic metres, and Δ is in centimetres, or by

$$E'G_R = 11.2 \times 10^9 \Delta^{0.554}$$

where $E'G_R$ is in pounds squared per cubic inches, and Δ is in inches. Residual strengths calculated from this equation using conventional instability analysis are also shown in Fig. 9*a*. The agreement is very slightly better than for Newman's SEFA, the average error being less than 3 percent. The estimated R-curve and the Newman ERCs are shown in Fig. 9*b*, and as expected the differences are small. Although these data tend to support the concept of a unique R-curve, the differences are so small as to be within the bounds of probable data scatter.

Concluding Remarks

The results of this study lead to the following conclusions:

1. For each SEFA there is an ERC whose magnitude and shape are determined by the SEFA formulation and its empirical parameters. The ERC is equivalent in that it predicts exactly the same relationship between fracture stress and initial crack length (residual strength) as the SEFA.
2. If, for a given set of data, a SEFA correlates residual strength closely, its ERC will closely approximate the effective R-curve of the test material.
3. Of the five SEFAs examined, Newman's [*4*] appears to be the most generally useful. Bockrath's SEFA [*5*], which is only formulated for quasi-infinite bodies, is too restrictive for widespread use. Three references, namely *1* through *3*, do not appear to warrant further consideration.
4. If the effective R-curve is indeed unique, then the various empirical parameters cannot be constant, and vice versa.

The analytical comparisons made herein indicate that the variations in Newman's parameters are small enough that the differences may well be within the range of normal data scatter for real materials. Thus, a very carefully planned and conducted experiment would be required to determine which concept (R-curve or SEFA) is more appropriate.

APPENDIX

Semi-Empirical Fracture Analyses

Paul Kuhn (1968)

Equations 3 and 4 of Ref *1* give the fracture stress for a finite-width center-crack plate. For an infinite plate, these may be rewritten and differentiated as

$$f(a_o) = \sigma_u{}^2 [1 + C_m \sqrt{a_o}]^{-2} \tag{21}$$

$$f'(a_o) = -f(a_o) \cdot (1 + C_m \sqrt{a_o})^{-1} \cdot C_m/\sqrt{a_o} \tag{22}$$

where C_m is an empirical parameter having units $(L^{-1/2})$.

T. W. Orange (1969)

Equation 8 of Ref *2* gives the fracture stress for a finite-width center-crack plate. For an infinite plate, this reduces to

$$f(a_o) = K_u{}^2 [\pi a_o + (K_u/\sigma_u)^2]^{-1} \tag{23}$$

$$f'(a_o) = -f(a_o) [a_o + K_u{}^2/\pi\sigma_u{}^2]^{-1} \tag{24}$$

where K_u is an empirical fracture toughness parameter having units $(FL^{-3/2})$.

C. E. Feddersen (1970)

For an infinite plate, Eqs 6 and 10 of Ref *3* reduce to

$$f(a_o) = \sigma_{ys}{}^2 \left[1 - \frac{4\pi}{27} \left(\frac{\sigma_{ys}}{K_c}\right)^2 a_o\right]^2 \tag{25}$$

$$f'(a_o) = -f(a_o) \left[\frac{27}{8\pi} \left(\frac{K_c}{\sigma_{ys}}\right)^2 - \frac{a_o}{2}\right]^{-1} \tag{26}$$

for $a_o \leq (9/4\pi)(K_c/\sigma_{ys})^2$ and Eq 7 to

$$f(a_o) = K_c{}^2/\pi a_o \tag{27}$$

$$f'(a_o) = -f(a_o)/a_o \tag{28}$$

for $a_o \geq (9/4\pi)(K_c/\sigma_{ys})^2$, where σ_{ys} is the material's yield strength and K_c is an empirical fracture toughness parameter.

J. C. Newman (1972)

Equation 12 of Ref *4* for a finite-width center-crack plate can be rewritten and differentiated as

$$f(a_o) = K_f{}^2 \left[\sqrt{\pi a_o \sec(\pi a_o/W)} + \frac{m}{1 - \lambda_o} \frac{K_f}{\sigma_u}\right]^{-2} \tag{29}$$

$$f'(a_o) = -\frac{f(a_o)}{a_o} \frac{\left[1 + \frac{\pi a_o}{W} \tan\left(\frac{\pi a_o}{W}\right)\right] \sqrt{\pi a_o \sec\left(\frac{\pi a_o}{W}\right)} + \frac{2\lambda_o}{(1 - \lambda_o)^2} \frac{mK_f}{\sigma_u}}{\sqrt{\pi a_o \sec\left(\frac{\pi a_o}{W}\right)} + \frac{1}{1 - \lambda_o} \frac{mK_f}{\sigma_u}} \tag{30}$$

which, for an infinite plate, reduce to

$$f(a_o) = K_f^2 \quad [\sqrt{\pi a_o} + mK_f/\sigma_u]^{-2} \tag{31}$$

$$f'(a_o) = -f(a_o)\sqrt{\pi/a_o}\,[\sqrt{\pi a_o} + mK_f/\sigma_u]^{-1} \tag{32}$$

where K_f is an empirical fracture toughness parameter and m is a dimensionless empirical coefficient, which is not greater than unity. Note that if one allows $m = 1$ and $K_f = \sigma_u\sqrt{\pi}/C_m$, Eq 31 reduces to Eq 21.

G. Bockrath (1972)

Equation 13 of Ref *5* for a center-crack plate is limited to $\lambda_o \leq 0.1$, which approximates an infinite plate. Thus

$$f(a_o) = K_{Tc}^2(a_o) - \frac{2}{2+\omega} \tag{33}$$

$$f'(a_o) = -\frac{2}{2+\omega} f(a_o)/a_o \tag{34}$$

where ω is a dimensionless empirical coefficient and K_{Tc} is an empirical parameter having irrational units of (FL^{ω}).

References

[*1*] Kuhn, Paul, *Materials Research and Standards*, Vol. 8, No. 9, Sept. 1968, pp. 21-26.

[*2*] Orange, T. W., *Engineering Fracture Mechanics*, Vol. 3, No. 1, July 1971, pp. 53-67.

[*3*] Feddersen, C. E. in *Damage Tolerance in Aircraft Structures, ASTM STP 486*, American Society for Testing and Materials, 1971, pp. 50-78.

[*4*] Newman, J. C., Jr., *Engineering Fracture Mechanics*, Vol. 5, No. 3, Sept. 1973, pp. 667-689.

[*5*] Bockrath, G. F. and Glassco, J. B., "A Theory of Ductile Fracture," Report MDC-G2895, McDonnell Douglas Astronautics Co., April 1974.

[*6*] Heyer, R. H. in *Fracture Toughness Evaluation by R-Curve Methods, ASTM STP 527*, American Society for Testing and Materials, 1973, pp. 3-16.

[*7*] Orange, T. W., "A Relationship Between Semiempirical Fracture Analyses and R-Curves," Technical Paper TP1600, National Aeronautics and Space Administration, Washington, D.C., 1980.

[*8*] Broek, D., "The Effect of Finite Specimen Width on the Residual Strength of Light Alloy Sheet," Report NLR-TR M.2152, National Aerospace Laboratory (Netherlands), Sept. 1965.

[*9*] Feddersen, C. E., discussion in *Plane Strain Crack Toughness Testing of High Strength Metallic Materials, ASTM STP 410*, American Society for Testing and Materials, 1966, pp. 77-79.

[*10*] Orange, T. W., "Fracture Toughness of Wide 2014-T6 Aluminum Sheet at −320°F," Technical Note TND-4017, National Aeronautical and Space Administration, Washington, D.C., 1967.

[*11*] Eichenberger, T. W., "Fracture Resistance Summary," Report D2-20947, Boeing Airplane Co., June 1962.

K.-H. Schwalbe[1]

A Modification of the COD Concept and Its Tentative Application to the Residual Strength of Center Cracked Panels

REFERENCE: Schwalbe, K.-H., "**A Modification of the COD Concept and Its Tentative Application to the Residual Strength of Center Cracked Panels,**" *Fracture Mechanics: Twelfth Conference, ASTM STP 700,* American Society for Testing and Materials, 1980, pp. 500-512.

ABSTRACT: Simple assumptions are used to derive analytical expressions for the crack-tip opening displacement of center cracked tension panel (CCT) specimens with finite width. The formulas obtained thereby are used to describe the fracture behavior of CCTs of aluminum alloys. The results of 83 tests show that the crack opening displacement (COD) concept yields reasonable assessment of the fracture behavior of thin sheet material. The advantages and limitations are discussed.

KEY WORDS: COD concept, thin sheets, effect of finite width on COD, aluminum alloys, fractures (materials), crack propagation

Nomenclature

a	Crack length
a_o	Length of fatigue precrack
a_{eff}	Effective crack length
E	Young's modulus
$f(a/W)$	Linear elastic calibration function for stress intensity
UTS	Ultimate tensile strength
$2W$	Specimen width
δ	Crack tip opening displacement
δ_c	Critical δ

[1] GKSS, Research Centre Geesthacht, 2054 Geesthacht, West Germany.

δ_i δ at initiation of stable crack growth
δ_{max} δ at maximum load
σ Applied stress
σ_c Stress at maximum load
σ_y Yield strength
$\sigma_{0.2}$ Yield strength defined for 0.2 percent plastic strain
ω Length of plastic zone

In the linear elastic regime, critical values of fracture mechanics properties (K_c, K_{Ic}, K_{Iscc} etc.) are determined experimentally by measuring the critical stress, σ_c, and by computing the critical stress intensity using the appropriate calibration function of the specimen the test is done on

$$K_{Ic} = \sigma_c \sqrt{\pi a} \, | f(a/W) |_{\text{specimen}} \tag{1}$$

Assuming K_{Ic} to be a material constant, it can be applied to the behavior of a real structure taking now the appropriate calibration function of the structure. Asking for the critical stress one obtains

$$\sigma_c = \frac{K_{Ic}}{\sqrt{\pi a} \, | f(a/W) |_{\text{structure}}} \tag{2}$$

This procedure is outlined schematically in Fig. 1. Since there are numerous solutions for $f(a/W)$ in the literature, the step symbolized by Eq 2 can be done in many cases without any problems.

The situation in elastic-plastic fracture mechanics is quite different. Calibration functions for J-integral and crack opening displacement (COD) exist only for some very simple geometries. In the case of COD the calibration functions are lacking even for the simple fracture mechanics specimen geometries. There are indeed some numerical solutions [*1,2*];[2] however, closed form solutions would be preferable. It is common practice to determine the critical crack opening displacement, δ_c, by extrapolation of the crack mouth opening to the crack tip. There is no doubt that much of the scatter observed in δ_c is due to this experimental procedure [*3,4*]. It is believed that more consistent results would be obtained if δ_c would be determined via critical stress and calibration function.

In the present paper the development of such a calibration function for a simple specimen geometry and the application to the prediction of residual strength of thin sheets is described.

[2] The italic numbers in brackets refer to the list of references appended to this paper.

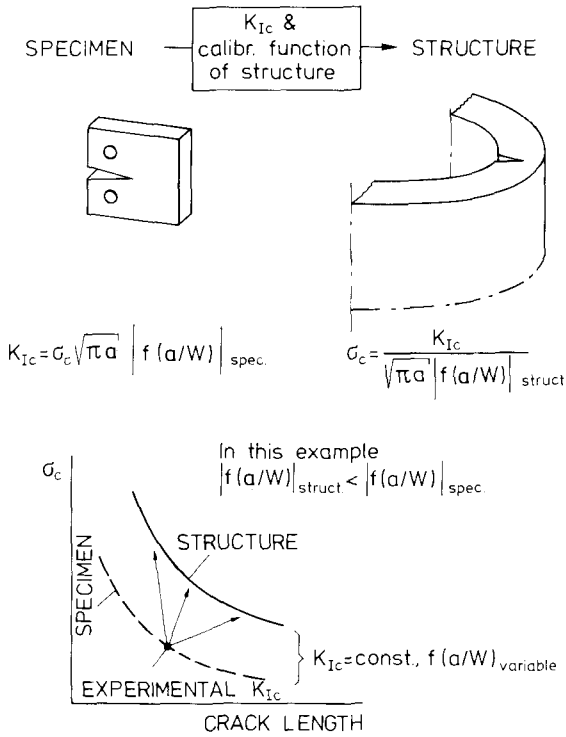

FIG. 1—*Application of fracture mechanics properties to real structures.*

Theory

For the infinitely extended plate Dugdale [5] derived his classical solution for the length of the plastic zone

$$\omega = a \left[\sec \frac{\pi \sigma}{2\sigma_y} - 1 \right] \tag{3}$$

The crack tip is opened by the amount [6]

$$\delta = \frac{8\sigma_y}{\pi E} a \ln \left[\sec \frac{\pi \sigma}{2\sigma_y} \right] \tag{4a}$$

$$= \frac{8\sigma_y}{\pi E} a \ln \left[\frac{\omega}{a} + 1 \right] \tag{4b}$$

Now the latter relation is assumed to be valid also in the case of finite

widths provided the proper expression for ω is inserted. For a strip of finite width Bilby et al [7] presented a solution for the plastic zone for a linear array of cracks

$$\omega = a\left\{\frac{2W}{\pi a}\arcsin\left[\sin\frac{\pi a}{2W}\sec\frac{\pi\sigma}{2\sigma_y}\right] - 1\right\} \tag{5}$$

This relation also represents, approximately, a strip of width 2 W. Combining (4*b*) with (5), one obtains the crack-tip opening displacement for a sheet of finite width subjected to a tensile stress σ

$$\delta = \frac{8\sigma_y}{\pi E}a\ln\left\{\frac{2W}{\pi a}\arcsin\left[\sin\frac{\pi a}{2W}\sec\frac{\pi\sigma}{2\sigma_y}\right]\right\} \tag{6}$$

The problem is that contrary to linear elastic fracture mechanics (LEFM) the calibration function does not only depend on geometry but also on the load σ/σ_y.

A normalized plot of δ is shown in Fig. 2. The individual curves of the normalized δ are terminated by the general yield envelope, which is obtained by equating the net section stress, σ_n, to the yield strength, σ_y. From this one obtains

$$\frac{\delta E}{4\sigma_y a} = \frac{2}{\pi}\ln\left\{\frac{2W}{\pi a}\arcsin 1\right\} \tag{7}$$

The influence of finite width on δ is obvious from Fig. 2. The results agree very well with numerical calculations of Erdogan and Bakioglu [1]. It is also obvious that at general yield, finite widths exhibit finite displacements.

If the critical value of δ, that is, δ_c, is considered as a material constant (for a given thickness) and if δ_c has been determined experimentally, the failure stress for all a and W can be calculated by solving Eq 6 for σ

$$\sigma_c = \frac{2\sigma_y}{\pi}\arccos\left|\frac{\sin\dfrac{\pi a}{2W}}{\sin\left\{\exp\left(\dfrac{\delta_c E\pi}{8\sigma_y a}\right)\dfrac{\pi a}{2W}\right\}}\right| \tag{8}$$

It can be seen from Fig. 2 that the use of a finite width solution is well justified since the infinite width solution yields nonconservative failure stresses if the defect length can no longer be neglected with respect of the width of the structural part. When using this relation numerical problems

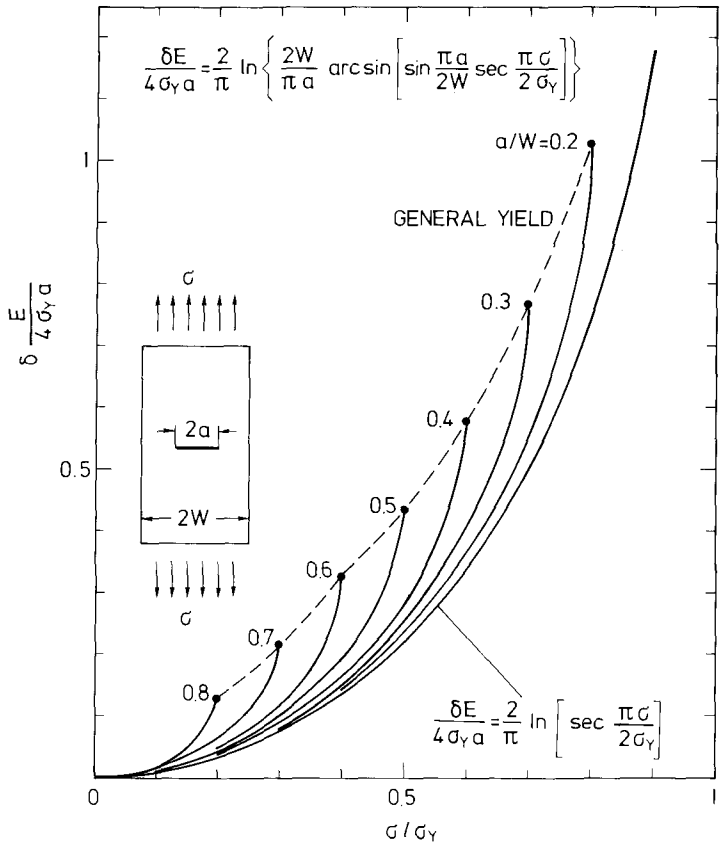

FIG. 2—*Normalized crack-tip opening displacement calculated by Eq 6.*

arise for low a/W values combined with net section stresses close to the yield strength; cut-off errors of the computer can cause nonconverging results.

An alternative approach for calculating the crack-tip opening displacement for finite widths is as follows: the infinite width solution

$$\delta = \frac{8\sigma_y}{\pi E} a \ln \left[\sec \frac{\pi\sigma}{2\sigma_y} \right] \tag{9}$$

is assumed to be applicable to finite width if an equivalent effective crack length

$$a_{\text{eff}}^{\text{eq}} = a \cdot f^2(a/W) \tag{10}$$

is inserted, where $f(a/W)$ is the linear elastic calibration function. In addition, the plasticity correction

$$a \rightarrow a + \frac{\omega}{2} \tag{11}$$

with ω from Eq 3 is included in $f(a/W)$. Setting

$$f(a/W) = \sqrt{\sec \frac{\pi a}{2W}} \rightarrow \sqrt{\sec \frac{\pi(a + \omega/2)}{2W}} \tag{12}$$

one obtains with these assumptions

$$\delta = \frac{8\sigma_y}{\pi E} a \sec \left\{ \frac{\pi a}{2W} \left[1 + \frac{1}{2} \left(\sec \frac{\pi \sigma}{2\sigma_y} - 1 \right) \right] \right\} \ln \left[\sec \frac{\pi \sigma}{2\sigma_y} \right] \tag{13}$$

This expression approaches analytically the infinite width solution (Eq 9) when $a/W \rightarrow 0$. Here the calibration function is given separately by the factor sec $\{ \ldots \}$; it contains both the effects of geometry and of the load level through the plasticity correction. In Eq 6 the calibration function cannot be separated from the remainder of the expression.

Equation 13 is plotted in Fig. 3. In spite of the crude approximation, applying a linear elastic solution to an elastic-plastic problem, the deviations from Eq 6 are not large. The greatest differences occur at δ for general yield; however, the errors in stress are small. The procedure underlying Eq 13 has the advantage that linear elastic solutions can be used that are available for numerous cases.

The formalism based on the Dugdale model is attractive since it is capable to describe the material behavior from linear elasticity to fully plastic situations. This effect has been already recognized and applied by various authors, that is, [*8,9*].

Check of Prediction Capability

If the critical COD, δ_c, were independent of geometric variables such as thickness, width, and crack length, and if Eq 6 were the exact solution to the finite width problem, predictions with high accuracy could be expected when applying Eq 8 to experimental results. However, the following problems may arise:

1. If δ_c is taken as a measure of crack growth initiation (δ_i), it is expected to be independent of specimen width and crack length within the scatter of material properties. Some experimental results [*10*] seem to

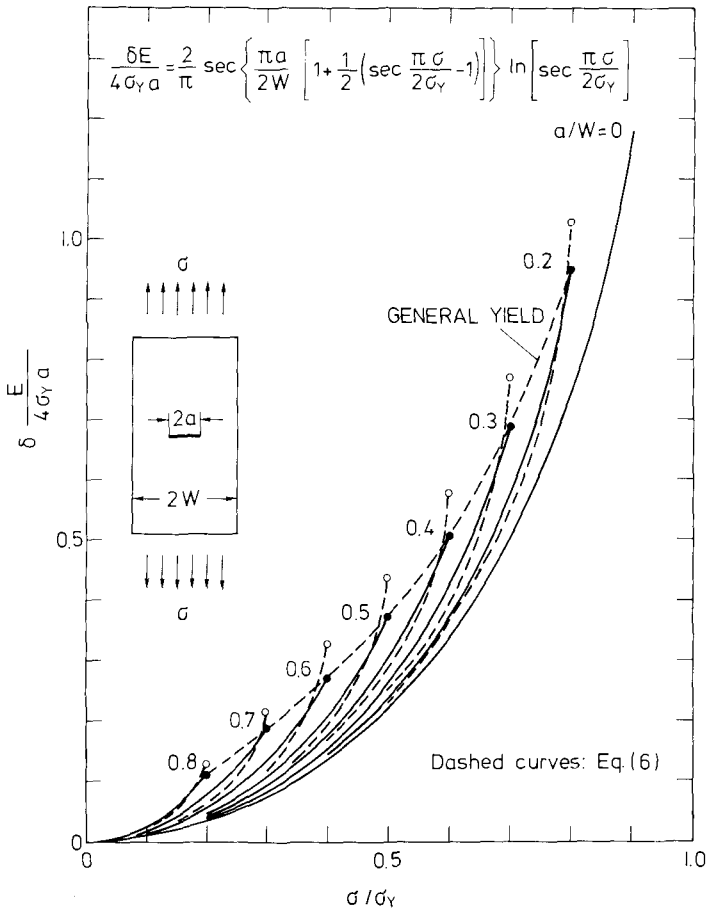

FIG. 3—*Normalized crack-tip opening displacement calculated by Eq 13.*

support this assumption. On the other hand, δ_{max}, the value of δ_c at instability, depends on width and crack length due to the R-curve effect, Fig. 4*a*. No δ_i-values obtained on center cracked panels and close enough to general yield to justify the application of an elastic-plastic analysis were available to the author. However, tests on center cracked panels with systematic variation of specimen width and crack length had been done in the author's laboratory [*11*]; δ_i is very low in the elastic range, whereas δ_{max} reflects elastic plastic conditions. This is shown schematically in Fig. 4*b*. Although δ_{max} varies with a and W, Fig. 5, the COD concept was tentatively applied to δ_{max} as described below. The error introduced thereby is not expected to be very large because the largest variations of $\delta_c = \delta_{max}$

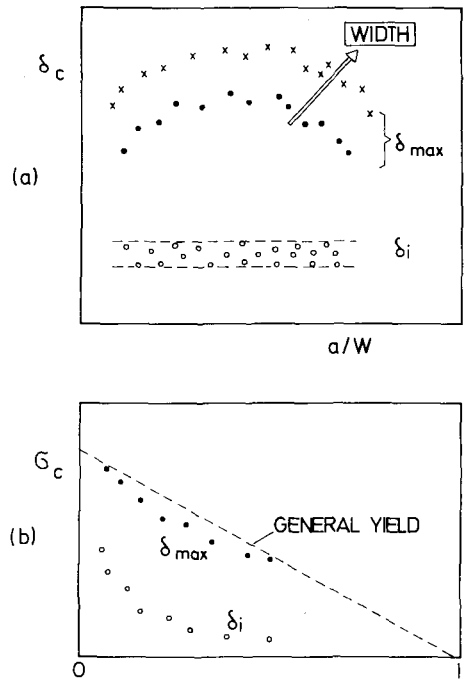

FIG. 4—(a) *Influence of specimen width and crack length on* δ_i *and* δ_{max}*; and* (b) *location of* δ_i *and* δ_{max} *with respect to general yield obtained in the tests analyzed by the COD concept.*

occur close to general yield where variations in δ are accompanied by small variations in σ (see Figs. 2 and 3).

2. Comparisons with numerical results of Ref *1* had shown that the accuracy of Eq 6 is fairly good. However, the Dugdale formalism is based on elastic-ideally plastic material behavior. To account for work hardening, a flow stress

$$\sigma_y \rightarrow 0.5(\sigma_{0.2} + \text{UTS}) \tag{14}$$

was used. This is a crude approximation of the real influence of work hardening.

The experimental data was obtained on 2-mm-thick center cracked tension specimens of 2024-T3, 7475-T761, and 7075-T6 aluminum. In addition, data of 7075-T6 clad aluminum were used. In the first step, the critical δ (δ at maximum load) was calculated for all experiments according to Eq 6. For the calculations the fatigue precrack length a_o was used.

The results for 2024-T3 aluminum are shown in Fig. 5. Due to the "R-curve effect," δ_c varies with specimen width and a_o/W. Part of the

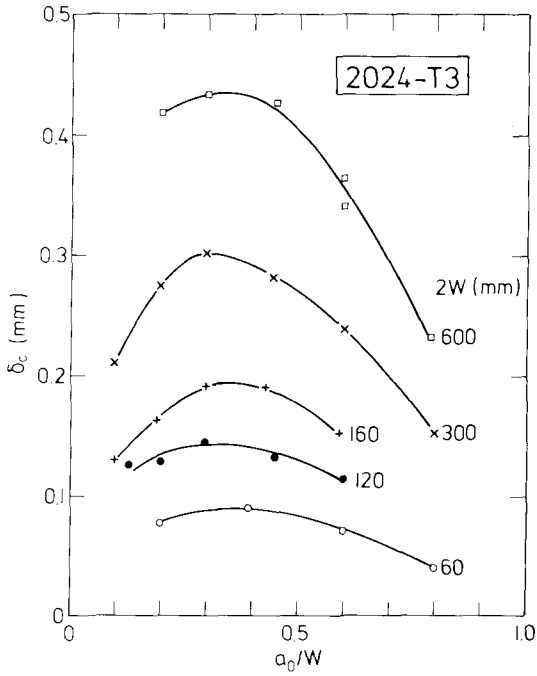

FIG. 5—δ_c *for 2024-T3 (2 mm thick) aluminum as a function of* W *and* a_0/W.

variation of δ_c is also due to yielding effects because at general yield different W and different a_o/W lead to different δ_c-values. In the second step, regardless of its variation, δ_c was assumed to be constant for each specimen width; that is, δ_c at $a_o/W = 0.6$ was taken as that value which is roughly representative for all a_o/W, Fig. 6. It will be seen immediately that the error introduced thereby is small. From these $\delta_c(a_o = 0.6)$ for each specimen width of the four materials investigated the failure stress, σ_c, was calculated by Eq 8, Fig. 6. Typical results are shown in Fig. 7. For $a_o/W \to 0$ the calculated critical stress approaches the flow stress used for calculation, in this case $0.5(\sigma_{0.2} + \text{UTS})$. Thus, unlike LEFM which overestimates the load carrying capacity of parts with small cracks, the COD-concept yields failure stresses that are automatically bounded by the flow stress used for calculation.

The accuracy of prediction was checked for all experimental data; the results are compiled in Fig. 8. It can be seen that the results are close to the 45 deg line.

Thus, in order to obtain the failure stress of a panel of a given width as a function of crack length the following three-step procedure is proposed:

1. Measure the critical stress, σ_c, of a specimen having the width the information is required for and having $a_o/W \approx 0.6$;

2. Calculate δ_c for $a_o/W = 0.6$ by Eq 8 or alternatively by Eq 13; and

3. Calculate $\sigma_c = f(a_o/W)$ by Eq 8 or alternatively by iteration when using Eq 13.

Compared with R-curve concepts the application of the COD-concept in the form described above has the following advantages:

1. No crack length measurement is required. The specimen must only be precracked and fractured. The only quantity to be measured is the critical load.

2. The fracture behavior of a given width can be approximately described by a single parameter, δ_c.

3. Unlike LEFM the fracture stress is automatically bounded by the flow stress.

However, the disadvantage is that no conclusion can be drawn from one width to another. This disadvantage may be overcome by a COD based R-curve. In this case, however, crack length measurements are again necessary. This problem of a COD R-curve is presently being investigated at the Research Centre Geesthacht.

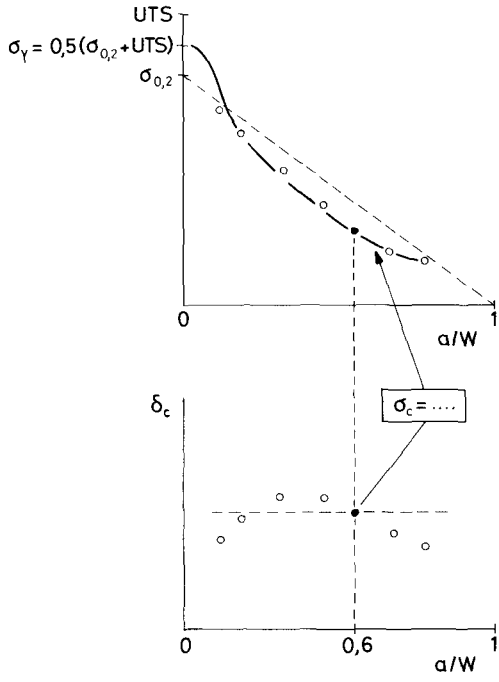

FIG. 6—δ_c *at* a/W = *0.6 is used to calculate the failure curve by Eq 8. This procedure is carried out for each specimen width separately.*

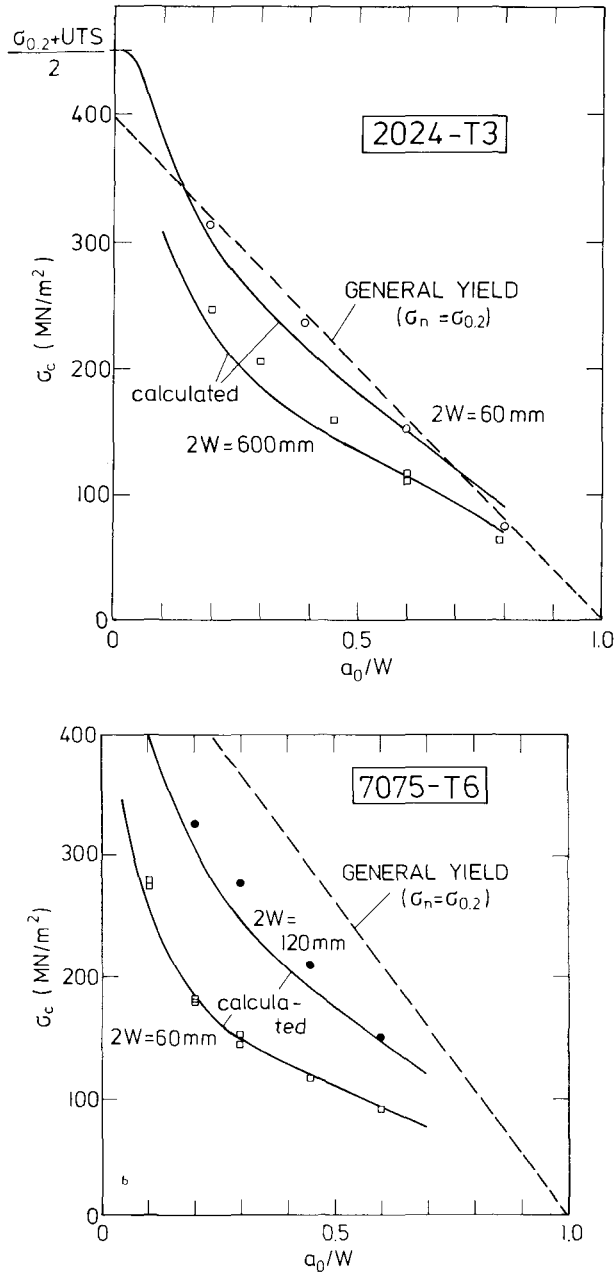

FIG. 7—*Calculated and measured fracture stress* (a) *for 2024-T3 aluminum, and* (b) *for 7075-T6 aluminum.*

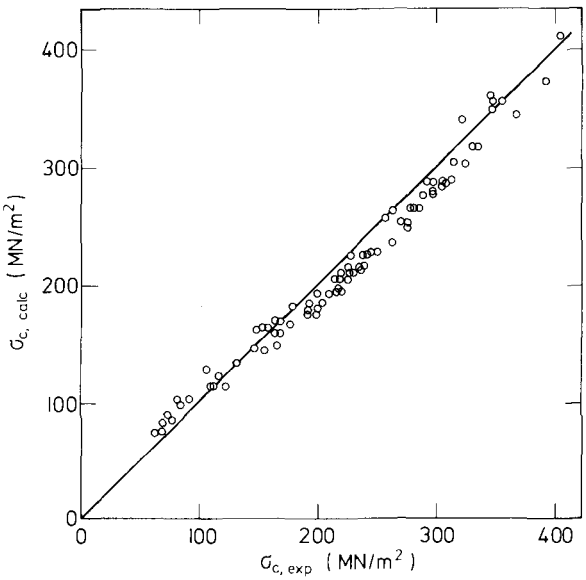

FIG. 8—*Compilation of 83 measured and calculated fracture stresses for 2024-T3, 7475-T761, 7075-T6, and 7075-T6 clad aluminum.*

Conclusions

1. By simple assumptions it is possible to derive two closed-form solutions for the crack tip opening displacement of a center cracked panel of finite width.

2. The effect of finite width is that the larger the width the closer the condition of net section yield is approached.

3. It is proposed to determine COD data via critical stress and appropriate calibration function instead of using empirical formulas relating δ to the clip gage displacement.

4. Test data of four aluminum alloys were used to calculate δ_c, which turned out to depend both on specimen width and crack length.

5. For a given width δ_c can be considered as constant to calculate the fracture stress as a function of crack length.

6. The fracture stresses calculated thereby represent reasonable assessment of the actual behavior of the specimens.

Acknowledgments

The financial support of this work by DFG (German Science Foundation) is gratefully acknowledged.

References

[1] Erdogan, F. and Bakioglu, M., *International Journal of Fracture*, Vol. 11, 1975, p. 1031.
[2] Hayes, D. J. and Williams, J. G., *International Journal of Fracture*, Vol. 8, 1972, p. 239.
[3] Hollstein, T., Blauel, J. G., and Urich, B., "Rissaufweitung COD/COS zur Beurteilung der Bruchgefährdung von Bauteilen aus 22NiMoCr37," Reaktortagung, 1976, Düsseldorf, Germany.
[4] Berger, C., "Round Robin Test as a Comparison of Crack Opening Displacements," *Proceedings*, Second European Colloquium on Fracture, Fortschr.-Ber. VDI-Z., Reihe 18, No. 6, 1978.
[5] Dugdale, D. S., *Journal of the Mechanics and Physics of Solids*, Vol. 18, 1960, p. 100.
[6] Goodier, J. N. and Field, F. A. in *Fracture of Solids*, Wiley, New York, 1963.
[7] Bilby, B. A., Cottrell, A. H., and Swinden, K. H., *Proceedings*, Royal Society, Series A, No. 279, 1964, p. 1.
[8] Hahn, G. T., Sarrate, M., and Rosenfield, A. R., *International Journal of Fracture Mechanics*, Vol. 5, 1969, p. 187.
[9] Harrison, R. P. and Milne, I. in *Fracture Mechanics in Engineering Practice*, Applied Science Publishers, London, 1977.
[10] Fearnehough, G. D., Lees, G. M., Lowes, J. M., and Weiner, R. T. in *Practical Application of Fracture Mechanics to Pressure-Vessel Technology*, The Institution of Mechanical Engineers, London, 1971.
[11] Schwalbe, K.-H. and Setz, W., "R-curve and Fracture Toughness of Thin Sheet Materials," in preparation.

Roland de Wit[1] *and J. H. Smith*[1]

Development of Some Analytical Fracture Mechanics Models for Pipeline Girth Welds

REFERENCE: de Wit, Roland and Smith, J. H., **"Development of Some Analytical Fracture Mechanics Models for Pipeline Girth Welds,"** *Fracture Mechanics: Twelfth Conference, ASTM STP 700,* American Society for Testing and Materials, 1980, pp. 513-528.

ABSTRACT: Analytical models based on fracture mechanics technology are developed to establish predicted critical defect sizes for sharp, circumferential defects in pressurized pipe. These models are only intended to provide a theoretical basis for establishing predicted critical defect sizes. The general problem considered here is that of a surface-defect in a plate; that is, the flat plate analogy is used here for a pipeline. Failure is considered to occur when the ligament ruptures and provides a leakage path. The fracture mechanics model used, called the collapsed ligament model, is based on the work of Erdogan and Bakioglu, which is in turn based on the Dugdale model. The collapsed ligament model assumes plastic collapse in the depth direction but any fracture mechanics model in the length direction. To illustrate the use of these theoretical models for defects in pressurized pipes, curves are derived that show the predicted critical defect sizes. In these curves, the defect depth is plotted versus the defect length for a given set of material properties and applied stress. Defects having sizes that fall below this curve are not expected to extend. On the other hand, it is assumed that defects with sizes which fall above the curve will extend.

KEY WORDS: collapse, cracks, defects, failure, fracture mechanics, girth welds, pipeline, plasticity, strength, stress, toughness, fractures (materials), crack propagation

Nomenclature

- a Defect depth
- a_1 Relative defect depth, a/B
- B Pipe wall thickness (or plate thickness)
- c Half defect length
- c_1 Relative defect length, $2c/W$

[1]Physicist and metallurgist, respectively, Fracture and Deformation Division, Center for Materials Science, National Measurement Laboratory, National Bureau of Standards, Washington, D.C. 20234.

E Young's modulus
F Geometrical factor in stress intensity factor
K Stress intensity factor
r Radius of pipe
W Pipe circumference, $2\pi r$ (or plate width)
α Geometry angle, $\pi c/W$
α_1 Dugdale angle, $\pi\sigma'/2\sigma_0'$
α_2 Geometrical Dugdale angle, $\alpha_1/(1 - c_1)$
δ Crack tip opening displacement (CTOD) at plastic zone
δ_0 CTOD at ligament
δ_1 Normalized CTOD at plastic zone, $E(\delta - \delta_r)/W\sigma_0$
δ_2 Normalized CTOD at ligament, $E(\delta_0 - \delta_r)/W\sigma_0$
σ Applied tensile stress
σ_0 Flow strength
σ' Equivalent applied stress
σ_0' Equivalent flow strength
σ_1 Normalized stress, σ/σ_0
σ_2 Normalized equivalent stress, σ'/σ_0

Fracture mechanics provides a relationship between the stress, strength, toughness, and geometry of a structure to predict a critical defect size. A critical defect size is one which the analysis predicts will extend under the defined service conditions. The material properties required for a fracture mechanics analysis are strength and toughness. The toughness can be classified by the failure mode. In order of increasing toughness they are: linear-elastic, elastic-plastic, and plastic collapse. Most pipeline girth welds under normal operating conditions are believed to behave in an elastic-plastic or plastic collapse fracture mode.

For the present study only "sharp" (crack-like) defects are considered from an analytic viewpoint. Furthermore, this paper will deal only with surface-defects; that is, defects that have not penetrated through the pipe wall. Girth-weld defects are typically oriented circumferentially, and consequently the axial stresses are used in the fracture mechanics analysis.

The analytic expressions, which are derived below, provide the theoretical basis for developing predicted critical defect sizes. Safety factors to account for uncertainties in stress, defect size, and material properties must be applied to these curves to establish the allowable defect size curves. From the theoretical models developed here, expressions are derived that relate the defect depth to the defect length for a range of selected design and material parameters. To illustrate the use of these theoretical models for developing predicted critical defect sizes, plots were made based on each model developed. The design and material parameters used as input data for these plots were assumed from values that are typical of steel pipe. The following values were assumed: thickness, $B = 12$ mm (0.47 in.); radius, $r = 60$ cm

(24 in.); circumference, $W = 377$ cm (150 in.); stress, $\sigma = 400$ MPa (58 ksi); flow strength, $\sigma_0 = 450$ to 550 MPa (65 to 80 ksi); Young's modulus, $E = 200\,000$ MPa (29 000 ksi); and crack tip opening displacement (CTOD), $\delta = 0.05$ to 0.2 mm (0.004 to 0.008 in.). The range for plotting of the typical defects dimensions was chosen as follows: defect depth to wall thickness ratio, $a/B = 0$ to 0.5; and defect length to circumference ratio, $2c/W = 0$ to 0.1.

The models that follow are based on a deterministic approach. This approach assumes that explicit input parameters predict explicit values of the results. However, it should be recognized that due to the natural variability of those input parameters it is more realistic to use a probabilistic approach in which this variability is quantitatively assessed. This would result in a sensitivity analysis with bands rather than curves in the plots below. However, it is then necessary to know the variability of the input parameters. Such information must come from the specific application for which the model is used. Since this paper addresses only the general problem of a pipeline, the probabilistic approach is left for future consideration.

The Models

Wilkowski and Eiber [*1*][2] have reviewed several analytical models for determining the critical size of through-wall cracks in pipes. Some of these theories took the curvature and bulging of the pipe wall into account. The theories differed from each other in their quantitative results. The scant experimental data available did not permit a critical assessment of the accuracy of the proposed theories.

The simplest approach reviewed was the flat plate analogy using the Dugdale crack model. Because defects in girth welds are oriented circumferentially, bulging is not significant and, therefore, defects in girth welds may be assumed to behave in a manner similar to a flat plate pulled in tension. Wilkowski and Eiber [*1*] further state that the Dugdale relationship has the unique feature that it is applicable for linear-elastic, elastic-plastic, and plastic collapse fracture behavior.

The authors therefore decided to adopt also the flat plate analogy for the present work. The general problem considered here is that of a surface-defect of length, $2c$, and depth, a, in a plate of thickness, B. Failure is considered to occur when the ligament, $(B - a)$, ruptures and provides a leakage path. The fracture toughness is measured by the CTOD. When this quantity exceeds the critical value for the material, it is assumed that defect extension occurs. This is taken as the failure criterion, even though the extension may not be unstable, as could be the case in a very tough material.

Under small-scale yielding, failure of the ligament can be treated using a

[2]The italic numbers in brackets refer to the list of references appended to this paper.

conventional linear-elastic fracture mechanics (LEFM) approach. However, when the net section stress on the ligament approaches the flow strength, σ_0, the LEFM approach is unconservative and elastic-plastic fracture mechanics (EPFM) must be used.

Two fracture mechanics models were chosen for the present study: the first due to Begley [*2*], and the second based on work by Erdogan and Bakioglu [*3*]. Both models use the flat plate analogy, and hence do not account for the curvature of the pipe. Both models are based on the collapsed ligament model.

The Collapsed Ligament Model

This model uses the CTOD for the measurement of fracture toughness. The defect geometry is illustrated in Fig. 1. A flat plate is considered under uniform tension, σ, with a defect of length $2c$ at its center. The thickness of the plate is B and the depth of the defect is a. For convenience the plate has also been given a width W. Initially this width is taken to be infinite, $W = \infty$. However, by taking W finite we also have the finite flat plate analogy, where the width of the plate equals the circumference of the pipe [*1*]. The ligament is the material that remains between the defect and the surface of the plate. Hence, it has a length $2c$ and a depth $(B - a)$.

The model works by analogy with a through-defect, $a = B$. For a through-defect under tension, σ, the defect will open up, with or without plastic zones at each tip. For the surface-defect, when $a < B$, the collapsed ligament model assumes that the whole ligament collapses, that is, yields plastically. It

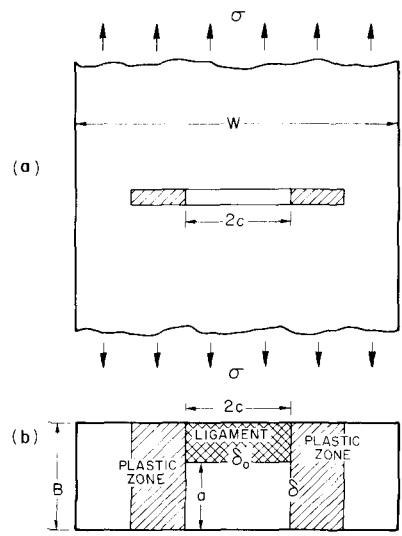

FIG. 1—*Surface defect with fully yielded ligament and plastic zones.*

is further assumed that the defect opens up as for an equivalent through-defect, but by a smaller amount, because the flow strength, σ_0, in the ligament opposes the applied stress, σ, and exerts a closing force, given by

$$F_c = 2c(B - a)\sigma_0 \tag{1}$$

The flow strength, σ_0, is often assumed to lie somewhere between the yield strength and the ultimate tensile strength, usually halfway [*1*]. If the closing force is taken to be distributed over the combined defect-ligament area, $2cB$, it gives a closing stress on the equivalent through-defect of

$$\sigma_c = \frac{F_c}{2cB} = \left(1 - \frac{a}{B}\right)\sigma_0 \tag{2}$$

which then opposes the remote stress, σ. Hence, the equivalent through-defect sees an equivalent stress of

$$\sigma' = \sigma - (1 - a/B)\sigma_0 \tag{3}$$

The model is then applied by using well-known fracture mechanics expressions derived for the through-defect, where the applied stress, σ, is replaced by the equivalent stress, σ'.

There are two CTODs of physical interest in this model. The first, termed δ, occurs at the equivalent through-defect tip, that is, at the boundary with the plastic zone. The second, termed δ_0, occurs at the midpoint of the surface-defect front, that is, at the boundary with the ligament. The basic assumption, which allows the application of fracture mechanics to this model, is that when either of these CTODs exceeds a particular critical value for the material then defect extension will occur. As mentioned above, this is taken as the failure criterion, even though the extension may not be unstable. Exceeding the critical value for δ will then lead to extension of the defect length, $2c$. Exceeding the critical value for δ_0 will lead to extension of the defect depth, a, and if enough extension occurs in this direction the surface-defect may become a through-defect.

It will be recognized that when the defect length, $2c$, is very large, the critical equivalent stress, σ', for defect extension will be very small. From Eq 3 this leads to the condition

$$\frac{\sigma}{1 - a/B} \to \sigma_0 \qquad \text{for } c \to \infty \tag{4}$$

that is, the net ligament stress equals the flow strength. This is the plastic collapse condition in its simplest form. For tough materials it will be a conservative condition, but for brittle materials it may not be conservative. This

point can be checked for any particular case by comparing Eq 4 with the corresponding fracture mechanics relation. This will be done in another publication.

Thus, in the collapsed ligament model one can use any appropriate relation from fracture mechanics in the width direction, but in the thickness direction the model always assumes plastic collapse.

The Begley Model

The Linear-Elastic Model

Begley [*2*] considered a linear-elastic CTOD model and a plastic-zone-corrected model. The latter will be discussed below. In the linear-elastic model the value of δ_0 is given by the elastic opening of the equivalent through-defect at its midpoint (see Ref [*4*], Eq 3.59)

$$\sigma_0 = \frac{4c\sigma'}{E} \tag{5}$$

where E is Young's modulus. Begley accounted for the effect of residual stresses by subtracting a residual portion δ_r from δ_0. If we do this in Eq 5, combine it with Eq 3, and solve for the defect depth, a,

$$a = B\left[1 - \frac{\sigma}{\sigma_0} + \frac{E(\delta_0 - \delta_r)}{4\sigma_0 c}\right] \tag{6}$$

This equation is the basic prototype relation between the critical defect sizes, a and $2c$, in terms of the applied stress, σ, and the material properties: the flow strength, σ_0, Young's modulus, E, and the CTOD, δ_0. Equation 6 is plotted as the dotted lines in Fig. 2 for several values of the CTOD, δ_0, and the typical values of the other parameters mentioned in the beginning of this paper. In the present study the authors have for convenience ignored the residual stresses and set $\delta_r = 0$.

It will be noted that for a large defect length, $2c$, the curves (Eq 6) approach the asymptotic value $a = B(1 - \sigma/\sigma_0)$, that is, the simple plastic collapse condition (Eq 4).

It is convenient to convert Eq 6 to dimensionless terms, because the number of free parameters is then reduced to a minimum, and hence a plot of the equation has then wider applicability. The following dimensionless terms are defined: relative defect depth, $a_1 = a/B$; relative defect length, $c_1 = 2c/W$; normalized stress, $\sigma_1 = \sigma/\sigma_0$; and normalized CTOD, $\delta_2 = E(\delta_0 - \delta_r)/W\sigma_0$.

In these relations the pipe circumference is introduced as W, even though

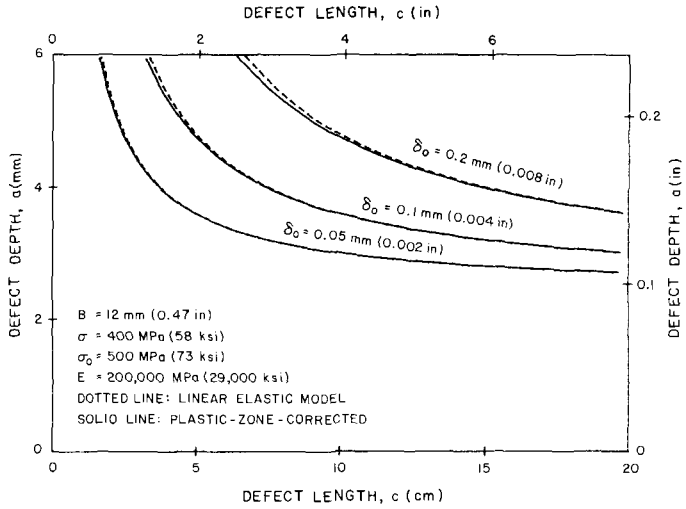

FIG. 2—*Predicted critical defect sizes for the Begley model. Comparison of the linear-elastic and plastic-zone-corrected models.*

it does not appear in Eq 6, because it provides a convenient measure of comparison for the defect length, $2c$. With these substitutions Eq 6 becomes

$$a_1 = 1 - \sigma_1 + \tfrac{1}{2}\delta_2/c_1 \tag{7}$$

Only two parameters, the normalized CTOD δ_2 and the normalized stress σ_1, now enter into the equation, and it is clearly simpler in form than Eq 6.

The Plastic-Zone-Corrected Model

Begley [*2*] corrected for the plasticity extending beyond the defect length with the Irwin plastic-zone adjustment. According to Irwin the effective defect length is given by

$$c_{\text{eff}} = c + (K/\sigma_0)^2/2\pi \tag{8}$$

where K is the stress intensity factor.

$$K = \sigma' \sqrt{(\pi c_{\text{eff}})} \tag{9}$$

By eliminating K between Eqs 8 and 9 one can solve for c_{eff}

$$c_{\text{eff}} = \frac{c}{1 - \tfrac{1}{2}(\sigma'/\sigma_0)^2} \tag{10}$$

Using c_{eff} for c in Eq 5 then provides a plasticity-adjusted δ_0

$$\delta_0 = \frac{4c\sigma'}{E[1 - \frac{1}{2}(\sigma'/\sigma_0)^2]} \tag{11}$$

This relation in conjunction with Eq 3 is also plotted in Fig. 2 (solid lines) and compared with Eq 6 (dotted lines). It is seen that the plasticity adjustment does not greatly alter the curves, but the adjustment does increase somewhat with increasing toughness, δ_0, and with increasing defect depth, a.

In dimensionless terms Eq 11 simplifies to

$$\delta_2 = \frac{2c_1\sigma_2}{1 - \frac{1}{2}\sigma_2^2} \tag{12}$$

where the normalized equivalent stress is defined

$$\sigma_2 = \sigma'/\sigma_0 = \sigma_1 - 1 + a_1 \tag{13}$$

the second equality following from Eq 3. In terms of σ_2 Begley's linear elastic model Eq 7 becomes simply $\delta_2 = 2c_1\sigma_2$ (compare Eq 12).

The Erdogan Model

The Model for δ_0

Erdogan and Bakioglu [*3*] base their model on the Dugdale model. In that model it is assumed that the plastic zone (Fig. 1) is fully yielded and exerts a closing stress, σ_0, on the applied stress, σ, giving a net stress on the plastic zone of $\sigma - \sigma_0$, Dugdale then derives the CTOD for a through-defect in terms of σ and σ_0. Erdogan and Bakioglu show that for a surface-defect the same equations apply with σ and σ_0 replaced by the equivalent stress, σ', and the equivalent flow strength, σ_0'. The CTOD for the ligament is

$$\delta_0 = \frac{4c\sigma_0'}{\pi E} \ln\left[\frac{1 + \sin(\pi\sigma'/2\sigma_0')}{1 - \sin(\pi\sigma'/2\sigma_0')}\right] \tag{14}$$

To obtain the equivalent flow strength, σ_0', note that the net stress on the plastic zone must be the same for a through-defect as for an equivalent through-defect

$$\sigma - \sigma_0 = \sigma' - \sigma_0' \tag{15}$$

From Eq 3 this gives

$$\sigma_0' = (a/B)\sigma_0 \tag{16}$$

For small values of $\pi\sigma'/2\sigma_0'$ Eq 14 approaches the linear-elastic Begley model (Eq 5).

In Eq 14 σ' and σ_0' are functions of a, given by Eqs 3 and 16. Hence, one can again plot c versus a as is done in Fig. 3 (solid lines) for the same parameters as used before. The linear-elastic Begley model (Eq 6) is also plotted for comparison (dotted lines). Comparing Figs. 2 and 3 shows that the Erdogan model gives a larger effect of plasticity than the plastic-zone-adjusted Begley model, especially for increasing toughness, δ_0, and increasing depth, a.

Relationships of Eqs 6 and 14 are again plotted in Fig. 4, but now indicates a fixed value of the CTOD and for several values of the flow strength, σ_0. The effect of plasticity increases with decreasing flow strength.

It is again convenient to convert Eq 14 to dimensionless form. For this it is useful to define the angle

$$\alpha_1 = \pi\sigma'/2\sigma_0' = \pi\sigma_2/2a_1 = \pi(\sigma_1 - 1 + a_1)/2a_1 \tag{17}$$

by Eqs 3, 16, and 13. Hence Eq 14 becomes

$$\delta_2 = \frac{2}{\pi} c_1 a_1 \ln\left[\frac{1 + \sin\alpha_1}{1 - \sin\alpha_1}\right] \tag{18}$$

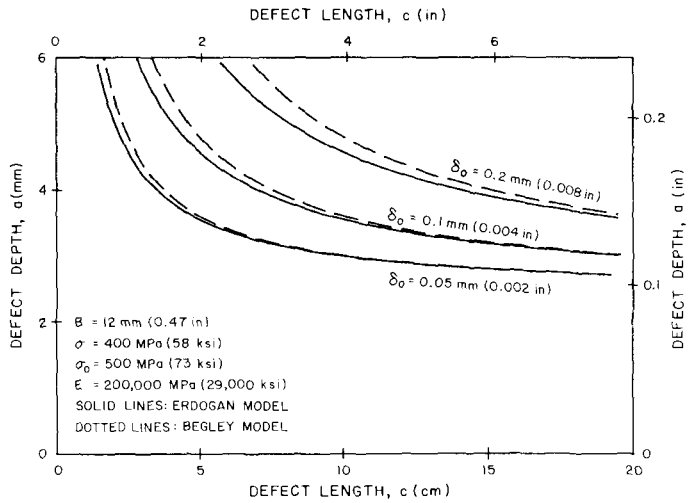

FIG. 3—*Predicted critical defect sizes. Comparison of the Erdogan model with the Begley model for three different values of the CTOD, δ_0, at the ligament.*

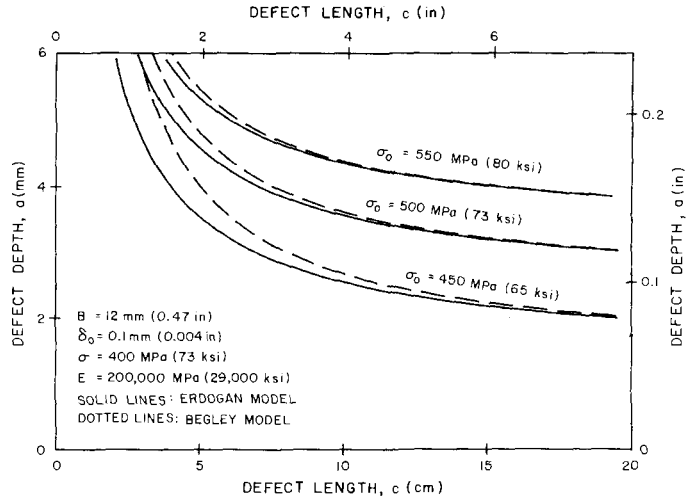

FIG. 4—*Predicted critical defect sizes. Comparison of the Erdogan and Begley models for the CTOD, δ_0, at the ligament and for three different values of the flow strength, σ_0.*

For small α_1 this reduces to Begley's linear-elastic model $\delta_2 = 2c_1\sigma_2$. In dimensionless form it is clear that still only two parameters, δ_2 and σ_1, are needed to plot the equation. Figure 5 shows several curves in approximately the same range as for Fig. 3, and Fig. 6 shows several curves in approximately the same range as Fig. 4.

The Model for δ

As mentioned before Erdogan and Bakioglu [*3*] also used the CTOD for the plastic zone, given by the well-known Dugdale expression

$$\delta = (8c\sigma_0'/\pi E) \ln \sec (\pi\sigma'/2\sigma_0') \tag{19}$$

The values of σ' and σ_0' are again given by Eqs 3 and 16. The linear-elastic value for the CTOD at the plastic zone is obtained when $\pi\sigma'/2\sigma_0'$ is small. Then Eq 19 reduces to

$$\delta = \pi\sigma'^2 c/\sigma_0' E \tag{20}$$

In dimensionless form the CTOD for the plastic zone (Eq 19) reduces to

$$\delta_1 = (4/\pi)c_1 a_1 \ln \sec \alpha_1 \tag{21}$$

and the linear-elastic CTOD (Eq 20) reduces to

$$\delta_1 = \pi\sigma_2^2 c_1/2a_1 \tag{22}$$

where the normalized CTOD at the plastic zone is defined by

$$\delta_1 = E(\delta - \delta_r)/W\sigma_0 \tag{23}$$

Equations 21 with 17 gives a relationship between a_1 and c_1 with the param-

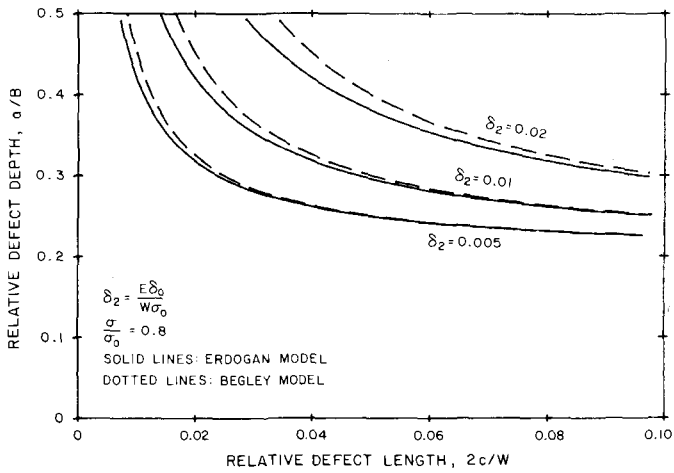

FIG. 5—*Predicted critical defect sizes. Presentation in dimensionless form. Comparison of the Erdogan and Begley models for three different values of the normalized CTOD, δ_2, at the ligament.*

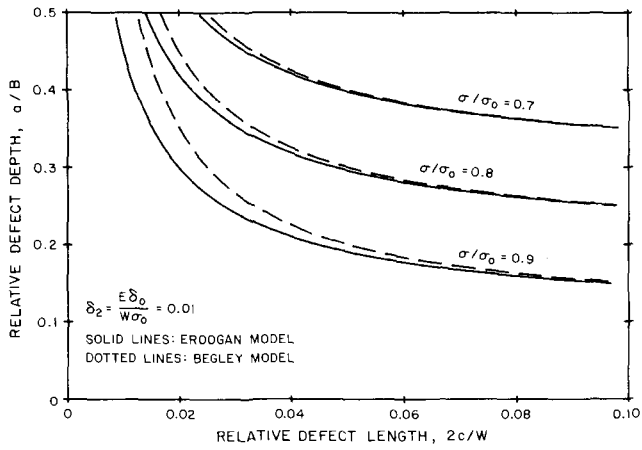

FIG. 6—*Predicted critical defect sizes. Comparison of the Erdogan and Begley models for the normalized CTOD, δ_2, at the ligament and for three different values of the normalized stress, σ/σ_0.*

eters δ_1 and σ_1. This relation is plotted in Fig. 7 (solid lines) over the same range and for the same parameters as in Fig. 5. The values of the normalized CTOD, δ_1, in Fig. 7 have been chosen, the same as the values for δ_2 in Fig. 5 for comparison. The curves for δ_1 are generally similar but lie somewhat higher than those for δ_2. This would indicate that for the parameters considered here the defect would tend to extend in the depth direction rather than the length direction. However, this conclusion could be altered if the fracture toughness is higher in the depth direction than in the length direction.

Equations 22 with 13 gives a relationship between a_1 and c_1 for the linear-elastic case. This relation is also plotted in Fig. 7 (dotted lines) for comparison.

Finally, Eqs 21 and 22 are also plotted in Fig. 8 for a fixed value of the normalized CTOD, δ_1, several values of the normalized stress, $\sigma_1 = \sigma/\sigma_0$, and the same values of the other parameters as in Fig. 6.

The Effects of a Finite Circumference

Using the results of Erdogan and Bakioglu [*3*] it is possible to modify the Dugdale expressions for CTOD (Eqs 14 and 19) in an approximate way to account for the finite circumference of the pipe, W. This is known as the finite flat plate analogy [*1*]. The result is lengthy and more conveniently written down in the dimensionless forms. The resulting modifications of Eqs 18 and 21 are

$$\delta_2 = \frac{c_1 a_1 (1 - c_1) F}{\pi \sqrt{(\alpha \tan \alpha)}} \ln\left[\frac{1 + \sin \alpha}{1 - \sin \alpha}\right] \ln\left[\frac{1 + \sin \alpha_2}{1 - \sin \alpha_2}\right] \tag{24}$$

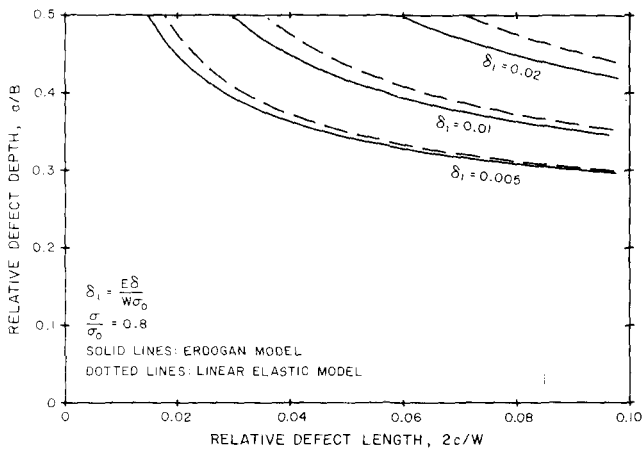

FIG. 7—*Predicted critical defect sizes. Comparison of the Erdogan and linear-elastic models for three different values of the normalized CTOD, δ_1, at the plastic zone.*

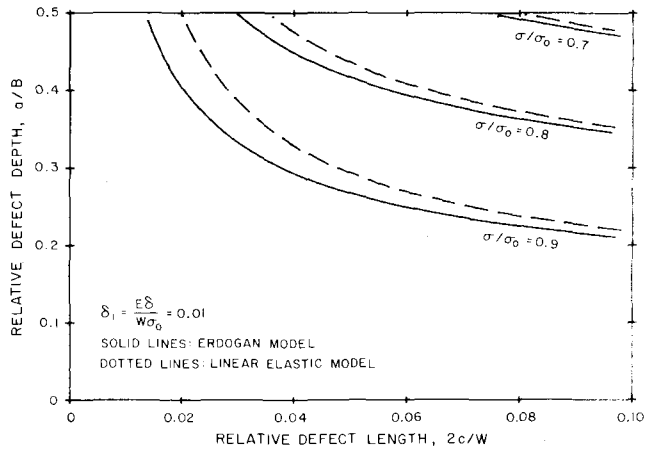

FIG. 8—*Predicted critical defect sizes. Comparison of the Erdogan and linear-elastic models for the normalized CTOD, δ_1, at the plastic zone and for three different values of the normalized stress, σ/σ_0.*

$$\delta_1 = (4/\pi)c_1a_1(1 - c_1)^2F^2 \ln \sec \alpha_2 \tag{25}$$

where the authors have defined

$$\alpha = \pi c/W = \pi c_1/2 \tag{26}$$

$$\alpha_2 = (\pi\sigma'/2\sigma_0')/(1 - 2c/W) = \alpha_1/(1 - c_1) \tag{27}$$

Here $F(\pi c/W)$ is the usual geometrical factor for the stress intensity factor. For a center cracked plate it is given by the Irwin expression

$$F(\alpha) = \sqrt{(\tan \alpha/\alpha)} \tag{28}$$

It was found that these modifications had a negligible effect on the curves in Figs. 2 through 8 for the parameters and range considered here. These equations will start showing a significant effect when the defect length, $2c$, approaches the circumference, W, and more details will be reported in another publication [*6*].

The Net-Section Flow-Strength Model

When the fracture toughness becomes very large it is seen that both Eqs 24 and 25 reduce to

$$\alpha_2 = \pi/2 \tag{29}$$

From Eqs 27 and 17 this is equivalent to

$$\sigma_1 = 1 - c_1 a_1 \tag{30}$$

$$\sigma/(1 - 2ca/WB) = \sigma_0 \tag{31}$$

The quantity $2ca/WB$ represents the fraction of cracked area in the cross-section of the plate or pipe. Hence, Eq 31 states that the net section stress equals the flow strength. This condition could be regarded as a generalization of the simple collapse condition (Eq 4). This criterion was found to account very well for fracture of Type 304 stainless steel plates and pipes by Kanninen et al [5].

For the values of the normalized stress, $\sigma_1 = \sigma/\sigma_0$, from 0.7 to 0.9, which are plotted in Figs. 6 and 8, it is found that the relation (Eq 30) falls outside the range considered for a/B and $2c/W$. In Fig. 9 the relation was plotted (Eq 30) for values of the normalized stress from 0.96 to 0.98. The authors conclude from these results that the net-section flow-strength model may not always give conservative answers if the fracture toughness is not large enough.

Summary

The curves in Figs. 2 through 8 represent the expected predicted critical defect sizes for the parameters and models considered. For a defect with a given depth and length, if the point falls below the curve on the plot it will not extend, but if the point falls above the curve it is assumed that the defect will extend and may lead to failure.

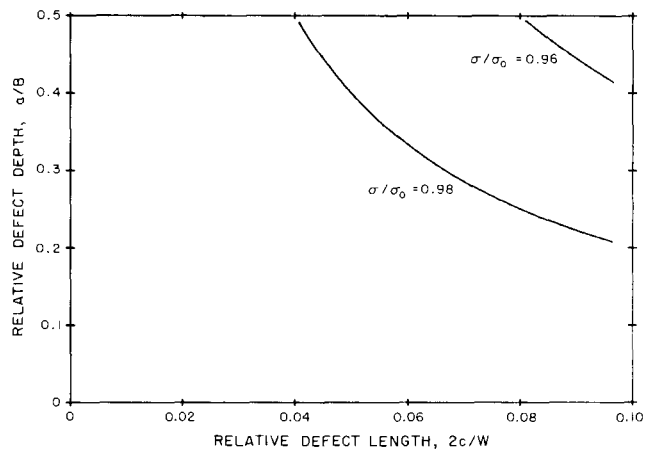

FIG. 9—*Predicted critical defect sizes for the net section flow strength model.*

The statistical variation in the material parameters has not been taken into account in this study. No safety factors have been assumed in these graphs. Verification experiments are now needed to assess the practical applicability of these theoretical curves.

Fracture mechanics methods have been used to develop several analytical models for predicted critical defect sizes of sharp circumferential surface-defects in pipes. Several theoretical limitations apply to these models, which are listed here for convenience:

1. Since the flat plate analogy for a pipe was used, the models do not account for bulging.
2. No bending of the sheet is assumed in the vicinity of the defect.
3. In the collapsed ligament model the defect is assumed to have a rectangular shape.
4. The ligament is always assumed to be completely yielded.
5. No work-hardening is assumed.
6. A critical value of the CTOD is assumed to be the fracture mechanics criterion for failure.
7. Slow stable crack growth is ignored.
8. The Irwin plastic zone in the Begley model and the Dugdale plastic zone in the Erdogan model are not realistic representations of plasticity at the crack-tip.

All of the above limitations have been used in previous work and have been claimed to offer satisfactory agreement between theory and experiment. However, how valid or accurate they are has never been explicitly assessed. Therefore, no quantitative measure of their validity can be given at this point.

Future plans call for experimental work to determine the overall predictability of the models. However, the validity and accuracy of the individual limitations cannot be assessed in the immediate future.

Acknowledgment

This research was supported in part by the Office of Pipeline Safety Regulation of the U.S. Department of Transportation, Washington, D.C. 20570.

References

[1] Wilkowski, G. M. and Eiber, R. J., "Review of Fracture Mechanics Approach to Defining Critical Size Girth Weld Discontinuities," WRC Bulletin 239, Welding Research Council, New York, 1978.

[2] Begley, J. A., "Defect Tolerance," Appendix B in the Alaska Pipeline Report, "Consideration of Fracture Mechanics Analysis and Defect Dimension Measurement Assessment for the Trans-Alaska Oil Pipeline Girth Welds," NBSIR 76-1154, Vols. I and II, National Bureau of Standards, 1976 (available from the National Technical Information Service, Springfield, Va.).

[3] Erdogan, F. and Bakioglu, M., *International Journal of Fracture,* Vol. 11, 1975, pp. 1031.

[4] Broek, D., *Elementary Engineering Fracture Mechanics*, Noordhoff International Leyden, The Netherlands, 1974.
[5] Kanninen, M. F., Broek, D., Hahn, G. T., Marshall, C. W., Rybicki, E. F., and Wilkowski, G. M., *Nuclear Engineering and Design*, Vol. 48, 1978, pp. 1-17.
[6] de Wit, R. and Smith, J. H., "Development of Some Analytical Fracture Mechanics Models For Surface Defects in Plates of Ductile Metals," Third International Symposium on Continuous Models of Discrete Systems, Freudenstadt, West Germany, 24-30 June 1979.

E. P. Cox[1] *and F. V. Lawrence, Jr.*[2]

Ductile Fracture Behavior of Wrought Steels

REFERENCE: Cox, E. P. and Lawrence, F. V., Jr., **"Ductile Fracture Behavior of Wrought Steels,"** *Fracture Mechanics: Twelfth Conference, ASTM STP 700,* American Society for Testing and Materials, 1980, pp. 529-551.

ABSTRACT: A two failure criteria model based on plasticity limit load (LL) theory and linear elastic fracture mechanics (LEFM) is proposed for characterizing the fracture behavior of ductile structural metals. Failure is considered to occur at the lower load predicted by the two failure criteria. The variables involved in the two failure criteria model are: fracture toughness (K_c), tensile strength (S_u), relative crack length (a/W), and geometry. A dimensionless parameter, $K_c/S_u W^{1/2}$ was defined. The fracture toughness failure criterion was found to dominate at low values of $K_c/S_u W^{1/2}$, and the LL failure criterion controls fracture at large values.

KEY WORDS: ductile fracture, fracture properties, mechanical properties, cracks, crack propagation, brittle fracture, plastic deformation toughness, steels, fractures (materials)

Nomenclature

- a Crack width or length
- Δa Change in crack length
- B Specimen thickness
- b Uncracked ligament
- d Span distance of bend specimen
- E Young's modulus
- J Value of the J-integral
- J_{Ic} Value of the J-integral at the onset of crack extension in plane strain
- K Stress intensity factor
- K_{Ic} Critical value of K in plane strain
- L Specimen length
- P Load

[1] Senior research engineer, Caterpillar Tractor Co., Peoria, Ill. 61629,
[2] Professor of Civil and Metallurgical Engineering, University of Illinois, Urbana, Ill. 61801.

P_m Maximum load (collapse load)
P_K Collapse load predicted by the fracture toughness failure criterion
P_L Collapse load predicted by the limit load failure criterion
S Gross section stress
S_m Gross section collapse stress (at maximum load)
S_o Tensile flow stress
S_y Tensile yield strength
W Specimen width
τ_o Shear flow stress

The ductile metals widely used in engineering applications may fracture at loads beyond the yield strength after extensive plastic deformation has occurred. The fracture loads of these high toughness metals often cannot be successfully predicted by linear elastic fracture mechanics (LEFM), particularly for the small thicknesses in common use. Attempts to characterize ductile, post-yield fracture of these materials using elastic-plastic fracture mechanics analyses have not been too successful. One of the most promising of these elastic-plastic analyses is the J-integral proposed by Rice [*1*].[3] Experiments have shown that the J-integral can be used to estimate the plane-strain fracture toughness of ductile metals undergoing elastic-plastic deformation [*2,3*]; thus, the J-integral may provide a single parameter characterization of post-yield fracture. However, a standard test method has yet to be established.

Recent investigations by the authors [*4–7*] and Dowling and Townley [*8*] have shown that post-yield fracture may be also characterized using both fracture mechanics and plastic limit-load failure criteria. The fracture toughness (FT) failure criterion predicts a fracture whenever the crack-tip stress intensity exceeds the material's fracture toughness. The limit load (LL) failure criterion predicts fracture (or collapse) when the load on the uncracked ligament reaches the limit load of the body. The limit load is the maximum load that a body can sustain without undergoing unlimited plastic deformation [*9,10*]. The two failure criteria concept is that the maximum (collapse) load or fracture stress of a body would be the lower value predicted by the two criteria.

Two Failure Criteria Model for Ductile Fracture

An example is given below of the two failure criteria model for a center-cracked-tension specimen (CCT). The gross section stress at collapse (S_m) for the CCT specimen geometry is [*11*]

[3] The italic numbers refer to the list of references appended to this paper.

$$S_m = \frac{P_m}{2BW} = 2\tau_o\left(1 - \frac{a}{W}\right) \tag{1}$$

where

P_m = collapse load,
B = specimen thickness,
$2W$ = specimen width, and
$2a$ = crack width.

The shear flow stress at fracture (τ_o) is replaced by either the von Mises or Tresca yield criterion. The collapse stress predicted using the von Mises yield criterion is

$$S_m{}^M = \frac{2}{3^{1/2}} S_u\left(1 - \frac{a}{W}\right) \tag{2}$$

Similarly, the collapse stress using the Tresca yield criterion is

$$S_m{}^T = S_u\left(1 - \frac{a}{W}\right) \tag{3}$$

The predicted values of collapse stress calculated using the von Mises and Tresca yield criteria are shown as solid lines in Fig. 1. The region between these lines labeled "limit load failure criterion" is the range in collapse stress predicted by the LL failure criterion. Most test data fall within this shaded region since most metals obey neither the von Mises nor Tresca yield criterion, exactly.

The collapse stress predicted by the fracture toughness failure criterion for the center-crack specimen geometry ($S_m{}^K$) is

$$S_m{}^K = \frac{K_c}{\left(\pi a \sec \frac{\pi a}{2W}\right)^{1/2}} \tag{4}$$

where K_c is the fracture toughness measured either by ASTM Test for Plane-Strain Fracture Toughness of Metallic Materials (E 399-78) test procedures (K_{Ic}) or by a J-integral test (J_{Ic}). The "fracture toughness failure criterion" is shown in Fig. 1 crossing the "limit load failure criterion" region. The value of $S_m{}^k$ is dependent on K_c, a, and W; whereas, $S_m{}^M$ and $S_m{}^T$ are dependent on S_u, a, and W. Consequently, as S_u, W, and K_c change, the values of S_m also change; and the intersection between the LL and FT failure criteria may be eliminated so that only one failure criterion prevails regardless of the relative crack length. For the case where an intersection

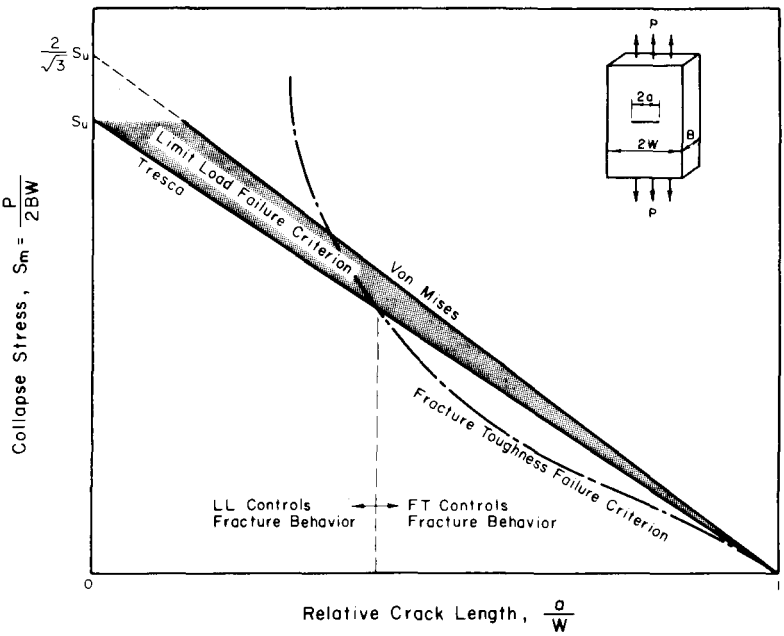

FIG. 1—*Illustration of the two failure criteria model for a center cracked tension specimen.*

does occur, such as shown in Fig. 1, the collapse stress will be that of the failure criterion which operates at the lower stress. In Fig. 1, the LL failure criterion controls fracture at smaller values of a/W, and the FT failure criterion controls fracture at larger values of a/W.

A transition from one failure criterion to another should occur whenever $S_m{}^T = S_m{}^K$. This condition will occur only at certain combinations of specimen dimensions, tensile strength, fracture toughness, and crack length (see Fig. 1). The crack length for this transition can be determined by equating the LL and FT collapse loads given by Eqs 2 to 4.

$$S_m{}^M \text{ or } S_m{}^T = S_m{}^K \tag{5}$$

which, for the CCT geometry and the Tresca yield criterion, becomes

$$S_u\left(1 - \frac{a}{W}\right) = \frac{K_c}{\left(\pi a \sec \frac{\pi a}{2W}\right)^{1/2}} \tag{6}$$

Equation 6 can be rearranged in terms of a/W to yield

$$\frac{K_c}{S_u W^{1/2}} = \left(1 - \frac{a}{W}\right)\left(\frac{\pi a}{W} \sec \frac{\pi a}{2W}\right)^{1/2} \tag{7}$$

The right-hand side of Eq 7 is multiplied by $2/3^{1/2}$ when the von Mises yield criterion is desired.

The quantity $K_c/S_u W^{1/2}$ relates the strength, fracture toughness and section size to the controlling failure criterion. This quantity is plotted versus a/W for the CCT specimen in Fig. 2 and for the three-point bend specimen in Fig. 3. When K_c is low and S_u is high (that is, a low value of $K_c/S_u W^{1/2}$) the fracture toughness failure criterion controls the fracture behavior. Increasing K_c and decreasing S_u raises the quantity of $K_c/S_u W^{1/2}$ into the limit load controlling region. Crack length also influences which failure criterion controls. Referring to Trajectory B in Fig. 2, at $K_c/S_u W^{1/2} =$

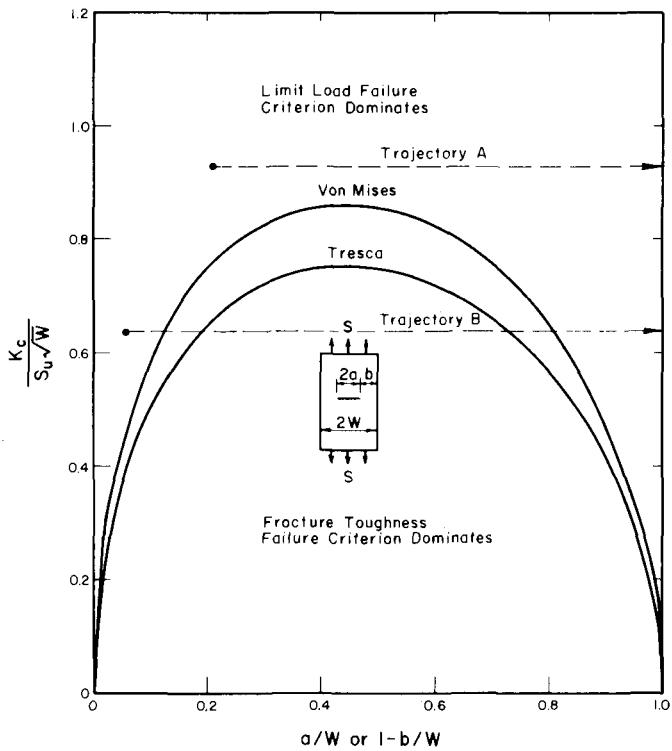

FIG. 2—*Limit load and fracture toughness failure criteria controlled fracture regions for the center cracked tension specimen. Trajectory "A" describes a failure that proceeds by limit only. Trajectory "B" describes a failure that begins as a limit load failure, changes to brittle fracture, and then back to limit load.*

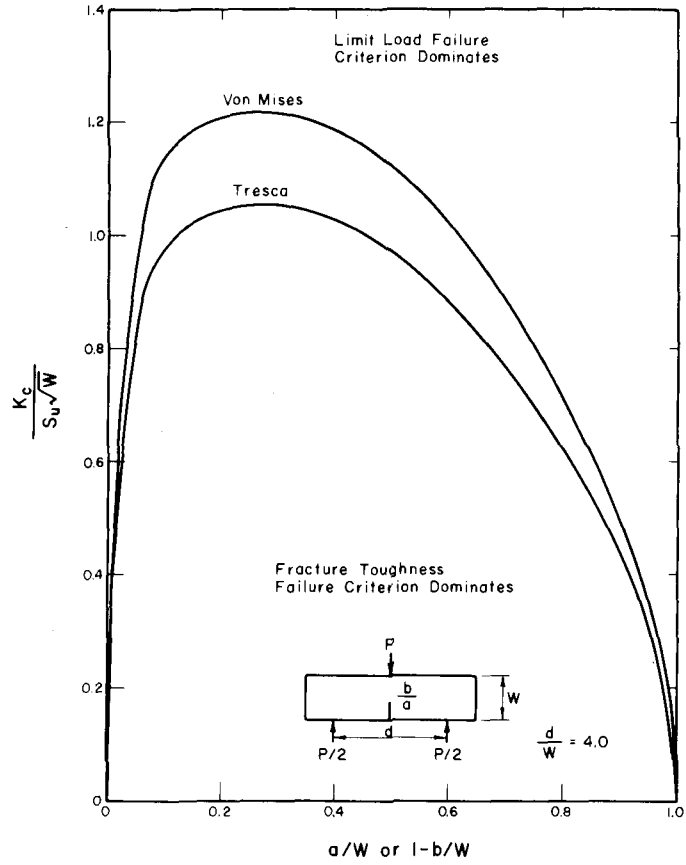

FIG. 3—*Limit load and fracture toughness failure criteria controlled fracture regions for the three-point bend specimen.*

0.65, the controlling failure criterion changes from LL to FT at small a/W (~ 0.1) and from FT back to LL at large a/W (~ 0.8).

A third illustration of the two failure criteria model is given for the compact specimen (CS). Since an exact limit load solution is not available, upper [*12*] and lower bound solutions are shown for both the von Mises and Tresca yield criteria. To be conservative, the lower bound LL solution was used in the analysis of the wrought steel data presented in a later section. The lower [*13*] bound LL expression for the collapse load is

$$P_L = \left[\left[2 + 2\left(\frac{a}{W}\right)^2\right]^{1/2} - \left[1 + \frac{a}{W}\right]\right] 2\tau_o BW \tag{8}$$

upon using the von Mises yield criterion Eq 8 becomes

$$\frac{P_L}{BW} = \left[\left[2 + 2\left(\frac{a}{W}\right)^2\right]^{1/2} - \left[1 + \frac{a}{W}\right]\right] \frac{2}{3^{1/2}} S_u \tag{9}$$

Using the Tresca yield criterion, the collapse load is

$$\frac{P_L}{BW} = \left[\left[2 + 2\left(\frac{a}{W}\right)^2\right]^{1/2} - \left[1 + \frac{a}{W}\right]\right] S_u \tag{10}$$

The FT failure criterion for a compact specimen is

$$\frac{P_K}{BW} = \frac{K_{Ic}}{YW^{1/2}} \tag{11}$$

where Y is the compliance function for a compact specimen given in the ASTM E 399 K_{Ic} test method. The concept of the two failure criteria model for the compact specimen is illustrated in Fig. 4.

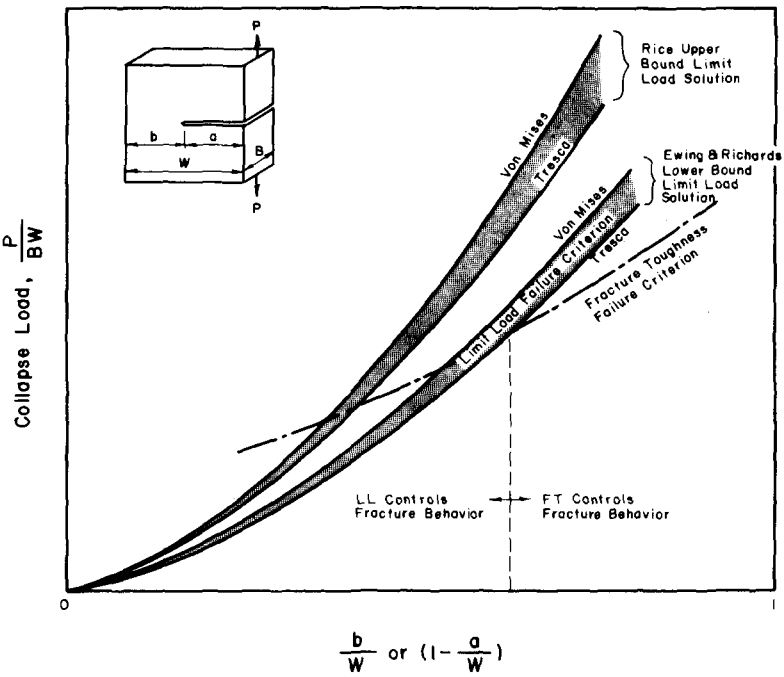

FIG. 4—*Illustration of the two failure criteria model for the compact specimen whose limit load failure criterion is approximated by upper and lower bound limit load solutions.*

Application of the Two Failure Criteria Model to Wrought Steels

Background

The use of the two failure criteria model to characterize the fracture behavior of wrought steels was tested by collecting and reanalyzing experimental data [*2,3,14-16*] for a variety of structural steels. These data were obtained from J-integral fracture toughness studies which used compact, three-point bend and four-point bend specimens. Only studies that reported both the collapse loads (maximum load values) and J-integral fracture toughness values were reanalyzed. The critical fracture toughness values determined from the J-integral tests have been denoted K_c to distinguish these values from the ASTM E 399 fracture toughness "K_{Ic}"; hence, all K_c-values are *J*-derived; that is

$$K_c^2 = J_{Ic}E \tag{12}$$

The steels considered range in yield strength from 283 MPa for the hot-rolled A570E steel to 1200 MPa for the quenched and tempered 4340 steel are indicated in Table 1.

Results

The reanalyses have been grouped by specimen geometry. For the CS specimens, the collapse loads were divided by the specimen width and thickness and plotted versus uncracked ligament per specimen width in Figs. 5-8. The collapse loads of the three-point and four-point bend specimens were divided by thickness and plotted versus uncracked ligament. These results are shown in Figs. 9 through 14, respectively. Using

TABLE 1—*The steels considered range in yield strength.*

Steel	Specimen Type	S_y (MPa)	Refs
A570E	CS[a]	283	*14*
A533B	CS, 3PB[b]	496	*3*
1EAEG	CS	731	*14*
1EAFD	CS	1110	*14*
Ni-Cr-Mo-V	3PB	855	*2,3*
AISI 4340	4PB[a]	779	*15*
A514	4PB	758	*16*
AISI 4340	4PB	1200	*15*

[a]CS = compact specimen.
[b]3PB = three-point bend specimen.
[c]4PB = four-point bend specimen.

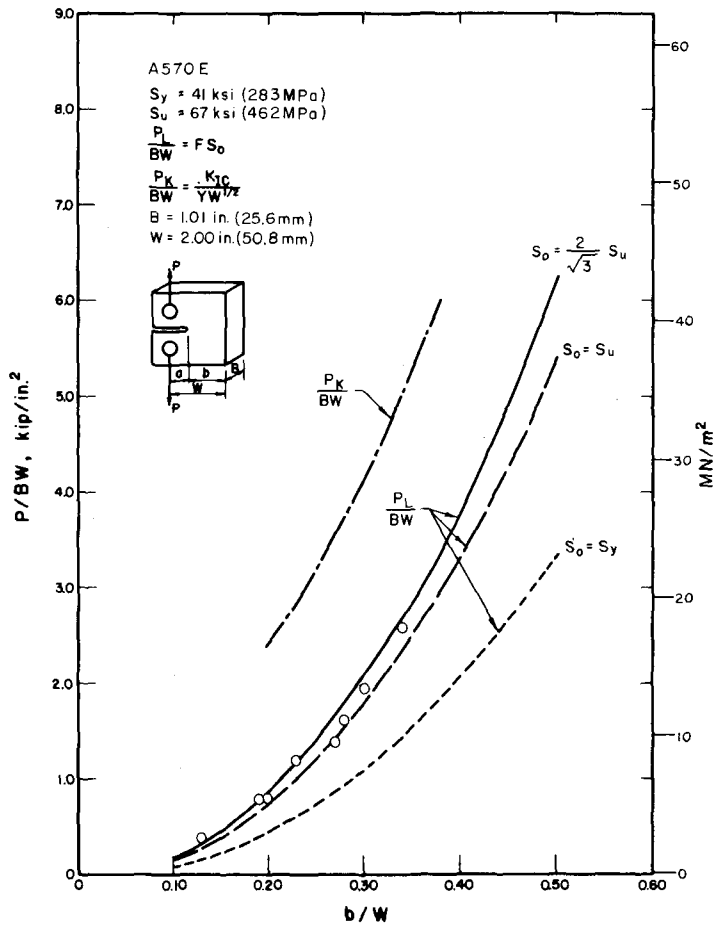

FIG. 5—*Comparison of A570E steel compact specimen data with collapse loads predicted by the limit load and fracture toughness failure criteria* [14].

the analysis previously discussed (Fig. 4), the collapse loads predicted by the LL and FT failure criteria are shown in each figure and compared with the experimental results. Also shown are the limit loads that were determined assuming a flow stress equal to the uniaxial yield strength of each material. Limit loads based on the uniaxial yield strength reflect the onset of net-section plastic deformation and permit the effect of work hardening on the LL failure criterion to be seen.

The reanalyses for which the measured collapse loads are predicted by the LL failure criterion are Figs. 5,6,9,11-13. The measured collapse loads generally lie between the von Mises and Tresca LL curves. The Tresca yield criterion is slightly conservative. Very conservative LL collapse

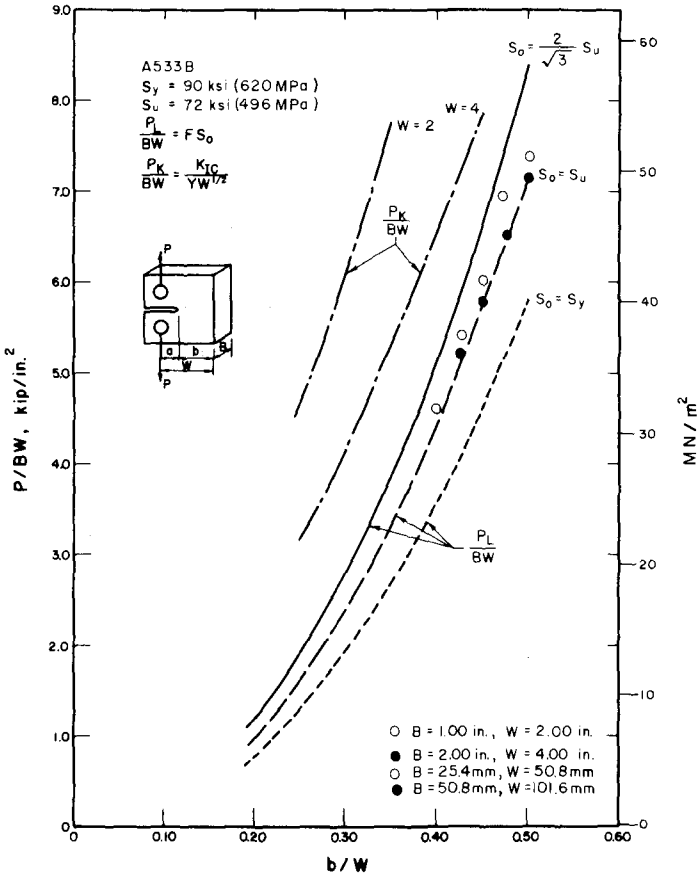

FIG. 6—*Comparison of A533B steel compact specimen data with collapse loads predicted by the limit load and fracture toughness failure criteria* [2,3].

load predictions result for the lower strength steels when the collapse stresses are calculated using the uniaxial yield strengths. Those materials that do not work-harden appreciably, that is, the higher strength quenched and tempered steels, exhibit little difference between the limit loads calculated using either the yield or tensile strengths. Reanalyses for which the measured collapse loads agreed with the FT failure criterion are shown in Figs. 7 and 8.

The effect of section size is illustrated in Fig. 6 in which the collapse loads agree with those predicted by the LL failure criterion for the specimen dimensions tested. However, the collapse loads predicted by the FT failure criterion decrease with increasing section size. Continuing to increase the section size should result in a change in the controlling failure criterion.

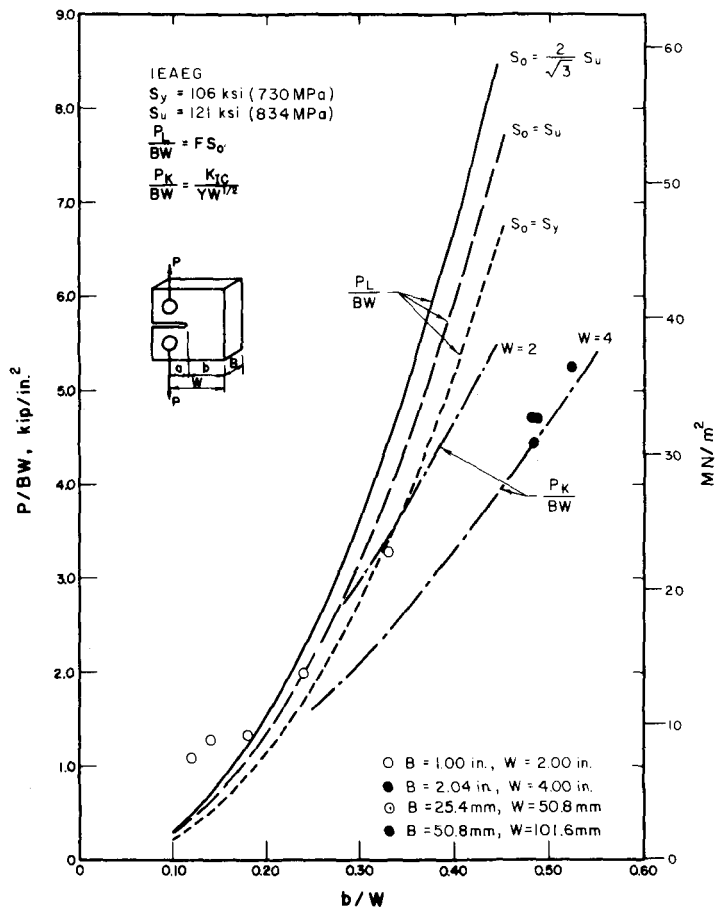

FIG. 7—*Comparison of IEAEG steel compact specimen data with collapse loads predicted by the limit load and fracture toughness failure criteria* [14].

An example of such a change is shown in Fig. 14 for the high-strength 4340 steel specimens. The 4340 steel collapse loads are characterized by the LL failure criterion for the smaller values of the uncracked ligament, but at the larger values of the uncracked ligament, the collapse loads are controlled by the FT failure criterion.

Discussion

Two Failure Criteria Model

The experimental results and analyses shown in Figs. 5–14 illustrate that ductile fracture can be understood using a two failure criteria model.

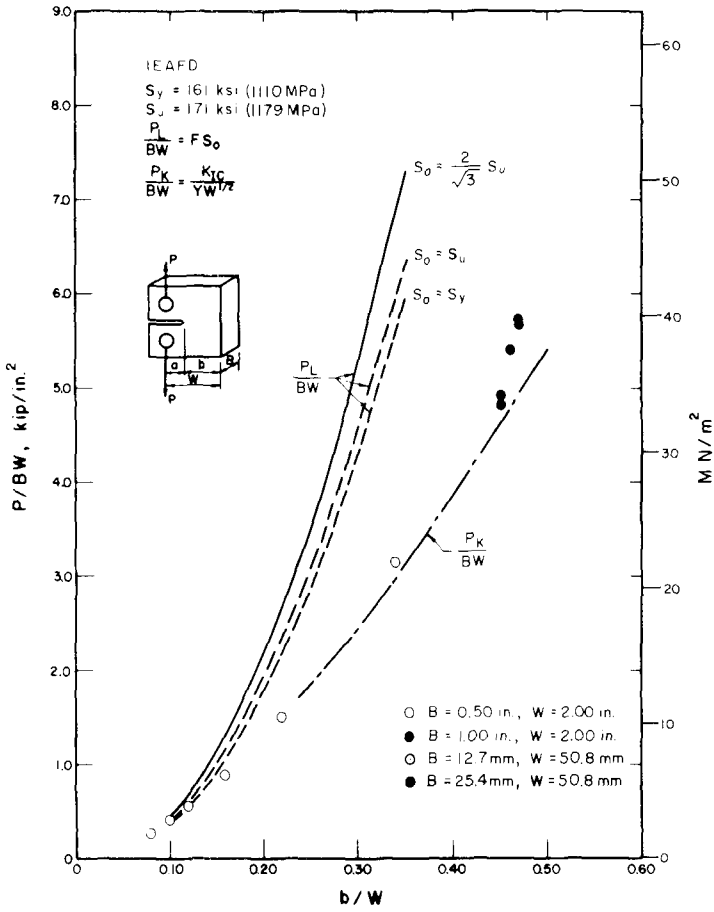

FIG. 8—*Comparison of IEAFD steel compact specimen data with collapse loads predicted by the limit load and fracture toughness failure criteria* [14].

In all instances, the experimental data agreed with the lower of the two collapse loads predicted by the two failure criteria model. The limit load controlled failures generally exhibited collapse loads lying between the values predicted using the von Mises and Tresca yield criteria. Limit loads based on the uniaxial yield strength showed no consistent relationship with measured collapse loads; consequently, predictions based on the limit load approach should be made equating the flow stress to the ultimate strength.

The FT failure criterion characterized the fracture behavior of the higher strength steels. The collapse loads of specimens controlled by the

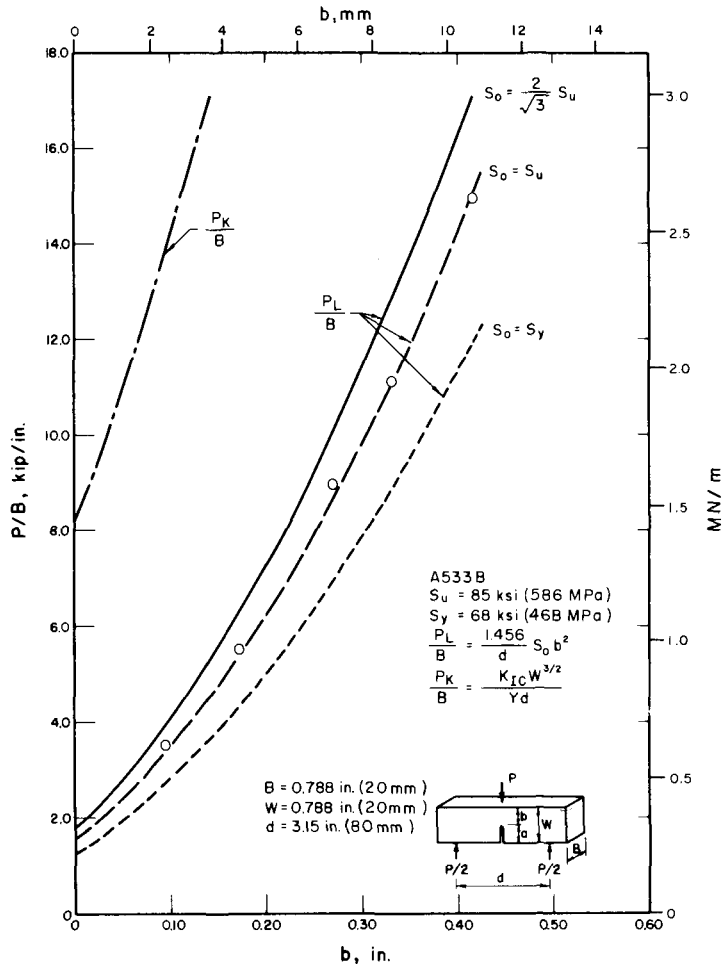

FIG. 9—*Comparison of A533B steel three-point bend specimen data with collapse loads predicted by the limit load and fracture toughness failure criteria* [2,3].

FT failure criterion were less than the loads necessary to cause net-section yielding (the yield strength limit loads).

A comparison between the predicted controlling failure criterion and experimental results is offered in Fig. 15 for the three-point bend specimens. All the reported data were apparently limit-load-controlled failures. Figure 15 illustrates an important aspect of the two failure criteria model, namely, the possibility of an *a priori* characterization of fracture behavior. If the tensile strength and fracture toughness are known, the controlling failure criterion can be predicted for a given geometry and section size.

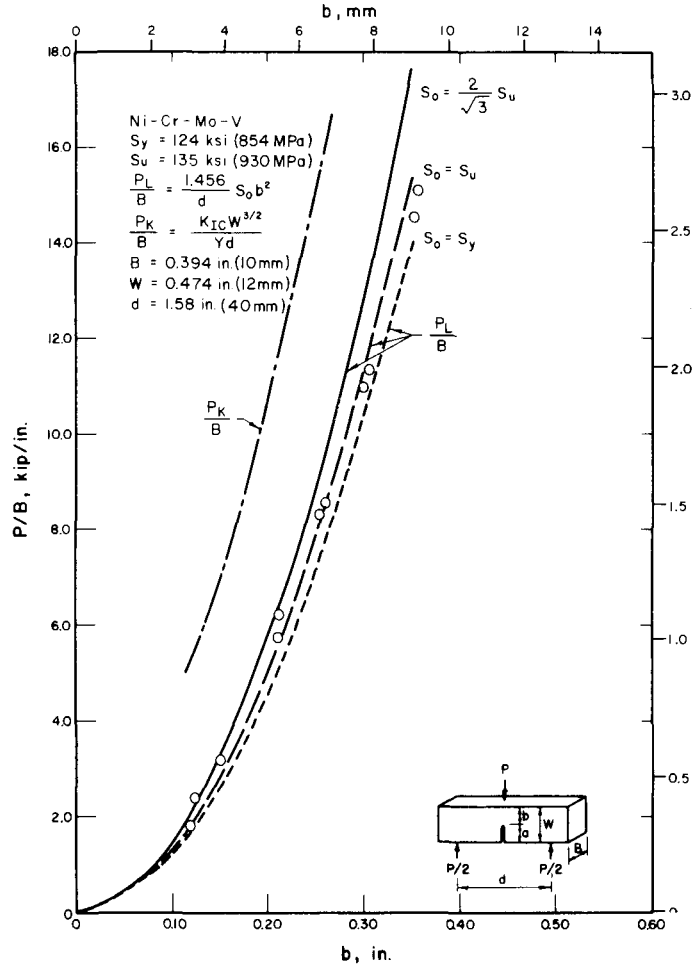

FIG. 10—*Comparison of Ni-Cr-Mo-V steel three-point bend specimen data with collapse loads predicted by the limit load and fracture toughness failure criteria* [2,3].

Effect of Subcritical Crack Extension

Subcritical crack extension is thought to affect the two failure criteria fracture model by altering the load-crack-length trajectory prior to collapse. Studies of resistance to crack extension (R-curves) using the J-integral have shown a geometry and section size dependence [*19*]. As a result, experimentally determined J_{Ic}-values may vary with specimen size and geometry. Subcritical crack extension begins when the applied J exceeds J_{Ic}. The stress-crack-length trajectory from this point to fracture is dependent on the tearing behavior of the material. Final fracture should

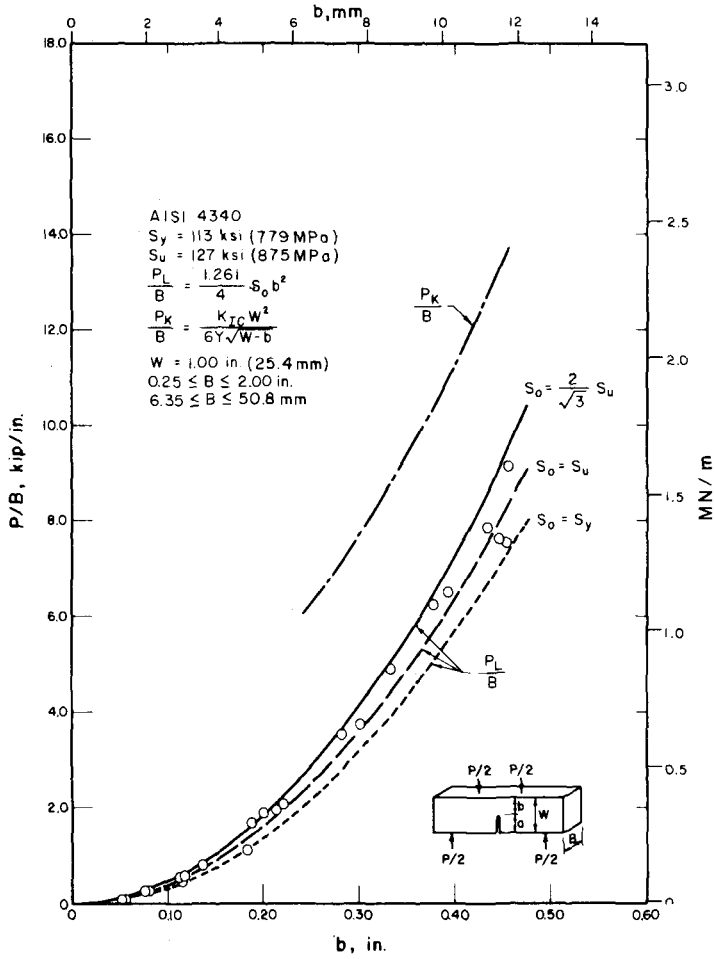

FIG. 11—*Comparison of low-strength AISI 4340 steel four-point bend specimen data with collapse loads predicted by the limit load and fracture toughness failure criteria* [15].

occur when the stress-crack-length trajectory intersects either the LL or FT failure criteria.

The effect of subcritical crack extension is illustrated in Fig. 16 for a butt weld containing an incomplete joint fusion. In the absence of subcritical crack extension, the stress-crack-length trajectories are depicted by the "A" lines. Subcritical crack extension is thought to alter the stress-crack-length trajectory in the manner of the curves labeled "B". Curves 2 and 4 in Fig. 16 illustrate how subcritical crack extension could change the controlling failure criterion.

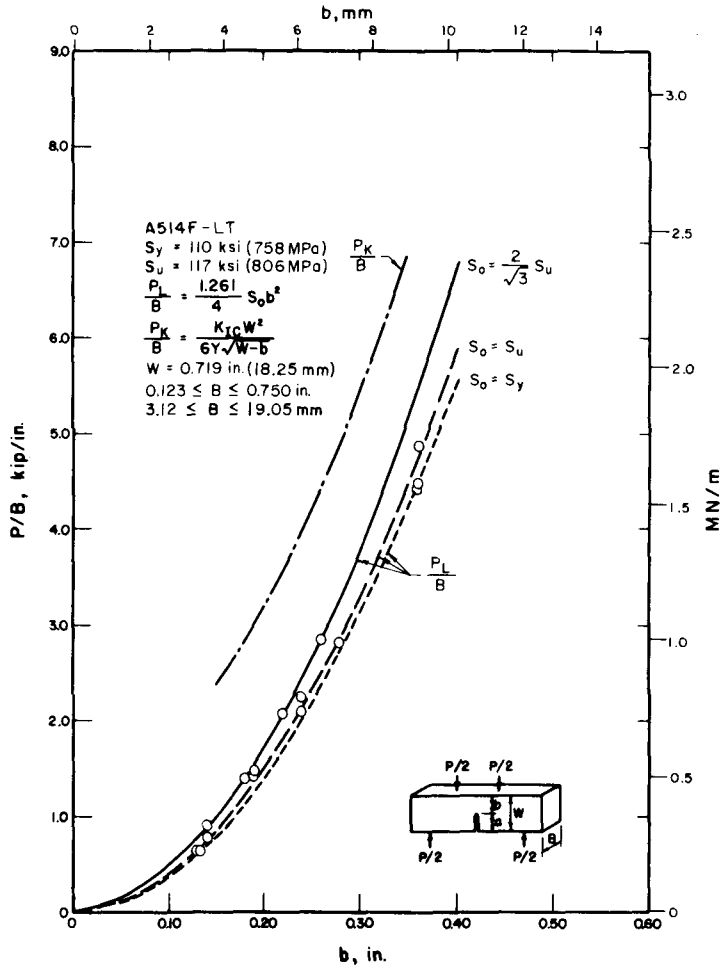

FIG. 12—*Comparison of A514F-LT steel four-point bend specimen data with collapse loads predicted by the limit load and fracture toughness failure criteria* [16].

The stable tearing behavior of structural materials has been described by Paris et al [*18*] in terms of a tearing modulus (T) (Fig. 17). The first crack extension is attributed to crack-tip blunting in proportion to the applied J

$$\Delta a \simeq \frac{J}{2S_o} \tag{13}$$

where S_o = the tensile flow stress. When the applied J reaches J_{Ic}, crack

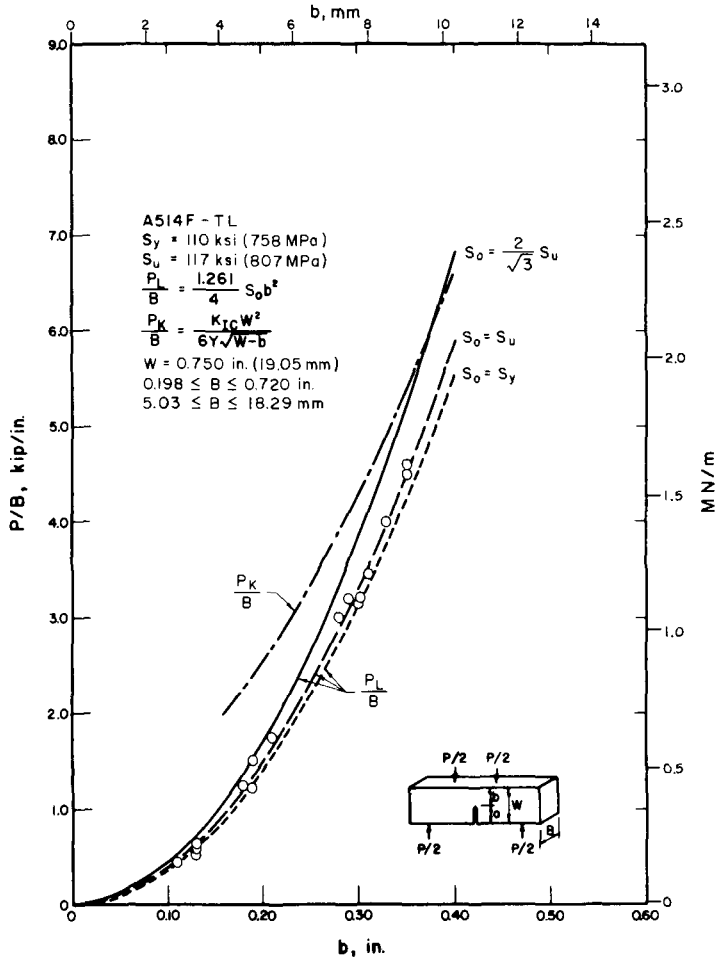

FIG. 13—*Comparison of A514F-TL steel four-point bend specimen data with collapse loads predicted by the limit load and fracture toughness failure criteria* [16].

extension by "stable tearing" begins. The slope of the stable tearing portion of the curve is used to determine T

$$T = \frac{dJ}{da} \frac{E}{S_o^2} \tag{14}$$

The effect of stable tearing can be incorporated into the two failure criteria model for a center-crack tension specimen since unstable tearing was stated to occur [*18*] whenever

$$T \leq \frac{L}{W} \tag{15}$$

Substituting Eq 12 into Eq 14 and combining this with Eq 15 results in

$$T \simeq \frac{dK^2}{da}\frac{1}{S_o{}^2} \leq \frac{L}{W} \tag{16}$$

When Eq 16 is integrated and subsequently divided by $W^{1/2}$

$$\frac{K_c}{S_o W^{1/2}} \leq \left(\frac{L}{W} \cdot \frac{a}{W}\right)^{1/2} \tag{17}$$

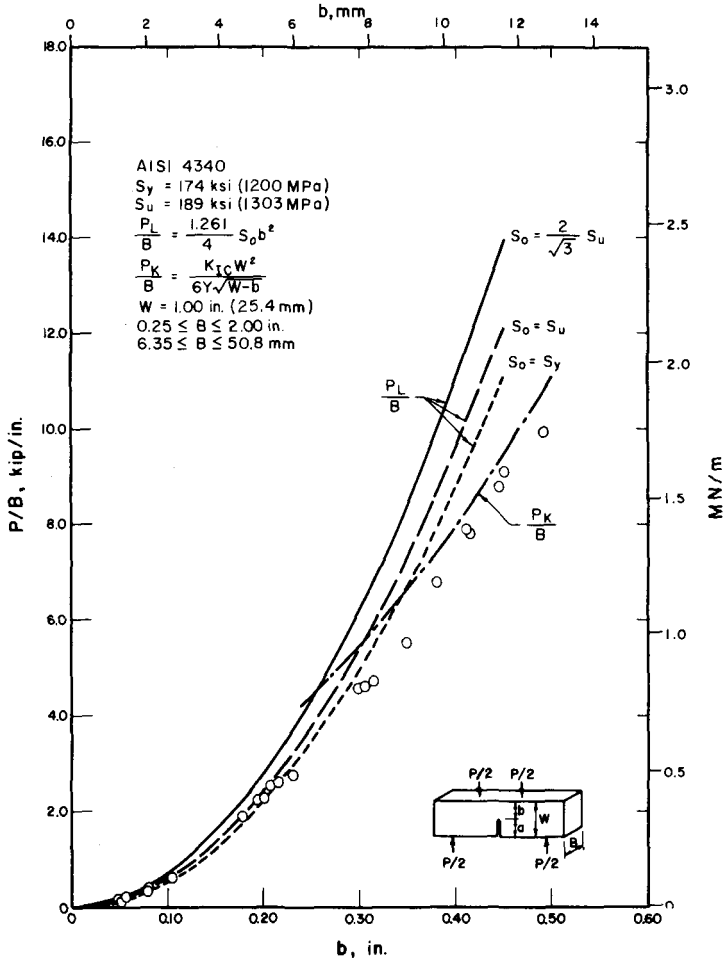

FIG. 14—*Comparison of high-strength AISI 4340 steel four-point bend specimen data with collapse loads predicted by the limit load and fracture toughness failure criteria* [15].

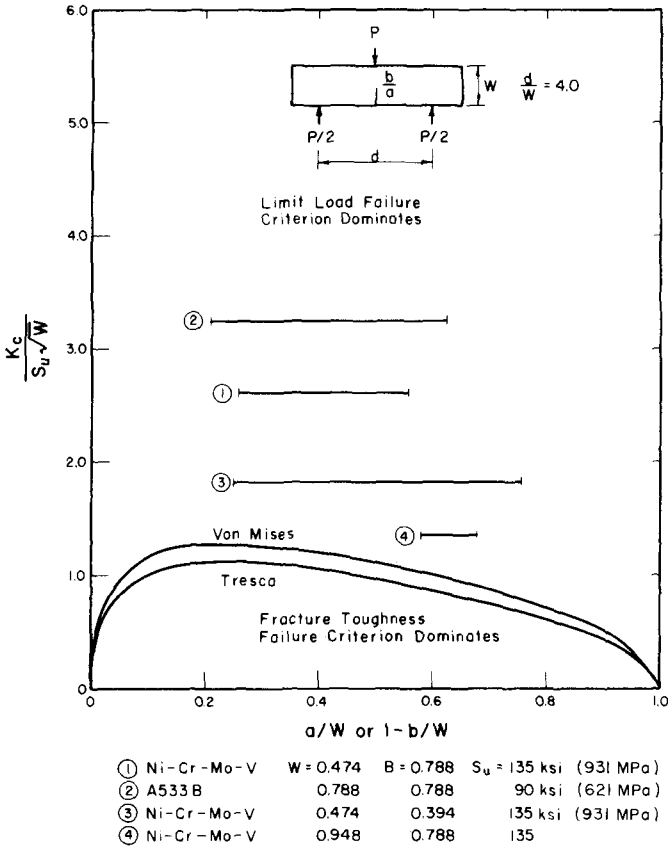

FIG. 15—*Comparison of the three-point bend specimen data from a variety of steels.*

Values calculated using Eq 17 for various values of $(L/W)^{1/2}$ are shown in Fig. 18 for the center-crack tension specimen. Subcritical crack extension precedes final fracture in the region lying above the appropriate $(L/W)^{1/2}$ line, and below this line, no subcritical crack extension occurs prior to fracture. Bodies prone to subcritical crack extension follow a $K_c/S_u W^{1/2} - a/W$ trajectory (horizontal lines in Figs. 2 and 18) until another of the failure criteria is encountered or the crack extends across the entire specimen.

Conclusions

The collapse stresses of flawed, wrought structural steels were predicted by a two failure criteria model that is based on plastic limit load theory and linear elastic fracture mechanics.

For a given geometry and crack length, the fracture behavior was shown

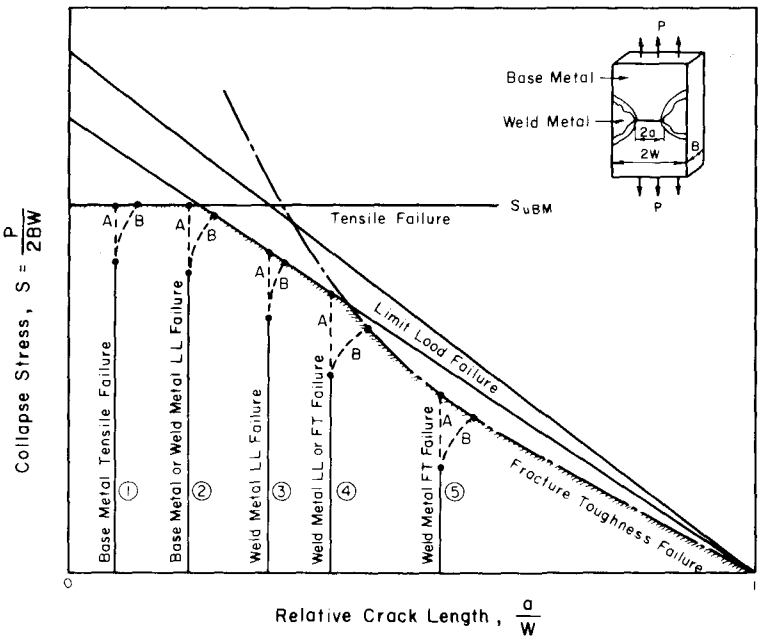

FIG. 16—*The effects of subcritical crack extension on the two failure criteria model for a centrally flawed butt weldment. For a given initial crack length, specimens not undergoing subcritical crack extension follow Trajectory "A"; while those that exhibit subcritical crack extension will follow a trajectory such as "B."*

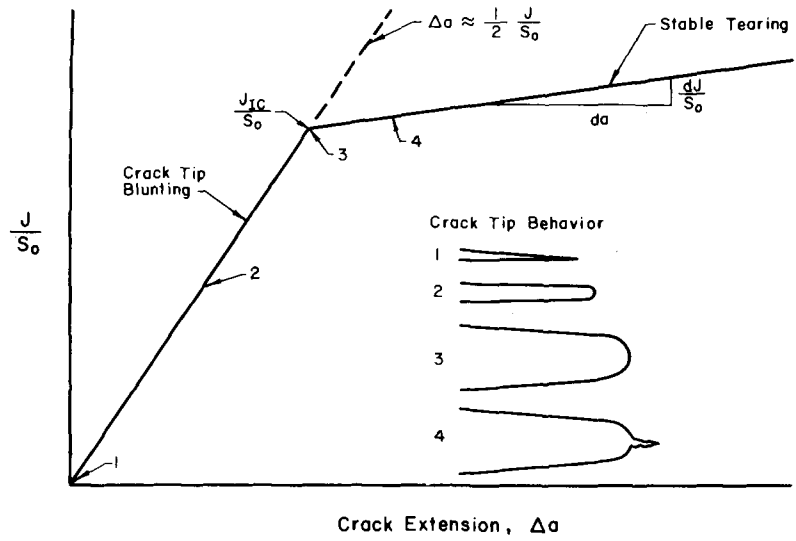

FIG. 17—*J-integral R-curve illustrating the crack tip behavior as* J *increases. The crack tip blunts in the region* $0 < J/S_o < J_{Ic}/S_o$ *followed by stable crack extension by tearing when* $J/S_o > J_{Ic}/S_o$.

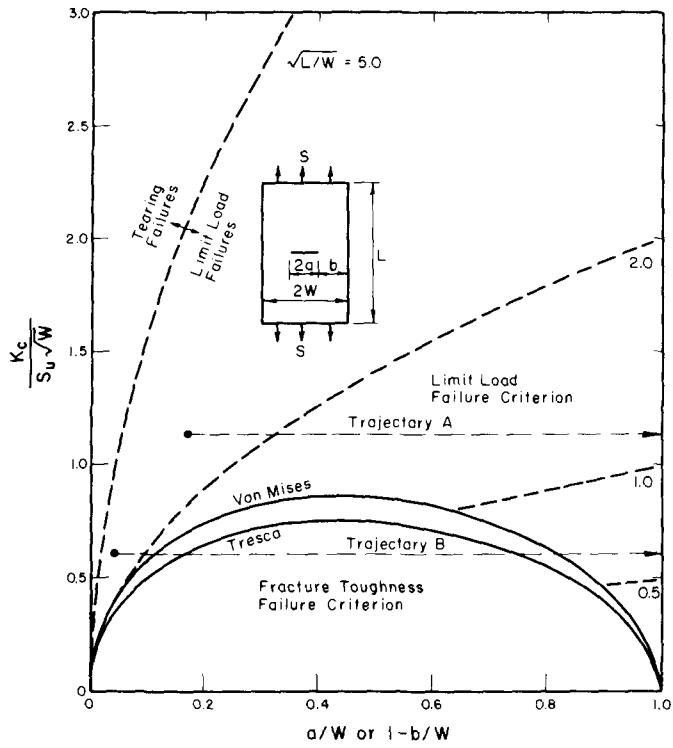

FIG. 18—*The effects of stable tearing on the fracture behavior of center cracked tension specimens. Subcritical crack extension may occur at a constant value of* $K_c/S_u\sqrt{W}$ *until either the limit load or fracture toughness failure criterion controlled region is encountered. Trajectory "A" predicts tearing followed by limit load. Trajectory "B" predicts, tearing, limit load, brittle fracture then, finally, limit load behavior during fracture.*

to depend on the fracture toughness, strength, and section size of the body. Fracture governed by the fracture toughness failure criterion occurred for low values of $K_c/S_u W^{1/2}$, and limit load controlled fractures occurred for high values of $K_c/S_u W^{1/2}$.

Subcritical crack extension by stable tearing was considered. Crack extension may change the controlling failure criterion, thereby resulting in a lower collapse stress. For specimens with very low length-width ratios, the entire fracture process may be controlled by stable tearing.

Acknowledgments

Portions of this investigation were supported by the University of Illinois Fracture Control Program, which is sponsored by a consortium of mid-

western ground vehicle industries and which is directed by Professor H. T. Corten of the Department of Theoretical and Applied Mechanics.

References

[1] Rice, J. R., *Journal of Applied Mechanics,* Vol. 35, 1968, pp. 379-386.
[2] Begley, J. A. and Landes, J. D. in *Fracture Toughness, ASTM STP 514,* American Society for Testing and Materials, 1972, pp. 1-23.
[3] Landes, J. D. and Begley, J. A. in *Fracture Toughness, ASTM STP 514,* American Society for Testing and Materials, 1972, pp. 24-39.
[4] Lawrence, F. V. and Cox, E. P., *Welding Journal Research Supplement,* Vol. 55, 1976, pp. 113s-120s.
[5] Lawrence, F. V., Jr. and Cox, E. P., "The Effect of Lack of Penetration Defects on the Static Tensile Behavior of High-Strength Structural Steel Weldments," Technical Report UICU-ENG-73-2011, Sept. 1973; also Construction Engineering Research Laboratory Technical Report M-123, Champaign, Ill. 1975.
[6] Lawrence, F. V., Jr., and Cox, E. P., "Influence of Heat Input and Lack of Penetration Length on Static Tensile Strength of High-Strength Structural Steel Weldments," Technical Report to Construction Engineering Research Laboratory, June 1974; also Construction Engineering Laboratory Technical Report M-135, Champaign, Ill., 1975.
[7] Cox, E. P., unpublished research.
[8] Dowling, A. R. and Townley, C. H. A., *International Journal of Pressure Vessels and Piping,* Vol. 3, 1975, pp. 2-31.
[9] Drucker, D. C., Prager, W. and Greenberg, H. J., *Quarterly of Applied Mathematics,* Vol. 9, 1952, pp. 381-389.
[10] Drucker, D. C. in *Fracture,* H. Liebowitz, Ed., Vol. 1, Academic Press, New York, 1968, pp. 474-529.
[11] McClintock, F. A., *Welding Journal Research Supplement,* Vol. 40, 1961, pp. 202s-208s.
[12] Rice, J. R. in *The Surface Crack: Physical Problems and Computational Solutions,* American Society of Mechanical Engineers, New York, 1972, pp. 171-185.
[13] Ewing, D. J. E. and Richards, L. E., *Journal of the Mechanics and Physics of Solids,* Vol. 22, 1974, pp. 27-36.
[14] Sailors, R. H., "Relationship Between Tensile Properties and Microscopically Ductile Plane Strain Fracture Toughness," TAM Report No. 37, University of Illinois, Urbana, Ill., 1973.
[15] Zaverl, F., Jr., "The Influence of Specimen Dimensions on a J_m Fracture Toughness Test," TAM Report No. 394, University of Illinois, Urbana, Ill., 1974.
[16] Carlson, K. W., private communication, 1977.
[17] Landes, J. D. and Begley, J. A. in *Fracture Analysis, ASTM STP 560,* American Society for Testing and Materials, 1974, pp. 170-186.
[18] Paris, P. C., Tada, T., Zohoor, A., and Ernest, H., "Instability of the Tearing Mode of Elastic-Plastic Crack Growth," Washington University Report No. NRC 77-1, St. Louis, Mo., 1977.

Richard Roberts, [1] *G. V. Krishna,* [2] *and Jerar Nishanian* [3]

Fracture Behavior of A36 Bridge Steels

REFERENCE: Roberts, Richard, Krishna, G. V., and Nishanian, Jerar, **"Fracture Behavior of A36 Bridge Steels,"** *Fracture Mechanics: Twelfth Conference, ASTM STP 700,* American Society for Testing and Materials, 1980, pp. 552-577.

ABSTRACT: This report examines the fracture toughness behavior of three heats of A36 steel in terms of Charpy V-notch (CVN) and critical stress intensity level (K_{Ic}) at an intermediate rate of loading (that is, one second rise time to failure). These results are contrasted with current toughness requirements of the American Association of State Highway and Transportation Officials (AASHTO) and the "H" testing frequency.

KEY WORDS: A36 steel, CVN testing, K_{Ic} testing, fractures (materials), fracture control, crack propagation

The Federal Highway Administration of the United States Department of Transportation proposed in 1972 that toughness requirements [*1*][4] be applied to the purchase of steels to be used in bridge construction. This proposal, which took the form of a requirement of a minimum Charpy V-notch (CVN) energy at a specified temperature, was taken up and modified by the American Iron and Steel Institute (AISI). This modified proposal [*2*] was presented to the American Association of State Highway and Transportation Officials (AASHTO) who subsequently adopted the proposal. The adoption of such requirements was the result of a number of recent fracture related bridge problems [*3,4,5*].

The specific details of the original AASHTO CVN requirements are set forth in Table 1. In addition to Table 1 it was required that the CVN testing be conducted in accordance with ASTM Sampling Procedure for Impact Testing of Structural Steel (A 673-77), such that all materials are tested to an

[1] Professor, Materials Research Center, Lehigh University, Bethlehem, Pa., 18015.
[2] Engineering associate, Air Products and Chemicals, Inc., Allentown, Pa. 18105.
[3] Structural research engineer, Office of Research, Federal Highway Administration, Washington, D.C. 20590.
[4] The italic numbers in brackets refer to the list of references appended to this paper.

TABLE 1—*AASHTO fracture-toughness specifications for bridge steels.*

ASTM Designation	Thickness	Energy Absorbed (ft·lb)/temperature, °F		
		Zone 1[b]	Zone 2[b]	Zone 3[b]
A 36		15/70	15/40	15/10
A 572[a]	up to 4 in. mechanically fastened	15/70	15/40	15/10
	up to 2 in. welded	15/70	15/40	15/10
A 440		15/70	15/40	15/10
A 441		15/70	15/40	15/10
A 242		15/70	15/40	15/10
A 588[a]	up to 4 in. mechanically fastened	15/70	15/40	15/10
	up to 2 in. welded	15/70	15/40	15/10
	over 2 in. welded	20/70	20/40	20/10
A 514	up to 4 in. mechanically fastened	25/30	25/0	25/−30
	up to 2½ in. welded	25/30	25/0	25/−30
	over 2½ to 4 in. welded	35/30	35/0	35/−30

Conversion factor:
1 ksi = 0.145 MPa
1 in. = 25.4 mm
1 ft·lb = 0.737 J
°C = (°F −32)/1.8

[a] If the yield point of the material exceeds 65 ksi, the temperature for the CVN value for acceptability shall be reduced by 15°F for each increment of 10 ksi above 65 ksi.

[b] Zone 1: Minimum service temperature 0°F and above; Zone 2: Minimum service temperature from −1 to −30°F; and Zone 3: Minimum service temperature from −31 to −60°F.

"H" frequency except the A514 material, which is to be tested to a "P" frequency. These frequencies are defined according to ASTM A 673 as

Frequency of Testing

5.1 Frequency (H) Heat Testing:

5.1.1 Plates and Shapes—One impact test (a set of three specimens) shall be made for each 50 tons (45 Mg) of the same type of product produced on the same mill from each heat of steel. The impact tests shall be taken from different as-rolled or heat-treated pieces of the heaviest gage produced unless there are insufficient pieces of the heaviest gage material produced to comply with the number of tests required in which case the testing shall proceed to the next heaviest piece produced. An as-rolled piece is the unit piece rolled from a slab, billet, bloom, or directly from an ingot.

5.2 Frequency (P) Piece Testing:

5.2.1 Plates and Shapes—One impact test, (a set of three specimens) shall be made from each as-rolled or as heat-treated plate or shape.

The fracture mechanics basis for the current AASHTO CVN requirements have been discussed by Barsom [*2*]. The essential features of the arguments put forward to justify the AASHTO specifications are very simple. Firstly, it was assumed that typical bridge loadings or stress time variations can be classified as an intermediate rate of loading when compared to static and impact loading. This is quite reasonable when compared to actual data [*6*] that show about a 1-s rise time to maximum load.

Secondly, the assumption was made that a definite temperature shift exists between the static and dynamic fracture response of bridge steels as measured by a critical stress intensity level, K_{Ic}. This is shown schematically in Fig. 1. The level of the temperature shift is dependent upon the static room temperature yield strength of the material and is expressed as [7]

$$T_s = 215 - 1.5\sigma_y \tag{1}$$

where

T_s = temperature shift in °F, and
σ_y = static room temperature yield strength, ksi.

The shift from the dynamic to the intermediate fracture response curves is estimated as approximately 75 percent of T_s [7]. This is also shown in Fig. 1.

Thirdly, another point behind the ASSHTO requirements was that the region of the dynamic K_{Ic} versus temperature curve where the K level begins to rise rapidly from the approximately horizontal portion of the K-curve corresponds to the temperature transition region of the CVN curve obtained for the same material. Figure 2 shows this schematically. Thus, the CVN curve can be used to locate the point of upswing of the dynamic K_{Ic}-curve along the temperature axis.

The final item as discussed by Barsom was that the fracture response of the two materials which he studied, ASTM steels A36 and A572, Grade 50 in thicknesses of 35.6 and 37.3 mm, respectively, showed a definite departure from plane-strain fracture behavior at approximately 27.8°C (82°F) above the temperature transition point. Furthermore, Barsom [2] proposed that the temperature of the CVN level can be used to conservatively estimate the temperature transition point. This is reasonable since at a CVN level of 20 J the corresponding K level is about 45 MPa$\sqrt{m}$. This is well above the K plateau or well into the transition region.

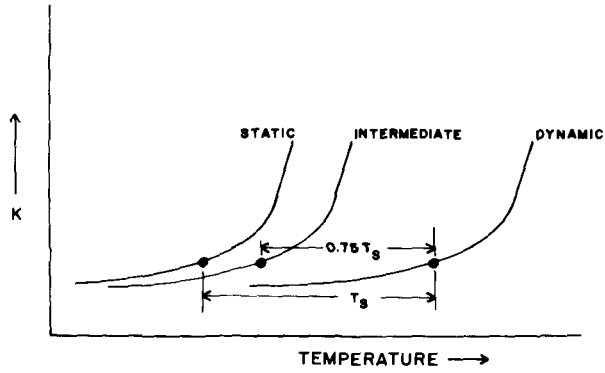

FIG. 1—*Schematic representation of* K *versus temperature for a structural grade steel.*

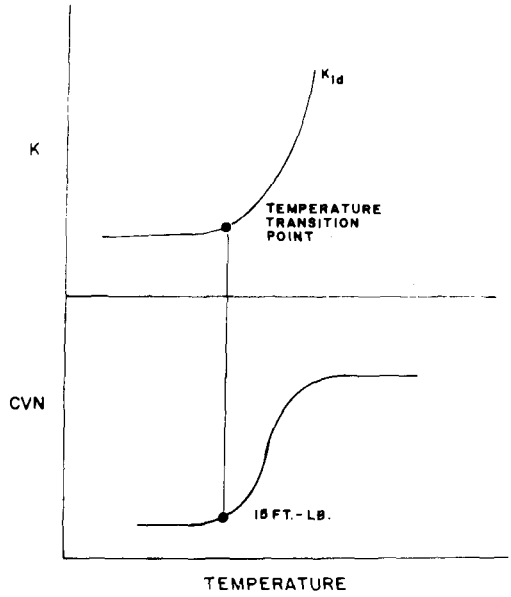

FIG. 2—*Schematic representation of correspondence of temperature transition regions and the temperature transition point with the 20 J (15 ft·lb) temperature.*

The above four items, (1) 1-s or intermediate loading for bridges, (2) definite temperature shift T_s, (3) CVN-K correspondence of temperature transition regions, and (4) temperature transition point plus 27.8°C (82°F) for nonplane-strain behavior were then combined with the philosophy that the materials shown in Table 1 should have adequate notch toughness so that at the lowest expected service temperature nonplane-strain behavior can be guaranteed at an intermediate rate of loading. All of this is illustrated in Fig. 3 for a hypothetical 248-MPa yield strength material with a lowest expected service temperature of −17.8°C (0°F).

To achieve the objective of nonplane-strain behavior at −17.8°C (0°F) it is required that the 20 J temperature transition point occur for an intermediate loading rate 27.8°C (82°F) below the −17.8°C (0°F) temperature or −45.6°C (−50.1°F). Since an intermediate rate of loading is appropriate for bridges, the temperature transition point on the dynamic curve should occur 0.75 T_s above the −45.6°C (−50.1°F) point. For a 248-MPa yield strength material T_s as per Eq 1 is approximately 88.9°C (192°F) or 75 percent of T_s is 66.7°C (152.1°F). Thus, the transition point should occur on the dynamic K_c-curve at −45.6°C (−50.1°F) plus 66.7°C (152.1°F) or at 21.1°C (70°F). Since the 20 J CVN temperature is proposed as a conservative estimate [2] of the dynamic fracture toughness transition point, a material with a measured CVN response of 20 J or better at 21.1°C (70°F) would meet the desired re-

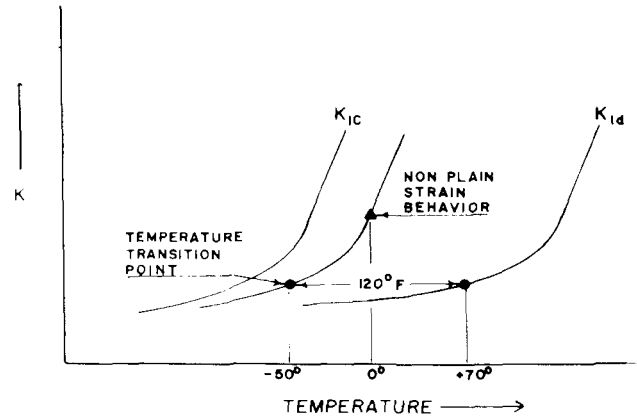

FIG. 3—*Schematic representation of AASHTO requirements for a −17.7°C (0°F) lowest expected operating temperature.*

quirements. It is obvious that the use of CVN tests for specification purposes is much more sensible than the use of the more costly K_c tests assuming all of the previous discussion is correct.

As already noted, the 1973 AASHTO CVN specification further required for quenched and tempered steels, such as A514, a "P" or piece testing frequency be employed for the CVN tests (ASTM A 673). For all other bridge steels and "H" or 45-Mg increment, heat testing frequency is used for the CVN tests. The use of a "P" frequency certainly offers more comfort in the knowledge of the properties of a specific piece of steel than an "H" test procedure. Furthermore, its use for quenched and tempered steels is generally reasonable. For the nonquenched and tempered steels the ability of the "H" testing frequency to adequately describe the CVN properties of each piece of steel plate from a single heat of steel is certainly open to question.

The primary goal of the research described in this report was to examine the suitability of an "H" testing frequency for the nonquenched and tempered bridge steels. The material chosen for this was an ASTM A36 bridge steel. Along with the primary goal it was hoped that further justification for the temperature shift T_s could be found in the present results.

Experimental Program

Test Material

The A36 material tested in this program was obtained from three plates of steel, each from a different heat. These plates were purchased to the 1973 AASHTO Class 2 CVN requirements for bridge steels as shown in Table 1. Two of the plates were 38.1 mm thick while the third was 50.8-mm thick.

Three locations were tested from each plate for a total of nine test locations. Details of the specific locations tested relative to the larger plates are shown in Fig. 4. The chemical compositions of the nine test locations are given in Table 2. Measured mechanical properties as well as mill reports are given in Table 3. Due to material size limitations, standard 12.7-mm round tension specimens were used for the tension tests rather than plate type specimens.

CVN Testing

Standard CVN tests were performed for each of the nine test locations. The CVN tests were performed in accordance with ASTM Standard for Notched Bar Impact Testing of Metallic Materials (E 23-72). Thirty specimens were prepared from each test location. All specimens had their notch normal to the plate rolling direction or in the L-T orientation as described in ASTM Test for Plane-Strain Fracture Toughness of Metallic Materials (E 399-78). All specimens were from the quarter thickness point of the plates. Five specimens were tested at the AASHTO specification temperature 4.4°C (39.9°F), three at −12.2°C (10°F), and three at 21.1°C (70°F). The remaining 19 specimens were tested to indicate the full CVN response of the plates.

Nil-Ductility Transition

Six nil-ductility transition (NDT) specimens, as per ASTM Method for Conducting Drop-Weight Test to Determine Nil-Ductility Transition Temperature of Ferritic Steels (E 208-69) were prepared from each of the nine

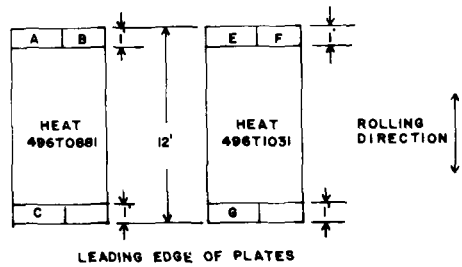

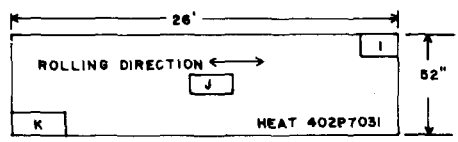

FIG. 4—*Approximate positions of test locations (1 in. = 25.4 mm).*

TABLE 2—*Chemical composition.*

Location	Heat Number	C	Mn	P	S	Si	Ni	Cr	Mo	V	Al	Ti	Cu	B
A	496T0881	0.11	1.04	0.004	0.026	<0.01	0.03	0.03	0.004	<0.002	<0.004	<0.004	0.03	<0.001
B	496T0881	0.21	1.03	0.003	0.024	<0.01	0.03	0.03	0.005	<0.002	0.005	<0.004	0.03	<0.001
C	496T0881	0.16	0.97	0.003	0.018	0.01	0.03	0.03	0.004	<0.002	0.010	<0.001	0.03	<0.001
E	491T1031	0.19	1.08	0.004	0.022	0.01	0.02	0.02	0.003	<0.002	0.005	<0.004	0.03	<0.001
F	491T1031	0.20	1.09	0.005	0.026	<0.01	0.02	0.02	0.003	<0.002	0.004	<0.004	0.03	<0.001
G	491T1031	0.23	1.13	0.004	0.032	<0.01	0.02	0.05	0.003	<0.002	0.004	<0.004	0.03	<0.001
I	402P7031	0.19	1.04	0.004	0.033	0.01	0.02	0.03	0.003	<0.002	0.052	<0.004	0.04	<0.001
J	402P7031	0.17	0.99	0.004	0.028	0.18	0.01	0.03	0.002	<0.002	0.064	<0.004	0.03	<0.001
K	402P7031	0.20	1.03	0.005	0.033	0.19	0.01	0.03	0.003	<0.002	0.052	<0.004	0.04	<0.00

TABLE 3—*Tensile properties.*

Test Location	Heat Number	Yield, ksi	Tensile Strength, ksi	Elongation Gage, %	Reduction of Area, %
A[a]	496T0881	33.1	62.1	2/38.6	65.7
B[a]	496T0881	33.1	62.2	2/38.7	64.8
C[a]	496T0881	30.5	57.5	2/39.7	69.8
E[a]	491T1031	34.1	61.5	2/38.9	67.9
F[a]	491T1031	33.6	62.1	2/38.2	67.4
G[a]	491T1031	33.8	66.0	2/37.2	65.9
I[a]	402P7031	34.6	62.6	2/36.3	64.8
J[a]	402P7031	34.5	62.6	2/36.7	65.9
K[a]	402P7031	34.6	62.6	2/36.3	65.3
X[b]	491T1031	40.8	68.5	8/28.5	...
Y[b]	496T0881	40.7	66.1	8/39.0	...
Z[b]	402P7031	44	70	2/34	...

Conversion Factor—1 ksi = 0.145 MPa.
[a] Average of two readings.
[b] Mill report data, average of two plate type specimens.

test locations. These were tested in accordance with ASTM E 208 requirements.

K_c *Fracture Toughness Testing*

Four 3-point bend fracture toughness specimens were prepared from each of the nine test locations (see Fig. 5). These specimens were 304.8 mm long, 76.2 mm high, and 38.1 mm thick. Each specimen contained a crack approximately 25.4 mm long which had been extended to its final length by means of low amplitude fatigue loading. All cracks were normal to the rolling direction of the plates or of the L-T variety as per ASTM E 399.

The fracture toughness specimens were all tested at an intermediate rate of loading so that a time to failure of about 1 s occurred. Two specimens were tested at the lowest ambient temperature corresponding to the Group 2 category, −34.4°C (−29.9°F). The remaining two specimens were tested at a temperature which corresponded to the 20 J CVN temperature level minus (−17.4°C) (0.75(215 − $1.5\sigma_y$)°F). Details of the K_c testing procedure have been described extensively elsewhere [*8,9*].

Experimental Results

CVN Results

The CVN response in terms of adsorbed energy, lateral expansion, and fracture appearance data for each test location are presented in Figs. 6 through 14.

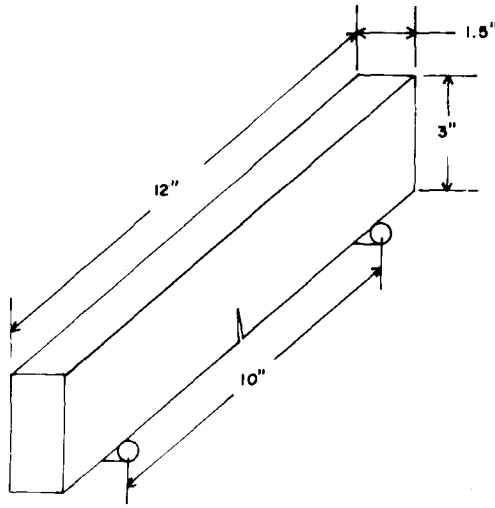

FIG. 5—*Three-point bend* K *specimens (1 in. = 25.4 mm).*

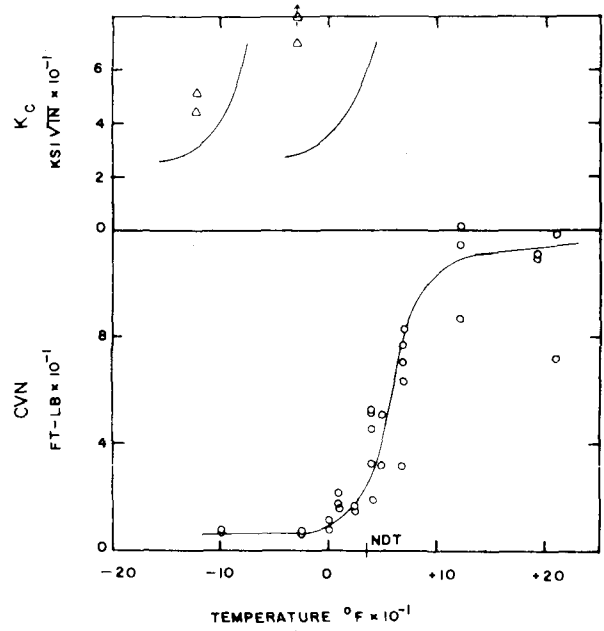

FIG. 6*a*—K_c *and CVN versus temperature—location A (1 ksi*$\sqrt{in.}$ *= 0.9 MPa*$\sqrt{m}$*, 1 ft·lb = 0.737 J, °C = (°F − 32)/1.8.*

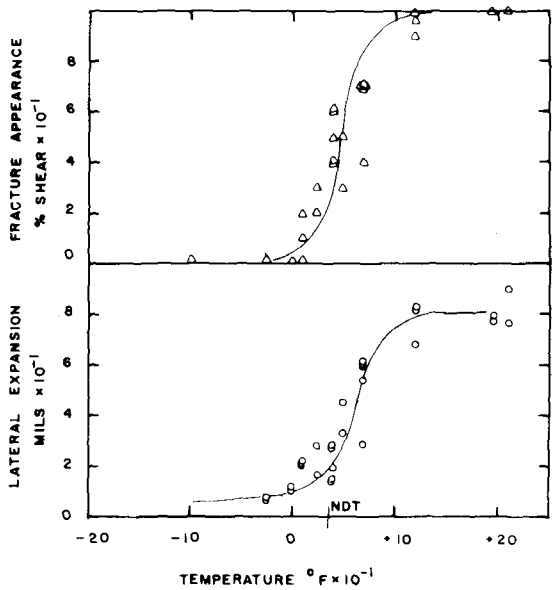

FIG. 6b—*Fracture appearance and lateral expansion versus temperature—location A (1 mil = 0.025 mm, °C = (°F − 32)/1.8).*

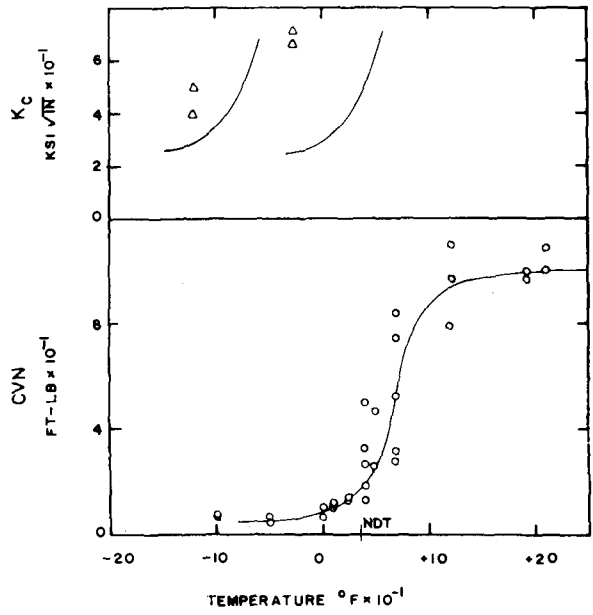

FIG. 7a—K_c *and CVN versus temperature—location B (1 ksi*$\sqrt{in.}$ *= 0.9 MPa*$\sqrt{m}$*, 1 ft · lb = 0.737 J, °C = (°F − 32)/1.8).*

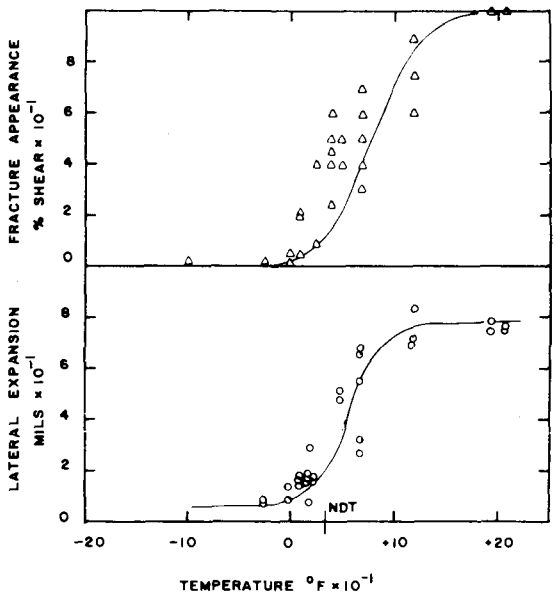

FIG. 7b—*Fracture appearance and lateral expansion versus temperature—location B (1 mil = 0.025 mm, °C = (°F − 32)/1.8).*

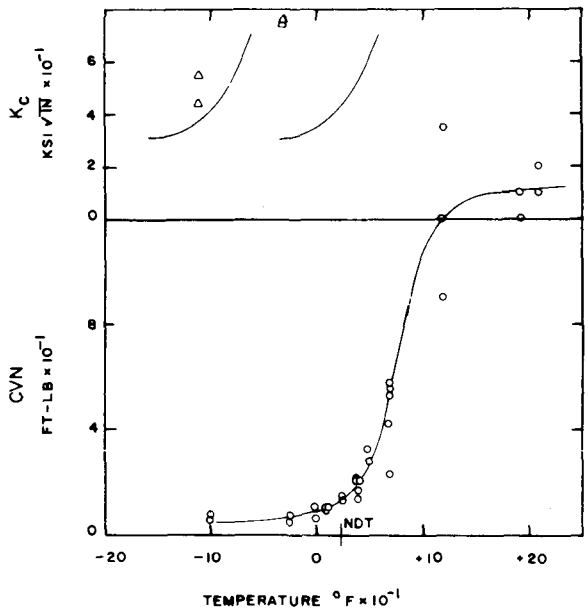

FIG. 8a—K_c *and CVN versus temperature—location C (1 ksi*$\sqrt{in.}$ *= 0.9 MPa*$\sqrt{m}$*, 1 ft·lb = 0.737 J, °C = (°F − 32)/1.8).*

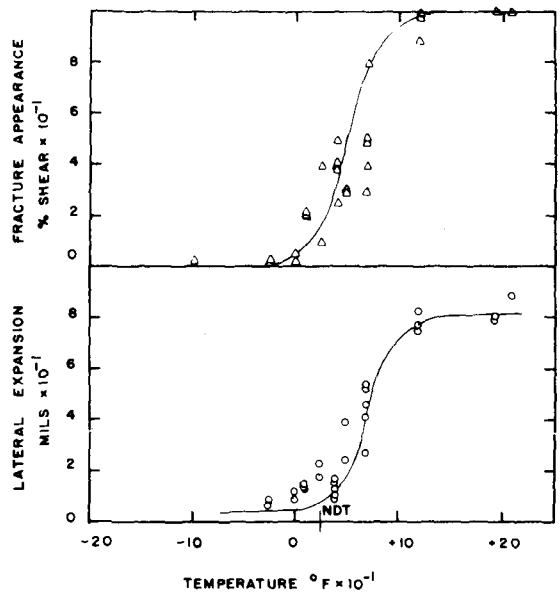

FIG. 8*b*—*Fracture appearance and lateral expansion versus temperature—location C (1 mil = 0.025 mm, °C = (°F − 32)/1.8).*

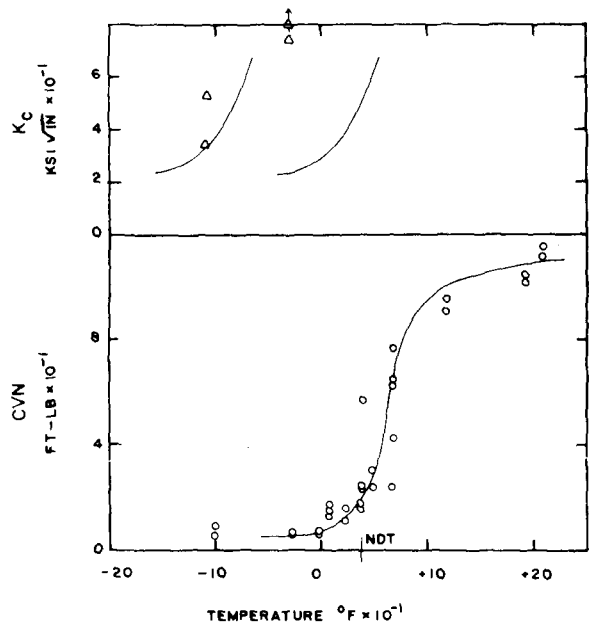

FIG. 9*a*—K_c *and CVN versus temperature—location E* (1 *ksi*$\sqrt{in.}$ = 0.9 *MPa*$\sqrt{m}$, 1 *ft·lb* = 0.737 *J*, °C = (°F − 32)/1.8).

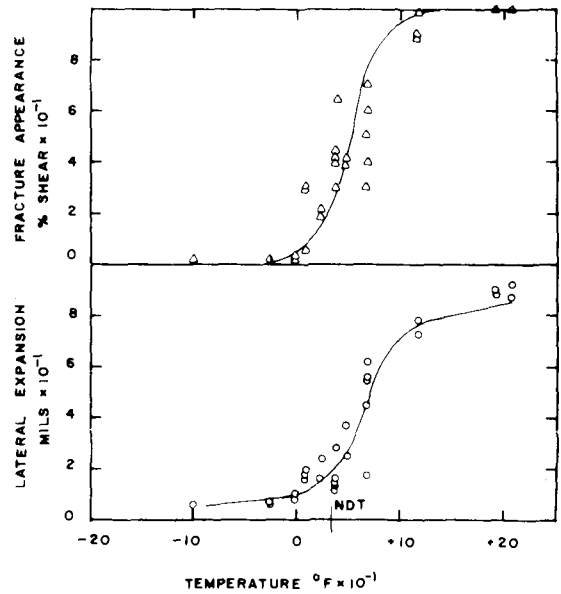

FIG. 9*b*—*Fracture appearance and lateral expansion versus temperature—location E (1 mil = 0.025 mm, °C = (°F − 32)/1.8).*

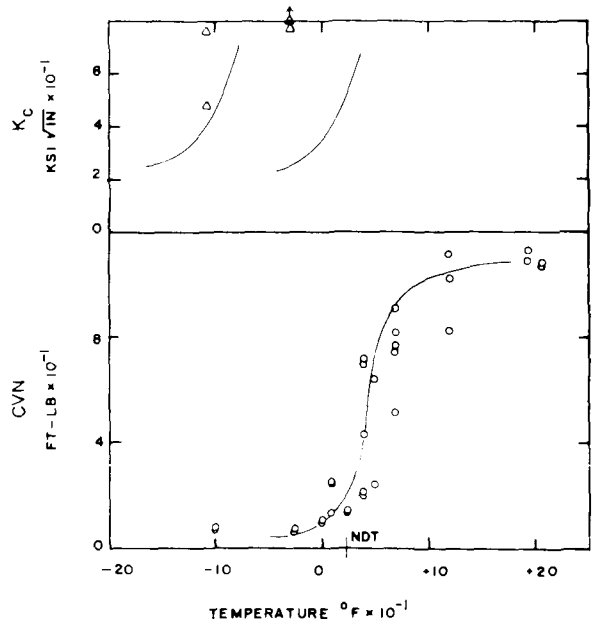

FIG. 10*a*—K_c *and CVN versus temperature—location F (1 ksi*$\sqrt{in.}$ *= 0.9 MPa*$\sqrt{m}$*, 1 ft·lb = 0.737 J, °C = (°F − 32)/1.8).*

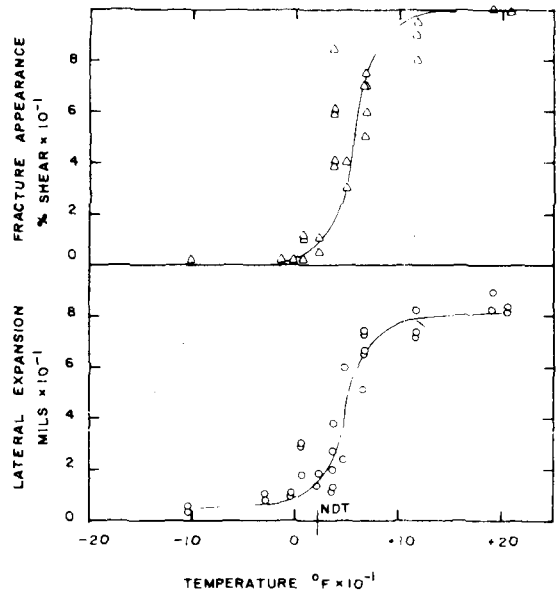

FIG. 10*b*—*Fracture appearance and lateral expansion versus temperature—location F (1 mil = 0.025 mm, °C = (°F − 32)/1.8).*

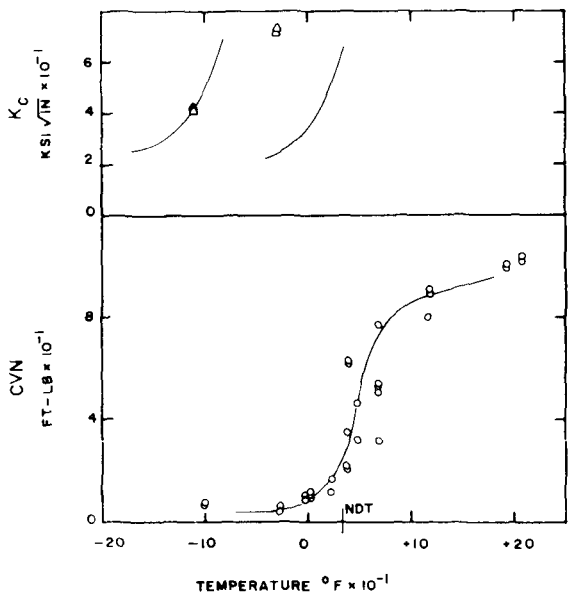

FIG. 11*a*—K_c *and CVN versus temperature—location G (1 ksi*$\sqrt{in.}$ *= 0.9 MPa*$\sqrt{m}$*, 1 ft·lb = 0.737 J, °C = (°F − 32)/1.8).*

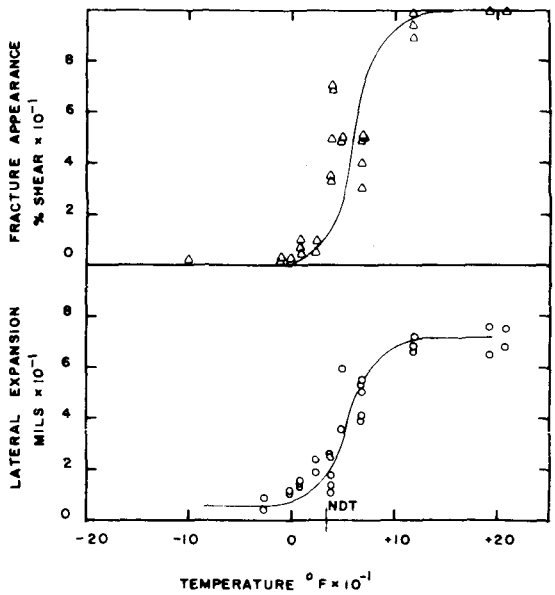

FIG. 11*b*—*Fracture appearance and lateral expansion versus temperature—location G (1 mil = 0.025 mm, °C = (°F − 32)/1.8).*

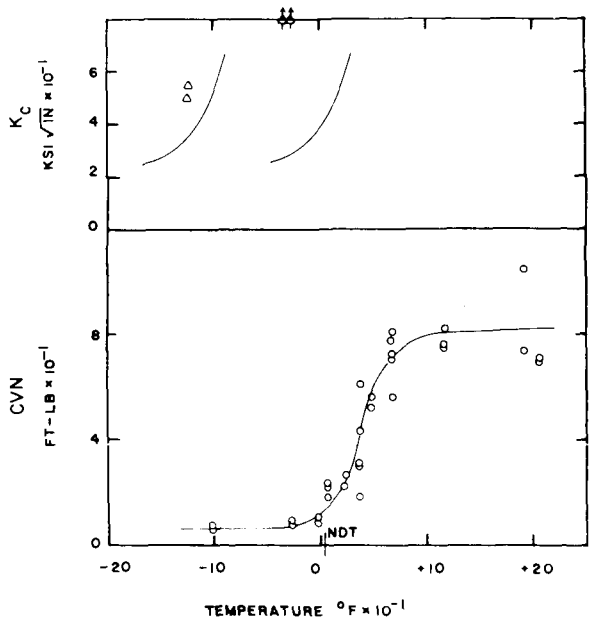

FIG. 12*a*—K_c *and CVN versus temperature—location I (1 ksi*$\sqrt{in.}$ *= 0.9 MPa*$\sqrt{m}$*, 1 ft·lb = 0.737 J, °C = (°F − 32)/1.8).*

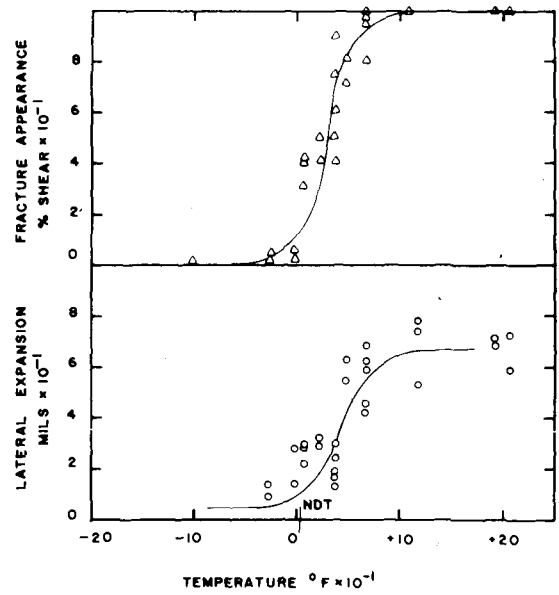

FIG. 12*b*—*Fracture appearance and lateral expansion versus temperature—location I (1 mil = 0.025 mm, °C = (°F − 32)/1.8).*

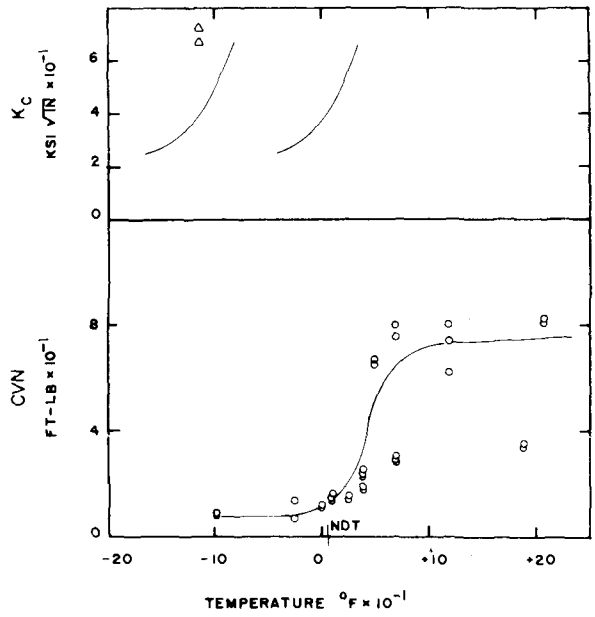

FIG. 13*a*—K_c *and CVN versus temperature—location J (1 ksi*$\sqrt{in.}$ *= 0.9 MPa*$\sqrt{m}$*, 1 ft·lb = 0.737 J, °C = (°F − 32)/1.8).*

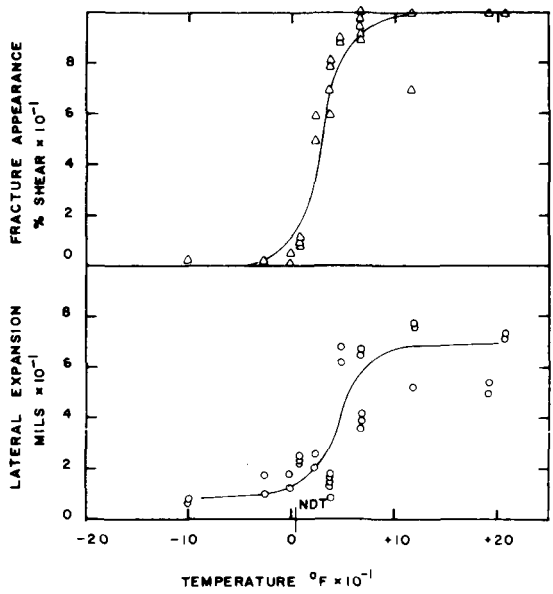

FIG. 13*b*—*Fracture appearance and lateral expansion versus temperature—location J (1 mil = 0.025 mm, °C = (°F − 32)/1.8).*

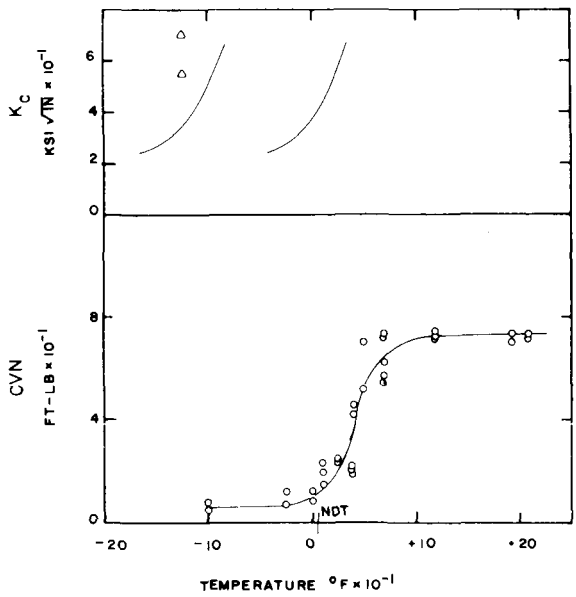

FIG. 14*a*—K_c *and CVN versus temperature—location K* (1 *ksi*$\sqrt{in.}$ = 0.9 *MPa*$\sqrt{m}$, 1 *ft·lb* = 0.737 *J*, °C = (°F − 32)/1.8).

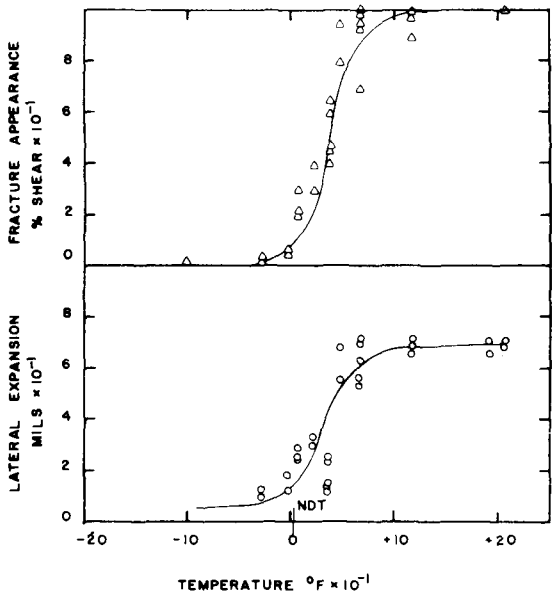

FIG. 14*b*—*Fracture appearance and lateral expansion versus temperature—location K* (*1 mil* = *0.025 mm*, °*C* = (°*F* − *32*)/*1.8*).

NDT Temperature Results

The results of the NDT tests are listed in Table 4 and are shown in Figs. 6 through 14.

K_c *Results*

The results of the individual K tests are presented in Table 5. The results were analyzed using the equation for K proposed by Wilson [*10*]. All values reported in Table 5 are for fracture toughness levels that reflect a plasticity correction and were computed with the formula [*10*]

$$K = \frac{PL}{(W - a')^{3/2}/B} \tag{2}$$

where

B = specimen width (38.1 mm),
W = specimen depth (76.2 mm),
P = maximum applied load,
L = span length (254 mm),
a' = effective crack length,

TABLE 4—*NDT test data.*

Material	−40	−20	0	+20	+40	+60	NDT, °F
A				x[a] x x	o[b] o o		+35
B				x x x	o o o		+35
C				x o o	o o		+25
E				x x o	o o o		+35
F				x o o	o o		+25
G				x o x	o o o		+35
I			x	o o o	o		+5
J		x	o x	o o	o		+5
K		x	o x	o o	o		+5

Conversion Factor—°C = (°F −32)/1.8.
[a] x indicates break.
[b] o indicates no break.

a = measured crack length,
r_y = plastic-zone size, and
$a' = a + r_y$.

The plastic zone size, r_y, was defined as

$$r_y = \frac{1}{2\pi}\left(\frac{K}{\sigma_y}\right)^2 \tag{3}$$

where σ_y is yield stress.

TABLE 5a—*Slow bend fracture toughness data.*

Temperature, °F	K_c (ksi$\sqrt{\text{in.}}$)								
	A	B	C	E	F	G	I	J	K
−30	71.0	67.4	76.1	82.5	83.1	75.0	93.5	[a]	[a]
	81.9	72.7	75.6	75.1	78.3	73.2	86.8		
−110			55.1	54.7	48.8	43.0			
			45.2	35.5	76.6	43.0			
−115								74.6	
								68.1	
−125	51.9	51.1					55.6		72.8
	45.2	40.7					39.5		57.2

Conversion Factor:
°C = (°F −32)/1.8
1 ksi$\sqrt{\text{in.}}$ = 0.9 MPa$\sqrt{\text{m}}$
[a] Iteration scheme for calculating K did not converge.

Equations 2 and 3 were solved by a simple interaction method [*8*]. The value of σ_y corresponded to the temperature and loading speed of the test conditions. This was determined by the following equation [*8*]

$$\sigma_{Yd} = \sigma_{Ys}|_{+75°F,t_o} + \frac{174\,000}{(T + 459)\log(2 \times 10^{10}t)} - 27.4 \qquad (4)$$

where

t = loading time to maximum load (second),
t_o = time of load application for a static test (50 s),
T = testing temperature (°F),
σ_{Ys} = yield stress (ksi), and
σ_{Yd} = yield stress adjusted for temperature and strain rate at test conditions (ksi).

Discussion of Results

Nominal Material

The results of the chemical analysis as shown in Table 2 for each test location meet the ASTM's compositional specifications set out for A36 material (see ASTM Standard for Structural Steel (A 36-77a)). The mechanical tests: yield strength, ultimate strength, and elongation as measured by the mill tests also meet the ASTM A 36 specification. However, the tension tests as run in this program fell short of the 248-MPa yield strength level. The data

TABLE 5*b*—*Fracture data.*

Test Location	A_i[a,b] (in.)	T[c] (°F)	P_{max}[d] (kips)	t[e] (sec)	K_c[f] (ksi$\sqrt{in.}$)
A	1.02	−30	31.0	1.6	71.0
A	1.07	−30	34.5	1.8	81.9
A	1.20	−125	19.5	1.3	51.9
A	1.01	−125	19.9	1.3	45.2
B	1.03	−30	29.2	1.6	67.4
B	1.05	−30	31.0	1.6	72.7
B	1.01	−125	22.5	1.3	51.1
B	1.02	−125	17.8	1.2	40.7
C	1.03	−30	33.0	1.5	76.1
C	1.08	−30	31.6	2.6	75.6
C	1.05	−110	23.5	1.5	55.1
C	1.03	−110	19.6	1.5	45.2
E	1.12	−30	33.2	1.3	82.5
E	1.04	−30	32.4	1.6	75.1
E	1.04	−110	23.5	1.5	54.7
E	1.02	−110	15.5	1.0	35.5
F	1.07	−30	35.0	1.9	83.1
F	1.04	−30	33.8	2.5	78.3
F	1.11	−110	19.8	1.3	48.8
F	1.06	−110	32.4	1.9	76.6
G	1.07	−30	31.6	1.3	75.0
G	1.05	−30	31.2	1.3	73.2
G	1.04	−110	18.5	0.9	43.0
G	1.02	−110	18.8	1.5	43.0
I	1.04	−30	40.2	2.5	93.5
I	1.67	−30	20.5	1.0	86.8
I	1.06	−125	23.6	1.7	55.6
I	1.08	−125	16.5	1.0	39.5
J	1.05	−30	40.0	2.0	[g]
J	1.05	−30	37.0	2.2	[g]
J	1.05	−115	31.8	1.9	74.6
J	1.25	−115	34.5	1.1	68.1
K	1.10	−30	40.0	2.0	[g]
K	1.10	−30	42.0	2.3	[g]
K	1.30	−125	25.0	1.1	72.8
K	1.02	−125	25.0	1.2	57.2

Conversion Factor:
1 in. = 25.4 mm
°C = (°F − 32)/1.8
1 kip = 224 N
1 ksi$\sqrt{in.}$ = 0.9 MPa$\sqrt{m}$

[a] Initial crack length—average of three readings as per ASTM E 399-78.
[b] Test temperature.
[c] Fracture load.
[d] Time to attain fracture load.
[e] K_c calculated as per Eq 2 of text.
[f] Fracture surface of all specimens showed absolutely no evidence of shear lips.
[g] Iteration scheme for calculating K did not converge.

reported in Table 3 for each location are the average of two 12.7-mm round tensile tests conforming to specimen Type 1 of Fig. 6 of ASTM Methods and Definitions for Mechanical Testing of Steel Products (A 370-77). The ultimate strength, percent elongation for a 50.4-mm gage length and reduction of area all meet the ASTM A 36 requirements. The 19.2 MPa difference between the minimum standard for A36 material and the values measured with the 12.7-mm round specimens is not felt to be of significance in relationship to the overall objectives of the project since all other areas of material performance were satisfactory. While various reasons for the differences between mill reported and current measured values of the tensile properties were carefully examined, no satisfactory explanation was uncovered.

CVN Results

The general results of the CVN tests as illustrated in Fig. 6 through 14 do not show any outwardly surprising results. All test locations exhibited the normal upper and lower shelf behavior with a definite temperature transition region. The results from locations A, B, and C, which came from heat 496T0881, show more dispersion than do the results from the other two heats of steel when comparing the CVN test results from location to location. Test locations E, F, and G show reasonable agreement while locations I, J, and K show very close agreement in overall CVN response. Heats 496T0881 and 491T1031 generally showed higher transition temperatures and higher upper shelf behavior than heat 402P7031.

The observation that for an A36 type material the NDT corresponds to approximately the 20 J temperature [*11*] is well-founded based on the current data. Table 6 highlights this. For a given heat of steel, the NDT showed no more than a 12.2°C (10°F) variation between test locations while the 20 J level showed a maximum difference of 9.4°C (48.9°F) for heat 491T1031. The maximum difference between the NDT and the 20 J temperature was 8.3°C (46.9°F) and occurred for Location G.

The five CVN tests that were run at the specification temperature of 4.4°C (39.9°F) are set out in Table 6 as a means of convenient comparison. It is obvious from this table that all test locations met the 20 J requirement at 4.4°C (39.9°F). Also, if the worst three CVN tests out of the five run had occurred first (that is, 14.9, 23.0 and 33.9 J for test location B), the results of these three tests would still have passed the 20 J average at 4.4°C (39.9°F). There is a fair amount of scatter in the average levels for the five 4.4°C (39.9°F) CVN tests within a specific heat. This is to be expected as this test temperature is in the transition region for the material.

Based on the above observations about the CVN results, the question of the suitability of "H" testing to establish the fracture response of each piece of steel from a 45-Mg piece of steel can be considered. The best way to do this for the current data is to carefully examine the 20 J temperatures for a

TABLE 6—*NDT, T_{15} and 40°F CVN data summary.*

Test Location	Energy Absorbed, ft·lb								
	A	B	C	E	F	G	I	J	K
	31.0	11.0	12.5	57.5	60.0	20.0	28.0	16.5	19.0
	50.0	49.0	20.0	17.5	20.0	52.0	30.0	21.0	21.0
	52.0	25.0	20.0	22.5	60.0	52.0	17.0	11.5	46.0
	16.8	17.5	16.0	23.5	42.0	35.0	42.0	22.5	20.0
	44.0	31.5	20.0	15.0	18.5	20.5	60.0	22.5	42.0
Average Energy Absorbed	38.7	26.8	17.7	27.2	40.1	35.9	35.4	20.0	29.6
NDT (°F)	35	35	25	35	25	35	5	5	5
T_{15}[a] (°F)	22	32	32	35	18	20	10	10	12

Conversion Factor:
1 ft·lb = 0.737 J
°C = (°F −32)/1.8
[a] 15 ft·lb CVN temperature.

given heat. First, suppose that the lowest observed 20 J temperature was the actual specification temperature. For heat 491T1031, test Locations E, F, and G, this would mean the imaginary specification temperature would be −7.8°C (18°F) corresponding to location F. If this was the case, test locations E and G would not meet the specifications. In terms of the 20 J temperature, test location E would miss by 9.4°C (48.9°F). For the other two heats, the temperature difference would not be as great, 5.6°C (42.1°F) for heat 496T0881 and 1.1°C (34°F) for heat 402P7031.

The preceding thoughts and the data considered indicate for materials similar to the A36 material tested in this program that if a heat of steel is tested according to an "H" testing frequency and if the chosen test location nominally meets the 20 J requirement then there is a possibility that other areas of the heat of steel tested may not meet the specification. This is not surprising when one considers the statistical value of any material property. The exact difference is not evident from the limited data of this research. It certainly can be at least 9.4°C (48.9°F) as shown by the 20 J temperature difference for heat 491T1031. The question of whether or not such behavior is acceptable within the philosophy and intent of the AASHTO CVN requirements is quite important.

In the original deliberations, which resulted in the 1973 AASHTO specification, it was decided that a suitable minimum operation temperature for a given strain rate would be 27.8°C (82°F) above the point where K/σ_{ys} is about 0.9. This plus conservatism in Eq 5 (see in next section) was felt to cover the variability that can be encountered in a 45-Mg piece of steel. The current CVN data when compared with the K data that follows does not provide any basis for disagreement with this philosophy. However, where it is desirable to know the fracture properties within closer tolerances, such as in fracture critical members, it certainly is reasonable to test each piece rather than rely on an "H" testing frequency.

K *Results*

The results of the intermediate or 1-s K tests are listed in Table 5 and shown in Figs. 6, 8, 10, 12, and 14. Along with these data are shown the trend line or curve based on the measured CVN data for the test location and the relationship proposed by Barsom [2]

$$K_c = \sqrt{5E\text{CVN}} \tag{5}$$

where

K_c = stress intensity level in psi$\sqrt{\text{in.}}$ corresponding to K_{Ic} for slow bend CVN results and K_{Id} for standard impact CVN results,
E = Young's modulus in pounds per square inch,
CVN = Charpy energy in foot-pounds.

The trend curve shown on the right is the predicted dynamic K_{Id} response based on the CVN data and Eq 5. The trend curve to the left is the result of shifting the dynamic trend curve by 0.75 T_s as previously discussed in the introduction.

The K data, which was obtained at test temperatures equal to the 20 J temperature minus 0.75(215 − 1.5σ_y), all show reasonable agreement with the intermediate trend line. In all cases the prediction by Eq 5 is conservative. Also the phenomenon of K suppression discussed by Barsom et al [*12*] is evident in all K tests at −34.4°C (−29.9°F). For this temperature the specimen thickness did not meet the size requirements of ASTM E 399. The K tests at the lower temperatures did meet the specimen requirements for valid K_{Ic} measurements. The phenomenon of a K suppression is highlighted in Fig. 15 after Barsom et al [*12*].

In general the K data at −34.4°C (−29.9°F) all exhibited nonplane-strain type behavior only in terms of specimen size requirement. At the lower temperature the results did meet the size requirements for valid K_{Ic} measurements. Also the levels of fracture toughness observed are consistent with the concept of a temperature shift and also with proposed techniques for predicting K levels based on CVN information.

Conclusions

With the foregoing in mind it is now possible to reflect on the data collected and draw a few modest conclusions. These are:

1. The temperature shift, T_s, appears real as reflected through the use of 0.75 T_s to predict intermediate rate behavior.

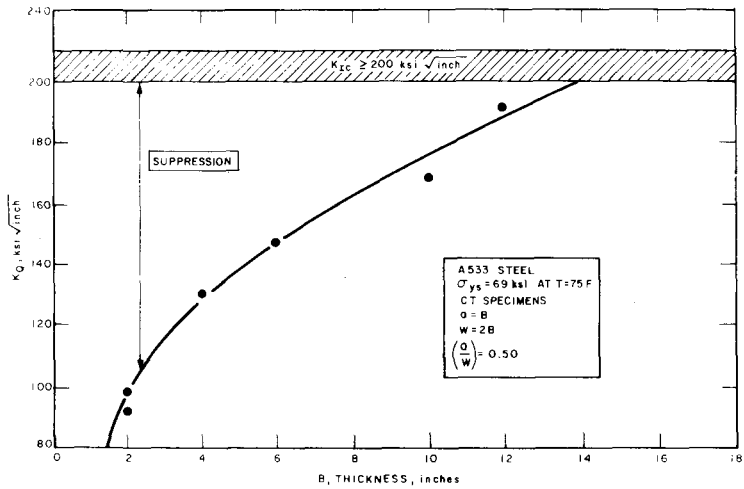

FIG. 15—*Effect of suppression on* K_{Ic} *for proportional specimens of A533 steel taken from Ref* 12 (*1 ksi*$\sqrt{in.}$ *= 0.9 MPa*$\sqrt{m}$, *1 in. = 25.4 mm*).

2. The use of Eq 5 gives conservative results for the data collected.

3. The use of an "H" testing frequency for fracture critical members of A36 material may not prove adequate where detailed knowledge of the fracture properties of each piece are desired.

References

[1] Frank, K. H. and Galambos, C. F., "Application of Fracture Mechanics to Analysis of Bridge Structures," *Proceedings,* Specialty Conference on Safety and Reliability of Metal Structures, American Society of Civil Engineers, Nov. 1972, pp. 279-306.

[2] Barsom, J. M., *Engineering Fracture Mechanics,* Vol. 7, No. 3, Sept. 1975, pp. 605-618.

[3] Highway Accident Report, "Collapse of U.S. 35 Highway Bridge, Point Pleasant, West Virginia, December 15, 1967," Report NTSB-HAR-71-1, National Transportation Safety Board, 1971.

[4] *Engineering News Record,* 20 Aug. 1970.

[5] *Engineering News Record,* 7 Jan. 1971.

[6] Highway Research Board of the NAS-NRC Division of Engineering and Industrial Research, "The AASHO Road Test," Report 4, Bridge Research, Special Report CID, Publication No. 953, 1962.

[7] Barsom, J. M., "Toughness Criteria for Bridge Steels," Technical Report No. 5 for American Iron and Steel Institute Project 168, 8 Feb. 1973.

[8] Roberts, R., Irwin, G., Krishna, G., and Yen, B., "Fracture Toughness of Bridge Steels—Phase II Report," Report No. FHWA-RD-74-59, Sept. 1974, prepared for Federal Highway Administration, Office of Research and Development, Washington, D.C. 20590.

[9] Madison, R. B., "Application of Fracture Mechanics to Bridges," Ph.D. dissertation, Lehigh University, 1969.

[10] Wilson, W. K., *Engineering Fracture Mechanics,* Vol. 2, No. 2, 1970, pp. 169-171.

[11] Irwin, G. R. and Roberts, R., "Fracture Toughness of Bridge Steels—Phase I Report," Fritz Engineering Laboratory Report, July 1972.

[12] Barsom, J. M., Sovak, J. F., and Novak, S. R., "Fracture Toughness of A36 Steel," Technical Report No. 1 for American Iron and Steel Institute Project 168, May 1, 1972.

[13] "The Variation of Product Analysis and Tensile Properties—Carbon Steel Plates and Wide Flange Shapes," American Iron and Steel Institute, Washington, D.C., Sept. 1974.